A BIORESPONSIVE POLYMERIC IMPLANT FOR SITE-SPECIFIC PROLONGED DRUG DELIVERY

by

LISA CLAIRE DU TOIT

A Thesis submitted to the Faculty of Health Sciences, University of the Witwatersrand, in fulfillment of the requirements for the degree of Doctor of Philosophy

Supervisor:
Professor Viness Pillay
Department of Pharmacy and Pharmacology, Faculty of Health Sciences, University of the Witwatersrand, South Africa

Co-Supervisors:
Professor Trevor Carmichael
Department of Neurosciences, Division: Ophthalmology, Faculty of Health Sciences, University of the Witwatersrand

Professor Thirumala Govender
Department of Pharmaceutics, School of Pharmacy and Pharmacology, University of KwaZulu-Natal, South Africa

Johannesburg, 2013

DECLARATION

I, Lisa Claire du Toit, declare that this thesis is my own work. It has being submitted for the degree of Doctor of Philosophy in the Faculty of Health Sciences in the University of the Witwatersrand, Johannesburg. It has not been submitted before for any degree or examination at this or any other University.

……

This …….. day of …….. 2013

RESEARCH OUTPUTS

Research Publications related to Doctoral Research (refer to Appendix, Section 9.2)

1. Lisa C. du Toit, Thirumala Govender, Viness Pillay, Yahya E. Choonara, Tetsuya Kodama. Investigating the Effect of Polymeric Approaches on Circulation Time and Physical Properties of Nanobubbles. *Pharm Res*, 2011, 28:494-504 *[Research Article]. Accreditation: ISI; IF: 4.742.*

2. Lisa C du Toit, Viness Pillay, Yahya E Choonara, Thirumala Govender, Trevor Carmichael. Ocular drug delivery - a look towards nanobioadhesives. *Expert Opin Drug Deliv*, 2011, 8:1 *[Review]. Accreditation: ISI; IF: 4.869.*

3. Lisa C. du Toit, Thirumala Govender, Trevor Carmichael, Pradeep Kumar, Yahya E. Choonara, and Viness Pillay. Design of an Anti-Inflammatory Composite Nanosystem and Evaluation of its Potential for Ocular Drug Delivery. *J Pharm Sci*, 2013, 102(8):2780-2805 *[Research Article]. Accreditation: ISI; IF: 3.13.*

4. Lisa C. du Toit, Trevor Carmichael, Thirumala Govender, Pradeep Kumar, Yahya E. Choonara and Viness Pillay. *In Vitro, In Vivo,* and *In Silico* Evaluation of the Bioresponsive Behavior of an Intelligent Intraocular Implant. *Pharm Res,* 2013, Available online 4 September 2013, DOI: 10.1007/s11095-013-1184-3 *[Research Article]*. *Accreditation: ISI; IF: 4.742.*

Additional Research Publications generated during Doctoral Research (refer to Appendix, Section 9.2

1. Lisa C. du Toit, Viness Pillay, Yahya E. Choonara. Nano-microbicides: Challenges in drug delivery, patient ethics and intellectual property in the war against HIV/AIDS. *Adv Drug Deliv Rev*, 2010, 62:532-546 *[Review]*. *Accreditation: ISI; IF: 12.888.*

Research Outputs at Conference Proceedings

1. Lisa C. du Toit, Viness Pillay, Thirumala Govender, Trevor R. Carmichael and Yahya E. Choonara. An Intelligent Intraocular Implant: Conceptualization and Identification of Design Parameters. ***(Poster Presentation).*** *Annual Meeting of the American Association of*

Pharmaceutical Scientists, Los Angeles Convention Center, Los Angeles, California, United States of America, November 08 - 12, 2009.

2. Lisa C, du Toit, Thirumala Govender, Viness Pillay, Yahya E. Choonara, Tetsuya Kodama. Novel polymeric approaches in the enhancement of nanobubble lifetime. (***Podium Presentation).*** *Cross-Faculty Postgraduate Symposium*, University of the Witwatersrand, Johannesburg, South Africa, October 25-29, 2010.

3. Lisa C. du Toit, Viness Pillay, Trevor Carmichael, Thirumala Govender, and Yahya E. Choonara. Conceptualisation and Experimental Optimisation of an Intelligent Intraocular Implant for Exemplification of the Bioresponsive Potential. ***(Podium Presentation)***. *6th International Conference on Pharmaceutical and Pharmacological Sciences*, Durban, South Africa, 25-27 September 2011.

4. Lisa C. du Toit, Viness Pillay, Thirumala Govender, Trevor Carmichael, Yahya E. Choonara. *In Vivo* Verification of the Bioresponsive Potential of an Intelligent Intraocular Implant. ***(Poster Presentation).*** *Association for Research in Vision and Ophthalmology (ARVO) Annual Meeting 2012*, Fort Lauderdale Florida, USA, 6-10 May 2012 ***(*Winner of ARVO International Travel Grant, 2012***).

Patents Filed

1. An Intelligent Inflammation-Responsive Multipolymeric Implantable System, Lisa C. du Toit, Viness Pillay, Yahya E. Choonara, Thirumala Govender and Trevor R. Carmichael. SA Patent Application Number 2010/03748, 12 October 2010. PCT filed.

ABSTRACT

Effective treatment of ocular diseases presents a formidable task, dually attributed to their nature, and the presence of the ocular barriers. This was exemplified in the presented review of developments in ocular drug delivery systems. Conceptualization of novel polymeric systems with intelligent (e.g. stimulus-responsive) mechanisms and advances in nanotechnology are at the forefront of achieving directed and controlled delivery for treating vision-threatening diseases. It was thus the pertinent goal of this investigation to assimilate these observations in the design of an intelligent ocular drug delivery system. The design of an autofeedback polymeric platform, employing biodegradable polymers is exemplified through the implementation of two-way communication systems between our bodies and the delivery platform to create innovative drug delivery systems that recognize a biochemical process that is characteristic of a disease, and then responding via drug release. To achieve this intelligence in design, the delivery platform was based on novel stimulus-responsive polymeric materials. The concept of an autofeedback polymeric platform was intrinsically implemented in the design of an intelligent intraocular implant - called the I^3 - employing inflammation-responsive polymers, having application as a smart release system capable of delivering controlled therapeutic levels of anti-inflammatory and/or antibiotic drug/s for posterior segment disorders of the eye in response to inflammation and infection. Inner and outer bioresponsive polymeric matrices (BPMs) were designed that released the incorporated anti-inflammatory and antibiotic in a fashion responsive to a stimulus, such as the highly reactive intermediates including hydroxyl radicals ($OH^{\cdot}$) that are released from activated leukocytes both *in vitro* and during acute and chronic intraocular inflammatory reactions *in vivo* (Hawkins and Davies, 1996).

The first step in developing the intelligent device implicated design of an anti-inflammatory nanosystem (NS) with satisfactory size and surface properties, adequate permeation potential, uptake by inflamed cells, low cellular toxicity, and enhanced anti-inflammatory effect availed to the incorporated drug. A composite lipoidal-polymeric NS was developed (Lipo-Chit-PCL NS) and compared to a purely polymeric NS. The NS was ultimately enclatherated as a NS-polymer superlattice, forming the inner BPM of the I^3. The designed composite lipoidal-polymeric NS attested its significant potential for selective drug delivery to inflamed tissues, demonstrating significantly enhanced tissue permeation, cell uptake, and anti-inflammatory activity compared to an indomethacin suspension. Subsequent molecular modeling revealed that the composite NS displayed an enhanced lipophilicity and superior cellular internalization efficiency. The preferred NS was subsequently selected for optimization via a Plackett-Burman Statistical Design Method.

Design of the NS was proceeded by development and optimization of the inner and outer BPMs, being the stimulus-responsive component of the device, via implementation of a novel methodology for simultaneous design of the two intimately crosslinked matrices. Inflammation-responsive polymers such as hyaluronic acid, alginate, poly(acrylic) acid, and chitosan, were ultimately selected for design of the I^3drug delivery system. Intensive device optimization was then undertaken, first employing a Response Surface Methodology, embodied by the Box-Behnken Design, ensued by Artificial Neural Networks. Characterization of the drug release kinetics from the optimized I^3 is pivotally provided, as well as molecular modeling. The reagent (*N*-hydroxysuccimide, NHS) and catalyst employed (aluminium chloride, $AlCl_3$) had a significant or notable effect on the mean dissolution time of indomethacin under normal and pathological conditions, respectively ($p=0.048$; $p=0.058$). The interaction between the inflammation-responsive hyaluronic acid and carbodiimide crosslinker emanated in a significant effect on the change in mean dissolution time of indomethacin from normal to inflammatory conditions ($p=0.050$). Subsequent execution of ANN with further training of the data confirmed the adequacy of the design. Analysis of the drug release kinetics from the optimum I^3 under both normal and pathological conditions was in coherence with the anticipated behavior of an inherently bioresponsive device. Molecular simulations generated provided clear evidence for the catalytic effect of the hydroxyl radicals, specifically in hyaluronic acid hydrolysis.

It was imperative to elucidate the intricate *modus operandi* of the optimized I^3. The intricately crosslinked polymeric system comprising the I^3 responds at an innate level predicted by its molecular make-up to inflammatory conditions as indicated by the results of the rheological analysis, MRI and SEM imaging. FTIR explicated the formation of pivotal intra- and intermolecular bonds within and between the inflammation-responsive polymers of the I^3, while TMDSC confirmed the extent to which the composite polymeric system had altered from its native consituents to form a device of the desired functionality. Tensile analysis provided an indication of the overall mechanical performance of the implant. The porosity ascertained for both the inner and outer BPMs was a predictor of the overall internal architecture and potential drug release characteristics of the BPMs comprising the I^3, as were critical morphological changes, visualized via SEM and interpreted via image analysis displayed during device erosion. Furthermore, molecular mechanics simulations were carried out to model the interaction between the polymeric components of the inner and outer BPM and confirmed the formation of a 'secure-fit' dual polymeric matrix system by highlighting the anticipated interconnectivity between the inner and outer BPM of the I^3.

The *in vivo* performance of the device was assessed to further provide a convincing argument as to the ocular suitability and overall contrasting performance under normal and inflammatory conditions. Histological assessment was key to predicting significant inflammatory changes, as well as reductions in inflammation initiated by the I^3. Analysis of ocular drug levels under normal and inflammatory conditions was undertaken for correlation with *in vitro* results, for ultimate establishment of an *in-vitro-in-vivo* correlation (IVIVC). The device was well-tolerated following implantation in the rabbit eye. Investigations of drug concentrations attained and device erosion were a good indication that the I^3 expresses bioresponsive capabilities *in vivo.* There was enhanced release of both drugs in the inflamed rabbit eye even after 7 days (the maximum period in which the induced inflammation was permitted to ensue), with indomethacin levels of 0.749±0.126µg/mL and 1.168±0.186µg/mL, and ciprofloxacin levels of 1.181±0.150µg/mL and 6.653±0.605µg/mL being attained in the normal and inflamed eye, respectively. At 28 days in the normal eye, concentrations of indomethacin detected were only 0.564±0.111µg/mL and those of ciprofloxacin were 1.226±0.209µg/mL. Furthermore, the enhanced erosion of the I^3 in the inflamed eye is also exemplified, with the I^3 eroding 1.504±0.505% in the normal eye and 22.609±2.421% in the inflamed eye after 7 days; and only reaching 13.830±1.010% erosion after 28 days in the normal rabbit eye. Elaboration of the IVIVC undertaken for both indomethacin and ciprofloxacin approached or attained a Level A correlation, respectively, and provided further evidence for the feasibility of the I^3 and for advancement of this concept toward application in a clinical setting. Establishment of such a correlation for the inflamed rabbit eye would be the main consideration in prospective investigations.

ACKNOWLEDGEMENTS

In completing this work, I would like to express my deepest gratitude to all who have gone over-and-above in providing their unwaivering guidance and support towards the completion of this study. I would like to acknowledge the following people for their great contribution:

- Foremost to my most amazing family: my parents, Martin and Terry du Toit; my sister, Megan du Toit; and nephew, Liam du Toit; for their endearing love and support, and for lifting my spirits when times were tough. It is beyond comprehension how truly blessed I am to have had the endearing support of my family during this time.
- To my partner, Angelo Lee Shong, thank you for coming into my life, always encouraging me and having faith in me.
- To my supervisor, Prof. Viness Pillay, without whom none of this would be possible. Prof. Pillay has been a true inspiration and mentor, not only in guiding my research, but in providing direction and life lessons, which have been pivotal in forging my career path. Furthermore, I will always be grateful for his true compassion during this quest.
- To my co-supervisor, Prof. Trevor Carmichael, whose commitment, guidance and assistance, particularly with the animal studies was greatly appreciated. Thank you for all the interesting discussions, both here in South Africa and abroad!
- To my co-supervisor, Prof. Thirumala Govender, whose expertise and kindness were both unfailing. I am truly grateful for the motivation and support.
- To Dr. Aubrey Makgotloe, I could not have done without your assistance during the animal surgeries. Thank you so much for your help.
- To Mr. Pradeep Kumar whose expertise and unwaivering assistance with the molecular modeling component of this study was greatly appreciated.
- To my dear friends in the Department of Pharmacy: Deanne Johnston, Shirona Naidoo, Nurit Esperance Dahan-Farkas, and Angeliki Stephanou, the supportive chats and endearing company were irreplaceable. Thank you all so much for everything!
- To the students and staff of the Department of Pharmacy and Pharmacology, University of the Witwatersrand: their contributions, great and small, have aided me in numerous ways.
- This research would also not have been possible without the financial assistance of the National Research Foundation (NRF) of South Africa, their support is sincerely appreciated.
- To the Almighty Father, without Whom none of this would be possible.

DEDICATION

This work is dedicated to my nephew, Liam Matthew du Toit, who is growing to be such a handsome young man.

TABLE OF CONTENTS

LIST OF FIGURES

LIST OF TABLES

LIST OF COMMONLY-USED ABBREVIATIONS

ALG - alginate
BAB - blood-aqueous barrier
BPMs - bioresponsive polymeric matrices
BRB - blood-retinal barrier
Chit-PCL NS - chitosan-poly(*ε*-caprolactone) nanosystem
CMV - cytomegalovirus
COX - cyclooxygenase
DCC - *N*,*N*′-dicyclohexylcarbodiimide
DIE - Drug incorporation efficiency
DSPC - distearoylphosphatidylcholine
DSPE - distearoylphosphatidylethanolamine
EIU - endotoxin-induced uveitis
ELISA - enzyme-linked immunosorbent assay
FTIR - Fourier-transform infrared spectroscopy
HA - hyaluronic acid
I^3 - Intelligent Intraocular Implant
Lipo-Chit-PCL NS - Lipoidal-chitosan-poly(*ε*-caprolactone) nanosystem
LPS - lipopolysaccharide
MMER - Molecular Mechanics Energy Relationships
MMW - medium molecular weight
MRI - magnetic resonance imaging
NBD-Cl - 4-chloro-7-nitrobenzo-2-oxa-1,3-diazole)
NFκB - Nuclear factor kappa-light-chain-enhancer of activated B cells
NHS - *N*-hydroxysuccimide
NPs - nanoparticles
NS - nanosystem/s
NSAIDs - nonsteroidal anti-inflammatory drugs
$OH^{\cdot}$ - hydroxyl radicals
PAA - crosslinked poly(acrylic) acid
PBS - phosphate-buffered saline
PCL - poly(*ε*-caprolactone)
PLGA - copolymers of lactic and glycolic acids
PMNs - polymorphonuclear leukocytes
RCS - retinal pigment epithelium-choroid-sclera
RPE - retinal pigment epithelium

SD – standard deviation

SEM - scanning electron microscopy/ micrograph

SVH - simulated vitreous humor

TEM - transmission electron microscopy/ micrograph

WAC - water absorption capacity

CHAPTER 1

INTRODUCTION

'The eye is the jewel of the body.'

Henry David Thoreau *(1817-1862)*
American naturalist, poet and philosopher

1.1. The Eye

The eye - an anatomically isolated specialized sensory organ - exhibits unique pharmacodynamic and pharmacokinetic properties, and is a prime site for practically investigating drug delivery system implantation. This is a consequence of its seclusion from systemic access by the blood-retinal, blood-aqueous, and blood-vitreous barriers. The eye is divided into two cavities (the anterior and posterior segment) in which ocular fluids circulate, creating a wide space of implantation. Furthermore, the surface of tissues to be targeted is large despite their associated small volume. It also benefits from an 'immune privilege', mainly evident in the anterior chamber and in the sub-retinal space; reducing the risk for exaggerated inflammatory reactions to foreign antigens and cell graft rejection. The visual functions of the eye are, however, exceptionally delicate, and more complex means of drug targeting are required. Significantly, the eye can be viewed as an apt 'laboratory' for the investigation of drug delivery in inflammatory and infectious afflictions. According to Robinson (1993) 'no other organ is so readily accessible or as visible for observation'; undoubtedly a distinct test for the pharmaceutical scientist in drug delivery system design. Successful drug delivery is thus considered the limiting factor for an optimal therapeutic strategy (Henderer and Rapuano, 2011).

1.2. Rationalization of an Innovative Drug Delivery System

1.2.1. Problem identification - Selection of a drug delivery system

Embodied in this research is the need to bridge the gap between the indispensable drug therapies that are available and their safe and effective transfer to practice through the pragmatic design of effective drug delivery systems. In terms of research spurring the pharmaceutical scientist, ophthalmic drug delivery is an increasingly demanding sector (Nanjawade et al., 2007). In their investigations, authors have pointed to inflammatory posterior segment ocular (vitreoretinal) disorders as the foremost contributors to visual impairment, and ultimately blindness (Herrero-Vanrell and Refojo, 2001; Del Amo and Urtti, 2008). Ensuring delivery of the indicated bioactive to the posterior segment of the eye (which includes the

vitreous humor, retina, choroid and optic nerve) is fundamental for the effectual treatment of internal eye structure disorders (Del Amo and Urtti, 2008). Nonetheless anterior segment drug delivery systems, most notably eye drops, still lead trends in the ocular market. When it comes to the disorders perpetuating visual impairment and even blindness, inflammatory disorders of the posterior segment are the ultimate perpetrators (Del Amo and Urtti, 2008).

As emphasized by Yasukawa and co-workers (2005), progress in the field of ocular drug delivery is delayed when problems of drug availability to the posterior segment are encountered; furthermore indirect bioactive pathways (topical, systemic, or periocular) to the vitreous suffer from the disadvantage of poor penetration of the biophysiological blood-ocular barriers, necessitating direct intravitreal drug delivery for successful management of posterior segment disorders (Haesslein et al., 2006). Intravitreal injection of drug, and sustained drug delivery systems fabricated from polymers (biodegradable or non-biodegradable) for delivery via injection or implantation, target the posterior segment (Herrero-Vanrell and Refojo, 2001; Haesslein, et al., 2006). Implementation of a sustained drug delivery strategy is preferred to repeated injections (Herrero-Vanrell and Refojo, 2001).

The field of ocular therapeutics is at the stage where appropriate active compounds for the treatment of posterior segment disorders are available; but in order to render the pharmaceutical intervention a success, intraocular controlled drug delivery systems are essential. Sustained and controlled release of the drug can be fulfilled through the use of polymeric drug delivery systems, for bioavailabiity optimization and potential side effect minimization (Ligório Fialho et al., 2007). Simultaneously, advances in nanotechnology could elaborate nano-sized delivery vehicles for enhanced drug permeation of blood-ocular barriers (de la Fuente et al., 2010).

1.2.2. Intraocular inflammation and infection

Because there may be significant damage to retinal and uveal tissues, Rao (1990) noted that visual prognosis is most critical where severe intraocular inflammation is a presenting feature; the process is initiated by T- and B-lymphocytes, but augmented and maintained by polymorphonuclear leukocytes (PMNs) and macrophages. Chemical mediators, such as arachidonic acid metabolites, proteolytic enzymes, and oxygen metabolites are responsible for the tissue damage evident in ocular inflammatory conditions, such as uveitis (infectious or non-infectious) (Rao, 1990). The emerging focus on reactive oxygen metabolites (oxygen free radicals) released by PMNs and macrophages during the initial phase of inflammation was

highlighted by Rao (1990). Such chemical mediators warrant attention as stimuli for responsive drug delivery. Champagne (2001) specified the topical and systemic use of corticosteroids and nonsteroidal anti-inflammatory drugs (NSAIDs) for the management of adnexal, corneal, and intraocular inflammation. Corticosteroid suppression of inflammation and cicatrization was reiterated by Holekamp et al. (2005), attained in part by their inhibition of inflammatory cytokines. Intravitreal corticosteroids (e.g. dexamethasone, fluocinolone acetonide, triamcinolone) are purported to result in improvements in patients with many chronic, inflammatory and proliferative intraocular diseases (Reichle, 2005; Haesslein et al., 2006), such as macular edema secondary to diabetes (Jonas and Sofker, 2001), pseudophakia (Jonas et al., 2003) central retinal vein occlusion (Park et al., 2003), and uveitis (Young et al., 2001); as well as in the prevention of proliferative vitreoretinopathy (Jonas et al., 2000). NSAIDs (e.g. flurbiprofen, keratolac, acetylsalicylic acid) are being used with increasing frequency, with exploration of further applications (Champagne, 2001).

Posterior segment pathologies further encompass intraocular infections e.g. bacterial endophthalmitis, which can occur post-operatively, post-traumatically, or via bacterial metastasis from an endogenous site. The clinical presentation of endophthalmitis varies from mild inflammation to complete loss of vision or loss of the eye (Callegan et al., 2007). Callegan and coworkers (2007) referred to experimental evidence, demonstrating the necessity to initiate treatment with intravitreal antibiotics in a timely manner. Vancomycin, aminoglycosides, cephalosporins, or the promising fourth generation fluoroquinolones, are often used empirically, with corticosteroids as an adjunct to limit the bystander damage caused by intraocular inflammation (Callegan et al., 2007).

Despite drug advances, the pharmacological management of these severe ocular pathologies is still a major hurdle, but a surmountable one. There is widespread procedural occurrence of elevated intraocular pressure and cataract progression (Roth et al., 2003). Other risks, particularly associated with intravitreal injection of corticosteroids, include endophthalmitis (Moshfeghi et al., 2003), retinal detachment (Jonas et al., 2003), hemicentral vein occlusion (Gillies et al., 2004), preretinal hemorrhage (Jonas et al., 2001), pseudohypopyon (Jonas et al., 2001), and vitreous hemorrhage (Moshfeghi et al., 2003). Furthermore, the combination of antibiotic and corticosteroid in the therapeutic management of endophthalmitis is still controversial due to corticosteroid-related effects (Callegan et al., 2007).

Research has been implicit in conveying that controlled polymeric drug delivery systems are essential for realizing a superlative pharmaceutical intervention, where effective bioactives are available for intraocular disease treatment. The current market leader representing intraocular implantable systems for the treatment of uveitis is Retisert™, incorporating a corticosteroid (fluocinolone 0.59mg intravitreal implant, Bausch and Lomb, Inc.), the first FDA approved intravitreal implant for the treatment of chronic posterior non-infectious uveitis. It is a sterile implant that releases fluocinolone initially at a rate of 0.6µg per day to the posterior segment of the eye decreasing over the month to 0.3-0.4µg per day over approximately 30 months. The Retisert™ provides continuous delivery of the corticosteroid (Ahn and Moshfeghi, 2008). Because there is uninterrupted release of anti-inflammatory drug, irrespective of alterations in the presence or absence of inflammation, there is an enhanced propensity for the occurrence of side effects, such as cataract development, intraocular pressure elevation, procedural complications and eye pain (Thilek Kumar et al., 2001).

Further developments in intraocular delivery systems, highlighting the diversity of approaches, have seen various modifications of photo-crosslinked poly(propylene fumarate)/poly(*N*-vinyl pyrrolidone) (PPF/PNVP) matrices by Haesslein et al. (2009) to investigate their effect on the release kinetics of acetazolamide and timolol maleate. The hydrophilicity of solid PPF/PNVP matrices was increased by adding various amounts of poly(ethylene glycol) or by increasing the amount of *N*-vinyl pyrrolidone in the polymer mixture prior to crosslinking. Barcia et al. (2009) tested the short- and long-term ability of dexamethasone-loaded poly(lactic-co-glycolic acid) (PLGA) microspheres to reduce ocular inflammation in rabbits elicited by intravitreal lipopolysaccharide (LPS) injection. Dexamethasone-loaded microspheres effectively reduced intraocular inflammation caused by LPS in both short- and long-term studies. Saliba et al. (2008) synthesized and characterized a nanostructured biodegradable intraocular implant based on PLGA (75:25) with Cyclosporine A (CyA) and evaluated its *in vitro* drug delivery profile. The results confirmed the chemical and biological drug stability, the drug distribution into the polymeric matrix and the possibility of a cyclosporine prolonged delivery system profile. No *in vivo* studies have been undertaken on this system. Allergan Inc. (2007) have developed biocompatible intraocular implants including a steroid and a polymer associated with each other to facilitate release of the steroid into an eye for a period of time greater than about two months (specified in European Patent 1750688). Two embodiments are described: in one, the steroid was associated with a biodegradable polymer matrix. Alternatively, the steroid was associated with a polymeric coating having one or more openings permitting release of the steroid into the

external environment. Previous investigations in our laboratories have also seen the design of a novel doughnut-shaped minitablet (DSMT) as a biodegradable intraocular drug delivery system for rate-modulated prolonged delivery of antiviral bioactives e.g. delivery of ganciclovir (GCV) in the treatment of CMV retinitis in AIDS patients. Extensive *in vitro* and *in vivo* investigations have been undertaken in this regard (Choonara et al., 2006; Choonara et al., 2007; Choonara, 2009). Manufacture of the DSMT device was via a special set of punches fitted with a central-rod in a Manesty tableting press. The DSMT device released the GCV at a first-order rate without any dose dumping. On average 2.02±0.01µg/h of GCV was released into the vitreous humor from every 5mg GCV-loaded DSMT device over 72 days. The DSMT device possessed a degree of flexibility which could be effective for long-term intravitreal delivery of drugs for the treatment of various posterior segment eye diseases. These are just a few examples of burgeoning investigations underway in the field of intraocular implantable devices. Their delivery mechanisms are either based on increasing or decreasing the rate of delivery of opthalmic drug, or providing sustained delivery of drug over prolonged periods.

In summary, currently available implantable systems generally attain 'controlled and sustained' levels of drug, for purported bioavailability optimization and side effect minimization in inflammatory posterior segment disorders (Ligório Fialho et al., 2008). However, what must be kept in mind is that available intraocular implants for controlled high-dose corticosteroid delivery have suffered from a notably high complication rate, as highlighted during clinical trials conducted by Holekamp et al. (2005). This begs the consideration of progressive and enhanced delivery system design strategies. Current promising developments have highlighted various polymeric modifications to implantable systems with the purpose of altering their release kinetics. However, no ocular system describes the responsive intraocular delivery of bioactives from an implantable, and potentially nano-enabled, system that is activated by a stimulus pertaining to a specific aberration, such as inflammation. Such a system would be designed to deliver the required drugs within the posterior segment of the patient's eye in accordance with presence or absence of intraocular inflammation experienced by the patient on a particular day. Furthermore, by incorporation of applicable drug/s within a nanosystem (e.g. nanoparticles) for loading into the implantable system, responsive targeted delivery of drug to the intraocular structures, via nanosystem-enabled permeation of ocular barriers, could be achieved on erosion of the implant.

1.2.3. Significance of the research - drug delivery system design strategy

Of current and pertinent interest is the incorporation of a two-way communication between the body and polymeric delivery platforms for the creation of systems that recognize a biochemical process pertaining to a disease and respond aptly via drug release (Alvarez-Lorenzo and Concheiro, 2004; Barbu et al., 2006). Barbu and co-workers (2006) proposed that sustained drug delivery from biodegradable implants incorporating 'smart' materials, combining the capabilities of stimulus response and molecular recognition, could possess enhanced potential for posterior segment disorder management. Furthermore, a number of inflammatory ocular diseases are chronic and hence require prolonged drug therapy. Release of an inflammation-reducing agent in a fashion responsive to a stimulus, e.g. the time-specific presence of inflammatory reactions, will purportedly minimize adverse reactions related to the drug. Extrapolating current research on inflammation-responsive systems (Panyam, 2008), design of a controlled release ocular delivery system that delivers drugs at a rate that is responsive to inflammation intensity would be particularly advantageous.

A proposed intelligent intraocular implant, referred to henceforth as ***the I^3***, employing bioresponsive polymers, would have application in the development of a smart release system capable of delivering controlled therapeutic levels of an anti-inflammatory drug and possibly an antibiotic within the posterior segment in response to a stimulus, which is preferably internal (e.g. pH, temperature, certain biochemicals, inflammation), or alternatively external (e.g. light intensity, ionic strength, magnetism, ultrasound). The I^3 would possess the intrinsic capability to respond to inflammatory molecules, such as the afore-described chemical mediators, or conditions created within the eye inherent of the infection and/ or inflammatory response, that contribute to the pathology of intraocular diseases such as posterior uveitis (which may be non-infectious or have an infectious etiology). Uveitis is the inflammation of one or more parts of the uvea of the eye. The uvea can be considered as the middle layer of the eye lying below the sclera (the white part of the eye). It consists of the iris, ciliary body and choroid. It is pertinent to note, however, that eye afflictions such as uveitis possess their origin in various structures of the eye (e.g. the retina and choroid), but cause secretion of cells into the vitreous (Asencio-Duran et al., 2012). Thus, multiple inflammatory sites must be considered for targeting of drug for amelioration of the condition.

Significantly, the anticipated system will be nano-enabled (i.e. incorporating a functional nanosystem), comprising crosslinked bioresponsive polymeric matrices (BPMs), incorporating

an antibiotic, and fixated with a uniformly interspersed nanosystem (NS); such as nanospheres, nanocapsules, nano/microbubbles, nanotubes or nanofibres; as anti-inflammatory drug reservoirs for inflammatory tissue targeting to yield a *'secure-fit dual bioresponsive polymeric matrix system with a NS enclatherated as a superlattice'*. The described NS would serve as a reservoir for selected anti-inflammatory drugs. The incorporation of synthetic biodegradable polymers or natural polymers as nanostructured systems within the delivery platform has substantial potential for ophthalmics for efficient delivery of drugs to the ocular tissues. The use of nanotechnology-based drug delivery systems prolongs exposure of the drug by controlled release for improved therapeutic efficacy. When released within the vitreous, Sahoo et al. (2008) reported that NS did not induce inflammatory reactions in the retinal tissue, nor was the organization of the surrounding ocular tissues compromized. The potential of a dispersion of solid NS to dramatically improve a delivery platform's thermal and mechanical integrity was noted by Balazs and Buxton (2004). Furthermore, these systems demonstrate the intrinsic potential to serve as targeted, bioresponsive/ self-regulated delivery systems (Li et al., 2005). NS, when injected into the vitreous, have the propensity to migrate through the retinal layers and tend to accumulate in the retinal pigment epithelium (RPE) cells (Bourges et al., 2003). Thus, inflamed tissues can be specifically targeted, and this tendency will be specifically engineered into the proposed NS. The proposed NS would thus be released in a responsive manner upon erosion of the BPMs and target inflamed tissues within the eye to achieve enhanced drug delivery.

Several design criteria for the I^3 were investigated, as delineated by López and coworkers (2007). These include: (i) polymer biodegradability and biocompatibility as inherent properties of both the matrix platforms and NS, with minimal propensity to induce inflammation, or uveal or retinal toxicity upon implantation, and sterilizability, (ii) the capability to act in a bioresponsive manner (e.g. respond to inflammation or other proposed stimuli at the implantation site), and to maintain the drug concentration above therapeutic levels in the vitreous cavity for the duration of the infection and the inflammatory state, and (iii) easy insertion of the implant into the desired ocular site (e.g. vitreous cavity), possessing an acceptable size with respect to the anatomy.

The pivotal thrust of this research is that the described system is a step forward from other described ocular systems owing to its combined bioresponsive nature and nano-based targeting capabilities, which would not provide sustained levels of drug for intraocular inflammatory condition-treatment (e.g. uveitis), but rather levels that are aligned with the presence or absence

of intraocular inflammation experienced by a specific patient at a specific time. Thus the described side effects that have been reported for products on the market such as Retisert™; including cataract development, intraocular pressure elevation, procedural complications and eye pain; would be minimized through the proposed system which would provide enhanced drug release when exposed to an inflammatory stimulus compared to when the implant is subjected to normal intraocular conditions. Furthermore, surgical complications (e.g. choroidal detachment, endophthalmitis, hypotony, retinal detachment, vitreous hemorrhage, vitreous loss, exacerbation of intraocular inflammation and wound re-opening) (Ahn and Moshfeghi, 2008) would be reduced in the I^3 due to the biodegradability of the device, obliterating the need for removal of the device which is necessitated in non-biodegradable implants such as Retisert™.

1.2.4. Model drugs and methodological design of the intelligent intraocular implant

The intraocular inflammatory process intrinsic to inflammatory disorders of the posterior segment such as uveitis and endophthalmitis has been introduced. Preservation of vision necessitates intensive management of inflammation. For non-infectious uveitis, corticosteroids remain a first-line therapy, with intraocular administration heralded an appealing method of delivery attributed to an enhanced anti-inflammatory effect and relative absence of systemic side effects. However, treatment of uveitis with steroids, even via the intraocular route, leads to complications such as cataract formation, poor wound healing, toxicity to corneal epithelium, and increased intra-ocular pressure (Thilek Kumar et al., 2001; Barañano et al., 2009). The inherent disadvantages of steroids have caused a shift to consideration of NSAIDs such as indomethacin (Thilek Kumar et al., 2001). NSAIDs potently inhibit all isoforms of cyclo-oxygenase (COX), a significant enzyme in the inflammatory process, which catalyzes the first two steps in the biosynthesis of eicosanoids from arachidonic acid. NSAIDs reduce postoperative inflammation and macular edema following cataract surgery, possessing both antiproliferative and antiangiogenic effects (Thilek Kumar et al., 2001).

Single intravitreal injections of NSAIDs have demonstrated efficacy in reducing intraocular inflammation caused by LPS in an animal model. Inflammatory changes induced by LPS include recruitment of macrophages, serous and hemorrhagic exudation, disruption of the blood-retinal barrier, and development of epiretinal membranes (Hiscott et al., 1988; Ruiz-Moreno et al., 1992; Yang et al., 1997; Zhang et al., 2005). This is due to the pathological effects of prostaglandins that propogate blood-ocular barrier disruption, vascular permeability changes, promotion of leukocyte migration, and angiogenesis stimulation (Adamis et al., 1994; Aiello et

al., 1995; Ayalasomayajula and Kompella, 2003; Leung et al., 2003). Proposed intraocular sources of endogenous prostaglandin production include the ciliary body, iris epithelium, RPE, and specific cells in the retina, which all express COX enzymes (Chin et al., 2001; Ju et al., 2002). NSAIDs are thus effective intraocularly in reducing prostaglandin production dramatically and attenuating leukocyte recruitment. With specific reference to indomethacin, data has indicated that although COX inhibition may partially explain the protection afforded the blood-aqueous barrier by this NSAID, indomethacin may also exert anti-inflammatory effects that are independent of COX inhibition (Fleisher et al., 1991), as presented in Table 1.1.

Topical NSAIDs have been demonstrated to 'reduce leukocyte release, prostaglandin production, and disruption of the blood-aqueous barrier in a rabbit model of endotoxin-induced ocular inflammation' (Waterbury and Flach, 2004; Waterbury and Flach, 2006), but do not achieve adequate levels of drug to the posterior segment which limits their potential applicability for the treatment of posterior segment inflammation (Rabiah et al., 1996). Barañano and co-workers (2009) thus assessed the intraocular efficacy of two commercially available NSAIDs: ketorolac and diclofenac, following intravitreal injection, via their propensity to reduce inflammation in an animal model of endotoxin-induced uveitis (EIU) induced by LPS injection as well as their intraocular pharmacokinetics and penetration into the retina (Barañano et al., 2009). They demonstrated excellent penetration of both NSAIDs into the retina but rapid clearance by 48 h. The group thus reiterated that novel implantable drug delivery technologies for sustained delivery of intraocular NSAIDs are currently feasible and may ultimately be necessary to maximize their efficacy; and that intraocular delivery of NSAIDs heralds a novel approach for treating uveitis (Barañano et al., 2009). It is of further significance that NSAIDs are not associated with cataract formation or glaucoma (which are related to corticosteroid use) and could thus be proffered as a safer alternative (Gillies et al., 2005; Jonas et al., 2005). At the higher drug concentrations achievable from an implantable system, enhanced therapeutic effects on posterior segment inflammatory disorders may be observed (Barañano et al., 2009).

Posterior segment disorders such as uveitis and endophthalmitis may have an infectious etiology. Intraocular infections are reportedly the cause of 40% of the cases of severe forms of uveitis. Treatment involves potential institution of an antibiotic (ClinicalTrials.gov(a)). As highlighted, bacterial endophthalmitis commonly occurs postoperatively, but may also result from penetrating ocular trauma or systemic infection (Yagci et al., 2007). In terms of antimicrobials for intraocular admininistration, the fluoroquinolone, ciprofloxacin, has been proposed as a single

agent for the treatment of intraocular polymicrobial infections (such as those implicated in bacterial endophthalmitis) because of its broad *in vitro* activity spectrum. Ciprofloxacin has shown good penetration into inflamed ocular tissues and exhibits a high degree of activity against many intraocular pathogens with a minimum inhibitory concentration (MIC_{90}) of less than 1µg/mL (Hainsworth et al., 1996; Yagci et al., 2007). Ciprofloxacin was employed as a model antimicrobial and included or excluded from the I^3 based on the posterior segment disorder targeted and the associated etiology. The pertinent properties of both the anti-inflammatory and antimicrobial drugs instituted in the proposed I^3 are provided in Table 1.1.

The preceding discussion provided the basis for conceptualization of the implantable device proposed. The I^3 would thus be formulated as a 3 component system incorporating two differential release BPMs and the anti-inflammatory agent-loaded NS (Figure 1.1). The outer BPM would incorporate the antibiotic and be designed and chemically engineered to provide a controlled intermediate drug release rate for the therapeutic management of an initial infection (if present - an antibiotic may or may not be included depending on the posterior segment disorder targeted and whether the etiology is infectious or not). The inner crosslinked core matrix, incorporating an indomethacin-loaded NS, would also be chemically modified, and enclosed within the outer BPM, to release the NS at a slower rate than the outer matrix for chronic responsive management of the ensuing inflammatory condition. The outer encapsulating BPM would further serve to control the drug release rate from the inner BPM. The differential release BPMs would be simultaneously originated from polymers susceptible to free radical degradation employing the concept of interpenetrating network formation in the presence of suitable crosslinking agents. The proposed sites of implantation for the I^3, based on preferred routes of intraocular administration, would be intrascleral, sub-Tenon (periocular), and at the pars plana of the eye (intravitreal).

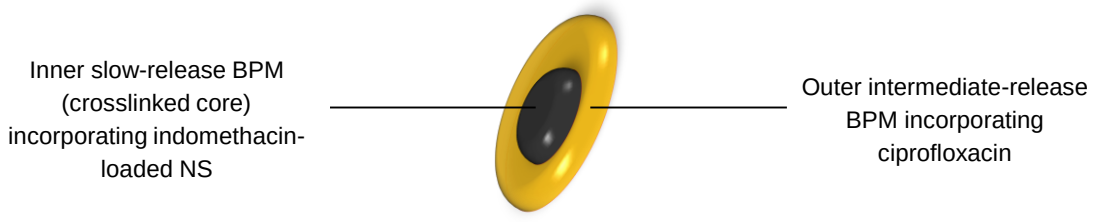

Figure 1.1: The proposed configuration of the intelligent intraocular implant possessing a 'fried egg' appearance

Table 1.1: Characterization of model drugs (data extracted from DrugBank, 2008)

Property	Indomethacin	Ciprofloxacin
3-D Chemical Structure	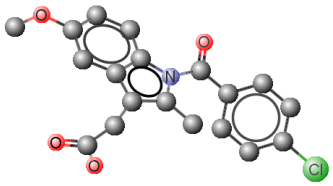	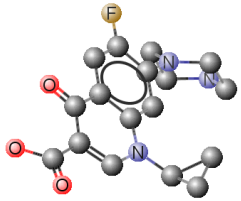
Pharmacodynamics	Indomethacin is known to inhibit two well-characterized isoforms of COX, COX-1 and COX-2, with greater selectivity for COX-1. COX-1 is a constitutively expressed enzyme that is involved in gastric mucosal protection, platelet and kidney function. It catalyzes the conversion of arachidonic acid to prostaglandin (PG) G_2 and PGG_2 to PGH_2. COX-1 is involved in the synthesis pathways of PGE_2, PGD_2, PDF_{2a}, PGI_2 (also known as prostacyclin) and thromboxane A_2 (TXA_2). COX-2 is constitutively expressed and highly inducible by inflammatory stimuli. It is found in the central nervous system, kidneys, uterus and other organs. It also catalyzes the conversion of arachidonic acid to PGG_2 and PGG_2 to PGH_2. In the COX-2-mediated pathway, PGH_2 is subsequently converted to PGE_2 and PGI_2 (also known as prostacyclin). PGE2 is involved in mediating inflammation, pain and fever. Decreasing levels of PGE_2 leads to decreased inflammation.	Ciprofloxacin is a broad-spectrum anti-infective agent of the fluoroquinolone class. Ciprofloxacin has *in vitro* activity against a wide range of Gram-negative and Gram-positive microorganisms. The mechanism of action of quinolones, including ciprofloxacin, is different from that of other antimicrobial agents such as beta-lactams, macrolides, tetracyclines, or aminoglycosides; therefore, organisms resistant to these drugs may be susceptible to ciprofloxacin. There is no known cross-resistance between ciprofloxacin and other classes of antimicrobials. Notably the drug has 100 times higher affinity for bacterial DNA gyrase than for the mammalian counterpart.
Mechanism of Action	Indomethacin antagonizes COX by binding to the upper portion of the active site, preventing its substrate, arachidonic acid, from entering the active site. Indomethacin, unlike other NSAIDs, also inhibits phospholipase A2, the enzyme responsible for releasing arachidonic acid from phospholipids.	The bactericidal action of ciprofloxacin results from inhibition of the enzymes topoisomerase II (DNA gyrase) and topoisomerase IV, which are required for bacterial DNA replication, transcription, repair, strand supercoiling repair, and recombination.
Experimental Properties	Melting point: 158 ^{o}C Water solubility: 0.937 mg/L logP: 3.4 logS: -4.62 Caco2 permeability: -4.69 pKa: 4.5	Melting point: 255-257 ^{o}C Water solubility: 1.1 mg/L logP: 2.3 pKa: 6.09

1.3. Aim and Objectives

The aim of this investigation is the design of a bioresponsive implantable device as a nano-enabled intelligent intraocular implant, which incorporates a two-way communication between the body and the I^3 to create a delivery system that recognizes biochemical processes pertaining to inflammation and then responds via a complex in-built mechanism to effect polymeric erosion with resultant drug release. For pragmatic fulfilment of the aim, the following objectives are apparent:

1. To design a novel methodology for anti-inflammatory NS design which culminates in a reproducible, scalable, nanotechnology-based preparation process to promote the anti-inflammatory potential of the drug via controlling drug release, overcoming ocular barriers where necessary, and targeting and enhancing delivery of the anti-inflammatory drug to inflamed sites within the eye.
2. To conceptualize, optimize, and computationally corroborate the inflammation-responsive BPMs. This would implicate construction of a statistical Response Surface Methodology derived from preliminary mathematical feasibility studies employing Design of Experiments (DoE), following fabrication of the nano-enabled I^3, for elucidation of the effect of independent variables; the upper and lower limits of which would be set during preliminary investigations of BPM and NS fabrication (with subsequent validation via Artificial Neural Networks). This would facilitate a mechanistic evaluation of possible correlations between independent variables and would ultimately emanate in the design of the optimum implant to meet several criteria dictated by current knowledge garnered in infectious and inflammatory conditions within the eye, and based on *in vitro* inflammation-responsiveness of the device investigated in the presence of inflammatory chemical mediators. Determination of the drug release kinetics from the device under normal and inflammatory conditions is also tantamount.
3. To elucidate the mechanisms of controlled drug delivery and the bioresponsive nature exemplified via the investigation and explication of the physicochemical and physicomechanical dynamics of the I^3 through determination of the inflammation-responsive rheological transitions, crystalline structure, thermal diffusivity, in-depth topographical investigations, bioerosional and hydration dynamics in simulated vitreous media, and tensile strength of the I^3.
4. Following the successful design and testing of a prototype I^3 based on its ability to meet the design criteria *in vitro*, its clinical potential in a suitable animal model would be ascertained in terms of *in vivo* release kinetics, anti-inflammatory effect induction as

assessed histologically, biodegradability and biocompatibility. Pertinently, an *in vitro-in vivo* correlation would be sought for intraocular drug release and absorption from the I^3. Subsequently the feasibility of the device in human patients can be corroborated.

1.4. Overview of the Thesis

The thesis was deconstructed as follows, with an associated confluence of design questions, as summarized in Figure 1.2, to provide a logical and pragmatic overview of the process implicated in the origination of the I^3.

Chapter 1 is essentially the blueprint of this thesis delineating the rationalization of this research undertaking, the challenges encountered to date in the treatment of posterior segment disorders of the eye, as well as the aim and objectives of this research.

Chapter 2 ushers in an overview of the drug delivery site of interest in this research - the eye. Its anatomy, physiology and pathophysiology are defined. This progresses into a critical multifaceted review of ocular drug delivery systems, in terms of the merits and downfalls of past approaches and the situation as it stands today. The concept of a 'stimulus-responsive system' and its application to inflammatory ocular afflictions is described. Furthermore, in this chapter, we delve into the world of nanotechnology and elaborate on the pertinence of consideration of an ocular nanoparticulate system ('nanosystem'). Nanopharmaceutical approaches to ocular drug delivery are presented with consideration of the most commendable strategies.

Following on from the theoretical basis established in Chapter 2, in Chapter 3, proposed anti-inflammatory NS for incorporation in the I^3 are assessed for their potential to penetrate ocular membranes, be subject to particle uptake by cells, and exert a notable anti-inflammatory effect. The preferred system is ultimately selected for optimization via a Plackett-Burman Design where its destination would be enclatheration within the inner BPM of the I^3.

The successful design of the anit-inflammatory agent NS for incorporation within the inner BPM of the I^3, lead onto the design of the stimulus-responsive component of the device in Chapter 4. The novel methodology for design of the BPMs is presented, and methodologies for appropriately defining the inflammation-responsive nature of the devices are elaborated on. Intensive device optimization was then scrupulously undertaken, first employing a Response Surface Methodology, embodied by the Box-Behnken Design, ensued by Artificial Neural

Networks. Characterization of the drug release kinetics from the optimized I^3 is pivotally provided. In order to prove the rationality and applicability of the constituent polymers in the formation of the multipolymeric complex, molecular mechanics and dynamics simulations were carried out. Of importance was the undertaking of a brief modeling simulating a pathological inflammatory intraocular state created in the presence of hydroxyl radicals to elucidate the effect of the inflammatory agents on the polymers forming the outer BPM.

It is imperative to elucidate the intricate *modus operandi* of the optimized I^3 developed in Chapter 4 - this forms the crux of Chapter 5. In-depth physicochemical and physicomechanical analysis of the I^3 was undertaken to explicate the inflammation-responsive rheological transitions, pertinent molecular and thermal transitions exemplifying the crosslinked form, hydrational behavior hinging on fluid imbibement, initial device porosity as a predictor of the overall make-up and potential drug release characteristics of the BPMs comprising the I^3, and critical morphological changes displayed during device erosion. Furthermore, energetic profiles for the important complexation reactions were generated using Molecular Mechanics Energy Relationships (MMER) by exploring the spatial disposition of energy minimized molecular structures.

Following the thorough *in vitro* characterization of the I^3 in Chapter 5, the *in vivo* performance of the device is assessed in Chapter 6 to further provide a convincing argument as to its ocular suitability and overall contrasting performance under normal and inflammatory conditions. Histological assessment is key to predicting significant inflammatory changes. Analysis of ocular drug levels under normal and inflammatory conditions is undertaken for correlation with *in vitro* results, for ultimate establishment of an *in-vitro-in-vivo* correlation.

Ultimately, in Chapter 7, conclusions are drawn regarding the overall success of this investigation, with regard to the current ocular drug delivery system market; followed by recommendations for scale-up of I^3 manufacture and implementation of further investigations to see the commercial potential of the I^3 realized.

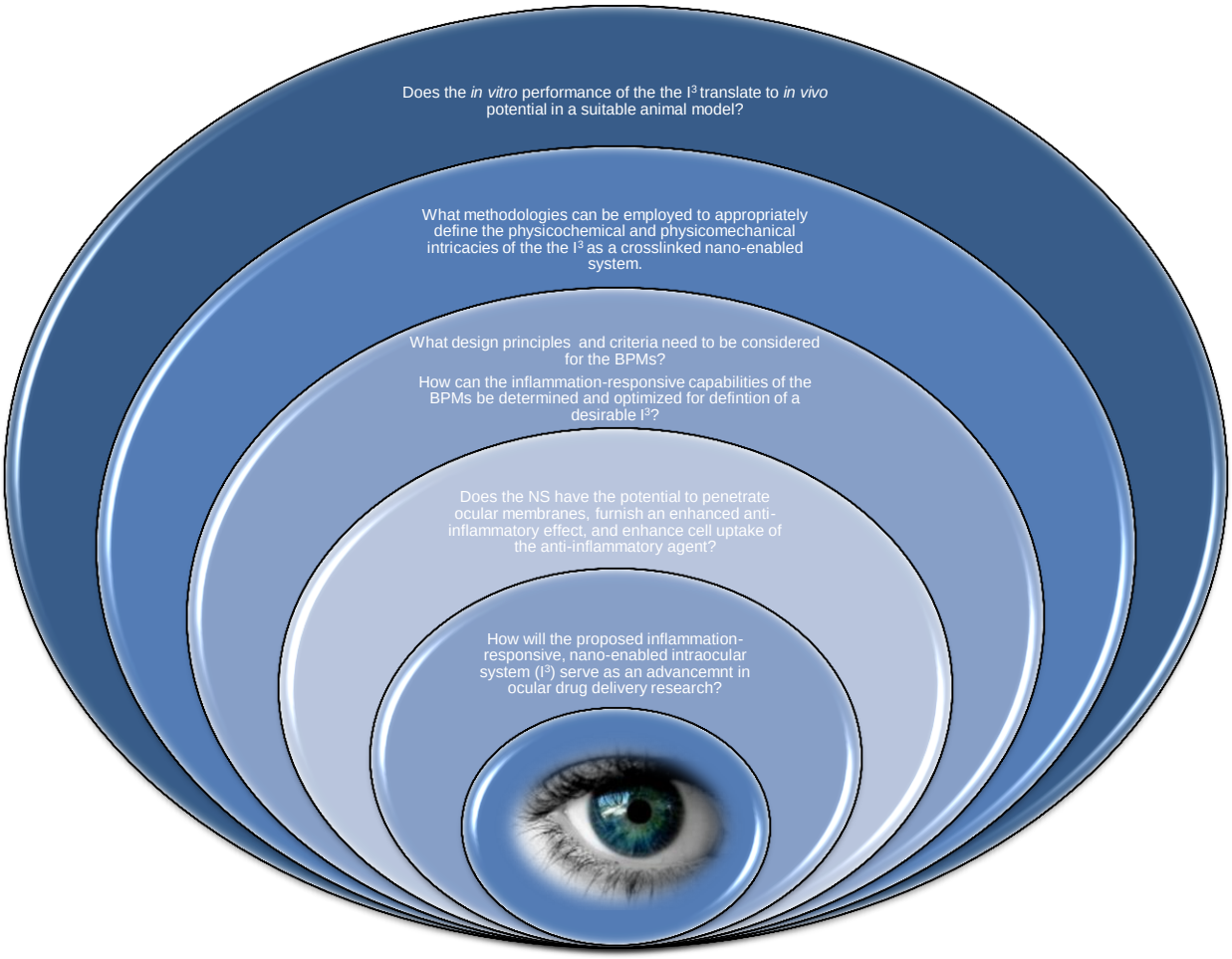

Figure 1.2: Outflow of critical pharmaceutical design questions which form the basis on which this thesis is built

1.5. Concluding Remarks

In this chapter, the overall design strategy and system rationalization for the proposed intraocular device was illuminated. In summary, this investigation rests on the design of an intelligent intraocular implant that would deliver bioactives in accordance with the biologically-predicted needs of the patient, which is, as yet, an unexplored approach to ocular drug delivery. This would proposedly be achieved through the selection and design of intelligent polymeric systems and application of progressive nanotechnological principles.

Before ensuing with the experimental synthesis of the conceptualized I^3, it is important to review the intricacies of inflammatory response modulation and ocular tissue damage mediation for elucidation of a predictable stimulus basis. Furthermore, it is of pertinence to obtain insight into

the potential to modify and functionalize the candidate, potentially inflammation-sensitive, polymeric materials to design innovative stimulus-responsive material platforms with unique or unusual properties for fabrication of the inner and outer BPMs of the I^3. This is accompanied with establishment the molecular basis of their intelligent capabilities. The role of nanotechnology in ocular drug delivery is also reviewed in the ensuing chapter.

CHAPTER 2

OCULAR DELIVERY SYSTEMS – THE NEED FOR A BIORESPONSIVE APPROACH

2.1. The Eye - Anatomy, Physiology and Biochemistry

2.1.1. Extraocular structures

The design of an innovative and effective ocular drug delivery system rests on a sound knowledge of ocular and orbital anatomy, which is discussed henceforth. The eyelids and the orbit protect the eye. The eye is aligned within the orbit by connective tissue (Tenon's capsule) and adipose tissues, together with six extraocular muscles. Posterior to the globe is the retrobulbar region. The eyelids serve several functions. Foremost, their dense sensory innervation and the attachment of eyelashes serve as a mechanical and chemical defence. The coordinated movement of the orbicularis oculi, levator palpebrae, and Müller's muscles (blinking), serves to distribute tears over the cornea and conjunctiva. The fornix is the reflection of the palpebral and bulbar conjunctivae, located superiorly and inferiorly behind the upper and lower eyelids, respectively. Topical medications are usually delivered in the inferior fornix. The lachrymal system consists of secretory glandular and excretory ductal elements. The secretory system is composed of the main lachrymal gland, located in the temporal outer portion of the orbit, and accessory glands of Krause and Wolfring, located in the conjunctiva. The lachrymal gland is innervated by the autonomic nervous system. The tear drainage system originates through small puncta located on the medial aspects of both the upper and lower eyelids. Following the action of blinking, tears enter the puncta and continue to drain through the canaliculi, lachrymal sac, nasolachrymal duct, and then into the nose. The nose is lined by a highly vascular mucosal epithelium; it follows that, topically applied medications that pass through this nasolachrymal system have direct access to the systemic circulation (Henderer and Rapuano, 2011).

2.1.2. Ocular structures

There is anatomical and physiological division of the eye into anterior and posterior segments. The anterior segment structures include the cornea, limbus, anterior and posterior chambers, trabecular meshwork, Schlemm's canal, iris, lens, zonule, and ciliary body. The posterior segment comprises the vitreous, retina, choroid, sclera, and optic nerve (Henderer and Rapuano, 2011).

2.1.2.1. Anterior segment

The cornea is the anterior-most layer of the eye and essentially a mechanical barrier limiting the entry of exogenous substances into the eye as well as having a protective role (Mannermaa et al., 2006). It is a transparent and avascular tissue organized into five layers: epithelium, Bowman's membrane, stroma, Descemet's membrane, and endothelium. The hydrophobic epithelial layer, comprising five to six cell layers, represents an important barrier to foreign matter, including drugs; additionally the basal epithelial cells lie on a basement membrane. Adjacent to this is Bowman's membrane, a collagenous fibre layer. The stroma is a hydrophilic layer constituting approximately 90% of the corneal thickness, distinctly organized with collagen lamellae synthesized by keratocytes - and presenting a formidable barrier to permeation of lipophilic drug molecules. Beneath the stroma lies Descemet's membrane, the basement membrane of the corneal endothelium. Lying most posteriorly, the endothelium is a monolayer of hexagonal-shaped cells cells adhering to each other by tight junctions, which maintain corneal integrity/ transparency by active transport processes and serve as a hydrophobic barrier. These layers thus constitute a barrier to diffusion of the drug from the tear fluid to the anterior chamber of the eye (Mannermaa et al., 2006; Gaudana et al., 2010). It is thus evident that drug absorption across the cornea requires penetration of the trilaminar hydrophobic-hydrophilic-hydrophobic domains of the various anatomical layers (Henderer and Rapuano, 2011).

At the periphery of the cornea and adjacent to the sclera lies a transitional zone (1 to 2mm wide) called the limbus. Limbal structures include the conjunctival epithelium, which contains the stem cells, Tenon's capsule, episclera, corneoscleral stroma, Schlemm's canal, and trabecular meshwork. Limbal blood vessels, as well as the tears, provide important nutrients and immunological defense mechanisms for the cornea. The anterior chamber holds approximately 250µL of aqueous humor. The peripheral anterior chamber angle is formed by the cornea and the iris root. Located above the apex of this angle is the trabecular meshwork and canal of Schlemm. The posterior chamber is encompassed by the boundaries of the ciliary body processes, posterior surface of the iris, and lens surface and holds approximately 50µL of aqueous humor (Henderer and Rapuano, 2011).

2.1.2.2. Posterior segment

As the I^3 would potentially be implanted in, and exposed to environment of the posterior segment of the eye, we must concern ourselves with its anatomical and biochemical make-up, as this will

ultimately impact on the intrinsic mechanism of operation of the implanted device. It comes as no surprise that drug delivery to the posterior segment is particularly challenging due to the anatomical and vascular barriers to both local and systemic access.

The sclera is the outermost coat of the eye, covering the posterior portion of the globe. The sclera is composed of collagen fibers and proteoglycans embedded in an extracellular matrix and is continuous with the cornea, originating from the limbus and extending posteriorly and globally. It possesses comparable permeability to that of the corneal stroma (Gaudana et al., 2010). The external surface of the scleral shell is covered by an episcleral vascular coat, Tenon's capsule, and the conjunctiva. The tendons of the six extraocular muscles insert into the superficial scleral collagen fibres, with blood vessels supplying and draining the choroid, ciliary body, optic nerve, and iris. Inside the scleral shell, the vascular choroid nourishes the outer retina by a capillary system in the choriocapillaris. The retina is composed of neural retina and RPE. Bruch's membrane and the RPE are situated between the outer retina and the choriocapillaris; their tight junctions provide an outer barrier flanking the choroid and retina. The multifunctional RPE is a polarized monolayer of highly specialized cells implicated in vitamin A metabolism, phagocytosis of the rod outer segments, and multiple transport processes (Henderer and Rapuano, 2011).

The neurosensory retina, the most extensively investigated structure of the eye, boasts a combination of neurons, glial cells, and blood vessels, with a high degree of organization. The inner border of the neural retina faces the vitreous and is composed of nine layers and the outer border is adjacent to the RPE. Between the apical microvilli of RPE cells is where the outer segments of photoreceptors are positioned. The surface area of RPE cells is increased by basolateral infoldings. Bruch's membrane, lying between the RPE and choriocapillaris, provides a basal lamina for RPE cells. The blood supply to the inner two thirds of the retina is via retinal vessels, whereas the outer one third of the neural retina and RPE is supplied by the choroidal circulation. The blood-retinal barrier (BRB) possesses properties comparable to the blood-brain barrier and restricts the movements of substances after systemic and periocular administration to the retina (Steuer et al., 2005). The two components forming the BRB are the outer part formed by the RPE and the inner part composed of the endothelial cells of retinal vessels (Cunha-Vaz, 2004). Tight junctions connect the cells of the RPE and retinal endothelium and it is these junctions that ultimately form the permeation barrier to hydrophilic substances. Thus the transfer of compounds both inward (blood to vitreous) and outward (vitreous to blood) is limited.

The overall drug flux (*J*) across the BRB is contingent on the concentration gradient of drug (*dC*), its barrier permeability (*P*) (retinal capillaries or RPE) and the barrier surface area (*S*) (Mannermaa et al., 2006).

The optic nerve is a myelinated nerve conducting the retinal output to the central nervous system. It is composed of: 1) an intraocular portion, which is visible as the 1.5mm optic disk in the retina; 2) an intraorbital portion; 3) an intracanalicular portion; and 4) an intracranial portion. The nerve is ensheathed in meninges continuous with the brain (Henderer and Rapuano, 2011).

Approximately 80% of the eye's volume is the vitreous (~4mL in the human eye), which is a clear medium containing collagen type II, hyaluronan/ hyaluronic acid (HA), proteoglycans, and a variety of macromolecules including glucose, ascorbic acid, amino acids, and a number of inorganic salts (Henderer and Rapuano, 2011). The overall composition exemplifies a delicate, transparent gel composed of a highly hydrated double network of protein fibrils and charged polysaccharide chains. By weight, vitreous is ~99% water and 0.9% salts. The remaining 0.1% is divided between protein and polysaccharide components. Most of the protein is found in or associated with 10-20nm heterotypic collagen fibrils composed a thick layer of collagen type II (75% of the fibril by mass) enveloping a small collagen type V/XI core. The exterior of each fibril is decorated with covalently bound collagen type IX and other glycoproteins. Collagen IX contains four short, coiled noncollagenous domains separated by three triple-helical collagenous domains. Two of the collagenous domains are aligned with, and crosslinked to, the axis of the fibrils, but the third strut-like collagenous domain is sterically forced to project out from the fibril by a heparin-sulfate glycosaminoglycan (GAG) chain that is covalently bound to the adjacent, hinge-like noncollagenous domain. The network of collagen fibrils has been presumed responsible for the mechanical properties of the vitreous because of the load-bearing capacity of collagen, and because the vitreous does not fully collapse with the enzymatic removal of HA. It has been suggested that HA polysaccharide chains play a passive role in the vitreous by filling the space between the fibrils to prevent extensive aggregation. Literature indicates that the vitreous shrinks after removal of HA, and morphologically the collagen network ‘relaxes’ from having relatively straight to significantly curved fibrils (Bishop, 2000).

2.1.2.3. Inflammation-induced pathophysiological changes to the posterior segment

In Chapter 1, the concept of intraocular inflammation was introduced as a significant perpetrator of damage to retinal and uveal tissues (initiated by T- and B-lymphocytes, but augmented and

maintained by PMNs and macrophages), with chemical mediators, such as arachidonic acid metabolites, proteolytic enzymes, and reactive oxygen metabolites (oxygen free radicals) being responsible for the tissue damage evident in ocular inflammatory conditions, such as uveitis and endophthalmitis (Rao, 1990).

With specific reference to the vitreous, inflammatory diseases of various etiologies emanate in opacification, liquefaction, and shrinkage. Should inflammation be protracted further alterations include cellular proliferation and transformation resulting in fibrosis, which may be cortical or extensive. Excessive outpouring of a fluid exudate emanates in detachment of the vitreous from the posterior eye. Vitreo-retinal adhesions are a common occurence at the sites of inflammation of young eyes. In numerous vitreal inflammations, exudate has a propensity to pool at the vitreous base where it organizes into scar tissue. The retina and ciliary body generally form the scar; however, there is also transformation of fibrosis-produced monocytes into fibroblasts (Hogan, 1975).

2.2. Current Drug Delivery Approaches

A brief step back in time, prior to the mid-1970s, divulges that somewhat archaic approaches were implemented for the treatment of endophthalmitis, including the intensive application of topical antibiotics used in conjunction with intravenous and subconjunctival therapy (Allen and Mangiaracine, 1964; Okada et al., 1994). Unsurprisingly, suboptimal outcomes were attained and the prognosis for visual recovery was poor. Treatment failure, with reference to extraocular treatment modalities for intraocular disorders such as endophthalmitis and uveitis has, as emphasized, been largely ascribed to the poor penetration of the drug of interest into the posterior segment (Peyman and Ganiban, 1995).

Previously, where the institution of intraocular drugs was restricted to the treatment of endophthalmitis, intraocular drug therapy is now considered for other disorders, such as proliferative vitreoretinopathy (PVR), viral retinitis and uveitis. Four routes of administration can be employed for drug delivery to the posterior segment of the eye: topical, systemic, intraocular, and periocular (including subconjunctival, sub-Tenon’s and retrobulbar). The diverse routes of ocular administration and associated kinetic pathways are divulged in Figure 2.1.

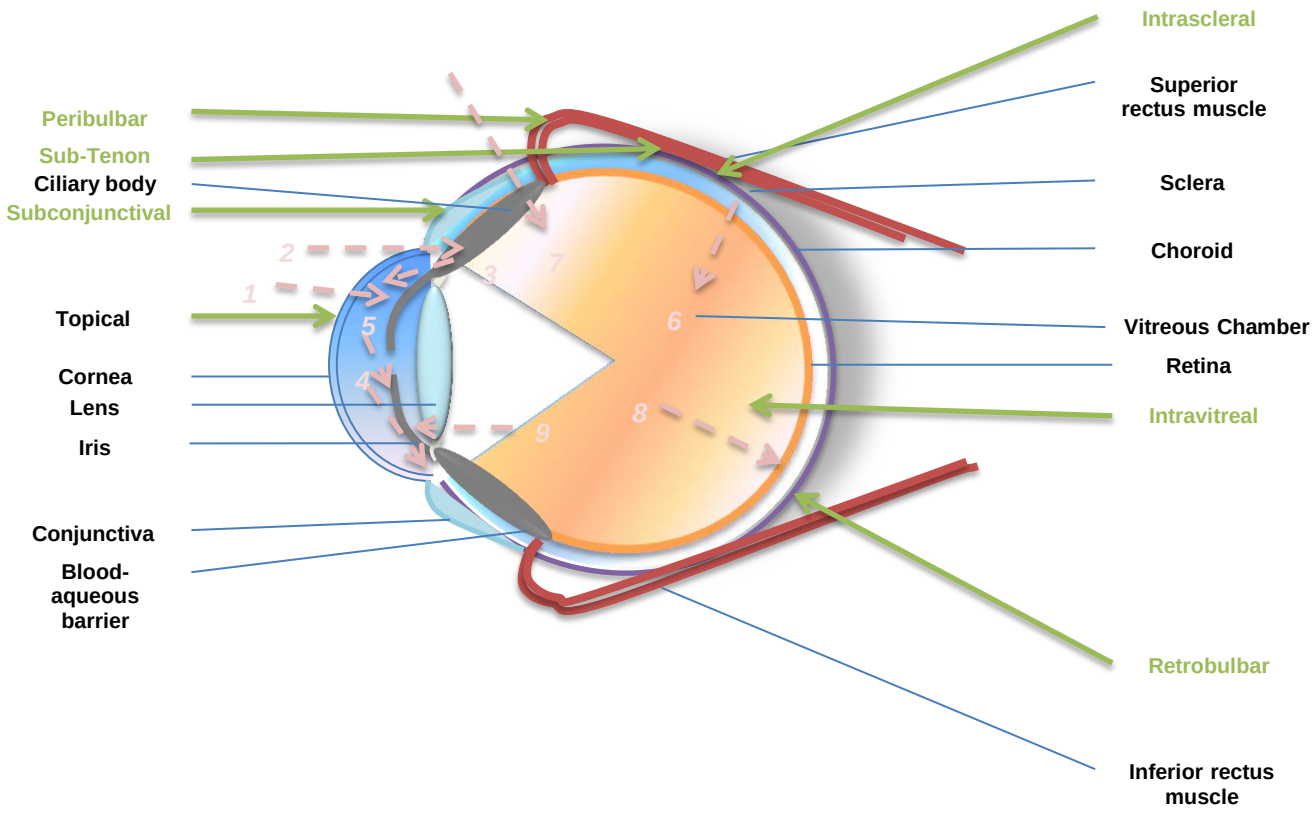

Figure 2.1: Schematic representing the ocular structures, routes of drug administration to the eye (adapted from Gaudana et al., 2010), and drug kinetic pathways. Note that the iris, ciliary body and choroid form the uvea. The following processes are referred to: (1) trans-corneal permeation from the lachrymal fluid into the anterior chamber, (2) non-corneal drug permeation across the conjunctiva and sclera into the anterior uvea, (3) drug distribution from the blood stream via blood–aqueous barrier into the anterior chamber, (4) elimination of drug from the anterior chamber by the aqueous humor turnover to the trabecular meshwork and Sclemm's canal, (5) drug elimination from the aqueous humor into the systemic uveoscleral circulation, (6) drug distribution from the blood into the posterior eye across the BRB, (7) intravitreal drug administration, (8) drug elimination from the vitreous via posterior route across the blood retina barrier, and (9) drug elimination from the vitreous via anterior route to the posterior chamber

Static barriers, which comprise the different layers of cornea, sclera, and retina including the blood aqueous barrier (BAB) and BRB; and dynamic barriers, comprising the choroidal and conjunctival blood flow, lymphatic clearance, and tear dilution; as well as efflux pumps present a significant challenge for ocular drug delivery, most specifically to the posterior segment. These barriers to ocular drug delivery are intrinsic and distinctive to the anatomical and physiological functioning of the eye and are encountered via most administration routes, i.e. topical, systemic, and periocular. It must be noted that most of these are anatomical and physiological barriers that are in place to protect the eye from toxicants. Most significant efforts gathering momentum in

recent years to overcome these barriers have focused on identification of influx transporters on various ocular tissues, together with the design of a transporter-targeted delivery of a parent drug. Concurrently, colloidal embodiments of drug delivery systems (e.g. nanoparticles, nanomicelles, liposomes, and microemulsions) have undergone in-depth investigations in attempts to establish their efficacy in overcoming various static and dynamic barriers. Furthermore, other innovative drug delivery strategies have been designed to achieve targeted and sustained release such as bioadhesive gels. Designing fairly noninvasive sustained drug delivery systems for availing drugs to the posterior segment seems the most feasible option prospectively for providing acceptable means for clinicians and patients to address posterior segment disorders (Gaudana et al., 2010). Consideration of diverse delivery routes, preformulation, and formulation factors is thus paramount in the design of an effective ocular delivery system (Gaudana et al., 2010).

2.2.1. Systemic administration

The major barriers encountered following systemic administration in ocular drug delivery are the BAB (anterior segment) and BRB (posterior segment). The BAB is composed of two cell layers situated in the anterior segment of the eye, being the endothelium of the iris/ ciliary blood vessels and the nonpigmented ciliary epithelium, both of which express tight junctional complexes (zonular occludens) thus obstructing the movement of solutes into the intraocular environment such as the aqueous humor (Barar et al., 2008). The BRB restricts the entry of the bioactives from blood into the posterior segment and is represented by two types of cells - the retinal capillary endothelial cells and the RPE, referred to as the inner and outer BRB, respectively. It is these tight junctions of the RPE, ultimately, that effectively restrict intercellular permeation. Should a drug be orally or intravenously administered, it can easily enter into the choroid due to its high vasculature compared to retinal capillaries. The fenestrated choriocapillaris permits swift equilibration of circulating drug molecules with the extravascular space of the choroid. However, the outer BRB (RPE) restricts further entry of drugs from the choroid into the retina, which is the challenge of systemic administration. There is thus a need for specific oral or intravenous targeting systems to enable transport of molecules through the choroid and into the underlying confines of the retina (Urtti 2006; Gaudana et al., 2010). Reports have highlighted poor concentrations in the vitreous following intravenous administration; with bactericidal antibiotic concentrations in the posterior chamber being problematic to attain (Espana et al., 1993). Ultimately, the passage of materials, including antibiotics, into the vitreous cavity is inhibited by these tight junctions. These junctions may be disrupted in cases of infection

or inflammation, to allow increased concentrations of intravitreal drugs; however, and unfortunately at this stage, permanent destruction of the retina has occurred (Peyman and Ganiban, 1995).

Researchers have been spurred by the current advancements in nanotechnology to investigate approaches to overcome the BRB. One investigation had researchers demonstrating that intravenously administered 20nm gold nanoparticles traverse the BRB and distribute in all the retinal layers without cytotoxicity (demonstrated in C57BL/6 mice), without affecting the viability of RPE cells, astrocytes, and retinoblastoma cells. In contrast, larger 100nm nanoparticles were not detected in the retina (Kim et al., 2009a). More recently, dual-functionalized PLGA nanoparticles were created for the IV route and found to be successful in targeted delivery of antivascular endothelial growth factor intraceptor plasmid to choroidal neovascularization (CNV) lesions, but this result was mainly attributed to the leaky BRB as a result of CNV in the laser-treated rat eye (Singh et al., 2009).

Certain drugs in themselves are distributed in ocular tissues upon intravenous administration, as demonstrated in pharmacokinetic studies, e.g. micafungin (Suzuki et al., 2008), marbofloxacin (Regnier et al., 2008), and amphotericin B (Goldblum et al., 2002). Visudyne® is a marketed intravenously administered formulation applied in age-related macular degeneration (AMD) as photodynamic therapy. However, intravenous administration is not favored for treating ocular disorders because of associated toxicity and delivery issues (Gaudana et al., 2010).

2.2.2. Topical administration

Eye drops are the most common topical preparation and are generally employed to treat anterior segment diseases, possessing their site of action in the various layers of the cornea, conjunctiva, sclera, and the other tissues of the anterior segment such as the iris and ciliary body (anterior uvea). Upon topical drug administration, the resistance encountered to drug penetration across the cornea, aqueous humor and crystalline lens generally emanates in non-therapeutic levels of drug in the posterior vitreous, retina and choroids (Herrero-Vanrell and Refojo, 2001). Precorneal factors (solution drainage, blinking, tear film, tear turn over, and induced lachrymation) and anatomical barriers significantly reduce the bioavailability of topical formulations following instillation (Ananthula et al., 2009). The first defence encountered is the tear film which has a high turnover rate. Mucin, as a component of the tear film, plays a protective role by forming a hydrophilic layer that is distributed over the glycocalyx of the ocular

surface, clearing debris and pathogens (Gipson and Argueso, 2003). Consider this: human tear volume is estimated to be 7μL, and the cul-de-sac can transiently hold ~30μL of the administered eye drop, but because tear film is rapidly restored within 2-3 min; most of the topically administered solutions are thus washed away within ~15-30 s following instillation. All these factors emanate in a short contact time with the absorptive membranes, the rationale for less than 5% of the applied dose gaining access to the intraocular tissues (Ahmed, 2003). Furthermore, the drug has yet to encounter and permeate the various layers of the cornea, conjunctiva, and sclera. Permeation mechanisms across the corneal epithelium include passive paracellular, and transcellular permeation, as well as transporter-mediated influx and efflux across the cell membrane on the apical and basolateral side, respectively. The lipioidal corneal epithelium contains 90% of the total cells in the cornea, exerting significant resistance towards permeation of hydrophilic drugs that are topically applied. Additionally, as discussed, superficial corneal epithelial cells conjoined by desmosomes are encapsulated by the zonula occludens, retarding paracellular drug permeation from the tear film into the intercellular spaces of the epithelium in addition to the inner layers of the cornea (Gaudana et al., 2010). As the corneal endothelial junctions are leaky, they facilitate the passage of macromolecules between the aqueous humor and stroma (Sunkara, 2003). Ultimately the corneal layers such as the epithelium and stroma impose themselves as major barriers to ocular drug delivery. A pertinent consideration is thus that the permeant should have an amphipathic nature to facilitate permeation through these layers (Barar et al., 2008).

Investigations have highlighted that bioactive permeability across the sclera is inversely proportional to the molecular radius, indicating that compounds with linear structures are less likely to permeate than globular compounds (Geroski and Edelhauser, 2001). Permeability across the sclera is also affected by the charge of the drug molecule, with positively charged molecules exhibiting poor permeability as a result of attachment to the negatively charged proteoglycan matrix (Kim et al., 2007; Gaudana et al., 2010), although this method has been exploited to enhance corneal retention time of nanosystems.

Although investigators continue to develop new topical drug delivery systems (Bar-Ilan et al., 1993; Keller et al., 1993; Umemoto et al., 1993), efforts to realize reasonable therapeutic drug levels in the posterior segment have fallen short (Peyman and Ganiban, 1995).

2.2.3. Oral administration

There have been diverse reasons for the investigation of oral delivery (Kampougeris et al., 2005; Shirasaki et al., 2006; Santulli et al., 2008), often in combination with topical delivery (Sakamoto et al., 2007); one being that isolated use of topical delivery did not achieve therapeutic concentrations in the posterior segment. Secondly, the lower degree of invasiveness and higher patient acceptance of the oral route spurred consideration of this approach (compared to IV route). The restrictions, however, are apparent: there is limited accessibility to many of the targeted ocular tissues which then requires high dosage to observe significant therapeutic efficacy, especially in the vitreous-retina, resulting in systemic side effects (Herrero-Vanrell and Refojo, 2001; Haesslein et al., 2006). This route is, therefore, not the primary choice and only a limited number of compounds have been investigated for ocular drug delivery e.g. analgesics (Coppens et al., 2002), antibiotics (Rajpal et al., 2009; Samtani et al., 2009), antivirals (Chong et al., 2009), antineoplastic agents (Takahashi et al., 2009), and omega-6 fatty acids (Kokke et al., 2008). Should a bioactive be considered for the oral route, it must possess a high oral bioavailability and have the propensity to cross the BAB and BRB (Gaudana et al., 2010).

2.2.4. Periocular and intravitreal administration

The periocular route encompasses subconjunctival, sub-Tenon, retrobulbar, and peribulbar administration and is advantageously less invasive than the intravitreal route (see Figure 2.1). Following administration of a drug via periocular injection, it may gain access to the posterior segment by three different pathways: 1) transscleral; 2) systemic circulation via the choroid; and 3) the anterior pathway traversing the tear film, cornea, aqueous humor, and the vitreous humor (Ghate et al., 2006; Gaudana et al., 2010).

Administering drug directly to the subconjunctival space could be more advantageous than topical delivery for anterior segment disorders (Clement and Tailor, 1987). Subconjunctival injection obviates the conjunctival epithelial barrier (which limits the permeation of water-soluble drugs). However, investigators have reported in the past that this route was not entirely successful in achieving effective therapeutic drug concentrations in the posterior segment (Axelrod et al., 1987; Sharir et al., 1989; Peyman and Ganiban, 1995). A transscleral route bypasses the cornea-conjunctiva barrier, but there are still various dynamic (conjunctival blood and lymphatic circulation), static, and metabolic barriers that limit drug access to the posterior segment. Dynamic barriers attain rapid drug elimination following subconjunctival administration and the formulation is essentially drained into the systemic circulation, lowering ocular

bioavailability (Hosseini et al., 2008; Kim et al., 2008). The major determinant of vitreous drug levels following conjunctival administration is therefore drug elimination from the subconjunctival space, and molecules evading the conjunctival vasculature permeating through the sclera (which is not a significant barrier, more permeable than the cornea, and independent of lipophilicity but dependent on the molecular radius). It would then permeate the choroid, gaining access to the neural retina and photoreceptor cells (Urtti, 2006). The choroid nonetheless poses a formidable obstacle as high choroidal blood flow can also eliminate an extensive amount of drug before it arrives at the neural retina (Gaudana et al., 2010). The BRB is subsequently encountered which limits drug availability to the photoreceptor cells, however, the periocular route necessitates smaller amounts of drugs compared to systemically, and in essence achieves therapeutic drug levels in the vitreous-retina with lower systemic side effects (Herrero-Vanrell and Refojo, 2001). This route is thus still a contender for drug delivery considerations.

Overall, where the indirect route attains inefficient access of bioactives to the vitreous; the direct intravitreal delivery of drugs is necessitated for the effective treatment of a number of posterior segment diseases. Compared to periocular injections, intravitreal injections avail direct insertion of drug molecules into the vitreous, which furnishes an advantage. A challenge, however, is that drug distribution in the vitreous is non-uniform with small molecules rapidly distributing throughout the vitreous, and restricted diffusion of larger molecules. Factors such as the pathophysiological condition and molecular weight of the administered drug also affect distribution (Mitra et al., 2006). HA, the negatively charged glycosaminoglycan discussed earlier and present in the vitreous, can interact with cationic lipid and polymeric DNA complexes leading to extensive aggregation and immobilization of the complexes (Pitkanen et al., 2003; Peeters et al., 2005). Nanoparticle structure and surface charge further has pertinent effects on mobility in the vitreous (Peeters et al., 2005). This is where surface modification of nanosystems comes into play and hydrophilic PEG chains are often included. Studies have also demonstrated that anionic nanoparticles diffused more freely in the vitreous than cationic particles (Kim et al., 2009b).

The cell layer separating the retina and the vitreous known as the inner limiting membrane (ILM) serves as a barrier for retinal delivery following intravitreal administration. In addition, the presence of the RPE presents an inherent complexity in drug transport from the vitreous to the outer segments of retina and choroid. Therapeutic efficacy is also affected by the half-life in the vitreous. Elimination pathways play a role as drug is cleared either by the anterior route or

posterior route following intravitreal injection. The anterior elimination route involves passive drug diffusion across the vitreous into the aqueous humor via zonular spaces. This is ensued with further clearance via aqueous turnover and uveal blood flow. Elimination via the posterior pathway implicates BRB permeation by the drug; therefore optimum passive permeability or active transport mechanisms are necessitated. The half-life of compounds is thus increased by hydrophilicity and large molecular weight (Urtti, 2006; Gaudana et al., 2010).

Intraocular drug delivery can be achieved through application of intravitreal drug injection and sustained drug delivery systems fabricated from either biodegradable or non-biodegradable polymers that are injected (i.e. micelles, liposomes, microspheres, microcapsules, nanospheres, nanocapsules) or implanted (i.e. nail-like scleral plugs, discs, pellets, rods, sheets, osmotic pumps, hydrogel reservoirs) in the posterior segment of the eye and maintain therapeutic levels over an extended period of time. Sites at which these systems can be introduced include the vitreous cavity, the subretinal space, the sclera, and the peribulbar space. Other alternatives include transdermal patches and iontophoretic devices. Biodegradable devices are inherently advantageous when compared to non-erodible systems in that as they are degrading, they are gradually disappearing from the site of implantation, and eliminating the risk of fibrous encapsulation and the necessity of surgical removal (Peyman and Ganiban, 1995; Haesslein et al., 2006; del Amo and Urtti, 2008).

Before implants made an appearance on the ocular drug delivery front, intravitreal injection into the posterior segment was deemed adequate (Peyman and Ganiban, 1995). Intravitreal injection can achieve targeted therapeutic concentrations, thus diminishing systemic side effects. The concept of an intravitreal injection was presented in 1944 by von Sallmann and co-workers but was not widely implemented at that stage because of lack of toxicity studies on the directly-injected intraocular drugs (Von Sallmann et al., 1944; Von Sallmann, 1948). From their investigations emanated reports that therapeutic levels of penicillin could be maintained in the posterior segment by intravitreal injection. In a series of experiments, Peyman and associates (as reported in Peyman and Ganiban, 1995), successfully determined the toxic levels of various intravitreal antibiotics, measured clearance times, and compared intravitreal injection with combined intravenous and subconjunctival administration to obtain clarity on this treatment modality (Peyman and Ganiban, 1995). Currently treatment of various acute and chronic posterior segment diseases, including proliferative vitreoretinopathy, endophthalmitis, recurrent uveitis, acute retinal necrosis, and CMV retinitis, is by repeat intravitreal injections for

maintainance of drug concentrations within the therapeutic window. However, the side effects of these multiple intraocular injections required to achieve high efficacy rates for the treatment of a variety of chorioretinal disorders are manifold, being not only disagreeable to patients, but also instigating the risk of cataract formation, retinal detachment, endophthalmitis and vitreous hemorrhage. Because the majority of drugs employed for posterior segment disorders possess a low therapeutic index, this can necessitate intravitreous injections at drug concentrations fast approaching the toxic level for the retina (Herrero-Vanrell and Refojo, 2001).

2.2.4.1. Sustained polymeric intraocular delivery systems

Sustained drug delivery devices are proffered as a superlative alternative to multiple intravitreous injections (Herrero-Vanrell and Refojo, 2001). The fabrication of an intraocular sustained release system that can maintain a therapeutic level of drug within the vitreous cavity would proposedly embody a significant advance for the treatment of ocular disease. Systems investigated in the recent past such as biodegradable microsystems, emulsions, and liposomes offer the advantage of being injected into the posterior segment, but ocular media clarity may be impaired if they ultimately become suspended in the vitreous. Trans-scleral iontophoresis is a non-invasive technique that has been described as holding some promise for intravitreal delivery, the disadvantages being the complicated procedural requirements and limited application to only ionizable drugs (Haesslein et al., 2006).

Scientists have pinpointed biodegradable polymeric nanoparticles as demonstrating significant innovative potential as drug delivery devices for the eye. Biodegradable polymers can be combined with drugs at the nano-level in such a way to enable drug release from the nanosystem into the eye in a predesigned fashion, which may be constant or cyclic over an extensive period, or stimulus-responsive. Following delivery of the drug load, the polymeric carrier is naturally degraded in the body (Corcoran, 2006). According to Tsibouklis in Barbu et al. (2006), 'the formulation of biodegradable or bioerodible polymers as colloidal [nanosystems] holds significant promise for ophthalmic drug delivery.' However, 'formulation stability, particle size uniformity, control of drug release rate, and the large-scale manufacture of sterile preparations are challenges that still require directed investigation' (Corcoran, 2006). These systems are further elaborated on in Section 2.5 below.

Systems that permit intraocular perfusion or microdialysis offer the advantages of allowing continuous drug administration into the vitreous cavity and possess the ability to change or stop

drug administration at any time. Nevertheless, because there is permanent access to the intraocular space, the risk of intraocular infection and patient discomfort are increased (Haesslein et al., 2006).

Conditions such as proliferative vitreoretinopathy (PVR), an infrequent complication of retinal re-attachment surgery that culminates in blindness, are ineffectively managed via conventional routes of drug therapy such as systemic or intravitreal injection - a result of the existence of the BRB and the short drug half-lives of effective agents. It is hypothesized that a controlled-release multiple-drug implant providing therapeutic drug levels for over a month (for simultaneous prevention of cell proliferation and modulation of the inflammatory response) inserted directly into the vitreous following re-attachment surgery would be the most feasible treatment of PVR (Zhou et al., 1998).

Various biodegradable and nonbiodegradable polymeric systems have developed for the treatment of ocular pathologies, some of which were introduced in Chapter 1, and archetypal corticosteroid-loaded systems represented in Figure 2.2. Holekamp et al. (2005) developed a polymer-based drug delivery platform in which fluocinolone acetonide, a corticosteroid that has been shown to inhibit choroidal neovascularisation (CNV) in an animal model of CNV, was compressed into tablets, introduced into a silicone elastomer and attached to a polyvinyl alcohol suture tab. The drug delivery system could be engineered to release a constant amount of corticosteroid over a prolonged time period (approximately 3 years) following surgical placement in the posterior segment of the eye. The fluocinolone acetonide sustained drug delivery device also has been used in the treatment of severe uveitis. Haesslein et al. (2006) fabricated a photo-crosslinked monolithic fluocinolone acetate-loaded poly(propylene fumarate)/ polyvinyl pyrrolidine rod-shaped matrices for the prevention of PVR and treatment of intraocular and inflammatory proliferative diseases. Ligório Fialho et al. (2007) developed and characterized biodegradable poly(ε-caprolactone) implants, for intraocular prolonged and controlled release of dexamethasone. SurModics' I-Vation™ intravitreal implant delivers controlled levels of triamcinolone acetonide; and in 2007, was reported as being evaluated in Phase I clinical trials in the treatment of diabetic macular edema (www.surmodics.com).

While these afore-described advancements in ocular delivery hold a number of advantages, they are not without their pitfalls, which are summarized in Table 2.1.

Rein Ulijn, a biomedical materials specialist at the University of Manchester, UK, highlighted that a major challenge is tackling the incorporation of a two-way communication between the body and the polymeric materials to 'create systems that recognize a disease-specific biochemical process and respond to it by releasing a drug' (Corcoran, 2006). Controlled drug delivery from preferably biodegradable polymeric implants that combine the capabilities of stimulus responsiveness and molecular recognition embody significant capacity for enhanced therapy of posterior segment disorders and ease patient discomfort (Barbu et al., 2006). There are a selection of polymers that display roles as sustained release vehicles, while ‘smart’ hydrogels that react to disease-specific environmental triggers and/ or chemical signals to elicit drug release are emerging as the backbone of a new generation of therapeutics (Barbu et al., 2006).

Furthermore, a number of inflammatory diseases are chronic and hence require prolonged drug therapy. Release of the inflammation-reducing agent in a fashion responsive to the presence or absence of inflammatory reactions would purportedly minimize adverse reactions in autoimmune diseases, wound healing and other pathological situations. Thus, a sustained release delivery system that delivers anti-inflammatory drug to a greater extent when inflammation flares would be desirable (Panyam, 2008).

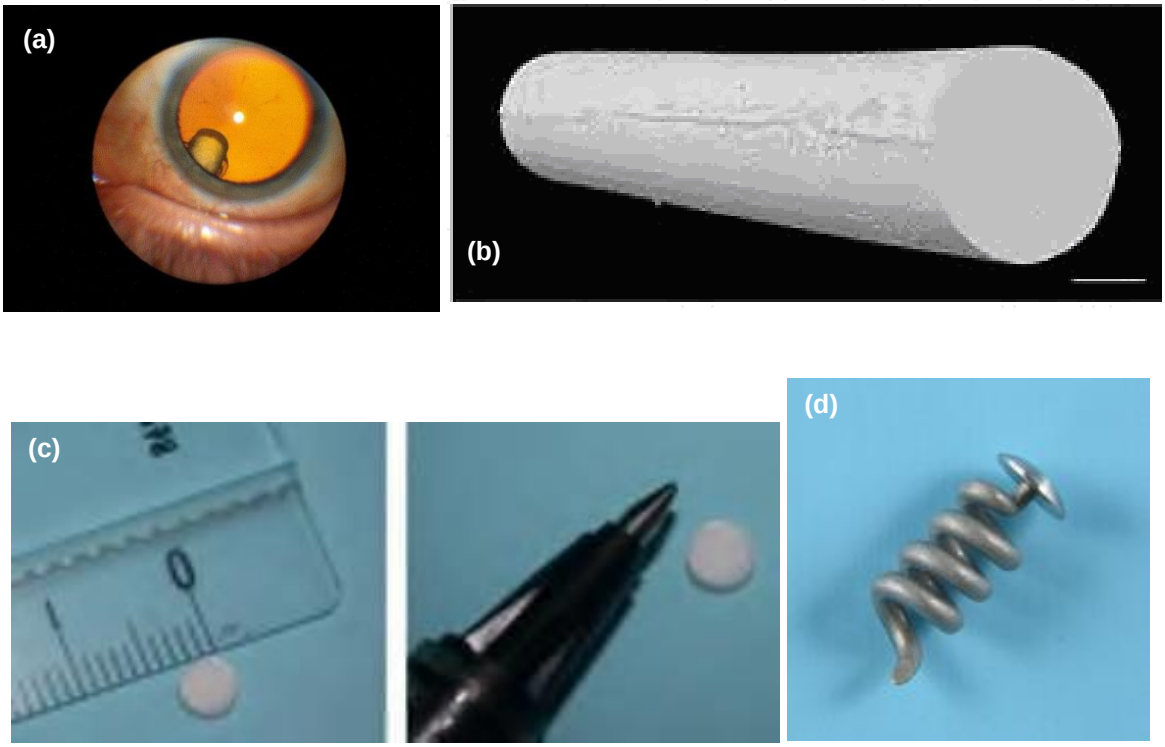

Figure 2.2: Examples of corticosteroid-loaded ocular implants: (a) Fluocinolone implant device in situ through a dilated pupil (Holekamp et al., 2005). (b) Images of photo-crosslinked poly(propylene fumarate)/ polyvinyl pyrrolidine rod-shaped drug delivery systems (Haesslein et al., 2006). (c) Macroscopic view of the developed poly(ε-caprolactone) implants (Ligório Fialho et al., 2007). (d) Intravitreal implant (I-vation™ Sustained Drug Delivery System) (www.surmodics.com)

Table 2.1: Advantages and disadvantages of the current ocular delivery systems (adapted from Amo and Urtti, 2008)

Eye delivery system	Advantages	Disadvantages	Examples of ocular systems for anti-inflammatory agent delivery
Drops, topical gels	- Ease of use and good patient acceptance - Non-invasive	- Resistance encountered to drug penetration across the cornea, aqueous humor and crystalline lens can result in non-therapeutic levels of drug in the posterior vitreous, retina and choroids i.e. Poor ocular bioavailability (Herrero-Vanrell and Refojo, 2001) - Comparatively short duration of action - Ineffective in treatment of posterior segment disorders - Possible ocular and systemic toxicity with frequent administration or high concentrations require frequent instillation of highly concentrated solutions, due to the rapid pre-corneal loss from the eye - Relies on patient compliance	- Ibuprofen-loaded polymeric Eudragit RS100 nanoparticle suspensions (Pignatello et al., 2002a) - Flurbiprofen-loaded acrylate polymer nanosuspensions (Pignatello et al., 2002b)
Systemic administration	- More effective to treat diseases of the posterior segment of the eye than drops	- Administered drugs may fail to by-pass blood–ocular barriers - Systemic toxicity	- Thalidomide and dexamethasone diluted in a saline solution (NaCl, 0.9%) (Rodrigues et al., 2007)
Intravitreal, periocular and subconjuctival injections	- Various acute and chronic posterior segment diseases (i.e. proliferative vitreoretinopathy, endophthalmitis, recurrent uveitis, acute retinal necrosis and cytomegalovirus retinitis) are often treated with repeated intravitreous injections to maintain drug concentrations within the therapeutic window - Improved drug absorption compared to systemically and topically administered agents - Lack of systemic toxicity - safer delivery to the posterior segment of the eye than systemic - Targeted drug delivery	- Multiple intraocular injections are required to achieve high efficacy rates for the treatment of chorioretinal disorders. Frequency of injections increase the risk of cataract formation, retinal detachment, endophthalmitis and vitreous haemorrhage - Low therapeutic index of the majority of the drugs used for posterior segment diseases may necessitate intravitreous injections at drug concentrations close the toxic level for the retina (Herrero-Vanrell and Refojo, 2001) - First-order kinetics (this rapid rise may cause difficulties with toxicity, and drug efficacy can diminish as the drug concentration falls below the targeted range) - Short half-life (few hours) - Poor patient acceptance by patients	- Intravitreal triamcinolone acetonide in balanced salt solution (Dot et al., 2007)
Intraocular perfusion/ Microdialysis	- Allow continuous drug administration into the vitreous cavity and possess the ability to change or stop drug administration at any time	- Permanent access to the intraocular space - risk of intraocular infection and patient discomfort are increased (Haesslein et al., 2006).	
Transdermal therapeutic systems (TTS)	- TTS avoid the peaks and valleys in the drug plasma levels that occur with oral dosing (Myles et al., 2005)	- Frequently do not release the entire amount of the active substance present therein within the time interval recommended for application by the manufacturer. - Disadvantages of systemic administration	- Prednisolone-TTS (Isowaki et al., 2003)

Implants (e.g. nail-like scleral plugs, discs, pellets, rods, sheets, osmotic pumps)	-	Various application sites include the vitreous cavity, the subretinal space, the sclera, and the peribulbar space	-	Device implantation is invasive and with associated ocular complications (retinal detachment and intravitreal haemorrhage)	-	Fluocinolone acetonide tablet (Retisert®)
	-	Biodegradable devices possess inherent advantages over non-erodible systems - as they degrade, they gradually disappear from the site of implantation, eliminating the risk of fibrous encapsulation and the necessity of surgical removal (Haesslein et al., 2006)	-	Non-biodegradable require surgery to harvest the device once is depleted of the drug (risk of ocular complications)	-	Fluocinolone acetonide cylindrical tube (Medidur®)
	-	Increase half-life of the drug and minimize peak-to-trough fluctuations	-	Biodegradable implants generally demonstrate a final uncontrollable 'burst' in their drug release profile	-	Dexamethasone microsized implant (Posurdex®)
	-	Can improve patient acceptance and compliance			-	Dexamethasone-loaded poly(ε-caprolactone) implants (Ligório Fialho et al., 2007)
	-	Drug stabilization			-	Fluocinolone acetate-loaded poly(propylene fumarate)/ polyvinyl pyrrolidine rod-shaped matrices (Haesslein et al., 2006)
Micelles, liposomes, microspheres, microcapsules, nanospheres, nanocapsules	-	Biodegradable microspheres, microcapsules, emulsions, and liposomes offer advantage of being injected into the posterior segment (Haesslein et al., 2006).	-	Risk associated with injections		*Micro- and nanoparticles*
	-	Drug stabilization	-	May impair the clarity of the ocular media if they ultimately become suspended in the vitreous (vitreous clouding) (Haesslein et al., 2006)	-	Ibuprofen-loaded acrylates and copolymers
	-	Increased drug half-life of drugs and decreased injection frequency	-	Formulation stability, particle size uniformity, control of drug release rate, and the large-scale manufacture of sterile preparations are challenges that still require directed investigation (Corcoran, 2006)	-	Ibuprofen-loaded Eudragit RS 100
	-	Micro- and nanoparticles minimize 'burst' release and decrease peak plasma concentrations			-	Flurbiprofen-loaded Eudragit
	-	Localized delivery of drug (RPE cells)			-	Ketorolac-loaded *N*-isopropylamide copolymers
	-	Improved patient compliance and convenience			-	Indomethacin-loaded chitosan-coated PECL particles
	-	Biodegradable polymer nanoparticles as demonstrating significant promise as drug delivery devices for the eye.			-	Piroxicam-loaded pectin
	-	Release of drug can be constant or cyclic over an extensive period, stimulus-responsive (Corcoran, 2006)			-	Piroxicam-loaded albumin (Ludwig, 2005)
					-	Betamethasone phosphate-loaded poly(lactic acid) (Sakai et al., 2006)
Cell encapsulation	-	Long-lasting and continuous expression of the given protein (avoiding repeated injections) without genetic alteration of the host tissues	-	Side effects: invasive method with the complications related to the surgical insertion and removal		
	-	Targeted delivery	-	Patient acceptance yet to be established		
	-	Easy retrieval of the implant when desired (making the treatment reversible)				
	-	Potentially improved patient compliance				
Iontophoresis (trans-scleral)	-	Non-invasive method and easy to use	-	Complicated procedural requirements and limited application to ionizable drugs (Haesslein et al., 2006)	-	Coulomb-controlled iontophoresis of acetylsalicylic acid (Voigt et al., 2002; Myles et al., 2005)
	-	May combine with other drug delivery systems	-	No sustained half-life - requires repeated administrations		
	-	Ability of modulate dosage (less risk of toxicity)	-	Side effects include mild pain in some cases		
	-	Good drug penetration to anterior and posterior segment of the eye	-	Risk of low patient compliance because of the frequent administrations that may be needed		
	-	Good acceptance by patients, no risk of infections or ulcerations				
	-	Broad applicability - can deliver a range of drugs or genes to treat several ophthalmic diseases in the posterior segment of the eye				

2.3. Alternative Approaches to Ocular Drug Delivery

The design of a progressive system begs a concerted consideration of alternative approaches for enhanced intraocular drug delivery.

2.3.1. Metabolism-based approaches for the design of ophthalmic delivery systems

2.3.1.1. Chemical delivery systems

A chemical delivery system (CDS) describes a therapeutic device where there is the incorporation of predictable metabolic activation (Bodor, 1988). CDSs for site-specific therapy have demonstrated success for drug delivery to the brain as well as for the eye (Bodor and Brewster, 1983). These systems possess an in-built propensity to convert from the inactive CDS to the active CDS upon recognition of enzymatic processes (often incorporating more than one bioactivation step) associated exclusively or preferentially at the target tissue. Ultimately cognisance must be maintained of the fact that barrier transport and site-specific delivery has multifunctional requirements (Bodor, 1984; Visor, 1994).

2.3.1.2. The soft drug approach

Another avenue which exploits a metabolism-based approach is the use of soft analogues in the design of ophthalmic agents. This is a class of compounds that are close structural analogues (isosteric, isoelectronic) of known active drugs or endogenous substances that differ from the lead compound in that they possess an in-built, specific metabolic (preferentially hydrolytic) ‘handle’ (functional moiety for metabolic transformation) in their structure that provides a one-step pathway for controllable detoxication, which occurs rapidly following receptor interaction without the formation of reactive intermediates. This principle has been applied for the creation of soft corticosteroids (Visor, 1994; Bodor and Buchwald, 2005).

2.3.1.3. Exploitation of transporters in the eye

Traditional approaches to improve ocular bioavailability have generally looked at chemical modification of the drug such that the desired solubility and lipophilicity is attained. Purportedly, transporter-targeted modification of the drug is considered to be a more rational approach. Transporters are membrane-bound proteins present in various ocular tissues, exercising a key role in active transport of nutrients across biological membranes. Transporters located in the epithelia of the cornea, conjunctiva and retina may be amenable to bind and transport specific-targeted ligands attached to drug moieties (Gaudana et al., 2010).

Two types of transporter systems are of interest in ocular drug delivery: efflux transporters (belonging to the ATP binding cassette superfamily) and influx transporters (belonging to the solute carrier superfamily).

Transporter-targeted prodrugs have thus been investigated and developed following the identification and description of these transporter superfamilies on ocular tissues in order to enhance of ocular absorption of a poorly permeating parent drug. Prodrugs are recognized by the membrane transporters as substrates resulting in their translocation across the epithelia (Gaudana et al., 2010). Further research is required in this area due to variabilility in the presence, type or amount of transporter of interest, which may also vary with cell lines generated, compared to *in vivo*.

2.4. Considerations for the Design of Bioresponsive Systems in Ocular Drug Delivery

During the past century we have seen the institution of polymers in elementary drug delivery functions for the creation of controlled release systems, but with the dawn of the new millennium, progressive drug delivery strategies are the key for the enhanced therapeutic management of the patient - we want polymeric drug delivery systems that are intelligent and capable of adapting to their environment to ensure an optimization of their behavior or that of the system of which they form an intrinsic component.

Nature is constantly providing solutions; various natural systems embody stimulus-responsive mechanisms, which we as pharmaceutical scientists ultimately embrace. A case in point: using sea cucumber skin for design inspiration, scientists have developed a new material that may improve treatment for Parkinson's disease, stroke and spinal cord injuries (Figure 2.3). The research is published in the journal *Science* (Capadona et al., 2008). The material, which resembles the skin of the sea cucumber and can switch between rigid and flexible states, may purportedly be used in the future in biomedical implants ‘as a protective sheath around brain microelectrodes, which would be stiff when implanted but could then become flexible, reducing the impact on surrounding tissue’ according to AAAS, publisher of *Science* (Capadona et al., 2008).

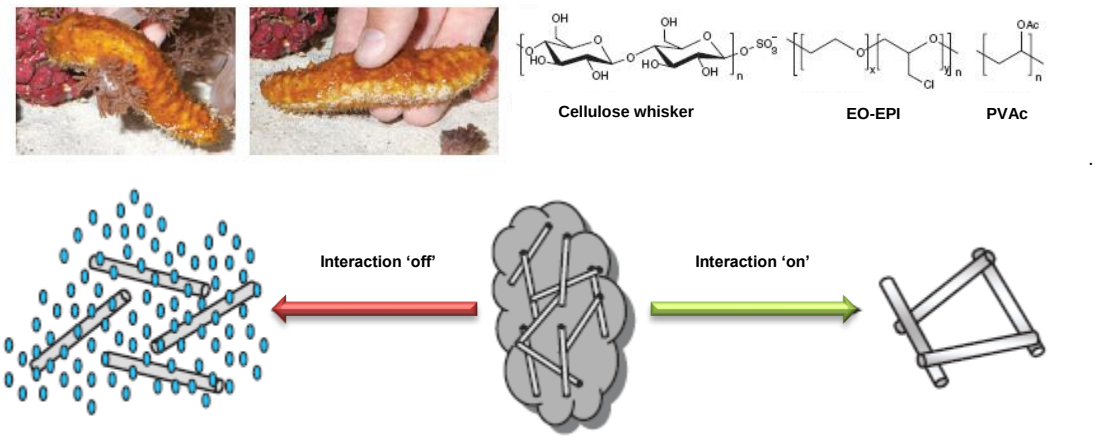

Figure 2.3: Sea cucumbers inspired the design of stimuli-responsive polymer nanocomposites with adaptive mechanical properties (Capadona et al., 2008)

To further elaborate on the stimulus responsive approach, one can delve into the 'Degrees of Intelligence':

1. A basic response implicates a polymer receiving a stimulus from its environment that involves the adaptation of one of its properties according to the intensity of the stimulus.
2. The sophistication of an intelligent system supercedes this through interpretation of the property changes of the smart polymer. It may even comprise a stimulus-emitting material and an adaptive material that controls the adaptations of a certain property to counterbalance the stimulus and to maintain a stable state of the system (Biron, 2005).

The universal intelligent polymer does not exist. However, in this investigation several approaches based on the intelligent polymer principle (Figure 2.4) were applied to generate an innovative intelligent polymeric system.

Figure 2.4: The intelligent polymer principle for responsive drug release

An increasingly broad panoply of stimulus-adaptation couples (Table 2.2) are under development to fulfil all the biotechnological and medical sectors. Well-established and employed couples include heat-shrinkage or heat-color, whereas others possess very specific applications or are still in early phases of development leading to more concrete uses (Biron, 2005).

Table 2.2: Coupled stimuli and responses (adapted from Biron, 2005)

Stimulus	Response/ Adaptive property
Temperature	Color
	Shape
	Rheology
	Swelling/shrinkage in a liquid
	Adhesive strength
Chemical	Deformation
	Color
	Release of active product
Mechanical Stress	Colour
	Shape
	Chemical property
	Electrical property
	Solubility of an aqueous solution
	Rheology
Electric	Shape
	Color
	Rheology
Light, UV	Colour
	Deformation
	Dichroism
	Shape
	Permeability
Magnetic	Mechanical properties
	Rheology

In recent years, intelligent polymers have been promulgated as valuable tools in biotechnological applications including controlled drug release, immunodiagnostics, and gene therapy. Intelligent or stimuli-responsive polymers mimic biological systems in a crude way in that they exhibit notable reversible physical changes in response to an external stimulus such as temperature, pH, ionic strength, solvents, electrical or magnetic field, radiation, redox potential, or concentration of biomolecules (e.g. electrolytes, glucose). These polymers may be in solid hydrogel form, immobilized on solid surfaces, or existing as water-soluble chains. A stimulus, proposedly an increase in temperature over a certain critical value causes a response, which can be manifold: dissolution/ precipitation, degradation, drug release, change in hydration state, swelling/ collapsing, alteration of hydrophilic/ hydrophobic balance (modification of the polymeric chains from water-soluble coils to water-insoluble globules in aqueous media), change in shape, conformational change and micellization;

often with ensuing release of an incorporated bioactive molecule (Pişkin, 2004; Schmaljohann, 2006).

The consequent advantages of stimuli-responsive systems in drug delivery have fuelled investigation into the fundamental and scientific exploitation of non-covalent supramolecular interactions in polymer matrices. This concept formed the foundation for the design and implementation of functional polymer blends. Rather than designing and synthesizing novel, complex functional macromolecules 'from scratch' (*de novo*), minor fractions of functional polymers or additives are blended with inert matrix polymers in order to create (employing specific crosslinking and/ or nanotechnological processing protocols) new and novel stimuli-responsive material platforms with unique or unusual matrix properties (Barbu et al., 2006).

Zeimer and Goldberg (2001) have developed a method for local targeting of drugs in the eye based on a straightforward mechanism. The method, called light-targeted delivery (LTD), implicated the encapsulation of a drug in heat-sensitive liposomes, ensued with intravenous injection, and ultimate release of their content at the site of preference by non-invasively warming up the targeted tissue with a light pulse directed through the pupil of the eye. The temperature needed for the phase transition and release was 41°C (within physiological range) (Zeimer and Goldberg, 2001).

The institution of stimuli-responsive systems with a specific affinity for the implanted tissue has also been of considerable interest in developing a drug delivery platform. Substantial advances have been made towards the understanding of the structure and biochemistry of mucins. The exploitation of specific structural or chemical features for the development of drug delivery platforms represents a new area of research; advances in this area may lead to materials with selective affinity for the corneal tissue. Natural limiting factors present obstacles for its institution, namely the low concentration of mucins on the ocular tissue and the high mucin turnover rate (Barbu et al., 2006).

Consideration of imprinted polymers for biomedical applications, including drug delivery, is on the rise. Feedback-regulated drug delivery is proposedly attainable by a combination of imprinted, stimuli-sensitive materials that would allow high drug-loading-capacity molecularly imprinted polymers (MIPs) to respond to slight changes in external stimuli (e.g. pH, temperature, ionic strength, concentration of biomolecules) or to furnish a response in the presence of specific receptors and/ or ligands. The resultant modulation in the affinity of the network for the target molecules (bioactives) provides a regulatory capability for the release process (Barbu et al., 2006).

It is essential to conceptualize an autofeedback polymeric platform, employing biodegradable polymers. The design of the platform hinges on its degradation, which is to occur via a selected internal signal, possessing a lifetime of adequate duration, for evolution of the sought after degradation (Yui et al., 1992).

In this investigation this forward-thinking approach was proposed to be exemplified through the implementation of a two-way communication system between our bodies and the delivery platform to create an innovative drug delivery system that recognizes a biochemical process that is characteristic of a disease and is then capable of responding via drug release. To achieve this intelligence in design, the delivery platform is based on novel stimulus-responsive polymeric materials. Since inflammation is a characteristic embodiment of most posterior segment disorders of the eye, it was pinpointed as the stimulus of interest.

Thus, of fundamental significance in this research was the discovery of novel inflammation (stimulus)-responsive materials for implantable drug delivery. Yui et al. (1992) prepared a biodegradable hydrogel of HA crosslinked with glycidylether and investigated its degradation by hydroxyl radicals *in vitro* and by inflammation *in vivo*. *In vitro*, hydroxyl radicals produced by Fenton's reaction of hydrogen peroxide (H_2O_2) and iron sulfate ($FeSO_4$) induced a rapid yet limited degradation of the crosslinked HA gels. Lipid microspheres which could potentially serve as drug microreservoirs were incorporated in a crosslinked HA matrix (Yui et al., 1993). These microspheres could be released during degradation of the matrix. Implantation *in vivo* highlighted the degradability of the HA gel in response to inflammation. Therefore, crosslinked HA gels may be promising devices as 'inflammation-responsive degradable matrices for implantable drug delivery'.

2.4.1. The stimulus: Inflammation

In conceiving this research, it is of pertinence to establish a mechanistic understanding of the inflammatory process and how this process can be simulated *in vitro* and replicated *in vivo* in an appropriate animal model to definitively establish the efficacy of a delivery system created for anti-inflammatory applications.

Inflammation is not a singular event; instead it is the composite of 'multiple immune responses elicited against a particular stimulus'. It may be compared to a 'battle' in which the immune system uses every weapon in its 'arsenal' in the hope that at least one of them will be effective. Among the many immune responses contributing to inflammation are the following (Doan et al., 2007):

- Chemoattraction and activation of neutrophils, phagocytes, and lymphocytes
- Complement activation
- Degranulation of mast cells, basophils and eosinophils to release inflammatory mediators
- Heightened natural killer (NK) cell activity
- Increased body temperature
- Increased vascular permeability
- Infiltration of tissues by fluids (containing antibodies and complement) and cells (particularly phagocytes and T lymphocytes
- Secretion of acute phase proteins
- Secretion of pro-inflammatory cytokines and chemokines
- Secretion of type 1 interferons (IFN)

The presence of microbial products (e.g. LPS) at the site of injury and infection induces local phagocytes to release a variety of pro-inflammatory cytokines (e.g. interleukin-1, IL-6, IL-8, IL-12, and tumor necrosis factor: TNF) that 'recruit additional players to the immunologic team' (Figure 2.5). Pro-inflammatory cytokines such as TNF-alpha and IL-1 from activated phagocytes cause increased vascular permeability and stimulate increased local blood flow to the affected area. IL-6 promotes the synthesis and release of C-reactive protein (CRP) by the liver. CRP, whose levels slowly elevate within 24 to 48 hours of infection, readily binds to phosphocholine (a molecule expressed in some microbes) and acts as an opsonin. CRP is one of a set of serum proteins known as acute phase proteins that inhibit the spread of infectious organisms and also include complement components, type I IFNs, fibronectin, and protease inhibitors. IL-12 stimulates NK cell activity, resulting in increased production of IFN-gamma. Large numbers of neutrophils are drawn to sites of inflammation and infection, attracted by chemokines secreted by activated phagocytes (e.g. IL-8) and by anaphylatoxins (e.g. C5a, C4a, C3a). Their numbers increase rapidly during infection and they are the most numerous lymphocytes infiltrating inflammatory sites. Elevated neutrophil levels in the blood are evidence of infection in the body and are the major contributors to the clearance of infectious organisms and cellular debris (Doan et al., 2007).

Inflammation continues until the stimulus is eliminated and healing begins. Sometimes, inflammatory stimuli cannot be eliminated, and the inflammation becomes chronic (e.g. chronic intraocular inflammation as seen with uveitis).

Most of the actual destructive actions that occur during inflammation are carried out by the elements of the innate immune response, such as complement and phagocytic cells. Inflammation is an excellent example of the manner in which the innate system and adaptive immune system are complementary, the adaptive system acting to focus and intensify the innate response. Antibodies, in initiating the classical pathway of complement activation, can target the resulting inflammation at specific microbes, molecules or sites. Anaphylotoxins (C3a, C4a, and C5a) resulting from complement activation can act as chemical signals promoting vascular permeability as well as attracting leukocytes to the site and activating them (Doan et al., 2007).

Injection of LPS is a documented approach for induction of intraocular inflammation in an animal model for evaluating the efficacy of an anti-inflammatory delivery system. LPS instigates numerous inflammatory changes including recruitment of macrophages, serous and hemorrhagic exudation, disruption of the BRB, and development of epiretinal membranes (Ruiz-Moreno et al., 1992). The diverse physiological and pathological functions of prostaglandins within the eye have been introduced (i.e. disrupting the BAB and BRB, increasing vascular permeability, promoting leukocyte migration, and stimulating angiogenesis). The ciliary body, iris epithelium, RPE and specific cells in the retina all express COX enzymes and are therefore potential originators of endogenous prostaglandin production (Chin et al., 2001; Ju et al., 2002). Prostaglandins are the presumed cause of cystoid macular edema in uveitis (Miyake and Ibaraki, 2002). As highlighted, NSAIDs are potent inhibitors of COX enzymes and consequently the synthesis of prostaglandins, which has been demonstrated in an animal model of uveitis (Barañano et al., 2009).

As introduced in Chapter 1, as a result of the aforedescribed inflammatory cascade, it is the chemical mediators released, such as arachidonic acid metabolites, proteolytic enzymes, and oxygen metabolites that are responsible for the tissue damage evident in ocular inflammatory conditions, such as uveitis. Such chemical mediators became the pivotal focus of this investigation for the fabrication of an inflammation-responsive drug delivery system.

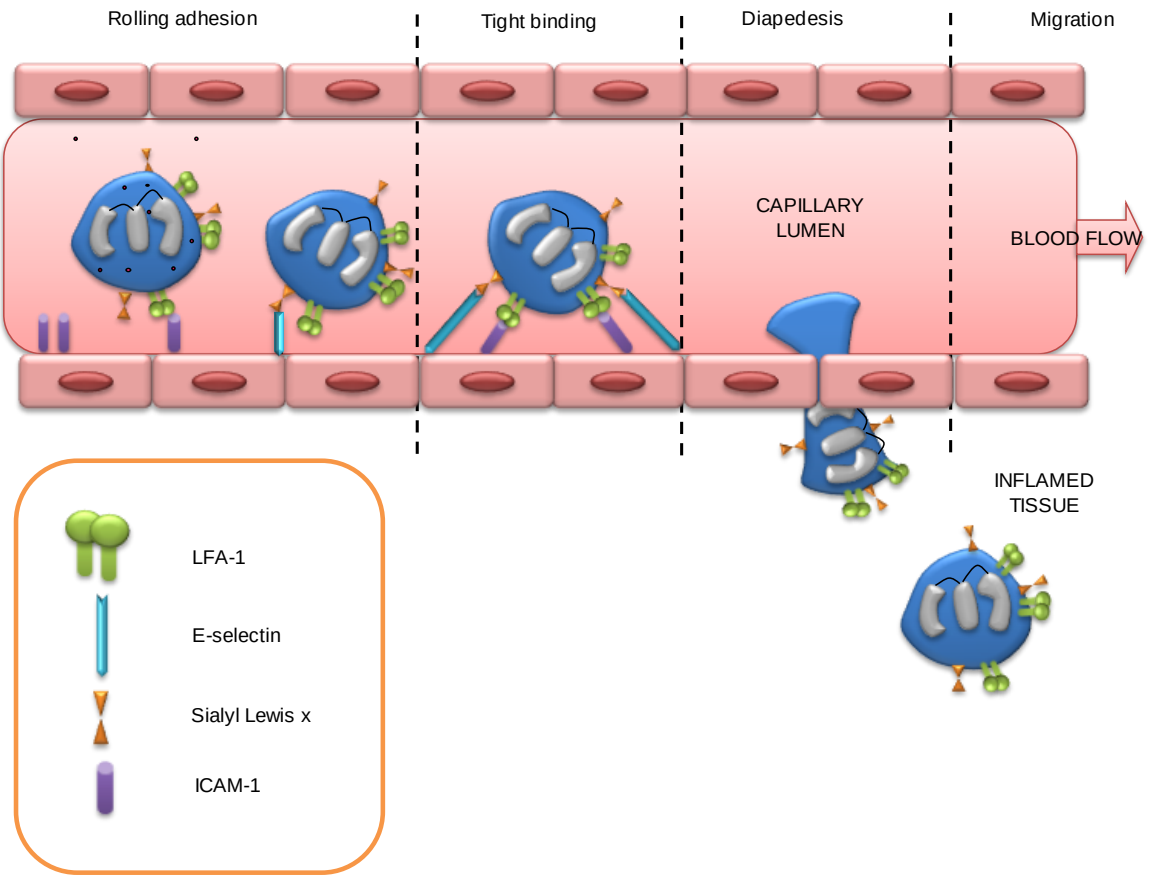

Figure 2.5: Leukocyte migration in response to an inflammatory stimulus (e.g. response induced by LPS as an animal model of uveitis) in the presence of adhesion molecules as directors of leukocyte migration. Activated leukocytes migrate from the blood vessels by a four-step process known as extravasation. 1. Rolling adhesion: P-(CD62P) then E-selectin (CD62E) expressed by endothelium in response to TNF-α or to LPS interacts with sialyl Lewis x on leukocytes causing them to roll along the endothelial surface. 2. Tight binding: interaction between leukocyte integrins (e.g. LFA-1, Mac1) with endothelial ICAM-1 causes leukocytes to tightly adhere to the endothelium. 3. Diapedesis: a process in which endothelial-bound leukocytes enter tissues underlying the endothelium. 4. Migration: leukocytes migrate to the site of microbial invasion, attracted by chemokines (adapted from Doan et al., 2007)

2.4.2. Selection of an implant type

As the implant is built, an initial point to stress is the issue that a biodegradable, bioabsorbable device such as the one exemplified in this research will generally deliver drug for only a few weeks or months, whereas non-biodegradable devices can deliver the drug for a year or more. However, this does not imply that a device that can deliver drug for long periods is necessarily superior to a short-acting device. The inherent consideration underlying device success is that a 'sufficient dose for a reasonable duration' is attained for the targeted disease, where 'sufficient dose' is defined as the steady-state concentration of drug required to cause a desirable therapeutic effect in an appropriate animal model then humans, and 'reasonable duration' is the time needed to either be curative or to ameliorate and maintain suppression of disease manifestations (Weiner and Marsh, 2008). In the case

of a bioabsorbable stimulus-responsive device, an aggressive acute disease state would dictate a shorter lifetime for the device; a chronic low-degree/ residual disease state would mean a longer lifespan for a device of the same weight.

2.4.3. Selection of bioresponsive polymeric platforms for componential implant development

Polymers have become an indispensable part of drug delivery systems, be it conventional or novel drug delivery. The proposed polymeric platform should fulfill the prerequisites of (Barbu et al., 2006):

1. Sufficient loading capacity to ensure therapeutic doses
2. Ability to penetrate to and/or reside at the desired site of action, and release the active in a controlled manner
3. Lack of toxicity, biocompatibility and biodegradablity - the latter particularly for intraocular administration
4. The carrier should not impede vision (tolerability and acceptance by the patient are critical factors)
5. Mucoadhesivity (a potential consideration for the nanosystem to be incorporated)
6. Ability to enhance drug penetration through ocular barriers in intraocular ailments where the drug delivery system is placed/ implanted on the ocular surface or within the ocular tissues
7. Bioresponsive capabilities.

The polymeric materials to be employed may be natural or synthetic, and the ultimate architecture would be critical in determining the controlled release of the active. Notably, increasing the crosslinking density of a polymeric network lowers diffusion rates, thereby improving the sustained release properties of the system, but reducing mucoadhesive capabilities. To effect sustained release from hydrophilic hydrogel networks that are freely permeable to water, strong association of the drug with the macromolecular chains is recommended (Barbu et al., 2006).

Essentially the platform would be founded on the art of matrix erosion, changes in hydration/ gelling area, and alteration of chemical and ionic interactions. It would therefore be a self-correcting system that leads to carefully controlled erosion (on exposure to vs. removal of the stimulus) as well as a predictable release of the active ingredient incorporated within the therapeutic matrix.

Diverse polymeric materials have been investigated for ocular drug delivery. Thiomers, which can form covalent disulfide bridges with cysteine-rich subdomains of mucins, have been examined as materials for mucoadhesive drug delivery. Ocular inserts formulated from thiolated poly(acrylic) acids have illuminated promise in tests on human volunteers (Bernkop-Schnurch, 2005). Other non-biodegradable bioadhesive materials for drug delivery have been investigated, such as copolymers based of vinylpyrrolidone and/or (meth)acrylic acids; poly(dimethylsiloxane) and poly(*N*-isopropyl acrylamide) interpenetrating networks; and, poly(amidoamine) dendrimers (Barbu et al. 2005; Liu and Sheardown, 2005; Sultana et al., 2005; Vandamme and Brobeck, 2005).

Recent research has concentrated on the institution of biodegradable polymers, which are commonly of natural origin. Among the biodegradable polymers that have been investigated for intraocular drug delivery are gelatin, albumin, polyortho-esters, polyanhydrides, and polyesters, particularly poly(lactic acid) and poly(glycolic acid), and copolymers of lactic and glycolic acids (i.e. PLGA) (El-Sayed et al., 2005; Twaites et al., 2005; Barbu et al., 2006; Qiu and Bae, 2006).

Work on biodegradable crosslinkers that are commonly used for the construction of three-dimensional hydrogel networks has been reviewed (Thomas et al., 2005). Materials based on poly(lactic) and poly(glycolic) acid, or their copolymers and derivatives, have been formulated as implants, as micro-/ nanospheres and nanocapsules and as films for glaucoma treatment (Andrieu-Soler et al., 2005; Fialho and Cunha, 2005; Huang et al. 2005). In the described materials, the mechanism of drug release is bulk erosion of the matrix following the cleavage of the polymeric chains via autocatalytic hydrolysis (Oh et al., 2006). Low molecular weight polymers tend to degrade rapidly; copolymers such as PLGA degrade faster than the corresponding homopolymers. These materials are particularly suitable for implantable devices or injectable micro/ nanospheres (Yasukawa et al., 2005).

Poly(anhydrides) and poly(orthoesters) have demonstrated promising characteristics, the controlled release properties being dominated by surface degradation (rather than drug diffusion) (Ha and Gardella et al., 2005). Poly(anhydrides) are a unique class of polymers for drug delivery combining near zero-order drug release with biocompatibility and relatively rapid *in vivo* biodegradation. Further, the release rate from a polyanhydride-fabricated vehicle may be significantly altered by simple changes to the polymer backbone (Jain et al., 2005). Bioerodible poly(ortho esters) have demonstrated excellent ocular biocompatibility and sustained controlled drug release (Heller, 2005). As reported, poly(*ε*-caprolactone) rod-

shaped implants loaded with triamcinolone acetonide displayed good tolerability by retinal tissue and released drug over a period of at least 4 weeks (Beeley et al., 2005).

Distinctly, hydrophilic polymers of natural origin (chitosan, gellan, scleroglucan and HA) are non-toxic, biocompatible, biodegradable, and significantly improve the bioavailability of the active (Coviello et al., 2005; Liao et al., 2005; Prabaharan and Mano, 2005). In particular, chitosan (essentially a cationic polysaccharide copolymer of 1,4-[2-amino-2-deoxy-*β*-D-glucopyranose] and 1,4-[2-acetamido-2-deoxy- *β*-D-glucopyranose]) has received increasing attention (Bodnar et al., 2005; Prabaharan and Mano, 2005). Grafting of chitosan with poly(*N*-isopropyl acrylamide) formed a thermally-responsive ophthalmic delivery vehicle for sustained release (Cao et al., 2005). Chitosan ocular implants are regarded as safe and effective for the release of drug into the implanted tissue (Barbu et al., 2006). Because of the ability of chitosan nanoparticles to penetrate corneal and conjunctival epithelia; a greater affinity of chitosan for certain types of conjunctival cells has been proposed (De Campos et al., 2004), as further elaborated on in this work in Chapter 3. Other modified polysaccharides, such as chondroitin-6-sulphate-*graft*-poloxamer copolymer, have been investigated as transparent *in situ* gel-forming drug carriers (Yoo et al., 2005).

The proposed implantable device would be formulated on the polymer matrix principle, fixated with an anti-inflammatory agent-loaded NS. It would be engineered with a combination of biodegradable, biocompatible polymers, which provide superior mechanical strength and restricted swelling. These are not inherent properties of commonly employed biodegradable and biocompatible polymers; such properties would thus be induced through synthetic approaches. Accordingly, this study proposes the application of novel crosslinking technology to modify the physicochemical and physicomechanical characteristics of the polymers to attain increased control over the dissolution and erosional behavior of the matrix architecture. This may be achieved through the institution of carefully selected chemical crosslinkers, rendering the polymer chains more rigid through the introduction of chemical bonds between the monomers.

2.4.4. Potential polymeric systems possessing inflammation-responsive capabilities and proposed degradation mechanisms of the polymers implicated in BPM fabrication

The first step in the pragmatic design of an I^3 proposes the incorporation of a two-way communication between the body and the polymeric delivery platform to create a delivery system that recognizes biochemical processes pertaining to a disease and then responds via a complex in-built mechanism to effect polymeric erosion with resultant drug dissolution and release. Thus the platform on which the I^3 is based would incorporate novel stimulus-

responsive polymeric materials for implantable drug delivery. The premise is the design of BPMs that erode and release the incorporated NSAID and antibiotic in a fashion responsive to a stimulus, such as the highly reactive intermediates including superoxide (O^{2-}), H_2O_2, chloramines and hydroxyl radicals ($OH^{\cdot}$) that are released from activated leukocytes both *in vitro* and during acute and chronic intraocular inflammatory reactions *in vivo* (Hawkins and Davies, 1996). Thus, release of incorporated drugs from the bioresponsive system will be individualized and synchronized directly with the needs of the patient, in other words, anti-inflammatory agent and/ or antibiotic release from the implant would correlate with the presence (increased release) or absence (decreased release) of inflammation experienced by that patient on a particular day. Polymers considered for their incorporation within the BPMs for their potential inflammation-responsive capabilities are elaborated on in the subsequent discussion.

HA, a large and ubiquitous polysaccharide, was first discovered by Meyer and Palmer in 1934, with diverse biological roles, including acting as a vital structural component of extracellular matrix and as a key instigator of leukocyte adhesion and migration (Tammi et al., 2002; Zhao et al., 2002). It is a long polysaccharide comprising repeating disaccharide units of N-acetylglucosamine and D-glucuronic acid. The HA molecule possesses unique rheological properties, enabling it to behave as a viscoelastic gel even at low concentrations. Its wide distribution in the body is especially evident in the vitreous humor of the eye as elaborated earlier, synovial fluid of joints, and the umbilical cord. It is a general constituent of the extracellular matrix together with collagen, chondroitin sulphate and other glycosaminoglycans where it is able to support cell and tissue growth. Because of its hydrophilic nature and viscoelasticity, it is able to retain the tonicity and elasticity of the tissue components in which it is incorporated. The combination of its physicochemical properties, biocompatibility, and non-immunogenicity, consolidate it as a molecule for use in a diverse range of clinical applications. Thus in addition to its applications in wound healing, prevention of post-surgical adhesions, correction of dermal deformities, it has also seen increasing attention for institution in controlled drug delivery (Zhao et al., 2002). Extensive cable-like structures or HA fibrils can be generated in response to various stimuli such as inflammation, viral infection, hyperglycaemia and endoplasmic reticulum stress, which possess specific leukocyte-binding properties not attributed to free HA (Day and de la Motte, 2005). Day and de la Motte (2005) propose that the presentation of HA cables in a crosslinked form leads to receptor clustering on leukocytes and that, although this is proadhesive specifically for non-activated mononuclear leukocytes, including monocytes, T and B lymphocytes, it is likely to be counter-inflammatory. The biologically-observed free radical degradation (i.e. inflammation-responsive degradation) of HA is appreciated (Yui et al., 1992; 1993); however

it is this rapid degradation (which is also observed in the presence of enzymes such as hyaluronidase) that precludes the isolated use of the native polymer for certain applications, such as drug delivery. It is thus a prerogative of this investigation to design a stable matrix, incorporating HA; this can be effected by crosslinking of HA molecules, however, it is imperative that the inflammation-responsiveness of the system is not compromized. The selection of candidate polymers for inclusion in the BPM necessitates careful consideration of the chemical make-up of said polymers. The reaction of HA with hydroxyl radicals has been reported to ensue preferentially via abstraction of the hydrogen on the carbon adjacent to the carboxyl group in the glucuronic acid unit - this leads to glycosidic cleavage. Hydroxyl radicals boast the shortest life time among active oxygen species due to their high reactivity (Yui et al., 1992). Crosslinked HA gels can be degraded specifically by generated hydroxyl radicals in the presence of other oxidizing agents; the degradation can take place in a pulsatile (stimulus-sensitive) mode. In order to control the rate of drug delivery in response to the biological need of a patient, it should be possible to discontinue the degradation of the drug-loaded polymer matrix when the biological requirement is eliminated. The observed degradation characteristics of the crosslinked HA gel, in principle, highlights its suitability for application in an auto feed-back drug delivery system.

Alginate, polygalacturonate, and methylcellulose (polyacetals), and poly (ethylene) oxide are also susceptible to free radical-induced degradation. Such polymers are conjoined by ether and acetal (i.e. glycosidic linkages). Their monomers are linked wholly or mainly by -C-O-C- bonds to form polyethers or polyacetals. This classification encompasses the uronic acids, which are a class of sugar acids with both carbonyl and carboxylic acid functional groups, where the terminal carbon's hydroxyl group has been oxidized to a carboxylic acid. For example, the structure of alginate is a polymeric uronic acid consisting largely of D-mannuronic acid residues. The proposed mechanism is based on a known disproportionation of ether free radicals, which is induced by hydroxyl radicals (in periodate solutions). Scission of the polymeric chains could occur solely by ether-type disproportionation, or by glycol cleavage once ring opening has occurred due to disproportionation in which the ring oxygen atom is implicated. The susceptibility of glycuronans to periodate degradation might be in part due to the known ease of formation of free radicals from alpha-hydroxy acids by removal of H-5 followed by ring opening and glycol fission by periodate (Scott and Tigwell, 1973). Uronic acids (e.g. alginate) should be susceptible to attack by hydroxyl radicals, and the especially rapid depolymerization of alginate and polygalacturonate would occur (Figure 2.6). Polyacrylate could give rise to $-O_2C-C^{\cdot}-C-$, but there is no disproportionation reaction comparable to that of stage 3 (Figure 2.6), which disrupts the polymer, and decarboxylation, recombination, and termination steps are anticipated to intervene (Scott and Tigwell, 1973).

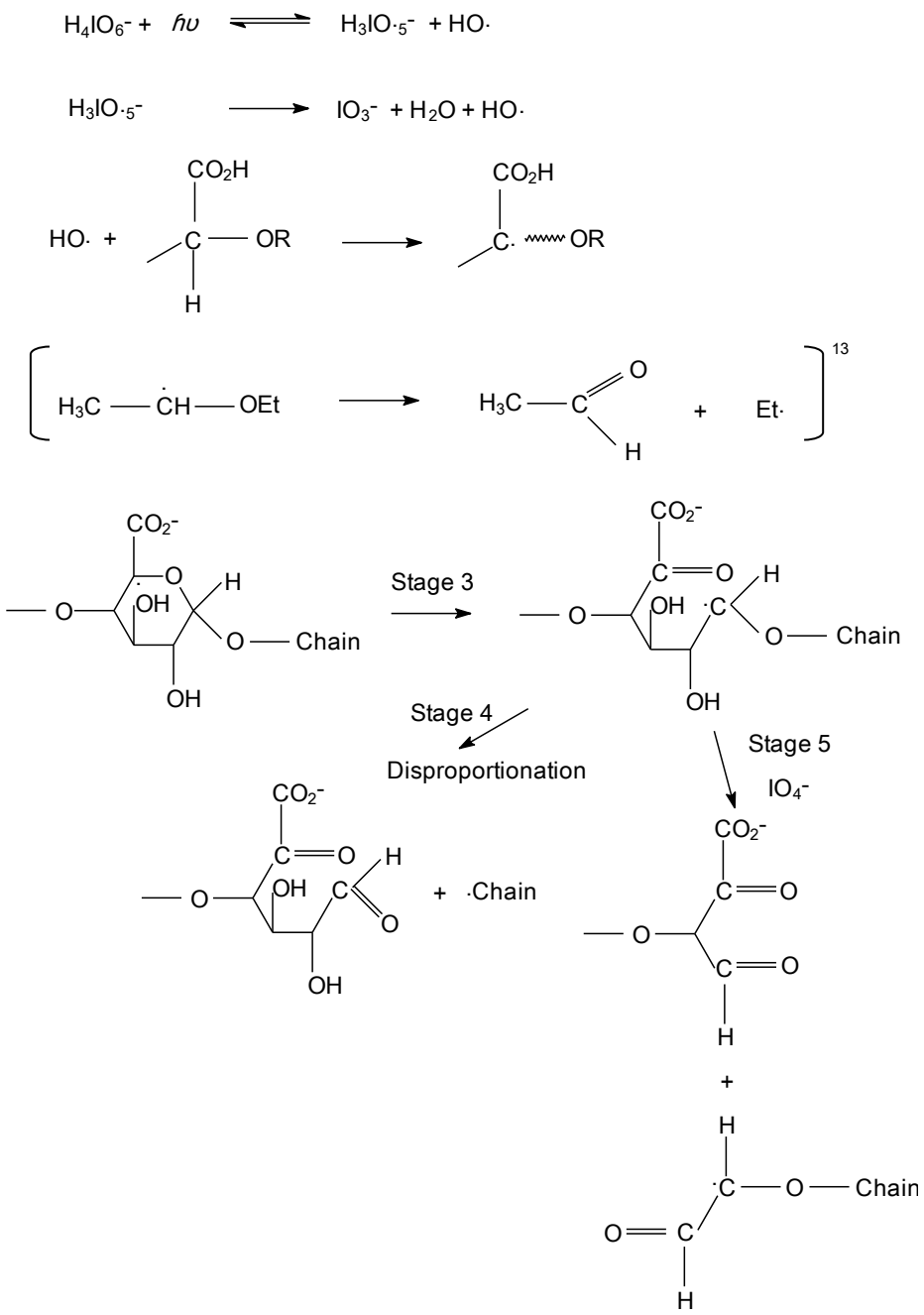

Figure 2.6: Free radical degradation of HA and other uronic acids (e.g. alginate). Stages 1 and 2 establish the feasibility of the route to the glycuronan free-radical. The disproportionation of the ethyl ether free-radical (in parenthesis) is the prototype reaction of those shown in Stages 3 and 4, which could, in principle, be undergone by any polysaccharide. Stage 5 demonstrates the possibility of chain scission, specific to periodate and glycol-containing polysaccharides, secondary to disproportionation involving the ring oxygen atom (Scott and Tigwell, 1973)

The free radical degradation of chitosan has also been described (Ulanski and von Sonntag, 2000). Hydroxyl radicals react with low-molecular-weight carbohydrates by abstraction of

carbon-bound hydrogens (Figure 2.7). One of the most important radical-induced reactions of oligo- and polysaccharides is the scission of the glycosidic bond. The initiated degradation would ultimately depend on the molecular weight and conformation of the macromolecules and, to a certain extent, on their concentration (Ulanski and von Sonntag, 2000).

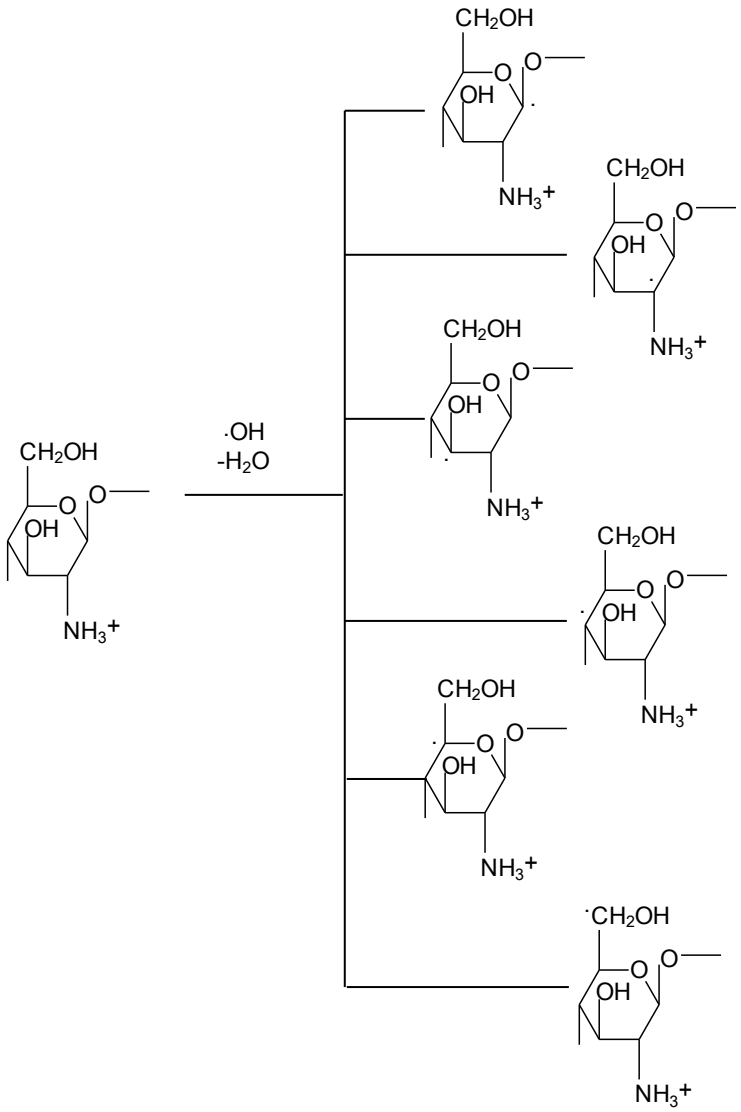

Figure 2.7: Chain scission of the polycationic chitosan in the presence of hydroxyl radicals (Ulanski and von Sonntag, 2000)

2.4.5. Chemical modification of the inflammation-responsive polymers

As described, HA possesses a bioresorbable nature and ease of degradation *in vivo* due to the action of the enzyme hyaluronidase and free radicals, however, this ultimately restricts its use for applications where a more enduring effect is required. Thus, modification of HA while maintaining its bioresponisive potential is necessary so as to increase its residence lifetime

and extend its potential applications (Zhao et al., 2002). HA essentially has four reactive groups (acetamido, carboxyl, hydroxyl and the reducing end) available for crosslinking to itself or other polymers. Researchers have derived a variety of crosslinked HA derivatives employing diverse crosslinking agents possessing enhanced residence time. Chemical modification is the most common means and can be divided into chemical derivatization and chemical crosslinking. Total or partially esterified HA can be produced by chemical derivatization of the carboxyl group of the polymer with an alcohol. The properties can be further tailored by the degree of esterification. The exploitation of chemical crosslinking yields strong hydrogels employing crosslinkers such as divinyl sulfone, polyepoxide and gluteraldehyde. Crosslinking the hydroxyl groups on the HA molecules enhances their biostability and other physical properties. Institution of water soluble carbodiimide purportedly instigates crosslinking of HA via reaction between the carboxyl and hydroxyl groups of HA, as well as available amine groups. Furthermore, the reaction between HA and biopolymers and synthetic polymers to form stable conjugates has been reported. Another common crosslinker possessing a high reactivity and good performance as a biostability and mechanical property enhancer is expoxide (e.g. 1,4-butanediol diglycidylether, 1,4-bisepoxybutane, and polyethylene glycol diglycidyl ether), which reacts with carboxyl and hydroxyl groups (Zhao et al., 2002). A pertinent observation is that an intricately crosslinked network can be assembled through crosslinking between both carboxyl/ carboxyl and hydroxyl/ hydroxyl groups of HA or HA/ polymer combinations - termed double-crosslinking technology, which is a stepwise process (Figure 2.8):

1. Stable ether-linkages are established by hydroxyl group crosslinking
2. Synthesis of additional ester-linkages via carboxyl group crosslinking.

Zhao et al. (2002) demonstrated this principle through crosslinking of HA with non-ionic synthetic polymers such as polyvinyl alcohol and ionic biopolymers such as sodium alginate.

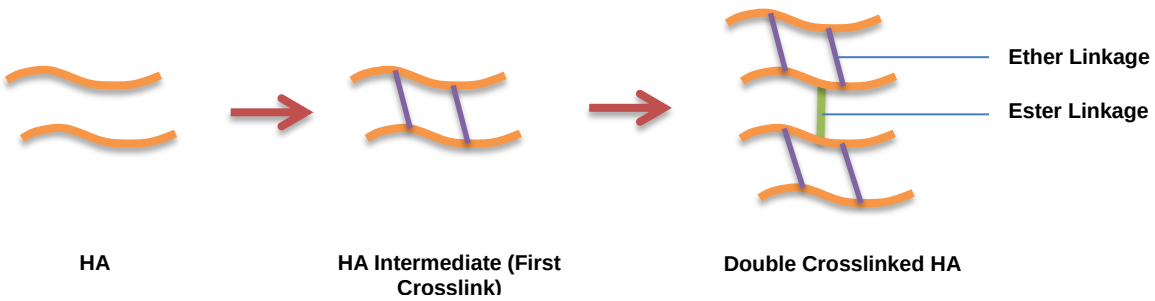

Figure 2.8: Proposed mechanism of formation of double crosslinked HA (adapted from Zhao et al., 2002)

A fine balance between the biostability and bioresponsiveness of the derived crosslinked device is imperative. Such characteristics can be established through the crosslinked system's innate response to the presence or absence of free radicals (created in the presence of Fenton's reagent) as well as its water absorption capacity (WAC). Being a hydrogel, the measurement of the WAC of the crosslinked polymeric system provides a useful indicator of the degree of crosslinking. An increased degree of crosslinking emanates in a reduction in the WAC. Whereas single crosslinking produces water-soluble or high water-uptake products, double crosslinking elaborates water insoluble counterparts with varying WACs, which are related to the combination of crosslinking conditions HA and its selected polymeric partners are exposed to (Zhao et al., 2002). When a combination of HA and sodium alginate has been employed, the presence of calcium ions was shown to increase the WAC of the resultant gel by reducing the reactivity of the carboxyl group through ionic complexation, leaving the carboxyl group available for water absorption. Exclusion of unnecessary cations at the initial crosslinking stages must thus be considered.

2.5. The Benefits of a Nanosystem Component in an Ocular Drug Delivery System

Advances in micro- and nanotechnologies have accelerated the development of innovative drug delivery technologies that are required to transform biological potential into medical reality (Hilt and Peppas, 2005). Nanotechnology is an 'umbrella term' that describes a rapidly evolving interdisciplinary field of technology, which implicates engineering or manipulation of matter at a sub-micron scale. It embraces objects, mechanisms, assemblies, and various systems based on size scales smaller than the micrometer and larger than 1 nanometer (nm) or about 10 atomic diameters (Bawa, 2004).

The goal in ocular therapeutics is to achieve and maintain an effective drug concentration at the site of action of adequate duration, in order to elicit the appropriate pharmacological response (Bucolo et al., 2008). Drug delivery systems undoubtedly form a crucial component of the 'therapeutic armamentarium' in ophthalmology. Accordingly, investigators have stated that, 'ophthalmic drug delivery, probably more than any other route of administration, may benefit from the characteristics of nanotechnology-based drug delivery systems' (Raju et al., 2008; de la Fuente et al., 2010). Promising results obtained from drug delivery systems employing non-ocular routes of administration has stimulated researchers to discover applications for nanotechnology in ophthalmology.

The inherent advantages of nanopharmaceutical systems (nanosystems, NS) are intrinsic to their colloidal nature. NS are poised, and have thus been conceptualized and fabricated, to circumvent the problems associated with conventional ocular systems to essentially increase

the ocular bioavailability of drugs (especially of poorly water soluble or poorly permeable drugs) and maintain activity at the site of action thus enhancing the therapeutic effect (due to reduced cellular and tissue clearance of drugs, sustained drug delivery, enhanced precorneal residence and uptake of drugs by ocular epithelia). NS have the ability to provide protection of the entrapped bioactive while conveying it to the desired compartments of the eye, as well as providing targeted delivery of bioactives (De Campos et al., 2001; Bourges et al., 2003; De Campos et al., 2004; Kayser et al., 2005; Sanchez and Alonso, 2006; Badawi et al., 2008; de la Fuente et al., 2008). This is a result of the capability to overcome blood-ocular barriers and efflux of the parent drug. Additionally, various stability-related concerns of drug molecules are bypassed or overcome through creation of a nanocarrier, as evidenced for proteins and peptides (Gaudana et al., 2010). Additionally, NS can provide controlled drug delivery for extended periods of time; an attractive benefit for the treatment of certain chronic ocular diseases (Mainardes et al., 2005; Vandervoort et al., 2005; de la Fuente et al., 2008). Furthermore, NS purportedly greatly reduce toxicity compared to the free drug and they overcome the poor acceptability of viscous or tacky preparations, including ointments, which cause extensive blurring of vision on correct administration (Nagarwal et al., 2009). Compared to normal eyedrop formulations, drug-loaded NPs, as a colloidal dispersion, possess the added advantage of enhancing patient compliance, due to less frequent application and prolonged retention in the extraocular portion due to the extended intraocular half-life of the drug (which is important where use of the drug preparation by the patient is lifelong e.g. glaucoma) (Araújo et al., 2009; Nagarwal et al., 2009). Significantly, with future developments firmly in mind, NS are paramount to exploitation of the emerging field of new gene therapies for the treatment of ocular disorders (Bloquel et al., 2006; de la Fuente et al., 2010).

In order to visualize how NS ‘slot in’ to the ocular delivery world, one must be cognisant of the peculiarities of the drug administration routes in the eye. As emphasized, local delivery of the drug is preferred over systemic delivery and diverse modalities exist for ocular drug administration. Most commonly, liquids are topically applied to the anterior of the eye in the form of eye-drops, sub-conjunctival or sub-Tenon’s injection in the conjunctival tissue or below the Tenon’s capsule, and intravitreal injection. In a significant advancement, drug-loaded intraocular implants fabricated from either biodegradable or non-biodegradable polymers have been employed to provide prolonged drug release at the implantation site. It must be accentuated that with conventional topical drug administration, symptoms are merely alleviated and the treatment is not usually curative but just palliative. The need for the design of an intelligent carrier for ocular drug delivery is thus pertinent to attain adequate bioavailability.

The main colloidal carriers under scrutiny for ocular delivery due to their favorably small size include liposomes and NPs. These NS can be coated with a hydrophilic polymer or further functionalized with antibodies for the enhancement of the targeting potential. Diverse methods exist for the preparation of NS and loading with therapeutic molecules. Ultimately NS are a highly adaptable drug delivery system, having the ability to surmount physiological barriers and transporting the drug to specific cells or intracellular compartments via passive or ligand-mediated targeting mechanisms (Sahoo and Labhasetwar, 2003; Vasir et al., 2005; Sahoo et al., 2008; Hamidi et al., 2008; Nagarwal et al., 2009). The last two decades have thus seen directed efforts in the rational design of ocular drug delivery NS. The starting point in the ocular drug delivery field was the development of hydrophobic NS consisting of polyalkylcyanoacrylate (Losa et al., 1991; 1992; 1993) and polyesters, particularly poly(*ε*-caprolactone) (Calvo et al., 1996a; 1996b; 1996c) as well as PLGA (Dillen et al., 2008), highlighting the affinity or bioadhesive potential of these systems for the corneal epithelium due to an appropriate surface charge or zeta potential (Vandervoort et al., 2004), but also emphasizing their unattractive propensity to aggregate upon contact with the mucosal surface. Thereafter, the aim was to create NS with a hydrophilic coating with the purpose of improving their stability and their interaction with the mucosa. This was achieved via optimization of ocular drug delivery NS to obtain prolonged bioadhesion/ residence time by the so-called 'mucoadhesive concept', based on entrapment of particles in the ocular mucus layer and interaction of bioadhesive polymer chains with mucins. Application of this concept generally emanates in a significant increase in precorneal residence time of the preparation (Ludwig, 2005; Dillen et al., 2008). Hydrophilic materials such as polyethyleneglycol (PEG) and chitosan (Calvo et al., 1997a,b; De Campos et al., 2003) were selected, because of their protein rejecting properties (shielding effect), and mucoadhesive and penetration-enhancing properties and good biocompatibility with ocular structures, respectively (Lehr et al., 1992; Schipper et al., 1997; Felt et al., 1999; Alonso et al., 2003). De la Fuente et al. (2010) elaborated on the evolution in the design of ocular NS, with specific reference to chitosan (Figure 2.9).

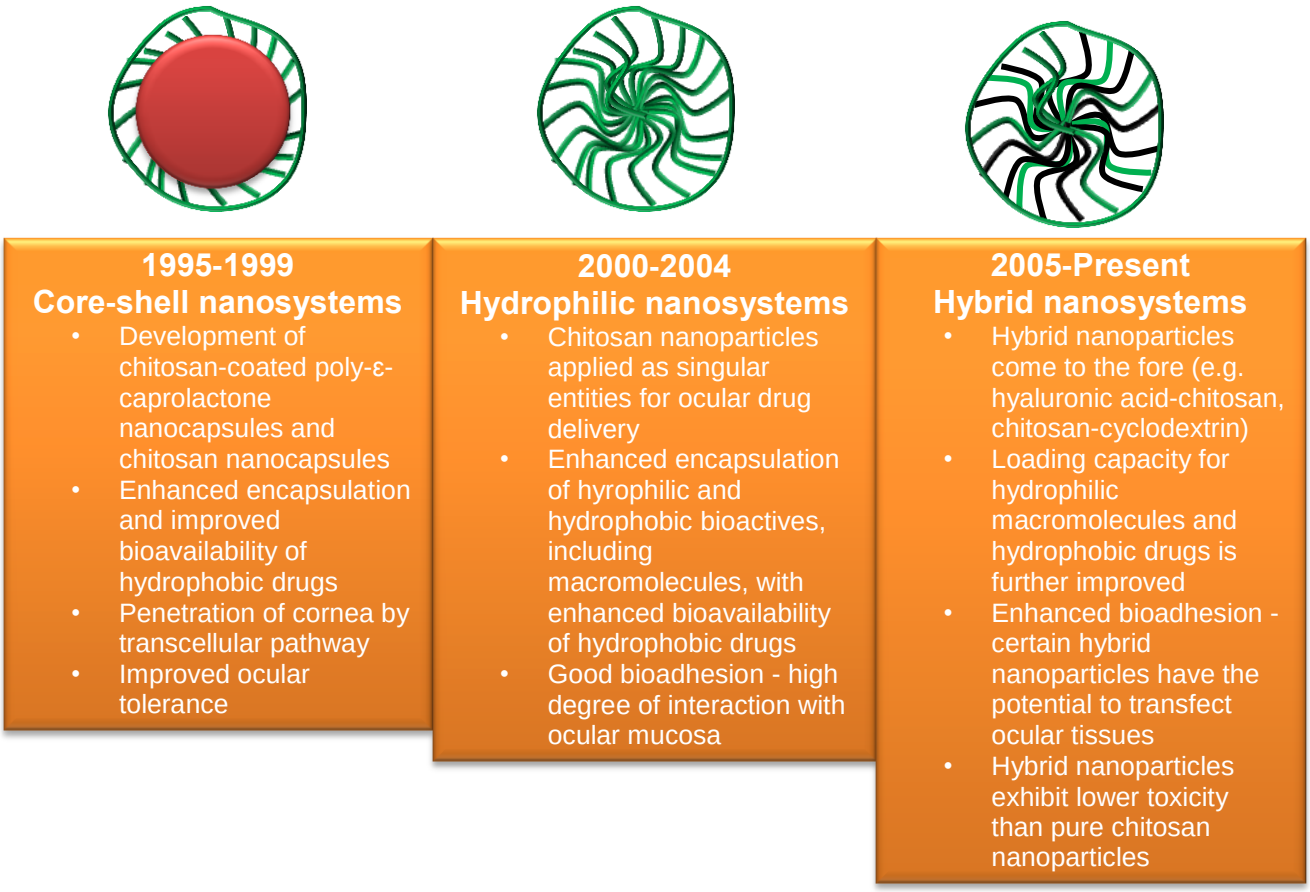

Figure 2.9: Time course highlighting the progression in design of nanosystems for ocular drug delivery, with a focus on the application of chitosan (adapted from de la Fuente et al., 2010)

Thus, falling under ocular NS, one can find an extensive array of polymeric formulations comprised of non-degradable polymers and biodegradable polymers that are either hydrophilic or hydrophobic. Examples of NS that differ in composition and application for ocular drug delivery are highlighted in Table 2.2. The possible manipulation of these systems for enhanced ocular delivery is depicted in Figure 2.10, appearing later in the text.

Table 2.2: Elaboration of potential nanosystems for ocular drug delivery (adapted from Carafa et al., 1998; Svenson and Tomalia; 2005; Barbu et al., 2006; Sahoo et al., 2007; Gaudana et al., 2009; Diebold and Calonge, 2010; Kaur et al., 2010; du Toit et al., 2011a)

Nanosystem	Definition	Composition	Potential/ manipulation for ODD*
Nanoparticles (NPs)	Nanoparticles for drug delivery are mostly polymerically based and vary in size from 1 to 1000 nm. Varying drug-loading configurations are evident; either the drug is attached to a nanoparticle matrix, dissolved, encapsulated or entrapped, leading to different terminologies, all of which embody the nanosize characteristic - i.e. nanospheres or nanocapsules	Natural or synthetic polymers, metals, lipids, phospholipids	Yes
Liposomes and niosomes	Liposomes can be defined as biocompatible and biodegradable microscopic vesicles consisting of membrane-like lipid bilayers, composed of mostly of phospholipids, surrounding aqueous compartments. These phospholipids are amphiphilic having a hydrophilic head and a lipophilic tail, which spontaneously arrange in aqueous solution as bilayers (the fatty acid tails, being non-polar, are located in the membrane's interior, and the polar heads point outward) to form closed vesicles. Niosomes, a variant of liposomes, are non-ionic surfactant vesicles. Like liposomes, niosomes are bilayered structures which can entrap both hydrophilic and lipophilic drugs either in an aqueous layer or in the lipid vesicular membrane	Phospholipids Non-ionic surfactants (niosomes)	Yes
Emulsions and microemulsions	Consist of interfacially stabilized (with surfactant and co-surfactant) oil-in-water or water-in-oil mixtures	Oil-in-water and water-in-oil mixtures that require surfactants	Yes
Nanosuspensions	-	Inert polymer resins	Yes
Dendrimers	The term dendrimer was first proposed by Tomalia in 1985 and originates from the Greek word 'dendron,' meaning tree; the structural shape yielding its unique attributes. Dendrimers are dissimilar from conventional polymers in that they have a multi-branched, three-dimensional architecture with minimal polydispersity and high functionality. Dendrimers are archetypically comprised of three different topological components of	Synthetic polymers	Yes

	chemical significance: 1) a poly-functional core, 2) interior layers, and 3) a multivalent surface are promising new scaffolds for drug delivery, especially if formulated as micelles, and may prove effective vehicles for ocular drug delivery		
Nanoparticle-loaded contact lenses	-	Various hydrogel-based lenses incorporating different drug-loaded nanoparticulate formulations into the lens matrix	Yes
Nanotubes and fullerenes	A fullerene is a form of carbon having a large spheroidal molecule consisting of a hollow cage of atoms. Carbon nanotubes are a fullerene having a cylindrical or toroidal configuration. They are large molecules, approximately 1-3nm in diameter, and hundreds to thousands of nanometers long	Carbon-based materials. There is a shift to producing nanotubes from polymeric materials to enhance safety	Not tested yet
Quantum dots	A quantum dot is a semiconductor whose excitons are confined in all three spatial dimensions	Semiconductor materials with fluorescent properties covered with other materials	Yes (Diagnostic)
Cyclodextrins	Cyclodextrins are a group of cyclic oligosaccharides capable of forming inclusion complexes with numerous drugs		Yes

**ODD = ocular drug delivery*

2.5.1. Considerations in nanosystem design for ocular drug delivery

The first consideration in the design of a colloidal delivery system for any ocular disease is of the molecular properties of the drug and the carrier in which it is destined for incorporation, such as size, charge, and affinity towards various ocular tissues and pigments.

In terms of transcorneal delivery, the overall make-up of each layer of the cornea must be considered, with the corneal epithelium and stroma existing as formidable barriers for hydrophilic and hydrophobic drugs, respectively. Because the corneal epithelial mucosa possesses an overall negative charge, permeability of positively charged molecules is promoted at physiological pH (Rabinovich-Guilatt et al., 2004). The type of lipid selected is of importance when designing a liposome-based formulation. As further elaborated on in subsequent sections, cationic liposomes have been demonstrated to achieve maximum drug transport across the cornea relative to anionic and neutral liposomes (Nagarsenker et al., 1999). Synonymous results have been observed for other colloidal dosage forms such as

NPs and microemulsions. Chitosan-coated NPs have demonstrated greater permeation relative to uncoated NPs. Transscleral and conjunctival absorption, in addition to transcorneal absorption; all have an important impact following topical administration (Gaudana et al., 2010).

The propensity of a compound to attain transscleral permeation is also dependent on bioactive and carrier molecular properties, such as overall size, charge and hydophilicity. Additionally, with regard to factors impacting the *in vivo* performance of colloidal dosage forms, dynamic barriers such as blood and lymphatic flow, affinity of the encapsulated drug towards melanin, and surface conjugation of NS, are all pertinent. NS size thus has a considerable effect subsequent to periocular administration as clearance of 20nm particles by conjunctival, choroidal, and lymphatic circulations has been demonstrated to be significantly higher, whereas particles of 200nm diameter could be found at the injection site for over 2 months. Furthermore, 20nm particles have been shown to cross the scleral tissue to a very low extent, while 200nm particles did not permeate (Amrite et al., 2005; Amrite et al., 2008a). A size range between 20-200nm could thus be seen as most preferable. Ocular disposition has also been influenced by bioactive affinity towards melanin pigment present in the choroid-RPE, thus delaying delivery to the inner retinal layers and the vitreous humor (Cheruvu et al., 2008). Drug targeting by functionalization has demonstrated some success. Drug availability into the inner retinal tissues is also impacted on by disease states (Cheruvu et al., 2009). The fate of colloidal carriers depends on numerous critical parameters following intravitreal delivery of a dosage form. It has been highlighted that vitreous humor is a colloidal fluid containing small amounts of solutes, ions, and low-molecular weight compounds; containing mainly collagen (40-120µg/mL) and HA (100-400µg/mL). Positively charged molecules display a propensity for aggregation in the vitreous humor due to the negative charge of vitreal HA. Hence, it is crucial to ascertain the zeta potential of a colloidal dosage form under physiological conditions (Pitkanen et al., 2003). PEGylation or alternative hydrophilic coatings on particles can significantly minimize this problem (Peeters et al., 2008). The ILM (separating the retina and vitreous) is also known to restrict the movement of particles from vitreous humor to inner retinal layers (Gaudana et al., 2010).

NS of various sizes for the improvement of ocular drug delivery have been based on polymers and biomaterials such as PLGA, poly(lactide) (PLA), poly(ε-caprolactone), albumin, and chitosan (Lang, 1995; Zimmer and Kreuter, 1995; Calvo et al., 1997a,b; Ding, 1998; Meadows et al., 2002; Ludwig, 2005; Barbu et al., 2006). The versatility of NS in terms of their size, shape, surface charge, and other physicochemical features, in addition to drug loading enhances, their attractiveness for drug delivery; however, these features also

influence their cellular uptake and intracellular trafficking, as well as interaction with vitreal proteins, other intraocular components (Dobrovolskaia et al., 2008), and with immune cells (Dobrovolskaia and McNeil, 2007), all of which are relevant to their ultimate distribution. Opsonization of NS (emanating in the covering of the NS by opsonins) furnishes a 'molecular signature' (Aggarwal et al., 2009) predicting the route of NS internalization in phagocytic cells and eventually their fate. Covering the NS surface with a hydrophilic coat prevents opsonization via the 'stealth effect' (Gref et al., 1994), and thus reduces the rate of cellular uptake, enhancing NS presence (Diebold and Calonge, 2010).

Therapeutic targets for drugs can be located extra- or intracellularly. On consideration of classical drugs possessing sizes greater than 1 kDa, stability conditions or hydrophilicity render them unable to cross the plasma membrane. NS enable the loaded bioactive molecule to cross cell membranes and epithelial barriers through exploitation of different internalization pathways - which highlights a very significant feature of NS and is one of the most interesting aspects of this technology. As early as the 1970's, Couvreur and co-workers (1977) demonstrated that submicrometer delivery systems such as NS can 'enter cells and become concentrated into nondiffusible molecules' (Couvreur et al., 1977). As emphasized, it is the physicochemical traits of nanocarriers, i.e. size; shape; surface charge, coating, and functionalization with targeting ligands; as well as the target cell type, that determine the internalization pathway and the intracellular fate (Bareford and Swaan, 2007; Frenkel, 2008; Hillaireau and Couvreur, 2009). The established internalization pathways are:

1. Phagocytosis - the typical pathway for intravenously administered NS implicating the involvement of specific cells with phagocytic capacity that will ingest the NS. NS and their payload ultimately become accessible to lysosomes and experience enzymatic degradation in the cytoplasm. This is a pivotal step to ensure drug release.
2. Endocytosis - occurs in all mammalian cells by means of pitted membranes coated by clathrin, or invaginated membrane regions that are coated with caveolin. Pitted membranes are formed by receptor-mediated and receptor-independent processes displaying varying internalization rates; invaginated membranes may also conduct receptor-mediated endocytosis. Targeting NS interaction with cell receptors of interest facilitates internalization by either of these receptor-mediated endocytic mechanisms. Following internalization of a drug-loaded NS by clathrin-mediated endocytosis, it would be guided to lysosomal degradation pathways. Alternatively, those internalized by caveolin-mediated endocytosis accumulate in the endosomes (caveosomes) for conveyance to other non-lysosomal subcellular compartments. Employment of this mechanism has been evidenced, for example, for delivery of

chemotherapeutics to cancer cells. Furthermore, clathrin- and caveolin-independent endocytosis mechanisms have been described.

3. Macropynocytosis - occurs in all kind of cells. Being the least specific pathway, it is directed by actin-driven membrane protrusions which create large endocytic vesicles known as macropinosomes. Eventually, those vesicles fuse with lysosomes.

It is of importance to note that several endocytic mechanisms can take place simultaneously. Remarkably, there is a scarcity of studies regarding internalization pathways and intracellular trafficking of NS intended for ocular drug delivery. Internalization pathways are a significant consideration as this will impact on the intracellular metabolism of delivered drugs, and implies that NS physicochemical make-up will determine the degradation ratio, which ultimately impacts on the pharmacological activity of the encapsulated molecule.

The release profiles of drugs from NS are controlled by various kinetic processes, namely: (i) desorption of the surface-bound or adsorbed drug, (ii) diffusion through the NS matrix or the polymer wall, (iii) erosion of the NS wall, and (iv) a combination of erosion and diffusion processes (Soppimath et al., 2001; Harush-Frenkel et al., 2008). Uniformly distributed or dissolved drug in the NS matrix displays kinetic release attributes dependent on diffusion and biodegradation of the matrix. Should polymeric degradation be slower than drug diffusion, drug release will ensue mainly through diffusion; alternatively, drug release occurs through degradation of the polymer.

Lastly, consideration of the mode of administration (e.g. injection, implantation) is required during the design of the NS. These complexities all tie together to furnish the requirements of minimal potential toxicity and improved efficiency. A number of investigations have been undertaken in the search for alternative NS in ophthalmic drug delivery (Diebold and Calonge 2010).

2.5.2. Nanosystems and transcorneal penetration for posterior segment delivery

As drug delivery scientists, the need to attain what initially seems impossible is commonplace, which is why transcorneal penetration of topically administered ophthalmic drugs is constantly sought even though the cornea constitutes one of the most selective barriers to foreign molecules for the eye. The rationalization of this seemingly fruitless pursuit is that currently, the ‘gold standard’ for treatment of intraocular inflammation, either infectious or non-infectious, is intravitreal drug injection. The vitreous is capable of retaining molecules and also delivering them to nearby structures (e.g. ciliary body or RPE) because of its gelatinous, acellular nature. However there is a necessity for frequent intraocular injections

for the satisfactory treatment of retinal disorders. This high injection frequency comes hand-in-hand with potential undesired side effects, which have already been described - hence a look toward NS as drug carriers. Of course this presents a challenge as less than 5% of drugs applied as liquid eye-drops penetrates the cornea as a result of tear turnover associated with blinking and the nasolachrymal drainage system (Keister et al., 1991). In addition, the drug diffusion pathway between the ocular surface and intraocular targets is protracted. This culminates in eye-drops failing to reach sufficient drug concentration in the posterior ocular tissues. Furthermore it has been highlighted that systemic drug administration delivered through the blood vascular system is not effective because of the uveal BAB and BRB. Hence, a poor dose-response profile is observed for vitreoretinal disorders and a large amount of the drug is required to maintain therapeutic levels, generally with inadequate duration, and with resultant systemic side effects (Geroski and Edelhauser, 2001). Furthermore, the high concentration of drugs necessitated to penetrate the blood-ocular barriers is commonly linked to systemic side effects.

We undertook a critical and chronological review of all ‘nanobioadhesives’ (du Toit et al., 2011a), that is, NS designed for ocular drug delivery with the goal of attaining prolonged ocular retention, from their reported point of inception to the present (du Toit et al., 2011a). This review can be referred to for an in-depth analysis of the numerous ocular NS have been developed based on this premise, and their characteristic nano-architecture is shown in Figure 2.10. However, most of the systems discussed herein were largely described in terms of their retention on the ocular surface, and transcorneal permeation rather than their ability to attain penetration into the posterior segment, which is achieved via alternative pathways.

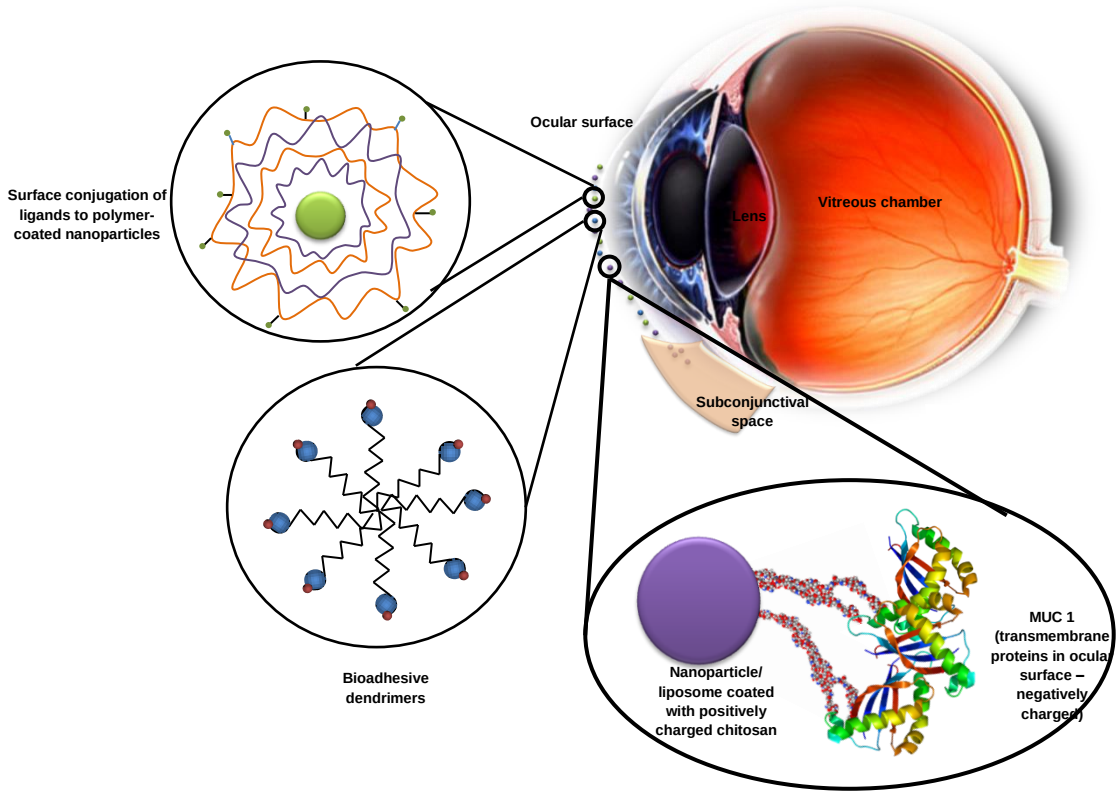

Figure 2.10: Interaction of diverse nanobioadhesives with the ocular surface (cornea, conjunctiva) and subconjuctival space of human eye. In the case of systems coated with positively charged polymers (e.g. chitosan), there is interaction of the chitosan molecules coating the nanoparticle with the negatively charged transmembrane proteins. Chitosan molecules develop molecular attraction forces by electrostatic interactions with the negative charges of mucin, which is determined by the formation of either hydrogen bonds, or ionic interactions between the positively charged amino groups of chitosan and negatively charged sialic acid residues of mucin, depending on environmental pH (adapted from Ludwig, 2005 and Nagarwal et al., 2009 in du Toit et al., 2011a).

2.5.3. The concept of inflammatory tissue targeting as achievable by nanosystems

As emphasized, the use of nano-scaled carriers in drug delivery is expected to increase the specificity of drugs, thus increasing bioavailability and thereby reducing side effects such that the dose of the administered drug may be reduced. In other words, nanoencapsulation can alter the pharmacokinetics of the incorporated drug. A particularly notable gain that nanoscaled drug carriers hold over conventional drug delivery systems is the ability to direct the drug to the site of action - this is ‘drug targeting’ which can be classified as active and passive targeting approaches (Ulbrich and Lamprecht, 2010).

Passive targeting is attainable in the absence of additional integration of a specific targeting moiety on the particle surface. It is achieved via different administration routes, via

intravenous or epithelial application. Pertinently, macrophages which initiate an inflammatory response are the primary target cells in this drug targeting approach (Kumar et al., 2001).

Several circumstances activate the cellular immune response in inflammatory diseases. An increased presence of immune-related cells such as macrophages is common in the inflamed area. Tabata and co-workers (1996) demonstrated that microspheres and NPs can be successfully engulfed up by macrophages, mainly by phagocytosis (Figure 2.11) or endocytosis as the particle size decreases. Thus, particle uptake into those immune-related cells or the disruption of the epithelium could facilitate the selective accumulation of the NS in the desired area (Stein et al., 1998). Therefore, passive targeting can be achieved in inflammatory diseases due to the immune response. Properties such as NS size and surface charge play a key role in attaining efficient uptake into those immune-related cells.

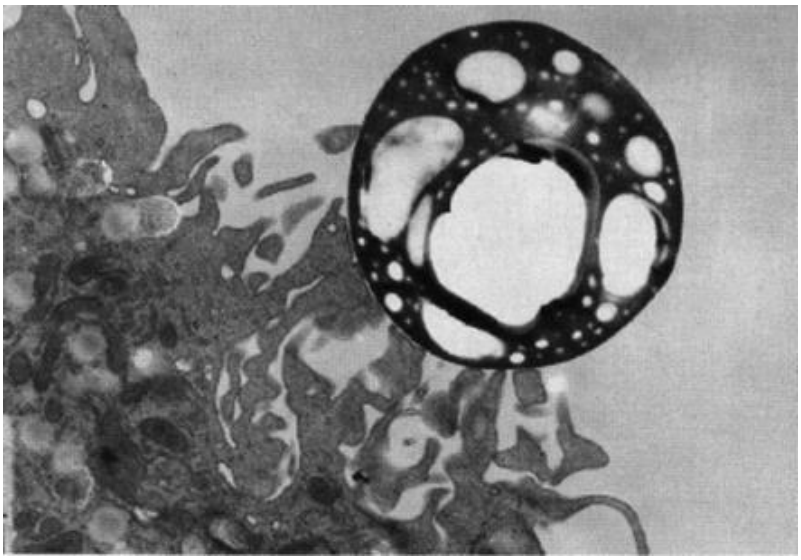

Figure 2.11: Transmission electron micrograph demonstrating adhesion of a NP on pseudopods of a macrophage (8500x magnification; Ulbrich and Lamprecht, 2010)

In order to achieve active targeting, integration of targeting entities, such as antibodies or specific adhesion molecules, onto the surface of particles is undertaken. These targeting moeities then recognize antigens or other specific adhesion molecule counterparts on the surface of the cells to be targeted (Steeber et al., 2005; Simone et al., 2009). The drug is anticipated to be specifically delivered to the site of action followed by potential intracellular uptake (Ulbrich and Lamprecht, 2010).

2.5.4. Nanosystems conceptualized for enhancing anti-inflammatory agent bioavailability, for intraocular drug delivery, or for inflammatory tissue targeting

An important goal of this investigation is an improvement in intraocular availability of the NSAID, indomethacin, to the posterior segment of the eye for the treatment of inflammatory disorders such as of uveitis. The limitation of NSAIDs and corticosteroids is their poor water solubility which results in them being excluded from intraocular sites by the various blood-ocular barriers, and thus generally failing to reach intraocular targets (Diebold and Calonge, 2010).

2.5.4.1. Nanosystems for enhancing anti-inflammatory agent bioavailability

In attempts to enhance the bioavailability of NSAIDs (specifically indomethacin) and corticosteroids, diverse approaches have been instituted.

Poly(*ε*-caprolactone)-based nanosphere, nanocapsule and nanoemulsion formulations of indomethacin (mean size = 225nm) prepared by interfacial deposition, nanoprecipitation and spontaneous emulsification have been reported (Calvo et al., 1996a). *In vitro* comparison of colloidal carriers with commercial eye drops revealed a threefold higher corneal penetration of indomethacin from colloidal systems. Further, *in vivo* evaluation of these colloidal systems in the rabbit eye highlighted a threefold higher drug concentration in aqueous humor at 0.5 h post instillation and a 300% increase in ocular availability of indomethacin compared with a commercial solution dosage form; while a polymeric microparticle formulation (mean size = 6.5μm) did not increase the ocular availability (Calvo et al., 1996b). The colloidal carriers penetrated the corneal epithelium by endocytosis without damaging the membrane. Ultimately, it is the colloidal nature of the carriers that have been proposed to be responsible for increased ocular availability of indomethacin. The ocular pharmacokinetics data of nanoformulations indicated, however, that the aqueous humor half-life of indomethacin ($t_{1/2}$ = 65-74 min) did not increase on instillation of colloidal formulations indicating inability of the dosage forms to have a prolonged effect.

Eudragit® RS100 NPs were designed for the encapsulation of ibuprofen and therapeutic efficiency was investigated after topical administration to rabbits in which eye inflammation was induced using sodium arachidonate (SA) (Bucolo et al., 2002). They observed significant reductions in the primary signs of ocular inflammation, the protein levels, and the number of leukocytes in the aqueous humor compared with the free drug. Furthermore, the aqueous humor drug concentration of the ibuprofen-containing NP group was higher than that of the free-drug group.

Pignatello et al. (2002a) developed ibuprofen-loaded NPs composed of inert polymeric resins (Eudragit® RS100) optimized as a pharmaceutical preparation for application in surgical traumas, such as cataract surgery, that cause miosis and require treatment with NSAIDs. *In vitro* profiles demonstrated controlled ibuprofen release, and *in vivo* studies in an ocular trauma model highlighted good efficacy in reducing miosis at lower drug concentrations than the eye-drop formulation.

Subsequently, Vega and co-workers (2006) coated flurbiprofen-loaded PLGA NPs with Poloxamer 188 and obtained zeta potential values of -25mV and a particle size of 230nm for topical administration. Poloxamer 188 was included as a surface modifier with cationic polymers. *In vivo* testing was undertaken in rabbit eyes in which a mild conjunctival inflammation was induced following topical instillation of SA. Results highlighted good anti-inflammatory efficacy in the absence of toxicity or irritation to ocular tissues. The anti-inflammatory response was notably enhanced compared to commercial eye-drops (Ocuflur®) containing the equivalent concentration of flurbiprofen ($0.03\%^{w}/_{v}$). This was attributed to the bioadhesive properties of the polymer emanating in an increased residence time of the colloidal system on the ocular mucosa, but avoiding the ocular penetration of SA. The residence time of NPs in inflamed eyes was higher than in healthy eyes due to physiological changes in inflamed ocular tissues.

Preparation via high-pressure homogenization of various nanosuspensions of three insoluble glucocorticoids (hydrocortisone, prednisolone and dexamethasone) was undertaken by Kassem et al. (2007). The NPs were instilled into the lower cul-de-sac of normotensive rabbits to determine whether the glucocorticoid-associated NPs could provide enhanced absorption and improved intensity of drug action following measurements of the intraocular pressure (IOP). They discovered improvements in both, as well as prolongation of the glucocorticoid action.

Bioadhesive systems, as described, have also been investigated for targeting ocular structures. Indomethacin was prepared as a bioadhesive nanoemulsion and was found to be effective in reducing corneal ulceration (Badawi et al., 2008). The nanoemulsion was able to achieve therapeutic concentrations of indomethacin in the inner ocular structures.

2.5.4.2. Nanosystems for drug delivery to the posterior segment

Few reports emphasize the intravitreal delivery of drugs through ocular barriers via NS, however some recent studies have shown commendable results on the use of intravitreally injected NPs. For example, ganciclovir-loaded albumin NPs have been developed as

ganciclovir is one of the standard treatments for CMV retinitis (Figure 2.12). These carriers were prepared by a coacervation method and chemical crosslinking with glutaraldehyde. Sustained drug release was evident following *in vitro* experiments (Merodio et al., 2001), as well as a significant improvement of drug uptake by CMV-infected human cells (Merodio et al., 2002a,b). Following single intravitreal injections in rats, safety and tolerance was demonstrated and drug levels were detected in the vitreous and ciliary body for at least two weeks (Irache et al., 2005). The risks associated with injectable systems, however, must be borne in mind.

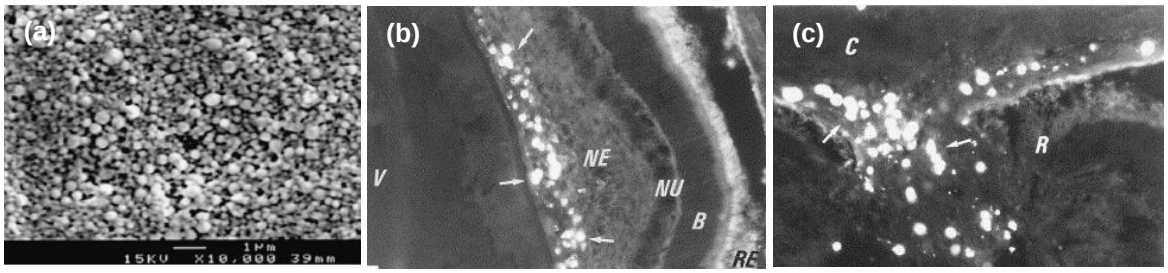

Figure 2.12: (a) Scanning electron micrograph of albumin nanospheres developed for the treatment of cytomegalovirus retinitis possessing an average diameter of ~250nm (Merodio et al., 2001) and biotin-labeled NP immunochemical detection by streptavidin-FITC staining 2 weeks after (a) their injection in the vitreous cavity and (b) in the BAB adjacent area and ciliary muscle (200x magnification). B: Bacillary layer; C: ciliary muscle; NE: neuronal interplay area; NU: outer and inner nuclear layers; R: retina; RE: retinal epithelium; and V: vitreous cavity (Merodio et al., 2002b)

Because RPE cells have the capacity to take up various kinds of NPs (Bourges et al., 2003; Bejjani et al., 2005; Normand et al., 2005), they therefore possess the capacity for treatment of disorders associated with ageing or photoreceptor dystrophies. These cells should be targeted with specific molecules or genetic material capable of reversing or discontinuing the processes culminating in the described diseases. Bourges et al. (2003) developed intravitreal PLA NPs loaded with fluorochromes and tested them in rats; they demonstrated a preferential localization at the RPE cells after 24 h. Notably, the RPE cells retained the NPs, allowing continuous delivery of the fluorochrome for months following a single injection.

Bejjani et al. (2005) undertook *in vitro* and *in vivo* investigations on PLA and PLGA NPs loaded with fluorochromes and model plasmids. Twenty-four hours following intravitreal injection in rats, NPs entrapping a plasmid encoding red nuclear fluorescent protein were localized in the RPE and plasmid expression was achieved four days subsequent to injection. There was no apparent tissue damage or toxicity and red fluorescence associated with expression was detectable in RPE cells for the following three weeks, with no apparent tissue damage or toxicity.

Other intravitreal systems include injectable NPs for gene therapy as extensively reviewed by Conley and Naash (2010). Ocular gene therapy is becoming a well-established field. Of late, development of nonviral gene therapies has been an area of intense focus and one technology, polymer-compacted DNA NPs, is becoming an excellent candidate for a retinal gene delivery vehicle. Safety, tolerability, and extensive and persistent expression throughout the retina, have been observed for these NPs. The ability to target NPs to different cell types and/ or regions of the cell furnishes them customizable for diverse applications. The remaining concerns facing the use of these vectors is a means to efficiently target the vast array of disease genes, and actually curing genetic diseases diagnosed following the inception of degeneration.

2.5.4.3. Nanosystems for inflammatory tissue targeting

Certain NS have been conceptualized, having specific applications in uveitis and associated intraocular inflammatory disorders. Drug-loaded liposomes have been employed for intraocular injections to reduce dosing frequency. The fate of fluorescent PEG-coated liposomes after intravitreal injections in healthy rats was investigated by Camelo et al*.* (2008). Liposomes were largely identified in the vitreous humor, the inner retina and to a lesser extent at the level of the iris root and ciliary body. Macrophages and neutrophils in the conjunctiva internalized the fluorescent liposomes. Lajavardi et al*.* (2007) developed sterically stabilized PEG-coated liposomes incorporating vasoactive intestinal peptide (VIP) for the purposes of stability enhancement in biological media and controlled release. The VIP-loaded liposomes were injected intravitreally in rats in which EIU was induced. Their findings demonstrated that VIP was only efficient at reducing EIU when encapsulated in liposomes (Ulbrich and Lamprecht, 2010).

Ryu et al. (2011) investigated the potential of NPs composed of poly(γ-glutamic acid) conjugated with L-phenylalanine (γ-PGA-Phe NPs) for management of retinal diseases. The γ-PGA-Phe NPs (200nm) were evaluated with macrophages and microglia *in vitro* and by intravitreal administration into normal or pathological rat eyes. The NPs were efficiently taken up by cultured macrophages or microglia and still detectable in the cytoplasm of these cells at day 7. No accumulation of NPs was noted in the retinas of normal rat eyes with no inflammatory cells recruitment. Pathological conditions saw the converse outcome, with NPs localized in activated CD11b-positive cells in the retina. Suppression the expression of TNFα and MCP-1 in cultured macrophages or microglia was thus achieved by dexamethasone NPs. Data generated suggested that γ-PGA-Phe NPs could be a powerful tool for lowering

the inflammatory cell burden in pathological conditions in the retina, and also demonstrated the concept of a more bioresponsive approach towards ocular drug delivery.

Groups have focused on the intravenous administration of NS for inflammatory tissue targeting. The effect and localization of poly(lactic acid) (PLA) NPs encapsulating betamethasone phosphate on rats with experimental autoimmune uveoretinitis (EAU) receiving a single IV injection was evaluated by Sakai et al. (2006). On confocal images it was highlighted that no NPs could be found in the normal retina of healthy rats whereas several NPs accumulated in the retina and a few NPs were detected in the outer nuclear layer, observed 3 hours after injection in EAU rats. These NPs remained in the retina of EAU rats up to 7 days after the administration. The anti-inflammatory effects observed were rapid and prolonged, being equal to a five-times-higher dose of free betamethasone phosphate. Further investigations are necessary to reveal whether either repeated injections or higher doses of betamethasone phosphate enhance the anti-inflammatory effect. However, even though intravenously administered NPs achieved ocular targeting from the endothelial side and sustained release in ocular inflammation, more than 95% of the NPs were trapped in the liver and spleen. Hashida et al. (2008) brought a second approach to endothelial delivery to the inflamed eye to the fore in their work in which an active targeting strategy was exploited. Novel sialyl-Lewis X (sLe^X) conjugated liposomes (sLe^XL) were loaded with dexamethasone and were injected into EAU mice. The interaction of PMNs and endothelial cells plays a crucial role at inflammatory sites and is characterized by E-selectin- and P-selectin-mediated 'rolling' of PMNs along the endothelium (McEver, 1992). E-selectin and P-selectin display recognition of the tetrasaccharides sLe^X and A, which are either protein- or lipid-bound on the PMN surface (Polley et al., 1991; Foxall et al., 1992). Dexamethasone-sLe^XL achieved a two-fold higher dexamethasone concentration and selective targeting to the inflamed eye, compared with 1mg free dexamethasone. A binding assay was performed to confirm whether sLe^XL liposomes target E-selectin, P-selectin or both - this highlighted that sLe^XL liposomes were able to target both selectin types on the activated endothelial cells *in vivo* (Ulbrich and Lamprecht, 2010). sLe^XL can be a highly efficacious site-directed system *in vivo.* Instituting sLe^XL as a vehicle for drug delivery in inflammatory diseases could see substantial pharmacologic effects with minimum side effects.

The results of the afore-described studies are promising and shine a new light on the treatment of retinal and uveal disorders, but implementation of these kinds of delivery systems in a clinical setting could be a limiting factor and further functional studies are required such that diminishment of the retinal function and vision, and development of accompanying chronic inflammatory processes are dismissed (Diebold and Calonge, 2010).

The total cost implications of implementing active targeting approaches is a further pertinent consideration.

It is apparent that design of an anti-inflammatory-loaded NS could be the key to enhancing overall anti-inflammatory drug bioavailability for the treatment of posterior segment inflammation. To add to this, instituting the afore-described approaches, several kinds of NS encapsulating diverse active molecules are currently in pre-clinical studies (Bourges et al., 2003; Bejjani et al., 2005; Normand et al., 2005; Irache et al., 2005; Farjo et al., 2006; Paasonen et al., 2007). A further consideration, however, is that implantable drug delivery systems are also moving to the fore as alternatives to intravitreal or periocular injections. Ocular implants provide the capacity to achieve long-term drug delivery in the retina and nearby tissues. Realization of the advantages of combining these two drug delivery approaches would appear to be an intuitive step. The concept here is to exploit the implant capacity to retain and deliver molecules to tissues that it has close or direct contact with and employ it as a biological reservoir for the NS. The key is to attain therapeutic levels of a drug for at least a month following implantation which would see a vast improvement in the quality of life of many patients.

2.6. Concluding Remarks

Effective treatment of ocular diseases presents a formidable task, dually attributed to the nature of intraocular diseases and the presence of ocular barriers. Challenges in ocular drug delivery have been partially addressed through the design of innovative drug delivery systems which all strive to enhance drug bioavailability, as well as identification of transporters and modification of drug substances to target these transporters. Development of compliance-promoting and disease-responsive delivery techniques will revolutionize ocular drug delivery. Evolution of sustained drug delivery systems integrating advanced polymers is infinite, and conceptualization of novel polymeric systems with intelligent (e.g. stimulus-responsive) mechanisms and advances in nanotechnology are at the forefront of achieving directed and controlled delivery for treating vision-threatening diseases. It is thus the pertinent goal of this investigation to assimilate these observations in the design of an intelligent ocular drug delivery system.

CHAPTER 3

DESIGN AND OPTIMIZATION OF A COMPOSITE OCULAR LIPOIDAL-POLYMERIC NANOSYSTEM AND EVALUATION OF ITS ANTI-INFLAMMATORY POTENTIAL

3.1. Introduction

Forward-thinking approaches are required to address the challenges previously described in the treatment of ocular diseases (Bucolo et al., 2008). The overall outcome of this chapter is promulgation of these sophisticated approaches through experimental elaboration of the pertinence of nanotechnology to ocular drug delivery. The preliminary design of an anti-inflammatory nanoparticulate system (Part A) and subsequent optimization of the preferred system (Part B) was undertaken. The optimum NS was destined for incorporation within the core of the I^3.

The aim of this ensuing investigation was to build on past successes and employ a combinatory drug delivery approach via developing a safe and effective NS (ultimately made readily available to the eye in the form of an implantable device) possessing the potential to permeate ocular barriers of interest and passively target inflammatory cells, while enhancing the anti-inflammatory potential of the incorporated drug.

3.2. PART A: Preliminary Design of an Anti-Inflammatory Nanosystem

3.2.1. Identification of a desirable nanosystem architecture

In designing an applicable NS for the treatment of inflammatory afflictions of the posterior segment, cognisance must be maintained of the fact that a drug delivery system is more than a simple (nano) carrier. There is an intricate science and technology behind the design of drug delivery systems such that directed solutions are achieved for enhanced treatment. Thus for the proposed I^3, the following components of NS must be exploited:

1. Controlling the release of the active agent so that a therapeutic concentration is achieved when exposed to an inflammatory stimulus, while maintaining drug within the implant over a prolonged period of time
2. Developing disease-specific targeting capabilities (inflammatory tissue targeting)
3. Providing new or more convenient routes of administration for the intraocular implant, through demonstration of the permeation potential of the designed NS,

such that drug still reaches the posterior segment of the eye (Diebold and Calonge, 2010).

Through our published investigations (du Toit et al., 2011b; Appendix 9.2.3) we have identified the combinatory advantages of polymerically-enhanced lipoidal NS, which include: (a) incorporation of poorly water-soluble drugs, which is largely independent of the liposome bilayer physicochemical properties, (b) prolonged lifetime attributed to the polymeric component, (c) tissue distribution, which will be largely lipid dose independent, such that therapeutic dose escalation produces increasing drug effects with minimal changes in pharmacokinetics, and (d) inflammatory tissue targeting based on the careful selection of lipoidal and polymeric components.

Based on the afore-described findings, and elaborated via the principles of liposomology and ionotropic gelation, a composite lipoidal-polymeric NS was thus developed which incorporated suitable phospholipids, the hydrophobic poly(*ε*-caprolactone) (PCL), and the mucoadhesive, permeation-enhancing chitosan.

3.2.1.1. Lipoidal component

The field of liposomology has its origins in the works of Alec Bangham since 1965 following his investigation of cell membranes and the role of phospholipids in blood clotting (O'Doherty, 2004). Liposomes are described as microscopic, spherical vesicles originating on hydration of phospholipids which self-assemble in circular sheets with consistent head-tail orientation, forming a lipid bilayer membrane enclosing water and water-soluble material in its core. As a result, liposomes enable water-soluble and water-insoluble materials to be combined in the absence of surfactants or other emulsifiers (Ebrahim et al., 2005). Phospholipids, including phosphatidylcholines (PC), phosphatidylethanolamines (PE), and phosphatidylserines (PS), constitute the primary make-up of naturally occurring bilayers; their amphiphilicity being their commonality (O'Doherty, 2004). PCs are widely employed in liposome fabrication and include distearoylphosphatidylcholine (DSPC). PCs are zwitterionic at all relevant pHs, thus emanating in lamellar structures independently of the pH in the solution. Phosphatidylethanolamines such as distearoylphosphatidylethanolamine (DSPE) possess a pH-dependent phase behavior - at physiological pH where the PEs have zwitterionic headgroups they are unable to form lamellar structures. However, above pH ~ 9 the headgroup becomes charged and lamellar structures can be formed. Compared to other PCs such as egg PC, DSPC is expected to create a more ordered membrane and hence fewer defects are formed. The addition of DSPE to DSPC introduces an amine group in the headgroup region, further reducing the permeability. The presence of the amine might

promote hydrogen bond formation with the phosphate group of DSPC, which could give rise to a membrane less prone to pore formation. When DSPE is conjugated to PEG, its use in the modification of liposome surfaces and for influencing the survival of liposomes *in vivo* is pertinent, furnishing a further leakage-reducing effect (Bergstrand, 2003).

Liposomes can be classified in accordance with their structural properties or on the basis of their preparation (O'Doherty, 2004). The different types of liposomes that can be formed are unilamellar, multilamellar, and multivesicular. Following their momentous discovery, further studies into liposomes and their application in various fields such as medicine and research have been explored (O'Doherty, 2004; Ebrahim et al., 2005). Phospholipids were incorporated within the NS to enhance distribution within the inflamed tissues, and to enhance intracellular uptake, with tubulin interaction identified as one potential mechanism (Klausner et al., 1981; Caron and Berlin, 1987; Fenske et al., 2001).

3.2.1.2. Polymeric component

Chitosan, a natural linear biopolyaminosaccharide, is generally obtained by the alkaline deacetylation of chitin, which is the primary cuticle-forming component of crustaceans s and cell walls of certain fungi. Chitosan is composed of copolymers of glucosamine and *N*-acetyl-glucosamine. Chitosan has one primary amino and two free hydroxyl groups for each C6 building unit. It carries a positive charge due to the availability of free amino groups thereby reacting with many negatively charged surfaces/ polymers and undergoing chelation with metal ions. Being a weak base it is insoluble in water and organic solvents, however, it is soluble in dilute aqueous acidic solution (pH <6.5), which can convert the glucosamine units into a soluble form, i.e. $R\text{-}NH_3^+$ (Sahoo et al., 2010). Chitosan has also been demonstrated to display antimicrobial activity (Susan et al., 1991). The permeability-enhancing properties of chitosan are available for exploitation (Lemarchand et al., 2004). Positively charged chitosan binds to cell membranes and is reported to increase transcellular and paracellular permeability. These features have made chitosan NPs an apt carrier for oral vaccine delivery (Chadwick et al., 2010) possessing the propensity to transfect mammalian cells arising from its potential to overcome the cellular transport processes, i.e. cell uptake, release from endosomes, and nuclear transport (Cadete et al., 2012). Thus, chitosan is a suitable hydrophilic material for incorporation in the proposed ocular NS because of its protein rejecting properties (shielding effect), mucoadhesion, penetration-enhancing properties and good biocompatibility with ocular structures (du Toit et al., 2011a). Furthermore, chitosan purportedly prevents NS degradation caused by the adsorption of lysozyme and reduces opsonization and complement activation. There are an extensive number of investigations reporting on the low toxicity and good biocompatibility of chitosan following topical

administration to rabbits and cell cultures (Alonso and Sanchez 2003; Diebold et al*.,* 2007; Suri et al*.,* 2007; Badawi et al*.,* 2008; Ulbrich and Lamprecht, 2010).

The institution of the cationic chitosan has already established a firm place in the design of ocular NS. Coating with cationic polymers such as chitosan was first reported by Calvo et al. (1997b) for ocular nanocapsules and was found to increase particle size and result in a net positive charge. The presence of the coatings did not alter the release profile to any extent but significantly affected ocular permeation of drug due to the penetration-enhancing capabilities of chitosan (Bilensoy et al., 2009). Motwani et al. (2008) and others have identified the cationic polymer chitosan as a polymer of choice because of its unique properties including acceptable biodegradability, biocompatibility (Knapczyk et al., 1989; Hirano et al., 1990), as well as the ability to increase membrane permeability, both *in vitro* and *in vivo* (Takeuchi et al., 1996), and enhance paracellular transport.

PCL is a biodegradable polyester which has attracted attention for its application in controlled drug delivery due to its lack of toxicity and low cost when compared to other biodegradable polyesters. It possesses a slow degradation rate *in vivo* due to its high crystallinity and hydrophobicity, which is useful for controlled drug delivery applications. However, biodegradability can be enhanced through copolymerization (Cai et al., 2000) and/ or blending with a variety of other polymers (Zhu et al., 1990). Polymer blending represents an appropriate means of tailoring the hydrophilicity of a matrix without significantly affecting its mechanical integrity (Ratajska and Boryniec, 1998; Sahoo et al., 2010). In terms of its ocular and inflammatory-targeted delivery potential, PCL purportedly possesses an affinity for inflamed tissue (by showing a high selectivity in adhesion to the inflamed tissue areas) (Pertuit et al., 2007) and possessing the potential to undergo corneal penetration by an endocytic process (Calvo et al., 1996a). It has also been demonstrated to reduce the cytotoxicity when employed as a coating on gold NPs (Mao et al., 2007).

Chitosan-PCL polyionic complexes are anticipated to form through ionotropic gelation via interactions between the carboxyl groups of PCL and the amine groups of chitosan. The combination of chitosan and PCL as the polymeric counterpart of the NS was proposed to avail a superior biomaterial where the limitations of chitosan are complemented by PCL. The combination could provide a superior biodegradable and biocompatible material, which would potentially limit the release of the encapsulated bioactive more effectively than either polymer alone (Sahoo et al., 2010). Their combination for topical ocular delivery was exploited by Calvo et al. (1997b), who demonstrated that introduction of a chitosan coating to the PCL

NPs dramatically improved the bioavailability of indomethacin in the cornea as well as in the aqueous humor after topical ocular instillation.

Bearing these considerations in mind, the institution of chitosan, together with PCL, and in combination with the liposomal counterpart for the preparation of an ocular NS for incorporation in an implantable device, is a novel means to enhance delivery of the anti-inflammatory agent to the ocular tissues.

3.2.2. Nanosystem characterization and investigation of the anti-inflammatory efficacy, ocular flux and toxicity

Drug delivery to the appropriate site of action within the eye is a challenging endeavor, owing to anatomical and physiological barriers as discussed. In order to overcome these challenges in ocular therapeutics, it is fundamental to maintain an effective drug concentration at the site of action for an appropriate period of time, in order to achieve the expected pharmacological response (du Toit et al., 2011a). The goal was to design a NS that would evade the downfalls associated with conventional systems, assisting the encapsulated molecule's transport to the eye compartment of interest on its diffusion out of the implantable device and allowing for targeted delivery of the bioactive. In addition, the NS should control drug delivery for prolonged periods of time for application in chronic ocular diseases.

In order to establish whether inclusion of the phospholipid component in the NS conferred a notable advantage to the NS for targeting ocular inflammatory diseases, it was compared to a purely polymeric NS. This preliminary investigation (Part A) sought to compare and elaborate on the potential of two specific embodiments of an ocular NS; one portraying a purely polymeric system (including chitosan and PCL), referred to as the Chit-PCL NS, and the other based on a composite lipoidal-polymeric NS architecture utilizing phospholipids (DSPC and DSPE), referred to as the Lipo-Chit-PCL NS. The preferred NS would ultimately be incorporated within the crosslinked core of the I^3 to achieve long-term delivery to the posterior segment of the eye. Implantation of the I^3 would be at the following proposed sites: sub-Tenon, intrascleral or at the pars plana. The following attributes of the designed NS were implicit to warrant efficacy and safety for possible inclusion in a delivery system for the intelligent treatment of ocular inflammatory disorders:

1. Appropriate size, surface stability, drug incorporation efficiency, and morphology of the NS. The overall stability and architecture of the formed NS would also be corroborated via generation of energetic profiles for the nanoformation of the ocular NS (polymeric and lipoid-polymeric based nanostructures) employing Molecular

Mechanics Energy Relationships (MMER) by exploring the spatial disposition of energy minimized molecular structures.

2. Acceptably low toxicity of the NS
3. Improved permeation of the NS across ocular barriers of interest compared to an indomethacin suspension
4. Enhanced internalization/ cell uptake potential (employing a generic cell line - in this instance Caco-2 cells were employed) as investigated via fluorescence and confocal microscopy compared to an indomethacin suspension, Overall results for each NS were substantiated via generation of energetic profiles via hydrophilic-lipophilic modeling employing MMER by exploring the spatial disposition of energy minimized molecular structures
5. Ability of the NS to enhance the efficacy of the incorporated anti-inflammatory agent as investigated through the propensity to reduce inflammation in a generic cell line in which inflammation would be induced compared to an indomethacin suspension
6. Potential to decrease inflammatory markers as ascertained via the appropriate enzyme-linked immunosorbent assay (ELISA) compared to a hydrocortisone suspension.

3.3. Materials and Methods (Part A)

3.3.1. Materials

Chitosan (low molecular weight M_w<6000 Da, viscosity ~20 000cps), poly(*ε*-caprolactone) (PCL), indomethacin (99% TLC minimum), DL-α disteroylphosphatidylcholine (DSPC), L-α distearoylphosphatidylethanolimine methoxypolyethylene glycol conjugate (DSPE-mPEG, referred to as DSPE, henceforth), and Tween® 80 were all purchased from Sigma-Aldrich® Inc. (St. Louis, MO, USA). Acetone and hydrochloric acid (HCl, 32%) were obtained from Unilab (Merck Chemicals (Pty) Ltd, Wadeville, Gauteng). Chloroform spirit was purchased from Wako (Pure Chemical Industries, Ltd. Japan). All other reagents were of analytical grade and were used as received.

Toxicology: White walled tissue culture plates compatible with luminometer and fluorometer, AAF-Glo™ substrate and reagent, 25mL assay buffer, 40µL Digitonin, and Lysis Reagent were obtained from Promega Corporation (Madison, USA).

Ex vivo permeation studies: Fluorescite™ 10% (sodium fluorescein) was purchased from Alcon® Laboratories (Bryanston, Johannesburg, South Africa). Enucleated eyes from euthanized New Zealand Albino rabbits (Ethics Clearance No. 2009/02/05) were obtained

from animals housed in the Central Animal Service, University of the Witwatersrand, Johannesburg.

ELISA: A Transfactor Extraction Kit and Transfactor NFκB p65 Colorimetric Kit were purchased from Clontech Laboratories (Clontech Laboratories, Inc. California, USA), Dulbecco's Modified Eagles Medium, chloroform spirit, bovine serum, USP phosphate buffered saline, Amphotericin B solution, and 1% penicillin-streptomycin solution were purchased from Sigma-Aldrich® (Sigma-Aldrich® Inc., St. Louis, USA). Hydrogen peroxide (3%) was obtained from Medical & Hospital supplies CC (Pretoria West, South Africa).

3.3.2. Culturing of a generic cell line (Caco-2 cells) and subsequent inflammation induction in cell lines

Caco-2 cells were employed as a generic cell line. The rationale for this being that they are a well-characterized line that grows quickly in culture and are representative of epithelial cells from all tissues of the body and has been previously employed in additional ocular studies such as the investigation of human CMV retinitis infection (Jarvis et al., 1999). The Caco-2 cells were cultured at 37°C in humidified air containing 5% CO_2. The Caco-2 cells were maintained in a 250mL sterile cell flask with Dulbeccos Modified Eagle's Medium, 1uL/mL of penicillin-streptomycin solution, and 1µL/mL of Amphotericin B solution. The cells were passaged by trypsinization (0.1% trypsin-0.5 mM EDTA) before the nuclear extraction procedure; all cell cultures had an approximated cell density of 1.6 million cells/mL determined via hemocytometry.

Inflammation was induced in cell lines in certain ensuing experiments via exposure to UV irradiation. UV irradiation reportedly initiates similar effects on cells as pro-inflammatory cytokines, promulgating the inflammatory cascade (Romero et al., 2006). There is membrane leakage of lactate dehydrogenase, generation of intracellular reactive oxygen species, increase in cell/ plasma membrane permeability (allowing more sodium and other ions to diffuse into the cell causing osmosis of water into the cell), and expression of inflammatory markers such as vascular cell adhesion molecule-1 and intercellular adhesion molecule-1, (Sun et al., 2011).

3.3.3. Synthesis of chitosan-poly(*ε*-caprolactone) and lipo-chitosan-poly(*ε*-caprolactone) nanosystems

PCL (50mg) and the anti-inflammatory, indomethacin (20mg), were dissolved in 3mL acetone. For the lipoid-based NS (Lipo-Chit-PCL NS), the phospholipids, DSPC (20mg) and DSPE (5mg), were dissolved in 2mL chloroform and the organic phases mixed. The

liposomal constituents were omitted in the Chit-PCL NS. Chitosan (low molecular weight) (50mg) was dissolved in 15mL 0.05M HCl. Tween® 80 (0.01mL) was included as a surfactant. The chitosan solution was slowly added to the phospholipid-PCL-indomethacin solution with sonication at a relative amplitude of 80 for 1 minute (20 kHz sonicator, VibraCell, Sonics and Materials, Inc., Danbury, CT, USA). The organic solvent was subsequently evaporated with gentle stirring for 3 hours. The interaction between the carboxyl or hydroxyl groups of the anionic PCL and the amine groups of chitosan formed immediate polyionic nanogels. The stability of the formed NS suspension was maintained through freezing at -80^{o}C in an ultra-low freezer (Sanyo VIP™ Series, Sanyo North America Corporation, Wood Dale, IL, USA) prior to incorporation as the core of the I^3 (described hereafter in Section 3.3.5).

3.3.4. Characterization of the size and stability of nanosystems

The size distribution (as well as the associated polydispersity index (PdI) as a measure of the size variability within a formulation), average diameter and zeta potential of the respective NS was assessed using the Zetasizer Nano ZS (Malvern Instruments Ltd, Malvern, Worcestershire, UK) operating at a light source wavelength of 532nm and a fixed scattering angle of 173° for detection. The Zetasizer Nano ZS employs dynamic light scattering and allows the size and zeta potential of NS to be measured on a particle-by-particle basis. It takes into account both positively and negatively charged particles moving under Brownian motion. Changes in the zeta potential distribution with particle size can thus be studied, and aggregation can be measured quantitatively. Aliquots of 0.8mL of NS suspensions were placed into the appropriate cuvette and the software configured with the specific parameters of refractive index and absorption coefficient of NS materials and solvent viscosity.

3.3.5. Morphological analysis of the transitions and interactions of NS formulations embedded within a chitosan core employing light, transmission and scanning electron microscopy

Imaging and analytical characterization of NS by Transmission Electron Microscopy (TEM) is often performed to define the size, shape and elemental distribution within the NS. TEM was performed on both NS formulations following initial sonication at a relative amplitude of 80 for 1 minute (20 kHz sonicator, VibraCell, Sonics and Materials, Inc., Danbury, CT, USA). Thereafter one drop of the respective NS suspension was placed on a TEM sample support mesh and samples were allowed time to dry (~10 minutes), followed by placement into the TEM airlock/ specimen stage. Images were acquired at 10 000x magnification, being optimal in this instance for good resolution images (TEM, JEOL 1200 EX, Japan). The TEM was operated at a voltage of 80kV.

The ultimate destination of the NS is incorporation within the core of the I^3, which would be composed of a crosslinked chitosan matrix. Chitosan (MMW) was hydrated in the NS suspension to yield a final MMW chitosan concentration of 13.33%$^{w}/_{v}$. In the case of the Lipo-Chit-PCL NS, an interesting phenomenon was noted during the stage of incorporation - this interaction of the comparatively larger chitosan molecules with the composite NS was progressively observed via stereomicroscopy (Olympus® Model SZX7, Japan) coupled with a digital camera and image analysis software (analySIS® Soft Imaging System, Japan).

Subsequent crosslinking of the chitosan to form a preliminary 'core' matrix in an acidified 2.5%$^{v}/_{v}$ gluteraldehyde solution was undertaken, followed by purification and drying at ambient conditions - the formed pellet was subjected to scanning electron microscopy (SEM). The surface morphology of dried NS incorporated within the core BPM was evaluated on a desktop SEM system (Phenom™ Scanning Electron Microscope, FEI Company, OR, USA) to view the overall and in-depth surface architecture to qualitatively elucidate factors such as shape, size, and degree of aggregation. Different magnifications at 10keV were employed to view the overall and in-depth surface structure. Samples were made electrically conductive prior to analysis through the process of gold-sputter coating (SPI Module™ Sputter Coater, SPI Supplies, PA, USA). Samples were attached to a SEM stub using adhesive carbon tape. The stub was inserted into the stub holder and the glass chamber and sputter head were replaced. Argon gas was allowed to flush the system before the leak valve was sealed and the vacuum was turned on. The sputter coater was run for 90 seconds when the plasma current reached 18mA, after which the system was turned off and the vacuum released.

The interaction of the NS with a generic cell line was also investigated via visualization under SEM. For both NS preparations, 1mL of the suspension was placed in a small glass petridish and Caco-2 cell culture (4mL) was added with incubation for 15 minutes at 36.7^{o}C, followed by freezing at -80^{o}C (Sanyo VIP™ Series, Sanyo North America Corporation, Wood Dale, IL, USA) with subsequent lyophilization at 25 mtorr for 48 hours (FreeZone® 2.5, Labconco®, Kansas City, Missouri, USA) and inspection for any remarkable interactions under SEM at various magnifications.

3.3.6. Assessment of the toxicological profile of the nanosystems

In noting the advantages of new developments in ocular NS for enhancing drug delivery, the other side of the coin must also be considered. It comes as no surprise that the innate NS architecture creating its advantages in biomedical applications may confer reactivity in

biological systems and lead to toxicity, blocking cell metabolic processes and impairing tissue function on aggregation. Thus, a critical issue with nanomaterials is the clear understanding of their potential toxicity. Furthermore, distortion of the ocular tissue architecture leading to altered function could result from indiscriminate NS accumulation in ocular tissues (Diebold and Calonge, 2010). A very important consideration with NS is toxic effects that may occur due to the actual approaches that are instituted to enhance ocular drug bioavailability, which is the presence of high levels of the loaded drug in a non-target tissue - the reason why effective targeting strategies should be considered. A number of physicochemical parameters have been proposed to be critical determinants in NS toxicity: size, crystalline structure, chemical composition, surface area, oxidation status, etc; none of which are singularly responsible. Moreover, another important factor to take into account is the nature of the cell type studied as each cell type has its own function and therefore may not respond the same way as another cell type after exposure to a single nanomaterial (Lanone et al., 2009), the reason for institution of a generic cell line.

The aim of this study was to determine whether the fabricated ocular NS are toxic to living cells and to ascertain whether the rate of apoptosis was significantly increased with the introduction of increasing levels of the NS to a cell culture.

The viable cell number was determined instituting the formula:

$$Total\ Cell\ Number - Dead\ Cell\ Number = Viable\ Cell\ Number \qquad \text{[Equation 3.1]}$$

The % cell viability (%CV) was determined as:

$$\%\ Cell\ Viability = \frac{Viable\ Cell\ Number}{Total\ Cell\ Number} \times 100 \qquad \text{[Equation 3.2]}$$

The CytoTox-Glo™ Cytotoxicity Assay is a single-reagent-addition, homogenous, luminescent, assay that allows measurement of the number of dead cells in cell populations. The CytoTox-Glo™ Cytotoxicity Assay measures a distinct protease activity associated with cytotoxicity and employs a luminogenic peptide substrate (alanyl-lanylphenylalanyl-aminoluciferin; AAF-Glo™ substrate) to measure ‘dead-cell protease activity’. The AAF-Glo™ substrate cannot cross the intact membrane of live cells and does not generate any appreciable signal from the live-cell population. The CytoTox-Glo™ Assay relies on the properties of a thermostable luciferase (Ultra-Glo™ Recombinant Luciferase - this furnsihes a stable ‘glow-type’ luminescent signal.

The inclusion of Lysis Reagent enables generation of a luminescent signal associated with the total number of cells in each assay well. Cell viability is subsequently determined by the difference in the luminescent signal resulting from experimental death and total luminescent values.

Part 1

Initially a 1:3 dilution with PBS solution and both NS samples were made (resulting in an indomethacin concentration of 0.33mg/mL). The two NS solutions were then placed into tissue culture plates, Chit-PCL NS in the first row and Lipo-Chit-PCL in the second row, in increasing increments of 5µL (ranging from 5-40µL), from well 1 to well 8, and left for a 24 hour period. Caco-2 cells (80µL) were then added into each well. These mixtures were then incubated at 36.7°C for a 24 hour period.

Part 2

A cell culture of Caco-2 cells was placed into a quartz cuvette. The Caco-2 cells were then exposed to ultraviolet light within a UV chamber (UV Stericab chamber, Life Steriware, New Delhi, India) at successive time intervals to instigate various degrees of cell damage replicating inflammation. Cells (80µL) were drawn up at each time interval and placed into the third row of wells of the tissue culture plate.

Wells 1 and 2 → cells not been exposed to UV radiation
Wells 3 and 4 → cells exposed to UV radiation for 1 minute 30 seconds
Wells 5 and 6 → cells exposed to UV radiation for 4 minutes
Wells 7 and 8 → cells exposed to UV radiation for 8 minutes
Wells 9 and 10 → cells exposed to UV radiation for 10 minutes
Wells 11 and 12 → cells exposed to UV radiation for 15 minutes.

Part 3

The CytoTox-Glo™ Cytotoxicity Assay was subsequently performed. The contents of the wells were then drawn up and placed into a white tissue culture plate in order to ascertain the toxicity to the cell samples. Firstly, 20µL of AAF-Glo™ reagent was placed into each well using a multichannel pipettor, which was then mixed and incubated for 15 minutes at room temperature. The white plate was then placed into a luminescence plate reader (Victor™ X3 2030 Multilabel Reader, which includes luminescence, fluorescence intensity [both top and bottom reading] and UV-absorbance [UV-VIS] technologies; PerkinElmer Ltd., Beaconsfield, UK) to measure the luminescence, in order to determine the number of dead cells. Thereafter, the Digitonin was prepared in an assay buffer to form the Lysis Reagent. The

Lysis Reagent (20µL) was then added into each well plate, mixed, and incubated for 15 minutes at room temperature. The white plate was subsequently placed into the luminescence plate reader in order to determine the total cell number.

3.3.7. *Ex vivo* drug-loaded nanosystem permeation across ocular barriers

The proposed NS, following implantation as an intraocular device, would potentially encounter and/ or permeate through the various ocular structures such as the sclera, choroid and RPE (and their associated barrier functions e.g. the blood-retinal barrier, BRB) depending on the site of implantation of the device (i.e. sub-Tenon, intrascleral or at the pars plana). For this investigation, and in line with the proposed sites of implantation, enucleated New Zealand Albino rabbit eyes were employed, as obtained from *in vivo* Pilot Study A conducted concurrently (Chapter 6, Section 6.2.2.1). The snap-frozen eyes (immediately frozen following enucleation at -80^{o}C in an ultra-low freezer (Sanyo VIP™ Series, Sanyo North America Corporation, Wood Dale, IL, USA) and used within 3 days of enucleation) were thawed at room temperature (25^{o}C) and cleaned by removing the external connective tissues and muscles and rinsed with PBS. The eyes were opened by giving a circular cut just posterior to the limbus and dissected to include the RPE, choroid and sclera (RCS) as the semi-permeable membranes on the Franz diffusion cell (Figure 3.1a and b). The receptor compartment of each Franz diffusion cell was filled to the graduated line with PBS (pH 7.4) and the donor compartment contained 0.5mL of the respective NS suspension or pure indomethacin suspension (comprising 20mg of indomethacin in 1mL chloroform spirit and 14mL deionized water, to replicate the drug concentration of the NS suspension). A control experiment was undertaken employing drug-free NS (purely polymeric and composite lipoidal-polymeric formulations) to ascertain whether the observed permeation was due to only drug penetration or drug-loaded NS movement across the RCS; and to account for the effect of the lipid and polymer NS components on the componential UV absorbance within the receptor compartment at the reported wavelength. Furthermore the presence of ocular tissues and/or debris present in the PBS of the receptor compartment on the absorbance readings was also accounted for by running a blank experiment with 0.5mL of water: chloroform (14:1) in the donor compartment. At 0.5 hours, 1 hour, 2 hours, 4 hours and 6 hours, 1mL samples of solution were extracted from the receptor compartment, with balancing replacement with PBS to maintain sink conditions within the solubility range of indomethacin (0.937mg/L), and analyzed via UV spectrophotometry (Specord 40 UV spectrophotometer, Analytik Jena AG, Jena, Germany) at a λ_{max} of 318nm. The cumulative indomethacin diffusion per unit area of ocular membrane was ascertained. From this, the extent of indomethacin permeation across the ocular tissue was determined in terms of drug

flux. The flux (mg.cm^{-2}.hr^{-1}) of drug across the ocular tissue was calculated per unit area by linear regression analysis of permeation data using Equation 3.3.

$$J_S = \frac{Q_r}{A \times t} \qquad \text{[Equation 3.3]}$$

Where J_s is the flux, Q_r (mg) is the quantity of indomethacin that diffused through the RCS into the receptor compartment, A (cm^{-2}) is the effective cross-sectional area available for drug permeation and t (h) is the time of drug exposure to the ocular tissue. All measurements were conducted in triplicate (n=3). The permeability coefficient (P), following application of Ficks's law, can be calculated as follows:

$$P = \frac{J_S}{C_{donor}} \qquad \text{[Equation 3.4]}$$

The degree to which indomethacin flux across the RCS was enhanced following incorporation in a NS compared to the drug suspension was also expressed as the enhancement ratio (ER).

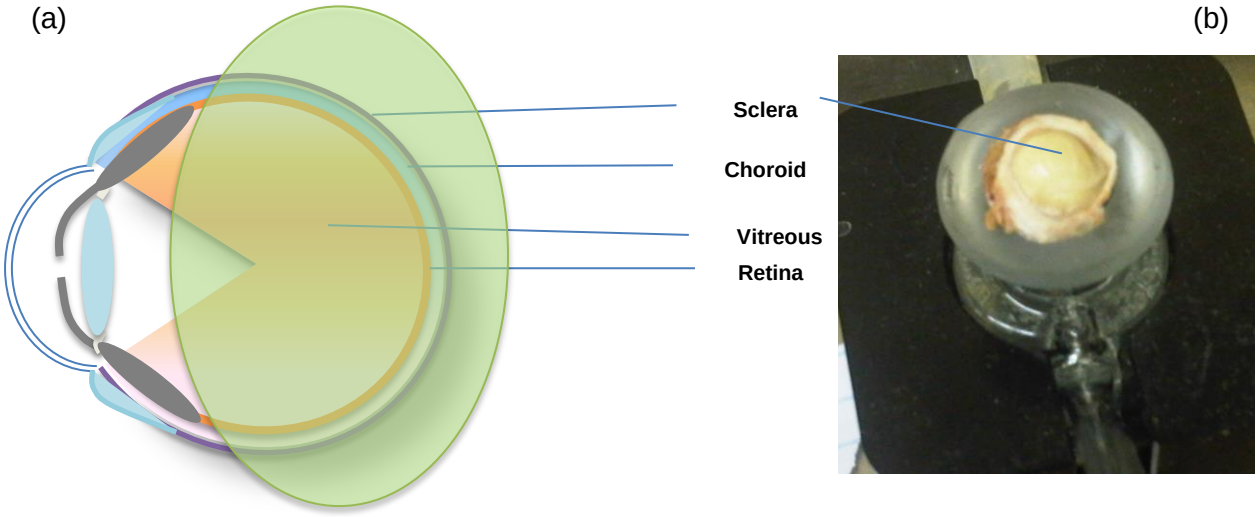

Figure 3.1: (a) Schematic highlighting the portion of the eye dissected for the permeation studies and (b) the experimental set up of the RCS membranes on the receptor compartment of the Franz diffusion cell apparatus

Additionally, utilization of fluorescence microscopy was undertaken to qualitatively inspect the potential for NS permeation (rather than merely drug permeation) through ocular tissue. In order to facilitate microscopic visualization of NS movement, fluorescein (Fluorescite®) was incorporated into the NS during the manufacture of both formulations in the aqueous phase. Permeation studies were performed as described above. The suspensions were allowed to diffuse through the ocular tissue for 6 hours, thereafter a section of the membrane

including all ocular layers employed in the permeation study of the ocular tissue was dissected and placed on a glass microscope slide on the created dimensional face (the face that prior to dissection would form the internal parenchyma of the sclera and cornea) with subsequent visualization via stereomicroscopy (Olympus® Model SZX7, Japan). An image was then acquired under maximum magnification (220x) in a darkened room with exposure of the tissue sample to the irradiation from a handheld UV torch.

3.3.8. Utilization of a superoxide probe for determination of the anti-inflammatory efficacy of nanosystems

The detection and measurement of the superoxide ion has been critical to the understanding inflammation in living organisms (Olojo et al., 2005). A UV spectrophotometric anti-inflammatory efficacy study was undertaken employing a 4-chloro-7-nitrobenzo-2-oxa-1,3-diazole (NBD-Cl) as a superoxide probe. The amount of superoxide ions and glutathione created by Caco-2 cells is an indication of the degree of inflammation occurring in a sample cell culture, thus the ability of a formulation to decrease the amount of these inflammatory markers indicates its effectiveness as a drug delivery system when compared to a control preparation (i.e. indomethacin suspension).

The superoxide ion probe, NBD-Cl, has been well documented in its use for fluorescent detection of reactive thiols as well as primary and secondary amines. Olojo and co-workers (2005) demonstrated that NBD-Cl has application in the rapid detection and quantification of superoxide ion production generated by a water-soluble enzymatic system (xanthine-xanthine oxidase), a membrane-bound nicotinamide adenine dinucleotide (NADH) oxidase, or in an organic solvent (Olojo et al., 2005).

Initially a 0.001M solution of NBD-Cl was prepared by dissolving 20mg of NBD-Cl in 1mL of chloroform spirit, which was made up to 100mL with deionized water, being the optimal concentration for superoxide ion concentration determination as stipulated by Olojo et al. (2005). The defined wavelength for determination of the concentrations of NBD-Cl complexes was 470nm (Olojo et al., 2005). An indomethacin suspension was prepared as described. All suspensions were buffered with PBS using a 1:3 dilution (indomethacin concentration = 0.33mg/mL). The reference solution (for UV spectrophotometer zeroing) for this experiment contained 1.5mL dilute cell culture further diluted with PBS (1:4) maintained at room temperature (this allowed a solution that permitted good transmittance; the dilute cell culture was kept in an incubator, not for longer than a day), 1mL NBD-Cl solution and 0.5mL of the indomethacin suspension. Thereafter the amount of superoxide ions produced after exposure to UV radiation was determined in the solutions that were not exposed to a

sufficient pharmacodynamic anti-inflammatory effect, in which the anti-inflammatory drug (indomethacin) was only added immediately prior to placing the solution in the UV chamber (UV Stericab chamber, Life Steriware, New Delhi, India). This ensured that very little time elapsed in which the drug could have an anti-inflammatory effect, thus not being able to effectively inhibit COX that would otherwise affect superoxide concentration by decreasing NADH oxidase activity and by decreasing glutathione (which also complexes with NBD-Cl) by glutathione S-transferase (GST) enzyme inhibition (Lampe et al., 2000).

The exact procedure implicated placing the cell culture dilution (1.5mL) into a cuvette together with 1mL NBD-Cl solution, followed by 0.5mL indomethacin suspension, and then placing the cuvette into a UV chamber where exposure to the UV radiation would induce inflammation. Exposure time was 1 minute and 30 seconds, as this was established as an optimal time to expose Caco-2 cells to UV radiation in order to create a non-necrotic inflammatory response; if cells lysed they would not produce inflammatory mediators as biomolecular processes would cease. The reason that NBD-Cl was added to the cell culture prior to placing it in the UV chamber is because as the superoxide probe binds to superoxide ions it does not allow them to undergo further reaction to peroxide or back to O_2 ($2O^{2-} + 2H_2O \rightarrow O_2 + H_2O_2 + 2OH^-$). The samples were then prepared by adding 0.5mL indomethacin suspension to 1.5mL dilute cell culture and incubating this solution at 36.7^oC for 30 minutes (in this instance, allowing the drug to exert a pharmacodynamic effect). Thereafter 1mL of NBD-Cl was added to the sample, which was subsequently placed in a UV chamber for 1 minute and 30 seconds. Absorbance readings were immediately obtained via UV spectrophotometry. The same procedure was followed for the two NS formulations (i.e. the NS suspensions also underwent a 1:3 dilution with PBS and possessed an indomethacin concentration of 0.33mg/mL, with addition of dilute cell culture and incubation for 30 minutes). This time was sufficient to enable the specific NS to commence availing indomethacin (either following cellular uptake or drug diffusion from the NS), versus the control, and to adequately inhibit the targeted enzyme systems as established *in vivo*, and achieved by 10 minutes, as demonstrated by Stofan et al. (2000). All measurements were conducted in triplicate (n=3).

3.3.9. Utilization of an Enzyme-Linked Immunosorbent Assay to ascertain nanosystem anti-inflammatory efficacy

Nuclear factor kappa-light-chain-enhancer of activated B cells (NFκB) constitutes a family of transcription factors consisting of five members, including Rel (c-Rel), RelA (p65), RelB, NFκB1 (p50 and its precursor p105), and NFκB2 (p52 and its precursor p100). NFκB regulates the expression of numerous genes, including IκBa, cytokines, chemokines,

adhesion targets, and acute phase proteins involved in growth, development, apoptosis, immune and inflammatory responses, and activation of various viral promoters (Brasier, 2006; Gilmore, 2006; Perkins, 2007). NFκB is a pertinent regulator of the immune response to infection (with kappa light chains being critical components of immunoglobulins). Incorrect regulation of NFκB has been linked to cancer, inflammatory and autoimmune diseases, septic shock, viral infection, and improper immune development (Albensi and Mattson, 2000; Meffert et al., 2003). The propensity of the designed NS to enhance the potential of the anti-inflammatory agent to decrease the concentrations of the NFκB transcription factor is a key indicator of the anti-inflammatory-enhancing potential of the designed system.

A TransFactor Kit (Transfactor NFκB p65 Colorimetric Kit, Clontech Laboratories, Inc. California, USA) was employed for efficient detection of transcription factor activities in cell extracts via an enzyme-linked immunosorbent assay (ELISA)-based format, which detects DNA binding by specific transcription factors (i.e. NFκB p65) (Shen et al., 2002). The transcription factors are detected by a Primary antibody, and the horseradish peroxidase (HRP)-conjugated Secondary Antibody detects the complex. On reaction of HRP with added substrate, an enzymatic product is formed that can be measured via an absorbance microtiter plate reader for colorimetric detection, or a luminometer for chemiluminescent detection (Benotmane et al., 1997).

Four 100mL Caco-2 cell suspensions were exposed for 30 minutes to a culture medium containing 2mM H_2O_2 as an established means of inducing inflammation in Caco-2 cell lines (Shin, 2011); three of these cultures were initially treated with a different formulation i.e. hydrocortisone-containing Chit-PCL-NS, hydrocortisone-containing Lipo-Chit-PCL NS and a hydrocortisone dispersion in a mixture of chloroform spirit in water ($1\%^{v}/_{v}$). The rationale for employing hydrocortisone rather than indomethacin in these formulations in this experiment is that it has a significant effect on decreasing the amount of activated NFκB that travels to cell nuclei from the cytoplasm by increasing the synthesis of anti-inflammatory proteins, such as annexin-1 (lipocortin-1), SLPI, IL-10, the inhibitor of NFκB, IκB-a, glucocorticoid-induced leucine zipper protein, which inhibits both NFκB and AP-1 (Barnes et al., 2003); it also decreases the amount of NFκB by decreasing the amounts of other cytokines such as TNF-α and IL-1 that stimulate NFκB activation. Thus a more notable effect would be emulated here, while still striving towards the overall goal of this investigation, being the ascertainment of the potential of the NS to enhance the anti-inflammatory potential of the incorporated drug. Each formulation solution was diluted with PBS (1:4 dilution), resulting in a drug concentration of 0.267mg/mL; 1mL of this dilution was then added to each of the three flasks to obtain a culture concentration of 2.6µg/mL of hydrocortisone. This concentration would be considered

effective as it is above the accepted mean effective concentration of 1ng/mL. After incubation, NFκB was extracted from the cell nuclei via the commercially available cell extraction kit; thereafter the amount of protein in the extracts was quantified using a Nanophotometer™ (Implen, Northstar Scientific, Germany) in order to ensure cell extracts were obtained that would allow a nuclear extract sample concentration of 5µg/µL for each sample set after dilution of the nuclear extract with blocking buffer, as this is generally the optimal concentration of protein extract required in order to achieve high absorbancies. The level of NFκB in the cell supernatant was determined by employing the commercially available ELISA kit utilized according to the manufacturer's protocols. Absorbance values were obtained at a wavelength of 655nm via an advanced plate reader (Victor™ X3 2030 Multi-label Reader, PerkinElmer Ltd., Beaconsfield, UK) in order to quantify the relative amount of NFκB that was present in each sample. Correction of the the optical density (OD) for each sample was via subtraction of the OD of the blank, with subsequent correction for total protein in the sample. All measurements were conducted in triplicate (n=3).

3.3.10. Utilization of confocal microscopy to confirm the extent of intracellular permeation of nanosystems in normal versus inflamed cells

Confocal microscopy has an important biomedical application in the imaging of either fixed or living cells and tissues that have usually been labeled with one or more fluorescent probes (Paddock et al., 2012). The objective of this study was to further visualize the degree of cellular uptake of both NS, in both normal cells and in cells exposed to UV irradiation in order to instigate inflammatory changes. Fluorescein was included as a fluorescent probe as described. Initially Caco-2 cell samples were prepared as a confluent monolayer having a cell count of approximately 1.5 million/mL (determined using a hemocytometer). The cell culture was placed in a cuvette, followed by exposure to UV radiation for 1 minute and 30 seconds, as this was established as an optimal time to expose Caco-2 cells to UV radiation in order to create a non-necrotic inflammatory response (as previously established).

The NS suspensions (0.25mL) were each placed into a 3mL microcentrifuge tube followed by the addition of 2.5mL of cell culture into each tube. The sample tubes were then incubated for 30 minutes. Thereafter, 0.5mL of 4%$^{v}/_{v}$ paraformaldehyde solution was added to the cell cultures to cease all biological processes and preserve the cells. One drop of each NS formulation was then placed on a microscope slide and each drop covered with a cover-slip and evaluated via confocal microscopy (Zeiss LSM 780, Carl Zeiss Microscopy GmbH, Goettingen, Germany). Quantification of the viable cell density of samples subjected to confocal analysis was undertaken via an advanced plate reader possessing a variety of counting modes (Victor™ X3 2030 Multi-label Reader, PerkinElmer Ltd., Beaconsfield, UK),

as described in Section 3.3.6 for determination of the total and dead cell count, to ensure that the visualized results could not be attributed to differences in cell density.

3.3.11. High speed fluorescence microscopy for live imaging of nanosystem uptake by inflamed cells

A high speed fiber-optic fluorescence microscope (Cellvizio® LAB, coupled with Microprobes and ImageCell™ Software; Visualsonics and Mauna Kea Technologies, USA) was employed for *ex vivo* cellular imaging to ascertain NS interaction and/ or uptake by a generic cell line (Caco-2 cells). It provides an *in situ* dynamic fluorescence microscopy solution, generating key information on the manner and location in which a molecular compound is taken up at the cellular level. Fluorescein-conjugated NS were prepared. Each NS suspension (0.5mL) was placed in a graduated sterile centrifuge tube. Caco-2 cell culture (1mL), which was exposed to UV irradiation as previously described, was introduced into each tube followed by centrifugation of the cell cultures at 280xg in a high-speed table microcentrifuge (Model TG16-WS, Shanghai Ronbio Scientific Co., Ltd., China) and extraction of the supernatant. Thereafter, the cells were re-suspended in PBS (pH 7.4). The NS-cell culture samples were incubated for 30 mins at 37^{o}C; thereafter the samples were viewed, and images acquired at successive time intervals for determination of NS-cell interactions. Images were also acquired of the fluorescein NS without the cell culture to serve as a control.

From data accumulated through the described investigations, the proposed mechanism of uptake of NS was constructed.

3.3.12. Molecular modeling simulations for prediction of nanosystem formation and cellular internalization of the nanosystems

3.3.12.1. Static Lattice Atomistic Simulations in vacuum

All modeling procedures and calculations, including energy minimizations in molecular mechanics, were performed using the HyperChem™ 8.0.8 Molecular Modeling System (Hypercube Inc., Gainesville, Florida, USA) and ChemBio3D Ultra 11.0 (CambridgeSoft Corporation, Cambridge, UK). DSPC (without the aliphatic chains), DSPE (without the aliphatic chains) and PCL were drawn using ChemBio3D Ultra in their syndiotactic stereochemistry as 3D models whereas the structure of chitosan (6 monomer chain) was built using polysaccharide editor module on HyperChem 8.0.8. The models were initially energy-minimized using MM+ force field and the resulting structures were again energy-minimized using the Amber 3 (Assisted Model Building and Energy Refinements) force field. The conformer having the lowest energy was used to create the polymer-polymer

complexes. A complex of one molecule with another was assembled by disposing the molecules in a parallel fashion, and the same procedure of energy-minimization was repeated to generate the final models: Chit-PCL, Chit-PCL-DSPC and Chit-PCL-DSPE (hypothetical molecular complexes), and Chit-PCL-DSPC-DSPE. Full geometry optimization was carried out in vacuum employing the Polak-Ribiere conjugate gradient algorithm until an RMS gradient of 0.001kcal/mol was reached. Force field options in the AMBER and MM+ methods were HyperChem 8.0.8 defaults (Kumar et al., 2011).

3.3.12.2. Static Lattice Atomistic Simulations in a solvated system

To generate the final models in a solvated system the MM simulations were performed for cubic periodic boxes with the molecular complex at the centre of the cubic box and the remaining free space filled with water molecules and the same procedure of energy-minimization was repeated to generate the solvated models except that the force fields were utilized with a distance-independent dielectric constant with no scaling (Table 3.1). Additionally, the force field options in the AMBER (with explicit solvent) were extended to incorporate cutoffs to Inner and Outer options with the nearest-image periodic boundary conditions, and the outer and inner cutoffs were to ensure that there were no discontinuities in the potential surface (Table 3.1) (Choonara et al., 2011).

Table 3.1: Computational parameters used to construct aqueous-phase model building and simulations

S. No.	Parameter	Description
1	Periodic box dimensions	15×15×35A°^{3}
2	Cut-offs	Switched
3	Dielectric (epsilon)	Constant
4	1-4 Scale factors	Electrostatic: 0.5 van der Walls: 0.5
5	Outer radius	7.5A°
6	Inner radius	3.5A°
7	Water molecules	261
8	Solvent/ Polymer distance	2.3A°

3.3.12.3. Molecular Mechanics Assisted Model Building and Energy Refinements

A molecular mechanics conformational searching procedure was employed to acquire the data employed in the statistical mechanics analysis, to obtain differential binding energies of a Polak-Ribiere algorithm, and to potentially permit application to polymer composite assemblies. MM+ is a HyperChem modification and extension of Norman Allinger's Molecular Mechanics program MM2 (Warhurst et al., 2003) whereas AMBER, is a package of computer programs for applying molecular mechanics, normal mode analysis, molecular

dynamics and free energy calculations to simulate the structural and energetic properties of molecules (Pearlman et al., 1995).

3.3.12.3.1. Molecular Mechanics Energy Relationship analysis

Molecular Mechanics Energy Relationship (MMER), a method for analytico-methematical representation of potential energy surfaces, was used to provide information about the contributions of valence terms, noncovalent Coulombic terms, and noncovalent van der Waals interactions for polymer/polymer and polymer/phospholipid interactions in the designed NS. The MMER model for potential energy factor in various molecular complexes can be written as:

$$\boldsymbol{E_{molecule/complex}} = V_{\sum} = V_b + V_\theta + V_\varphi + V_{ij} + V_{hb} + V_{el} \qquad \text{[Equation 3.5]}$$

Where, $V_{\sum}$ is related to total steric energy for an optimized structure, V_b corresponds to bond stretching contributions (reference values were assigned to all of a structure's bond lengths), V_θ denotes bond angle contributions (reference values were assigned to all of a structure's bond angles), V_φ represents torsional contribution arising from deviations from optimum dihedral angles, V_{ij} incorporates van der Waals interactions due to non-bonded interatomic distances, V_{hb} symbolizes hydrogen-bond energy function and V_{el} stands for electrostatic energy.

In addition, the total potential energy deviation, ΔE_{total}, was calculated as the difference between the total potential energy of the complex system and the sum of the potential energies of isolated individual molecules, as follows:

$$\boldsymbol{\Delta E_{Total(A/B)}} = E_{Total(A/B)} - (E_{Total(A)} + E_{Total(B)}) \qquad \text{[Equation 3.6]}$$

The molecular stability can then be estimated by comparing the total potential energies of the isolated and complexed systems. If the total potential energy of complex is smaller than the sum of the potential energies of isolated individual molecules in the same conformation, the complexed form is more stable and its formation is favored (Yu et al., 2008).

3.4. Results and Discussion

The ultimate aim of these investigations was to synthesize an anti-inflammatory NS with satisfactory size and surface properties, adequate permeation potential, low cellular toxicity, and enhanced anti-inflammatory potential availed to the incorporated drug. Specifically, we set out to determine whether inclusion of a lipoidal component within the designed ocular NS

notably enhanced the desired capabilities compared to a purely polymeric NS. The addition of phospholipids to the NS was anticipated to further improve the loading capacity of the hydrophobic drug, increases NS propensity for inflammatory cells, as well as augment the ability to transfect ocular tissues, and create a more biocompatible NS.

3.4.1. Proposed mechanism of formation of the lipo-chitosan-poly(ε-caprolactone) nanosystems

In this section, we briefly describe the proposed mechanism of formation of the composite NS. Phospholipid molecules exhibit amphiphilic properties and will thus aggregate either in their crystalline state or in polar solvents into ordered structures with typical lyotropic liquid crystalline symmetries (de Gennes, 1974). In aqueous solutions phospholipid molecules normally form self-closed spherical or oval structures where one or several phospholipid bilayers entrap(s) part of the solvent in its/ their interior. Where one bilayer separates the internal and external solvent, these structures are called small or large unilamellar vesicles (SUV and LUV, respectively), depending on the size, while the term multilamellar vesicles (MLV) is used in the case of many bilayers entrapping some of the solvent (Lasic, 1988).

Szoka and Papahadjopoulos (1978) elaborated the mechanism of vesicle formation by reverse phase evaporation technique (water-in-oil emulsions). The inverse micelles with phospholipid located on the organic solvent/ water phase boundary transform to vesicles upon removal of the organic phase. These micelles grow in size, transform into a gel composed of a continuous framework of curved bilayered surfaces, which disconnect upon addition of water, closing upon themselves, or else disassociating into curved bilayered phospholipid fragments (BPFs) which immediately vesiculate. A planar bilayer is a necessary intermediate structure in the transition reverse micelle-vesicle. If phospholipid is deposited on surfaces with special surface topography, BPFs of different sizes can be formed, which are already in the crystalline state. Upon hydration these peel off and form vesicles. The size is controlled by template surface topography while the formation of multilamellar structures is prevented by inducing surface charge on the bilayers (Lasic et al., 1988; Lasic, 1988). In this instance, the polymeric nanogel present during fabrication could serve as a template impacting on the overall liposome morphology.

Chitosan is known to form hydrogen bonds and hydrophobic interactions (Brunel et al., 2009). The interaction between the carboxyl or hydroxyl groups of the anionic PCL polymer and the amine groups of the LMW chitosan formed an immediate polyionic nanogel. With regard to the overall surface stability, the anionic fractions (DSPE and PCL have a negative surface charge which is pH-dependent) are anticipated to contribute to the resultant

negativity to the surface charge. DSPC exhibits no net charge; whereas chitosan would make a significant contribution to the positivity of the surface. Diffusion of the shorter PCL chains between the longer chitosan chains occurs as a result of strong ionic electrostatic interaction and complexation of the polymers to form a dense network. Furthermore, additional hydrophobic interactions promote the formation of a hydrated/ gelified core of neutralized chitosan and PCL chains surrounded by partially protonated chitosan chains extending outwards.

Combining theories of vesicle formation emanating from liposomology and the principles of polymer complexation on the nanoscale is necessary to obtain a tentative prediction of the overall NS architecture (Figure 3.2). Numerous liposomes are anticipated to spontaneously form, largely incorporating indomethacin within the phospholipid bilayer, located at the hydrophobic tail region. Chitosan and PCL are predicted to form diffuse nanogels (which may additionally entrap some of the drug) which interlock with and possibly serve as templates for one or more liposomes via adsorption. The adsorption of polysaccharides such as chitosan over liposomal membranes is due to an initial diffusion-controlled process by the polymeric components, ensued by lateral diffusion and subsequent interdigitation (interlocking) of adsorbed polysaccharide molecules into bilayers (Sihorkar and Vyas, 2001). The formed NS, in both formulatory instances, is anticipated to possess a coronal appearance, with a dense center emanating from crosslinking of chitosan and PCL, with interlocking of the liposomal structures, and a diffuse ‘atmosphere’ or chitosan polymeric chains extending outwards.

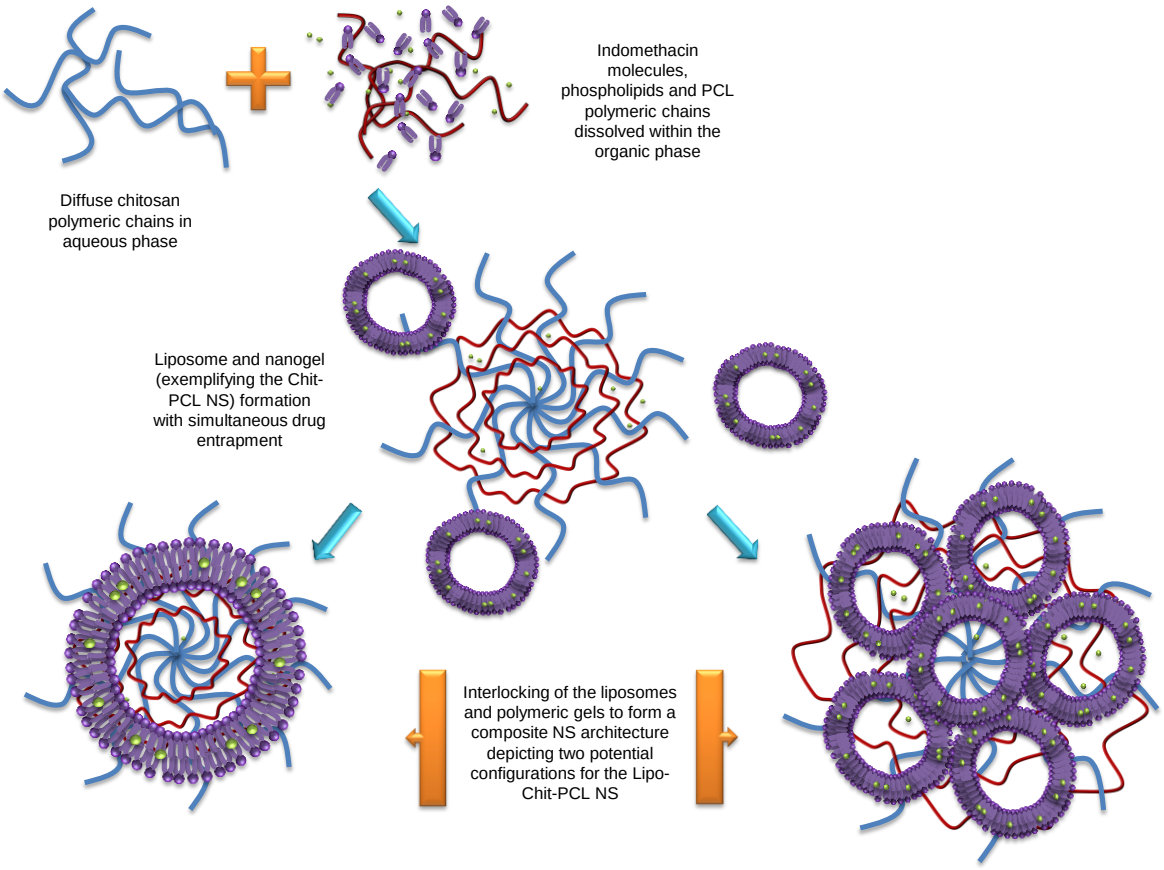

Figure 3.2: Proposed mechanism of formation of the composite nanosystem

3.4.2. Characterization of the size and stability of nanosystems

The average diameter of the Chit-PCL NS was 140.7nm (PdI=0.285) and that of the Lipo-Chit-PCL NS was 134.3nm (PdI=0.378) (Figure 3.3). Calvo et al. (1997b) reported nanocapsules of chitosan and PCL having a size range of 200-400nm. The normal size range of NS obtained employing this methodology fell between the desired size range of 100-200nm, thus promoting the potential for tissue permeation and cell uptake. Highly satisfactory zeta potentials were attained for both formulations, being +55.7mV and +49.4mV for the Chit-PCL NS and Lipo-Chit-PCL NS, respectively (Figure 3.4) - particles possessing zeta potentials between -30mV and +30mV typically tend to aggregate (www.nanosight.com). The slight split in the zeta potential peak for the Lipo-Chit-PCL NS may be attributed to the NS adopting different configurations in the presence of the lipoidal component due to spontaneous formation of the spherical liposomal structures, with certain particles accumulating a slightly lower ratio of chitosan polymeric strands per unit surface area than others, thus possessing an overall surface charge that is somewhat less positive.

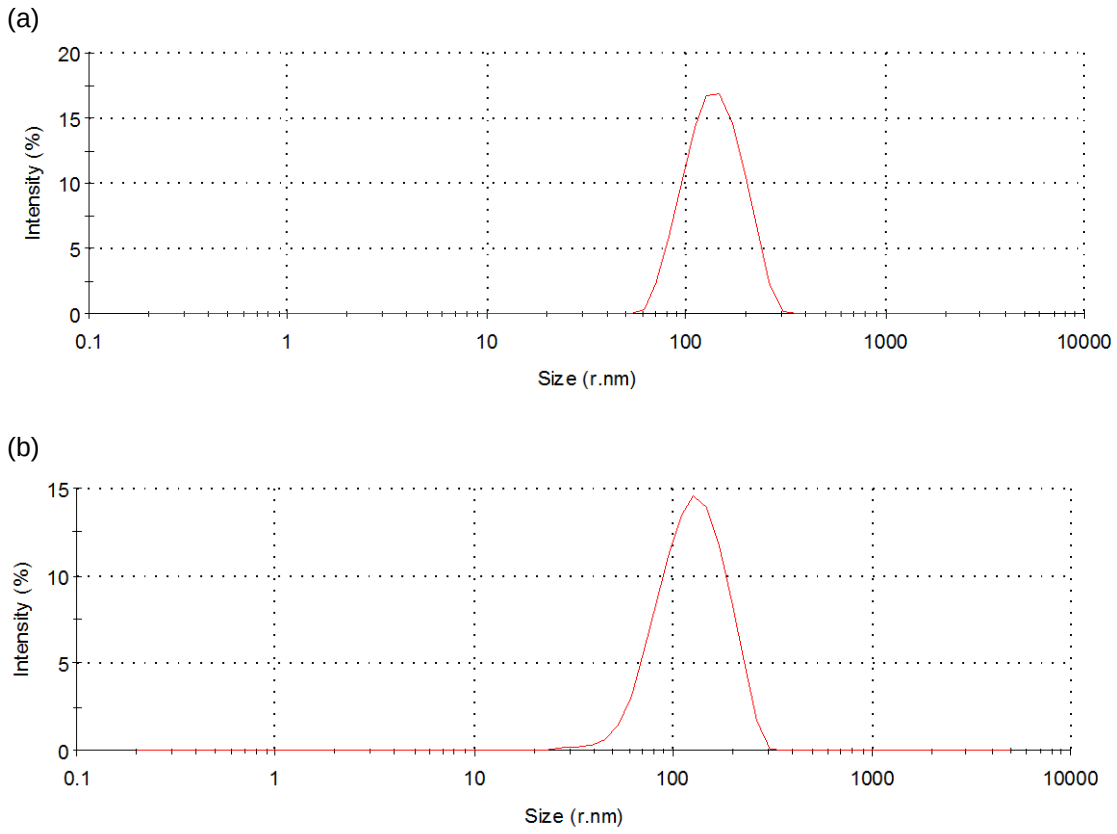

Figure 3.3: Size distribution of (a) Chit-PCL NS and (b) Lipo-Chit-PCL NS

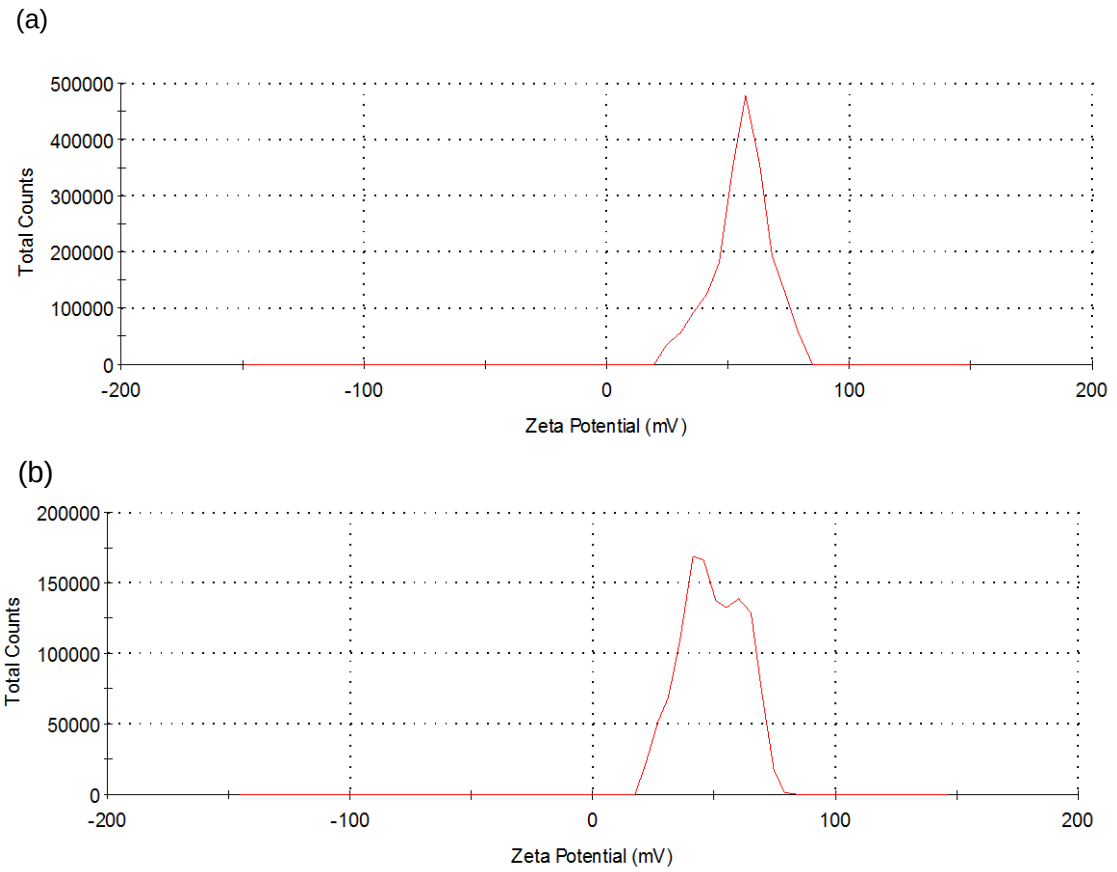

Figure 3.4: Zeta potential profiles for (a) Chit-PCL NS and (b) Lipo-Chit-PCL NS

3.4.3. Morphological analysis of the transitions and interactions of NS formulations embedded within a chitosan core employing light and scanning electron microscopy

Unique properties of the designed NS can lead to a high adsorption of impurities on their surface, complicating observation of individual structures. Thus it is fundamental to employ TEM for enhanced visualization. Structures were near-spherical and the proposed coronal appearance of the NS is clearly evident in the TEMs of both formulations, specifically apparent in the derived black-and-white contrast images (Figure 3.5aiii and biii). The observed size of both NS is congruent to measurements acquired via size analysis. The slightly larger size of the Chit-PCL NS compared to the composite NS is readily ostensible. The composite NS is more readily detected possibly due to the presence of a denser core in the presence of integrated liposomes in the nanogel structure.

Figure 3.6a depicts the phenomenon observed specifically for the Lipo-Chit-PCL NS. Incorporation of the NS (visualized as nanogels in suspension the photomicrograph Figure 3.6a) into the medium molecular weight-based chitosan matrix elaborated progressive coating with a respective increase in size of the nanogels due to surface adsorption of the long chain chitosan molecules at a perpendicular configuration to the NS surface, in a similar arrangement to the LMW chains comprising the NS (Figures 3.6b and c). The inflamed tissue-targeted systems ultimately boasted a ‘star-like’ appearance and were fundamentally ‘fuzzy’ microstructures. The NS essentially becomes maintained within the inner BPM composed of chitosan to become what is redolent of a ‘NS-polymer superlattice’, as elaborated by Taheri et al. (2011). The coating of the NS with the long chain chitosan (MMW chitosan) creates the compatibilizing layer enabling enclatheration of the NS within a polymeric matrix. It significantly increases the drug diffusion pathway from the NS by creating an extra layer and provides for the formation of hydrolyzable linkages which are established between the inner matrix and the NS; and the inner BPM would subsequently be formed via crosslinking, as visualized in the subsequent SEMs (Figure 3.7) and further elaborated in Chapter 4. These linkages hold the NS in place in the I^3 and ultimately release the NS on exposure to dissolution media. The hydrolysis of the matrix-NS linkages is anticipated to occur to a greater extent on exposure to inflammatory mediators (i.e. hydroxyl radicals) owing to the described responsive behavior of chitosan.

It is apparent that the surface topography of the Lipo-Chit-PCL NS coated and entrapped within the chitosan matrix (Figure 3.7b) differs from the surface architecture of the Chit-PCL NS (Figure 3.7a) as essentially, in the presence of phospholipids, the polymeric constituents are embedded and adsorbed in and around the lipoidal structure/s, whereas in their absence, the result is a purely polyionic nanogel structure. The outcome of generating the composite

structure is that the polymeric strands are adsorbed with consequent ionotropic interaction and chain entanglement around the lipoidal structures, which may comprise singular or multiple vesicular structures to create a multifaceted assemblage with diverse enabling features. This aforementioned point is an important consideration when dealing with the tissue permeation and cell uptake characteristics of each formulation. It was a prerogative of this study to predict the *in vivo* interaction between the designed NS and a generic cell line via *ex vivo* means. Images depicting the cultured Caco-2 cells and evident cellular adhesions are provided in Figure 3.8. It was further evident that the NS incorporating the phospholipids possessed an appeared to possess an enhanced propensity to be internalized via the biological processes of phagocytosis or endocytosis; as highlighted via the acquired SEM images (Figure 3.9b and c) compared to the polymeric NS (Figure 3.9a); this is attributed to the fact that phospholipids play an active role in biosynthetic molecular mimicry. Klausner et al. (1981) and Caron and Berlin (1987) discussed the fact that phospholipids (i.e. DSPC and DSPE) do in fact directly interact with tubulin, explaining the high concentration of microtubules 'attached' to the observed NS clusters. Furthermore the discovery of Fenske et al. (2001) explained the mechanism by which DSPE enhanced the intracellular uptake of NPs.

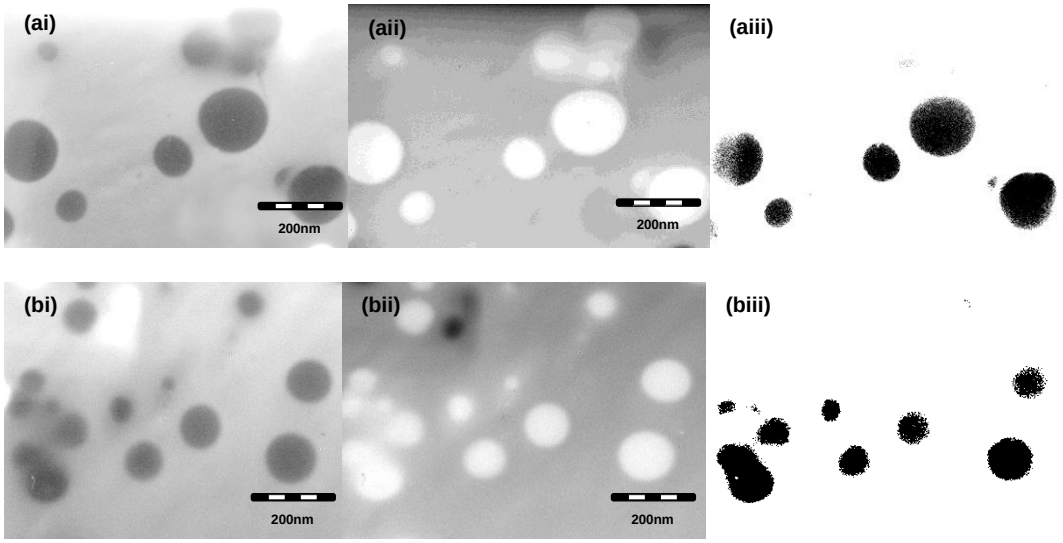

Figure 3.5: (i) Brightfield and (ii) darkfield TEMs acquired at 10000x magnification and (iii) black-and-white contrast images highlighting near-spherical coronal appearance of the NS for the (a) Chit-PCL NS and (b) Lipo-Chit-PCL NS formulations

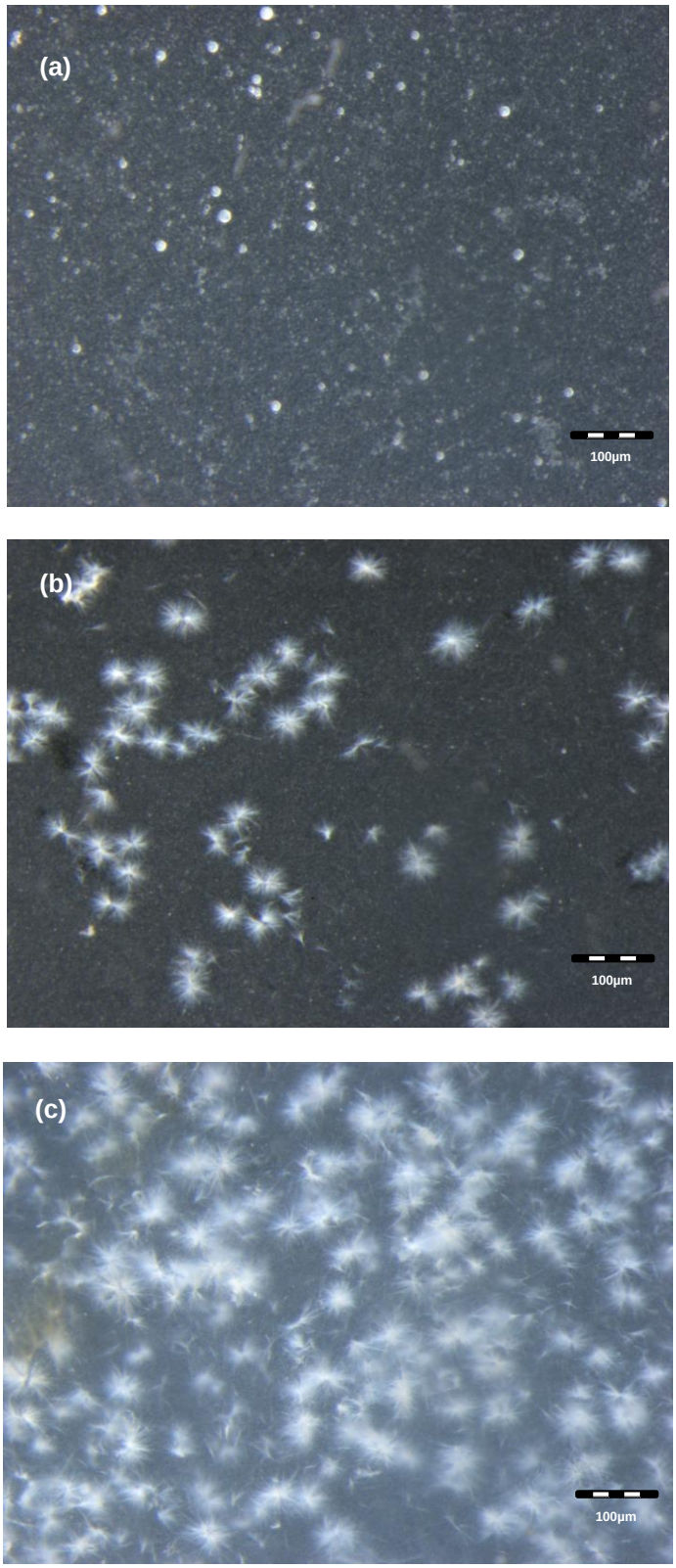

Figure 3.6: Progressive deposition of the polysaccharide coat on the Lipo-Chit-PCL NS at 32x magnification (scale bar redrawn for clarity: 1cm=100µm): (a) the uncoated NS, with time the coating emanated in the elucidation of 'fuzzy' microstructures, as viewed at (b) 12 hours and (c) 24 hours

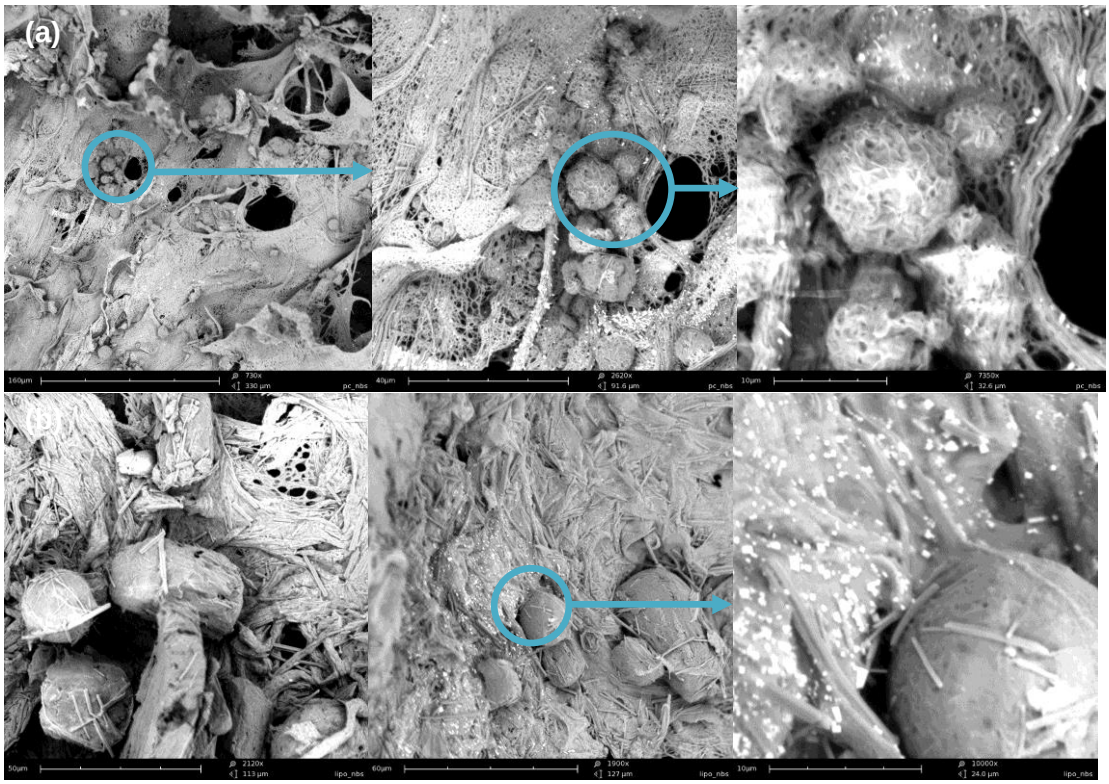

Figure 3.7: SEM images, at progressive magnifications, of the (a) Chit-PCL NS and (b) Lipo-Chit-PCL NS coated and embedded in the MMW chitosan matrix

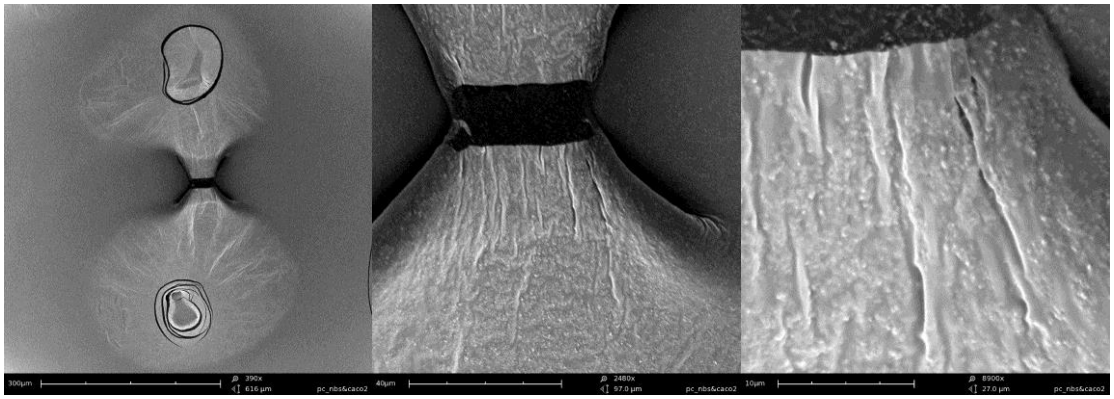

Figure 3.8: SEM images of Caco-2 cells, at increasing magnifications, highlighting cell adhesions

Figure 3.9: SEM images exemplifying the artefacts of NS-cell interactions for the (a) Chit-PCL NS and (b and c) Lipo-Chit-PCL NS. Microtubules interacting with the phospholipids in the NS enable the progressive intracellular transport of the internalized NS.

3.4.4. Assessment of the toxicological profile of the nanosystems

The results obtained highlighted acceptable toxicological profiles for both the Chit-PCL NS and the Lipo-Chit-PCL NS. The toxicity of both NS was found to be concentration-dependent; it can be seen that as the level of the NS increased the cell viability decreased, whereby the cell viability was maintained at lower NS levels of 15-25µL/ 80µL cell culture compared to higher levels of 40-50µL/ 80µL cell culture, where a more notable increase in toxicity was evident (Figure 3.10). With respect to Caco2 cells and UV Light exposure, as time of exposure increased, the cell viability dropped. The toxicology assay confirmed that 1 minute and 30 seconds was an adequate time period to expose Caco-2 cells to UV radiation (Figure 3.19). Overall, the results indicate that both NS exhibit a satisfactory toxicological profile for ocular administration. Ocular toxicity is a critical issue to consider for the design of nano-based ocular drug delivery systems; especially due to the fact that various clinical applications of drug delivery to the eye require chronic administration. It is thus fundamental to derive methods and assays to examine the immunosafety of NS, which are well-established and validated. From the results obtained, there is evidence of good tolerance and acceptability of the proposed NS from a toxicological perspective (this would be further put to the test via *in vivo* studies elaborated in Chapter 6). Furthermore, the incorporation of specific components into the NS has been shown to be of pertinence in this regard. The presence of PCL significantly improves the colloid stability and reduces the biological response to NS uptake (i.e. disorganization of the cytoskeleton) (Mao et al., 2007).

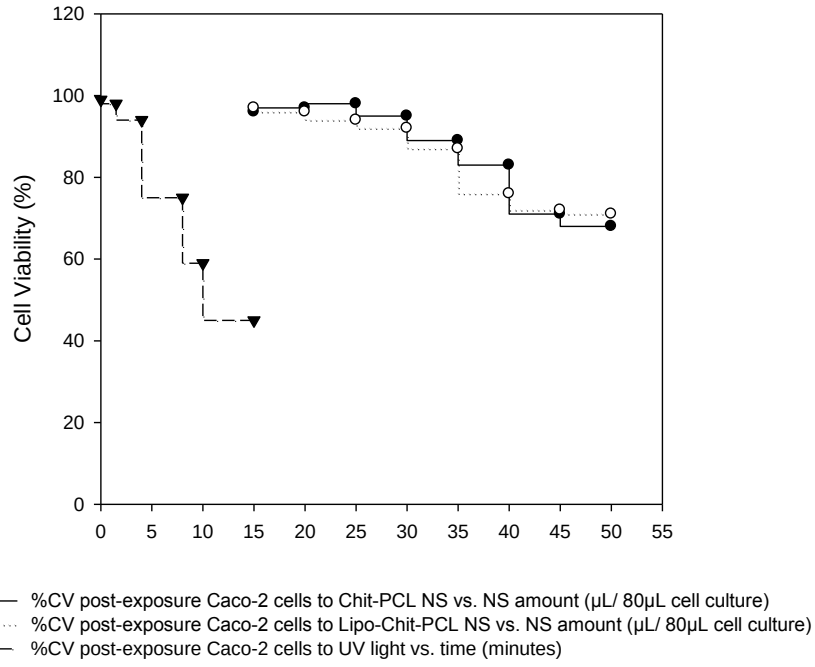

Figure 3.10: Composite cell viability (CV) plots following exposure of Caco-2 cells to UV light and NS

3.4.5. *Ex vivo* drug-loaded NS permeation across ocular barriers

An increase in absorbance values on measurement of the control solution compared to the blank revealed that permeation across the RCS into the receptor compartment was attributed to the drug-loaded NS and not solely the indomethacin. This was supported by the fluorescence data below. The permeation behavior of the NS were somewhat irregular, possibly due to the presence of some smaller NS and the differences in tissue sample thickness as a result of inter-subject variability (as evidenced by somewhat inflated standard deviations). It is reasonable to assume that NS of smaller size diffuse through and release the incorporated drug more rapidly thus explaining why the initial diffusion value obtained at 1 hour of the permeation study was highest (Figure 3.11). This correlates with the data obtained by Calvo et al. (1997b) where a burst release was observed during the first hour of *in vitro* studies followed by a more gradual drug release over 24 hours; it also correlates with the investigations of Motwani et al. (2008) where the tested NP formulation exhibited a burst release during the first hour followed by a more gradual drug release during a 24 hour period following a non-Fickian diffusion process. Furthermore, it was noted that the permeation and dissolution of the indomethacin suspension was inferior as compared to the NS formulations having a flux value across the RCS of only 0.00003342mg.cm^{-2}.hr^{-1} (Table 3.2); this is attributed to the fact that indomethacin is solely hydrophobic/ lipophilic and in the crystalline state, and rather than passing through the ocular tissue entirely with the hydrostatic gradient created by the PBS, it resides in the parenchyma of the ocular tissue. The reason the NS formulations permeate the ocular layers more effectively, specifically the NS incorporating a lipoidal component, is because of the penetration-enhancing capabilities of chitosan and, in the case of the Lipo-Chit-PCL NS, they possess an amphiphilic shell surface that enables their partitioning across the diverse barriers and fluids of the eye along the hydrostatic gradient. The low flux is also redolent of the poor solubility of unadulterated indomethacin. Although sink conditions were maintained for the duration of the experiment (all levels were <0.92mg/mL) flattening at the final time points for the NS formulations could be as a result of solubility limits being approached, specifically for the Lipo-Chit-PCL NS. However, it must also be noted that the state of indomethacin in the NS produced via the emulsion method as provided here is largely in the amorphous form (confirmed in Chapter 5 by the results of Temperature-Modulated Differential Scanning Calorimetric analysis, Figure 5.15b), with each NS creating an amorphous solid dispersion. This enhances the bioavailability of the low-solubility drug. The described NS, like other amorphous dispersions, is proposed to provide dissolved-drug concentrations higher than crystalline solubility, which emanates in the enhanced dissolution of indomethacin in the receptor compartment. Thus because of the enhanced bioavailability of the low-bioavailability drug availed by the NS, less drug would

ultimately need to be incorporated within the final dosage form and still achieve therapeutic levels.

The Chit-PCL NS had an average flux across the RCS of 0.001255mg.cm^{-2}.hr^{-1}, whereas the Lipo-Chit-PCL NS (i.e. containing DSPC and DSPE) had an average flux of 0.002951mg.cm^{-2}.hr^{-1}, indicating the superior tissue permeability of the composite lipoidal-polymeric NS and/ or enhanced drug release from the NS as compared to a purely polymeric system. The enhancement ratio highlighted the notable improvement in permeation compared to the drug suspension (Table 3.2). The lower flux rate anomaly associated with the purely polymeric system could indicate that more protein/ tissue binding or tissue retention occurs between this NS and ocular tissue, in essence rendering this system more bioadhesive, and potentially more suitable for the treatment of extraocular conditions such as keratoconjunctivitis sicca (du Toit et al., 2011a), the polymeric NS would be most appropriate to achieve this goal. However, in this instance, the NS is already incorporated within a 'reservoir' - the implant - and a system is desired that would achieve enhanced permeation properties through all ocular layers to reach inflammatory cells and attain adequate drug levels in the posterior segment of the eye, thus pinpointing the composite NS as a potentially suitable candidate in this instance.

Other investigators have developed solid lipid particle and structured lipid carrier dispersions containing indomethacin and have attained flux values of 0.0024 mg.cm^{-2}.hr^{-1} and 0.0012mg.cm^{-2}.hr^{-1}, respectively across the RCS (Hippalgoankar et al., 2009). The Lipo-Chit-PCL NS is thus a further improvement on these lipoidal systems.

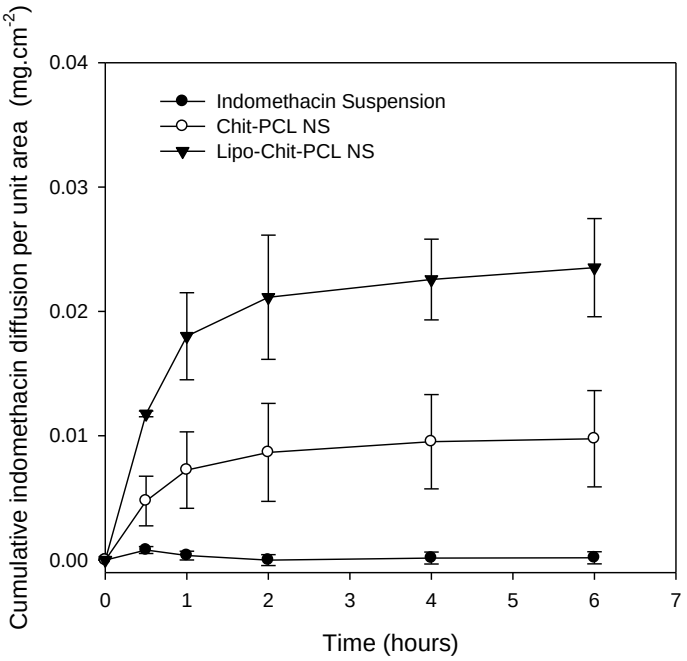

Figure 3.11: *Ex vivo* permeation profiles of an indomethacin suspension vs. the NS formulations through excised New Zealand Albino Rabbit ocular tissues (n=3)

Table 3.2: Indomethacin flux and associated permeability coefficients for the indomethacin suspension vs. the NS formulations through excised New Zealand Albino Rabbit ocular tissues (n=3)

Formulation	**Flux, J_S, (mg.cm^{-2}.hr^{-1})**	**Permeability Coefficient, *P***	**Enhancement Ratio***
Indomethacin suspension	$3.342E^{-5} \pm 6.359E^{-6}$	$2.507E^{-5}$	-
Chit-PCL NS	$1.255E^{-3} \pm 5.085E^{-5}$	$9.413E^{-4}$	37.552
Lipo-Chit-PCL NS	$2.951E^{-3} \pm 1.257E^{-4}$	$2.213E^{-3}$	88.300

**** Compared to indomethacin suspension***

The NS were clearly visible as fluorescent spheres dispersed within the tissues comprising the ocular layers of the posterior segment of the eye, specifically the lipoidal system, which is depicted in Figure 3.12; highlighting the potential of this technique for tracking and visualizing NS permeation. In the acquired micrograph (Figure 3.12) numerous fluorescent spheres were observed, representing the NS permeating the ocular tissues (RCS) potentially enabling their movement to the inflammatory cells of interest.

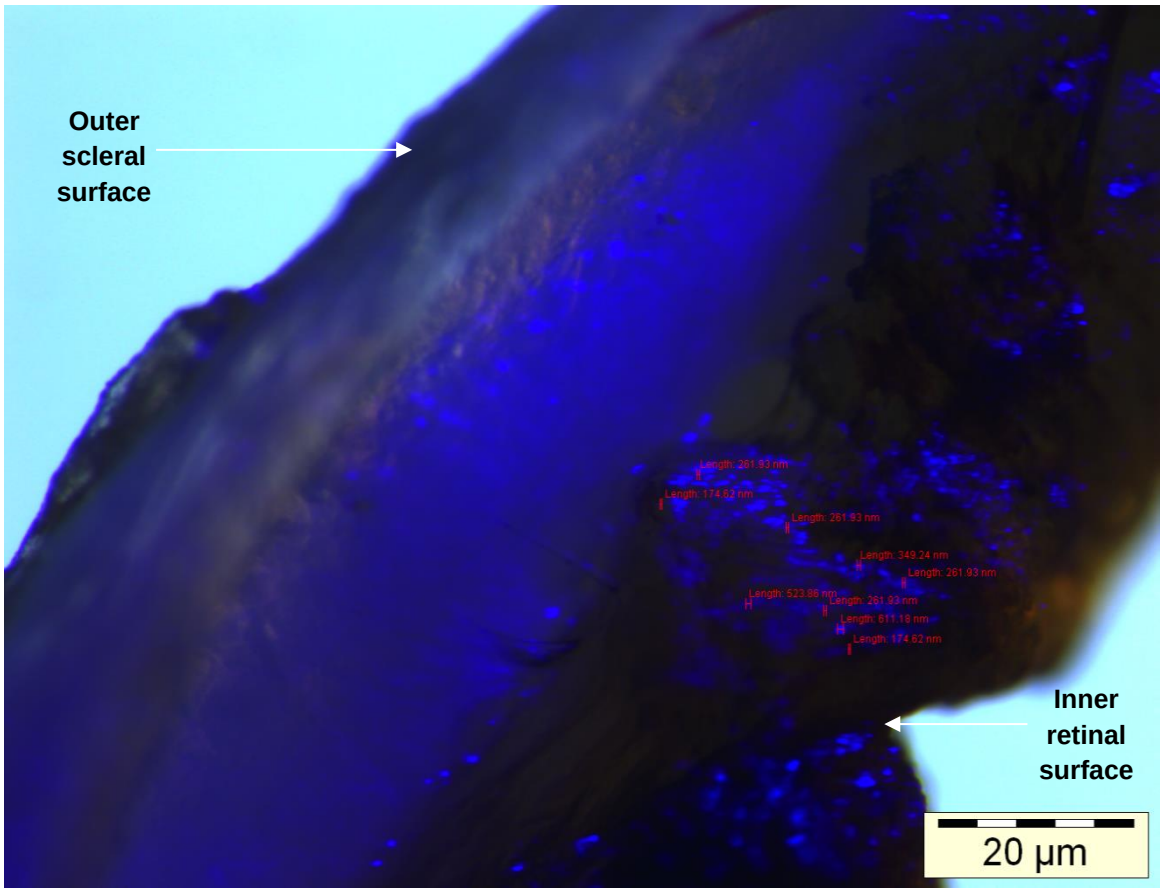

Figure 3.12: Photomicrograph indicating the various stages of penetration of the NS (visualized as fluorescent spheres) through the ocular tissues. The hyperpigmented retina is apparent. The larger diameter measurements in some cases is associated with NS clustering in the tissues

3.4.6. Utilization of a superoxide probe for determination of the anti-inflammatory efficacy of the nanosystems

The molar concentration of NBD-Cl complex was determined by using Beer-Lambert's Law and the molar absorption coefficient for the NBD-Cl complex of 14.5$mM^{-1}cm^{-1}$ (Lampe et al., 2000), employing a path length of 1cm.

The larger the decrease in NBD-Cl-superoxide and NBD-Cl-Glutathione complex value, the more superior the anti-inflammatory efficacy of the test formulation; this is because superoxide and glutathione concentrations are directly proportional to the level of inflammation, thus the more glutathione and superoxide the drug delivery system inhibits, the greater the obtained difference. Overall it can be seen that the both NS formulations exhibited greater anti-inflammatory efficacy than the suspension. This is due to enhanced solubility effects and thus notably improved bioavailability, and potentially reduced local side effects, afforded to indomethacin (and other poorly soluble drugs) by the NS (Ahuja et al., 2008). The pure polymeric Chit-PCL NS decreased NBD-Cl complex concentrations by 0.0023mmol/L, the Lipo-Chit-PCL NS decreased NBD-Cl complex formation by

0.0031mmol/L, while the indomethacin suspension lowered levels by 0.0015mmol/L (Figure 3.13). The Lipo-Chit-PCL NS possessed enhanced anti-inflammatory efficacy in relation to the pure polymeric NS; this can be primarily attributed to the promoted intracellular uptake of the lipoidal NS together with the enhanced incorporation of indomethacin in the amphiphilic NS. The constituent phospholipids play an active role in biosynthetic molecular mimicry; Klausner et al. (1981) discussed the fact that phospholipids (i.e DSPC and DSPE) interact directly with tubulin, thus enabling enhanced phagocytosis of NS constituted thereof. Furthermore Fenske et al. (2001) discovered that DSPE enhances intracellular uptake of NS. Additionally, investigators have demonstrated that the anti-inflammatory activity of liposomal indomethacin is significantly higher than that of free indomethacin (Srinath et al., 2000).

Even though the indomethacin suspension achieved adequate efficacy *in vitro*, the effect would potentially be short-lived *in vivo*. It is more desirable to have more controlled inhibition of inflammation during its presence (thus preventing cytokine flare up) in comparison to decreasing inflammation rapidly and briefly.

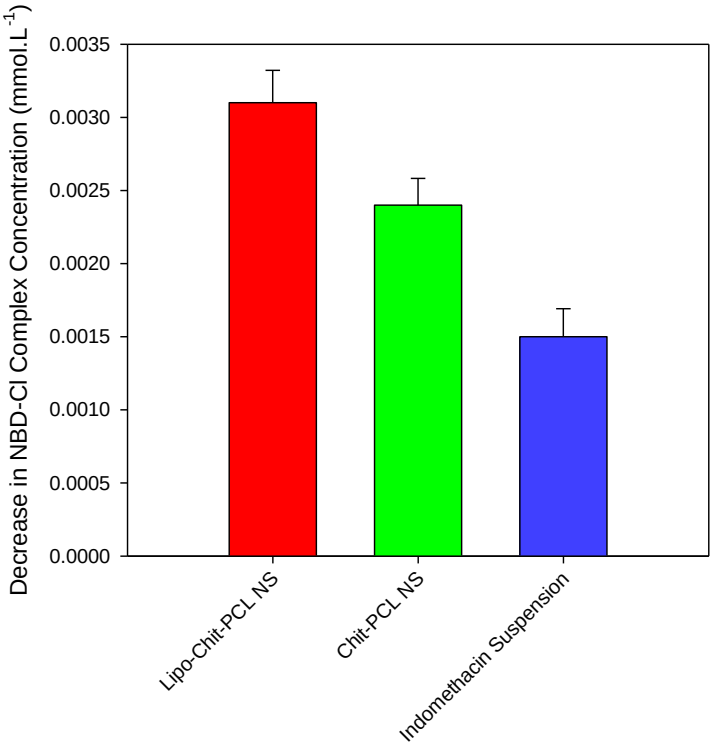

Figure 3.13: Decrease in NBD-Cl Complex for the NS formulations compared to an unaltered indomethacin suspension (n=3)

3.4.7. Utilization of an Enzyme-Linked Immunosorbent Assay to ascertain nanosystem anti-inflammatory efficacy

Interpretation of the results (Figure 3.14) acknowledges the fact that anti-inflammatory efficacy is inversely proportional to the relative quantity of NFκB produced. The control (i.e. cell culture exposed to H_2O_2 without any added hydrocortisone) produced an amount of NFκB similar to that in the positive control that was provided with the ELISA kit, indicating that inflammation was successfully induced.

The anti-inflammatory efficacy of the Lipo-Chit-PCL NS formulation was superior to that of the Chit-PCL NS, and both NS exhibited improved efficacy compared to the hydrocortisone suspension. This outcome is dependent on the level of drug bioavailability enhancement availed by the respective NS; the lipoidal system significantly enhanced the bioavailability of hydrocortisone to the cell within the 4 hour study period compared to the pure hydrocortisone suspension, whereas the purely polymeric NS achieved slightly improved results to the suspension. It is important to note that due to the fact that the Caco-2 cells were exposed to the different formulations for 4 hours means that different rates of NS uptake by Caco-2 cells had little effect on the overall anti-inflammatory efficacy of the NS formulation in this experiment as compared to the superoxide-probe experiment above (Section 3.4.6); overall it is unlikely that internalization rates have a large role to play in determining anti-inflammatory efficacy but rather overall drug bioavailability to the internal cell environment. The observation that the negative control (i.e. nuclear extract from the control sample introduced into mutant-oligo wells) demonstrated a low absorbance and hence low apparent value of quantified NFκB proves that the assay had a correct oligo design, that the dilution factor of the primary antibody was correct, and that the isolation of the cellular extract was successful.

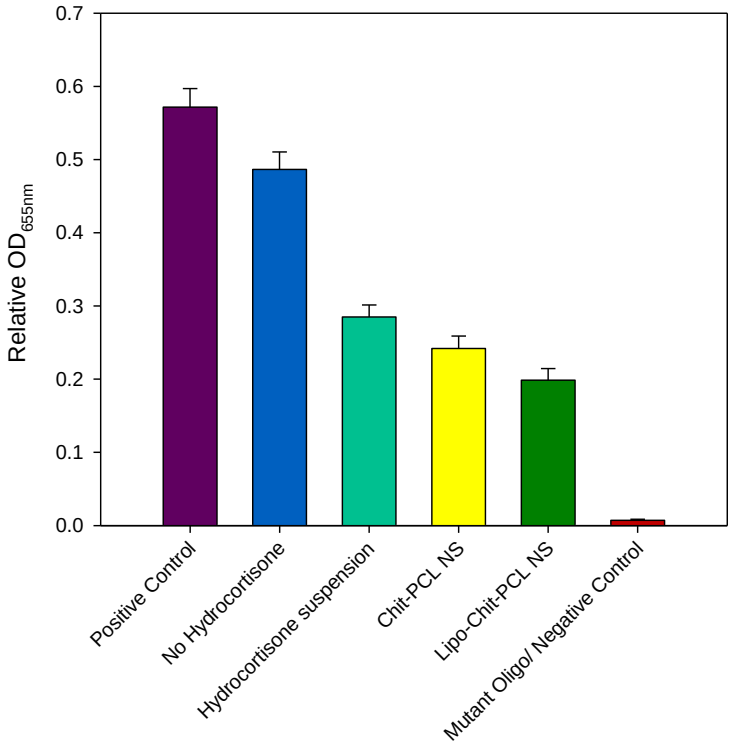

Figure 3.14: Detection of NFκB p65 for the NS formulations, hydrocortisone suspension, and controls

3.4.8. Utilization of confocal microscopy to ascertain the extent of intracellular permeation of the nanosystems in normal versus inflamed cells

The viable cell density for the prepared Chit-PCL NS with normal cells was 1.07 x 10^6/mL and for the Lipo-Chit-PCL NS with normal cells was 1.08 x 10^6/mL. The viable cell density for the Chit-PCL NS with inflamed cells sample was 9.58 x 10^5/mL whereas that of the Lipo-Chit-PCL NS with inflamed cells was 9.68 x 10^5/mL; thus samples in which inflammation was induced exhibited a predictably lower viable cell density, however, no significant differences in the cell density of compared samples within the normal or inflamed group was apparent. The uptake of NS by inflamed cells was enhanced compared to normal cells, even in the presence of a lower viable cell count (Figure 3.15b vs. a). The rationale for this is multifaceted. Firstly, inflammation causes an increase in the permeability of the cell membranes. Additionally, UV irradiation induces changes within the DNA of the exposed cells. UVA and UVB radiation possess the propensity to induce mutations. UVB radiation is site specific and is absorbed directly by cellular DNA; whereas UVA radiation is not direct in its mechanism, but is absorbed by intracellular chromophores such as riboflavin and membrane bound enzymes, and ultimately generates superoxide or hydroxyl radicals by Fenton's reaction leading to the development of single strand breaks, or induce oxidized

base formation in DNA via singlet oxygen production (Lyons and O'Brien, 2002). This could compromise overall cell integrity. Furthermore the formulatory components of the NS have a propensity for inflamed tissue: chitosan through electrostatic association, PCL through as yet undefined means, and phospholipids (in the composite NS) due to specific uptake by inflamed cells. Stable liposomal structures have been highlighted for their potential for passive inflammatory tissue targeting possibly due to selective uptake by inflamed cells (Love et al., 1990) - even though specific immune-related cells would be absent in a cell culture.

From the preceding investigations it is clear that the performance of the composite polymeric-lipoidal system (Lipo-Chit-PCL NS) exceeded that of the polymeric NS in terms of its permeation potential, cell uptake and anti-inflammatory potential. The somewhat enhanced uptake of the lipoidal NS was further exemplified qualitatively via confocal microscopy as increased and more concentrated areas of fluorescence indicative of NS uptake into the confined cell space, with a diffuse background of free-floating NS (Figure 3.15aii and bii). As mentioned the phospholipids (i.e. DSPC and DSPE) do directly interact with tubulin, explaining their enhanced internalization capabilities as compared to the purely polymeric NS. Once again it is helpful to acknowledge the discovery of Fenske et al. (2001) regarding the ability of DSPE to enhance intracellular uptake of NS when employed as a structural component of NS shells. The inclusion of phospholipids in the stable NS structure could create a 'Trojan horse' system (Figure 3.16) of 'tricking' cells into thinking that NS are in fact extracellular nutrient vesicles which enhances the level of internalization of these NS by endocytosis compared to the purely polymeric system.

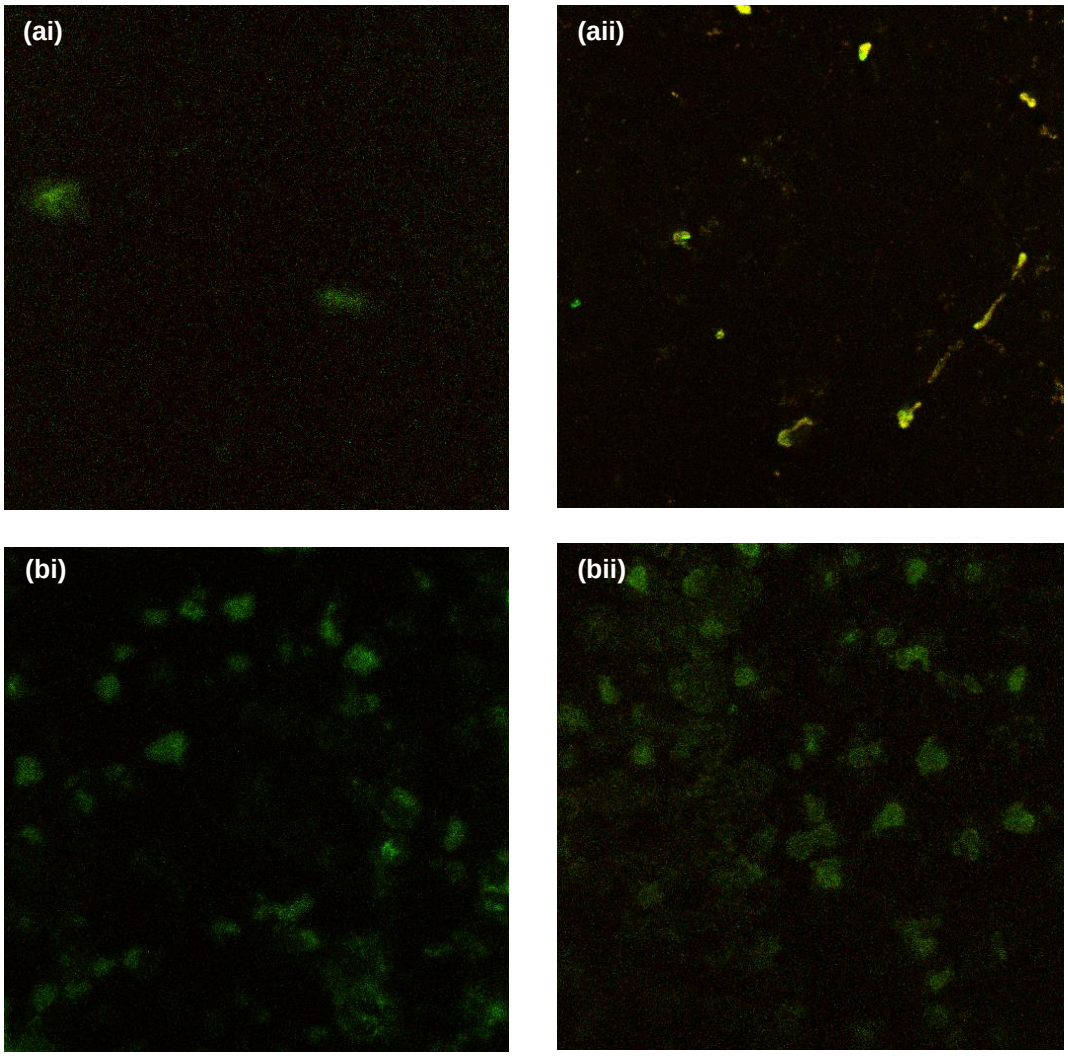

Figure 3.15: Confocal microscopy images acquired in (a) normal and (b) inflamed Caco-2 cells for fluorescent (i) Chit-PCL-NS (ii) Lipo-Chit-PCL NS

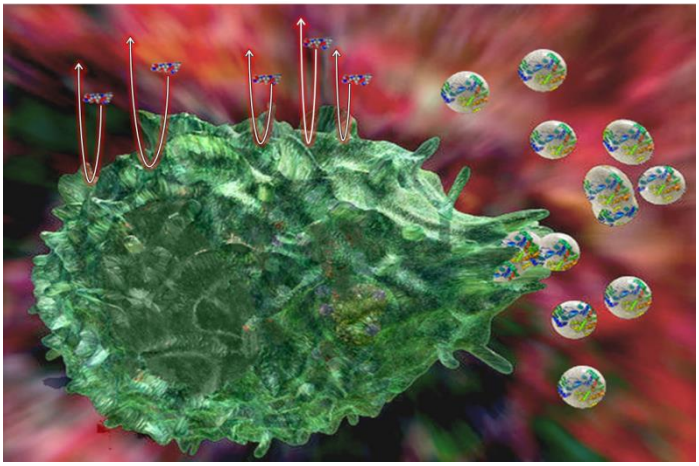

Figure 3.16: 'Trojan horse' mechanism demonstrating NS internalization for the entrapped drug compared to free drug

3.4.9. High-speed fluorescence microscopy for live imaging of nanosystem uptake

With reference to the isolated NS (without cells) observed under the magnification of the CellVizio® imaging system, fluorescent spheres were visualized as free-floating entities, with slight clustering at the fiber-optic probe (Figure 3.17a and c).

In combination with the cell culture composed of inflamed cells, there was more distinctive clustering of the fluorescent zones indicating uptake of the fluorescent particles into the cell via the processes of either endocytosis or cell fusion (Sharma and Sharma, 1997). According to cell theory derived from the field of cellular biology it can be predicted that the NS are taken up into the cells via interactions of with the penetration-enhancing chitosan (Figure 3.17b), or with the phospholipids in the Lipo-Chit-PCL NS (Figure 3.17d) and the cell membrane, where the NS are recognized as extracellular vesicles (due to biosynthetic mimicry imparted by inherent properties of phospholipids), enhancing internalization of the NS. Diebold and co-workers (2007) had also highlighted the successful uptake of liposome-chitosan NP complexes, for drug delivery to the ocular surface, into a conjunctival cell line, as demonstrated via confocal microscopy. The internalization of the NS could not be attributed to a complete disruption of cellular membranes because the NS did not contribute to significant changes in the cell viability, as evidenced via the toxicology assay. Chitosan interacts with cell membranes by non-specific electrostatic forces of attraction, which may initiate absorptive endocytosis (Schipper et al., 1997; Ma and Lim, 2003; Diebold et al., 2007). Ma and Lim (2003) further demonstrated that transformation of chitosan into NPs significantly promoted its association with Caco-2 cell monolayers by up to 1.97-fold. It also enabled the polymer to be internalized by the cells through clathrin-dependent pathways. Among the proteins identified to regulate endocytosis, clathrin, and caveolin are perhaps the most widely studied. Most likely, in combination with the presence of phospholipids, the NS were internalized by the Caco-2 cells by adsorptive endocytosis, an energy-dependent, saturable process that is preceded by nonspecific interaction of the cargo with the cell membrane.

The inclusion of PCL also plays a role in achieving intracellular drug release. Woodward et al. (1985) demonstrated rapid escape of hydrophobic PCL-coated NPs from endo-lysosomes to the cytoplasm (Singh and Lillard Jr., 2009). The ensuing interaction of the phospholipids and microtubules promotes further intracellular mobilization of the lipoidal NS.

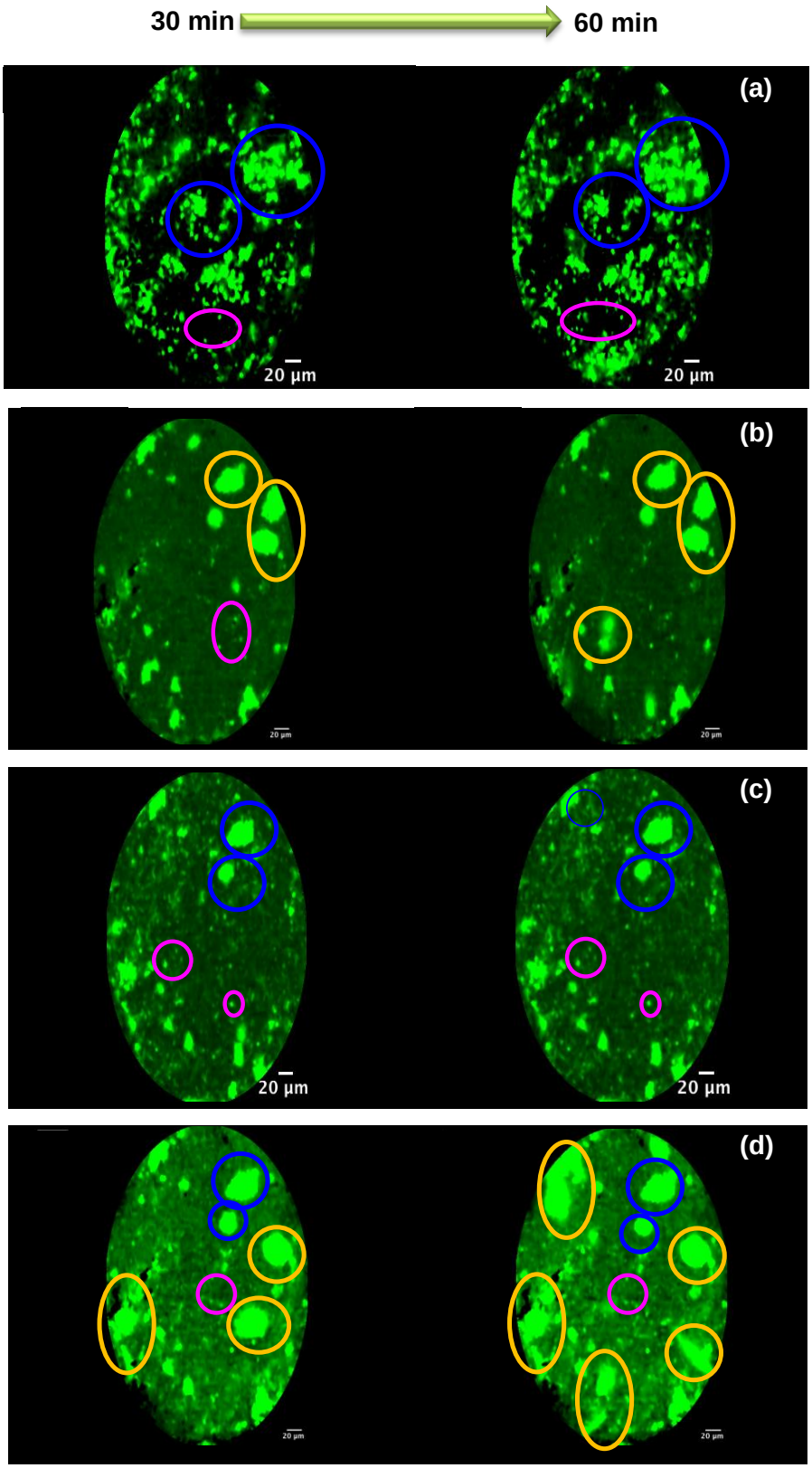

Figure 3.17: Time-lapse images acquired for (a) Chit-PCL NS (b) Chit-PCL-NS-Caco-2 cell suspension (c) Lipo-Chit-PCL NS (d) Lipo-Chit-PCL-Caco-2 cell suspension

- Slight random NS clustering on the fiber-optic probe
- Exemplary free floating fluorescent spheres
- Distinct NS clusters in Caco-2 cells

3.4.10. Molecular modeling simulations for prediction of nanosystem formation and cellular internalization of the nanosystems

Computational chemistry is essential to understanding the behavior of NS; and has been pinpointed as a gateway to the emerging and burgeoning field of nanotechnology (Ramachandran et al., 2008). In the present MM study, the global energy relationships for the various complexes derived after assisted model building and energy refinements were as follows:

$E_{Chit} = 23.418V_{\sum} = 1.971V_b + 11.420V_\theta + 15.980V_\varphi + 9.217V_{ij} - 15.171V_{el}$ [Equation 3.7]

$E_{PCL} = 6.413V_{\sum} = 0.337V_b + 1.329V_\theta + 0.052V_\varphi + 4.694V_{ij}$ [Equation 3.8]

$E_{Chit\text{-}PCL} = -2.591V_{\sum} = 1.897V_b + 10.463V_\theta + 15.670V_\varphi - 10.069V_{ij} - 20.553V_{el}$ [Equation 3.9]

ΔE = -32.422kcal/mol

$E_{DSPC2} = 24.094V_{\sum} = 0.986V_b + 9.934V_\theta + 8.786V_\varphi + 4.926V_{ij}$ [Equation 3.10]

$E_{Chit\text{-}PCL\text{-}DSPC} = -8.293V_{\sum} = 2.971V_b + 21.598V_\theta + 25.698V_\varphi - 24.708V_{ij} - 0.003V_{hb} - 33.850V_{el}$ [Equation 3.11]

ΔE = -62.218kcal/mol

$E_{DSPE2} = 111.800V_{\sum} = 1.402V_b + 95.628V_\theta + 7.68V_\varphi + 7.09V_{ij}$ [Equation 3.12]

$E_{Chit\text{-}PCL\text{-}DSPE} = 60.052V_{\sum} = 2.583V_b + 76.641V_\theta + 30.945V_\varphi - 32.995V_{ij} - 17.123V_{el}$ [Equation 3.13]

ΔE = -81.579kcal/mol

$E_{Chit\text{-}PCL\text{-}DSPC\text{-}DSPE} = 33.779V_{\sum} = 2.498V_b + 42.682V_\theta + 22.977V_\varphi - 29.939V_{ij} - 0.002V_{hb} - 4.438V_{el}$

ΔE = -63.999kcal/mol [Equation 3.14]

3.4.10.1. Formation of the nanosystems

The energy equations (Equations 3.7-3.14) demonstrated that the NS composed of Chit, PCL, DSPC, and DSPE were stabilized in terms of respective bonding and non-bonding energy factors. The preferred orientations of the polymers as binary and ternary polymeric systems are depicted in Figures 3.18-3.21.

The binary system modeled using Chit-PCL yielded energetically stabilized molecular complexes with an energy of interaction equivalent to -32.422kcal/mol suggesting good compatibility and miscibility. All the bonding and non-bonding energies played a significant role with van der Waals interactions (ΔE ~-24kcal/mol) and electrostatic forces (ΔE ~-5kcal/mol) being the major contributors, as evident from Equations 3.7 and 3.8. Interestingly, the hydrogen bonding played a minor role in the structure stabilization despite the fact of PCL possessing -COOH groups and Chit having -NH_2 groups. This is also visible in Figure 3.18. However, Figure 3.18 further displayed the formation of a helical bimolecular-structure which may be due to the involvement of non-bonding hydrophobic interactions as explained

above forming a closed-and-defined network structure. This is also supported by the fact that PCL is the more hydrophobic molecule among PCL and Chit. Furthering our modeling interventions, Chit-PCL was modeled with DSPC and DSPE to form Chit-PCL-DSPC, Chit-PCL-DSPE, and Chit-PCL-DSPC-DSPE to simulate the formation of the nanoliposystem. As per the findings of Lozano and Longo (2009), the addition of a lipophilic/ hydrophobic agent such as cholines and enolines to an already lipophilic system may further enhance the stability of binary systems (Lozano and Longo, 2009). Likewise, Chit-PCL modeled with DSPC or DSPE (theoretical systems), as well as with both DSPC and DSPE (as exists for the lipoidal NS) formed highly stabilized molecular structures with interaction energies of ΔE=-62.218kcal/mol, ΔE=-81.579kcal/mol, and ΔE=-63.999kcal/mol, respectively, as calculated from Equations 3.9-3.14. The higher stabilization of Chit-PCL-DSPE as compared to Chit-PCL-DSPC may be explained by the fact that DSPE contains a certain hydrophilic component which might have settled with the Chit component of Chit-PCL complex and hence forming a better geometrical conformation as compared to DSPC. In general, the complexes were stabilized by generalized energy times in terms of bond angles and torsional contributions (bonding energies) as well as London dispersion forces (non-bonding interaction). Interestingly, electrostatic interactions stabilized Chit-PCL-DSPC but destabilized Chit-PCL-DSPC-DSPE. Strikingly, DSPC introduced hydrogen bonding into the ternary systems with a value of -0.003kcal/mol which lead to a stabilized molecular entity. The van der Waals interactions further added to the stabilization of Chit-PCL-DSPE and retrieved high negative values which may be due to DSPE acting as a filler in the space lattice of the ternary system (Figure 3.20). Finally, the quaternary polymeric complex Chit-PCL-DSPC-DSPE (Figure 3.21), as expected, displayed intermediate energy stabilization (ΔE = -63.999kcal/mol) lying between that of Chit-PCL-DSPC and Chit-PCL-DSPE. Except for electrostatic interactions; all bonding and non-bonding energies contributed towards the stabilization of the final polymer matrix. The electrostatic destabilization in vacuum implies that the matrix may show significant 'aqueous-interaction profile' due to the high dielectric constant of water molecules. This successfully validates the computational method employed in the present simulations and additionally provides the evidence to the 'amphiphilic' nature of the developed final nanoliposomal structure as explained in the next section. These non-bonding interactions lead to the hydrophobic interactions arising from the inclusion of cholines and enolines which further lead to the formation of nanoliposomes in an excess of PBS (aqueous phase).

3.4.10.2. Investigation of cellular internalization of the nanosystems

To investigate the cellular-internalization of NS, the modeling was performed in the presence of water molecules (periodic box) as the hydrophilic phase. Notably, the modeling done in

vacuum in the previous section corresponds to the lipophilic phase. The hydrophilic-lipophilic modeling is based on the assumption that the more the complex is stabilized in vacuum, the more it leans towards the lipophilicity required for penetration of the cellular architecture. Inversely, the more it is stabilized in the water phase the more it contributes to the hydrophilicity of the complex. For cellular-internalization, the passing of a lipo-polymer conjugate through the cellular membrane requires a hydrophilic-lipophilic-balance (HLB) with lipophilicity on the higher side. Equations 3.9, 3.11, 3.13 and 3.14 display the energy profile of the molecular complexes and it is evident that DSPC and DSPE provided lipophilicity to Chit-PCL by stabilization in vacuum. The changes in the conformational space lattice of the Chit-PCL caused by the lipid chains might have contributed to its lipid-soluble behavior as the London dispersion forces stabilized (in vacuum).

$E_{Chit\text{-}PCL\text{-}H2O} = -2798.018V_{\sum} = 34.439V_b + 53.197V_\theta + 22.123V_\varphi + 1.587V_{ij} - 0.98V_{hb} - 2908.39V_{el}$

[Equation 3.15]

$E_{Chit\text{-}PCL\text{-}DSPC\text{-}H2O} = -2427.952V_{\sum} = 29.987V_b + 54.18V_\theta + 43.30V_\varphi - 61.77V_{ij} - 5.1V_{hb} - 2488.56V_{el}$

[Equation 3.16]

ΔE = +370.066kcal/mol

$E_{Chit\text{-}PCL\text{-}DSPE\text{-}H2O} = -2064.28V_{\sum} = 23.53V_b + 100.68V_\theta + 37.59V_\varphi - 47.62V_{ij} - 2.02V_{hb} - 2176.43V_{el}$

[Equation 3.17]

ΔE = +733.744kcal/mol

$E_{Chit\text{-}PCL\text{-}DSPC\text{-}DSPE\text{-}H2O} = -2138.564V_{\sum} = 23.997V_b + 74.552V_\theta + 30.018V_\varphi - 42.688V_{ij} - 2.217V_{hb} - 2222.23V_{el}$

[Equation 3.18]

ΔE = +659.454kcal/mol

The effect of adding solvated-phase on the reactional-profile and stabilization of the polymer-lipid aggregates was extracted via relative modeling of the peptide-lipid complex in presence of same number of water molecules (261) and with identical periodic box dimensions. Referring to Equations 3.15-3.18, the energetic profiles of molecular complexes revealed that the conjugated systems represent stable systems with negative potential energy. However, in comparison to the cumulative energy profile of the constituent molecules, the complex systems were highly destabilized with Chit-PCL-DSPC-H_2O > Chit-PCL-DSPC-DSPE-H_2O > Chit-PCL-DSPE-H_2O having energy of interactions ranging from ~370kcal/mol through ~659kcal/mol to ~733kcal/mol, respectively. These high energies of destabilization were mainly due to electrostatic interactions (V_{el}) and partially due to angle (V_θ) and torsional constraints (V_φ), as evident from Equations 3.15-3.18.

With reference to the results from the vacuum and solvated system simulations, it can be concluded that Chit-PCL-DSPC-DSPE-H_2O displayed an improved hydrophilic-lipophilic-balance (HLB):enhanced lipophilicity compared to Chit-PCL-DSPC-H_2O, and better hydrophilicity than Chit-PCL-DSPE-H_2O, thereby producing superior cellular internalization efficiency thanboth theoretical nanoliposystems, as well as the purely polymeric system. These results are in corroboration with the *ex vivo* data as discussed earlier in this chapter.

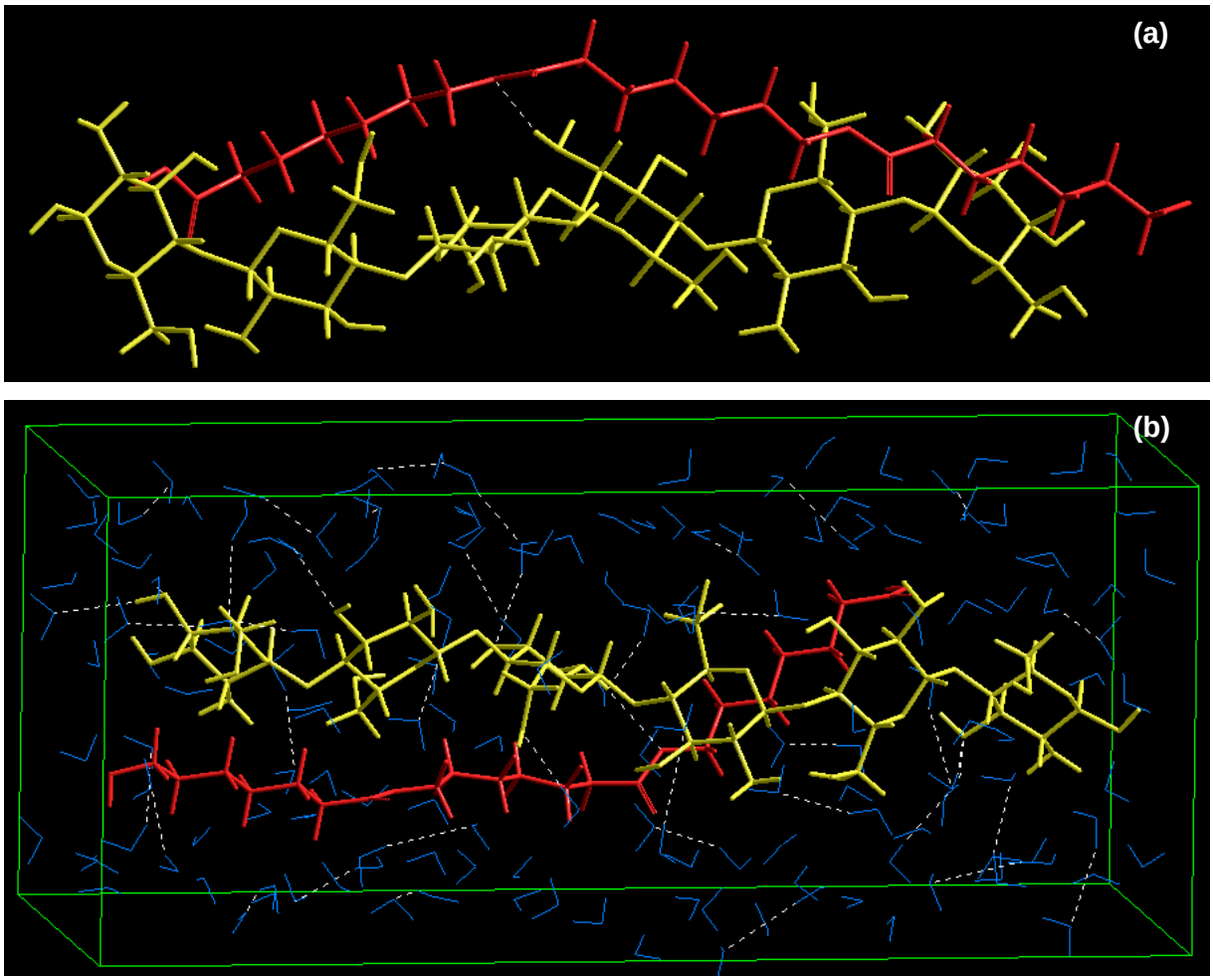

Figure 3.18: Visualization of geometrical preferences of Chit molecule (yellow) in complexation with PCL molecule (red) after molecular simulations in a) vacuum; and b) solvent system consisting of 261 water molecules (blue).

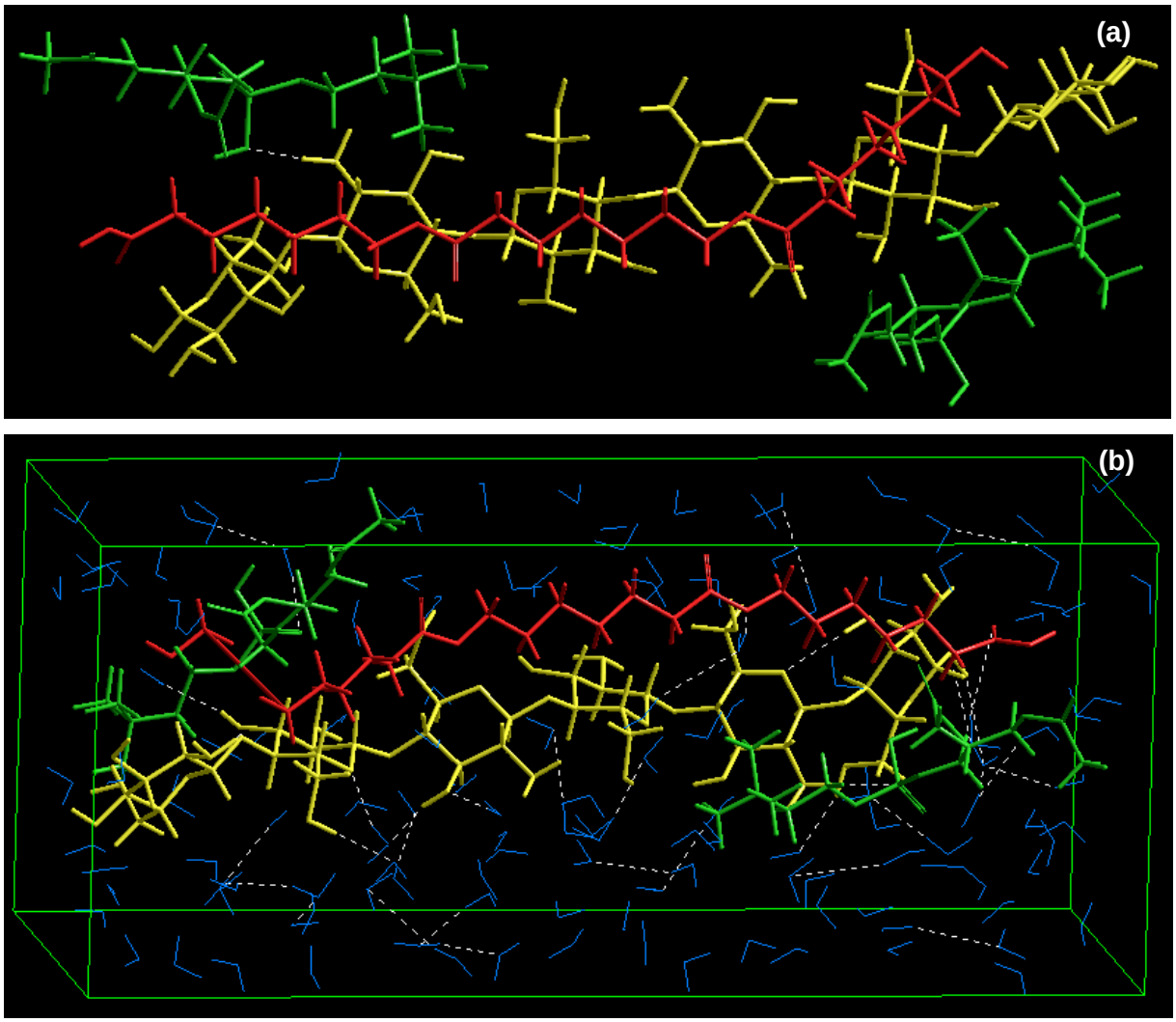

Figure 3.19: Visualization of geometrical preferences of Chit molecule (yellow) in complexation with PCL molecule (red) and DSPC (green) after molecular simulations in a) vacuum; and b) solvent system consisting of 261 water molecules (blue).

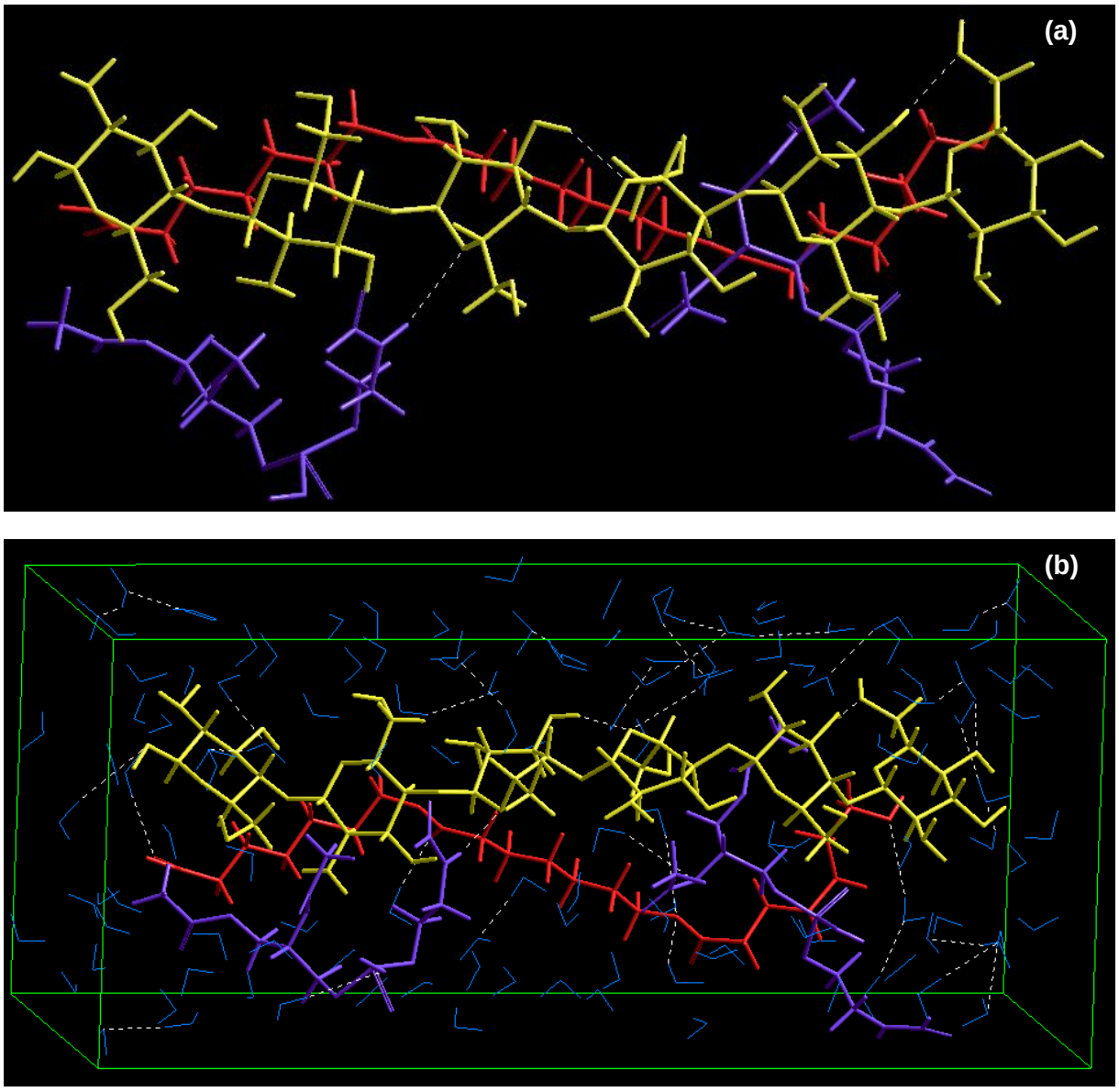

Figure 3.20: Visualization of geometrical preferences of Chit molecule (yellow) in complexation with PCL molecule (red) and DSPE (violet) after molecular simulations in a) vacuum; and b) solvent system consisting of 261 water molecules (blue)

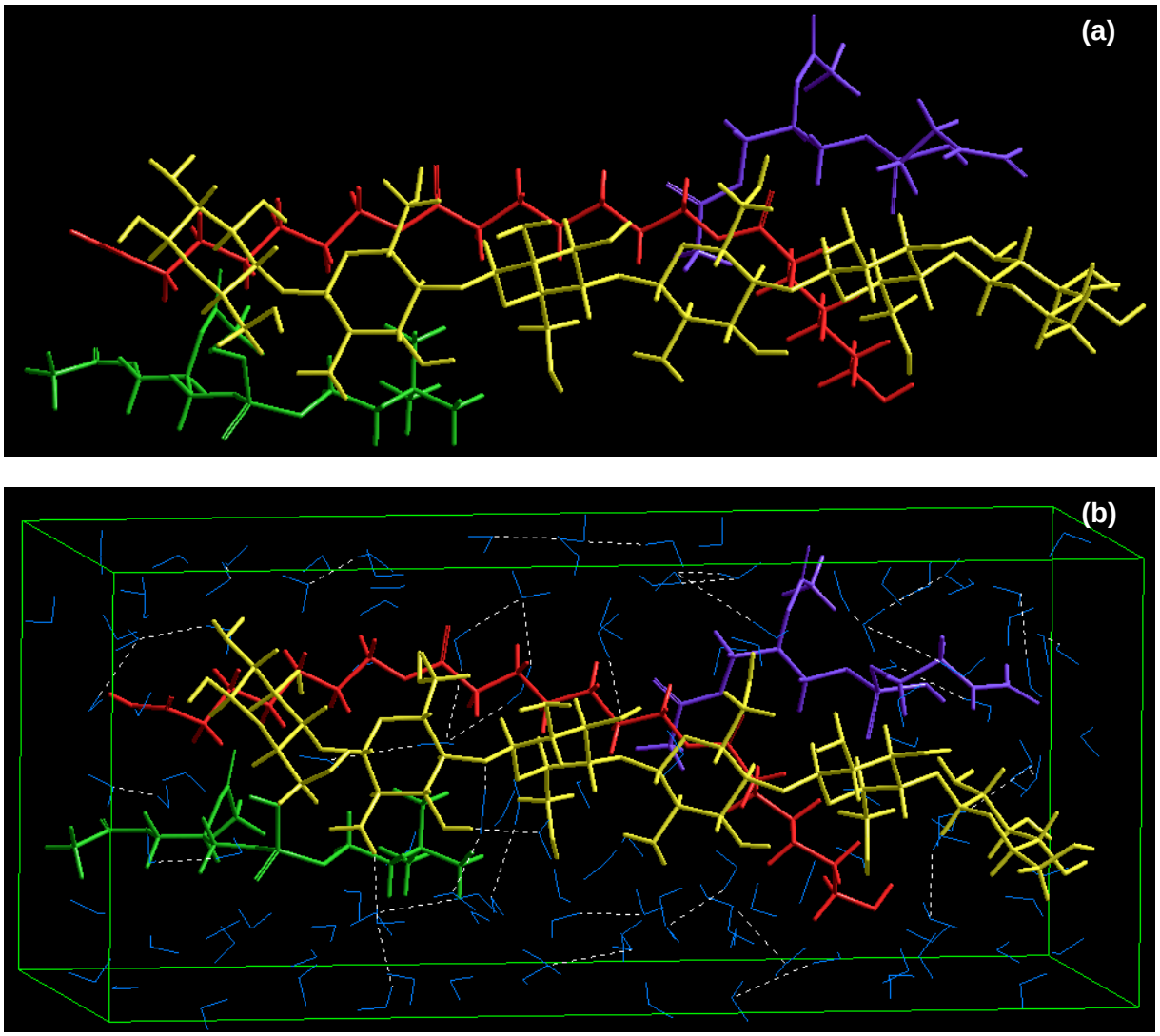

Figure 3.21: Visualization of geometrical preferences of Chit molecule (yellow) - PCL molecule (red) in complexation with DSPC (green) and DSPE (violet) after molecular simulations in a) vacuum; and b) solvent system consisting of 261 water molecules (blue).

3.4.11. Prediction of the overall mechanism of nanosystem attachment, uptake and anti-inflammatory action

Figure 3.22 is a proposed construction of the mechanism of attachment, uptake and ultimate action of the composite lipoidal-polymeric anti-inflammatory NS.

Previous investigation in Caco-2 cell lines have emphasized that the particle uptake depends on their size, with NPs demonstrating greater efficacy of uptake than microparticles (Desai et al., 1997; Davda and Labhasetwar, 2002). The uptake of NPs (~100-200nm) seems to be mediated by endocytosis (Qaddoumi et al., 2000).

Once the NS comes into contact with a biological system they may have a significant influence due to their nonbiological origin, and in the case of a living cell, the NS can be internalized into the cell. Ion channels exist in the cell membrane, however, colloidal particles are too large to pass through. One pathway for the colloid internalization is phagocytosis or endocytosis, with phagocytosis involving the uptake of particles larger than 500nm; therefore smaller colloids are endocytosed. This process generally causes changes to the cell morphology and cytoskeleton structure (Mao et al., 2007). What is envisaged is that the NS attaches to the cell via a receptor-mediated process (facilitated by chitosan), as discussed above in Section 3.4.9, and are gradually embedded by invagination of the membrane and endocytosed into the cell. A portion of the plasma membrane is invaginated and pinched off, forming membrane-bound vesicles or endosomes - these deliver their contents to lysosomes. The membranes of the two organelles fuse. Once inside the lysosomes, the ingested NS may either be broken down by the degradative enzymes (releasing indomethacin), or released from the lysosome. Concerning biodegradation, chitosan is degraded into oligomers by lysozyme, and then further degraded by *N*-acetyl-glucosaminidase, in animal cells. Both of these enzymes are present in the endosomal/ lysosomal vesicles, thus release of indomethacin could be immediate. Additionally, because lysozyme is present at inflammation sites, it would allow site-specific release should the NS not undergo endocytosis (Gonçalves et al., 2010). Should the NS be released from the lysosome, attachment to tubulin, enabling intracellular transport, and facilitated by the lipoidal component of the NS, is anticipated.

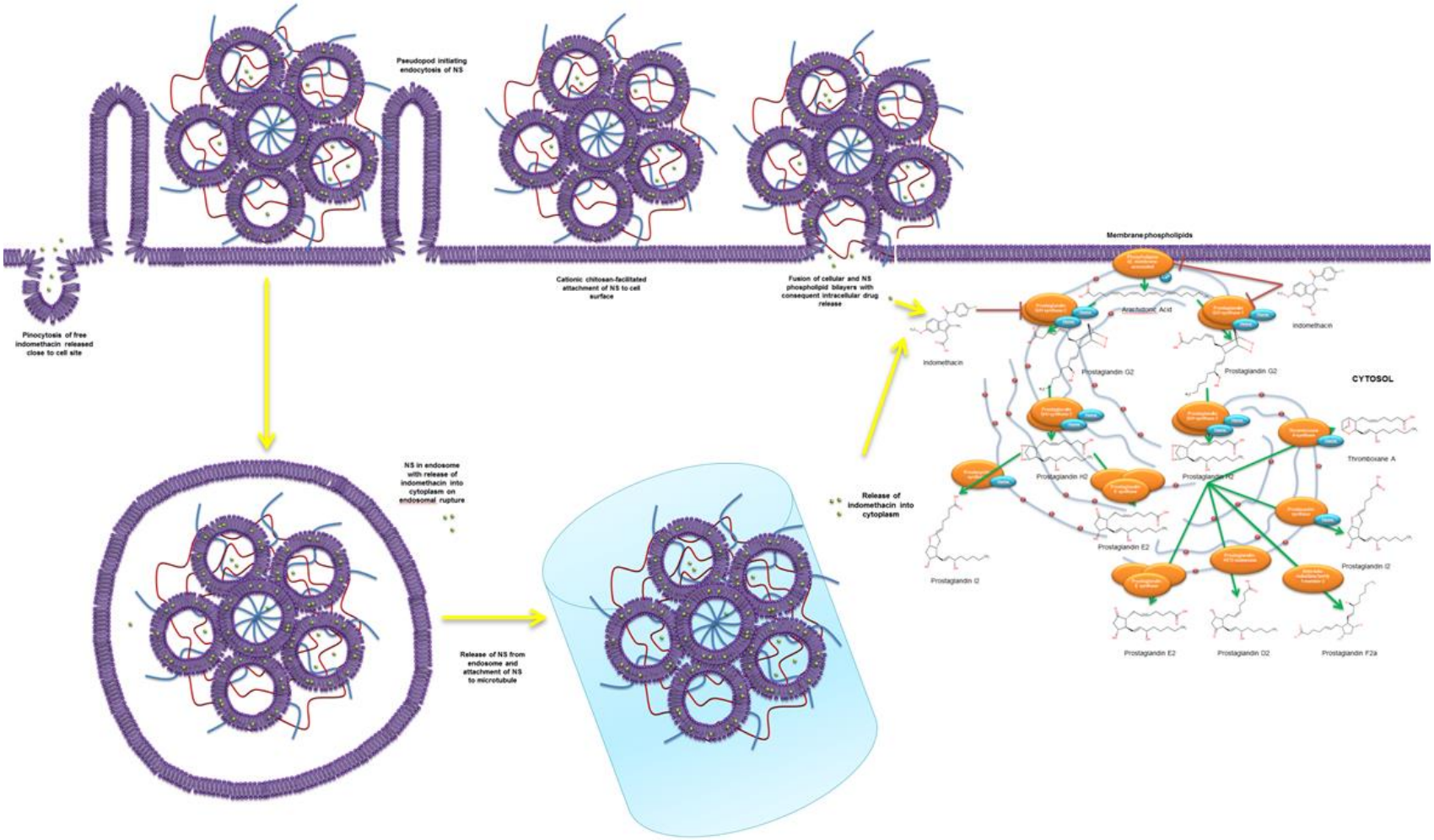

Figure 3.22: Schematic exemplifying the proposed overall *modus operandi* of the NS and ultimate intracellular indomethacin pathway in humans. The purported methods of cell entry are endocytosis, being the most anticipated approach, fusion, and pinocytosis to a lesser extent. Indomethacin is ultimately released exerting its effect via inhibition of prostaglandin G/H synthase (i.e. COX), acting on both prostaglandin G/H synthase 1 and 2 (COX-1 and -2) via binding to the upper portion of the active site, preventing its substrate, arachidonic acid, from entering the active site. Indomethacin, unlike other NSAIDs, also inhibits phospholipase A2, the enzyme responsible for releasing arachidonic acid from phospholipids. The resultant anti-inflammatory effect of indomethacin occurs as a result of decreased prostaglandin synthesis

3.5. PART B: Experimental Design and Optimization of the Nanosystem

In order to economically and efficiently design a matrix of NS to identify desirable levels of formulatory components for the NS synthetic approach, a Plackett-Burman (P-B) Statistical Design was employed. The significant paper of R.L. Plackett and J.P. Burman entitled 'The Design of Optimal Multifactorial Experiments' was published in *Biometrika* in 1946. This paper described the construction of highly efficient and economical designs with consideration of only the main effects and the run number being a multiple of four rather than a power of 2, i.e., a resolution III experiment that requires only 4n runs for 4n-1 factors, where n is any positive integer. A P-B design was considered appropriate for screening an appropriate lipoidal-polymeric NS composition that would ultimately be included in an implant for optimization.

3.6. Materials and methods (Part B)

3.6.1. Experimental design for the lipopolysaccaride-chitosan-poly(ε-caprolactone) nanosystem

A 14-experimental set P-B Statistical Design was generated (Table 3.3) and analyzed for the fabrication of Lipo-Chit-PCL NS by the reverse phase methodology described for description of the effect of important formulation and processing factors such as polymer and drug levels on the fractional drug release at t_{8h} in PBS (pH 7.4), drug incorporation efficiency, size, and zeta potential. Phospholipid and surfactant quantities were maintained at the described levels, after they were ascertained during studies conducted and published to be appropriate for formation of liposomal structures (du Toit et al., 2011b). From the experimental results, the surface plots were generated using statistical software (MINITAB®, V15, Minitab, USA).

Table 3.3: Lipo-Chit-PCL NS formulations derived from the PB design

Formulation	*Indomethacin (mg)*	*PCL (mg)*	*Chitosan (mg)*
1	25	25.0	25.0
2	5	50.0	50.0
3	15	37.5	37.5
4	25	50.0	25.0
5	5	50.0	25.0
6	15	37.5	37.5
7	5	25.0	25.0
8	5	25.0	25.0
9	25	50.0	50.0
10	25	25.0	50.0
11	25	25.0	50.0
12	25	50.0	25.0
13	5	50.0	50.0
14	5	25.0	50.0

3.6.2. Synthesis of the lipopolysaccharide-chitosan-poly(*ε*-caprolactone) nanosystems

PCL (25-50mg) and the anti-inflammatory, indomethacin (5-25mg), were dissolved in 3mL acetone. The phospholipids, DSPC (20mg) and DSPE-mPEG (5mg), were dissolved in 2mL chloroform and the organic phases mixed. Chitosan (low molecular weight) (25-50mg) was dissolved in 15mL 0.05M HCl. Tween® 80 (0.01mL) was included as a surfactant. The chitosan solution was slowly added to the phospholipid-PCL-indomethacin solution with sonication for 1 minute (20 kHz sonicator, VibraCell, Sonics and Materials, Inc., Danbury, CT, USA). The organic solvent was subsequently evaporated with gentle stirring for 3 hours. FTIR was undertaken to ensure complete removal of the organic solvent. The interaction between the carboxyl or hydroxyl groups of the anionic PCL and the amine groups of chitosan formed immediate polyionic nanogels. The stability of the formed NS was maintained through freezing at -80^{o}C (Ultra-low freezer, Sanyo VIP™ Series, Sanyo North America Corporation, Wood Dale, IL, USA) for a period not exceeding 48 hours prior to testing.

3.6.3. Size and surface stability of the experimentally-derived lipopolysaccharide-chitosan-poly(*ε*-caprolactone) nanosystems

NS stability was evaluated via zeta potential value determination - a high absolute zeta potential value indicating a high electric charge on the NS surface. Zeta potential was measured employing a Zetasizer Nano ZS (Malvern Instruments Ltd. UK). Size analysis was undertaken using multimodal analysis at a scattering angle of 90° and temperature of 25°C. The hydrodynamic particle size was calculated as the value of z-average size ± SD. The width of the size distribution is indicated by the polydispersity index (PdI).

3.6.4. Elucidation of Drug Incorporation Efficiency of the experimentally-derived nanosystems

For incorporation within the core of the I^3, the NS would be maintained in this suspension form, thus no drug would be lost during the fabrication sequence, however, it is of pertinence to identify the degree to which drug was actually incorporated into the NS rather than remaining as free drug within the suspension, such that it benefits from all the advantages the NS furnishes. For this purpose the NS suspensions for each formulation were lyophilized at 25 mtorr for 48 hours (FreeZone® 2.5, Labconco®, Kansas City, Missouri, USA. Samples of freeze-dried NS (10mg) were accurately weighed and placed in dialysis tubing cellulose membrane (flat width: 33mm, diameter: 22mm, MW: 12400g.mol^{-1}, Sigma-Aldrich®, St. Louis, MO, USA) and washed three times with acetone to remove any free/ surface indomethacin that was not incorporated within the shell or core of the NS. The NS was allowed to dry to constant weight. The NS were subsequently dissolved in 5mL PBS pH 7.4 by centrifugation (MSE Minor Laboratory Centrifuge, 5000rpm for 12 hours). Aliquots (1mL) were filtered through a 0.22μm filter (Millipore Corporation, Bedford, MA, USA) to remove non-soluble polymer residues and appropriately diluted. The filtered samples were centrifuged (5000rpm for 1 hour) and the supernatant was sampled. Drug incorporation efficiency (DIE) was determined spectrophotometrically at the λ_{max} for indomethacin of 318nm instituting the following equation:

$$Drug\ Incorporation\ Efficiency\ (\%) = \frac{Actual\ quantity\ of\ drug\ in\ NS}{Theoretical\ quantity\ of\ drug\ employed} \times 100$$

[Equation 3.18]

3.6.5. *In vitro* drug release analysis from experimentally-derived lipopolysaccharide-chitosan-poly(*ε*-caprolactone) nanosystems

A modified closed-compartment USP 31 dissolution testing apparatus was used. The NS suspension (1mL), equivalent to 0.33-1.67mg indomethacin, was placed in dialysis tubing cellulose membrane (flat width: 33mm, diameter: 22mm, MW: 12400g.mol^{-1}, Sigma-Aldrich, St. Louis, MO, USA) and was exposed to normal conditions following immersion in 4mL simulated vitreous humor (SVH) (comprising phosphate-buffered saline with 0.03% $^{v}/_{v}$ hyaluronic acid, 37^{o}C) at physiological pH (7.4). (Note: prior to testing, the dialysis tubing was immersed in deionized water for 3 hours to remove glycerol and sulfide from the tubing). The samples were placed in closed vials and placed in an oscillating laboratory incubator (Labcon® FSIE-SPO 8-35, California, USA), set to 20 rpm. Balancing withdrawal of samples was undertaken every hour for eight (8) hours, and the cumulative drug release at 8 hours ascertained. All aliquots withdrawn were subjected to filtration (0.22μm PVDF, Millipore

Corporation, Bedford, MA, USA) and appropriately diluted prior to spectrophotometric analysis at the λ_{max} for indomethacin (318nm) in SVH. All analyses were conducted in triplicate (n=3).

3.6.6. Optimization of the formulatory components

Following generation of the polynomial equations relating the dependent and independent variables, the formulation process was optimized under constrained conditions for the measured responses. Simultaneous equation solving for optimization of the formulation process was performed to obtain the levels of independent variables, which would attain optimal stability (in terms of the zeta potential), acceptable drug entrapment, and good control over drug release.

3.7. Results and Discussion

3.7.1. Characterization and optimization of the experimentally-derived PB formulations

Results generated from the P-B design highlighted the generation of statistically diverse formulations in terms of the investigated responses (Table 3.4). The presence of chitosan conferred a highly positive exterior to the NS, was a stability-enhancing trait, and was evidenced in various degrees with reference to the zeta potentials of the formulations, but overall attested to their enhanced stability and potential bioadhesive capabilities. The formulations possessed varying propensities to control the release of indomethacin from the composite polymeric lipoidal structure (fractional drug release at t_{8h} ranging from 0.330 to 1.022).

Table 3.4: Characterization of the experimentally-derived Lipo-Chit-PCL NS

Formulation	***Fractional Drug Release (t_{8h})***	***Size (d.nm)***	***Zeta Potential (mV)***	***DIE (%)***
1	0.380	81.5	0.664	67.20
2	0.960	276.6	3.410	30.69
3	0.646	400.1	26.400	42.32
4	0.330	67.4	61.900	75.00
5	1.022	308.3	49.100	36.72
6	0.288	4840.0	31.400	61.00
7	0.591	563.1	38.100	45.78
8	0.994	102.6	8.450	38.86
9	0.963	1140.0	46.200	50.36
10	0.363	328.0	57.800	71.96
11	0.970	222.7	50.300	47.96
12	0.524	375.8	35.100	49.04
13	0.790	74.8	36.500	46.00
14	0.780	171.9	4.290	42.72

Consequent response surface analysis and associated plots (Figure 3.23) highlighted NS components and interactions of significance. The amount of indomethacin had a significant effect on the DIE ($p=0.042$), which increased as larger amounts of indomethacin were employed during NS fabrication, possibly due to the presence of a thermodynamically more stable emulsion system during fabrication creating an enhanced propensity for drug intercalation within the lipoidal shell. In an interesting outcome, higher drug levels within the formulations emanated in lower fractional release of indomethacin from the composite NS structure. This is contrary to literary findings where a larger polymer: drug ratio increases the diffusion pathways within the drug delivery matrix, retarding drug release. This is purportedly due to the enhanced incorporation of the indomethacin within the lipoidal shell at increased drug levels, as described. The interactive effect between the relative amounts of chitosan and indomethacin had a significant effect on the zeta potential of the NS ($p=0.038$). Zeta potential was most positive, and thus most favorable, at high chitosan and indomethacin levels. It is clearly visualized from microscopic images (Figures 3.5 and 3.6) that the cationic chitosan furnishes a generous positive coating.

Response optimization procedure (MINITAB®, V15, Minitab, USA) was used to obtain the adjusted levels of drug and polymer incorporated into the NS. Simultaneous constrained optimization of fractional drug release from the NS and zeta potential, identified as the most pertinent responses for successful operation of a nanoparticulate ocular delivery system, was undertaken to obtain a system that would avail the highest achievable particle stability, while minimizing excessive burst release within the first few hours from the NS. The optimized levels of the independent variables that would achieve the desired drug release and stability and their predicted responses were then determined. The optimized levels of the independent variables, the goal for the response, the predicted response, y, at the current factor settings, as well as the individual and composite desirability scores are represented in Figure 3.24. Based on the statistical desirability function, it was found that the composite desirability of the formulations was > 0.9.

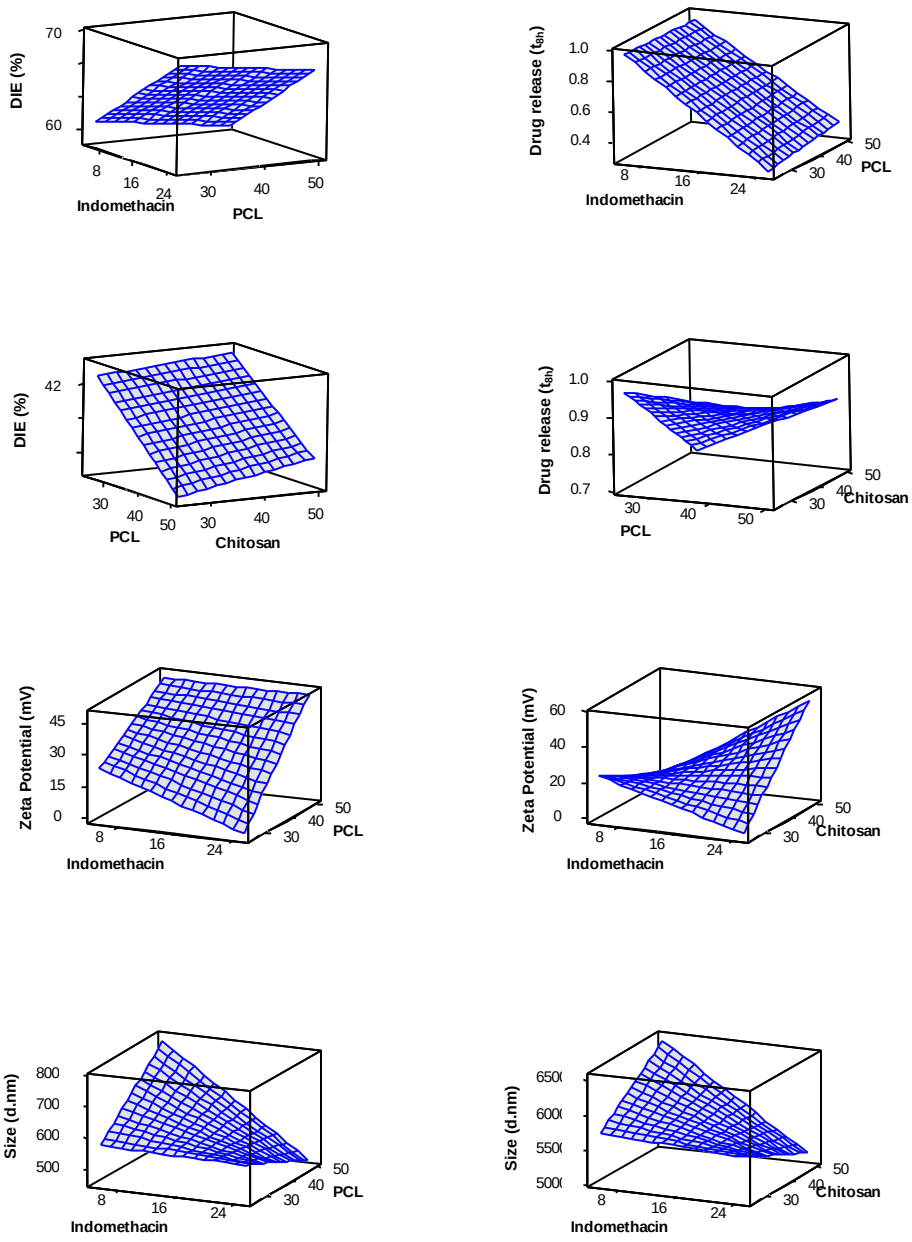

Figure 3.23: Surface plots highlighting the interactive effects of the defined variables on the responses for the P-B design

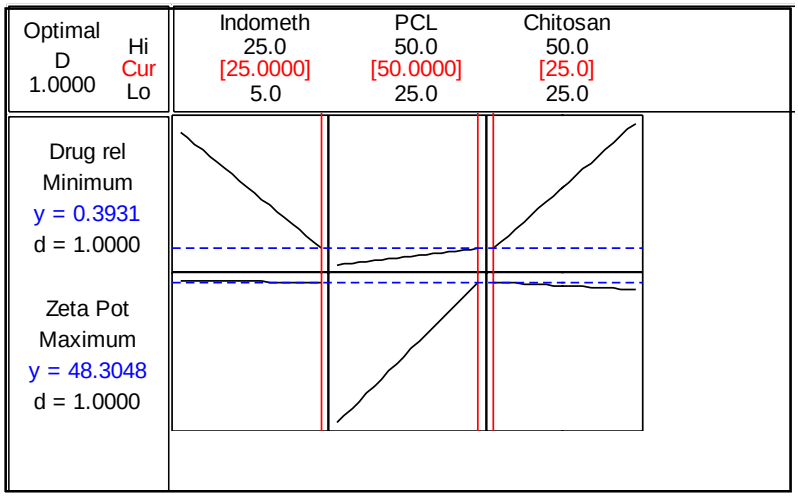

Figure 3.24: Optimization plot for definition of the optimum NS

The ideal formulation, incorporating desirable levels of the polymer and drug, was prepared according to the optimal predicted settings. The experimentally-derived values for the drug release and zeta potential of the optimal formulation was in close agreement with the predicted values (t_{8h} = 0.4123, zeta potential = 48.5mV), demonstrating the reliability of the optimization procedure in predicting the inherently distinct behavior of the preferred nano-architecture.

3.8. Concluding Remarks

This investigation demonstrated the efficacy of a composite lipoidal-polymeric system, embodied by the Lipo-Chit-PCL NS, for ocular drug delivery to the posterior segment of the eye. The designed and subsequently optimized composite lipoidal-polymeric NS holds significant potential for selective drug delivery to inflamed tissues, demonstrating significantly enhanced tissue permeation, cell uptake, and anti-inflammatory activity compared to an indomethacin suspension. Furthermore, the size (134.3nm vs 140.7nm); surface charge (+49.4mV vs. +55.7mV); flux across the RCS (0.002951mg.cm^{-2}.hr^{-1} vs. 0.001255mg.cm^{-2}.hr^{-1}); anti-inflammatory efficacy, demonstrated by a decrease in NBD-Cl complex formation (by 0.0031mmol/L vs. 0.0023mmol/L) and decrease in NFκB formation (observed as a decrease in relative optical density of 0.2027 vs. 0.2420); and enhanced inflammatory cell uptake, visualized via high-speed fluorescence and confocal microscopy; all highlighted the enhanced potential of the lipoidal system compared to the purely polymeric NS, and the potential of the NS to target inflammatory afflictions of the posterior segment of the eye.

Molecular modeling revealed that Chit-PCL-DSPC-DSPE-H_2O displayed an enhanced lipophilicity and therefore more favorable hydrophilic-lipophilic-balance (HLB) producing

superior cellular internalization efficiency than the theoretical Chit-PCL-DSPC-H_2O system and the purely polymeric NS, and corroborating the *ex vivo* data discussed earlier in this chapter.

In the second component of this Chapter, the optimal composition of the preferred composite lipoidal-polymeric NS was defined following response optimization of the formulations generated via a P-B design. This NS would be included in the inner BPM of the I^3 for further optimization in Chapter 4.

Since the exact target cells are still ubiquitous, further investigations are necessary in order to develop specific and disease-related adhesion mechanisms for active approaches. Passive targeting approaches thus highlight an important direction to achieve targeting to inflamed tissues from an implanted intraocular system, and can achieve controlled drug release, while enhancing the bioavailability of the incorporated anti-inflammatory drug.

CHAPTER 4

CONCEPTUALIZATION AND DETAILED STATISTICAL OPTIMIZATION OF AN INTELLIGENT INTRAOCULAR IMPLANT FOR EXEMPLIFICATION OF THE BIORESPONSIVE POTENTIAL

4.1. Introduction

The pragmatic design of an intelligent intraocular implant (I^3) proposed the incorporation of a two-way communication between the body and the polymeric delivery platform to create a delivery system that recognizes biochemical processes pertaining to a disease and then responds via a complex in-built mechanism to effect polymeric erosion with resultant drug dissolution and release, which was initially explicated in Chapter 1. Thus the platform on which the I^3 is based would incorporate novel stimulus-responsive polymeric materials for implantable drug delivery. The premise, which has been elaborated, is the design of inner and outer bioresponsive polymeric matrices (BPMs) that would erode and release the incorporated anti-inflammatory and antibiotic in a fashion responsive to a stimulus, such as the highly reactive intermediates including O^{2-}, H_2O_2, chloramines and $OH^{\cdot}$ that are released from activated leukocytes both *in vitro* and during acute and chronic intraocular inflammatory reactions *in vivo* (Hawkins and Davies, 1996). Thus release of the incorporated bioactives from the bioresponsive system would preferably be individualized and synchronized directly with the anti-inflammatory response of the patient, in other words, whether the anti-inflammatory agent would be released to a greater extent or not would correspond with the presence or absence of inflammation in the eye. Furthermore, the anti-inflammatory agent would be presented as a NS, as designed and optimized in Chapter 3 for inclusion within the inner core, which on its erosion, would avail the NS for targeting of inflammatory sites within the eye. The overall *modus operandi* of the I^3 is divulged in the animation below (Figure 4.1).

In this Chapter, the potentially inflammation-sensitive polymers introduced in Chapter 2 were formulated and optimized as multi-crosslinked simultaneously-originated BPMs forming a secure-fit dual bioresponsive polymeric matrix system with a NS enclatherated as a superlattice (i.e. each nanoparticle connected within the numerous periodic layers of the polymeric material). Chitosan constitutes the inner BPM in which the NS was embedded; and alginate, hyaluronic acid and crosslinked poly(acrylic) acid comprise the inflammation-responsive outer BPM. The I^3 would possess the inherent capabilities to meet the following design criteria, which would form the basis for ultimate optimization of the device:

1. Minimal drug release under *in vitro* conditions simulating a normal physiological intraocular state

2. Enhanced drug release (relative to the normal state) under *in vitro* conditions simulating a pathological inflammatory intraocular state created in the presence of hydroxyl radicals generated via the Fenton reaction. A triggered erosion of the BPMs with a more rapid response from the outer BPM (compared to the inner BPM) and antimicrobial release is necessitated for management of the initial infection (if present).
3. The inner (core) BPM should display prolonged, modulated inflammation-responsive erosion to release the anti-inflammatory agent-loaded NS for management of the acute inflammatory response and ensuing inflammation.
4. Minimal swellability or fluid imbibement, expressed as water absorption capacity (WAC), to prevent untoward eye irritation following implantation. Pertinently, WAC is a measure of the degree of crosslinking (as described in Chapter 2) that has been instigated in the polymers comprising the I^3.

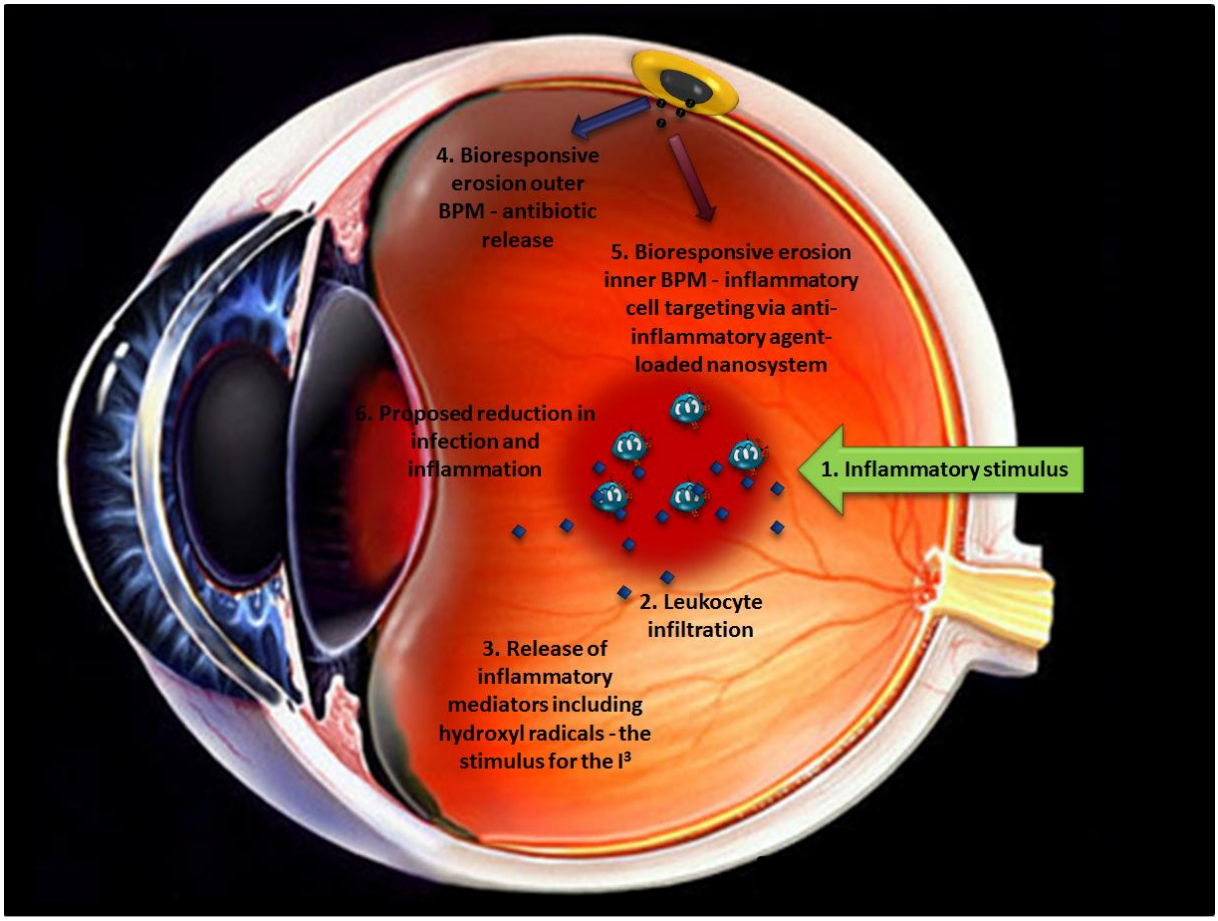

Figure 4.1 *(still)*: Animation explicating the overall *modus operandi* of the I^3 in the inflamed eye (superimposed on a diagram of a cross-section of the eye by Stephen E. Gordon) (See Video CD in the front cover of this Thesis for Figure 4.1 *(animated)*)

4.1.1. Optimization of complex drug delivery systems

Considering the aim of this Chapter is the elucidation of an optimum I^3, it is only fitting to mention that the sought-after goal of the pharmaceutical scientist is design of an impeccable drug delivery system, which consequentially encompasses multiple objectives. There has thus been a paradigm shift to modern delivery system optimization approaches, employing systematic Design of Experiments (DoE), which are being more widely instituted in the design of diverse embodiments of drug delivery devices with the aim of overcoming irregularities, such as failure to fix errors and unpredictability. The advantages of this systematic approach must be realized: the number of experiments required to achieve an optimum formulation is reduced, thus problem identification and rectification are simplified, pertinent drug/ polymer/ crosslinking agent interactions are revealed, product performance may be simulated, and the fabrication process is better comprehended which enables enhanced delivery system development and subsequent scale-up (Singh et al., 2005). Statistical experimental designs are thus strongly recommended in identifying critical formulation variables in the development of modified-release drug delivery systems and would be key in identifying the optimum I^3 (Sastry et al., 1997). An innovative approach was appointed for simultaneous origination of the BPMs employing multiple crosslinking steps with the proposed elaboration of both ionic and chemical interpolymeric associations. Response surface methodology (RSM) was thus importantly applied for the generation of mathematical models to adequately describe or predict the WAC, micromechanical properties, and drug release capabilities of the BPMs possessing an intricate structural basis; under conditions simulating both normality and inflammation of the intraocular environment.

In order to further describe the complex system exemplified by the I^3, and as a complementary tool to RSM, the institution of networks was considered apt. An artificial neural network (ANN) is a mathematical or computational model deriving inspiration from the structure and/ or functional aspects of biological neural networks. A neural network is composed of an interconnected group of artificial neurons, which process information employing a connectionist approach to computation. Furthermore, ANN is an adaptive system that implicates a learning phase; it is a non-linear statistical data modeling tool that models complex relationships between inputs and outputs. Both DoE and ANN are important approximation techniques, each with their own unique features, advantages and disadvantages over one another. Chen and Varadarajan (1997) reported on an integration strategy for DoE and ANN for complementary and verification purposes. The combinatory institution of both techniques was applied here. The same inputs fed into the response surface design were emulated in the ANN to ascertain the strength of correlation for a selected output.

Consequent to device optimization, further characterization in terms of the overall drug release kinetics of the I^3 was imperative. The I^3 in its entirety is essentially an intricate crosslinked hydrophilic polymeric matrix. Thus the drug release from this system (under both normal and inflammatory conditions) is anticipated to be a complex interaction between dissolution, diffusion and erosion mechanisms. Several mathematical models have been published in an attempt to elucidate the water and drug transport processes and to predict the resulting drug release kinetics from hydrophilic matrix systems such as those derived from hydroxypropyl methylcellulose (Korsmeyer et al., 1986a,b; Gao et al., 1995; Siepmann et al., 1999a,b). The manifestation of a mathematical description of the entire drug release process is somewhat difficult due to the number of physical characteristics that must be taken into consideration, which include diffusion of water (and/ or free radicals) into the BPMs, BPM swelling, drug diffusion from the I^3, polymeric chain scission or disentanglement and dissolution, axial and radial transport in the 3-dimensional implant, concentration dependent diffusivities of the species, moving boundaries, changing BPM dimensions, porosity, and variable composition of the I^3. Each model embodies certain assumptions, which restricts the applicability of the respective models to certain drug-polymer systems (Siepmann et al., 2000). Different dissolution models were thus applied to the drug release data obtained for the optimal formulation when exposed to normal and inflammatory conditions. The criterion for selecting the most appropriate model was based on linear and non-linear regression techniques (Shoaib et al., 2006).

Finally, in order to prove the rationality and applicability of the constituent polymers in the formation of the multipolymeric complex, molecular mechanics and dynamics simulations were carried out. The concept of computational chemistry and molecular modeling pertains to the application of theoretical methods and computational techniques for the modeling and simulation of small chemical and biological systems in order to predict and interpret their behavior, and is significantly applicable to polymeric systems implicated in the formation of a novel drug delivery system as exemplified, in this investigation, by the I^3. Molecular mechanics simulations were carried out to model the polymers comprising the outer BPM (alginate, HA and crosslinked poly(acrylic) acid), individually as well as in combination. The polymeric complexes were modeled in the presence of a solvated system with water as the solvent. Modeling simulating a pathological inflammatory intraocular state created in the presence of hydroxyl radicals was also performed to elucidate the effect of the inflammatory agents on the polymers, specifically the HA molecule. Furthermore, molecular dynamic simulations for the binary and ternary combinations were performed to validate the atomistic simulation results.

4.2. Materials and Methods

4.2.1. Materials

Hyaluronic acid (potassium salt, from human umbilical cord), chitosan (MMW) *N*,*N*′-dicyclohexylcarbodiimide, indomethacin (99% TLC) and gluteraldehyde 25%$^{v}/_{v}$ were all purchased from Sigma-Aldrich® Inc. (St Louis, MO, USA). *N*-hydroxysuccimide and ciprofloxacin were purchased from Fluka® Analytical via Sigma-Aldrich® Inc. (St Louis, MO, USA). Alginate (TICA-algin® 400 Powder, medium viscosity) was purchased from Texture Innovation Center® (White Marsh, MD, USA). Other materials employed were crosslinked poly(acrylic) acid (Carbopol 974P®) (Noveon Inc., Cleveland, Ohio, USA), as well as hydrochloric acid and aluminum chloride that were purchased from (Merck, Wadeville, Gauteng, South Africa). All other reagents were of analytical grade and used as received.

4.2.2. Formulation of the bioresponsive polymeric matrices

For the initial formulation of the outer BPM a 4%$^{w}/_{v}$ sodium alginate - 1%$^{w}/_{v}$ crosslinked poly(acrylic) acid (Carbopol® 974; referred to henceforth as PAA) - 3%$^{w}/_{v}$ *N*-hydroxysuccimide (NHS) - 0.25%$^{w}/_{v}$ hyaluronic acid (HA) - 2.5%$^{v}/_{v}$ gluteraldehyde - 0.25%$^{w}/_{v}$ ciprofloxacin aqueous solution was prepared, instituting carbodiimide coupling chemistry to increase the interconnectivity of the matrix. *N*,*N*′-dicyclohexylcarbodiimide (DCC), which is commonly used as a coupling agent or activator, was employed to facilitate coupling between the HA and alginate, and the PAA. DCC (300mg) was dissolved in ethanol and dispersed within the polymeric solution. This formed the anionic polymer-drug solution.

In this synthetic effort, the carbodiimide functionality acts as a dehydration agent and activates carboxylic acids towards amide or ester formation. The inclusion of additives or reagents in the polymeric composition, namely NHS, has the purpose of increasing the reaction yield, i.e., increasing interpolymeric crosslinking via, proposedly, amide formation, and decreasing side reactions (Hermanson, 2008).

For the inner (core) BPM, the cationic chitosan solution incorporating the Lipo-Chit-PCL NS was prepared as described in Chapter 3, Sections 3.3.3 and 3.6.2, employing the optimal solution of 25mg indomethacin, 50mg PCL and 25mg chitosan, ensued with hydration of chitosan (MMW) in the NS suspension to yield a final MMW chitosan concentration of 13.33%$^{w}/_{v}$. The anionic polymer-drug solution (0.3mL) was distributed to plastic moulds (diameter = 12mm, volume = 1cm^3, curvature = 10^o) containing 0.05mL of an acidified 3%$^{w}/_{v}$ $AlCl_3$ solution, where the $AlCl_3$ serves as a catalyst for the interpolymeric coupling reaction (Friedel-Crafts acylation). The cationic polymer solution (0.1mL) was added to the center of

the mould. Diffusional development of two separate interpenetrating networks, and simultaneous curing of the chitosan core and outer matrix, was allowed to occur over 12 hours. The final implants were washed thrice with double deionized water and allowed to dry for 48 hours under ambient conditions at 25^{o}C.

4.2.3. The implications of incorporation as a nano-enabled component on the drug release behavior of indomethacin

The specific advantages of the NS in its entirety as a drug delivery system was extensively evolved in Chapter 3 in terms of its potential to target and reduce inflammation. This exercise was undertaken to exemplify the differences in release behavior of indomethacin following direct incorporation within the inner BPM as opposed to initial incorporation into the NS, followed by incorporation within the inner BPM. For the non-nano-enabled I^3 (as opposed to the nano-enabled form prepared as detailed above), the outer BPM solutions were prepared as described in Section 4.2.2 above. For the inner BPM, 25mg indomethacin (equivalent to the drug amount employed in NS manufacture) and chitosan (MMW) (200mg) was dissolved in 15mL 0.05M HCl, and 0.1mL of this solution was employed for each inner BPM. Simultaneous origination of the inner and outer BPM was as described. Drug release studies were undertaken on both the nano- and non-nano-enabled I^3 under normal and inflammatory conditions as described in the ensuing Section 4.2.5.

4.2.4. Experimental design for the bioresponsive polymeric matrices for selection of pertinent variables impacting the formulation process

Preliminary investigations were undertaken for the identification of critical formulatory components and their upper and lower desirable levels. The fixed ratio presence of alginate: crosslinked poly(acrylic) acid was found to be integral for establishment of the outer matrix. The specified amount of chitosan and gluteraldehyde crosslinking agent also proved essential for the formation of a robust inner BPM. These factors were thus not subjected to variation via RSM. The NS intercalated within the inner core was previously optimized, as described in Chapter 3.

Factors were selected that would ultimately impact on the responses displayed by the preliminary system. Optimization of the I^3 was conducted by constructing and analysing a four-factor, three-level (3^4) Box-Behnken statistical design on MINITAB®, (V15, Minitab, USA) as depicted in Table 4.1. All formulations were prepared as two batches (one containing only ciprofloxacin in the outer BPM and a drug-free NS in the inner core, and the other containing only the indomethacin-loaded NS in the inner BPM and a drug-free outer matrix). Each batch comprised 24 implant replicates (n=24 for each of the 27 formulations) for subsequent tests.

Table 4.1: Formulations depiciting the levels of independent variables generated by the 3^4 Box-Behnken Design

Formulation	HA ($\%^{w}/_{v}$)	NHS ($\%^{w}/_{v}$)	DCC ($\%^{w}/_{v}$)	$AlCl_3$ ($\%^{w}/_{v}$)
1	0.25	3	8	8
2	0.50	4	6	6
3	0.25	4	6	8
4	0.25	3	6	6
5	0.25	3	4	8
6	0.00	2	6	6
7	0.25	3	8	4
8	0.00	3	6	4
9	0.25	2	8	6
10	0.25	4	6	4
11	0.50	2	6	6
12	0.25	2	6	8
13	0.00	3	4	6
14	0.50	3	6	8
15	0.25	3	6	6
16	0.00	4	6	6
17	0.50	3	6	4
18	0.25	4	4	6
19	0.25	2	4	6
20	0.25	2	6	4
21	0.00	3	6	8
22	0.00	3	8	6
23	0.25	3	6	6
24	0.50	3	8	6
25	0.25	4	8	6
26	0.50	3	4	6
27	0.25	3	4	4

4.2.5. Evaluation of the *in vitro* bioresponsive drug release behavior from the experimental design-derived bioresponsive polymeric matrices

In the selection of inflammation as a stimulus, the *in vitro* degradation of the crosslinked BPMs by varying levels of chemical inflammatory mediators (hydroxyl radicals) generated via the Fenton reaction (Yui et al., 1992) (Equation 4.1) was examined:

$$Fe^{2+} + H_2O_2 \rightarrow Fe^{3+} + OH^{\cdot} + OH^{-} \qquad \text{[Equation 4.1]}$$

A modified closed-compartment USP 31 dissolution testing apparatus was used. Each accurately weighed I^3 (separately loaded with either indomethacin in the core BPM or ciprofloxacin in the outer BPM) was either exposed to normal conditions (N) following immersion in 4mL simulated vitreous humour (SVH, comprising phosphate-buffered saline with $0.03\%^{v}/_{v}$ HA, 37^{o}C) at normal physiological pH (7.4), or pathological inflammatory conditions (F) in 4mL SVH containing 0.05M Fenton's reagent. Briefly, each accurately weighed BPM was placed in a filtered SVH solution which contained 100µmol of hydroxyl

radicals generated by combining 1mL 0.1M $FeSO_4$ and 1mL 0.1M H_2O_2, which had a pH of 5. This fell within the range of hydroxyl radicals reportedly generated during pathological inflammatory states, and pH range (3-6) for optimum reaction conditions (Yui et al., 1992). The drug release was thus reported at normal physiological and pathological conditions to enable assessment of an inflammation-responsive mode of degradation.

The samples were placed in closed vials and placed in an oscillating laboratory incubator (Labcon® FSIE-SPO 8-35, California, USA), set to 20 rpm. Balancing withdrawal of samples was undertaken at 3, 7, 14, 21 and 28 days. All aliquots withdrawn were subjected to filtration (0.22μm PVDF, Millipore Corporation, Bedford, MA, USA) and appropriately diluted prior to spectrophotometric analysis at the λ_{max} for indomethacin (318nm) and ciprofloxacin (278nm) in SVH. The componential polymeric absorbance of the I^3, together with the influence of the Fenton's reagent on the absorbance readings at the respective wavelengths were taken into account. As any unincorporated surface drug and NS could be lost during the rinsing of the formulations, the total amount of drug in each formulation was determined following grinding of the respective I^3 formulations in a pestle and mortar, followed by dispersion of the subsequent powder in SVH pH 7.4. These samples were placed in the oscillating laboratory incubator for 28 days at 50rpm, and then subjected to centrifugation at 15000×*g* for 1 hour. Centrifugation was repeated twice. The supernatant was isolated and filtered and samples were analyzed via UV spectroscopy as described. This procedure was found to be adequate for releasing all entrapped drug. All analyses were conducted in triplicate (n=3). A model-independent approach was used to compare the dissolution data for both the inner and outer BPM for ciprofloxacin and indomethacin release. For this purpose a mean dissolution time at 28 days (MDT) was calculated for each formulation, defined as the sum of different release fraction periods obtained for dissolution studies endured in SVH, divided by the initial loading dose (Pillay and Fassihi, 1998) as exemplified in Equation 4.2:

$$MDT = \sum_{t=1}^{n} ti \ \frac{M_t}{M\infty} \qquad \text{[Equation 4.2]}$$

M_t is the fraction of dose released in time $ti = (t_i + t_{i-1})/2$ and $M\infty$ corresponds to the loading dose and a maximum MDT refers to the fastest drug release achievable (Govender et al., 2005).

4.2.6. Investigation of the transitional micromechanical behaviour and fluid uptake of the experimental design-derived intelligent intraocular implants

All 27 formulations (ciprofloxacin- and indomethacin-loaded) were exposed to both normal (N) and pathological (F) testing conditions as described for *in vitro* drug release evaluation

(Section 4.2.5). At each time point (0, 3, 7 14, 21, and 28 days) the implant was removed from the simulated physiological fluid, excess liquid blotted with filter paper, and the WAC and textural attributes evaluated in triplicate. The hydrated implant was weighed at each time point to assess the swollen weight, as an indication of the WAC as follows:

$$WAC(\%) = \frac{W_s - W_d}{W_d} \times 100 \qquad \text{[Equation 4.3]}$$

Where W_s is the swollen weight and W_d is the dry weight of the I^3.

The physicomechanical properties were assessed through textural profiling of the I^3 at 0, 3, 7, 14, and 28 days, using a calibrated Texture Analyser (*TA.XT.plus Texture Analyser*, Stable Microsystems®, Surrey, UK) fitted with a 5kg load cell, for determination of the matrix hardness (N/mm, calculated as the gradient of the force-displacement profile during the compression phase) and deformation energy (N.m or J, calculated as the area under the force-displacement curve, AUC) of normal and pathological SVH-hydrated BPMs (except at day 0, at which point the device as in the unhydrated state), using a 2mm flat-tipped steel probe; and matrix resilience, using a 36mm cylindrical steel probe. The settings for analysis are highlighted in Table 4.2.

Table 4.2: Textural parameters for determination of matrix hardness, deformation energy and matrix resilience

Parameter	Matrix hardness and deformation energy settings	Matrix resilience settings
Pre-test speed	1.00 mm/s	1.00 mm/s
Test speed	2.00 mm/s	2.00 mm/s
Post-test speed	10.0 mm/s	10.0 mm/s
Target mode	Force	10 % strain
Target force	0.98067 N	-
Trigger type	Auto (force)	Auto (force)
Trigger force	0.04903 N	0.04903 N
Load cell	5 kg	5 kg

4.2.7. Optimization of the formulatory components

In order to evaluate the varied capabilities of the experimental design-generated formulations, diversely applicable responses were measured and analyzed, namely:

- MDT of indomethacin at 28 days under normal and pathological conditions (MDT I N and F, respectively)

- MDT of ciprofloxacin at 28 days under normal and pathological conditions (MDT C N and F, respectively)
- Change/ difference in the MDT of indomethacin from normal to pathological conditions (Δ MDT I)
- Change/ difference in the MDT of ciprofloxacin from normal to pathological conditions (Δ MDT C)
- Rate of change in WAC under normal and pathological conditions (Δ WAC N and Δ WAC F, respectively), ascertained via linear regression
- Overall rate of change in normalized textural properties i.e. averaged rate of change in resilience, hardness and deformation energy under normal pathological conditions (Δ Textural properties N and F, respectively), ascertained via linear regression
- Rate of change in each textural attribute (resilience, hardness, and deformation energy) under normal and pathological conditions (Δ Resilience N and F, Δ Hardness N and F, Δ Deformation Energy N and F), ascertained via linear regression.

Following generation of the polynomial equations relating the dependent and independent variables, the formulation process was optimized under constrained conditions for the most applicable and significant measured responses. Simultaneous equation solving for optimization of the formulation process was performed to obtain the levels of independent variables, which would exemplify the bioresponsive capabilities of the I^3 i.e. maximization of the Δ MDT, and minimization of the WAC, such that the device would release minimal drug under normal conditions but release increased levels of drug on exposure to an inflammatory stimulus, and swell minimally on exposure to the physiological fluids of the eye.

4.2.8. Concurrent optimization by ANN for statistical validation

Concurrent optimization was conducted by employing the feedback Multilayer Perceptron (MLP) neural network to train the empirical input Δ MDT I data (being the most pertinent indicator of bioresponsivness of the I^3) with static back propagation. Figure 4.2 illustrates the typical construction of the MLP network. The input data (obtained from the comparative drug release investigations under normal and pathological conditions) was trained. The main advantage of these networks is that they can approximate any input/ output map.

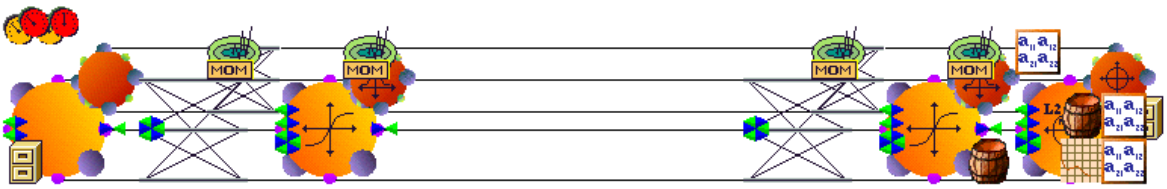

Figure 4.2: Constructed multilayer perceptron network. An artificial neural network is an interconnected group of nodes, akin to the vast network of neurons in the human brain (generated employing Neurosolutions Version 5.0, NeuroDimension Inc., Gainsville, Florida).

A genetic algorithm with a Sigmoid Axon transfer function and Conjugated Gradient learning rule was employed for the hidden input and output layers. A maximum of 10,000 epochs were run on NeuroSolutions Version 5.0 (NeuroDimension Inc., Gainsville, Florida) for ensuring optimal training of data.

4.2.9. Kinetic analysis of drug release from the optimum formulation

To analyze the *in vitro* release data of the optimum formulation various kinetic models were used to describe the release kinetics. The zero order rate equation (Equation 4.4) describes systems where the drug release rate is independent of its concentration (Hadjiioannou et al., 1993). The first order equation (Equation 4.5) describes a concentration-dependent release rate from a system (Bourne, 2002). Higuchi (1963) described the release of drugs from an insoluble matrix as a square root of time dependent process based on Fickian diffusion (Equation 4.6). The Hixson-Crowell cube root law (Equation 4.7) describes drug release from systems which is dependent on alterations in surface area and diameter of the drug delivery system (Hixson and Crowell, 1931).

$$C = k_0 t \qquad \text{[Equation 4.4]}$$

Where k_0 is the zero-order rate constant expressed in units of concentration/time and t is the time.

$$Log\ C = Log\ C_0 - \frac{k_t}{2.303} \qquad \text{[Equation 4.5]}$$

Where C_0 is the initial concentration of drug and k_t is the first order constant.

$$Q = Kt^{1/2} \qquad \text{[Equation 4.6]}$$

Where K is the constant reflecting the design variables of the system.

$$Q_0^{1/3} - Q_t^{1/3} = K_{HC}t$$ [Equation 4.7]

Where Q_t is the amount of drug released in time *t*, Q_0 is the initial amount of the drug in tablet and K_{HC} is the rate constant for Hixson-Crowell rate equation.

The following plots were constructed: *cumulative % drug release vs. time* (zero order kinetic model); *log cumulative of % drug remaining vs. time* (first order kinetic model); *cumulative % drug release vs. square root of time* (Higuchi model) *log cumulative % drug release vs. log time* (Korsmeyer model) and *cube root of drug % remaining in matrix vs. time* (Hixson-Crowell cube root law).

4.2.9.1. Mechanism of drug release

Korsmeyer et al. (1983) originated a simple relationship describing drug release from a polymeric system (Equation 4.8). To postulate the mechanism of drug release, the drug release data (generally less than 60%) was fitted in Korsmeyer-Peppas model:

$$\frac{M_t}{M\infty} = Kt^n$$ [Equation 4.8]

Where M_t/M_∞ is the fraction of drug released at time *t*, *K* is the rate constant and *n* is the release exponent. The *n* value is used to characterize different release mechanisms as for cylindrical shaped matrices, which may be n=0.45 for Fickian diffusion, $0.45 < n < 0.89$ for anomalous (non-Fickian) diffusion, n=0.89 for case-II transport, and $n > 0.89$ for super case-II transport.

4.2.9.2. Linear Mixed Effects Modeling

In order to construe the kinetic model which best described the drug release kinetics from the I[3], nonlinear/ linear mixed effects modelling was undertaken in addition to the generic linear modelling in order to generate statistical descriptors. The Linear Mixed Effects Modeling feature is based on the general linear mixed effects model, which can be represented in matrix notation as:

$$y = X\beta + Z\gamma + \varepsilon$$ [Equation 4.9]

Where *X* is a matrix of known constants and the design matrix for β, β is a vector of unknown (fixed effect) parameters, γ is a random unobserved vector (the vector of random-effects

parameters), normally distributed with mean 0 and variance *G, Z* is a matrix of known constants and the design matrix for γ, and $\boldsymbol{\varepsilon}$ is a random vector, normally distributed with mean 0 and variance *R*. γ and $\boldsymbol{\varepsilon}$ are uncorrelated.

WinNonlin's Linear Mixed Effects module (WinNonlin® V5.3, Pharsight Software, Statistical Consultants Inc., Apex, NC, USA) was employed, which institutes the smaller-is-better form of Akaike's Information Criterion (AIC):

$$AIC = -2L_R + 2s \qquad \text{[Equation 4.10]}$$

Where L_R is the restricted log-likelihood function evaluated at final fixed parameter estimates and the final variance parameter estimates, and *s* is the rank of the fixed effects design matrix *X* plus the number of parameters in θ (i.e. *s* = rank(*X*) + dim(θ)).

The Linear Mixed Effects module also uses the smaller-is-better form of Schwarz's Bayesian Criterion (SBC):

$$SBC = -2L_R + s\log(N - r) \qquad \text{[Equation 4.11]}$$

Where L_R is as described above, *N* is the number of observations used, *r* is the rank of the fixed effects design matrix *X*, and *s* is the rank of the fixed effects design matrix *X* plus the number of parameters in θ (i.e. *s* = rank(*X*) + dim(θ)).

The AIC and SBC values are a measure of goodness of fit based on maximum likelihood. When comparing several models for a given set of data, the model associated with the smallest value of AIC or SBC is regarded as giving the best fit. Lower values of the index indicate the preferred model, that is, the one with the fewest parameters that still provides an adequate fit to the data; although it is not the actual value but rather the difference between the values in a set. The value that is the lowest in the set represents the best fit. In this case each set is the different kinetic model. Thus the variation between the values among different sets is not a consideration.

4.2.10. On-off inflammation-responsive capabilities of the optimum formulation

Intrinsic to further assessment of the optimum formulation was its *in vitro* performance with interchanging exposure to *and* removal of the mitigating stimulus. The optimum implant was thus exposed to alternating normal and inflammatory phases as follows, in Table 4.3.

Table 4.3: Exposure conditions for assessment of the on-off inflammation-responsive capabilities of the optimum formulation

Time period	Condition	Media
Day 0-3	Normal	SVH
Day 3-7	Inflammatory	SVH+Fenton's reagent
Day 7-14	Normal	SVH
Day 14-21	Inflammatory	SVH+Fenton's reagent
Day 21-28	Normal	SVH

At 3, 7, 14, 21 and 28 days, the respective media was subjected to UV spectrophotometric analysis before being drained and replaced with new media, in order to ascertain whether any fluctuations in the drug release behavior could be detected.

4.2.11. Molecular modeling simulations for prediction of pertinent interactions within the polymeric system of the I^3 and between the I^3 and normal or inflammatory milieu

All modeling procedures, computations, and molecular simulations were performed using commercial softwares: HyperChem™ 8.0.8 Molecular Modeling System (Hypercube Inc., Gainesville, Florida, USA) and ChemBio3D Ultra 11.0 (CambridgeSoft Corporation, Cambridge, UK). Simulation approaches included molecular mechanics (MM) and molecular dynamics with the number of atoms, pressure and temperature held constant (NPT-MD).

4.2.11.1. Static Lattice Atomistic Simulations in vacuum

The decamer of crosslinked poly(acrylic) acid (PAA) was archetyped using ChemBio3D Ultra in its syndiotactic stereochemistry as a 3D model, whereas the structures of alginate (ALG; 6 monosaccharide units) and hyaluronic acid (HA; 6 monosaccharide units) was built from standard bond lengths and angles using the Sugar Builder Module on HyperChem 8.0.8. The models were primarily energy-minimized using the MM+ Force Field algorithm and the resulting structures were subsequently energy-minimized using the AMBER 3 (Assisted Model Building and Energy Refinements) Force Field algorithm. The conformer having the lowest energy was used to develop the polymer-polymer. A complex of one polymer molecule with another was assembled by parallel disposition and the energy-minimization was repeated to generate the final models: ALG-HA, ALG-PAA, PAA-HA, and ALG-PAA-HA. Full geometrical optimization was conducted in vacuum employing the Polak-Ribiere Conjugate Gradient method until an RMS gradient of 0.001kcal/mol was reached (Kumar et al., 2011).

4.2.11.2. Static Lattice Atomistic Simulations in a solvated system

To generate the final models in a solvated system, the MM simulations were performed for cubic periodic boxes with the polymer/ polymer at the centre of the cubic box and the remaining free space filled with water molecules and the same procedure of energy-minimization was repeated to generate the solvated models except that the force fields were utilized with a distance-independent dielectric constant with no scaling (Table 4.4). Additionally, the Force field options in the AMBER (with explicit solvent) were extended to incorporate cutoffs to inner and outer options with the nearest-image periodic boundary conditions, and the outer and inner cutoffs were to ensure that there were no discontinuities in the potential surface (Table 4.4) (Choonara et al., 2011).

Table 4.4: Computational parameters used to construct aqueous-phase model building and simulations

S. No.	Parameter	Description
1	Periodic box dimensions	15×15×20A°^{3}
2	Cut-offs	Switched
3	Dielectric (epsilon)	Constant
4	1-4 Scale factors	Electrostatic: 0.5 van der Waals: 0.5
5	Outer radius	7.5A°
6	Inner radius	3.5A°
7	Water molecules	149
8	Solvent/Polymer distance	2.3A°

4.2.11.3. Molecular Dynamics Simulations in vacuum

The polymer chains initially minimized by molecular mechanics were then minimized by molecular dynamics for 1.0ps (time step = 0.001ps) at 300K with the Nose-Hoover thermostat. For evaluation of the stability of a simulation and the extent of equilibration and for identification of the interesting low energy conformations, molecular dynamics calculations were averaged and saved as kinetic energy (EKIN), potential energy (EPOT), total energy (ETOT) and temperature (TEMP). Equilibrium was established before recording the measurements wherein the instantaneous potential and kinetic energy were monitored to determine when the system reached equilibrium. Thereafter, the simulation was allowed to run for 1000 time-steps before taking measurements (Guo et al., 2003).

4.2.11.4. Molecular Mechanics Assisted Model Building and Energy Refinements

A molecular mechanics conformational searching procedure was employed to acquire the data required in the statistical mechanics analysis, to obtain differential binding energies of a Polak-Ribiere algorithm, and to potentially permit application to polymer composite assemblies as described in Chapter 3, Section 3.3.12.3.

MMER was used as described in Chapter 3, Section 3.3.12.3.1 to provide information about the contributions of valence terms, noncovalent Coulombic terms, and noncovalent van der Waals interactions for polymer/ polymer interactions, employing Equations 3.5 and 3.6 to measure the total potential energies of the isolated and complexed systems. If the total potential energy of the complex is smaller than the sum of the potential energies of isolated individual molecules in the same conformation, the complexed form is more stable and its formation is favored (Yu et al., 2008).

4.3. Results and Discussion

The simultaneous formation of the multi-crosslinked BPMs culminating in the final I^3 (in plastic moulds of appropriate curvature as per the angles of curvature within the eye) as well as the diameter of the dried implant, is highlighted in Figure 4.3. There was dramatic shrinkage of the hydrogels implicated in implant formation due to a potentially high degree of crosslinking with resultant enhanced interconnectivity of the component polymers.

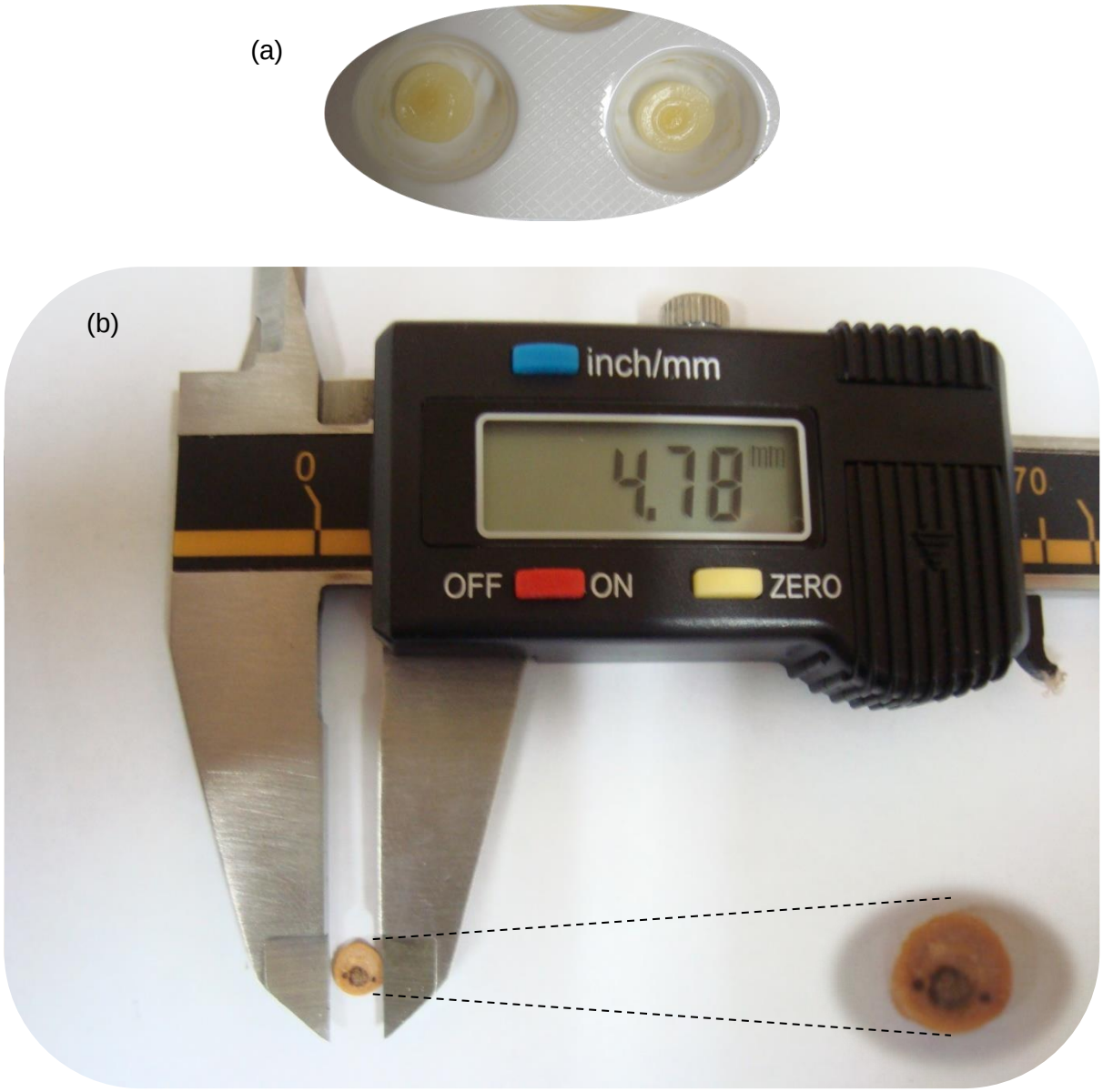

Figure 4.3: Photographic images depicting (a) simultaneous origination of the BPMs comprising the I^3 and (b) the final implant and resultant diameter

4.3.1. The implications of incorporation as a nano-enabled component on the drug release behavior of indomethacin

Drug release from the nano-enabled I^3 was lower than for the non-nano-enabled device under normal conditions, but enhanced under inflammatory conditions, attributed to the stimulus-responsive mechanism emanating in potential disruption of hydrolyzable linkages with release of the enclatherated NS, as evident in Figure 4.4. The creation of an additional diffusion barrier created through incorporation of indomethacin into the NS has the following implications depending on the polymeric degradation mechanism of the surrounding implant:

1. In the case of a high degree of fluid imbibement by the BPMs comprising the I^3, consequent hydration and swelling of the surrounding matrix may result in dislodgement of the NS from the matrix and diffusion of the NS from the implant with ultimate release of the drug from the NS (following tissue targeting as proposed in Chapter 3), or drug may be released from the NS while still entrapped within the matrix creating an extended diffusion pathway through both the NS wall and implant matrix where drug release is prolonged and diffusion controlled. The latter situation is not largely favored.
2. Should erosion be the primary mechanism of implant biodegradation, with minimal fluid penetration into the inner BPM, the NS will be dislodged from the inner matrix and the only diffusion pathway controlling drug release will be the NS wall. This is the preferred mechanism under inflammatory conditions for targeted and concise operation of the NS.

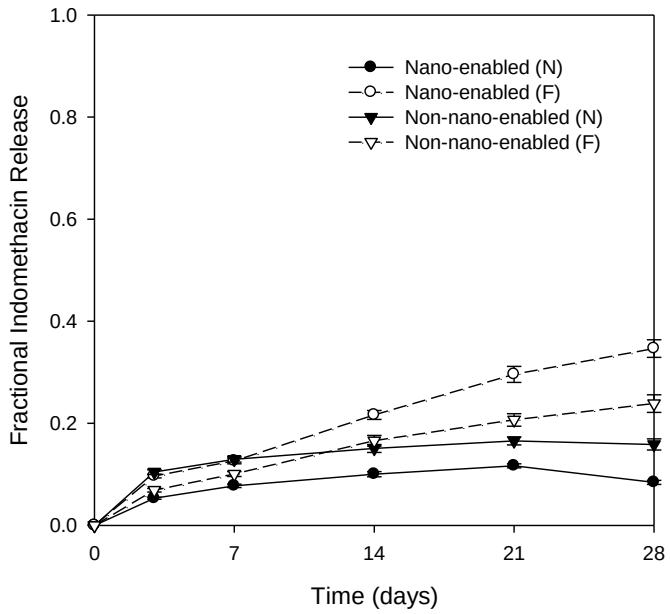

Figure 4.4: Comparative indomethacin release profiles for the nano- versus non-nano-enabled I^3 under normal (N) and inflammatory (F) conditions (n=3)

The NS is intricately embedded within the the I^3 due to the surrounding long chitosan chains that interact and attach to the surface of the NS through hydrogen bonding and ionic interactions as a result of self-deposition and crosslinking initiated by gluteraldehyde, as evidenced from the SEMs in Chapter 3 (Figure 3.7) thus in order for dislodgement to occur, hydrolysis of these linkages is necessitated. Thereafter release of indomethacin from the NS could be by the following mechanisms: (a) desorption of drug bound to the surface, (b)

diffusion through the NS matrix, (c) NS matrix erosion, or (d) a combined erosion-diffusion process (Ringe et al., 2004).

4.3.2. Characterization of the experimentally-derived formulations

There was little variation in the amounts of drug incorporated within all the I^3 formulations with 59.84±6.32µg (~60µg) indomethacin and 68.56±6.29µg (~70µg) ciprofloxacin detected. The drug release profiles generated for the experimentally-derived formulations attest to the bioresponsive potential of the implants, as in general, a higher degree of drug release was achieved when implants were exposed to pathological conditions (hydroxyl radicals generated by Fenton's reaction). Indomethacin *in vitro* levels were above the minimum effective concentration (MEC) of indomethacin (>0.225µg/mL) being >0.689µg/mL under normal conditions and >1.333µg/mL under inflammatory conditions for all formulations at all time points evaluated. *In vitro* levels of ciprofloxacin attained were above the MIC_{90} of common pathogens for ciprofloxacin (>0.8µg/mL, refer to Table 4.5) being >2µg/mL and >10µg/mL in all cases, under normal and pathological conditions, respectively. Intraocular levels achieved following topical application of ciprofloxacin were demonstrated by Yagci et al. (2007). Following infection with an intravitreal inoculum of *Staphylococcus aureus* in New Zealand Albino Rabbits, the efficacy of topical ciprofloxacin was evaluated 24 hours after the inoculation, and compared to topical application in normal eyes. In the normal and inflamed eyes, mean aqueous concentrations of ciprofloxacin were 2.16 and 3.65µg/mL, respectively. Mean vitreous concentrations of ciprofloxacin were 0.08 and 0.32µg/mL, in normal and inflamed eyes, respectively. This highlights the potential of this system to deliver adequate drug levels intraocularly. Whether these levels would successfully translate to *in vivo* performance would be ascertained in Chapter 6.

Table 4.5: MIC_{90} of common ocular pathogens for ciprofloxacin (adapted from Yagci et al., 2007)

Bacterial Species	**MIC_{90} (µg/mL)**
Escherichia coli	0.02; 0.083
Enterobacter	0.206
Klebsiella	0.295
Proteus	0.267
Pseudomonas	0.50; 0.626
Haemophilus influenzae	0.014
Staphylococcus aureus	0.57; 0.796
Staphylococcus epidermidis	0.25; 0.375
Streptococcus pyogenes	0.782
Propionibacterium acnes	0.35
Bacillus cereus	0.25
Serratia	0.12

**Cases where two values are quoted indicates differences in results obtained by investigators*

Various degrees of bioresponsiveness were attained for the experimentally-derived I^3 devices, with ΔMDT of indomethacin ranging from 0-32.606. For ciprofloxacin the ΔMDT ranged from 5.109-25.956. Diverse correlatory relationships were derived between the MDT and WAC of the formulations under normal and inflammatory conditions (Figure 4.5, Table 4.6); an indication of the differing types and degrees of crosslinking attained through variation of the formulatory components. The measured responses for all experimentally-derived formulations are provided in Table 4.7. Drug release profiles clearly highlight that for the majority of formulations, there was enhanced release of both indomethacin and ciprofloxacin from the matrices when exposed to inflammatory conditions created by the presence of hydroxyl radicals (Figures 4.6-4.9). Preliminary release studies conducted in normal SVH of pH 5 proved that a lowered pH in itself actually reduced the MDT of indomethacin by ~2% and ciprofloxacin by ~7% from the I^3 due to a slightly lower degree of ionization, and therefore less erosion, of the largely anionic polymers of the outer BPM, yet insufficiently notable ionization of the cationic chitosan of the inner BPM at the lower pH (in comparison to drug release observed in normal PBS, pH 7.4). Thus the anticipated mechanism for promoting drug release under inflammatory conditions is the free radical presence.

There was generally a strong positive correlation between the MDT of both indomethacin and ciprofloxacin with the WAC of the I^3 under normal conditions (Table 4.6) indicating that the drug release in this case exhibited dependence on the overall hydration of the device; whereas a negative correlatory relationship was essentially observed between the WAC and MDT when exposed to inflammatory conditions created in the presence of hydroxyl radicals, which may be redolent of the fact that alternative polymeric degradation mechanisms were implicated in controlling the release of drug from the I^3 in an inflammatory milieu. The transitions in the textural properties of the formulations with time are depicted in Figures 4.10-4.13. All formulations exhibited an overall slight decrease in the textural properties of resilience, hardness and deformation energy with time, with the rate of change ranging from -3.62×10^{-3} to $-2.01 \times 10^{-2} day^{-1}$ as a result of softening of the device with fluid imbibement with time. There were no notable differences between the changes in hardness and deformation energy from normal to inflammatory conditions. The change in resilience under normal conditions was greater than that observed in the presence of hydroxyl radicals possibly due to more extensive hydration of the device under normal conditions.

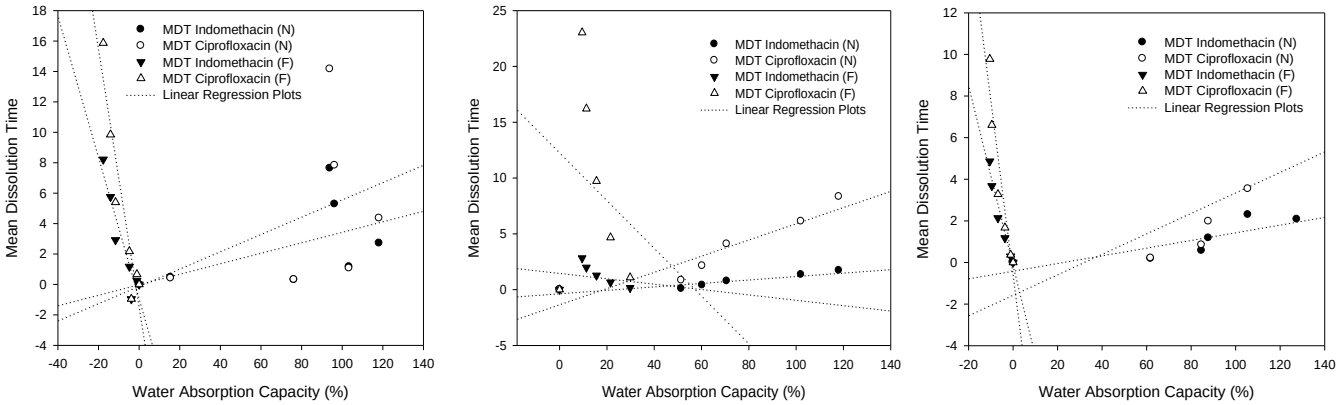

Figure 4.5: Exemplary graphical depictions of the correlation between the WAC and MDT of the I^3 under normal and inflammatory conditions representing (a) high correlation under inflammatory conditions (Formulation 10) (b) high correlation under normal conditions (Formulation 20) (c) high correlation under normal and inflammatory conditions (Formulation 24).

Table 4.6: The relationship between the mean dissolution time and fluid imbibement of formulations

Formulation	Correlation coefficient (R^2) for MDT vs. WAC			
	Indomethacin (N)	***Ciprofloxacin (N)***	***Indomethacin (F)***	***Ciprofloxacin (F)***
1	0.1856	0.1782	-0.2364	-0.2608
2	0.7647	0.7721	-0.8961	-0.9025
3	0.7621	0.6714	-0.1731	-0.1904
4	0.2688	0.1215	-0.3015	-0.3416
5	0.8953	0.8790	-0.9597	-0.9753
6	0.7845	0.7562	-0.6888	-0.6932
7	0.7844	0.7803	-0.4481	-0.4547
8	0.7776	0.7001	-0.7547	-0.7704
9	0.6009	0.5467	-0.6643	-0.6705
10	0.4672	0.4090	-0.9603	-0.9514
11	0.7370	0.7124	-0.4827	-0.5278
12	0.1819	0.2326	-0.8202	-0.8733
13	0.3681	0.3745	-0.8365	-0.8278
14	0.7523	0.7897	-0.1958	-0.1926
15	0.2688	0.1215	-0.3015	-0.3416
16	0.8972	0.8956	-0.4670	-0.5024
17	0.7199	0.7148	-0.5144	-0.5276
18	0.7118	0.6998	-0.1809	-0.2239
19	0.7890	0.7569	-0.7033	-0.6922
20	0.9243	0.9368	-0.2254	-0.2423
21	0.9061	0.8060	-0.6416	-0.6604
22	0.6045	0.5866	-0.1132	-0.1204
23	0.2688	0.1215	-0.3015	-0.3416
24	0.8378	0.7918	-0.9787	-0.9497
25	0.8018	0.8197	-0.5375	-0.5481
26	0.8466	0.6887	-0.8913	-0.8870
27	0.6577	0.5568	-0.3867	-0.3981

Table 4.7: Measured responses for the I^3 formulations

Form	MDT I N	MDT I F	MDT C N	MDT C F	Δ MDT I	Δ MDT C	Δ Textural Properties (day^{-1})	ΔWAC N (day^{-1})	Δ WAC F (day^{-1})	Δ Resilience N (day^{-1})	Δ Hardness N (day^{-1})	Δ Deformation Energy N (day^{-1})	Δ Resilience F (day^{-1})	Δ Hardness F (day^{-1})	Δ Deformation Energy F (day^{-1})
1	6.77	7.99	13.02	18.99	1.22	5.97	-1.60E-02	8.86	-0.06	-1.09E-01	-1.27E-01	-1.04E-01	-5.73E-02	-1.30E-01	-1.14E-01
2	10.17	20.74	10.70	30.65	10.57	19.95	-3.62E-03	30.26	-1.75	-8.51E-02	-1.16E-02	-2.22E-02	3.30E-03	-9.00E-03	-1.70E-03
3	18.01	26.23	35.34	39.16	8.21	3.82	-1.11E-02	65.97	-0.30	-1.16E-01	-1.06E-01	-1.58E-02	-1.06E-01	-1.30E-01	-6.00E-04
4	6.33	19.46	14.90	26.78	13.13	11.88	-8.18E-03	10.96	-0.74	-3.41E-02	-7.44E-02	-7.52E-02	3.10E-03	-7.89E-02	-8.08E-02
5	14.99	23.55	13.24	31.89	8.55	18.65	-5.66E-03	15.72	-2.07	-2.50E-02	-5.12E-02	-3.14E-02	4.00E-03	-3.56E-02	-2.87E-02
6	13.20	24.18	18.94	26.69	10.98	7.75	-2.01E-02	51.46	-2.64	-5.03E-02	-1.40E-01	-9.26E-02	-7.03E-02	-2.05E-01	-1.89E-01
7	15.23	29.32	14.03	35.09	14.09	21.06	-1.61E-02	22.64	-1.67	-8.07E-02	-1.24E-01	-1.33E-01	-1.84E-02	-1.25E-01	-1.44E-01
8	12.56	22.99	9.44	19.14	10.43	9.71	-5.52E-03	19.48	-6.32	-8.88E-02	-2.97E-02	3.20E-03	-2.58E-02	-2.49E-02	-2.59E-02
9	5.75	5.57	12.85	17.28	-0.17	4.43	-1.35E-02	53.30	-2.62	-5.44E-02	-6.30E-02	-2.63E-02	-1.03E-01	-1.07E-01	-1.25E-01
10	17.10	27.73	18.32	33.95	10.63	15.63	-2.60E-03	15.56	-3.83	-5.08E-02	-1.56E-02	-1.60E-03	-2.50E-03	1.90E-03	2.70E-03
11	9.08	19.59	8.13	25.21	10.51	17.08	-1.25E-02	46.85	-1.01	-2.17E-02	-1.25E-01	-1.07E-01	-4.10E-03	-1.14E-01	-7.38E-02
12	45.30	48.65	42.50	50.36	3.35	7.87	-5.90E-03	8.12	-2.73	-3.23E-02	-4.37E-02	-1.42E-02	-7.50E-03	-5.46E-02	-4.09E-02
13	12.21	21.01	7.74	20.93	8.80	13.19	-5.20E-03	10.85	-2.01	-6.48E-02	-3.08E-02	-1.23E-02	-2.67E-02	-3.04E-02	-2.10E-02
14	6.15	8.80	26.35	39.90	2.65	13.55	-1.51E-02	65.25	0.37	-2.58E-02	-1.42E-01	-1.22E-01	-1.72E-02	-1.47E-01	-1.45E-01
15	6.74	20.11	15.33	26.95	13.89	12.01	-8.87E-03	11.13	-0.80	-3.76E-02	-7.52E-02	-7.83E-02	3.45E-03	-8.25E-02	-8.13E-02
16	38.82	43.31	45.20	56.16	4.49	10.96	-5.60E-03	68.75	-0.69	-3.04E-02	-7.77E-02	-3.94E-02	1.02E-02	-5.48E-02	-4.11E-02
17	7.91	11.08	28.85	54.80	3.18	25.96	-1.70E-02	35.13	-1.05	-9.50E-03	-1.56E-01	-1.20E-01	-1.26E-02	-1.73E-01	-1.41E-01
18	34.18	46.25	28.85	53.27	12.07	24.42	-1.50E-02	48.47	-0.02	-6.00E-02	-1.34E-01	-1.18E-01	1.66E-02	-1.46E-01	-1.50E-01
19	13.34	21.43	11.67	29.86	8.09	18.19	-5.07E-03	16.03	-1.97	-2.25E-02	-4.62E-02	-3.62E-02	4.20E-03	-3.17E-02	-2.93E-02
20	4.31	6.89	21.51	54.71	2.57	33.20	-1.20E-02	21.50	-0.39	-8.30E-03	-1.11E-01	-1.12E-01	-1.41E-02	-1.07E-01	-1.24E-01
21	12.47	38.80	13.40	29.67	26.33	16.27	-1.05E-02	23.24	-1.08	-4.43E-02	-1.08E-01	-8.14E-02	2.70E-03	-7.69E-02	-6.81E-02
22	11.56	44.17	53.17	58.28	32.61	5.11	-1.14E-02	30.89	0.22	-2.32E-02	-9.75E-02	-7.23E-02	3.16E-02	-1.29E-01	-1.24E-01
23	6.24	19.14	14.87	26.44	12.95	11.65	-7.88E-03	10.11	-0.72	-3.23E-02	-7.27E-02	-7.19E-02	2.84E-03	-7.34E-02	-7.08E-02
24	6.31	13.78	12.14	21.70	7.47	9.56	-3.14E-03	22.05	-2.31	-7.10E-03	-3.27E-02	-2.27E-02	-2.40E-03	-3.36E-02	-2.20E-02
25	32.10	48.72	21.56	34.42	16.62	12.86	-1.90E-02	52.84	-1.99	-1.06E-01	-1.31E-01	-1.15E-01	-1.25E-01	-1.32E-01	-1.29E-01
26	10.41	21.29	13.37	34.57	10.88	21.19	-9.65E-03	44.54	-2.86	-4.18E-02	-8.35E-02	-3.32E-02	-2.50E-03	-1.02E-01	-1.09E-01
27	17.75	23.07	13.17	29.96	5.32	16.79	-5.47E-03	11.63	-1.0037	-3.29E-02	-6.28E-02	-5.03E-02	1.30E-02	-4.34E-02	-4.56E-02

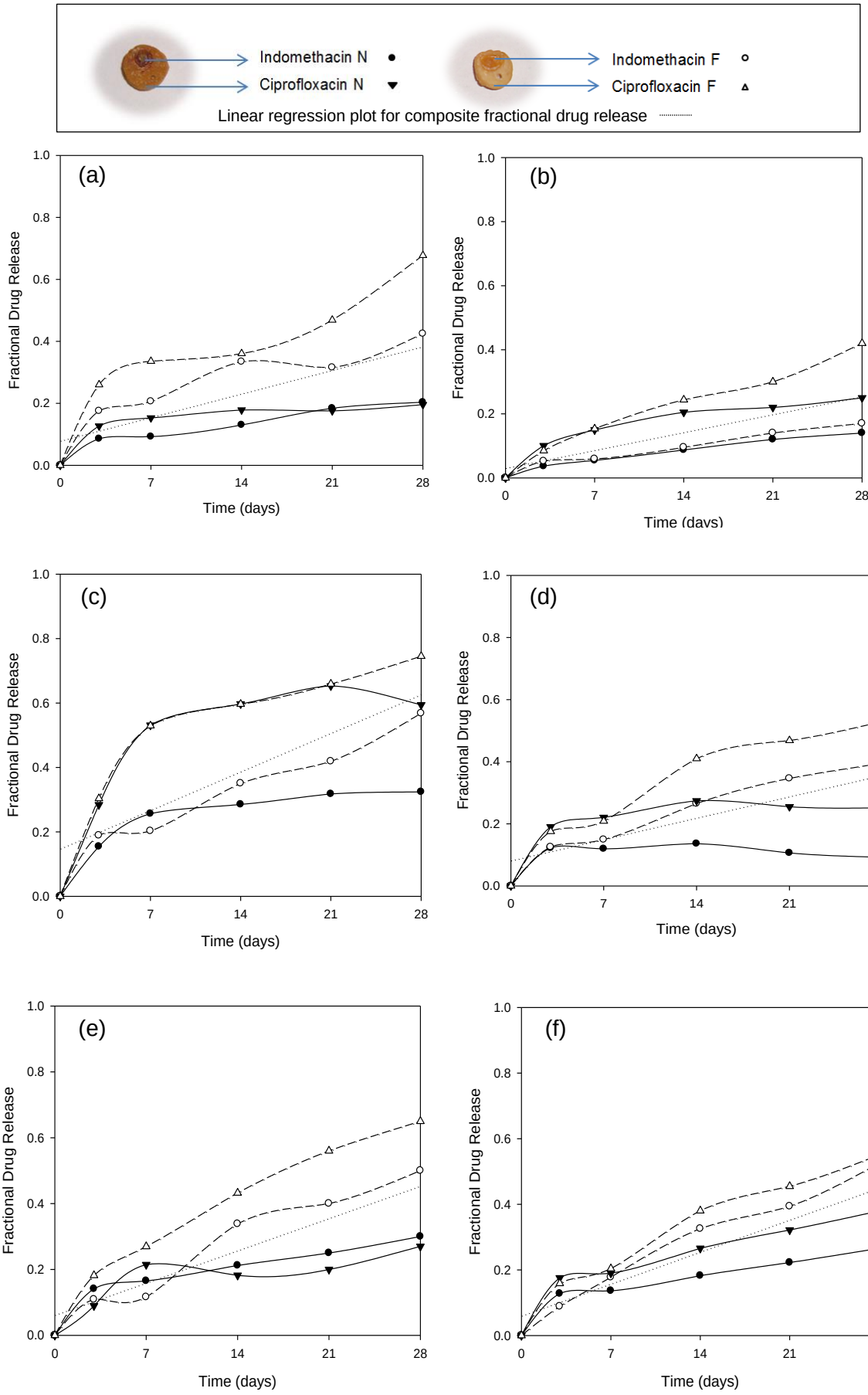

Figure 4.6: Drug release profiles for formulations 1-6 (a-f) (n=3, standard deviation (SD) < ±0.03042 for indomethacin and SD < ±0.05607 for ciprofloxacin in all cases)

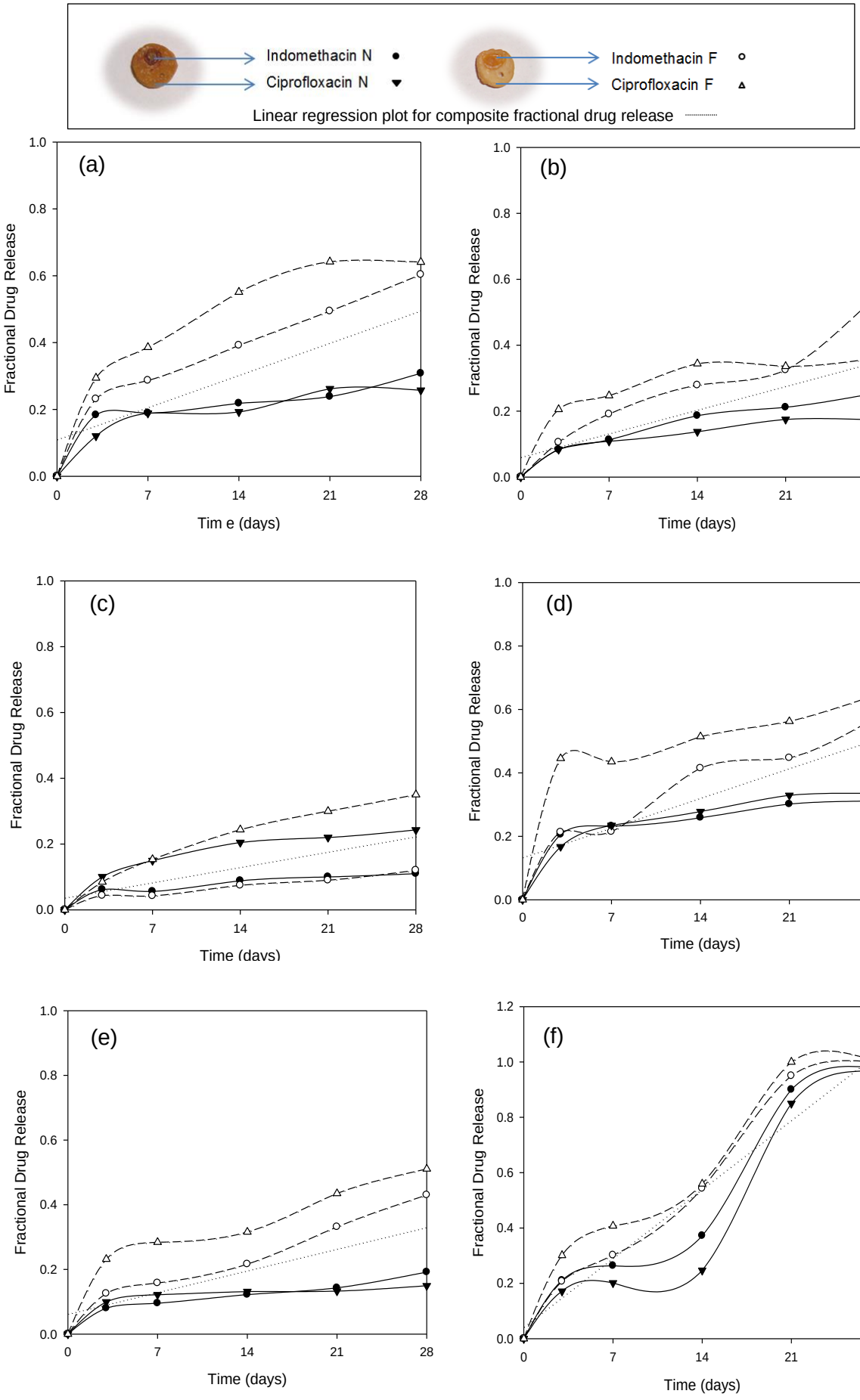

Figure 4.7: Drug release profiles of formulations 7-12 (a-f) (n=3, SD < ±0.03042 for indomethacin and SD < ±0.05607 for ciprofloxacin in all cases)

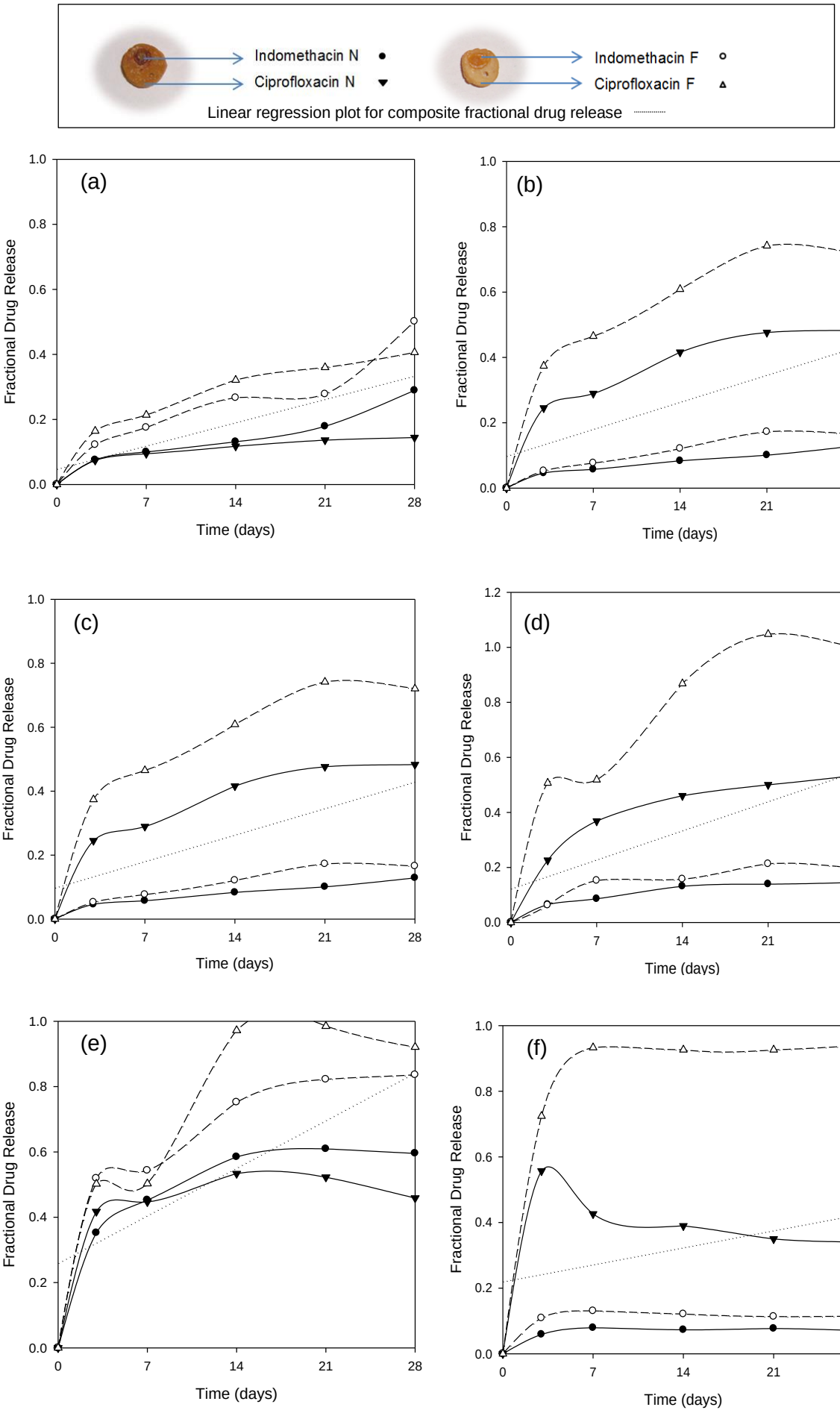

Figure 4.8: Drug release profiles for formulations 13 and 14 (a,b), 16-18 (c-e), 20 (f) (n=3, SD < ±0.03042 for indomethacin and SD < ±0.05607 for ciprofloxacin in all cases)

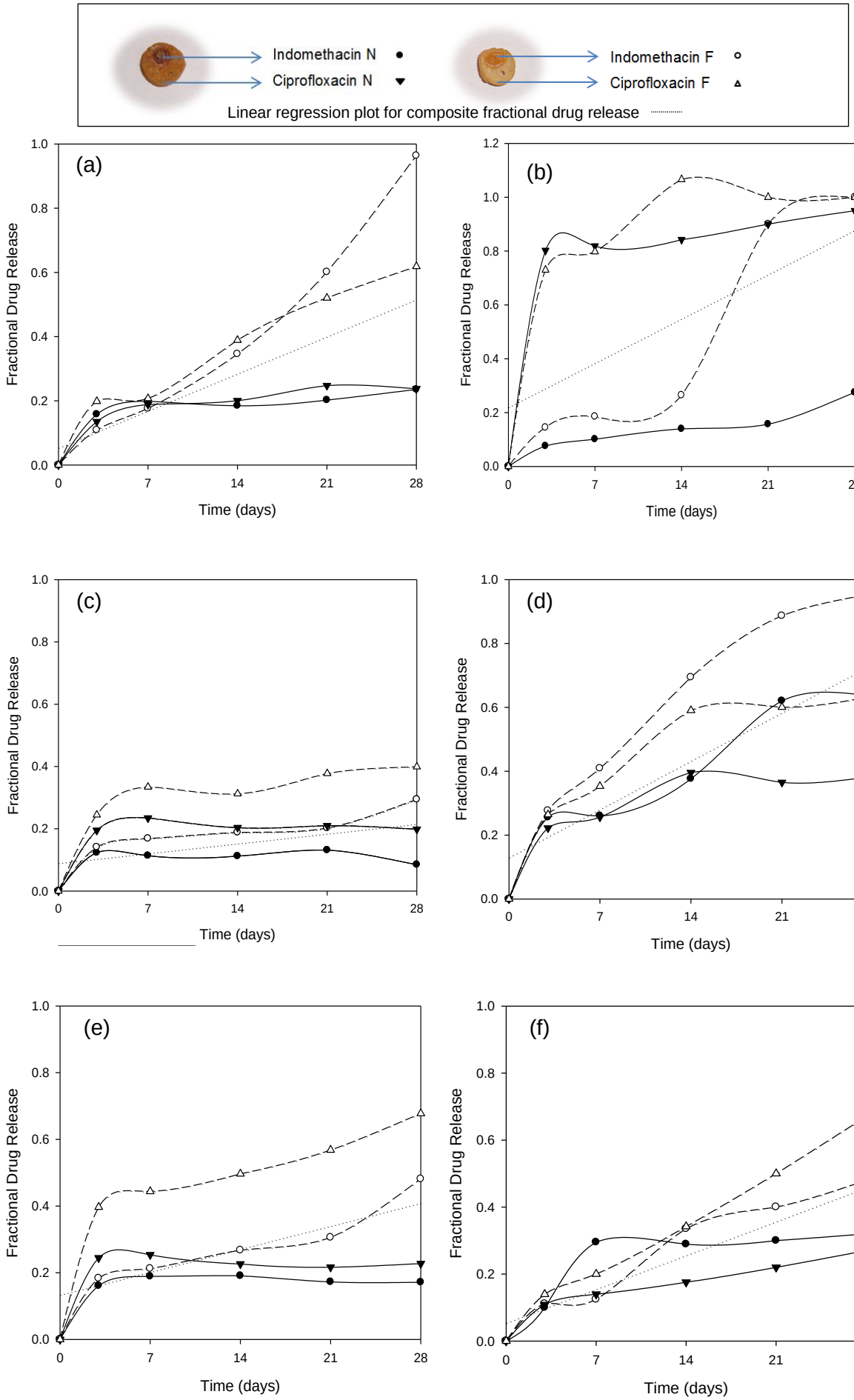

Figure 4.9: Drug release profiles for formulations 21 and 22 (a,b), 24-27 (c-f) (n=3, SD < ±0.03042 for indomethacin and SD < ±0.05607 for ciprofloxacin in all cases)

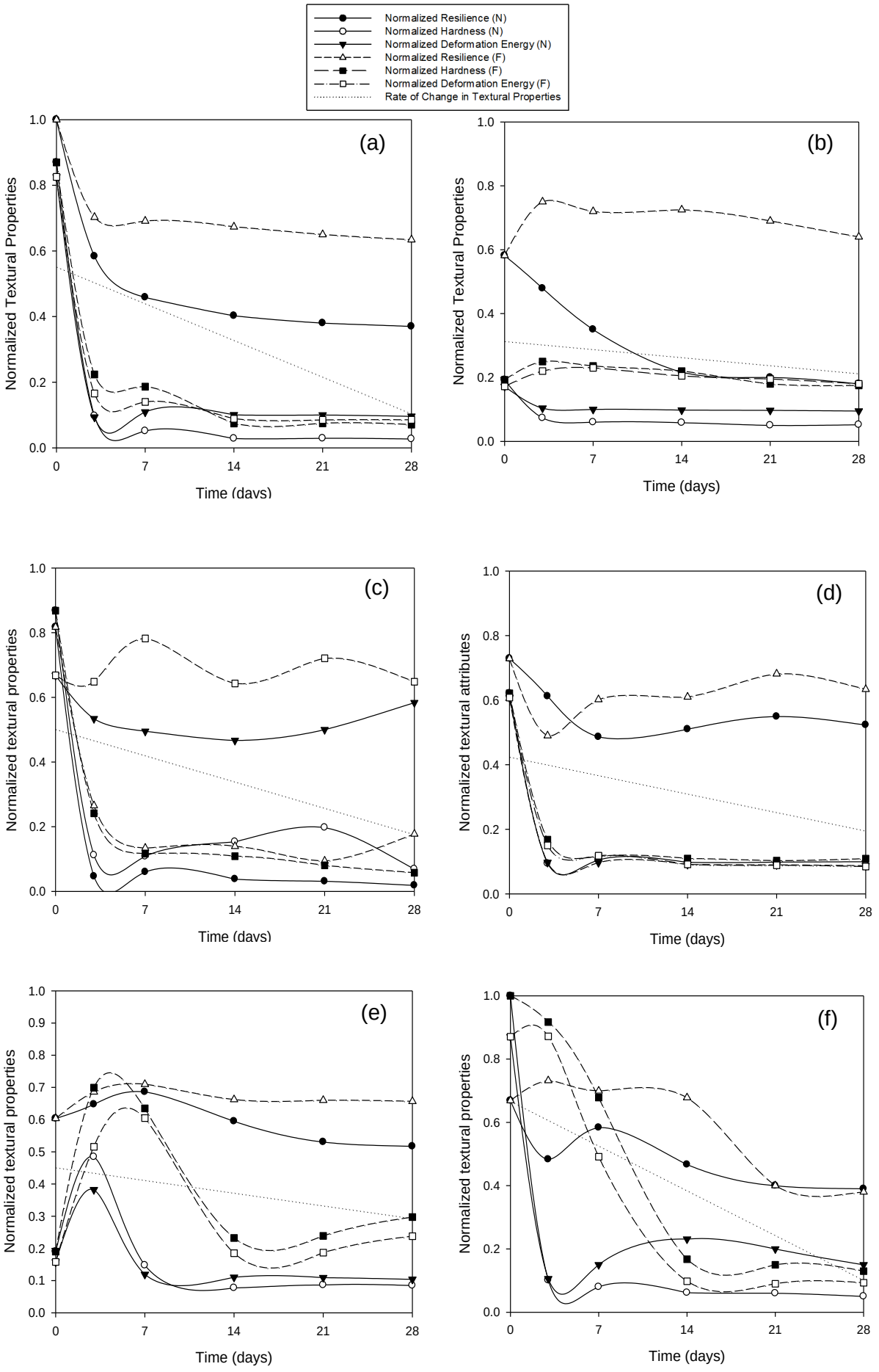

Figure 4.10: Normalized transitional textural profiles for formulations 1-6 (a-f) (n=3, SD < ±0.08112 in all cases)

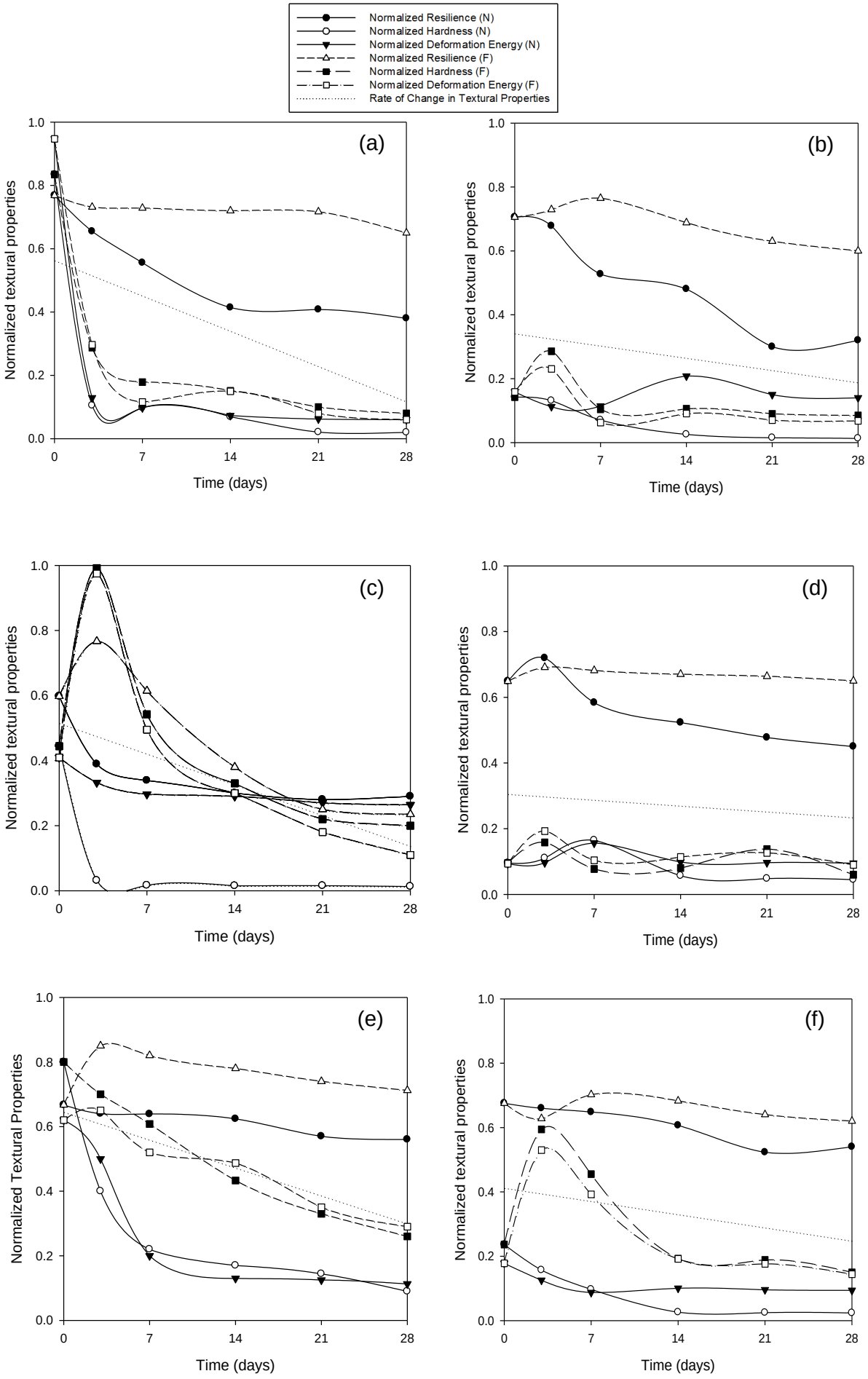

Figure 4.11: Normalized transitional textural profiles for formulations 7-12 (a-f) (n=3, SD < ±0.08112 in all cases)

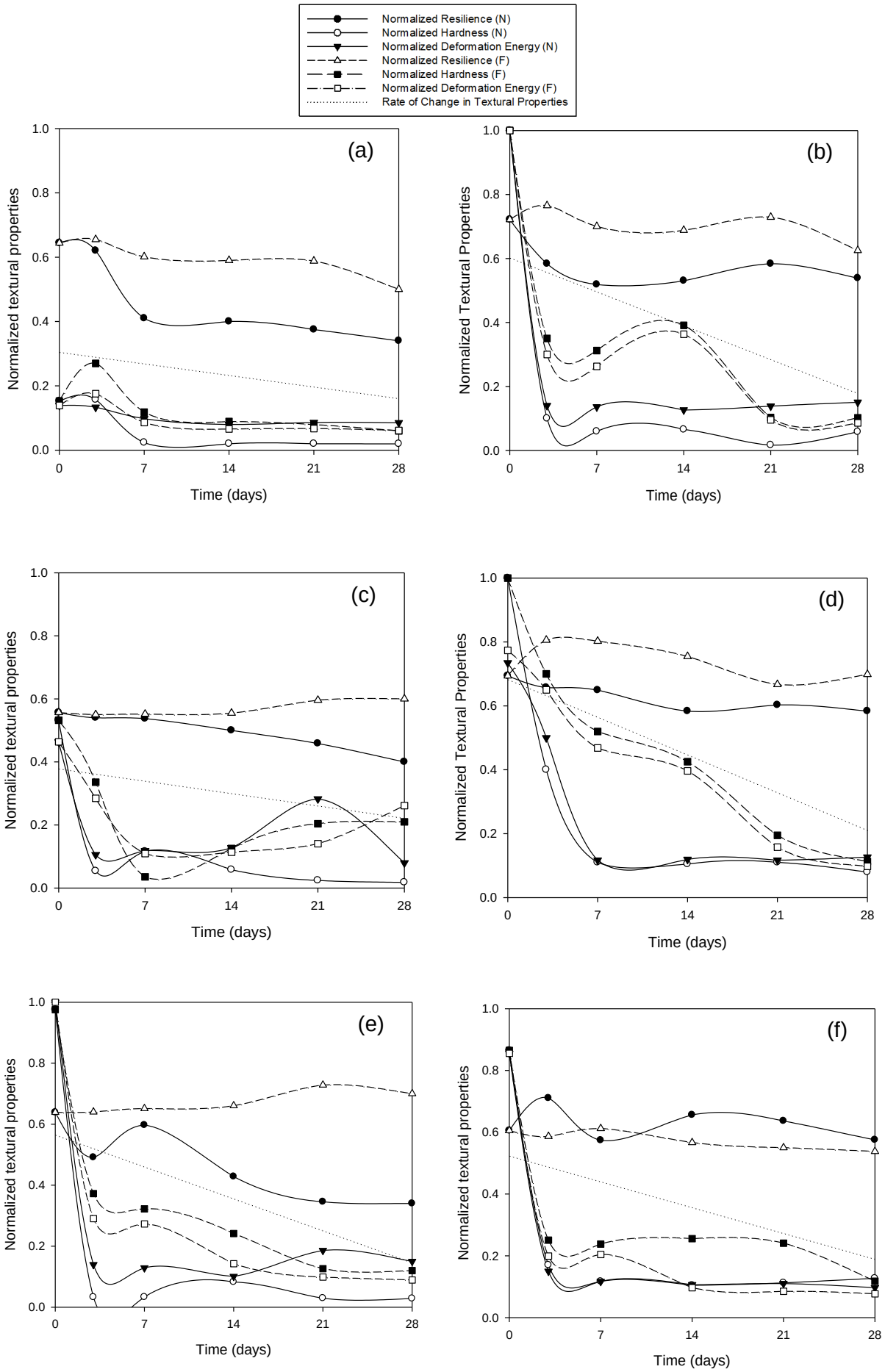

Figure 4.12: Normalized transitional textural profiles for formulations 13 and 14 (a,b), 16-18 (c-e), 20 (f) (n=3, SD < ±0.08112 in all cases)

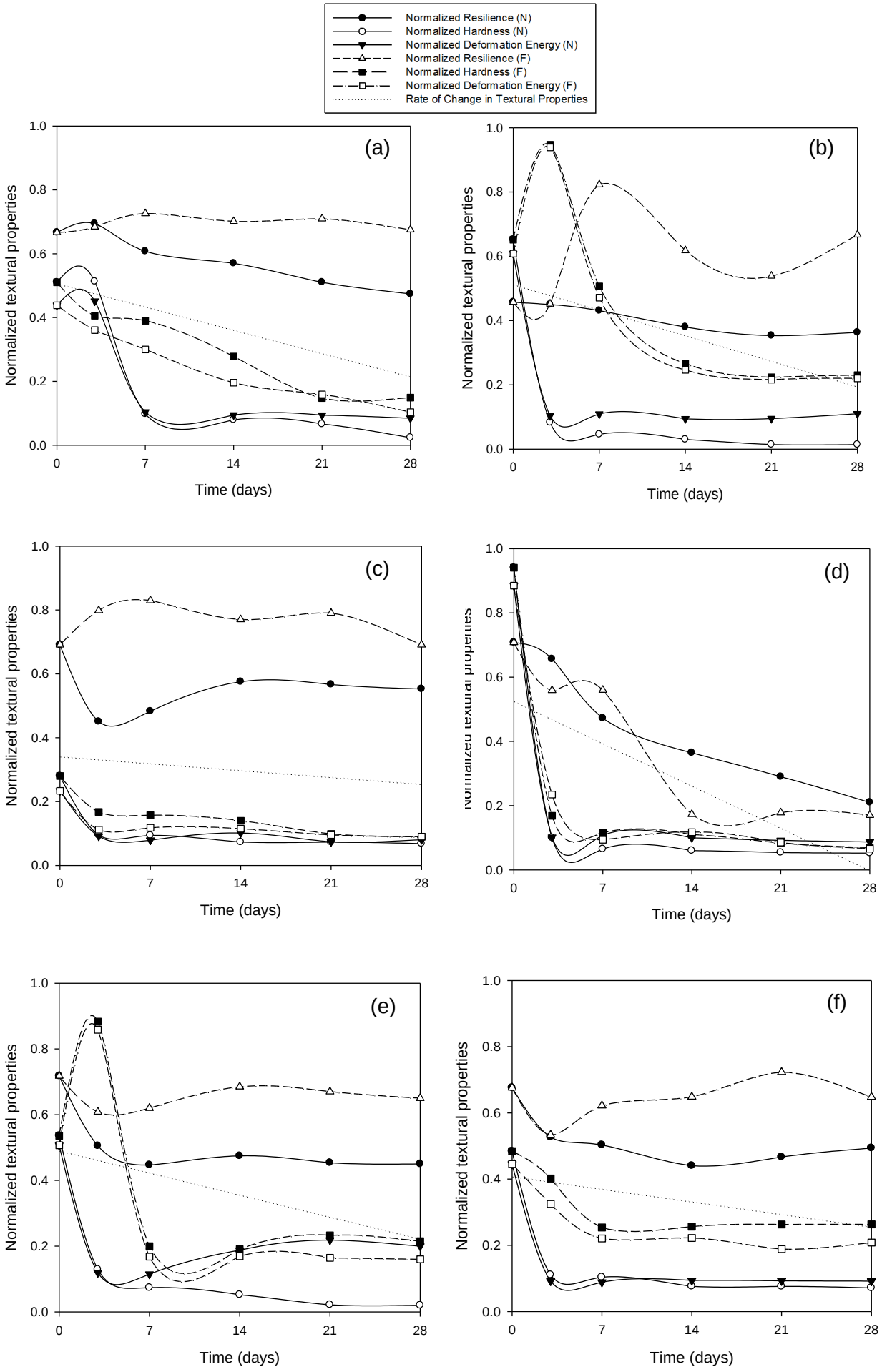

Figure 4.13: Normalized transitional textural profiles for formulations 21 and 22 (a,b), 24-27 (c-f) (n=3, SD < ±0.08112 in all cases)

4.3.3. Response surface analysis of the Box-Behnken Design

Factors having notable or significant effects on investigated responses have been further elaborated on to highlight the intricate relationship between the formulatory components of the resultant experimentally-derived formulations. The MDT I N, MDT I F, Δ MDT I, Δ WAC N, and Δ WAC F as measured responses for the experimentally synthesized formulations were included in the statistical design for identification of a formulation with an optimal bioresponsive potential.

Residual analysis (run order, predicted values) for the significant responses of the response surface design data (Figure 4.14) generally showed random scatter i.e. no trends, indicating none of the underlying assumptions of the multiple regression analysis were grossly violated; however some fanning and an outlier was observed for MDT I N (Figure 13a) indicative of a degree of nonconstant variance. The normal probability plots of the residuals fell on a straight line indicating the data to be normally distributed with no evidence of unidentified variables.

The residuals and standardized residuals indicated that the majority of cases were adequately fitted by the response surface model. Cook's distance (values not shown) was interpreted an overall measure of the combined impact of each observation on the fitted values and considers whether an observation is unusual with respect to both x- and y-values. Unusual observations generated by the model were minimal. The significance of the ratio of mean square variation due to regression and residual error was tested using ANOVA. The theoretical (predicted) values and observed (experimental) values were in fairly close agreement for MDT I N (R^2=0.8516), MDT I F (R^2=0.8368), Δ MDT I (R^2=0.8039), Δ WAC N (R^2=0.8476), Δ WAC F (R^2=0.7237), respectively, thus indicating the applicability of the regression models and usefulness of response surface plots.

The Pearson correlation coefficient (R and R-adjusted) represents the proportion of variation in the response that is explained by the model. The R^2 and R^2-adjusted values for the MDT I N (66.5%), MDT I F (70%), Δ MDT I (64.6%), and Δ WAC N (71.8%) models were satisfactory. The coefficient for Δ WAC F (52.4%) was less than satisfactory, indicating that this response should possibly be excluded from device optimization. Ultimately, statistical predictors validated and indicated the soundness of the statistical design for generating an optimal formulation.

The significance of linear and higher-order interaction terms is depicted by the p-values in Table 4.8.

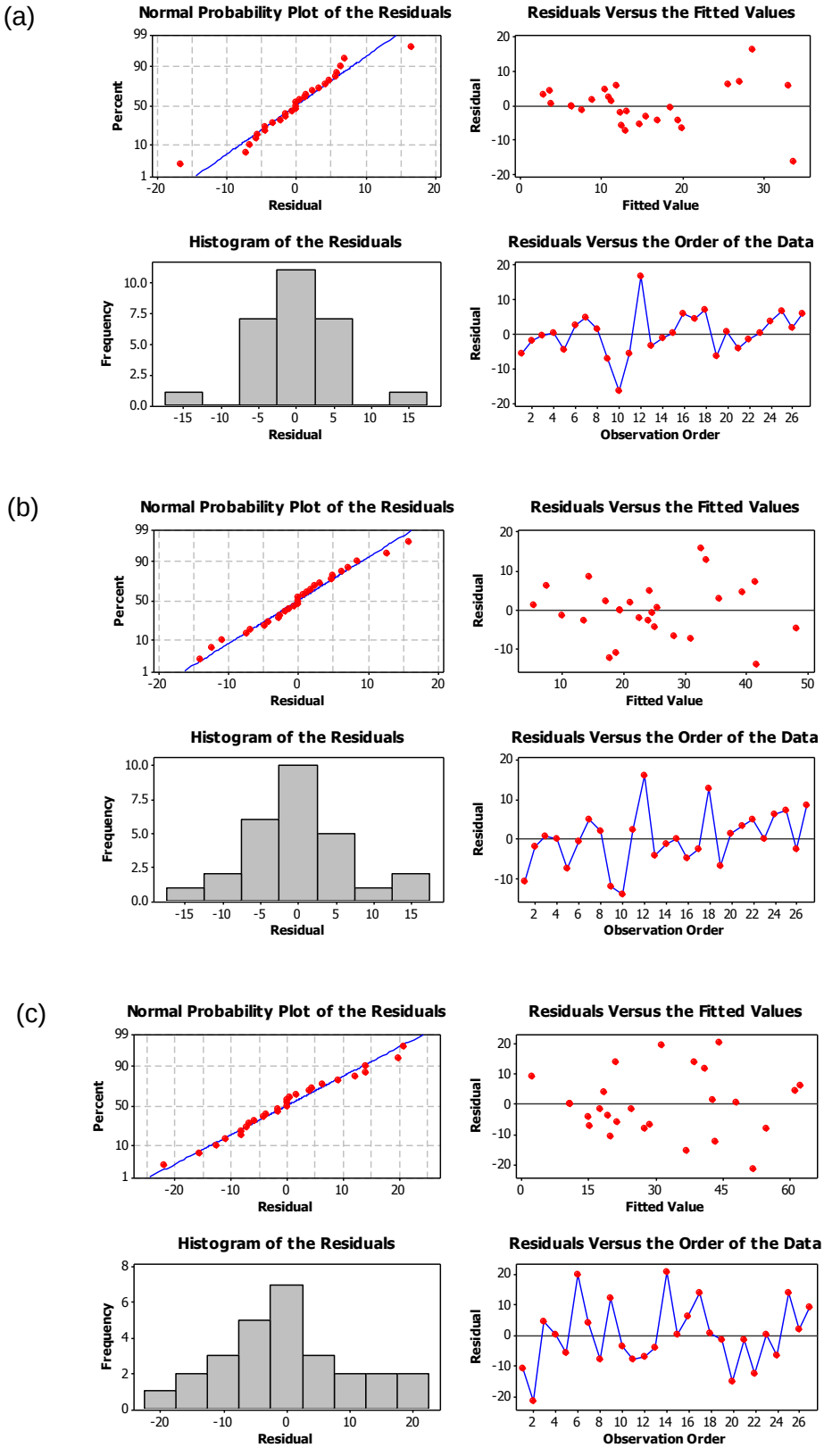

Figure 4.14: Exemplary residual plots for (a) MDT I N, (b) MDT I F, and (c) WAC N

In fabricating a bioresponsive device, it is imperative that these features are implicitly accentuated via the drug release behavior. A low MDT for the drugs from the BPMs is favored when the implant was exposed to normal physiological conditions. The interaction between NHS and $AlCl_3$ had a significant effect on the MDT of indomethacin (p=0.048) (Figure 4.15a). With DCC serving as the activator, activating the HA towards amide formation with alginate and poly(acrylic) acid, NHS as the reagent, and $AlCl_3$ as the catalyst; a stoichiometric ratio of these components was required for optimal crosslinking. Crosslinking was best promoted at lower concentrations of NHS and $AlCl_3$ (Figure 4.17a). An enhanced degree of crosslinking within the outer BPM forms an intact structure around the inner BPM, retarding swelling and and/ or erosion of both the inner and outer BPMs and subsequent NS release.

A similar result was seen for the MDT of indomethacin when exposed to inflammatory conditions. The interaction between NHS and $AlCl_3$ had a notable effect on the MDT of indomethacin (p=0.058) (Figure 4.15b). The crosslinked patency of the outer BPM enclosing the inner BPM, and thus impacting on its erosion in the presence of hydroxyl radicals, was optimal at lower concentrations of NHS and $AlCl_3$ (Figure 4.17b). An enhanced degree of crosslinking within the outer BPM forms an intact structure around the inner BPM, retarding swelling and subsequent erosion of both the inner and outer BPMs and subsequent NS release.

A large difference in the values of the MDT of the drug from the device is preferable as the aim is to achieve a system which is innately bioresponsive, releasing more drug when exposed to pathological conditions. [$AlCl_3$] had a notable effect (p=0.065) on ΔMDT of indomethacin from normal to pathological conditions (Figure 4.15c). The difference in MDT was highest at median levels of the catalyst (Figure 4.17c). The potential of the catalyst to promote intermolecular and interpolymeric crosslinking to create a matrix which was more responsive to the effects of hydroxyl radicals was optimal at this level indicating a stoichiometrically sound molar presence of the catalyst in relation to the activator, reagent, and polymers employed for creating a stimulus-responsive system. The interaction between the inflammation-responsive HA and DCC emanated in a significant effect on the change in MDT (p=0.050) (Figure 4.15c). The MDT was lowest when either correspondingly high levels or low levels of the DCC activators and bioresponsive HA were instituted (Figure 4.17c), indicating once again the dependency of origination of an optimally crosslinked BPM on the stoichiometric use of components.

A low WAC is an indication of a high degree of crosslinking achieved within the I^3 and is the most favorable situation for an implant that is to be placed within the relatively small and isolated environment of the eye in order to avoid discomfort as the implant imbibes fluid. NHS had a significant effect on the rate of change in WAC under normal conditions (p=0.023) (Figure 4.16a). The interaction between [NHS] and the catalyst [$AlCl_3$] had a notable effect on the WAC (p=0.060). The WAC was lowest at median levels of NHS and low levels of $AlCl_3$ (Figure 4.18a).

As observed under normal conditions, the interaction between NHS and $AlCl_3$ also had a notable effect on the WAC observed when exposed to pathological conditions (p=0.066) (Figure 4.16b), even though hydration was minimal in this instance. Here the imbibement of physiological fluids was limited when low [$AlCl_3$] and high [NHS] were employed (Figure 4.18b). Higher $AlCl_3$ concentrations could potentially increase the hydrophilicity of the implant, and hence fluid uptake, due to potential incorporation of the electrolyte ions into the BPMs.

It is important that the device withstands stresses that it is exposed hence maintaining its resilience once implanted into the eye to avoid fragmentation and potential discomfort. The [NHS] significantly affected the resilience of the device when exposed to pathological conditions (p=0.047) (Figure 4.16c).The resilience was most satisfactory at median levels of $AlCl_3$ (Figure 4.18c).

Table 4.8: Estimated p-values for the measured responses, highlighting significant effects

Term (%w/v)	**p-value**					
	MDT IN	**MDT I F**	**Δ MDT I**	**Δ WAC N**	**Δ WAC F**	**Δ Resilience F**
HA	0.4880	0.192	0.239	0.901	0.078	0.320
NHS	0.336	0.689	0.447	0.023	0.952	0.047
DCC	0.461	0.775	0.541	0.588	0.821	0.400
$AlCl_3$	0.612	0.116	0.065	0.454	0.720	0.252
HA*HA	0.993	0.780	0.656	0.021	0.347	0.762
NHS*NHS	0.014	0.120	0.177	0.007	0.471	0.113
$AlCl^3$*$AlCl_3$	0.392	0.903	0.159	0.910	0.449	0.560
HA*NHS	0.203	0.400	0.610	0.293	0.371	0.385
HA*DCC	0.853	0.163	0.050	0.192	0.575	0.487
HA*$AlCl_3$	0.929	0.398	0.213	0.408	0.213	0.690
NHS*DCC	0.768	0.392	0.325	0.306	0.656	0.677
NHS*$AlCl_3$	0.048	0.058	0.803	0.060	0.066	0.200

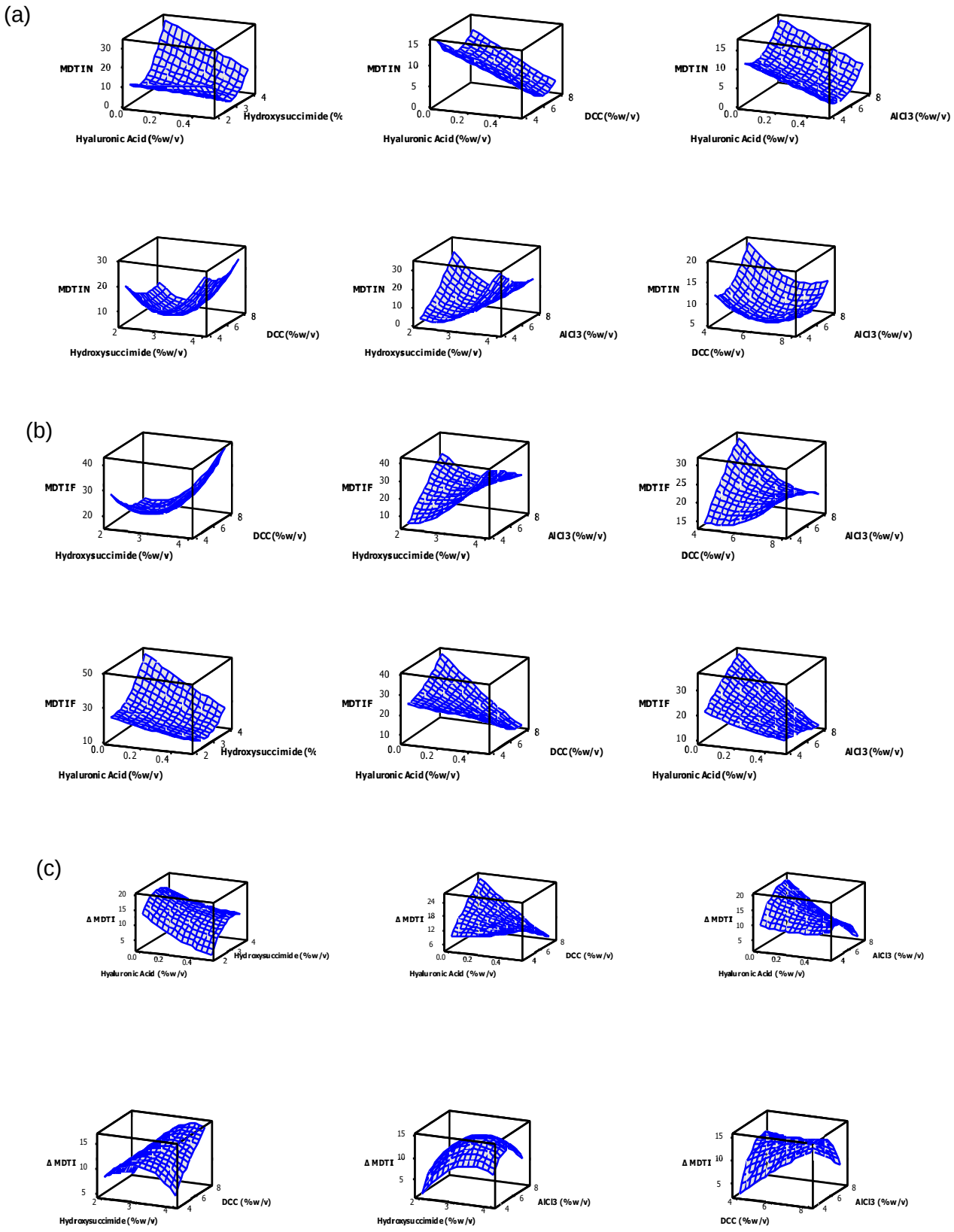

Figure 4.15: Response surface plots for the significant responses (a) MDT I N (b) MDT I F (c) Δ MDT I

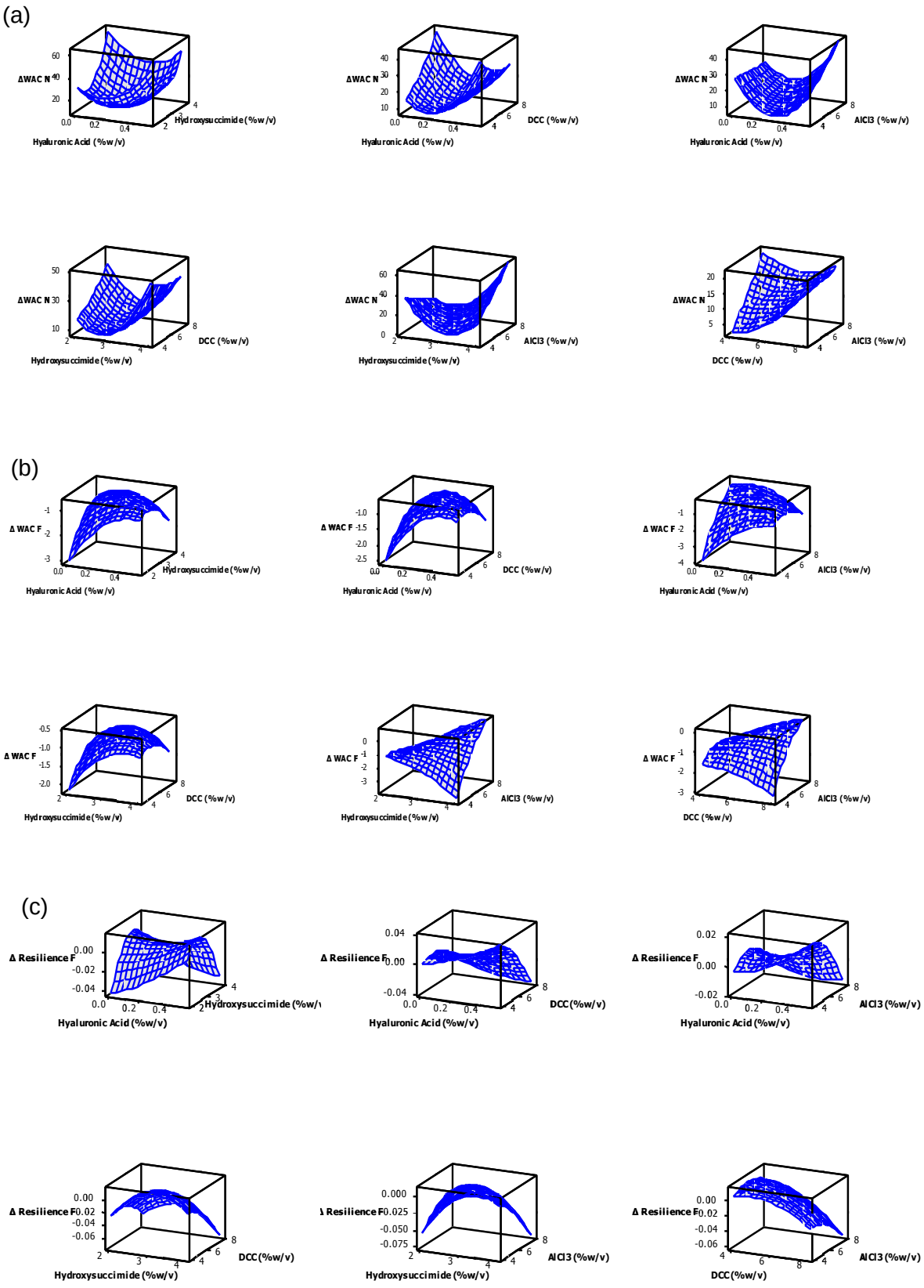

Figure 4.16: Response surface plots for the significant responses (a) Δ WAC N (b) Δ WAC F (c) Δ Resilience F

(a)

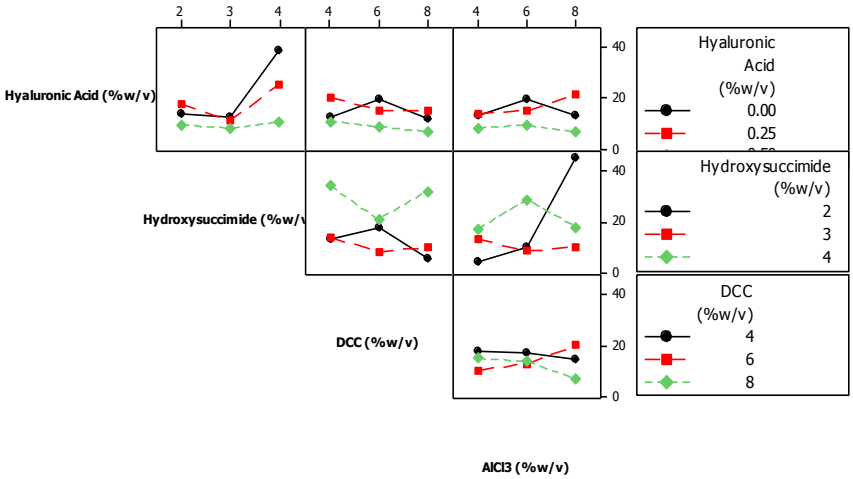

(b)

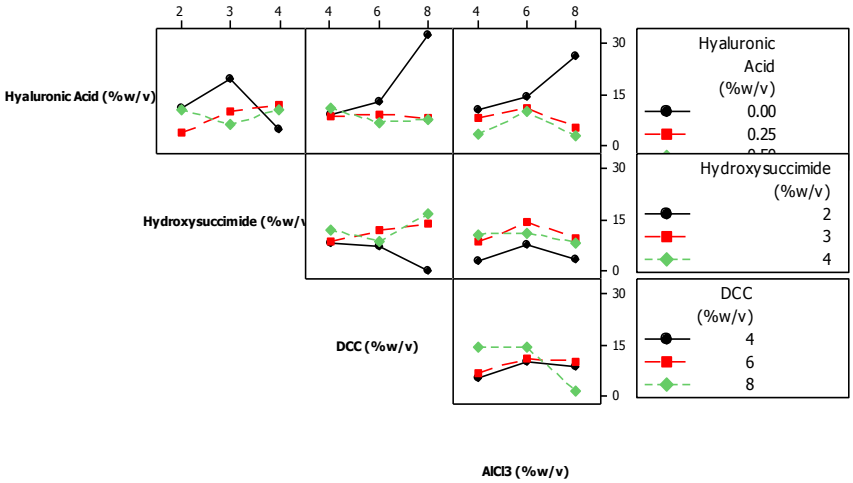

(c)

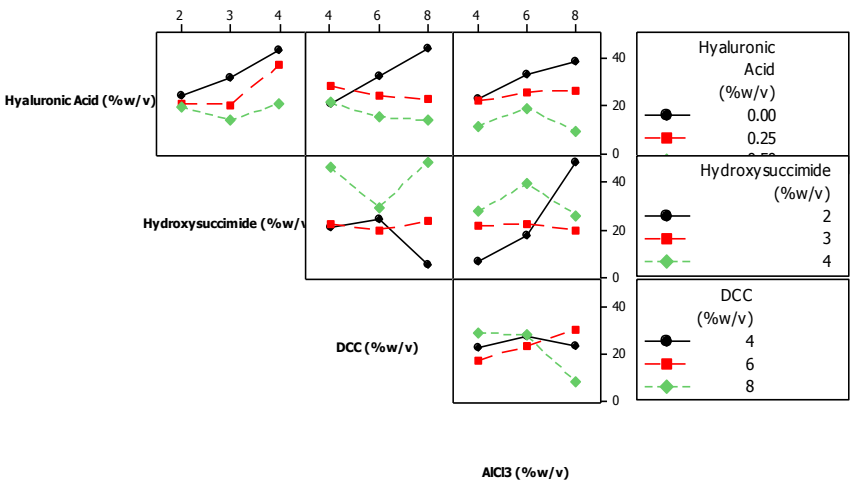

Figure 4.17: Interaction plots for (a) MDT I N, (b) MDT I F and (c) change in MDT I

(a)

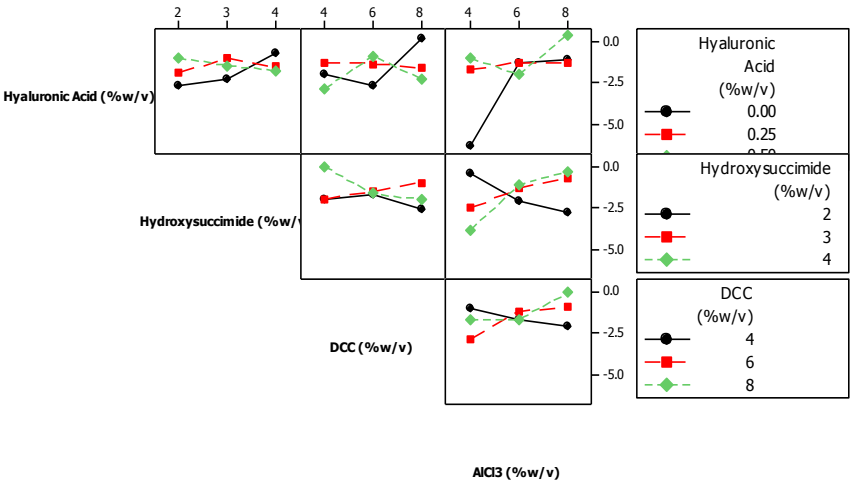

(b)

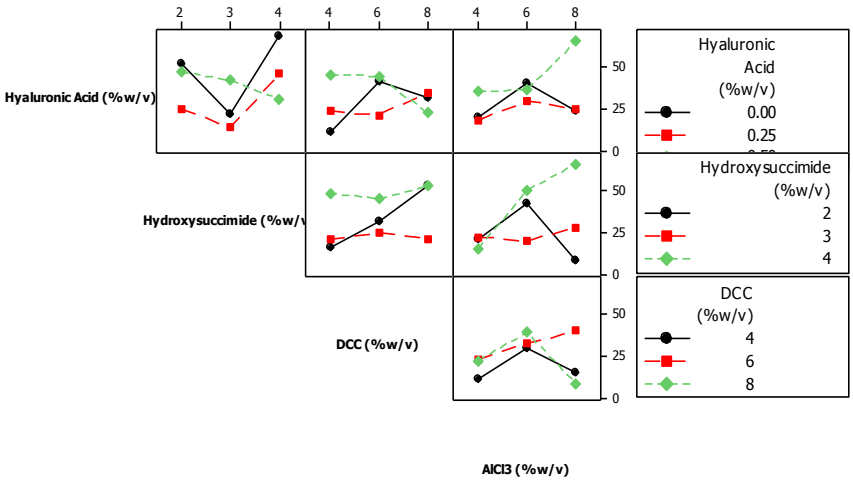

(c)

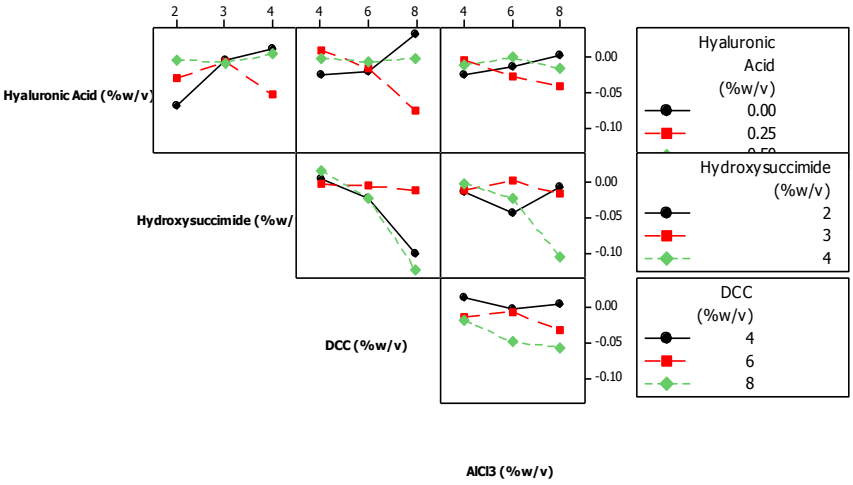

Figure 4.18: Interaction plots (data means) for (a) change in WAC (N), (b) change in WAC (F), and (c) change in resilience (F)

4.3.4. Response optimization of the I[3]

Response optimization procedure (MINITAB®, V15, Minitab, USA) was used to obtain the preferred levels of the selected formulatory components. An optimal formulation was developed following simultaneous constrained optimization of MDT I N, MDT I F, Δ MDT I, Δ WAC N, and Δ WAC F. The optimized levels of the independent variables that would achieve the desired drug release and fluid uptake and their predicted responses were then determined. The optimized levels of the independent variables, the goal for the response, the predicted response, *y*, at the current factor settings, as well as the individual and composite desirability scores are shown in Figure 4.19. Based on the statistical desirability function, it was found that the composite desirabilities for the formulation was 1.0. The constrained settings utilized are outlined in Table 4.9.

Table 4.9: Constrained settings for response optimization

Parameter	Goal	Constraint
MDT I N	Minimize	6-10
MDT I F	Target	12-18
Δ MDT I	Maximize	6-9
Δ WAC N	Minimize	15-20
Δ WAC F	Maximize	-2.5-(-1.5)

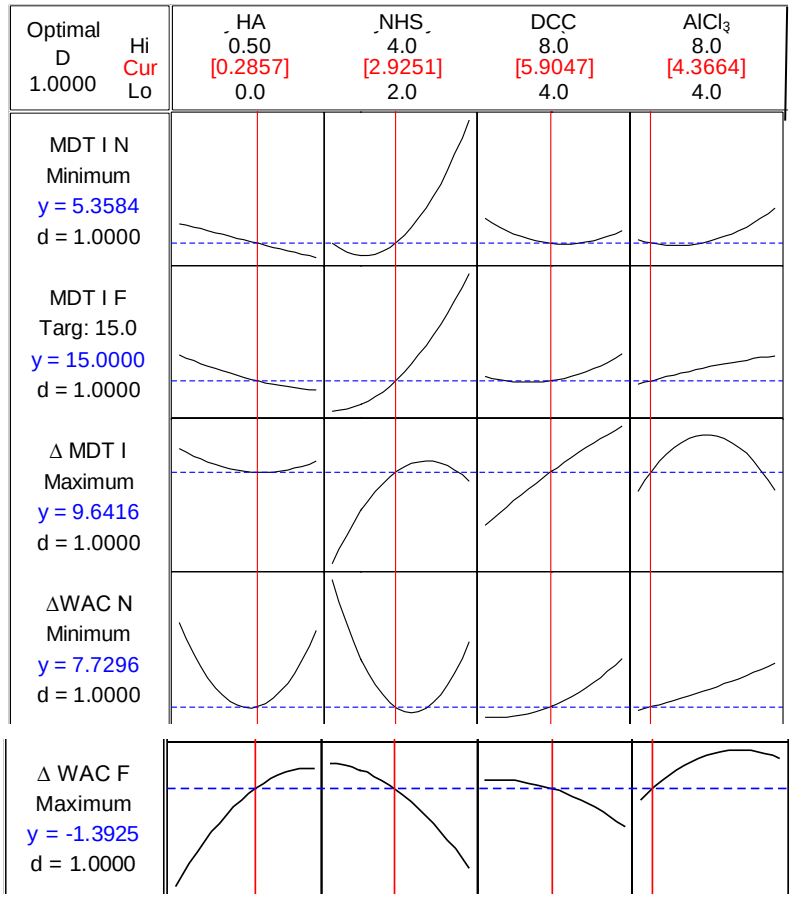

Figure 4.19: Optimization plots delineating factor settings and desirability values for the optimal formulation

The ideal formulation was prepared according to the optimal predicted settings. The experimentally derived values for the responses of the optimal formulation were in close agreement with the predicted values (Table 4.10), demonstrating the reliability of the optimization procedure in predicting the bioresponsive performance of the I^3 and ascertaining the significance of the effect of HA, NHS, DCC and $AlCl_3$ levels and their intricate interplay on the fluid uptake behavior, with disentanglement of the crosslinked polymeric composite and ultimate drug release.

Table 4.10: Experimental and predicted response values for the optimized formulations

Measured Response	Predicted	Experimental	R^2	Desirability
MDT I N	5.3584	5.6212		1.000
MDT I F	15.000	10.723		1.000
Δ MDT I	5.6416	5.1019	0.9674	1.000
Δ WAC N	7.7296	7.8824		1.000
Δ WAC F	-1.3925	-1.2735		1.000

4.3.5. Concurrent optimization by ANN for statistical validation

In order to obtain accuracy and a maximum degree of precision, the training was done twice (i.e. primary and secondary training). The leveling of the MSE with standard deviation (SD) boundaries for the training runs indicated a sequential improvement of data modeling as depicted in Figure 4.20. Table 4.11 depicts the average of the MSE values for the three runs of the primary training, the best network run at 10 000 epochs, and the overall efficiency and performance of the neural network during the data training.

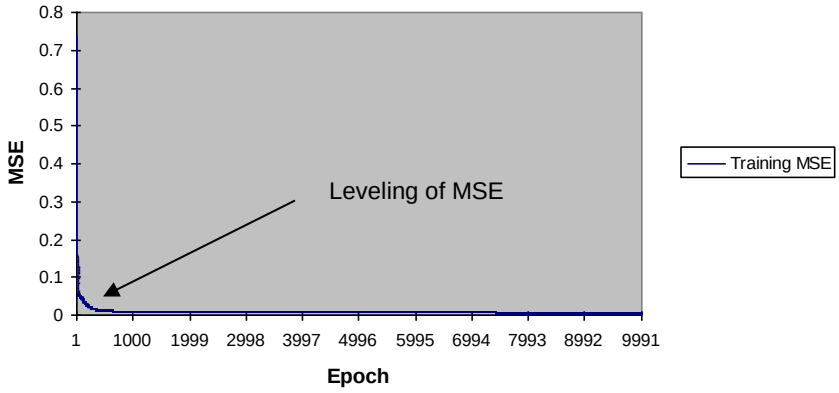

Figure 4.20: Graphical depiction of the training performed on Neurosolutions™

Table 4.11: Neural network indicators characterizing the efficiency and performance of data in the primary training as per ANN

Best Network	Training	Performance	Δ MDT I
Epoch #	10 000	MSE	3.9723
Minimum MSE	0.005	NMSE	0.08097
Final MSE	0.006	MAE	1.5740
		Min Abs Error	0.008375
		Max Abs Error	5.2342
		R^2	0.9589

MSE: Mean square error
NMSE: Normalized mean square error
MAE: Mean absolute error
Min Abs Error: Minimum absolute error
Max Abs Error: Maximum absolute error

Based on the obtained results, it is evident that the employed training model was efficient (MSE = 0.005). Results revealed a satisfactory fit for the input variables (R^2 = 0.96). The performance criterion employed to assess the closeness and correlation between the desired and the actual network output for Δ MDT I of each formulation is depicted in Figure 4.21. The sensitivity coefficient of each formulatory component (input variables) is depicted in Figure 4.22. It is apparent that each variable considered had a fairly high sensitivity against the Δ MDT I. An optimum formulation based on each of the proposed formulatory components is thus desirable.

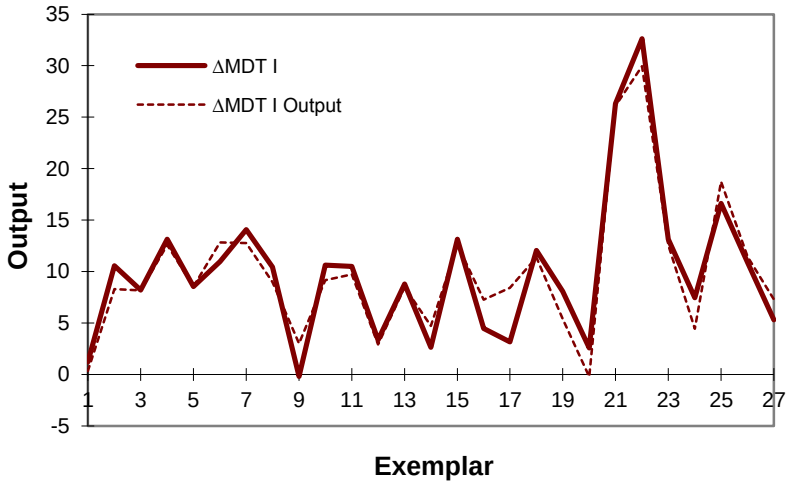

Figure 4.21: Graphical depiction of the correlation between the desired and the actual network output for Δ MDT I of each formulation

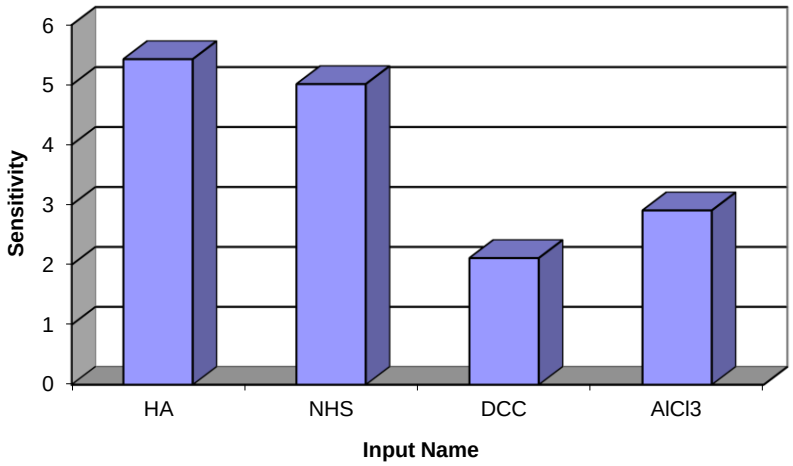

Figure 4.22: A typical bar chart graph depicting the sensitivity coefficients (sensitivity about the mean) of each variable implicated in I^3 manufacture against the Δ MDT I following the primary training

4.3.6. Kinetic analysis of drug release from the optimum formulation

The kinetic models generated were in congruence with the bioresponsive capabilities of the device embodied by the polymeric transitions on exposure to normal and pathological fluids. The degree to which each model describes the optimum formulation is represented in Table 4.12. The release kinetics of both indomethacin and ciprofloxacin under normal conditions were best exemplified by the Higuchi model (comparatively low AIC, SBC, and high R^2 of 0.9841 and 0.9892, respectively) indicating release of drug from the BPMs as a square root of time-dependent process based on Fickian diffusion. The Hixson Crowell cube root law was more applicable to the drug release kinetics of both indomethacin and ciprofloxacin under inflammatory conditions (comparatively lower AIC, SBC, and high R^2 of 0.9816 and 0.9906, respectively). This indicates the observed change in surface area and diameter of the I^3 with progressive bioresponsive erosion of the implant in the presence of hydroxyl radicals as a function of time. Interestingly, there was a lack of correspondence between the statistical predictors for zero order release. According to the linear model, the release kinetics attained for indomethacin and ciprofloxacin under inflammatory conditions emulate a close fit with zero order release (R^2 of 0.9858 and 0.9903, respectively) in the presence of constant inflammation. However, the linear mixed effects model indicated that the best fit for zero order release was achieved under normal conditions. This contradiction is possibly attributed to the complexity of the drug release behavior from the stimulus-responsive form. Ultimately, zero order release is the most desirable case for disease treatment. The Korsemeyer and Peppas (Power law) was employed to provide a prediction of the drug release mechanism. Only release under inflammatory conditions did drug release kinetucs fit the limits of this

model, where *n* (representing the diffusion exponent) fell between 0.45 and 0.89, which is indicative of anomalous (non-Fickian) diffusion.

Table 4.12: Release parameters and statistical descriptors of the optimum I^3

Form	Zero Order			
	k_0 (h^{-1})	AIC	SBC	R^2
Indo (N)	0.0127	24.648219	23.420808	0.9408
Indo (F)	0.0407	33.765658	32.538247	0.9858
Cipro (N)	0.0103	22.813537	21.586126	0.9781
Cipro (F)	0.0306	31.473764	30.246353	0.9903
	Higuchi			
	k_H ($h^{-1/2}$)	AIC	SBC	R^2
Indo (N)	0.4508	37.126297	36.735735	0.9841
Indo (F)	1.3737	43.182074	42.791512	0.9352
Cipro (N)	0.3594	41.062219	40.671657	0.9892
Cipro (F)	1.0535	48.025498	47.634936	0.9755
	Peppas			
	n value	K_{KP} (h^{-n})	AIC	SBC	R^2
Indo (N)	-0.4907	0.549	14.727099	14.336537	0.9892
Indo (F)	-1.9224	1.1655	16.159547	15.768985	0.9697
Cipro (N)	0.4695	0.2448	16.841935	16.451373	0.9855
Cipro (F)	0.4611	0.3646	19.208455	18.817893	0.966
	First Order			
	k_1 (h^{-1})	AIC	SBC	R^2
Indo (N)	-6.00E-05	22.947045	22.556483	0.9451
Indo (F)	-0.0002	22.833126	22.442564	0.9791
Cipro (N)	-5.00E-05	22.843544	22.452982	0.98
Cipro (F)	-0.0002	22.524279	22.133717	0.9904
	Hixson			
	k_{HC} ($h^{-1/3}$)	AIC	SBC	R^2
Indo (N)	-0.0002	31.276151	30.885589	0.9437
Indo (F)	-0.0007	31.112422	30.721860	0.9816
Cipro (N)	-0.0002	31.120598	30.730036	0.9794
Cipro (F)	-0.0006	30.656577	30.266015	0.9906

4.3.7. On-off inflammation-responsive capabilities of the optimum formulation

The optimum formulation displayed adequate responsive capabilities on exposure to and removal of the inflammatory stimulus, as exemplified in Figure 4.23. Ciprofloxacin was released to a greater extent due to its presence in the outer BPM, which is anticipated to erode at a faster rate, as well as its non-incorporation in a nanocarrier. A degree of loss in the bioresponsive capabilities of the device is anticipated as irreversible changes in the polymeric integrity of the I^3 will ultimately occur as chain scission is repeatedly initiated in the presence of hydroxyl radicals. The enhanced release of both drugs under inflammatory conditions is attributed to the stimulated surface erosion of the inflammation-responsive BPMs, specifically the encapsulating outer BPM, as predicted via *in silico* modeling.

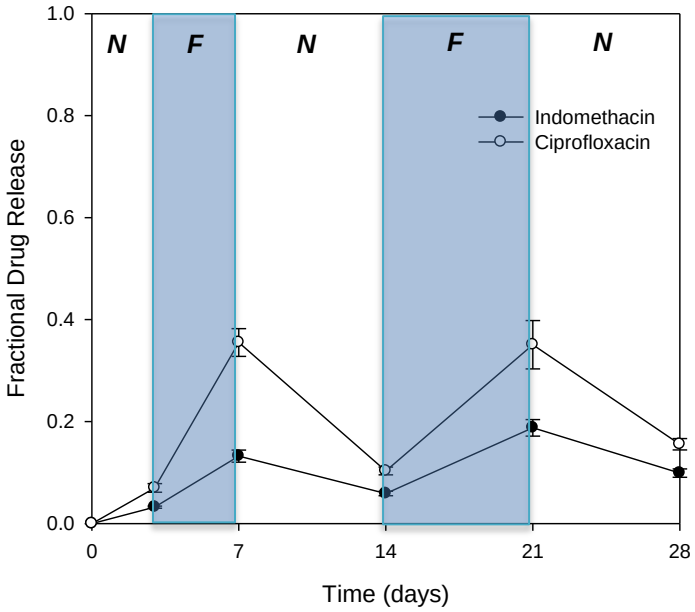

Figure 4.23: Drug release profiles signifying the on-off inflammation-responsive capabilities of the optimum formulation (n=3; *N* is representative of normal ocular conditions and *F* of inflammatory ocular conditions created in the presence of Fenton's reagent)

4.3.8. Molecular modeling simulations for prediction of pertinent interactions within the polymeric system of the I^3 and between the I^3 and normal or inflammatory environment

4.3.8.1. Molecular understanding of the coherent formulation of a tripolymeric over a bipolymeric architecture

To prove the rationality and applicability of the constituent polymers in the formation of the multipolymeric complex, molecular mechanics and dynamics simulations were carried out in vacuum and in a solvent phase. Typical simulation profiles consisted of an initial reactional testing of bipolymeric complexes such as alginate-hyaluronic acid (ALG-HA); alginate-poly(acrylic) acid (ALG-PAA); and hyaluronic acid-poly(acrylic) acid (HA-PAA) followed by the testing of the tripolymeric complex. The energetic stability of the formed complexes was considered as the benchmark for the determination of preferential orientation of the polymers to form the final coherent polymeric matrix.

4.3.8.1.1. Bipolymeric architectures

The bipolymeric complexes were well stabilized with a negative energy of formation with stabilization ranging from -15.722kcal/mol (ALG-HA) through -59.916kcal/mol (ALG-PAA) to -27.475kcal/mol (PAA-HA) (Equations 4.12-4.17):

$E_{ALG} = 28.304V_{\sum} = 4.084V_b + 33.109V_\theta + 39.138V_\varphi + 7.979V_{ij} - 0.581V_{hb} - 55.426V_{el}$ [Equation 4.12]

$E_{HA} = -27.922V_{\sum} = 4.006V_b + 37.315V_\theta + 40.375V_\varphi + 10.742V_{ij} - 7.769V_{hb} - 112.592V_{el}$ [Equation 4.13]

$E_{PAA} = 10.257V_{\sum} = 1.517V_b + 7.178V_\theta + 4.244V_\varphi - 2.540V_{ij} - 0.141V_{hb}$ [Equation 4.14]

$E_{ALG\text{-}HA} = -15.340V_{\sum} = 8.426V_b + 72.221V_\theta + 85.100V_\varphi - 0.777V_{ij} - 8.136V_{hb} - 172.174V_{el}$

$\Delta E = -15.722$kcal/mol [Equation 4.15]

$E_{ALG\text{-}PAA} = -21.355V_{\sum} = 5.473V_b + 33.177V_\theta + 61.269V_\varphi - 5.109V_{ij} - 2.797V_{hb} - 113.37V_{el}$

$\Delta E = -59.916$kcal/mol [Equation 4.16]

$E_{PAA\text{-}HA} = -45.140V_{\sum} = 4.941V_b + 44.337V_\theta + 48.071V_\varphi - 13.135V_{ij} - 8.095V_{hb} - 121.26V_{el}$

$\Delta E = -27.475$kcal/mol [Equation 4.17]

The principle difference among the individual bonding and non-bonding attributes of ALG [(1-4)-linked β-D-mannuronate and α-L-guluronate] and HA [D-glucuronic acid and D-N-acetylglucosamine] was observed in terms of electrostatic contributions with a difference of ≈70kcal/mol due to the presence of $-NH_2$ group which eventually lead to a more stabilized, equal, and negative numeric static energy value for HA. It was hypothesized that ALG-HA would form a highly connected combination matrix owing to the presence of -COOH and $-NH_2$ functionalities in ALG and HA, respectively [Hypothesis I]. The final geometrical conformation of ALG-HA displayed a van der Waals forces' rendered optimization (≈-18kcal/mol) slightly assisted by hydrogen bonding and electrostatic interactions (≈-5kcal/mol). However, close inspection of Figure 4.24 revealed that the only the -OH functionalities of ALG formed H-bonds with the -COOH/-OH groups of HA, with the $-NH_2$ functionalities being intact. This observation may be attributed to the repulsive behavior of the bulky hydrophobic groups present in both the polysaccharides leading to the formation of a strained structure eventually forming a destabilized structure which was 'balanced' by the non-bonding interactions to some extent. Energetically, this tautness was a result of bonding energies wherein $V_\theta + V_\varphi$ demonstrated an increase in value (Equations 4.12-4.15).

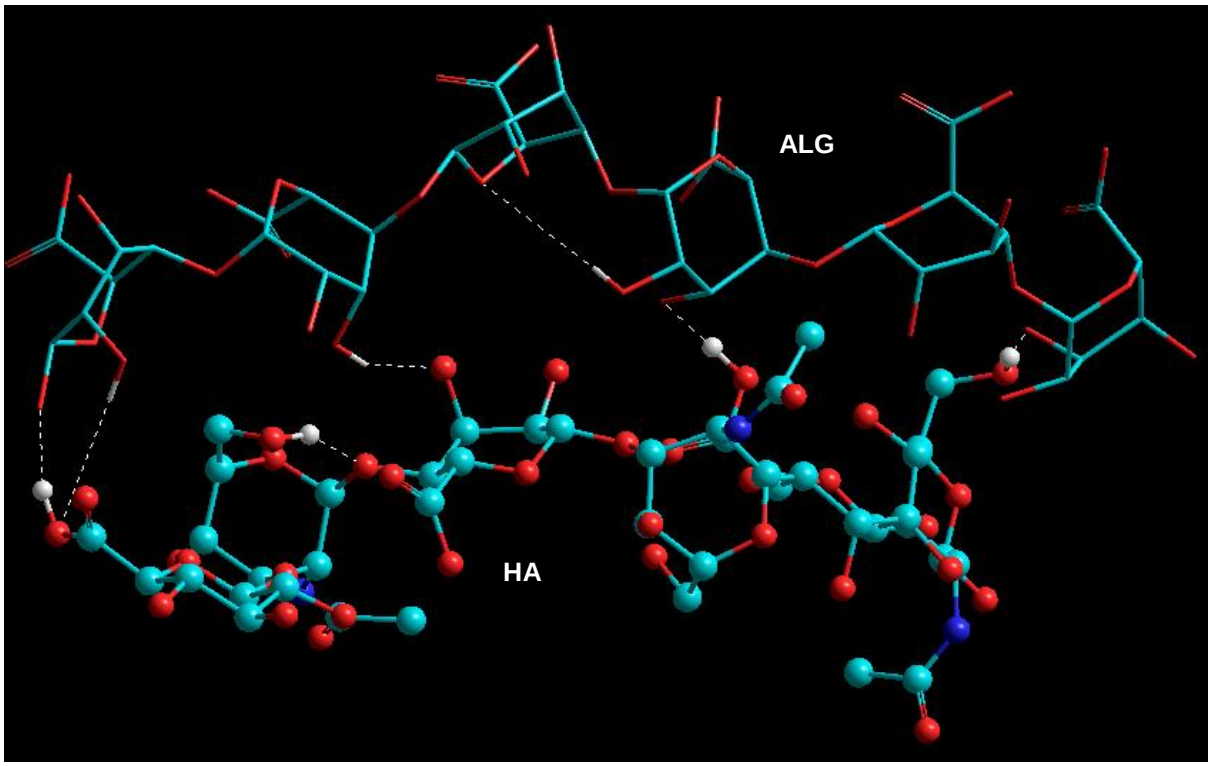

Figure 4.24: Energy minimized geometrical conformation displaying the bipolymeric complex of alginate (tubes) and hyaluronic acid (ball-and-tube) after molecular mechanics simulations. Color codes for elements: Carbon (cyan); Hydrogen (white); Nitrogen (blue); Oxygen (red).

With ALG-HA; it is evident that ALG and HA have comparatively less affinity among themselves as hypothesized above. This led to the prospective inclusion of another anionic polymer which may cover the surplus functional groups [Hypothesis II]. Formulation-wise; PAA was chosen among the various anionic polymers because of its biocompatibility, biodegradability, and potential inflammation-responsive properties. Computationally; the slender non-bulky chain-like structure of PAA, consisting of -COOH functionalities, was expected to fill the void space between ALG-HA thereby keeping the network volume unchanged. Before studying the potential of PAA towards the ALG-HA bipolymeric architecture; PAA was individually modelled with ALG and HA as ALG-PAA and HA-PAA, respectively, to idealize the inter- and intra-molecular interactions among the constituent polymers, as depicted in Figure 4.25. Interestingly, the extent of affinity in both the cases (ALG-PAA and PAA-HA) were significantly more than ALG-HA with static energy stabilization values of ≈-60kcal/mol and ≈-27kcal/mol, respectively (Equations 4.12, 4.13, 4.14, 4.16, 4.17). This partially proves the apt selection of PAA as the common third polymer as follows:

1. In the case of ALG-PAA; the structural optimization of the complex was the result of both bonding and non-bonding components with V_θ and V_{el}, respectively, being the deciding factors. Notably, V_θ was the destabilizing factor in the case of ALG-HA. Additionally, V_{el}, in case of ALG-PAA, was significantly ahead in terms of energetic minimization as compared

to that of ALG-HA. Furthermore, the inter- and intra-molecular H-bonds in the case of ALG-PAA presented a well-orientated matrix structure and hence a less strained structure.

2. With reference to HA-PAA; the structural optimization of the complex was the result of both bonding and non-bonding components with V_b and V_{ij}, respectively, being the deciding factors. Notably, V_θ is still the destabilizing factor as was in the case of ALG-HA. Notably again, V_{el} in the case of ALG-PAA does not provide much support in terms of energetic minimization as compared to that of HA-PAA. Significantly, the inter- and intra-molecular H-bonds in the instance of HA-PAA presented a well-orientated matrix structure identical with ALG-PAA and a less strained structure as compared to ALG-HA. Interestingly, the bonding contributions and van der Waals forces were because of the involvement of C-O-C and -OCH_3 functionalities, along with the carboxylic groups for both the polymers. Although the polymeric structure is well bonded, the -NH_2 groups were only involved in intramolecular interactions and no intermolecular interactions were observed.

Conclusively, the inclusion of PAA with ALG and HA proved to be an improved stabilization aspect as compared to ALG-complexed-HA. An array of almost all bonding and non-bonding energies were involved in the geometrical optimization. The non-involvement of -COOH groups of ALG and HA as well as of -NH_2 of HA led to the formulation and modelling of the tripolymeric complex, ALG-PAA-HA, as explained in the next section.

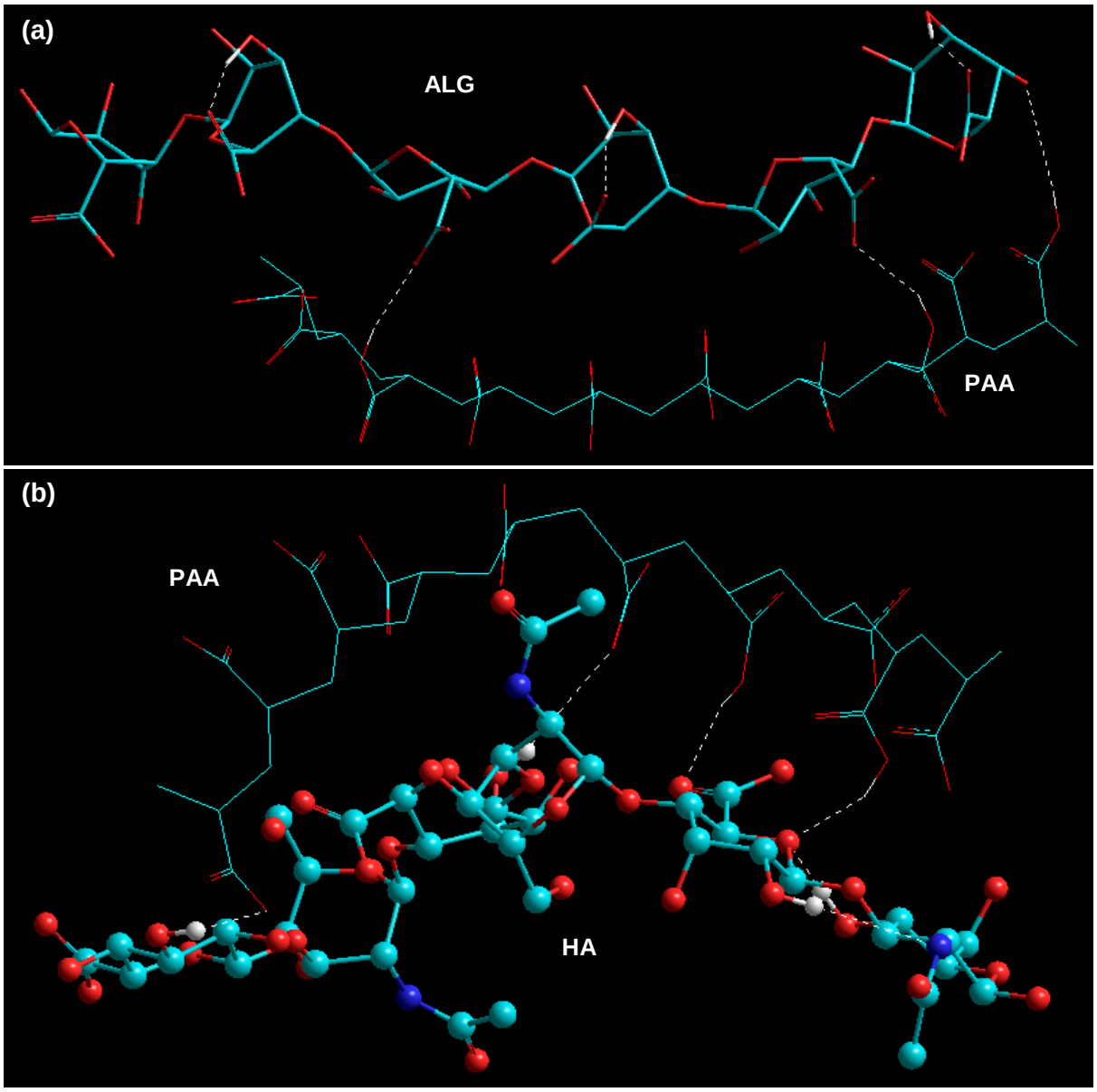

Figure 4.25: Energy minimized geometrically conformation displaying the bipolymeric complex of (a) alginate (tubes) and poly(acrylic) acid (stick); and (b) hyaluronic acid (ball-and-tube) and poly(acrylic) acid (stick) after molecular mechanics simulations. Color codes for elements: Carbon (cyan); Hydrogen (white); Nitrogen (blue); Oxygen (red).

5.3.9.1.2. Tripolymeric architectures

$$E_{ALG} = 28.304V_{\sum} = 4.084V_b + 33.109V_\theta + 39.138V_\varphi + 7.979V_{ij} - 0.581V_{hb} - 55.426V_{el}$$

[Equation 4.12]

$$E_{HA} = -27.922V_{\sum} = 4.006V_b + 37.315V_\theta + 40.375V_\varphi + 10.742V_{ij} - 7.769V_{hb} - 112.592V_{el}$$

[Equation 4.13]

$$E_{PAA} = 10.257V_{\sum} = 1.517V_b + 7.178V_\theta + 4.244V_\varphi - 2.540V_{ij} - 0.141V_{hb}$$

[Equation 4.14]

$$E_{ALG\text{-}PAA\text{-}HA} = -108.088V_{\sum} = 11.420V_b + 81.701V_\theta + 136.062V_\varphi - 15.867V_{ij} - 10.236V_{hb} - 311.17V_{el}$$

Δ**E = -118.727kcal/mol** [Equation 4.18]

Figure 4.26 and Equations 4.12, 4.13, 4.14, and 4.18 displays the optimized geometrical preference and the energetic profiling, respectively, for the ALG-PAA-HA tripolymeric complex. Evidently, the matrix structure is well-stabilized energetically with -118.727kcal/mol wherein the prominent stabilizing forces are the non-bonding interactions, namely, van der Waals forces, H-bonding, and electrostatic interactions. The bonding interactions altogether provided the strained-destabilization component to the final structural conformation. The formation of the tripolymeric complex thus followed a definite trend unlike the bipolymeric systems wherein the bonding and non-bonding components varied in their contribution towards geometry optimization. A pronounced decrease in the electrostatic energy value was the principle difference among the individual polymers' summation and the final structure. This was due to the extensive H-bonding and the involvement of almost all functional groups in the network formation (Figure 4.26b). All the possible complexing combinations such as -OH-OH, -OH-COOH, -COOH-NH_2, -OH-NH_2, and -O-NH_2 were apparent from the structure, thereby providing an ideal composite required for the adequate performance of the I^3. A closer view of the network structure in Figure 4.26b reveals that PAA, due to its linear, non-bulky, highly functionalized and slender structure, provided the much needed 'van der Waals radius filling' structure for the ALG-HA destabilized structure. The inclusion of PAA thus acted as a 'bridge mediating the space constrained structure' and could further create a series matrix in the form of ALG-PAA-HA-PAA-ALG-PAA-HA-PAA-ALG.

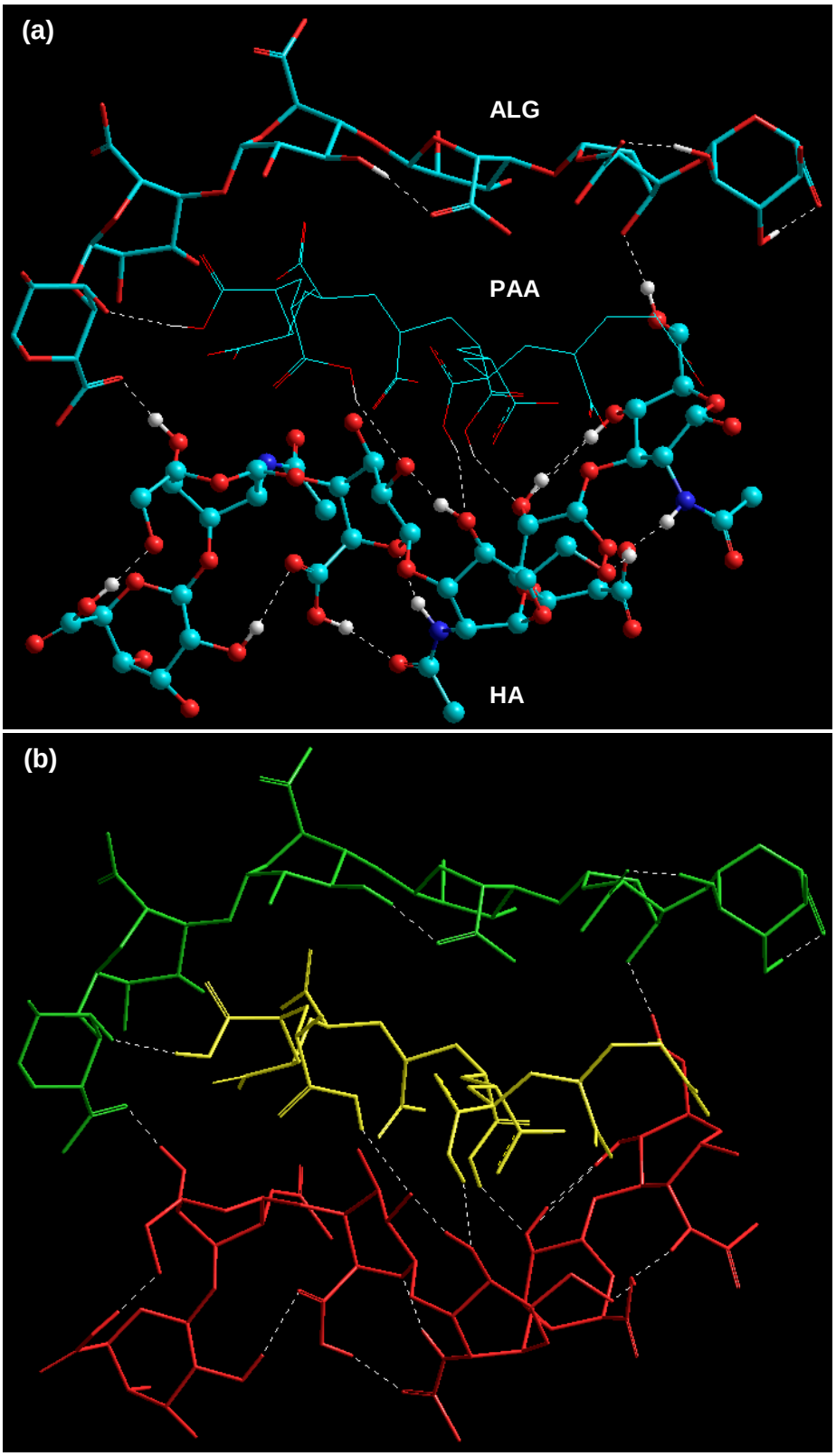

Figure 4.26: Energy minimized geometrical conformation displaying the tripolymeric complex of alginate (tubes), poly(acrylic) acid (stick), and hyaluronic acid (ball-and-tube) after molecular mechanics simulations (a). Color codes for elements in (a): Carbon (cyan); Hydrogen (white); Nitrogen (blue); Oxygen (red). Color codes for structures in (b): Alginate (green); PAA (yellow); Hyaluronic acid (red).

Furthering the simulation studies, the bi- and tri-polymeric complexes were modelled in the presence of a solvated system with water as the solvent at room temperature. The dimensions of the periodic box were maintained and hence the number of water molecules per molecular system was constant. The final optimized solvated architectures for the bipolymeric architectures were destabilized as compared to the monopolymeric (individual) molecules under similar conditions (Equations 4.19-4.24). This structural destabilization may lead to dislodgement of individual polymers from the bi-polymeric complex in order to stay as stabilized as the monopolymeric form in the solvated system. This very tendency of the polymers to stay in their original conformation rather than in complex form might lead to the separation of the polymers after implantation, hence affecting the performance of the polymeric system. Interestingly, the tripolymeric system demonstrated a substantial decrease in energy values with all the non-bonding energy components working towards the structural stabilization. The final optimized static energy for the ALG-PAA-HA-H_2O was much lower than either of the individual polymers: ALG-H_2O; PAA-H_2O; or HA-H_2O (Equations 4.19, 4.20, 4.21, 4.25) and the bi-polymeric molecular complexes: ALG-PAA-H_2O; PAA-HA-H_2O; or PAA-HA-H_2O (Equations 4.22-4.25). This minimization was rendered due to enhanced H-bonding (Figure 4.27) and electrostatic interactions which led to the formation of an intact complexed structure capable of acting in conjugation. The tripolymeric structure of the outer BPM thus has a good propensity to maintain its patency under normal ocular conditions.

$$E_{ALG\text{-}H2O} = -4182.155V_{\sum} = 47.936V_b + 73.647V_\theta + 51.075V_\varphi + 82.174V_{ij} - 16.299V_{hb} - 4420.69V_{el}$$ [Equation 4.19]

$$E_{HA\text{-}H2O} = -4154.776V_{\sum} = 49.986V_b + 84.461V_\theta + 79.982V_\varphi + 88.341V_{ij} - 14.607V_{hb} - 4442.94V_{el}$$ [Equation 4.20]

$$E_{PAA\text{-}H2O} = -3705.359V_{\sum} = 38.304V_b + 43.612V_\theta + 8.100V_\varphi + 78.321V_{ij} - 4.155V_{hb} - 3869.54V_{el}$$ [Equation 4.21]

$$E_{ALG\text{-}PAA\text{-}H2O} = -3826.993V_{\sum} = 43.983V_b + 73.445V_\theta + 74.001V_\varphi + 88.212V_{ij} - 33.950V_{hb} - 4072.68V_{el}$$ [Equation 4.22]

$$E_{ALG\text{-}HA\text{-}H2O} = -3882.668V_{\sum} = 49.303V_b + 121.86V_\theta + 104.302V_\varphi + 81.720V_{ij} - 40.815V_{hb} - 4199.04V_{el}$$ [Equation 4.23]

$$E_{PAA\text{-}HA\text{-}H2O} = -3675.562V_{\sum} = 41.485V_b + 75.155V_\theta + 60.084V_\varphi + 60.355V_{ij} - 26.229V_{hb} - 3886.41V_{el}$$ [Equation 4.24]

$$E_{ALG\text{-}PAA\text{-}HA\text{-}H2O} = -4592.788V_{\sum} = 59.645V_b + 134.86V_\theta + 150.876V_\varphi + 96.631V_{ij} - 49.856V_{hb} - 4984.94V_{el}$$ [Equation 4.25]

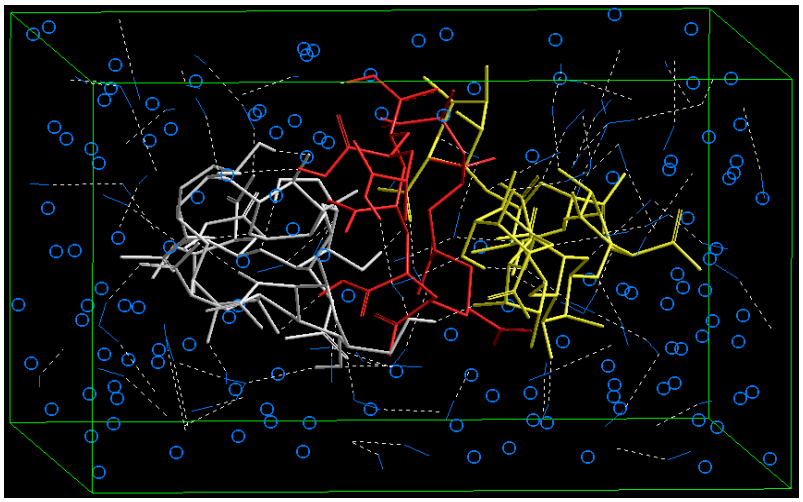

Figure 4.27: Visualization of the geometrical preference of the tripolymeric complex consisting of alginate (yellow), poly(acrylic) acid (red), and hyaluronic acid (white) after molecular simulation in a solvated system consisting of water molecules (blue molecules).

The inherent aspect of this study was to fabricate a inflammation-responsive polymeric system for stimuli-modulated ocular delivery of one or more drugs. In addition to the above simulations in water; a brief modeling simulating a pathological inflammatory intraocular state created in the presence of hydroxyl radicals was also performed to elucidate the effect of the inflammatory agents on the polymers, specifically the HA molecule. The -OH-mediated stimuli-responsive behavior of the outer BPM can be accredited to the action of the hydoxyl radicals on specific bonding/ functional sites on the polysaccharides as displayed in Figure 4.28. The MMER analysis confirmed the interaction potential of the hydroxyl radicals with polysaccharides accounting for stabilized binding energies of -3383.307kcal/mol (Equations 4.20 and 4.26) and -2541.329kcal/mol (Equations 4.25 and 4.27) for HA and ALG-PAA-HA molecular complexes, respectively. The complexes were hugely stabilized by ion pair-ion pair electrostatic non-bonding interactions. All other bonding and non-bonding interactions contributed to the destabilization of the structure proving the dominating role played by the ionized species. These energy attributes may indicate activation barriers for the first stage (abstraction of the hydrogen on the carbon adjacent to the carboxyl group in the *n*-glucuronic acid unit, leading to glycosidic cleavage) and second stages (formation of a hydrolytic product) (Yui et al., 1992). As can be deduced from the geometric configuration, the volume of polysaccharide fractions as well as the solvent-accessible surface obviously decreases during the catalytic process. This decrease in molecular size can be related to the ordering of polysaccharide fractions, which is usually accompanied with a lowering in steric energy (Tian et al., 2010). This ordering conformation provided clear evidence for the catalytic effect of the hydroxyl radicals in HA hydrolysis. The activation barriers of these reactions were lowered. In addition, the main forces that may cause the change of molecular size were analyzed by the final single point energies. Van der Waals and hydrogen bonding energies increased

significantly; whereas this was not the case for electrostatic energy during the simulation process. These findings were fully in agreement with the results that van der Waals attraction, hydrophobic forces, and electrostatic interactions were the dominant driving force in the formation of an ordered polymer structure (Xie and Soh, 2005). In general, the more negative the force energy is, the more thermodynamically favorable is the formation of the ordered structure. The change in bonded interaction was exothermal as can be adjudged from the enthalpy change (negative) indicating that the bonded interaction may also accelerate the hydrolysis of saccharide molecules.

$$E_{HA\text{-}H2O\text{-}OH} = -7538.083V_{\sum} = 86.210V_b + 125.944V_\theta + 85.995V_\varphi + 207.547V_{ij} - 12.752V_{hb} + - 8031.03V_{el}$$

[Equation 4.26]

$$E_{ALG\text{-}PAA\text{-}HA\text{-}H2O\text{-}OH} = -7044.117V_{\sum} = 96.147V_b + 215.22V_\theta + 157.456V_\varphi + 290.264V_{ij} - 52.878V_{hb} - 7750.33V_{el}$$

[Equation 4.27]

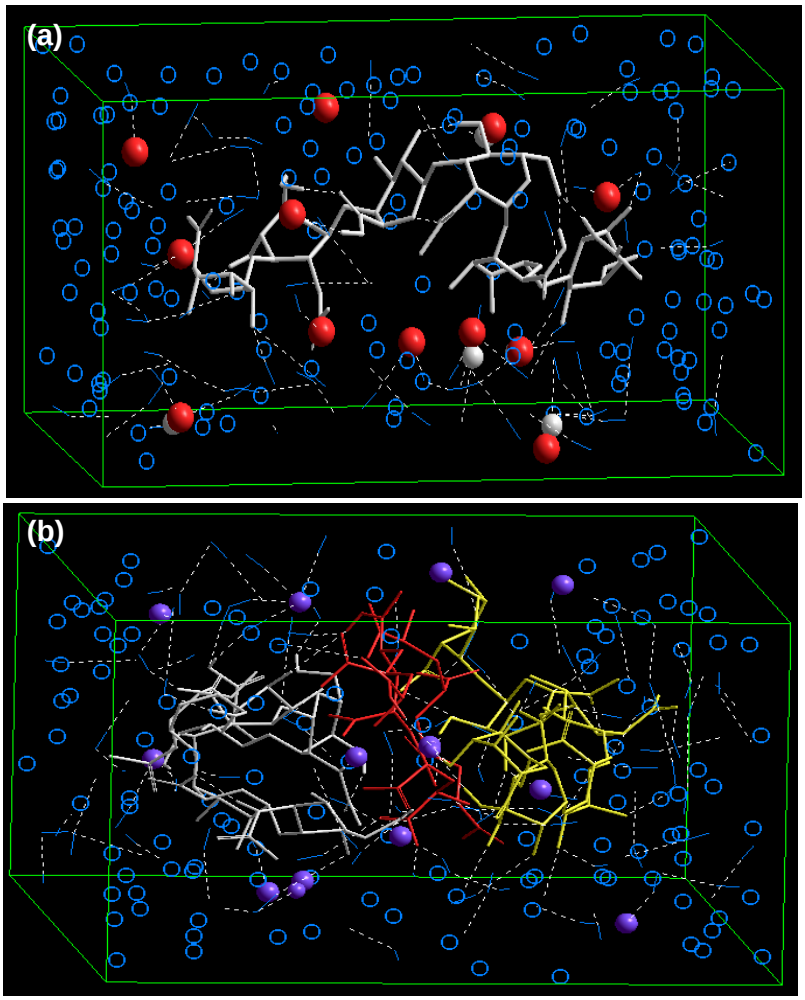

Figure 4.28: Visualization of geometrical preference of (a) hyaluronic acid (white tubes) and hydroxyl ions (red balls); and (b) tripolymeric complex consisting of alginate (yellow), poly(acrylic) acid (red), and hyaluronic acid (white) in response to addition of hydroxyl ions (purple balls) after molecular simulation in a solvated system consisting of water molecules (blue molecules)

4.3.8.2. Dynamic analysis of polymeric architectures

Molecular dynamic simulation was successfully used to further investigate the energy profile of interactions between the functional groups in the bipolymeric and tripolymeric architectures. Table 4.13 represents the main energy attributes inherent to the formation and properties of the ALG-PAA-HA - tripolymeric architecture (TPA). From Figure 4.29, it is evident that by 1000 time-steps, the potential (EPOT) and kinetic energy (EKIN) were fluctuating about equilibrium values. The atoms vibrate about fixed positions as a result of their thermal energy, and give rise to the graphs in Figure 4.29d depicting typical solid-type behavior.

In the case of ALG-HA, the preliminary bipolymeric structure, EKIN and EPOT displayed an atypical energy profile wherein EKIN and EPOT attained equal values in the initial time frame (0.5 picoseconds) followed by an increase in EKIN with a decrease in EPOT at a later time frame (Figure 4.29a). This anomalous behavior is in line with the static lattice simulations as explained in Section 5.3.9.1 on the interaction between the inner and outer BPM.

In case of ALG-PAA, EKIN and EPOT displayed equivalent values as evident from the energy overlap in Figure 4.29b. Correspondingly, HA-PAA displayed a non-equivalent but linearly-related energy profile as shown in Figure 4.29c. The final ETOT value in the case of the TPA was stabilized by ~134.841kcal/mol, further confirming the computational results (formation and conformation) obtained in molecular mechanics simulations (Table 4.13). Interestingly, the final optimized energy for the TPA was even less than ALG-HA proving that the addition of PAA has not disturbed the surface-to-volume ratio of ALG-HA. The energy minimization is mainly due to potential energy changes which are evident from the $EPOT_{TPA}$ displaying a significant flotation owing to the interaction among the atoms of ALG, PAA, and HA which is also evident from the oscillatory form of $EKIN_{TPA}$. Furthermore, the total energy varied in direct proportionality to kinetic energy, confirming the presence of a spring-mass system in the TPA which is in good corroboration with the resilience (Section 4.3.2) and nanotensile observations (Chapter 5, Section 5.3.5) obtained during experimental investigations. Interestingly, it was found that the potential energy decreased with an increase in the kinetic energy, obeying the well-known behavior of a high underdamping harmonic oscillator.

Table 4.13: Energy attributes calculated for the simulated outer BPM in a molecular dynamics setup performed using HyperChem^{TM} 8.0.8 (Hypercube Inc., Gainesville, FL).

Molecule	**Energy (kcal/mol)**		
	EKIN	EPOT	ETOT
ALG-HA	98.137	133.143	223.920
ALG-PAA	82.536	96.926	173.589
HA-PAA	89.562	85.939	168.582
ALG-PAA-HA	138.670	87.012	215.625[a]

[a] $\Delta E_{Total(TPA)} = [2(E_{Total(ALG\text{-}PAA\text{-}HA)}) - (E_{Total(ALG\text{-}HA)} + E_{Total(ALG\text{-}PAA)} + E_{Total(HA\text{-}PAA)}] = -134.841$kcal/mol

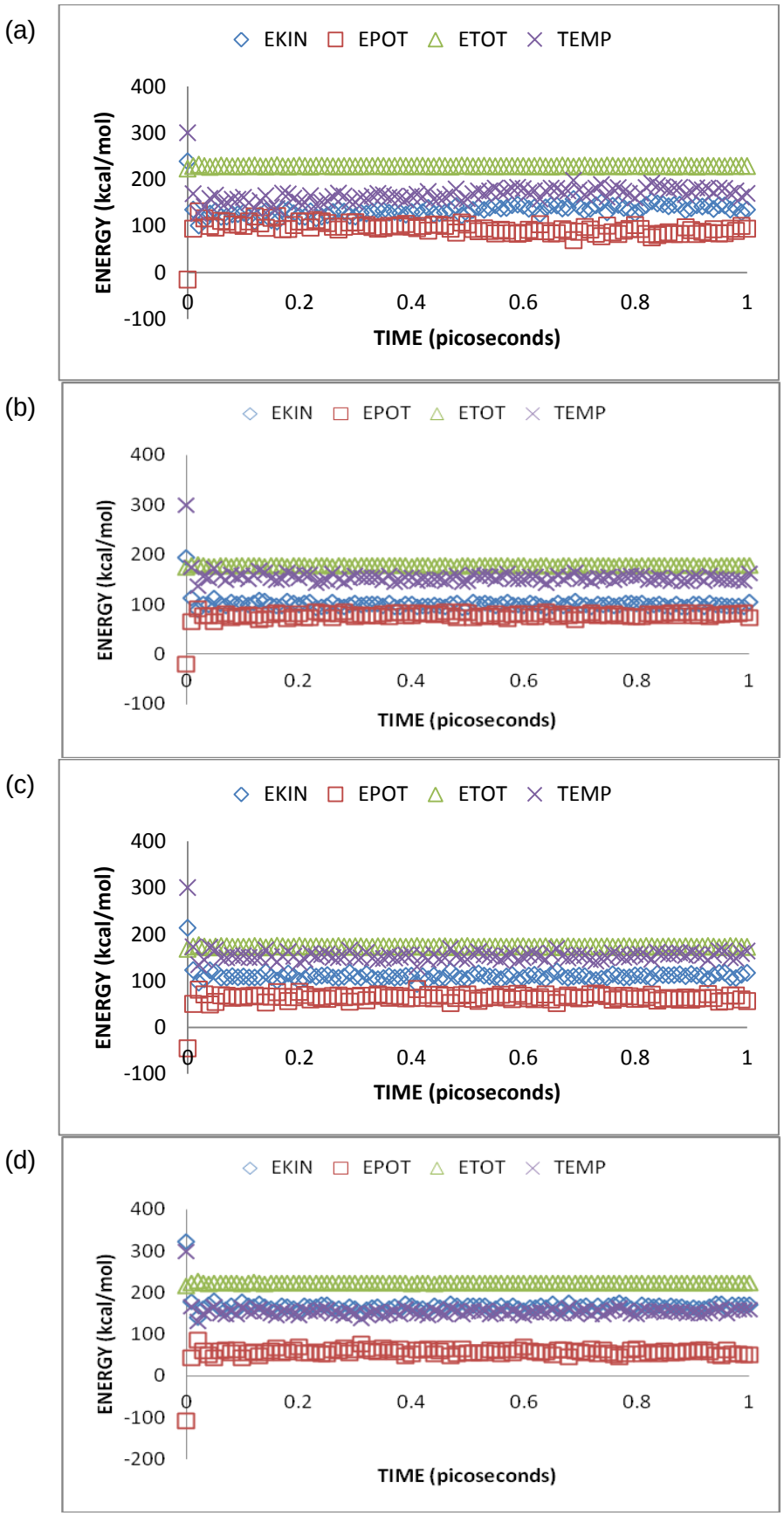

Figure 4.29: The total (ETOT), potential (EPOT) and kinetic energy (EKIN) (kcal/mol) for (a) ALG-HA; (b) ALG-PAA; (c) PAA-HA; (d) ALG-PAA-HA calculated by molecular dynamic simulations in vacuum. (EKIN = Kinetic energy, EPOT = Potential energy, ETOT = Total energy, TEMP = Temperature).

4.4. Concluding Remarks

[NHS] and [$AlCl_3$] had a significant or notable effect on the MDT of indomethacin under normal and pathological conditions, respectively (p=0.048; p=0.058). The interaction between the inflammation-responsive [HA] and [DCC] emanated in a significant effect on the ∆MDT of indomethacin (p=0.050). [$AlCl_3$] also had a significant impact on the WAC of the I^3 under normal conditions (p=0.023), whereas the effect of [NHS] was significant when considering the resilience of the device under pathological conditions (p=0.047). Subsequent execution of ANN with further training of the data confirmed the adequacy of the design. Analysis of the drug release kinetics from the optimum I^3 under both normal and pathological conditions was in coherence with the anticipated behavior of an inherently bioresponsive device. The reversibility of the inflammation-responsive drug release behavior of the I^3 was exemplified *in vitro*.

Molecular mechanics and dynamics simulations, carried out in vacuum and in solvent phase, successfully proved the rationality and applicability of the constituent polymers in the formation of the multipolymeric complex, as well as the inflammation-responsive attributes of the I^3, thus giving further gravity to the preceding physicochemical and physicomechanical observations. The inclusion of PAA with ALG and HA elaborated an enhanced stabilization aspect as compared to ALG-complexed-HA. An array of almost all bonding and non-bonding energies were involved in the geometrical optimization. PAA, due to its linear, non-bulky, highly functionalized and slender structure, provided the much needed 'van der Waals radius filling' structure for the ALG-HA destabilized structure.

Modeling simulating a pathological inflammatory intraocular state created in the presence of hydroxyl radicals was also performed for elucidation of the effect of the inflammatory agents on the polymers. The stimuli-responsive behavior of BPMs can be attributed to the action of the hydoxyl redicals on specific bonding/ functional sites on the polysaccharides. The MMER analysis confirmed the interaction potential of the hydroxyl radicals with polysaccharides.

Following the afore-described in depth optimization, *in vitro* drug release characterization, and *in silico* modeling of the I^3, it is important to further characterize all aspects of the bioresponsive behavior of the device through physicochemical and physicomechanical characterization of the I^3. This is undertaken in the following Chapter to ascertain whether the steps implicated in device development, optimization, and characterization, were sufficient to create a system of apt clinical potential, which can only be assessed succinctly *in vivo.*

CHAPTER 5

COMPONENTIAL EVALUATION OF THE INTELLIGENT INTRAOCULAR IMPLANT AND COMPUTATIONAL PREDICTION AS A MEANS OF ELABORATING DEVICE BIORESPONSIVENESS IN A SIMULATED NORMAL AND INFLAMMATORY OCULAR MILIEU

5.1. Introduction

The interaction of the I^3 with the ocular environment is tantamount to elaboration of the bioresponsive capabilities of the device. The drug delivery capabilities of the I^3 depends on the characteristics of the device, and can be engineered into the implant by varying the chemical or physical properties of the polymer (Saltzman, 2001). Thus, interpretation of the physicochemical and physicomechanical properties is a prerequisite in defining the behavior/ performance of the device following implantation.

There is an unequivocal relationship between the properties of the simultaneously originated crosslinked BPMs comprising the device and its structure in such a way that both characteristics cannot be considered in an isolated way; the multipolymeric composition, synthetic approach employed, and its nano-architectural component, decisively influence the structure of the I^3 as well as the final properties that the structure would have (Figure 5.1).

In order to gain an in-depth understanding of the crosslinking mechanisms instigated to derive the device with rheological demonstration of pertinent transitions at the fabrication stage, consequent altered thermal and nano/ micro-mechanical behavior of the implant, tortuosity of the device as predicted via porosity, and overall implant architecture; Fourier Transform-infrared spectroscopy, rheological investigations, Advanced Differential Scanning Calorimetric studies, nanotensile testing, textural analysis, porosity assessment, and Scanning Electron Microscopy were respectively and systematically performed. Additionally, to justify the formation of a ‘secure-fit dual bioresponsive polymeric matrix system with a NS enclatherated as a superlattice’, i.e. integration via crosslinking of the inner BPM within the outer BPM, the energetic profiles for the complexation of chitosan, forming the matrix in which the NS was embedded, with alginate, HA and PAA (forming the outer BPM) were generated using MMER by exploring the spatial disposition of energy minimized molecular structures. In most instances, evaluation of the I^3 implicated both nano- and non-nano-enabled embodiments.

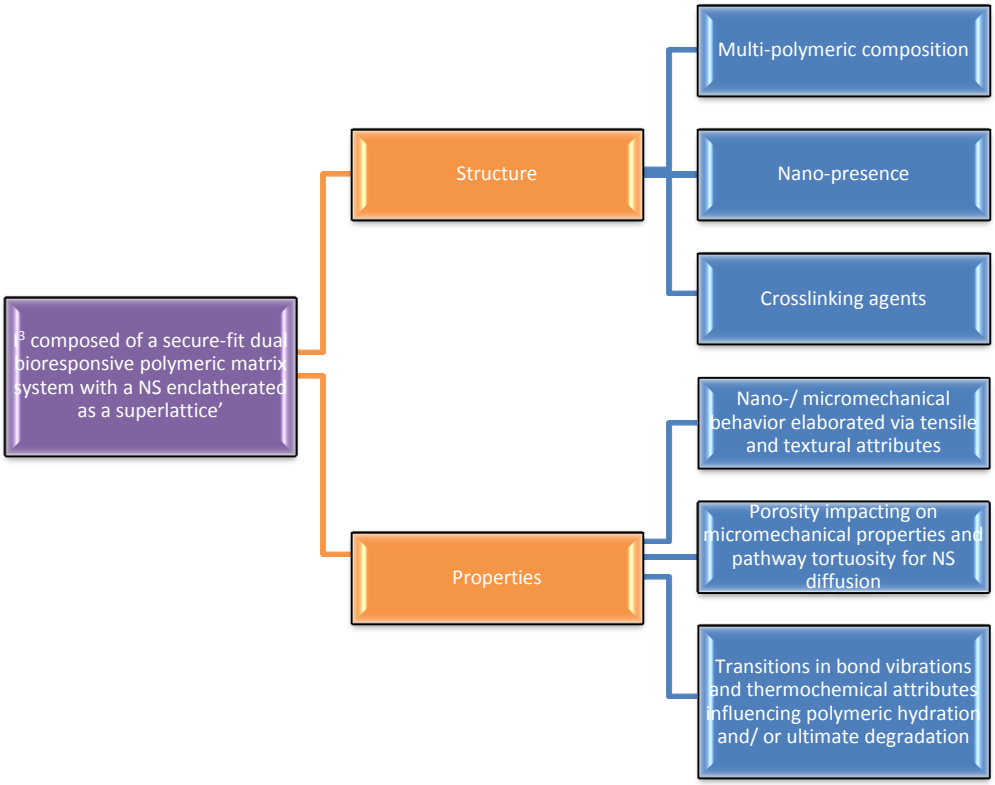

Figure 5.1: Relationship between structural variables and properties for the I^3

5.2. Materials and Methods

5.2.1. Materials

The optimum intraocular device (I^3, in both nano-enabled and non-nano-enabled embodiments), as defined, was employed for the ensuing investigations. The procedure employed for preparing the devices was as described in Chapter 4, Section 4.2.2 and 4.2.3, using the optimal settings defined in Section 4.3.4. The polymers, drugs and reagents implemented in their fabrication were also included in ensuing investigations: Hyaluronic acid (potassium salt, from human umbilical cord), chitosan (MMW) *N*,*N*′-dicyclohexylcarbodiimide, indomethacin (99% TLC) and gluteraldehyde 25%$^{v}/_{v}$, all purchased from Sigma-Aldrich® Inc. (St Louis, MO, USA). *N*-hydroxysuccimide (>97% TLC) and ciprofloxacin (>98% TLC) were purchased from Fluka® Analytical via Sigma-Aldrich® Inc. (St Louis, MO, USA). Alginate (TICA-algin® 400 Powder, medium viscosity) was purchased from Texture Innovation Center® (White Marsh, MD, USA). Crosslinked poly(acrylic) acid (Carbopol 974P®) was purchased from Noveon Inc. (Cleveland, Ohio, USA). Aluminum chloride was purchased from Merck® (Wadeville, Gauteng, South Africa). All other materials were of analytical grade and were employed as received.

5.2.2. Rheological analysis of the initiator polymer-crosslinker milieu for determination of the physicomechanical expression of the stimulus-responsive behavior

Rheology is defined as the study of the relationship between the deformation of physical bodies and the forces generated within them (Marriot, 2008; Gaudana et al., 2009). Understanding the fundamental nature of the polymeric system implicated in forming the implant is of most significance to these investigations (Herh et al., 1998; Partini et al., 2009).

Oscillatory studies are of vital importance for the evaluation of the multipolymeric hydrogels forming the matrices to be exposed to crosslinking agents, as they are anticipated to undergo macro- or micro-structural rearrangement with time. These rearrangements directly influence rheological performance, which in turn could provide the necessary information regarding 'stimulus-responsive' transitions in the polymeric components of the I^3 with time (Herh et al., 1998). Oscillatory studies consist of 3 main tests, namely yield stress, stress sweep and frequency sweep tests.

5.2.2.1. Preparation of the precursor stimulus-responsive hydrogel systems

For the stimulus-responsive hydrogel systems (SRHS) forming the intermediate release BPM, the optimal 4%$^{w}/_{v}$ sodium alginate-1% $^{w}/_{v}$ PAA (Carbopol 974)-2.925%$^{w}/_{v}$ NHS-0.286%$^{w}/_{v}$ HA-2.5%$^{v}/_{v}$ gluteraldehyde-0.25%$^{w}/_{v}$ ciprofloxacin aqueous solution was prepared, instituting carbodiimide coupling chemistry to increase the interconnectivity of the matrix. DCC (295mg) was dissolved in ethanol and dispersed within the polymeric solution. This SRHS constituted the outer BPM. Incremental volumes (1mL) of the cationic chitosan solution (inner BPM) incorporating the Lipo-Chit-PCL NS was added to the anionic solution, and the rheological transitions ascertained. Additionally incremental volumes (1mL) of an acidified 4.366%$^{w}/_{v}$ $AlCl_3$ solution was added to the anionic polymeric composition of certain samples, thus serving as the initiator solution.

5.2.2.2. Preliminary viscosity analysis

The rheological analysis studies of the respective SRHS were carried out employing the Thermo Scientific HAAKE MARS Rheometer (Thermo Fischer Scientific, Karlsuhe, Germany). The viscosity of the gel solutions were measured at 37°C at a speed of $1.25s^{-1}$. Three sample sets at five concentration levels were evaluated. The sample solutions were tested in different ratios (Table 5.1). Preliminary oscillatory studies (yield stress, stress sweep and frequency sweep) were also undertaken to identify the most discriminatory rheological test.

Table 5.1: Ratios of polymeric gel and initiator solutions in the SRHS for rheological interpretation

Outer BPM SRHS: Inner BPM SRHS (A:B)	Outer BPM SRHS: Initiator solution* (A:C)	Outer BPM SRHS: Inner BPM SRHS: Initiator solution* (A:B:C)
10:1	10:1	10:1:1
10:2	10:2	10:1:2
10:3	10:3	10:1:3
10:4	10:4	10:1:4
10:5	10:5	10:1:5

Initiator solution refers to $AlCl_3$

5.2.2.3. Oscillatory studies: frequency sweep tests

The oscillatory studies of the sample solutions were carried out employing the Thermo Scientific HAAKE MARS Rheometer (Thermo Fischer Scientific, Karlsuhe, Germany). The frequency sweep tests were carried out at the frequency range of 0.05-1Hz at a temperature of 37°C. Two sample gel systems were tested, as per the preferred ratio of components identified during preliminary analysis (Section 5.2.2.2):

(i) The outer and inner BPM solution (1mL: 0.5mL) and

(ii) The SRHS comprising of all three BPM components: the outer BPM, the inner BPM and the initiator solution in a ratio of 1mL: 0.5mL: 0.1mL, respectively.

These two systems (i and ii) in their respective concentrations were used to perform the frequency tests in response to simulated ocular inflammatory conditions and normal ocular conditions. Frequency sweep tests were carried out after exposing a set of each of the solutions to normal conditions in 4mL SVH (comprising PBS with 0.03%$^{v}/_{v}$ HA, 37^{o}C) and another set to inflammatory conditions in 4mL SVH containing 0.05M Fenton's reagent for a period of 28 days, simulating normal ocular physiological conditions and ocular inflammatory conditions, respectively. The frequency sweep tests were time dependent, carried out on days 0, 3, 7, 14, 21 and 28. A second set of frequency sweep analyses was performed by alternating the two systems between SVH and Fenton's Reagent in the same above mentioned conditions. Dialysis tubing cellulose membrane (flat width: 33mm, diameter: 22mm, MW: 12400, Sigma-Aldrich®, St. Louis, MO, USA) was used to encase and expose the respective systems to normal SVH and Fenton's Reagent in SVH. All investigations were conducted in triplicate (n=3).

5.2.3. Characterization of vibrational transitions by Fourier Transform Infrared Spectroscopy

Fourier Transform Infrared Spectroscopy (FTIR) was applied to the study of the I^3, for system exemplification and investigation of its structured properties e.g. crystallinity and hydrogen bonding. The vibrational molecular transitions of the outer and inner matrix (comprising the NS incorporated within a crosslinked core) in comparison with the native system components were characterized for the attainment of important microstructural information via their FTIR spectra, recorded on a PerkinElmer® Spectrum 100 Series fitted with a universal ATR Polarization Accessory (PerkinElmer Ltd., Beaconsfield, UK). Spectra were recorded over the range 4000-625cm^{-1}, with a resolution of 4cm^{-1} and 32 accumulations.

5.2.4. Characterization of thermal transitions of the I^3 by Advanced Differential Scanning Calorimetry

Differential Scanning Calorimetry (DSC) is a thermoanalytical materials characterization which is of considerable value in polymer description and forms an essential component of this investigation. Knowledge of the glass transition (T_g) is vital in the enhancement of the novel drug delivery device. It is reported that the modification in T_g of a polymer is dependent on the interaction degree between the componential polymers, and the polymers and drug. An increase in the temperature is considerably associated with a strong interaction, which is essentially dictated by a fall in the polymer chain mobility - the nature of the chemical crosslinking interactions is important to defining the success of the proposed implant. (Takka, 2003).

Because crosslinking increases the T_g of a polymer following the introduction of molecular restrictions, Nielson (1974) averaged the data in the literature to arrive at the following empirical equation:

$$T_g - T_{g0} = \frac{3.9\times10^4}{M_c} \qquad \text{[Equation 5.1]}$$

M_c is the average molecular weight between crosslinked points, to be considered with reference to the M_w of the native polymer. T_{g0} is the T_g of the uncrosslinked polymer having the same chemical composition as the crosslinked polymer.

Temperature modulated DSC (TMDSC) or Advanced Differential Scanning Calorimetry (ADSC) can be considered as a significant extension to DSC. The basic principle of TMDSC can be stated simply: in TMDSC, the constant rate of increase (or decrease) of temperature

that is used in conventional DSC is modulated through superimposition of a periodic temperature modulation (often sinusoidal) of a certain amplitude and frequency (or period). With the help of this periodic perturbation, quantities like complex heat capacity consisting of a real and an imaginary part or the reversing and non-reversing heat capacity can be obtained often in addition to the 'common' DSC signal (total heat capacity). The contribution of the structural changes within the sample during any one period will alter both the amplitude and the phase of the heat flow modulations. Thus C^*_p complex comprises two components, one in-phase with the heating rate modulations (C'_p), and the other out-of-phase (C''_p) defined as:

$$C'_p = C^*_p cos\emptyset \qquad \text{[Equation 5.2]}$$

$$C''_p = C^*_p sin\emptyset \qquad \text{[Equation 5.3]}$$

Where ϕ is the phase angle (Cheng, 2002; Jiang et al., 2002).

Assessment of the thermal transitions was performed on all native polymers and drugs and compared with the formed inner and outer BPMs employing a Temperature Modulated Differential Scanning Calorimeter (TMDSC) (Mettler Toledo DSC-1 STAR^e System, Schwerzenback, ZH, Switzerland). Normal and temperature-modulated DSC curves were generated. Thermal events of significance included the glass transition (T_g), measured as the reversible heat flow due to changes in the magnitude of the C_p-complex values (ΔC_p) melting (T_m) and crystallization (T_c) temperature peaks which are consequences of irreversible heat flow corresponding to the total heat flow. The temperature calibration was undertaken in accordance with the melting transition of indium. Samples were weighed on perforated 40µL aluminium pans and evaluated over the temperature range of interest under nitrogen atmosphere (Afrox, Germiston, Gauteng, South Africa) in order to diminish oxidation. The instrument parameters are highlighted in Table 5.2.

Table 5.2: TMDSC settings for thermal analysis

Segment Type	Parameter Setting
SINE[a]	
Start	0°C
Heating rate	1°C/min
Amplitude	0.8°C
Period	0.8°C
LOOP[b]	
To segment	1
Increment	0.8°C
End	≥200°C (varies with the polymer)

a) Sinusoidal Oscillations
b) Oscillation periods

5.2.5. Porosity analysis of the I^3

Physical adsorption processes in porous materials are controlled via the interplay between the strength of fluid-wall and fluid-fluid interactions as well as the effects of confined pore space on the state and thermodynamic stability of fluids confined to narrow pores. It is this interplay that is ultimately reflected in the shape or type of the adsorption isotherm, which emanated in the International Union of Pure and Applied Chemistry (IUPAC) publishing a classification of six types of adsorption isotherms that proposes to classify pores by their internal pore width (Sing et al., 1985).

The ultimate porosity of the I^3 would have a considerable impact on its physicomechanical performance and possibly have interplay on the drug diffusion kinetics depending on the overall release mechanism. The porosity of the implants was evaluated by the BET isotherm of adsorption/ desorption of nitrogen, employing a porositometer (ASAP 2020, Micromeritics Instrument Co., Georgia, USA). Amongst the plots generated via the instrumentation software, a few are of pertinence for analysis. The BET plot calculation obtains the device surface area value by determining the monolayer volume of adsorbed gas from the isotherm data. The t-plot calculation allows quantitative analysis of the area and total volume ascribed to micropores within the device matrix. The Barrett-Joiner-Halenda (BJH) calculation permits determination of the mesopore volume/ area distribution which accounts for both the change in adsorbate layer thickness and the liquid condensed in the pore cores of the respective BPMs of the I^3.

The porosity of the formed inner and outer BPMs was separately assessed. Samples were initially degassed to aid the removal of surface moisture and contaminants prior to analysis. At least 100mg was instituted for analysis. A glass filler rod was then inserted into the sample

tube to reduce the total free space volume within the tube facilitating a reduction in the time required for complete degassing to occur. Samples were completely degassed after a period of between 7 and 9 hours. The respective parameter settings are shown in Table 5.3.

Table 5.3: Evacuation and heating phase parameters employed for porositometric analysis

Parameter	Rate/ Target
Evacuation phase	
Temperature ramp rate	10°C/min
Target temperature	40°C
Evacuation rate	50mmHg/s
Unrestricted evacuation form	30mmHg
Vacuum set point	500µmHg
Evacuation time	60 min
Heating phase	
Temperature ramp rate	10°C/min
Hold temperature	30°C
Hold time	900min

5.2.6. NanoTensile™ analysis of the nano- versus the non-nano-enabled I^3

Measurement of the tensile properties was undertaken to indicate the manner in which the implant would react to forces being applied in tension (i.e. during and following implantation *in vivo*). A tensile test is a fundamental mechanical test where a carefully prepared specimen is loaded in a controlled manner while measuring the applied load and the elongation of the specimen over some distance, with the goal of determining the modulus of elasticity, elastic limit, elongation, proportional limit, reduction in area, tensile strength, yield point, yield strength and other tensile properties.

The software (nanoTensile^{TM}) that was employed to generate these values employs the general equations of stress and strain specified for the calculation of mechanical parameters using Equations 5.4 and 5.5, respectively:

$$\sigma = \frac{F}{A_0} \qquad \text{[Equation 5.4]}$$

$$\varepsilon = \frac{l_i - l_0}{l_0} \qquad \text{[Equation 5.5]}$$

Equation 5.4 signifies the determination of stress (σ) where the instantaneous load applied by force (F) measured in Newtons and the cross-sectional area (A_0) measures the area prior to deformation. Equation 5.5 represents the strain (ε), comparing the change in the fiber

length after deformation to that of the original fiber, in which [l_0] and [l_i] represent the original and final length of the fibers, respectively.

The Young's modulus is a result of the ratio of tensile stress to tensile strain, as represented in Equation 5.6.

$$E = \frac{\sigma}{\varepsilon} = \frac{F.L_0}{A_0.\Delta L} \qquad \text{[Equation 5.6]}$$

To facilitate tensile analysis of the I^3, the BPMs had to be presented in a fibrous configuration. The I^3 was thus prepared via syringe extrusion in a rubber tubular mould filled by the outer BPM in the $AlCl_3$ catalyst solution with the inner BPM running through the center in both nano- and non-nano-enabled embodiments (Figure 5.2).

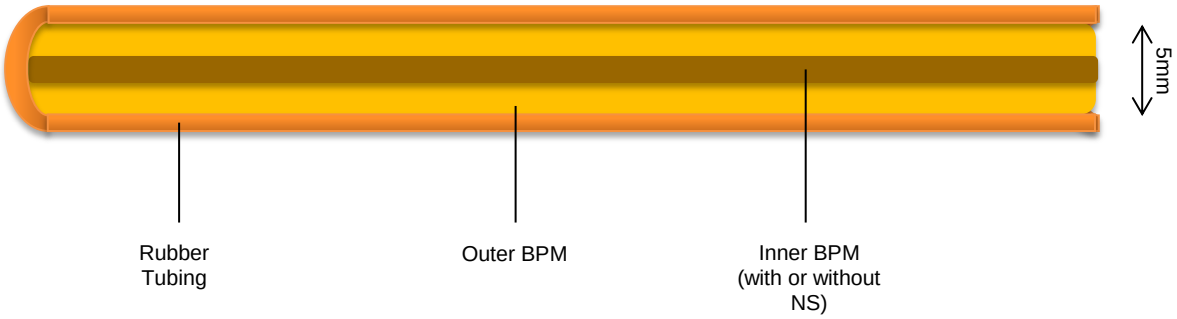

Figure 5.2: Preparation and configuration of the I^3 for nanoTensile™ analysis. The rubber tube had an inner diameter of 5mm and the tubing was 1.5mm thick

The mechanical properties of the nano- (NE) and non-nano-enabled (NNE) fibers were subsequently assessed according to their tensile strength employing a nanoTensile™ 5000 (NT) (Hysitron Inc., Minneapolis, USA). The Z force FP Gain was set to 100 and the Z Displacement FP Gain was set to 10. The settings on the system test window are detailed in Table 5.4.

Table 5.4: Standard NT transducer settings

Settings on the system test window	
Pieze stop voltage	8V
Piezo start voltage	0V
Time per cycle	30sec
Num points per half cycle	100
X, Y and Z NT Head transducer constants	
X Force FP Gain	100
X Force FP Filter (Hz)	300Hz
Y Force FP Gain	100
Y Force FP Filter (Hz)	300Hz
Z Displacement FP Gain	100
Z Displacement FP Filter (Hz)	300Hz
Z Force FP Gain	100
Z Force FP Filter (Hz)	300Hz

Following calibration, sample analysis was undertaken. The samples were weighed while mounted on the upper gripper of the NT head. Thereafter, the sample was centrally positioned between the upper and lower grippers, secured in place with tightening of the grippers, and cutting of the cardboard segments between the two lines on either side on the cardboard template prior to analysis. Interpretation of the generated plots was related to the strength and flexibility of the fiber formulation. The tensile load was controlled via the displacement and the load or strain rate through adjustment of the test velocity. The rate of velocity was regulated at 10µm/sec with a displacement limit of 150mm and a load limit of 1N. Data analysis produced values pertaining to yield stress, ultimate strength, ultimate strain and toughness as well as calculating the Young's modulus for the NE and NNE fibers.

5.2.7. Magnetic Resonance Imaging for live-acquisition of the inflammation-responsive transitions of the I^3

Magnetic Resonance Imaging (MRI) has specific application for its potential to monitor the fate of the dosage form *in vivo*, and attractively, to correlate *in vitro* with *in vivo* behavior. For complex systems comprised of a number of functional polymeric excipients, thorough comprehension of the drug release mechanism is difficult employing cumulative drug release profiles alone. The kinetics of water ingress into the drug delivery system has a significant contribution in controlling drug release from hydrogel matrices (Tajiri et al., 2010). Application of MRI to the long-term hydrational behavior of a complex polymeric system is a largely unexplored aspect. This investigation sought to gain further insight into the extent of water ingress into the I^3 over a prolonged period, as well as ascertaining the opposing intricacies of water uptake under normal versus pathological conditions. MRI thus forms an explanatory

role in this investigation for determining the transience in hydration of the I^3 on exposure to and following the removal of the inflammatory stimulus.

A magnetic resonance system with digital MARAN-i System configured with a DRX2 HF Spectrometer console (Oxford Instruments Magnetic Resonance, Oxon, UK) equipped with a compact 0.5 Tesla permanent magnet stabilized at 37^{o}C and a dissolution flow through cell was employed for the viewing of the hydrational morphological transitions of the I^3. After duly configuring, optimizing the shims and probe tuning, the cone-like lower part of the cell was filled with glass beads to provide laminar flow at 16mL/min of the solvents employed. The implant matrices were placed in position each time following dissolution analysis (described below) within the cell which in turn was positioned in a magnetic bore of the system and MR images were acquired every 3 minutes with MARAN-i version 1.0 software. The image was acquired after setting the frequency offset and testing gain employing RINMR version 5.7 under continuous solvent flow conditions. MARAN-i software comprises image acquisition software and image analysis software. The image acquisition parameters are depicted in Table 5.5.

The I^3 was exposed to SVH and another to SVH and Fenton's Reagent for a period of 28 days (n=3). The MR images were taken on days 0, 3, 7, 14, 21 and 28 in order to visually determine implant hydration. In a further investigation, the I^3 was alternated between SVH and Fenton's reagent at days 0, 3, 7, 14, 21 and 28; following exposure to conditions as described in the *in vitro* drug release study i.e. in the I^3 was placed in 4mL of the desired dissolution media and placed in an oscillating laboratory incubator (Labcon® FSIE-SPO 8-35, California, USA). The I^3 was removed at each successive time point for MRI analysis. Image acquisition was performed in triplicate at each time point (n=3). The gelled intensity and change in area of the I^3 was ascertained for each time point.

Table 5.5: Image acquisition parameters applied during magnetic resonance imaging employing the MARAN-i

S. No.	Parameter	Value
1.	Imaging protocol	FSHEF
2.	Requested gain (%)	4.17
3.	Signal strength	68.92
4.	Average	2
5.	Matrix size	128
6.	Repetition time (ms)	1000.00
7.	Spin Echo Tau (ms)	6.80
8.	Image acquired after	60min
9.	Total scans	64

MRI was undertaken concurrently with *in vitro* drug release evaluations in an effort to correlate the drug release behavior with the observed changes in the implant appearance and hydration state on exposure to and removal of the inflammatory stimulus. Thus, analysis of all corresponding dissolution samples via UV spectroscopy was performed, as described (n=3).

5.2.8. Morphological characterization and image processing analysis of erosional behavior of the I^3 via gross photographic and Scanning Electron Microscopic analysis

In the successful development of a novel dosage form, it is of pertinence to describe the overall architecture (bulk and nano-level) and changes in morphological attributes (e.g. surface texture) on exposure to the conditions it will encounter *in vivo*. Previously, it has been difficult to describe morphology in absolute terms, until the evolution of qualitative and quantitative digital image processing. Digital image processing is the use of computer algorithms to perform image processing on digital images. It enables a wide range of algorithms to be applied to the input data and can avoid problems such as the build-up of noise and signal distortion during processing. Since images are defined over two dimensions (perhaps more) digital image processing may be modeled in the form of multidimensional systems. *Mathematica*®, developed by Wolfram Research Inc., is one such program that achieves this. *Mathematica*® ultimately provides broad and in-depth built-in support for both programmatic and interactive modern industrial-strength image processing. This is fully integrated with *Mathematica®'s* powerful mathematical and algorithmic capabilities. An important concept common to many image enhancement operations is that of a histogram, which is simply a count (or relative frequency, if normalized) of the gray levels in the image. Analysis of the histogram provides useful information about image contrast.

The I^3 was exposed to normal and inflammatory conditions over 28, 56 and 72 days and transitions in surface architecture visualized via scanning electron microscopy (SEM). The implants were coated using the SPL module-Sputter Coater (Toronto, Canada). The sample implants were attached to the spud using carbon paper and were left in the SPL module-Sputter Coater for 120 seconds to ensure generously coated surfaces. The SEM images were taken with the objective of comparing surface changes related to the bio-erosion mechanism of the device, using the Phenom G2 Pro SEM (Germany), as well as determining the conditions that lead to mechanical failure of the implants when exposed to the afore-mentioned conditions.

To enhance characterization of the photographic images, image analysis was undertaken employing intricate mathematical software (Mathematica® v. 8.0, Wolfram Research Inc.,

Champaign, IL, USA). For bulk morphological changes, the 'ImageHistogram' command was employed to plot a histogram of the pixel levels for each channel in the image for assessment of changes occurring in the histogram output as a predictor of surface erosion changes (exemplified in Equation 5.7, where *'Image'* refers to the applicable photographic image file). This default function plots a histogram of the pixel levels for each channel in the image, which was represented as 'voxel intensity', where a voxel is a 'volumetric pixel', carrying the same color-intensity properties as pixels, plus the additional important property of transparency.

$$ImageHistogram['Image', Appearance \rightarrow "Separated"] \quad \text{[Equation 5.7]}$$

To enhance characterization of the microscopic images, image analysis was undertaken employing Mathematica® v. 8.0 (Wolfram Research Inc., Champaign, IL, USA) in accordance with an approach previously developed (Shaikh et al., 2012). For the erosional images acquired via SEM, image processing was performed on sixteen-bit greyscale images obtained by SEM of the inner and outer BPMs of the I^3. These images were low in contrast due to the effects of uneven illumination across the field of view. Thresholding of crude images was unable to capture all of the required details; therefore intermediate image-processing steps were employed to even out the background and increase contrast between the solid polymeric architecture, deep pores, and pores at the surface of the structure. Images in TIFF format were imported and converted to Mathematica™ 8.0 format.

The first processing step, blurring the image, provided a distorted version of the image making it unfocused, which can be obtained by convolving the image with a low pass filter. For this investigation, the quantity of blurring is increased by increasing the pixel radius (r) to 15 without compromising image detail. This was achieved in Mathematica™ 8.0 by applying a custom blurring function (Equation 5.8, where *'Image'* refers to the applicable SEM image file):

$$Blur['Image', 15] \quad \text{[Equation 5.8]}$$

After blurring the image, the next step was to ColorQuantize the blurred image at 5 which provided an approximation to an image that uses only 5 distinct colors. This was achieved in Mathematica™ 8.0 by applying a custom ColorQuantize function:

$$ColorQuantize['Image', 5] \quad \text{[Equation 5.9]}$$

The third step consisted of analyzing the images by plotting a histogram. Histograms of both the unmodified SEM and well as the color quantized image were plotted in order to exemplify the extent of refinement provided by the image manipulation, for assisting description of the overall implant architecture. Furthermore, separate histograms for each color channel were constructed. This was achieved in Mathematica^{TM} 8.0 by applying the custom ImageHistogram functions for default and separated algorithms as displayed above in Equation 5.7.

An analysis of the histogram was essential for the best choice of the threshold for discriminating between different morphological features seen in the SEM of the eroding I^3.

5.2.9. Molecular modeling simulations for prediction of pertinent interactions between the inner and outer bioresponsive matrices of the I^3

The concept of computational chemistry and molecular modeling pertains to the application of theoretical methods and computational techniques for the modeling and simulation of small chemical and biological systems in order to predict and interpret their behavior, and is significantly applicable to polymeric systems implicated in the formation of a novel drug delivery system as exemplified, in this investigation, by the I^3. As discussed in Chapter 3, the I^3 essentially comprises a NS-polymer superlattice forming the inner matrix which is bound via crosslinking within the outer BPM. The final step in this 'modeling trilogy' describing firstly the NS (Chapter 3, Section 3.4.10), followed by the outer BPM (Chapter 4, Section 4.3.8), is the intricacies of the interactions between the inner and outer BPM, which is implicit to the overall understanding of the underlying mechansims governing the physicochemical and physicomechanical attributes of the implantable device.

A number of potential interactions are possible between the polymeric components of the inner and outer BPM ultimately redolent of a 'secure-fit' dual polymeric matrix system. Molecular modeling is a necessary step to add further weight to the physicochemical ascertainments. All modeling procedures and calculations, including energy minimizations in molecular mechanics, were performed using the HyperChem^{TM} 8.0.8 Molecular Modeling System (Hypercube Inc., Gainesville, Florida, USA) and ChemBio3D Ultra 11.0 (CambridgeSoft Corporation, Cambridge, UK).

5.2.9.1. Static Lattice Atomistic Simulations in vacuum

The structure of chitosan, alginate, and HA (10 oligosaccharide units each) were built using polysaccharide editor module on HyperChem 8.0.8 while PAA (25 monomer units) was drawn using ChemBio3D Ultra in its syndiotactic stereochemistry as a 3D model. The models

were initially energy-minimized using MM+ force field and the resulting structures were again energy-minimized using the Amber 3 (Assisted Model Building and Energy Refinements) force field. The conformer having the lowest energy was used to create the polymer-polymer complexes. A complex of one molecule with another was assembled by disposing the molecules in a parallel manner, and the same procedure of energy-minimization was repeated to generate the final models: Chit-ALG, Chit-PAA, and Chit-HA. Full geometry optimization was carried out in vacuum employing the Polak-Ribiere conjugate gradient algorithm until an RMS gradient of 0.001kcal/mol was reached. Force field options in the AMBER and MM+ methods were HyperChem 8.0.8 defaults (Kumar et al., 2011).

5.2.9.2. Molecular Mechanics Assisted Model Building and Energy Refinements

A molecular mechanics conformational searching procedure was employed to acquire the data required in the statistical mechanics analysis using MM+ (a HyperChem modification) and AMBER, to obtain differential binding energies of a Polak-Ribiere algorithm, and to potentially permit application to polymer composite assemblies as described in Chapter 3, Section 3.3.12.3.

MMER was used as described in Chapter 3, Section 3.3.12.3.1 to provide information about the contributions of valence terms, noncovalent Coulombic terms, and noncovalent van der Waals interactions for polymer/ polymer interactions, employing Equations 3.5 and 3.6 to measure the total potential energies of the isolated and complexed systems. As discussed, ff the total potential energy of the complex is smaller than the sum of the potential energies of isolated individual molecules in the same conformation, the complexed form is more stable and its formation is favored (Yu et al., 2008).

5.3. Results and Discussion

5.3.1. Rheological analysis

The high molecular weight of HA solutions and its entangled coil formation renders them viscous with shear-thinning behavior. Rheology studies thus play a key role in evaluating the effect of crosslinking. Measurements on HA systems have been performed in steady shear mode or in oscillatory mode (Schante et al., 2011).

Initial rheological analysis revealed that the A:B SRHS demonstrated dilatant flow (Figure 5.3a). This gel fluid displayed an increasing viscosity with an increase in shear rate, therefore characterizing a dilatant fluid containing a high concentration (≥50%) of small, deflocculated particles (Marriott, 2008). In this instance, the polymer coil whose size is comparable in

solution to particle diameter creates a flexible bridge between two particles. When the particle and polymer concentrations are increased above a certain critical level, the suspension exhibits unique flow profiles exemplary of Newtonian viscosity at the zero shear rate limit, dilatant flow at moderate shear rates, and pseudoplastic flow at high shear rates. The existence of Newtonian viscosity is indicative of the quiescent constant formation, breakage, and re-formation of the polymer bridges, exemplifying a reversible adsorption-desorption process. An increase in shear rate causes rapid extension of the polymer coils, with restorative forces creating flow resistance. Dilatant flow arises due to bridge extension, with the network structure of unbounded flocs being a pertinent consideration. The percolation theory embodies this combinatory situation of extension of flexible bridges between particles and formation of a network structure (Otsubo, 1992).

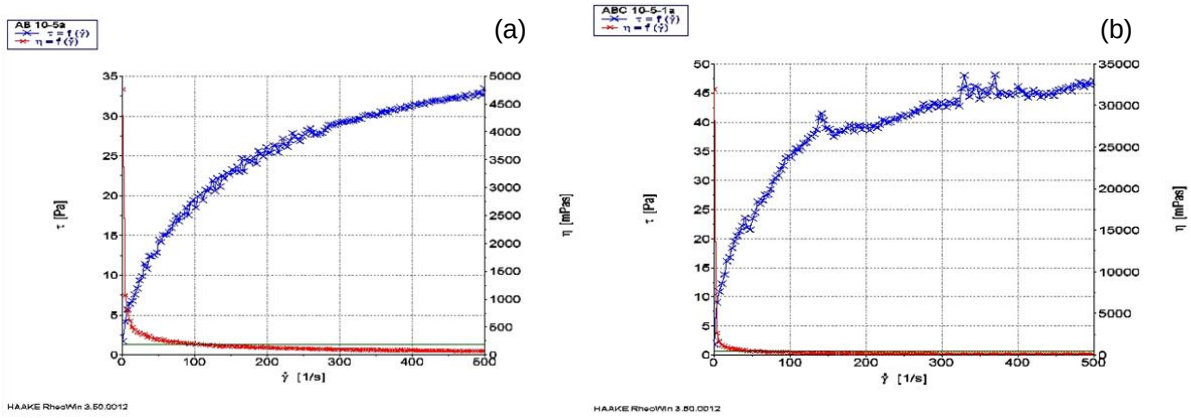

Figure 5.3: Initial rheograms depicting characteristic flow behavior of (a) A:B SRHS (10:5) and (b) A:B:C SRHS (10:5:1)

The A:C SRHS displayed uncharacteristic rheological flow and was therefore inconclusive in defining the flow type, due to inability to form a stable structure in the presence of the initiator solution yet absence of the cationic component (B). The A:B:C SRHS also demonstrated dilatant flow, with certain sharp increases in viscosity due to instigation of crosslinking between the polymeric solutions due to the presence of the initiator and migration of gluteraldehyde from A to B (Figure 5.3b).

The preliminary rheological analyses results are shown in Figure 5.4. Preliminary tests on the A:B:C combination displayed a yield stress average of 0.3288Pa. This is the minimum shear stress required for initiating flow. Ideal stress sweep test results should form a plateau before displaying a constant decline in *G'*, which is reminiscent of Figure 5.4b. Frequency sweep results show that *G'* is constantly greater than *G"* thus indicating that the material is transforming to the semisolid state (Figure 5.4c).

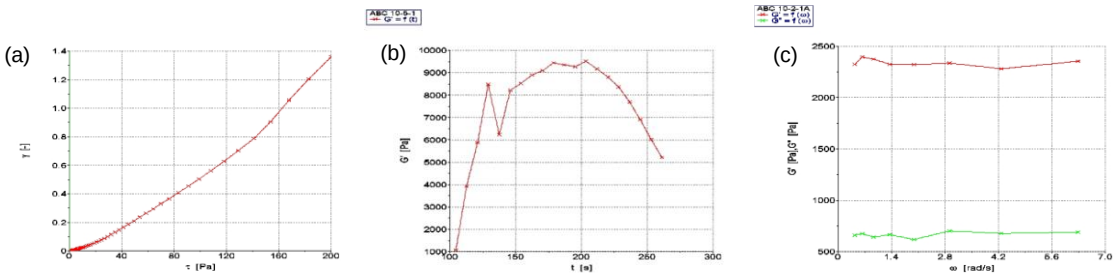

Figure 5.4: Preliminary (a) yield stress, (b) sweep stress, and (c) frequency results for the SRHS

The viscosity of both uncrosslinked and crosslinked HA gel are both dependent on the shear rate. However, in contrast, crosslinked HA gel exhibits a tendency to an increased dynamic viscosity even at low frequency.

With reference to the shear moduli, *G'>G"* at all times for the crosslinked gel. Zhao et al. (2002) also indicated that for double-crosslinked HA gels, *G'* is always greater than *G"*. For an uncrosslinked HA gel, there is generally a crossover at 1Hz, showing a viscous gel giving *G">G'* before this point and an elastic gel afterwards possessing *G'>G".*

In the preliminary rheological tests, the gel systems that displayed the best results were the outer and inner BPM SRHS (10:5), and the SRHS comprising of all three BPM components (10:5:1). These two solutions in their respective concentrations were employed to perform the rheological tests in response to simulated ocular inflammatory conditions and normal ocular physiological conditions. The frequency sweep test produced the most discerning results, thus frequency sweep tests were carried out as a time study of the BPM precursor solutions after exposing one set of the following solutions:

1. The outer and inner BPM SRHS (10:5)
2. A solution comprising of all three BPM components: the outer BPM: inner BPM solution: initiator solution SRHS (10:5:1)

To PBS (normal ocular physiological conditions) and another set to Fenton's Reagent (simulated ocular inflammatory conditions) for a period of 28 days. The frequency sweep tests were undertaken on days 0, 3, 7, 14, 21 and 28.

5.3.1.1. Oscillatory studies: Frequency sweep tests

Oscillatory shear experiments on crosslinked HA hydrogels enabled determination of the shear storage modulus (or elastic modulus), *G′*, and the shear loss modulus, *G″*, giving information on their viscoelastic characteristics. *G′* reflects the elasticity of the material whereas *G″* represents its viscous behavior. Barbucci et al. (2000) presented the results of

oscillatory shear experiments on HA solutions and the respective crosslinked gels. Unmodified HA solutions, being typical viscous liquids, display a *G″* higher than the elastic modulus *G′*, which simultaneously increase in a linear manner with. For HA hydrogels, the elastic modulus *G′* is higher than *G″*, and both moduli exhibit independence from the shear frequency, thus behaving as viscoelastic solids. Both forms of behavior were also demonstrated by Borzacchiello et al. (2010). According to Barbucci and co-workers (2000), these measurements enable differentiation between chemical hydrogels from entangled networks.

Results are reported in terms of the average loss tangent, where the loss tangent is the tangent of the phase angle - the ratio of viscous modulus to elastic modulus and a useful quantifier of the presence and extent of elasticity in a fluid, as per Equation 5.12. With a *tan* δ value of 1, the elastic (solid-like) and viscous (liquid-like) properties of the material are equal. The smaller the loss tangent is, the greater the elasticity of the material. *Tan* δ is often the most sensitive indicator of various molecular motions within the material. In general, the smaller the *tan* δ (or the greater *G'*), the stronger is the interaction.

$$tan\ \delta = \frac{G''}{G'} \qquad \text{[Equation 5.10]}$$

Exemplary rheograms obtained following oscillatory studies for the SRHS over 28 days under normal and inflammatory conditions, respectively, are presented in Figures 5.5 and 5.6. The rheograms obtained for the systems in Fenton's reagent were somewhat inconsistent possibly due to a more exacerbated degree of polymeric scission in randomized crosslinked zones.

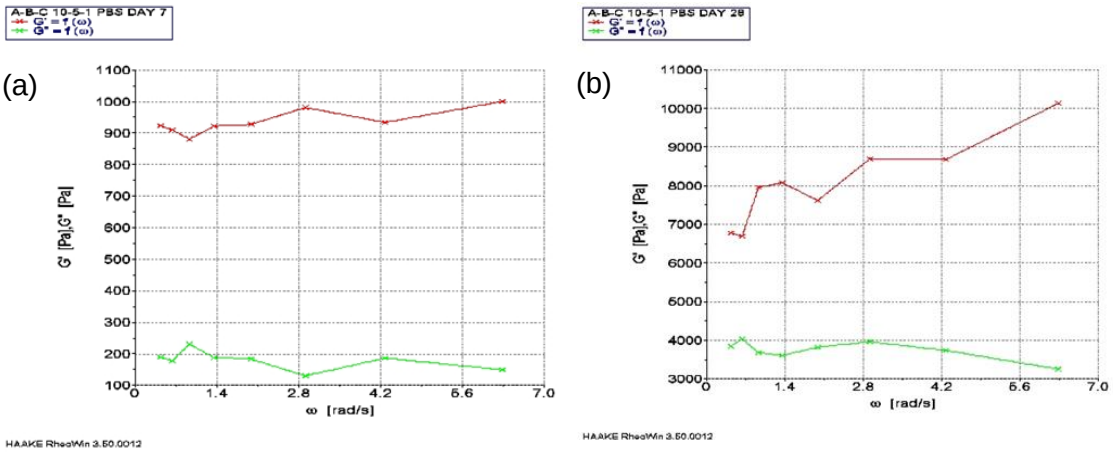

Figure 5.5: SRHS A:B:C following constant exposure to SVH on (a) day 7 and (b) day 28

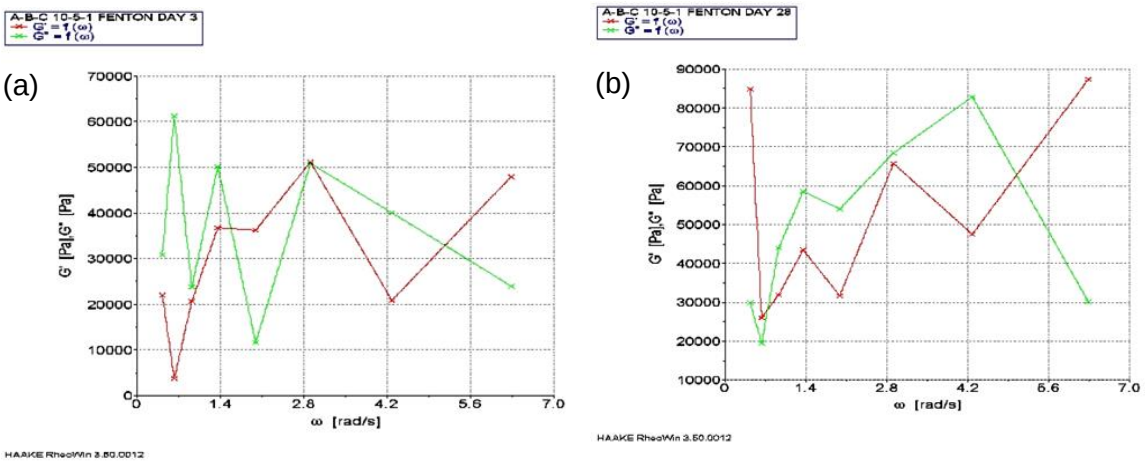

Figure 5.6: SRHS A:B:C following constant exposure to SVH + Fenton's Reagent on (a) day 3 and (b) day 28

It was noted from the results presented in Figure 5.7 that the SRHS of the inner and outer BPM (A:B), when exposed to PBS, displayed a loss tangent less than 1 throughout the study with a slight progressive increase in the loss tangent. Hence solid-like behavior predominated in the gel mixture, but a small degree of the structural integrity was lost.

The SRHS containing both the polymer mixtures as well as the initiator solution (A:B:C) displayed a lower average loss tangent with a progressive decrease in the loss tangent highlighting that enhanced solid-like performance prevailed when exposed to PBS (note Figure 5.7 and 5.9). The addition of the acidified $AlCl_3$ initiator solution, where the $AlCl_3$ serves as the catalyst for the Friedel-Crafts acylation interpolymeric coupling reaction, served to enhance the integrity of the interpolymeric system. This purportedly indicates that this polymeric system in which crosslinking is promoted would maintain good patency under normal (ocular) conditions.

Furthermore, Figure 5.7 depicts that both A:B and A:B:C displayed a progressive increase in the loss tangent, with the loss tangent exceeding 1 after only 3 days for A:B:C, thus liquid-like characteristics were observed and prevailed for the precursor BPM solutions, specifically where crosslinking was initiated, when exposed to inflammatory conditions. The interaction between the functional groups was disrupted in the Fenton's Reagent as compared with the PBS, as highlighted by the respective regression curves. The decreased interactions between the multipolymeric functional groups would purportedly facilitate enhanced erosion of the final BPMs under inflammatory conditions compared to normal conditions, fulfilling the purpose of inflammation-responsiveness.

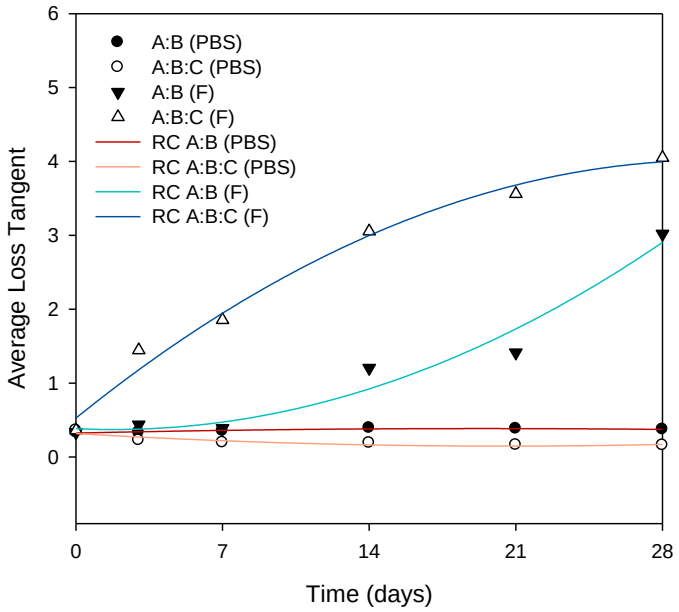

Figure 5.7: Frequency sweep results in constant normal or pathological media for the precursor SRHS combinations with associated regression curves (RC)

Both A:B and A:B:C exhibited stimulus-responsive rheological behavior on exposure to and removal of the inflammatory environment. The average loss tangent was highest when exposed to Fenton's reagent on day 7, specifically for A:B:C, with liquid-like characteristics predominating (Figure 5.8). In the presence of Fenton's Reagent, the solution displayed average loss tangent values of greater than 1. It can therefore be assumed that in response to inflammation, interpolymeric interactions are decreased and the overall system elasticity is reduced. This may be advantageous in allowing for surface erosion and hence the release of drug. Rheological synergism was observed in A:B:C, that is, the propensity to demonstrate gel-like properties when mixed, which is in excess of the original components (Hoare and Kohane, 2008), and confirms the computationally modeled molecular synergism described in Chapter 4. This synergism is typically a result of hydrogen bonding interactions between the polymer chains facilitated by the compatible geometries of the interacting polymers (Tammi et al., 2002).

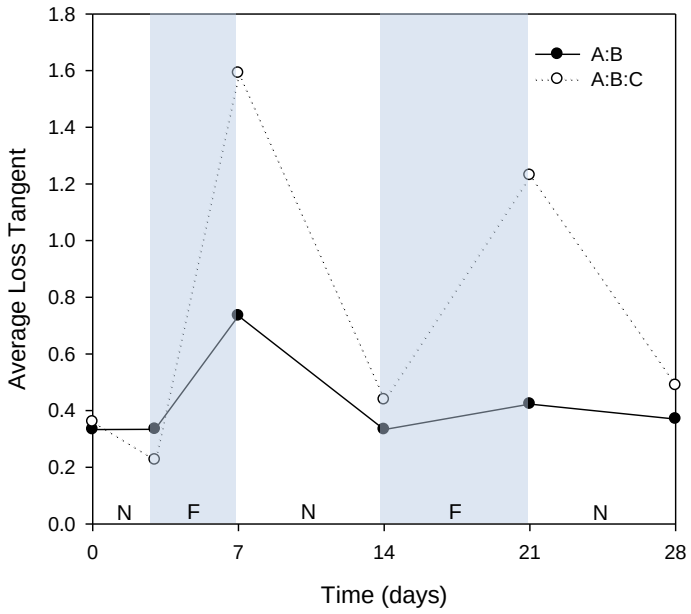

Figure 5.8: Frequency sweep results in alternating normal vs. pathological media for the precursor SRHS combinations. Note: A:B (outer: inner BPM SRHS) = 1mL: 0.5mL; A:B:C (outer BPM: inner BPM: initiator solution) = 1mL: 0.5mL: 0.1mL. N = normal conditions in SVH, F = pathological conditions with Fenton's reagent in SVH

5.3.2. Characterization of vibrational transitions by Fourier Transform Infrared Spectroscopy

In elaborating on the vibrational transitions evidenced within the I^3, it is of importance to expound on the underlying mechanisms of the proposed interactions that could occur within and between the incorporated polymers on fabrication of the device. In the outer BPM, essentially an environment was created for introducing side chains into HA (with participation of alginate and PAA) by carbodiimide-mediated coupling of primary or secondary amines to the carboxyl group of the glucuronic acid moiety employing an active ester intermediate.

With carbodiimides, crosslinking ensues via the initial formation of an anhydride on the polysaccharide, through reaction with neighboring carboxyl groups. The resulting anhydride subsequently reacts with proximate hydroxyls emanating in both inter- and intramolecular crosslinks. It has been postulated that crosslinking takes place via ester groups (Figure 5.9). The inclusion of NHS in this reaction serves to increase yields and decrease side reactions (Collins and Birkinshaw, 2007).

Scheme A

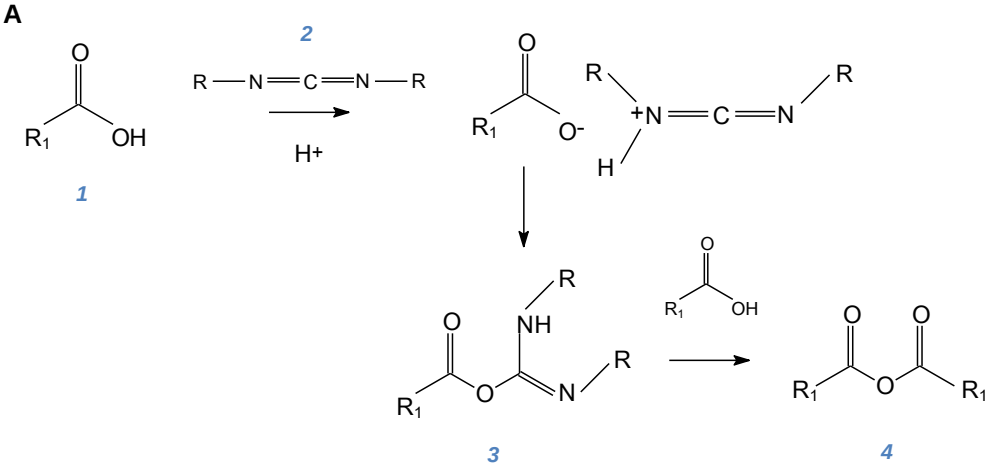

Scheme B

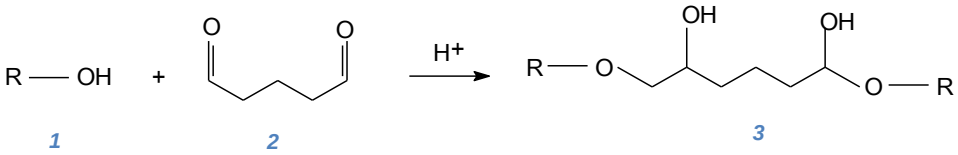

Figure 5.9: Proposed interactions of HA and other polymers with the chemical crosslinkers employed in I^3 fabrication. Scheme A: In the presence of carbodiimides (2) the crosslinking occurs through the formation of O-acylisourea (3) on the polysaccharide, through reaction with neighboring hydroxyl groups (1) an anhydride (4) is formed, and this anhydride then reacts with nearby hydroxyl groups to give both inter and intramolecular crosslinks. Scheme B: In the acidic conditions created, the OH (1) group on HA reacts with gluteraldehyde (2) to give hemiacetal or ether crosslinks (3) (adapted from Collins and Birkinshaw, 2007).

This reaction is similarly reported for alginate: the water-soluble carbodiimide catalyzes the formation of amide bonds between carboxylic acids and amines through activation of the carboxylate to form an unstable *O*-acylisourea intermediate, which undergoes rapid hydrolysis. Success of the procedure requires that the active form of alginate carboxyls are more stable than the *O*-acylisourea derivative. Such a condition was fulfilled by employing active esters, such as NHS (Polyak et al., 2004).

Gluteraldehyde was also included in the reaction system and is proposed to diffuse throughout the precursor implant matrix to initiate crosslinking of the inner and outer BPM. Dialdehydes are proposed to form crosslinks via formation of acetal and hemiacetal groups on neighboring chains, with the hemiacetal prevailing. Gluteraldehyde is believed to form either a hemiacetal or an ether link with HA under acidic conditions (Collins and Birkinshaw, 2007). Slow degradation of HA crosslinked by gluteraldehyde has been attributed to resistance of the hemiacetal bond (Tomihata and Ikada, 2000).

Furthermore, in the outer BPM, there exists the polymeric combination of HA, alginate and PAA, which exhibit multiple, often regularly spaced, carboxylic acid groups. Moreover, the amide groups of HA provide additional interaction possibilities. The blending of these polymers, with consequent undertaking of the crosslinking chemistries described herein, offers a complex new dimension for elaborating a chemically-modified polymeric matrix. The gel-forming properties of alginate enhances HA hydrogel formation in a blended material (Prestwich, 2001). Inclusion of the synthetic PAA affords the propensity to yield a stable composite material/ interpenetrating molecular network that features the desired properties of the individual polymers (which is already reported in the absence of chemical crosslinking). Blends of HA/ PAA sponges prepared by lyophilization of the blended aqueous polymers and crosslinking them at 130°C *in vacuo* have been reported (Prestwich, 2001).

With regard to inclusion of the phospholipid component in the NS assemblage, FTIR is a proven approach for monitoring lipid phase behavior. FTIR has application in monitoring subtle changes in the structure and function of the lipid assemblies through analysis of the frequency or the bandwidth changes of the different vibration modes representative of the acyl chains, the interfacial region and the head group region of lipid molecules. The information that can be obtained from frequency shifts in different regions of corresponding bands provides information about diverse physicochemical processes taking place within the NS (Lewis and McElhaney, 2002). An elevation in disorder in hydrocarbon chain conformation causes symmetric and asymmetric stretching vibrations of lipid hydrocarbon chains, and is visualized as increases in the frequencies of infrared absorption bands. This could indicate a poorly-formed NS. With respect to the inner crosslinked chitosan core, gluteraldehyde is anticipated to migrate into the chitosan-rich epicentre. The crosslinking of chitosan by gluteraldehyde has been described (Kildeeva et al., 2009). The reaction of the amino groups of chitosan with gluteraldehyde proceeds by a complicated mechanism, which involves the formation of chitosan derivatives containing unsaturated oligomeric products of the aldol condensation of gluteraldehyde capable of reacting further not only with each other, but also with the amino groups of chitosan after the completion of gel formation. Chitosan catalyzes the polymerization of gluteraldehyde to form irregular products (Figure 5.10), with the length of oligomeric chains in modified or crosslinked chitosan and the concentration of coupled bonds N=CHCH=C< and O=CHCH=C< being dependent on the conditions under which the process is conducted (the concentration of gluteraldehyde and pH of the reaction medium). This fact should be taken into consideration for the reaction of chitosan with gluteraldehyde in the creation of a drug delivery system for medicobiological applications (Kildeeva et al., 2009). Demonstration of sufficient crosslinking of the chitosan core is pertinent for ensuring adequate enclathration of the NS into the polymeric superlattice, onto

which adsorption of the long chitosan chains has occurred, within the inner BPM (see Chapter 3, Section 3.4.3). On exposure to hydroxyl radicals, there would be responsive hydrolysis of the formed lattice-like structure entrapping the NS.

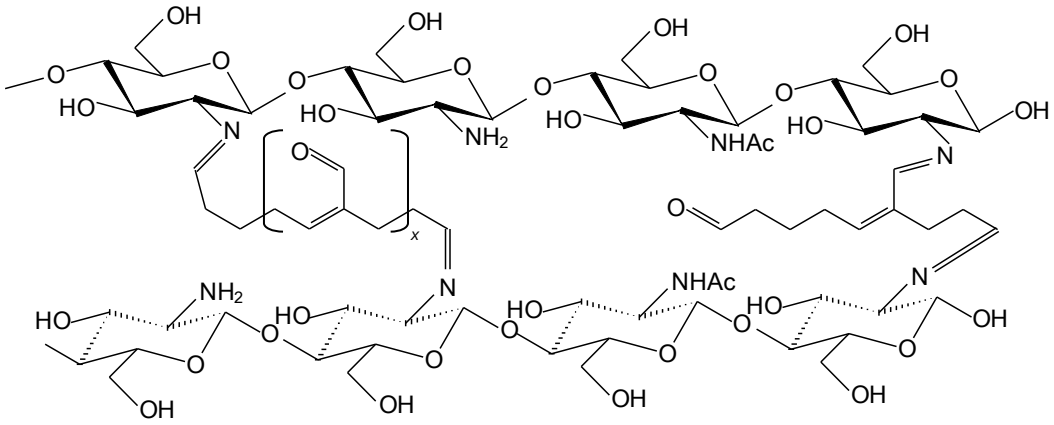

Figure 5.10: Structures of the products of reaction of chitosan and gluteraldehyde (adapted from Kildeeva et al., 2009)

At the interface of the inner and outer BPM polyanion/ polycation convergence is encountered. Chitosan is a polycationic polysaccharide in acidic medium (pKa 6.5) and is reported to form a complex with negatively charged moieties such as sodium carboxymethylcellulose, citrates, pectin, acacia, agar, sodium caprylate, stearic acid, gluteraldehyde, sodium tri-polyphosphate, lactic acid, malic acid, alginate and HA. These chitosan complexes are insoluble in alkaline buffer (Tiwary and Rana, 2010).

During fabrication of the I^3, simultaneous formation of the inner and outer BPM is anticipated due to an immediate interface originating between the outer polyanionic polymeric solution and the inner cationic solution. There is polymeric entanglement at the interface and a membrane is formed instantaneously between the counter-ionic constituent polymer solutions, leading to a patent network forming at the interface, preventing further diffusion of chitosan molecules into the outer matrix (Gaserod et al., 2008). Ionized $-NH^{3+}$ groups on the chitosan backbone (availed in the presence of chemical crosslinkers) are anticipated to interact with ionized –COO- groups on the backbones of the three anionic polymers (Ma et al., 2012). The ionic interaction is depicted in Figure 5.11 (Ravi Kumar, 2000).

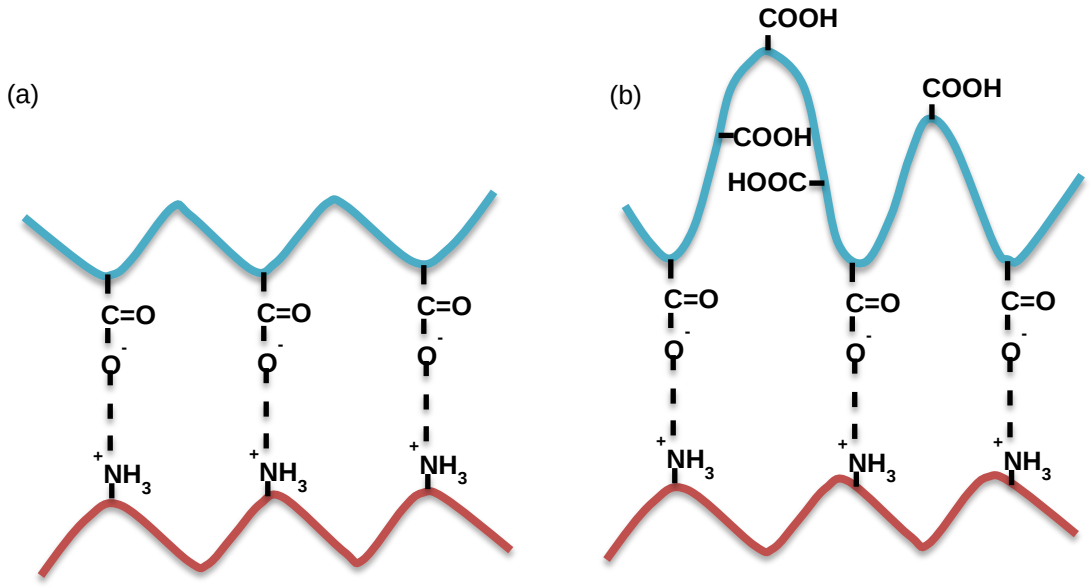

Figure 5.11: Schematic representation of the ionic interactions between the polyanions and chitosan at (a) higher pH ~5.4 and (b) lower pH ~2.0 (adapted from Ravi Kumar, 2000)

5.3.2.1. Chemical transitions of the nanosystem, inner and outer BPM, and BPM interface

FTIR studies confirmed the appropriate loading of indomethacin into the NS (as evidenced in the Lipo-Chit-PCL NS). As expected, two main characteristic C=O bands (Figure 5.12) were observed for crystalline indomethacin at 1691 and 1729cm^{-1}, and assigned to the aliphatic and aromatic carbonyl stretching bands, respectively (Rusu et al., 1998). The amino-glucose architecture of chitosan comprises a small proportion of amide groups connected via an amide linkage with acetic acid. In the IR spectrum, pure chitosan exhibited a broad peak at 3431cm^{-1}, representative of the N-H and hydrogen-bonded O-H stretch vibrational frequencies; whereas a sharp (shoulder) peak at 3610cm^{-1} highlights the stretching of the free O-H bond of glucopyranose units. Further, in the C-H stretch region of the spectrum, the higher intensity peak at 2923cm^{-1} is assigned to the asymmetric mode and the lower intensity peak at 2857cm^{-1} is assigned to the symmetric mode of CH_2 stretching. Pure chitosan also shows a distinct amide I and amide II band at 1662 and 1554cm^{-1}, respectively (Kolhe and Kannan, 2002; Gong et al., 2006). In addition, it also possesses a characteristic band due to CH_2 scissoring, which usually occurs at 1465cm^{-1}. Peaks at ~1100cm^{-1} signify the aliphatic amino group. In PCL, the peaks at 2929 and 1729cm^{-1} represent the characteristic peaks for C-H and ester carbonyl groups, respectively (Sarmila et al., 2009).

Distinctive shifts in the molecular transitions were observed. The FTIR band of indomethacin at 1729cm^{-1} appeared to shift to a lower wavenumber of 1725cm^{-1}, possibly indicative of the interaction of its carbonyl with the amino group of chitosan. The band representative of the carbonyl group of PCL was shifted to higher wavenumbers at 1748cm^{-1}, visualized as a composite peak with the characteristic indomethacin peaks, as well as a band at 1618cm^{-1} attributable to the hydrogen-bonded carbonyl groups with hydrogen-donating groups (-OH and -NH_2) of chitosan (Figure 5.12). Combinations of chitosan and PCL have previously shown a shift in the O-H stretching to the lower frequency side and a sharp peak at 3437cm^{-1} (Sahoo et al., 2010). The peak at 1166cm^{-1} is due to the C-O-C group. Furthermore, the Chit-PCL interaction occurence in the NS produced peaks between 3200 and 3700cm^{-1}, which were further increased in intensity due to incorporation of the NS into the inner BPM due to the overwhelming presence of chitosan.

For the NS, the general stability and slight decrease in intensity of the absorption bands between 2800-3000cm^{-1} could exemplify formation of a fairly stable composite structure. The absorption bands of the ester C=O are sensitive to changes in the polarity of their local environments and hydrogen bonding and other interactions have a disctinct influence. Therefore, changes in the contours of the ester C=O absorption band could be associated with structural and/or hydrational changes of the bilayer polar/apolar interface. Although not clearly evident in the NS due to its overall complexity, a change in the contour of the C=O band is detectable for the NS compared to native DSPC (Cong et al., 2009). The CH_2 scissoring and lipid carbonyl stretching modes of DSPC are visible at 1462cm^{-1} and 1734cm^{-1} respectively, confirming the presence of the lipid bilayer (Tamm and Tatulian, 1997). The shifts in peaks observed may thus also be attributed to the formation of hydrogen bonds, or weak van der Waals forces or dipole moments amongst the polar functional groups of the indomethacin, phospholipids moieties and polymers. These interactions may favor the formation of a vesicular shape, stability of the structure, and slower drug release (Layek and Mukherjee, 2010).

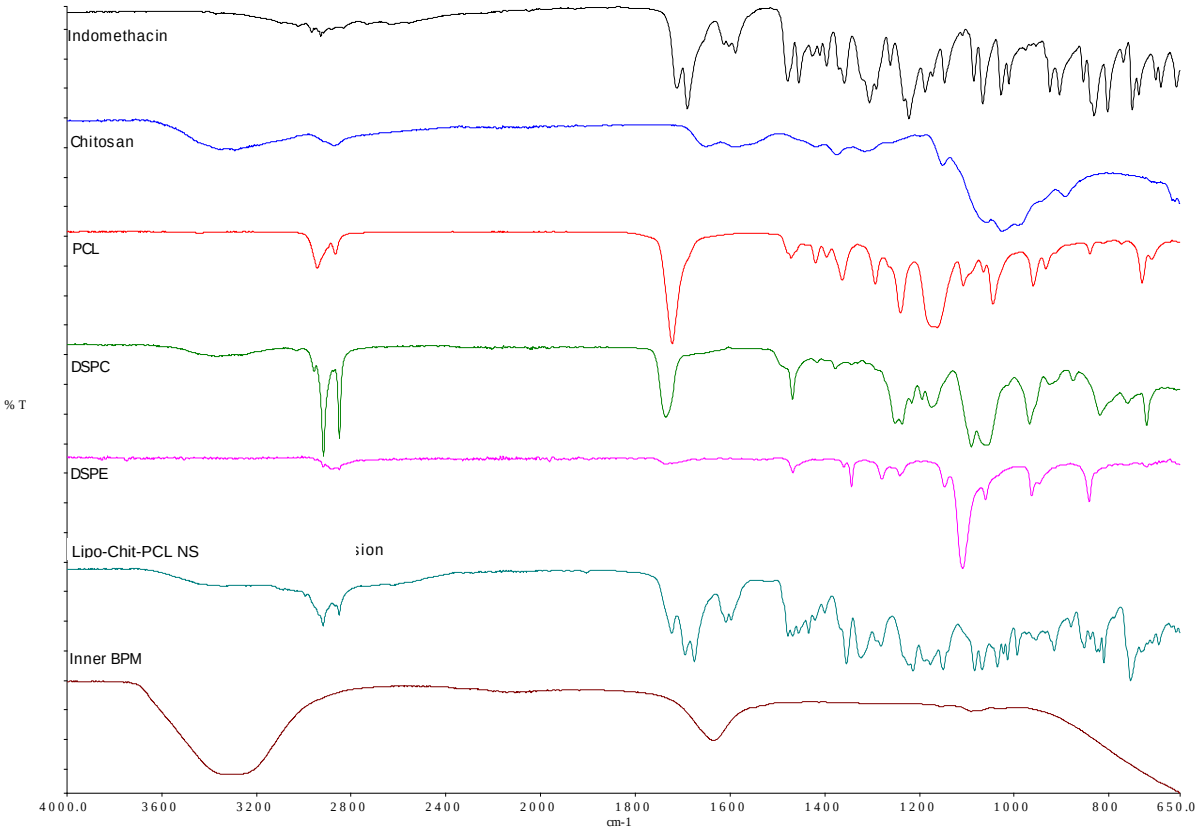

Figure 5.12: FTIR spectra of the native drug, polymers, phospholipids, and the resultant NS, which was ultimately embedded in the inner BPM

The observed chemical transitions for the outer BPM and inner BPM are compared in Figure 5.13a and elaborated for the outer BPM in Figure 5.13b. The final crosslinked BPMs showed the presence of bands inherent to all its components, with a reduction in intensity of selected bands and the appearance of new bands, attributable to the intra- and intermolecular crosslinking instigated in the presence of the chemical crosslinkers and initiators, namely DCC and NHS in the outer core and gluteraldehyde in the inner core, all of which migrate throughout the device during its formation. The resultant FTIR spectrum is a predictor of the type of bond formed during the polymeric crosslinking, with specific reference to HA. The additional band at 2934cm^{-1} points to the presence of additional alkyl chains on HA, alginate and PAA corresponding to -CH and -CH_2 vibrations (Mlčochová et al., 2006), introduced in the presence of DCC and NHS, as proposed in Figure 5.9. This could indicate both intramolecular and intermolecular crosslinking within the polyanions themselves, as well as between HA, alginate, and PAA. The participation of alginate and PAA in forming an intricately crosslinked structure is evident by the appearance of bands at 1628cm^{-1} and 1159cm^{-1} reminiscent of the ester functionality, being a pertinent indicator of intra- and intermolecular crosslink formation. Summative bond designations are proposed in Table 5.6.

An interpenetrating network at the site of conversion at the inner and outer BPM is anticipated to form between the cationic chitosan amino groups and the anionic alginate, HA and PAA carboxylic groups, potentially disrupting any hydrogen bonding already present between amino groups and hydroxyl groups in chitosan and elaborating an amorphous structure. Even though the inner and outer BPM are evident as separate entities, there is integration of chitosan into the outer BPM at the boundary and the crosslinking interaction between these entities is visualized in the FTIR spectrum of the outer BPM. The occurrence of a new band at 3232cm^{-1} is representative of ionization of amine groups. This corresponds with a comparative increase in intensity in the peak at 1650cm^{-1}, indicating the carbonyl group of amides. The increase in intensity of the peak at 1630-1650cm^{-1} are characteristic of the C=N group, which confirms the formation of Schiff's linkage, corresponding to ionic interactions between chitosan and the polyanions such as HA (Magnani et al., 2000).

With regard to the inner BPM, previous reports have shown that most substantial changes in the spectra of crosslinked chitosan occur in the absorption region of CH_2 groups (3000-2800cm^{-1}) and aldehyde, amide, and amino groups (1700-1300cm^{-1}) (Beppu et al., 2007; Kildeeva et al., 2009). The presence of the azomethin group in the product of reaction of chitosan with gluteraldehyde is easiest to follow from the peak of valence vibrations of the C=N bond which appears in the region of 1680-1620cm^{-1}. These products appear during the crosslinking of chitosan. The formation of the aldimine bond activates the added gluteraldehyde molecule and accelerates the elongation of the oligomeric chain of gluteraldehyde on chitosan. This is evidenced by the appearance of a band of valence vibrations of aldehyde groups in the IR spectra of the products of the reaction of chitosan and gluteraldehyde at ~1706cm^{-1}. Further transformations with the formation of the already crosslinked product can occur through the condensation of the amino groups of chitosan with the carbonyl groups of modified chitosan, or through the aldol reaction and condensation of oligomeric chains of modified chitosan with the formation of the products.

Comparison of the IR spectra of pristine and glutaraldehyde-crosslinked chitosan revealed significant transitions. The crosslinking of chitosan membranes with glutaraldehyde shows that an increase in the absorption at ~1655cm^{-1} is seen due to imine bonds (N=C). The slight shoulder at 1720cm^{-1} is due to free-aldehydic bonds. There is a high intensity broad peak extending from 3500 to 2900cm^{-1}, which could be attributed to the N-H and hydrogen bonded O-H stretch vibrational frequencies (at 3431cm^{-1} in pure chitosan) and an increase in the intensity of the C-H stretch increase at ~2936 cm^{-1}. The increase in the number of methylene groups in the products of condensation of chitosan and gluteraldehyde is known to manifest itself as changes in the ratio of band intensities in the region of 3000-2800cm^{-1}

(Kildeeva et al., 2009). The intensity of the peak at ~1100 cm^{-1} attributed to the presence of the aliphatic amino group is decreased drastically in the crosslinked BPM compared to native chitosan. This change pertinently highlights that the crosslinking with glutaraldehyde transforms the membrane to a more hydrophobic form as amino groups are blocked with aliphatic chains (Beppu et al., 2007). Summations inferred of polymeric interactions from FTIR would ultimately be corroborated via molecular modeling as reported in Section 5.3.9.

Table 5.6: Bond designations for the outer crosslinked BPM

Bond	Type of bond	Specific type of bond	Absorption peak	Appearance
C-H	Alkyl	Methyl	2930-2960	Medium to strong
C=O	carboxylic acids/derivates	saturated carboxylic acids	1710 cm^{-1}	
	carboxylic acids/derivates alcohols, phenols	Amides carboxylates (salts)	1650 cm^{-1} 1550-1610cm^{-1}	
	carboxylic acids primary amines	amino acid zwitterions high concentration amino acid zwitterions	1550-1610cm^{-1} 3200-3400cm^{-1} 1560-1640cm^{-1}	Broad Strong multiple broad peaks
O-H	secondary amines ammonium ions	Any	2400-3200cm^{-1}	Medium
	Alcohols	Tertiary Any	1150-1200cm^{-1} 1200cm^{-1}	
N-H	primary amines	Tertiary	1120cm^{-1}	
	phenols	Any aliphatic aromatic	1220-1260cm^{-1}	Two bands (distinct from ketones, which do not possess a C-O bond)
	Ethers	Any	1250-1300cm^{-1}	Often overlapped
	ammonium ions	Any	1100-1300cm^{-1}	Similar conjugation effects to C=O
C-O	carboxylic acids	Any	1020-1220cm^{-1}	
	esters aliphatic amines	Any	1615-1700cm^{-1}	

(a)

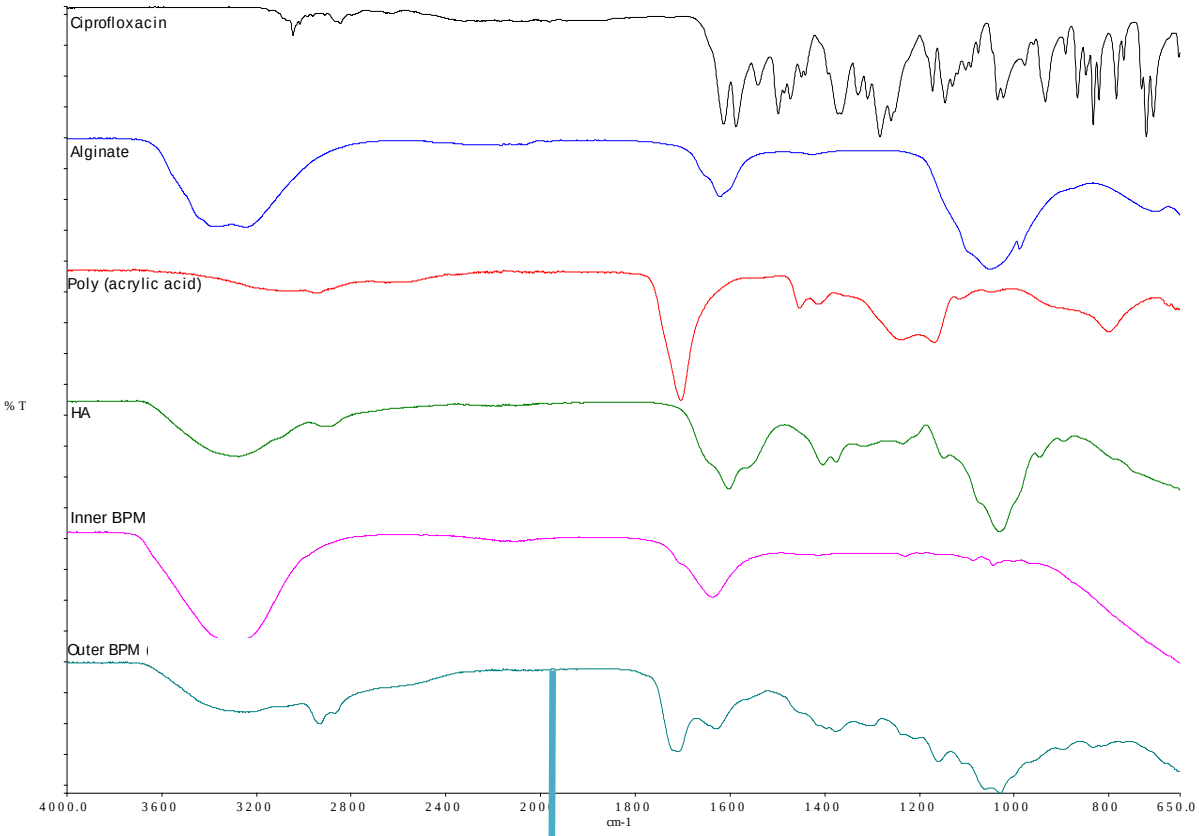

(b)

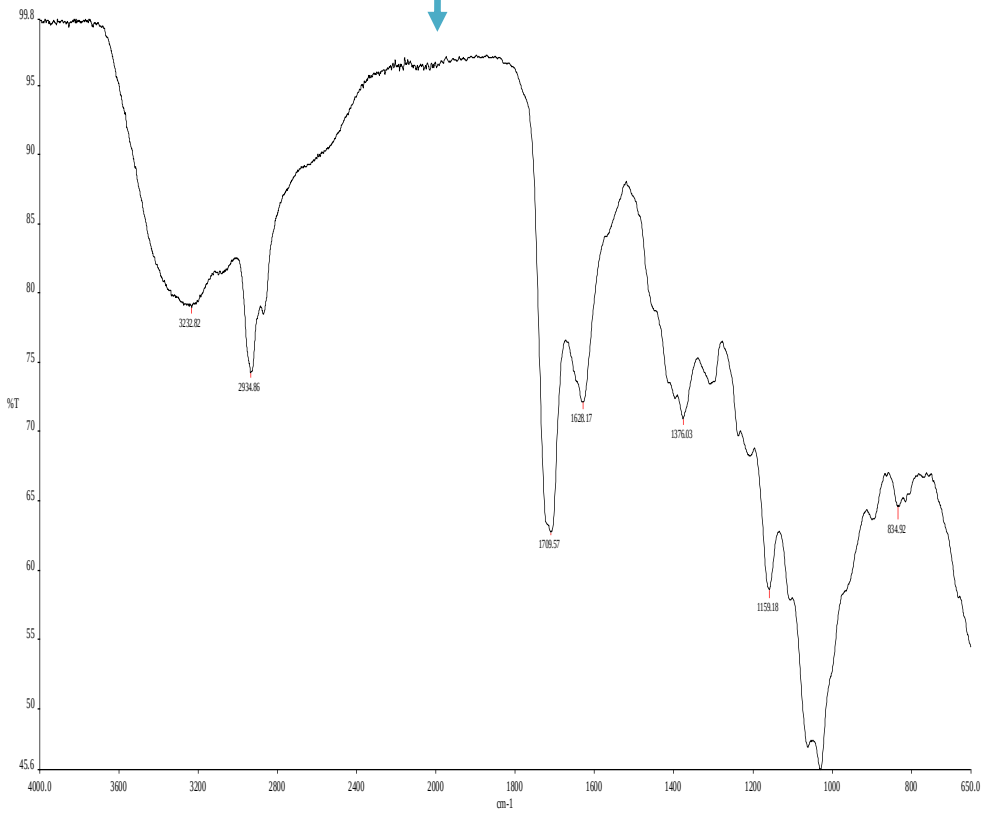

Figure 5.13: (a) Comparative FTIR spectra of the native polymers, inner BPM, and outer BPM (b) Expansive FTIR spectrum of the crosslinked outer BPM

5.3.3. Thermal analysis of the I^3

DSC is a pivotal technique for characterizing the thermal behavior of HA hydrogels in native and unmodified forms, furnishing information on their hydration properties (Collins and Birkinshaw, 2008). The DSC thermogram of native HA presented by Luo et al. (2000) highlights a broad endothermic peak at 89.5°C and two sharp exothermic peaks at 243.6 and 258.7°C, indicative of the crystalline nature of HA. The peaks above 300°C correspond to HA decomposition. Crosslinked HA is amorphous and the thermogram would no longer indicate an exothermic peak.

The thermal intricacies of the constituent polymers as well as the crosslinked multipolymeric I^3 were investigated by conventional DSC over a wide temperature range; and subsequently via TMDSC over a more focused temperature range with peak integration at significant thermal events (such as the T_g) to quantify the change in enthalpy (ΔH) and change in specific heat capacity (ΔC_p) at these points (Table 5.7). The corresponding conventional and modulated DSC thermograms are provided in Figures 5.14 and 5.15. In the case of conventional DSC analysis of the I^3, multi-transitional thermal behaviors were evidenced which were indistinguishable as T_g, T_m or T_c transitions, evidenced by diverse temperature inflection peaks that were attributed to the existence of reversing and non-reversing endothermic signals. The notable shift in glass transition in the crosslinked inner and outer BPMs of the I^3 compared to the native polymeric components is clearly apparent, as is the dramatic change in enthalpy and ultimately heat capacity (Figure 5.15b and c; Table 5.9).

Table 5.7: Critical thermal events as evidenced by conventional and temperature-modulated DSC

Sample	Critical Temperature Transition Points (^oC)					
	T_g			T_m		
	DSC	*ADSC*	*Ref*	*DSC*	*ADSC*	*Ref*
Indomethacin				162.06		158 (DrugBank, 2008)
Ciprofloxacin				258.50		255-257 (DrugBank, 2008)
Alginate	125.84	93.10	95-136 (Roger et al., 2004)	-	-	
Chitosan	128	208.04	140-150 (Dong et al., 2003), 203 (Sakurai et al., 2000)		268.59 (degradation)	Chitosan undergoes thermal degradation at 270 °C prior to melting (Sarasam et al., 2005)
HA	76	73.92	80 (Yadav et al., 2007)		{200.57 (T_c)}, 218.83	Crystallization peak prior to melting, 239.1 °C Ma et al. (2012)
PAA	108	145	106 (Chan and Chu, 2001), 130-140 °C, (Kanis et al., 2000).	258		
Outer BPM		188.84				
Inner BPM		217.69				

5.3.3.1. Conventional Differential Scanning Calorimetry for delineating primary thermal events

The following observations were inferred from the conventional DSC curves, as represented in Table 5.8. These critical thermal transitions were compared with those elucidated via TMDSC.

- The melting points of the drugs fell within the reported ranges.
- Alginate exhibited a T_g at 125.84^{o}C. No melting point signal was observed, as confirmed by Miura et al. (1999).
- The T_g observed for chitosan (128^{o}C) was comparable to the reported values.
- The T_g of HA was observed at 76^{o}C while its T_m was 107.32^{o}C.
- PAA had a T_g of 108^{o}C and a T_m of 258^{o}C.
- The outer BPM exhibited three indiscriminate endothermic peaks at 104.87^{o}C, 180.76^{o}C, and 220.56^{o}C.
- The inner BPM exhibited indiscriminate peaks at 219.7^{o}C and 249.2^{o}C.

Being a complex multipolymeric sequentially crosslinked device, it is not possible to differentiate the exact T_g of the inner and outer BPMs from analysis of the conventional DSC curves. TMDSC thus held a significant role in this regard.

5.3.3.2. Thermal Modulated Differential Scanning Calorimetry for further elaboration of the thermal events

TMDSC was further employed on all samples to provide thermochemical data on the various polymers and the implant that cannot be provided by conventional DSC. All samples were subjected to an initial run prior to analysis in order to remove any residual water. Curvature and baseline slopes were reduced, hence increasing the sensitivity to obtain more precise peaks. Events such as molecular relaxation and glass transitions could be differentiated to a greater extent. The multi-transitional thermal behaviors noted for the I^3 was potentially due to the significant contribution of inter- and intramolecular/ polymeric crosslinking, which conclusively impacted on the unique release capabilities of the device (Bhattarai et al., 2009). Intra- and intermolecular bond establishment was a result of disruption of initial bonds within the native polymers, with subsequent random alignment and new chemical bond formation in the presence of chemical crosslinkers and initiators that ultimately emanates in an intricately crosslinked structure.

The reversing peak emphatically reveals the T_g, and the non-reversing and total heat flow curves depicts the melting point and crystallization peaks. It is known that melting is an endothermic reaction and the peaks show a downward curve displacement, whereas crystallization is an exothermic reaction; hence the peaks display an upward curve displacement (Mettler Toledo, 2010). Furthermore, as evidenced from Figures 5.14 and 5.15, a phase angle (in radiums, rad) between the ADSC signal and the heating rate is created. The averaged ADSC signal yields the total heat flow, corresponding to the outcome of a conventional DSC experiment run at the underlying heating rate. The phase angle enables calculation of the in-phase and out-of-phase components of the complex heat capacity. The in-phase heat capacity then enables computation of the reversing heat flow, which allows determination of the non-reversing heat flow from the difference between the average or total heat flow and the reversing heat flow.

The following additional thermal transitions were further elaborated via TMDSC:

- For alginate, a T_m of 93.10^{o}C was deduced. The reversing curve did not reveal any distinctive T_g.

- A T_g of 208.04^{o}C was integrated for chitosan. Chitosan undergoes thermal degradation, observed at 268.59°C prior to melting, correlating with previous investigations (Sarasam et al., 2005).
- With respect to HA, the exothermic peak at 200.57^{o}C highlights the point of crystallization, prior to melting of the HA crystal at 218.83, which was slightly lower than the observations of Ma et al. (2012).
- A distinctive endotherm highlights the T_m of NHS at 98^{o}C.
- A T_g of 145^{o}C was apparent on the reversing curve of PAA
- For the outer BPM, a broad endotherm was observed, which following integration of the peak revealed a T_g of 188.84 ^{o}C
- With reference to the inner BPM, an endothermic peak at 217.69^{o}C represents the T_g of the system.

The wide temperature range employed for conventional DSC enabled detection of moisture loss remaining after the initial drying process. Essentially the greater degree of crosslinking in the implant would reflect lower water retention through the drying period. The reason may be that as molecular level complexes were formed, the powerful interaction of the polycation and polyanions prevented the multipolymeric network from combining with water. Essentially, crosslinking increases the hydrophobicity of the polymers implicated. The broad range also saw detection of sharp exothermic peaks at higher temperatures. Crosslinking affects the magnitude of the exothermic peaks. Where two peaks are evident, they represent, firstly, conversion into a less ordered state, and secondly, thermal degradation (Collins and Birkinshaw, 2008). It also emanates in shifts of the endothermic and exothermic peaks, generally to higher temperatures (Collins and Birkinshaw, 2007). Thus more energy was required to remove residual water adsorbed within the I^3, and less energy was released by breaking ionic interactions and during I^3 thermal decomposition.

Overall, there was a significant shift in the T_g in the I^3, represented as the outer and inner BPM, compared to the native components. This is a consequent predictor of the numerically predicted low molecular weight between crosslinks, relationally ascribed to each polymeric contributor, as provided in Table 5.8. Simply, this was further redolent of a highly crosslinked structure, even with regard to chitosan which already has a high T_g. The difference in ΔH at the glass transitions for each polymer compared to the I^3 was also calculated - the larger the difference, the more energy required to induce thermal transitions i.e. metamorphosis from a glassy to rubbery state, melting and ultimately thermal degradation, which was clearly the case for the multipolymeric device compared to its polymeric constituents.

Table 5.8: Thermodynamically-derived data for the I^3 (as the inner and outer BPM) compared to the native polymeric components

Relational Polymer	T_g-T_{g0}/ T_g (%)	M_c (gmol^{-1})	Difference in ΔH (Jg^{-1})
*Outer BPM**			
Alginate	95.74	407.35	101
HA	109.25	356.98	35.75
PAA	43.84	889.60	50.58
*Inner BPM***			
Chitosan	9.65	4041.45	-35.59

Compared to outer BPM thermal data
****Compared to inner BPM thermal data***

Intricate crosslinking within the I^3 essentially decreases the crystallinity of the device compared to the native polymers, such that the melting endotherms become vanishingly small and difficult to estimate exactly.

With reference to the structural integrity of the device, it would be unlikely to observe a disruption of the structure of the crosslinked device into its polymeric constituents over the scanned temperature range, specifically if an appreciable amount of covalent bonds are established, which are irreversible. Chemical alterations of the structure necessitated higher energy levels represented by an endotherm at greater temperatures.

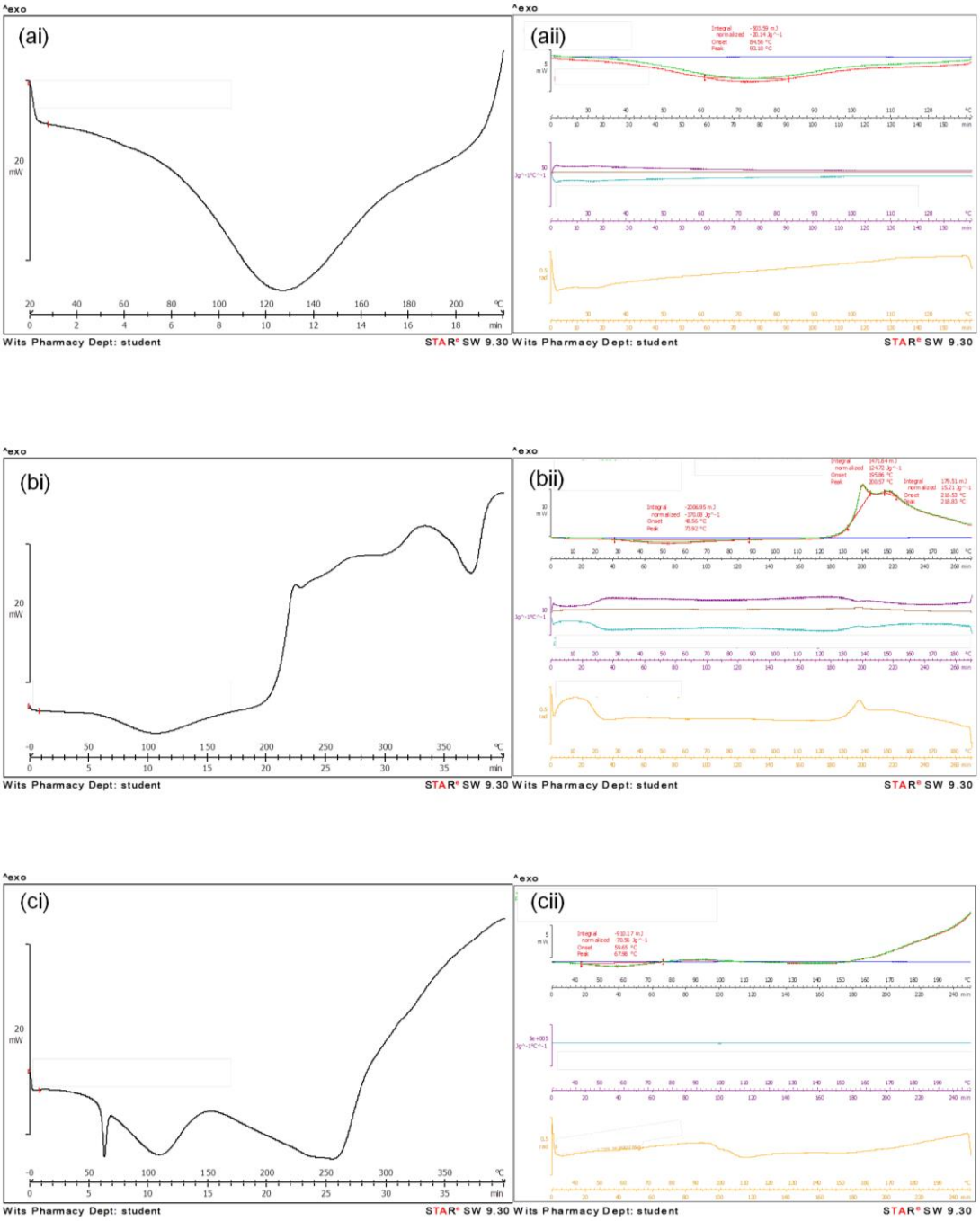

Figure 5.14: (i) Conventional and (ii) TMDSC thermograms for (a) alginate (b) HA and (c) PAA showing transition temperatures, transition enthalpies, and transition heat capacities elaborated via the reversing (dark blue), non-reversing (green) and total heat flow (red) curves; the C_p complex (purple) comprising the C_p in-phase (brown) and C_p out-of-phase (light blue) (see Equations 5.2 and 5.3); and the phase angle, ϕ, (orange)

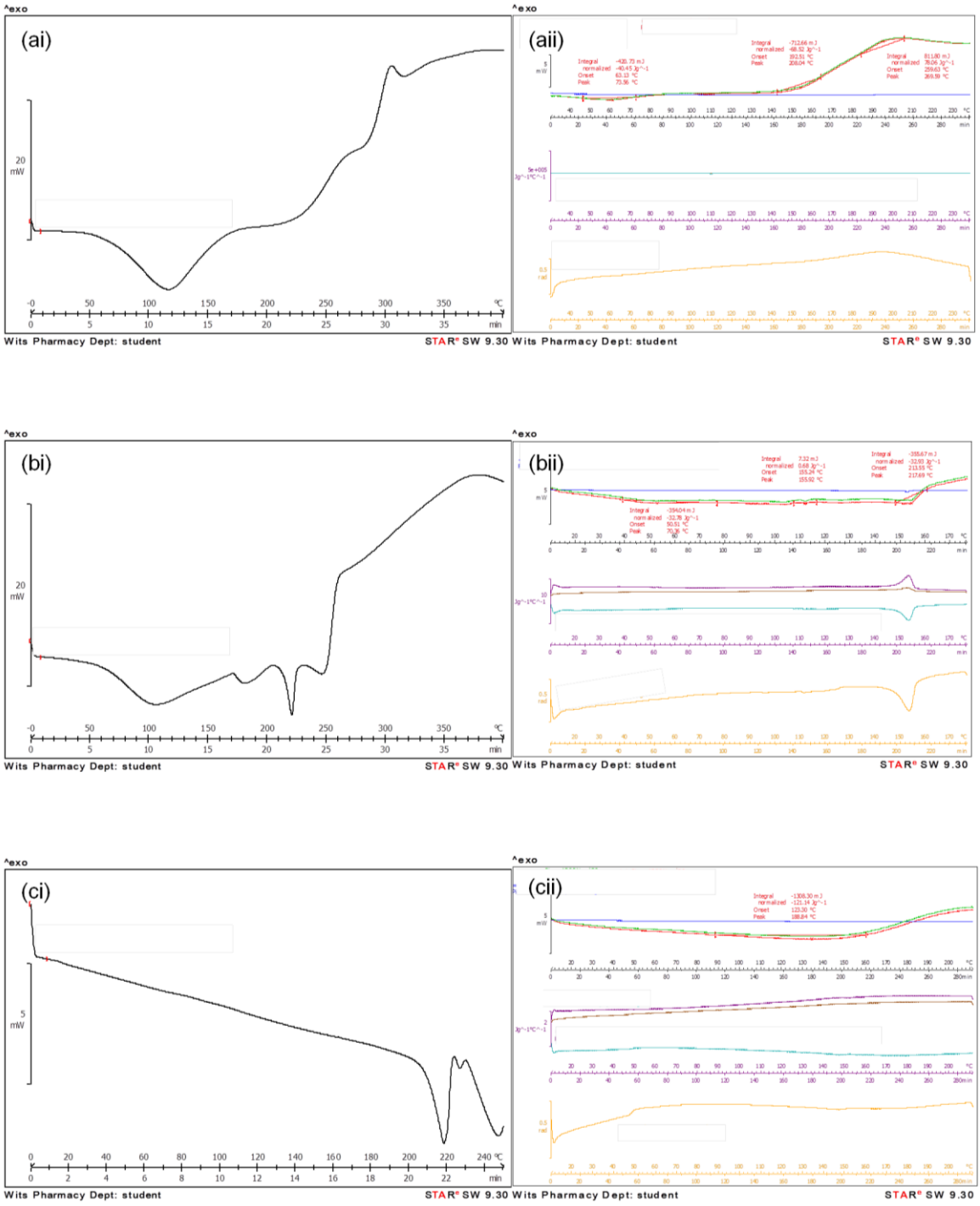

Figure 5.15: (i) Conventional and (ii) TMDSC thermograms for (a) chitosan (b) the inner BPM and (c) the outer BPM showing transition temperatures, transition enthalpies, and transition heat capacities elaborated via the reversing (dark blue), non-reversing (green) and total heat flow (red) curves; the C_p complex (purple) comprising the C_p in-phase (brown) and C_p out-of-phase (light blue) (see Equations 5.2 and 5.3); and the phase angle, ϕ, (orange)

5.3.4. Porosity analysis of the I^3

Analysis of pore characteristics of the inner and outer BPM comprising the I^3 was determined by a technique of physical gas adsorption, which was employed over a wide range of relative pressures (P/P_0) and N_2 adsorption isotherms, and provided significant insight regarding pore size distributions (Yang et al., 2002). The BJH model of determining pore volume and pore size distribution is based on the Kelvin equation and corrected for multi-layer adsorption (Kaneko, 1994).

Isotherm plots for the inner and outer BPMs highlighted that the implant exhibited type IV isotherms with a type H3 hysteresis loop (Figures 5.16 and 5.17). The implant can thus be considered to be mesoporous and possesses a high energy of adsorption with the formation of a multilayer material. The implant can be considered to be a porous adsorbent with pores in the range of 1.5-100nm. This correlates with the average pore widths and diameters calculated via BJH and BET methodologies (4.548nm-8.077nm for the inner BPM and 7.012-22.005nm for the outer BPM) (Table 5.9). The saturation level is attained at a pressure below the saturation vapor pressure due to gases condensing in the tiny capillary pores of the adsorbent at a pressure below the saturation pressure (P_S) of the gas. The slope indicates increased uptake of adsorbate as pores become filled at higher pressures; the inflection point typically occurs near completion of the first monolayer. The sorption behavior in mesopores depends not only on the fluid-wall attraction, but also on the attractive interactions between the fluid molecules. This leads to the occurrence of multilayer adsorption and capillary (pore) condensation (at $P/P_0 > 0.2$) (Thommes, 2010).

On the pore level, also regarded as the 'independent pore model', adsorption hysteresis is proposed to be 'an intrinsic property of the vapor-liquid phase transition in a finite volume system' (Monson, 2008). The simplest scenario is open uniform cylindrical pores of finite length. Typically, a hysteresis loop of type H1 is observed. However, hysteresis in the intricate pore networks of the I^3 is expected to be more complex, thus hysteresis loops which reflect the shapes of types H2 to H4 would be a more likely observation (Figures 5.16 and 5.17). For both the inner and outer BPM, a H3 hysteresis is essentially observed. A type H3 hysteresis loop is typical of slitlike mesopores formed by the platelike particles or layers of globule agglomerates. It reveals a loose assemblage between particles and matrix (Kuznetsova, 2003; Mosquera et al., 2003), which is anticipated for the I^3 structure, specifically for the inner BPM where the matrix is essentially built around the NS agglomerates. Furthermore, an inverse type H3 hysteresis is observed which may be associated with the occurrence of pore blocking as well. The desorption branch is less steep

than the adsorption branch in this instance. Summaries of BET and BJH measurements are provided in Table 5.9.

SEM micrographs of the inner and outer BPM attested to porous surface characteristics. Surface area and porosity results indicated that the porosity of the BPM followed a random distribution and an interconnected pore system. This was evidenced from SEM images at various magnifications for each matrix, as provided in Section 5.3.7, Figure 5.21.

These results presented in Table 5.9 correlate with the fact that, in the outer BPM, the pore size is much larger compared to the inner BPM, which exhibits a smaller pore size overall. This clearly exemplifies that, in the inner BPM, the pores are essentially occupied to a great extent by the NS, thus having an enhanced surface area (availed by the NS and numerous small pores), whereas in the outer BPM, the pores are larger, possessing a smaller surface area. The porosity of the device explains why, under normal conditions, an initial low level release of both drugs from the I^3 was still observed. The initial presence of and continued pore formation on exposure to dissolution media is a possible anticipated mechanism contributing to this. In the inner BPM, the pores are essentially occupied to a great extent by the NS, thus having an enhanced surface area (availed by the NS and numerous small pores), whereas in the outer BPM, the pores are larger, possessing a smaller surface area. On initial exposure of the I^3 to dissolution media, the pores of the outer BPM are anticipated to enlarge under normal conditions causing ciprofloxacin release and the release of indomethacin-loaded NS located at the boundary of the inner and outer BPM, which is reflected in the early phase release of low levels of indomethacin and slightly higher levels of ciprofloxacin. Indomethacin release could also be attributed to release of NS or indomethacin dissolution from the embedded NS located at the exposed surface of the inner BPM.

Table 5.9: Summative surface area, pore volume and pore size as an indication of the overall porosity of the I^3

Surface Area	**Inner BPM**	**Outer BPM**
Single point surface area at P/P_0	0.200530789: 0.7491 m²/g	0.200414083: 0.6256 m²/g
BET Surface Area:	1.2161 m²/g	0.7349 m²/g
t-Plot External Surface Area	1.8641 m²/g	0.9034 m²/g
BJH Adsorption cumulative surface area of pores between 17.000 Å and 3000.000 Å diameter:	1.084 m²/g	0.439 m²/g
BJH Desorption cumulative surface area of pores between 17.000 Å and 3000.000 Å diameter:	0.8094 m²/g	0.2342 m²/g
Pore Volume		
Single point adsorption total pore volume of pores less than 779.590 Å diameter at P/P_0 = 0.974527638:	= 0.975234986: 0.001383 cm³/g	= 0.997540920: 0.001288 cm³/g
t-Plot micropore volume:	-0.000480 cm³/g	-0.000117 cm³/g
BJH Adsorption cumulative volume of pores between 17.000 Å and 3000.000 Å diameter:	0.001770 cm³/g	0.001222 cm³/g
BJH Desorption cumulative volume of pores between 17.000 Å and 3000.000 Å diameter:	0.001634 cm³/g	0.001288 cm³/g
Pore Size		
Adsorption average pore width (4V/A by BET):	45.4843 Å	70.1166 Å
BJH Adsorption average pore diameter (4V/A):	65.322 Å	111.419 Å
BJH Desorption average pore diameter (4V/A):	80.773 Å	220.046 Å

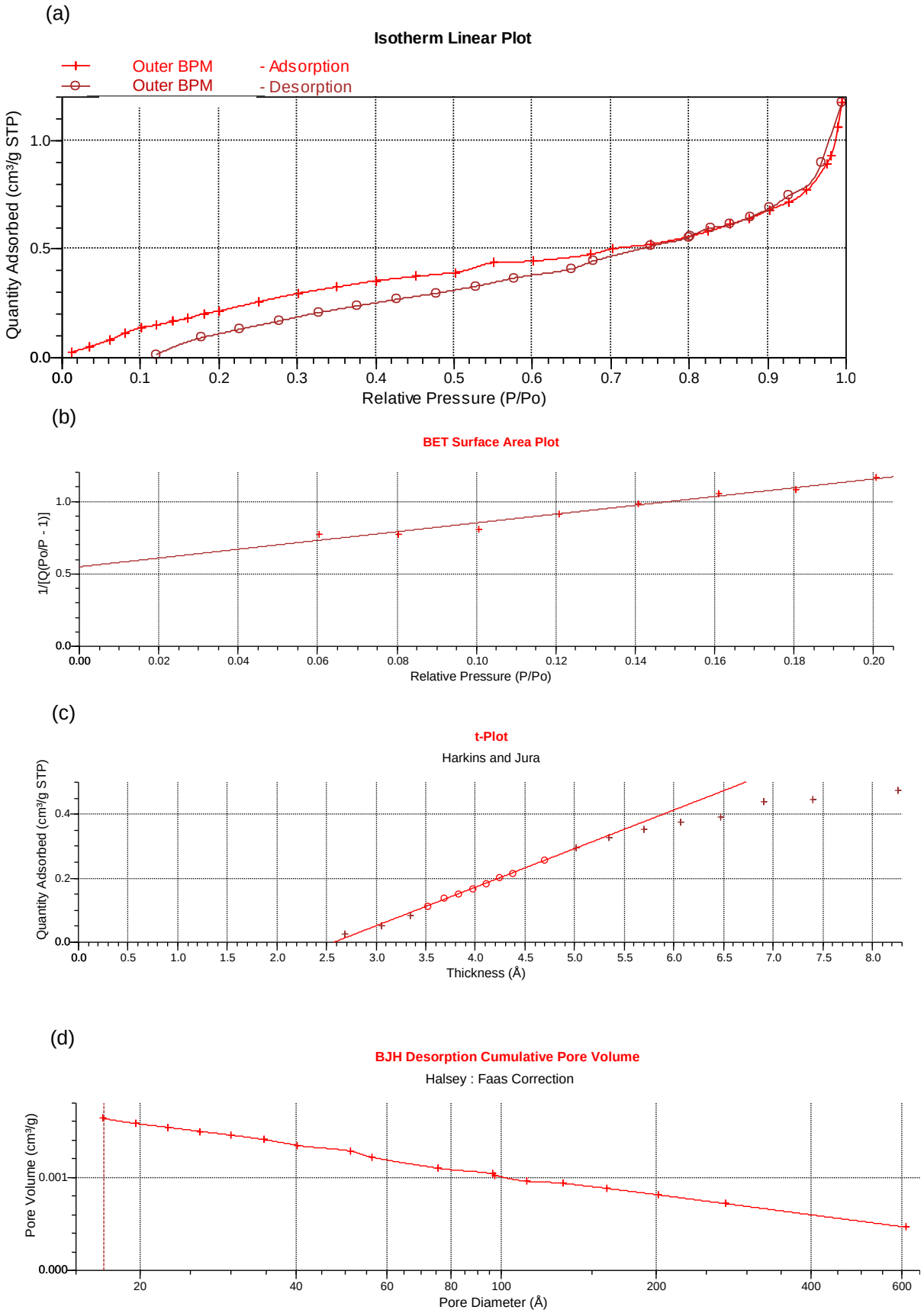

Figure 5.16: Outer BPM porosity plots: (a) isotherm linear plot (b) BET surface area plot (c) t-plot and (d) BJH desorption cumulative pore volume

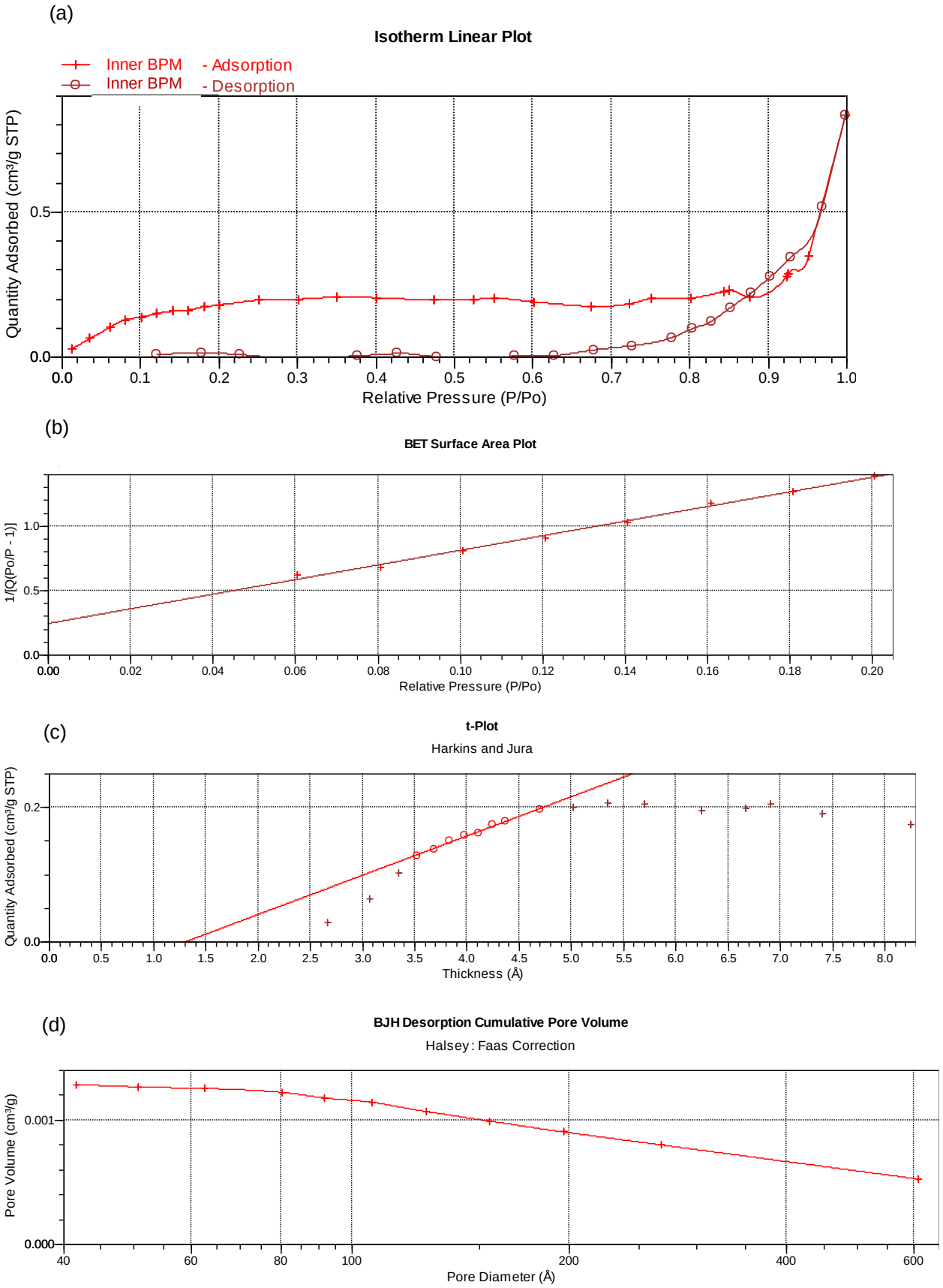

Figure 5.17: Inner BPM porosity plots (a) isotherm linear plot (b) BET surface area plot (c) t-plot and (d) BJH desorption cumulative pore volume

5.3.5. NanoTensile™ evaluation of the nano- and non-nano-enabled I^3 fibres

Tensile load analysis was undertaken on NE and NNE I^3 fibres, and results were obtained for all the measured mechanical parameters: Young's modulus, yield stress, ultimate strain, ultimate strength and toughness, as depicted in Table 5.10.

Table 5.10: Tensile analysis results comparing nano- and non-nano-enabled I^3 fibers

Tensile Parameter	NNE I^3 fiber	NE I^3 fiber
Young's modulus (MPa)	422.73	354.20
Yield stress(MPa)	0.98	1.86
Ultimate strength (MPa)	1.85	2.96
Ultimate strain (MPa)	0.017	0.028
Toughness ($J.cm^{-3}$)	0.02	0.06

The fracture of the fibres is a result of microfailure caused by formation of microvoids and/ or micro-cracks on exposure to stress. The formation of a micro-crack is essentially a stress-concentrator; the coalescence of several micro-cracks instigating macro-crack propagation. In the multipolymeric system represented by the fiber, formation of microvoids is caused by scission of both crosslinks formed within and between the polymers and covalent bonds between monomers within the macromolecules. The homogenously blended crosslinked networks exemplified by the inner and outer BPM forming the I^3 fiber could emanate in potentially wide-ranging tensile properties including good strength and high extensibility. The inclusion of a nano-component in the inner BPM also has significant consequences. A network consisting of multiple strands connecting NS crosslink sites is less prone to sequential bond failure as the force released by the scission of one chain will be spread over many neighboring chains thereby lessening the likelihood of micro-crack formation, as exemplified for the NE fiber.

It is evident that the NE fibers (Figure 5.18b) possess greater strength (with reference to the ultimate tensile strength) in comparison to the NNE fibers (Figure 5.18a). Goyal and co-workers (2009) found that NPs act as filler and enhance the mechanical properties of polymer fims within which they are embedded, which is evident in the inner slow-release BPM (crosslinked chitosan core) incorporating the indomethacin-loaded Lipo-Chit-PCL NS. They enhance the elasticity of the formulation, as evidenced by the comparatively lower Young's modulus of the NE fiber system (which indicates a decreased rigidity), hence creating a tougher more durable formulation, which is essentially important when the I^3 comes in contact with the ocular environment. Therefore, the NE system is anticipated to

possess a greater ability to withstand stresses it is exposed to, allowing it to respond appropriately to the stimulus of interest in the absence of extraneous effects.

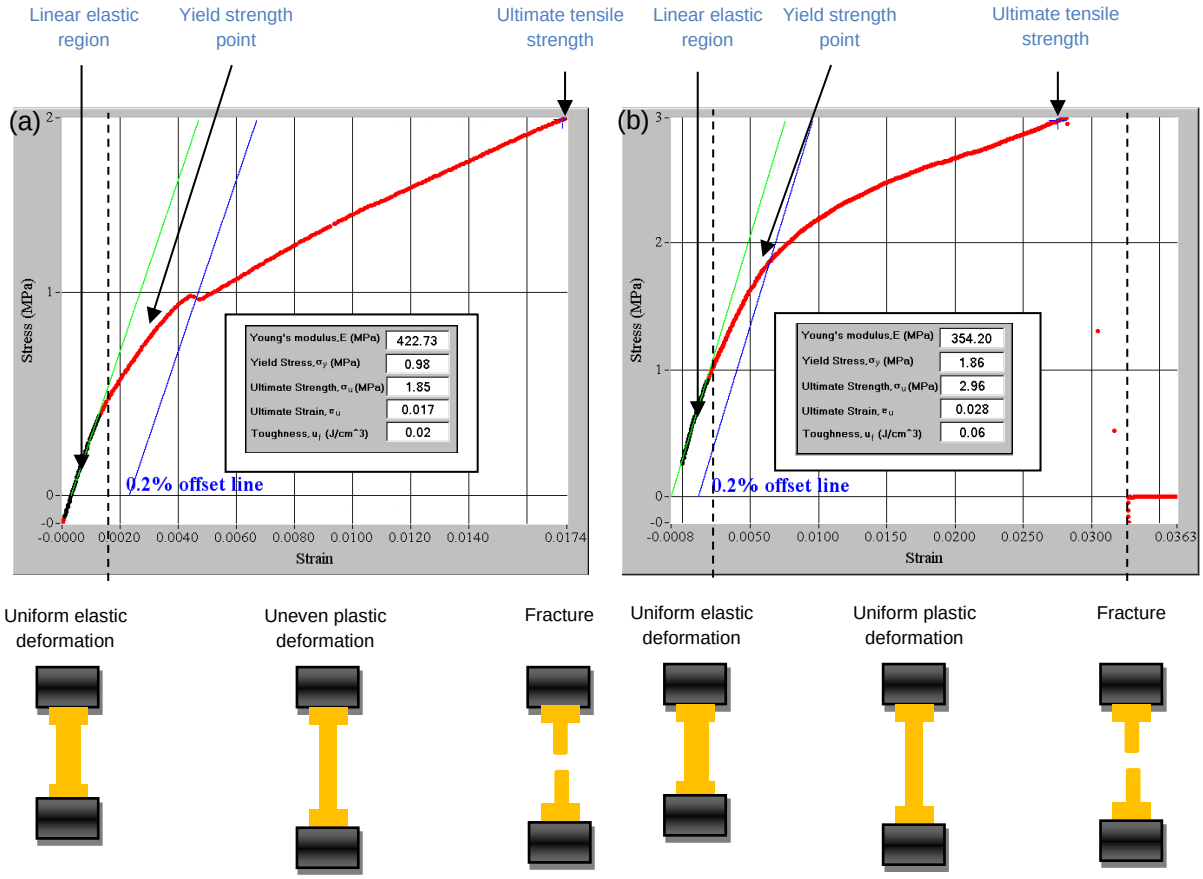

Figure 5.18: Exemplary Stress vs Strain profiles and corresponding schematic depiction of gross morphological changes for the (a) non-nano-enabled and (b) nano-enabled I^3 fibers

5.3.6. Magnetic Resonance Imaging of the I^3

The approach of Tajiri et al. (2010), which has been applied to hydrogel matrix tablets, was adapted to differentiate gelled (extensively hydrated) and non-gelled regions of the I^3 and the changes in hydration with time and on exposure to normal and inflammatory dissolution media. In each image, a lower degree of hydration or gelling of the I^3 is visualized as lower intensity, darker areas, whereas more extensive hydration or gelling of the implant possess an appearance falling towards the white side of the intensity scale (Fig. 5.19a) . The high-intensity areas of the hydrogels in MRI images (white part) possess a smaller relaxation time (T_1) than bulk dissolution media (gray region) due to the hydrogen bonds between the essentially hydrophilic polymers comprising the I^3 and water (Tajiri et al., 2010). The image of the I^3, which had not been exposed to dissolution media, is visualized in Fig. 5.19a. The MRI ^{1}H NMR images of the I^3 at subsequent stages of the dissolution test as visualized in the

flow-through apparatus under normal, inflammatory and fluctuating conditions, are represented in Fig. 5.19b-d.

Plotted results indicate the gelled intensity (i.e. the intensity of the white area of the I^3, which is the hydrated area), as well as the change in area of the I^3 on exposure to the various dissolution conditions compared to the unhydrated I^3 at day 0. The associated MRIs at each time point are also provided. Upon initial inspection at day 0, the I^3 was clearly observed as a small unhydrated device in accordance with the associated intensity scale (Fig. 5.19a). Following exposure to normal SVH a comparatively greater imbibement of dissolution fluid occurred (indicated by the largely white appearance of the implant corresponding to a high gelling intensity in the MRIs in Fig. 5.19b). As drug release studies undertaken at normal conditions concluded, drug release was at a minimum highlighting that fluid uptake in this instance enforces the crosslinked structure emanating in a highly interconnected multipolymeric hydrogel which hinders drug and NS diffusion out the gel. Following exposure to SVH, compared to the device at day 0, there is a prominent increase in the area of the I^3. This is due to swelling caused by the high concentration of charged ionic groups in the crosslinked multipolymeric structure due to osmosis and charge repulsion. The overall hydration of the implant is apparent with the gelling intensity being consistently >~79% over 28 days. Thereafter, the slight progressive decrease in the size of the gel with time is indicative of a low degree of erosion occurring at the implant surface. Drug release observed under these conditions is most likely attributed to self-diffusion initially, followed by matrix erosion as the device area decreases. Fluid ingress with device hydration, causing an initial increase in the area of the implant with subsequent limited erosion over the investigated period, can be considered as a significant predictor of the drug release profiles of the I^3. The change in the device area decreased with with time , concurrently with a limited increase in both indomethacin and ciprofloxacin release (R^2= -0.8856, and R^2= -0.8783, respectively). The high degree of device hydration (measured as gelling intensity) was thus important for limiting the drug release under normal conditions.

Subsequently, the transitions in the device area and gelling intensity was measured for the implant under pathological conditions created by Fenton's reagent in SVH (Fig. 5.19c). Ingress of fluid was minimal in Fenton's reagent, as evidenced by essentially a lower gelling intensity ranging between ~51 and 56% (with I^3 images appearing grey), however, there was a notable decrease in area with time, which corresponds with the predicted surface erosion of the device under inflammatory conditions due to chain scission initiated in the presence of hydroxyl radicals propogating the observed surface erosion of the device. There is limited overall hydration of the device highlighting that the polymeric degradation initiated by the free

radicals is largely a surface phenomenon. The change in the area of the implant increased with time and correlated positively and significantly with the observed drug release of both indomethacin and ciprofloxacin, with progressively increased erosion or the I^3 resulting in enhanced drug release (R^2= 0.9695 and 0.9888, respectively).

The behavior of the I^3 on exposure to alternating dissolution stresses is of importance in that the 'on-off' inflammation-responsive transitions of the device become quite evident (Fig. 5.19d). In the absence of the instigating stimulus (hydroxyl radicals), from days 0-3, the I^3 hydrates and gels, visualized as a high gelling intensity; and the device area increases. On exposure to inflammatory conditions from day 3-7, device hydration decreases and chain scission is initiated at the surface of the I^3 with the implant area drastically decreasing. Under normal conditions from days 7-14, fluid ingress into the device progresses further into the core. After exposure to hydroxyl radicals for another 7 days, there was a noted decrease in the size and hydration of the device once again. Interestingly, after a further 7 days exposure to normal conditions, prominent hydration of the implant occurs; the device area does again increase, although not as notably as before, due to more extensive device erosion with pieces of the implant. This reversible swelling and gelling and then 'collapsing' of the polymeric matrix on alternating exposure to and removal of the instigating stimulus is a hallmark of stimulus-responsive systems (Barbu et al., 2006). In this instance, collapse of the gel occurs in the presence of inflammation, which promotes erosion of the device. It is thus apparent that although the responsive behavior is reversible, a point is reached at which excessive stresses and polymeric chain scission may alter the mechanism of operation of the device to a degree. Large decreases in area of the implant were observed following exposure of the device to pathological conditions (subsequent to normal conditions) attributed to erosion in the presence of hydroxyl radicals with associated drug release. The correlation obtained between changes in device area and drug release was not remarkable for indomethacin (R^2=0.5049), but somewhat notable for ciprofloxacin release (R^2=0.7375), possibly due to the fact that ciprofloxacin was directly incorporated within the stimulus-responsive matrix; whereas following NS release from the eroding implant, indomethacin has yet to diffuse through its encapsulating boundaries.

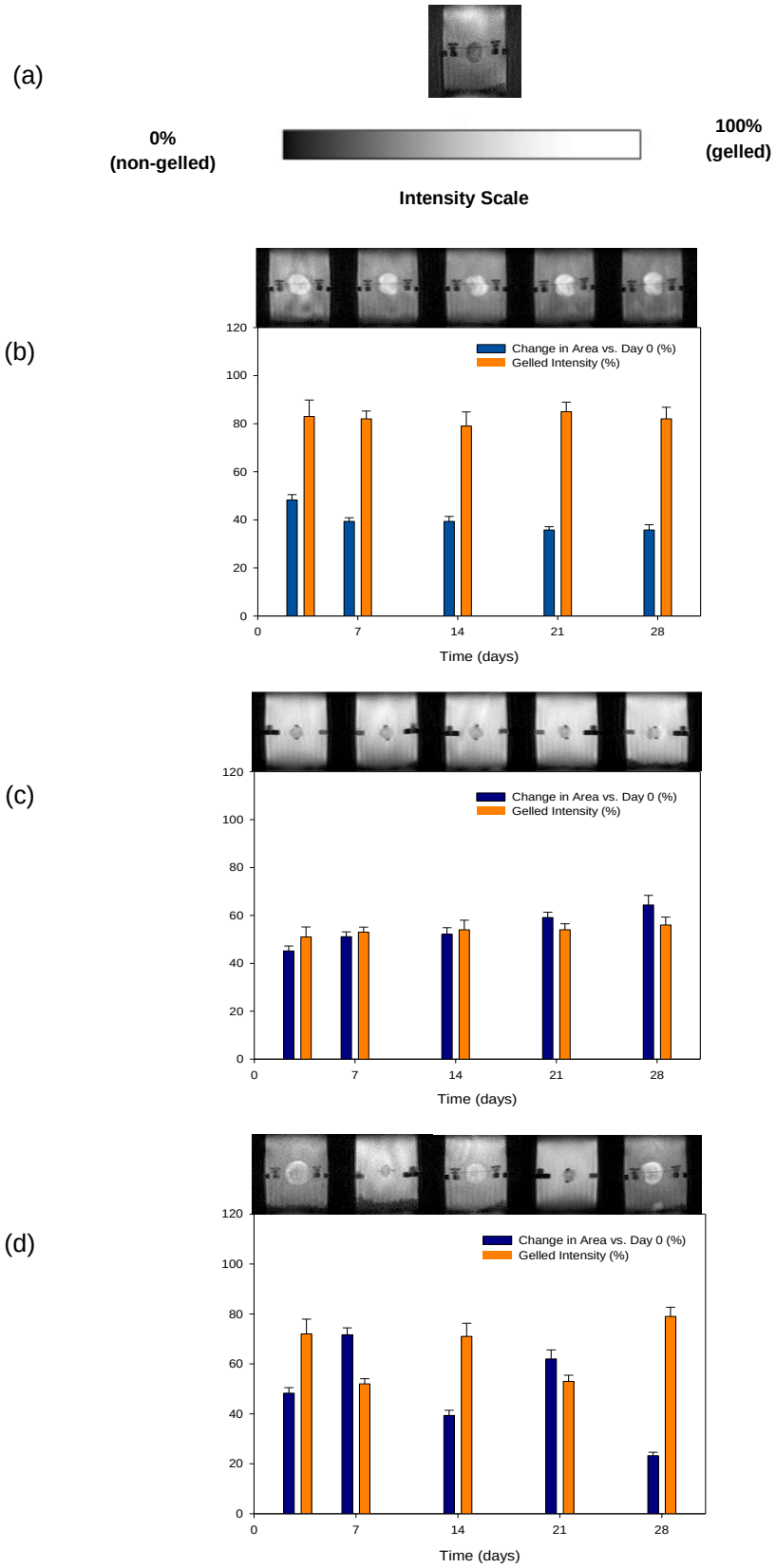

Figure 5.19: (a) MRI of the I^3 at day 0 and the intensity scale highlighting gelled and non-gelled areas; (b) graphical depiction and associated MRIs exemplifying hydration transitions of the I^3 over 28 days in normal SVH; (c) graphical depiction and associated MRIs exemplifying hydration transitions of the I^3 over 28 days in Fenton's Reagent in SVH; and (d) graphical depiction and associated MRIs exemplifying hydration transitions of the I^3 over 28 days in alternating media (n=3 for all evaluations)

5.3.7. Morphological characterization and image processing analysis of erosional behavior of the I^3 via gross photographic and Scanning Electron Microscopic analysis

Photographic images obtained for the eroding I^3 separated into the inner and outer BPM for visualization on exposure to normal and inflammatory conditions were analyzed by generation of image histograms, where changes in the saturation (y-axis) and pixel intensities (x-axis) of different colors were indicative of alterations of the overall polymeric make-up on exposure to differing dissolution conditions.

For the outer BPM under normal conditions, the color saturations did not alter notably and the polymeric structure was essentially maintaned. Each color channel demonstrated a shift to lower pixel intensities indicating a slight increase in porosity of the device. Exposure to an inflammatory milieu instigated significant changes in the morphology of the matrix (Figure 5.20a). With reference to the inner BPM, no pertinent changes were observed in the colour saturation nor intensity over time following exposure to normal conditions. Only a slight increase in porosity of the BPM predicted by a limited shift in intensity values was detected. After exposing the inner BPM to inflammatory conditions, the color saturation (specifically for the red color channel) notably decreased indicating a change in the polymeric structure due to disengagement of polymeric crosslinks/ chain scission. More peaks are seen at lower intensities indicating the formation of pores of diverse sizes due to the NS dislodging from the matrix structure (Figure 5.20b). For the entire I^3, succinct evaluation via the image histograms was complicated by the lack of correspondence of changes in the pixel saturations and intensities of the inner versus the outer BPM due to opposing polymeric compositions (Figure 5.20c).

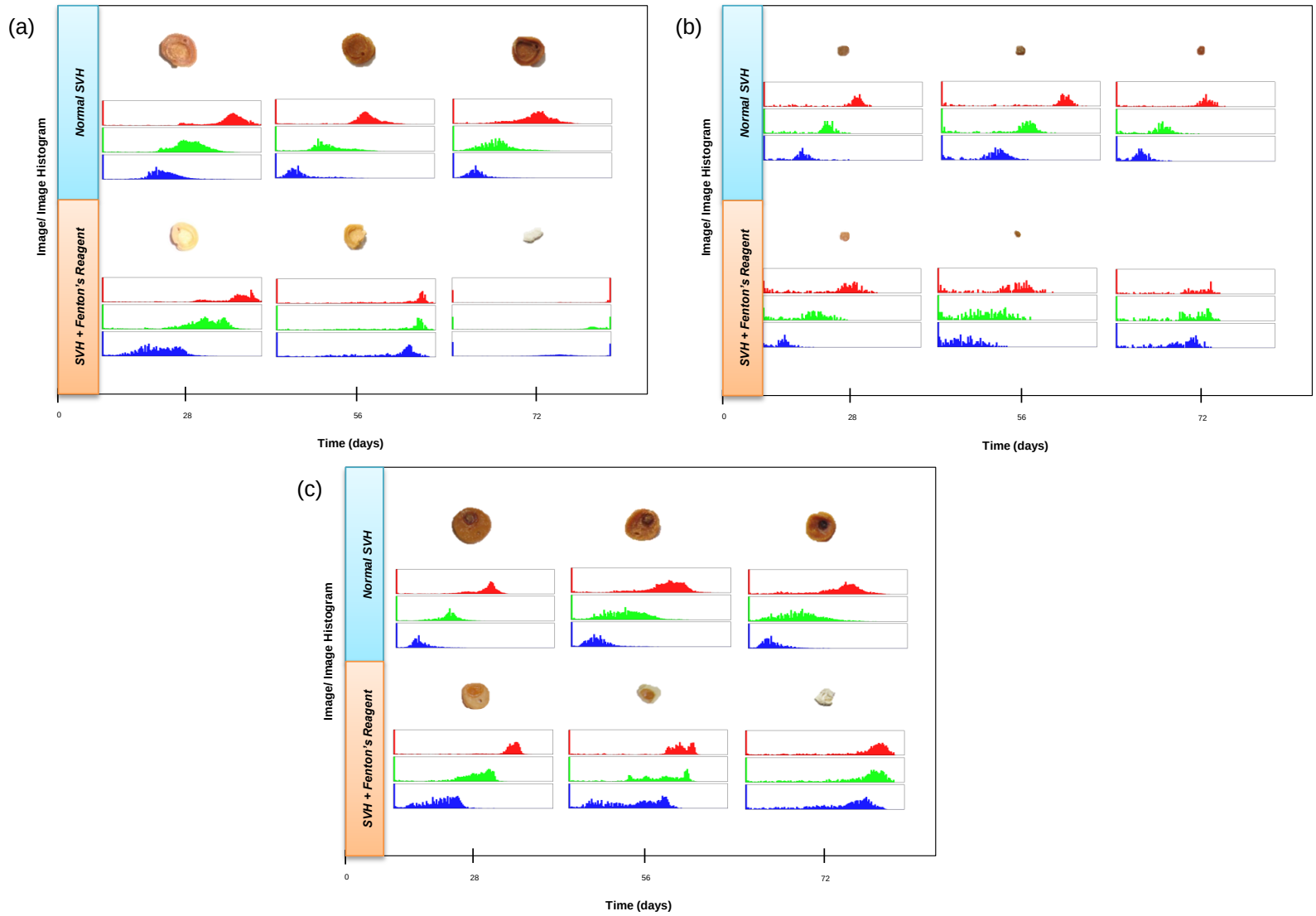

Figure 5.20: Photographic depiction of erosion of (a) the outer BPM, (b) the inner BPM, and (c) the entire I^3 under normal and inflammatory conditions with associated image histograms

Through analysis of the image histograms generated, transitions in morphological features on erosion of the device after 72 days, captured via SEM (raw images are depicted in Figure 5.21), could be discriminated. The comparative analysis of histograms, with the histogram of the original SEM shown as an inset to the histogram obtained after image processing, highlighted the effect of the processing steps on the clarity of the image histogram such that the respective erosional effects on BPM morphological features could be distinguished. Fig. 5.22a for the erosion of the outer BPM under normal conditions shows a tetramodal distribution of peaks with four of the peaks at voxel intensities of ~25, 85, 160 and 200 representing voxels for air-filled deep pores, pores reaching the second or third layer of the structure, solid polymeric architecture in the second or third layer of the structure, and the solid polymeric architecture of the top layer, respectively, in the order of increasing linear absorption coefficients. The black regions visualized in the processed images are representative of deep pores, cracks and crevices extending from the surface into deeper layers of the respective BPMs of the I^3 which become enlarged on erosion. The peaks on either side of these pores and solid interfaces are blurred because of the finite spatial resolution of the scanning system instigating an undesirable partial volume effect. The probability of finding intensity at a pore-solid polymer boundary was assumed to be equal for both features. The average of these peaks was thus established as the threshold (i.e. ~118) implying that voxels with an intensity equal to or smaller than 118 are pores, which is true for the peaks at 25 and 85, which were assumed as pores initially. This model was used for comparison with the images acquired for exposure of the outer BPM to inflammatory conditions (Fig. 5.22b). Here there was a tetramodal distribution of peaks with voxel intensities at ~30, 70, 100, 150, representing a significant shift towards a more porous structure on exposure to an inflammatory environment.

Analysis of the erosion of the inner BPM under normal conditions revealed a pentamodal distribution at 20, 95, 170, 220 and 245, representing voxels for air-filled deep pores, pores reaching the second or third layer of the structure, solid polymeric architecture in the second layer, solid polymeric architecture in the third layer of the structure, and the solid polymeric architecture of the top layer, respectively (Fig. 5.23a). The threshold was thus established at ~150, implying that pores are represented by peaks at or below this intensity. Thus, under normal conditions, the more solid architecture is attributed to the fact that the NS still occupies a great deal of the pores of the matrix until their ultimate dislodgement from the system on matrix erosion. When exposed to inflammatory conditions, analysis of the SEM image of the inner BPM highlighted a pentamodal distribution of peaks at ~27.5, 90, 110, 150 and 200, indicating a highly porous matrix with excessive loss of the embedded NS (Fig.

5.23b). The inner BPM was resolved into more layers than the outer BPM (pentamodal vs. tetramodal) due to pores arising which were artefacts of NS release from the matrix.

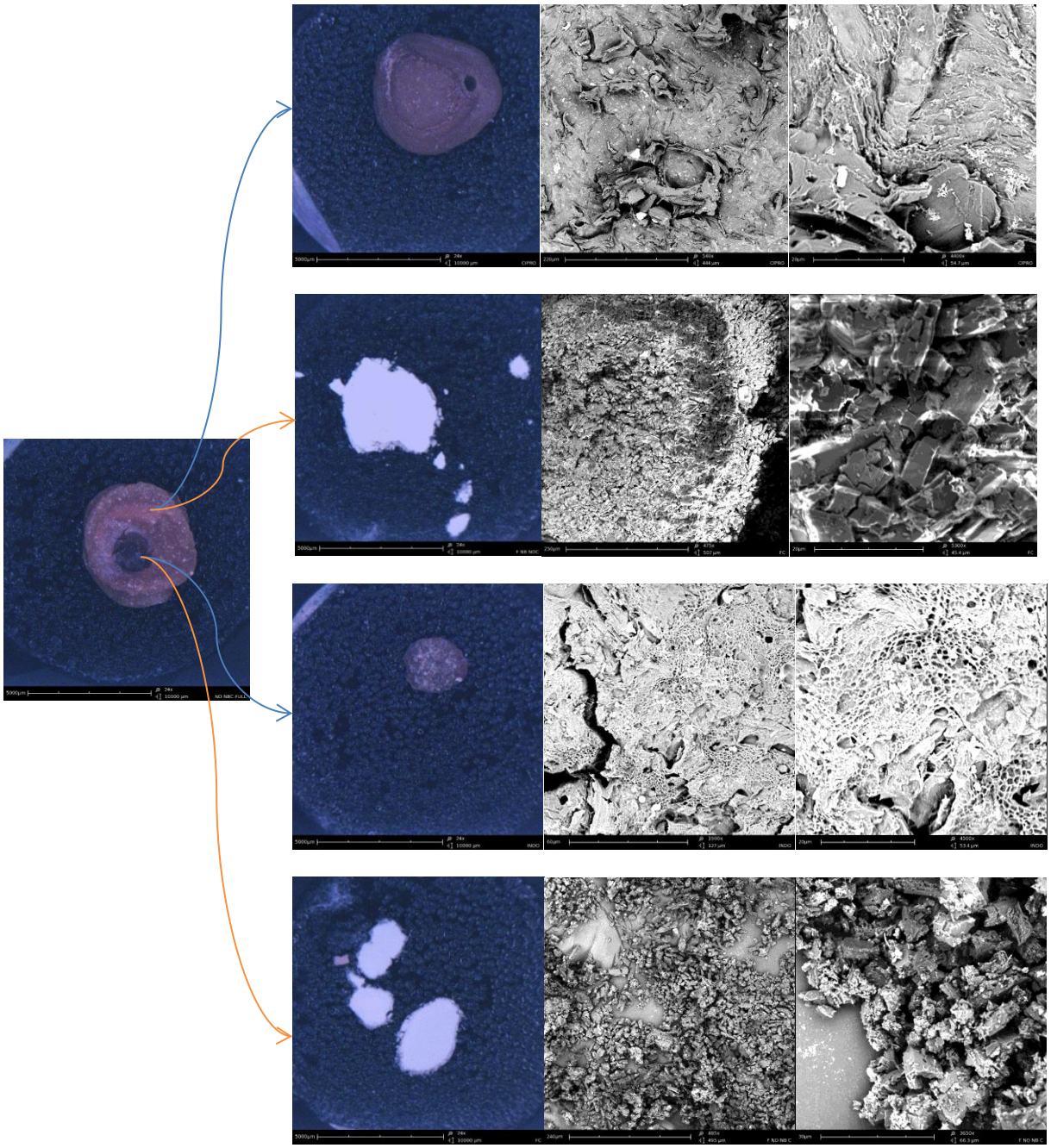

Figure 5.21: Componentially-derived scanning electron micrographs of the outer and inner BPMs under normal (blue arrow) and inflammatory (orange arrow) *in vitro* conditions after 72 days exposure (represented at incremental magnifications)

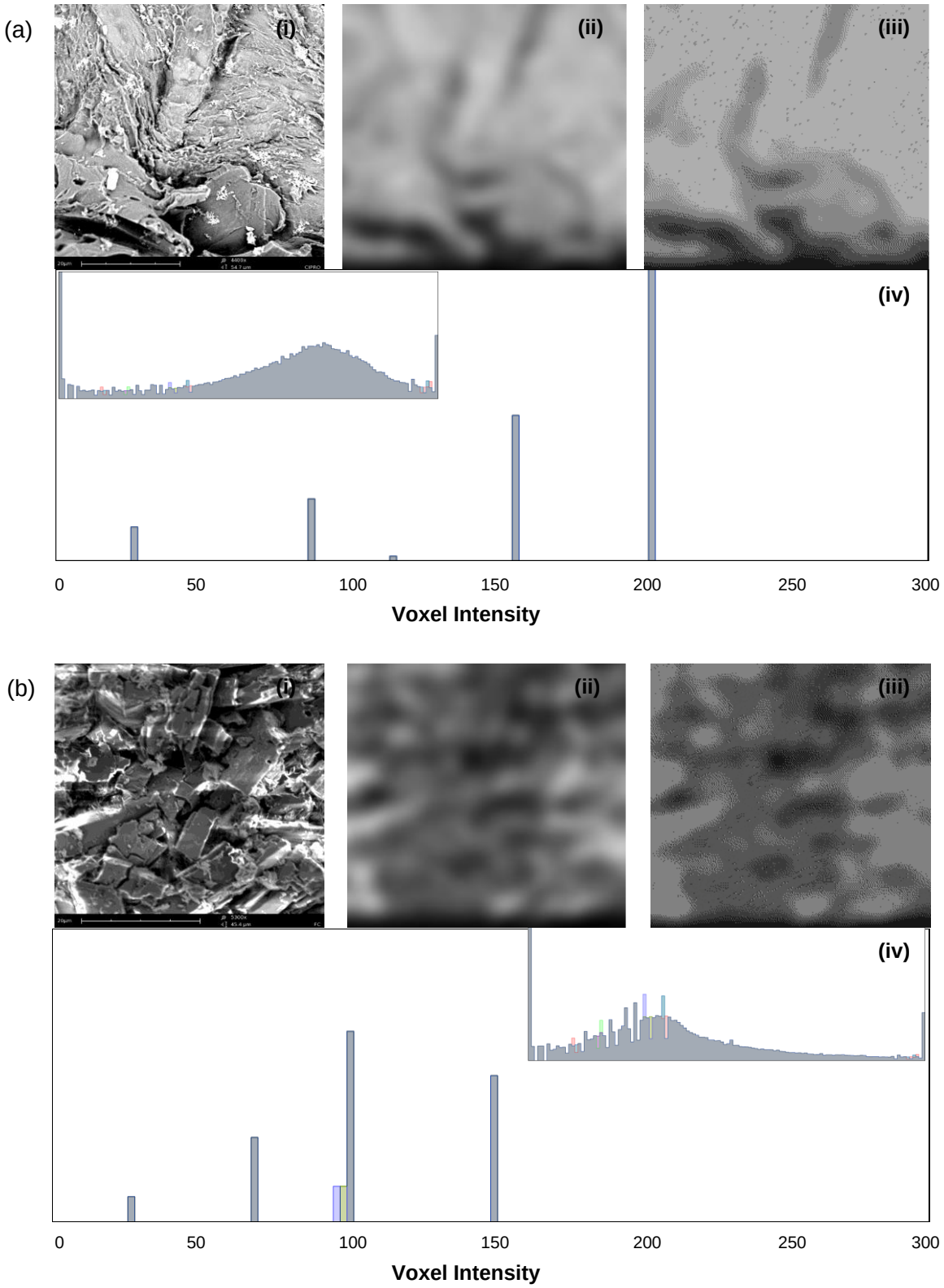

Figure 5.22: Image processing with subsequent (iv) image histograms generated for high-magnification images of the outer BPM under (a) normal and (b) inflammatory conditions showing the (i) original, (ii) blurred, and (iii) color quantized image. Note that each channel is capable of highlighting most of the pores and layers but not all

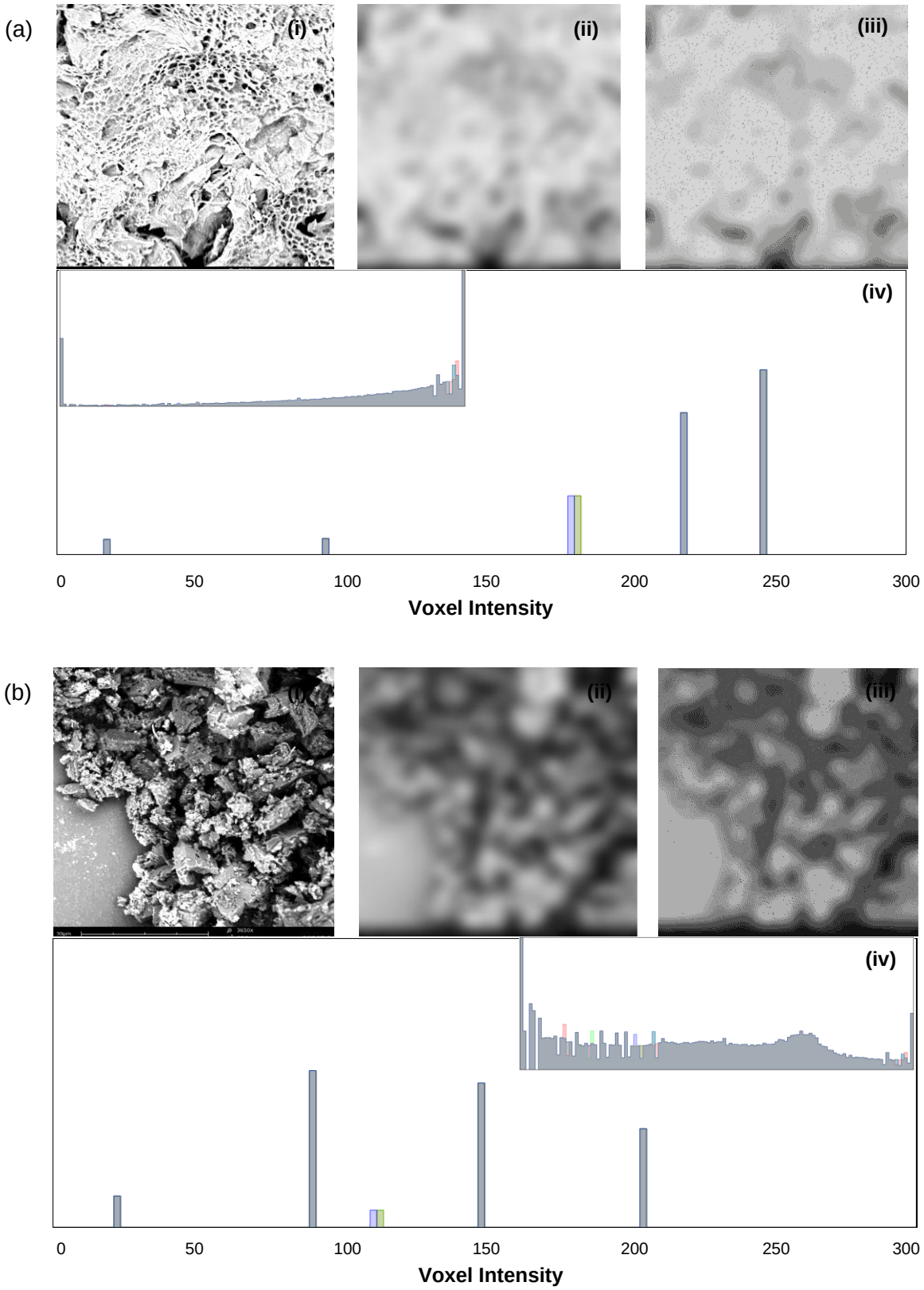

Figure 5.23: Image processing with subsequent (iv) image histograms generated for high-magnification images of the inner BPM under (a) normal and (b) inflammatory conditions showing the (i) original, (ii) blurred, and (iii) color quantized image. Note that each channel is capable of highlighting most of the pores and layers but not all

5.3.9. Molecular modeling simulations for prediction of pertinent interactions between the inner and outer bioresponsive matrices of the I^3

5.3.9.1. Formation of the chitosan-alginate polyelectrolytic structure

The formation of the chitosan/ alginate ionic gelation system is depicted in Figure 5.24 and the corresponding energy values were calculated employing Equations 5.11-5.13.

$E_{Chit} = 35.555V_{\sum} = 3.120V_b + 18.035V_\theta + 25.774V_\varphi + 13.323V_{ij} - 24.697V_{el}$ [Equation 5.11]

$E_{ALG} = 74.426V_{\sum} = 5.204V_b + 32.486V_\theta + 34.168V_\varphi + 30.708V_{ij} - 28.142V_{el}$ [Equation 5.12]

$E_{Chit\text{-}ALG} = -3.600V_{\sum} = 8.491V_b + 60.358V_\theta + 58.164V_\varphi + 8.608V_{ij} - 139.224V_{el}$ [Equation 5.13]

ΔE = -113.581kcal/mol

It is evident from the energy equations that the Chit-ALG complex was highly stabilized with a negative E_{total} energy value as compared to the individual polysaccharide entities Chit and ALG. The energy of stabilization ΔE ~ -114kcal/mol further confirms the favorable interaction of the cationic and anionic polymer chains with, as expected, the electrostatic energy counting for the majority of the stability (ΔE_{Vel} ~ -86kcal/mol) followed by the van der Waals forces (ΔE_{Vij} ~ -35kcal/mol). Interestingly; the bond angle contributions destabilized the structure by $\Delta E_{V\theta}$ ~ +10kcal/mol, compared to the reference values, as the structures' bond angles changed during the torsional strain caused by the cationic and anionic functional groups. During the geometrical minimization of chitosan; no intramolecular bonding was observed after the global minimization (Figure 5.24a). However; it was noted that alginate forms intramolecular H-bonds (two in number) in the same mannuronate unit (Figure 5.24b). After molecular mechanics simulation of the Chit-ALG complex; the scenario changed drastically with the formation of intramolecular H-bonds in chitosan; intermolecular H-bonds between Chit and ALG; and extensive intramolecular H-bonding in the alginate molecule as depicted in Figure 5.24c. A closer look at the Chit-ALG molecular complex highlighted the involvement of $-NH_2$ and -OH functionalities of Chit and -COOH and -OH functionalities of ALG. This corroborates with the structural transitions ascertained via FTIR furnished in Section 5.3.2 above. Furthermore; the connolly molecular surface structure of the complex (Figure 5.24d) confirmed the compact nature of the polyelectrolytic structure as the van der Waals radius of the constituent molecules overlapped to give a perfect fit.

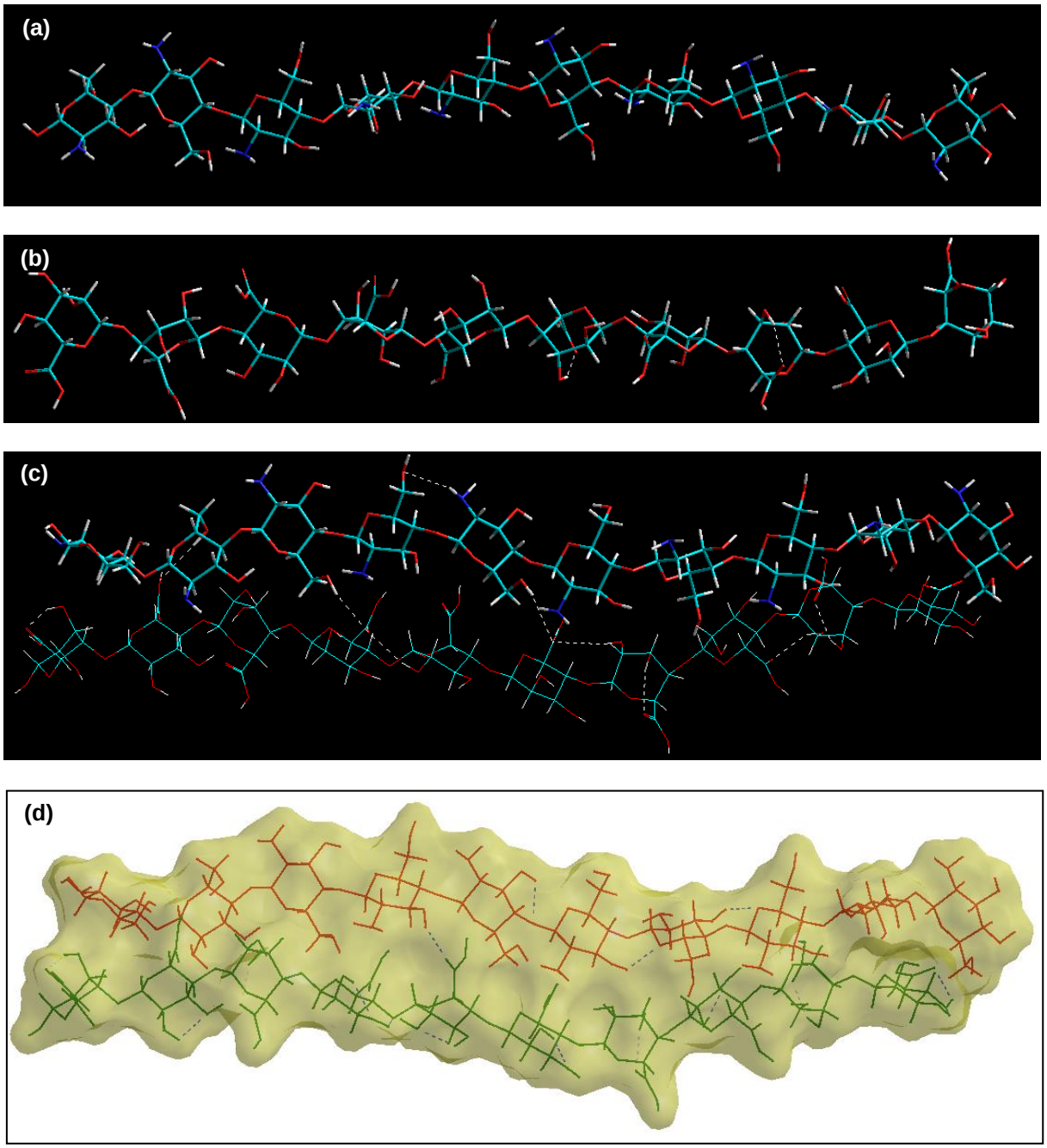

Figure 5.24: Visualization of geometrically minimized and energetically stable model of (a) Chitosan; (b) alginate; (c) chitosan (tube rendering) - alginate (stick rendering) complex; and (d) respective connolly molecular chitosan (red) and alginate (green) electrostatic potential surfaces in translucent display mode - after molecular simulations in vacuum. Color codes: C (cyan), O (red), H (white), and N (blue)

5.3.9.2. Formation of the chitosan-PAA polyelectrolytic structure

The formation of chitosan-PAA cation-anion conjugate is depicted in Figure 5.25 and the corresponding energy values can be calculated using Equations 5.11, 5.14 and 5.15. It is evident from the energy equations that the Chit-PAA complex was highly stabilized with a negative E_{total} energy value as compared to the individual polymer entities Chit and PAA. The energy of stabilization $\Delta E \sim -36$kcal/mol further confirms the favorable interaction of the cationic and anionic polymer chains with, unlike Chit-ALG, the van der Waals forces accounting for majority of stability ($\Delta E_{Vel} \sim -36$kcal/mol) followed by the electrostatic forces ($\Delta E_{Vij} \sim -3$kcal/mol). Interestingly; the torsional contributions rather than bond energy destabilized the structure by $\Delta E_{V\theta} \sim +3$kcal/mol which may have contributed to the formation of a constrained Chit chain as shown in Figure 5.25c. During the geometrical minimization of individual polymers: Chit and PAA; no intramolecular bonding was observed after the global minimization (Figure 5.25a and b). After molecular mechanics simulation of the Chit-PAA complex; the formation of intramolecular H-bonds in PAA and intermolecular H-bonds between Chit and PAA was observed as shown in Figure 5.25c. The Chit-PAA molecular complex displayed the involvement of $-NH_2$; -O- and -OH functionalities of Chit and -COOH and -OH functionalities of PAA. The connolly molecular surface structure of the complex (Figure 5.25d) confirmed the formation of a dense and highly constrained polyelectrolytic structure as the van der Waals radius of the constituent molecules overlapped to give a perfect fit in a small region in proximity of PAA.

$E_{Chit} = 35.555V_{\sum} = 3.120V_b + 18.035V_\theta + 25.774V_\varphi + 13.323V_{ij} - 24.697V_{el}$ [Equation 5.11]

$E_{PAA} = 46.074V_{\sum} = 3.946V_b + 40.124V_\theta + 33.706V_\varphi - 31.703V_{ij}$ [Equation 5.14]

$E_{Chit\text{-}PAA} = 45.202V_{\sum} = 6.864V_b + 58.079V_\theta + 61.771V_\varphi - 54.122V_{ij} - 27.390V_{el}$ [Equation 5.15]

$\Delta E = -36.427$kcal/mol

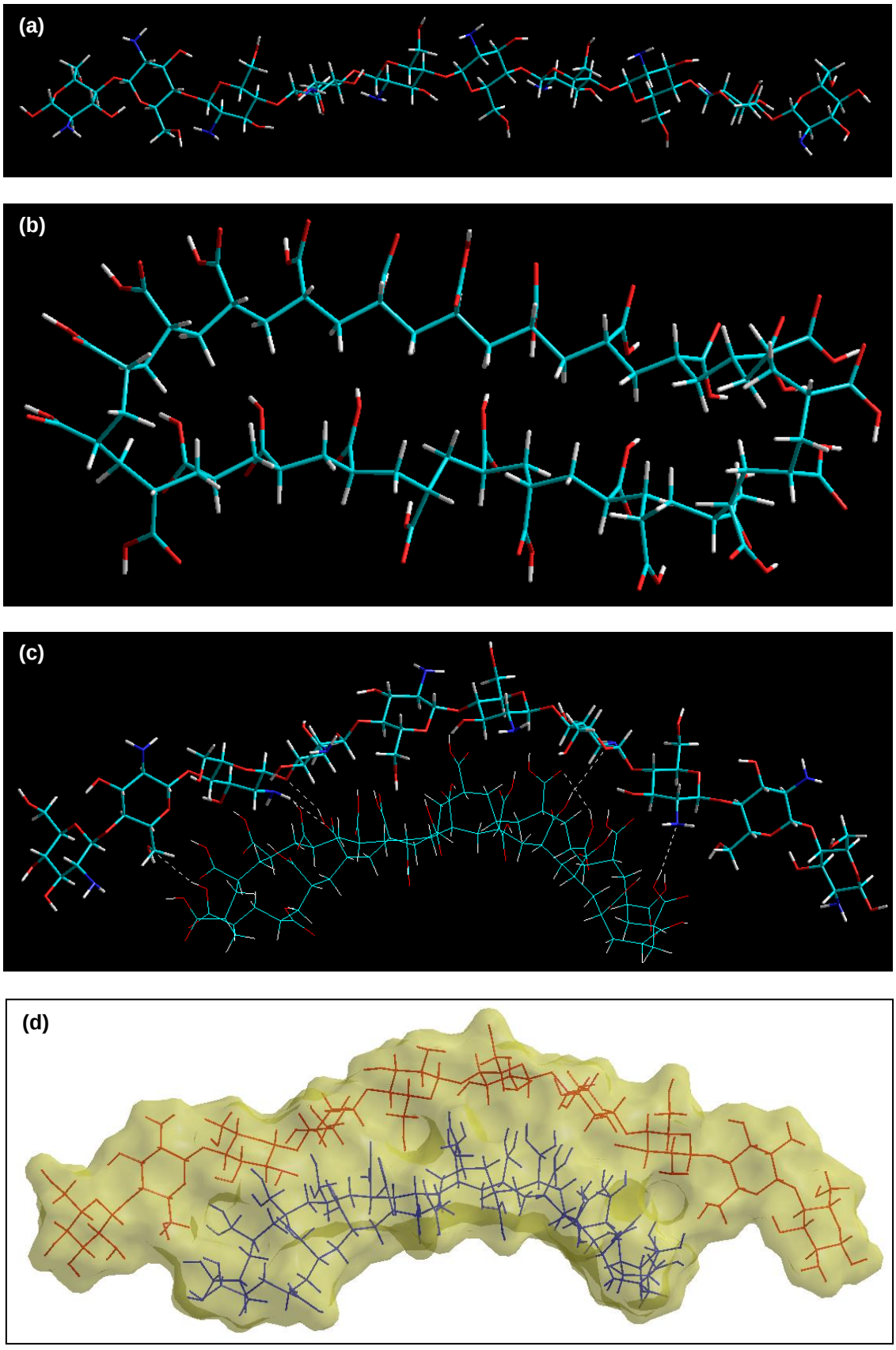

Figure 5.25: Visualization of geometrically minimized and energetically stable model of (a) Chitosan; (b) PAA; (c) chitosan (tube rendering) - PAA (stick rendering) complex; and (d) respective connolly molecular chitosan (red) and PAA (blue) electrostatic potential surfaces in translucent display mode - after molecular simulations in vacuum. Color codes: C (cyan), O (red), H (white), and N (blue)

5.3.9.3. Formation of the chitosan-hyaluronate polyelectrolytic structure

The formation of chitosan-hyaluronate polyampholyte is depicted in Figure 5.26 and the corresponding energy values can be calculated using Equations 5.11, 5.16, and 5.17. Similar to Chit-ALG and Chit-PAA; the Chit-HA polyampholyte was highly stabilized with a negative E_{total} energy value as compared to the individual polysaccharide entities Chit and HA. The energy of stabilization ΔE ~ -54kcal/mol confirms the interaction of the cationic (Chit) and cationic/anionic polymer (HA) chains. The involvement of $-NH_2$ groups of HA and Chit in the interactions contributed to the huge electrostatic energy stabilization (ΔE_{Vel} ~ -70kcal/mol) followed by the van der Waals forces (ΔE_{Vij} ~ -25kcal/mol) and H-bonding (ΔE_{hb} ~ -2kcal/mol). Interestingly; both the bond angle and torsional contributions destabilized the structure by $\Delta E_{V\theta}$ ~ +13kcal/mol and $\Delta E_{V\varphi}$ ~ +32kcal/mol which may be responsible for the atypical constrained structure of the polyampholytic matrix as revealed in Figure 5.26c. During the geometrical minimization, HA formed intramolecular H-bonds (seven in number; Figure 5.26b). After molecular mechanics simulation of the Chit-HA complex; the involvement of $-NH_2$ and -OH functionalities of Chit and -COOH; $-NH_2$; and -OH functionalities of HA resulted in the formation of intermolecular H-bonds between Chit and HA; and extensive intramolecular H-bonding in the HA molecule as shown in Figure 5.26c. The connolly molecular surface structure of the complex (Figure 5.26d), however, confirmed that the atypical constrained structure was still capable of forming an 'overlapped van der Waals radius' compact structure for the polyampholytic system.

$E_{Chit} = 35.555V_{\sum} = 3.120V_b + 18.035V_\theta + 25.774V_\varphi + 13.323V_{ij} - 24.697V_{el}$ [Equation 5.11]

$E_{HA} = -75.437V_{\sum} = 6.047V_b + 58.234V_\theta + 68.269V_\varphi + 13.857V_{ij} - 6.429V_{hb} - 215.417V_{el}$ [Equation 5.16]

$E_{Chit\text{-}HA} = -93.636V_{\sum} = 10.263V_b + 89.446V_\theta + 125.423V_\varphi + 0.529V_{ij} - 8.379V_{hb} - 310.92V_{el}$ [Equation 5.17]

ΔE = -53.754kcal/mol

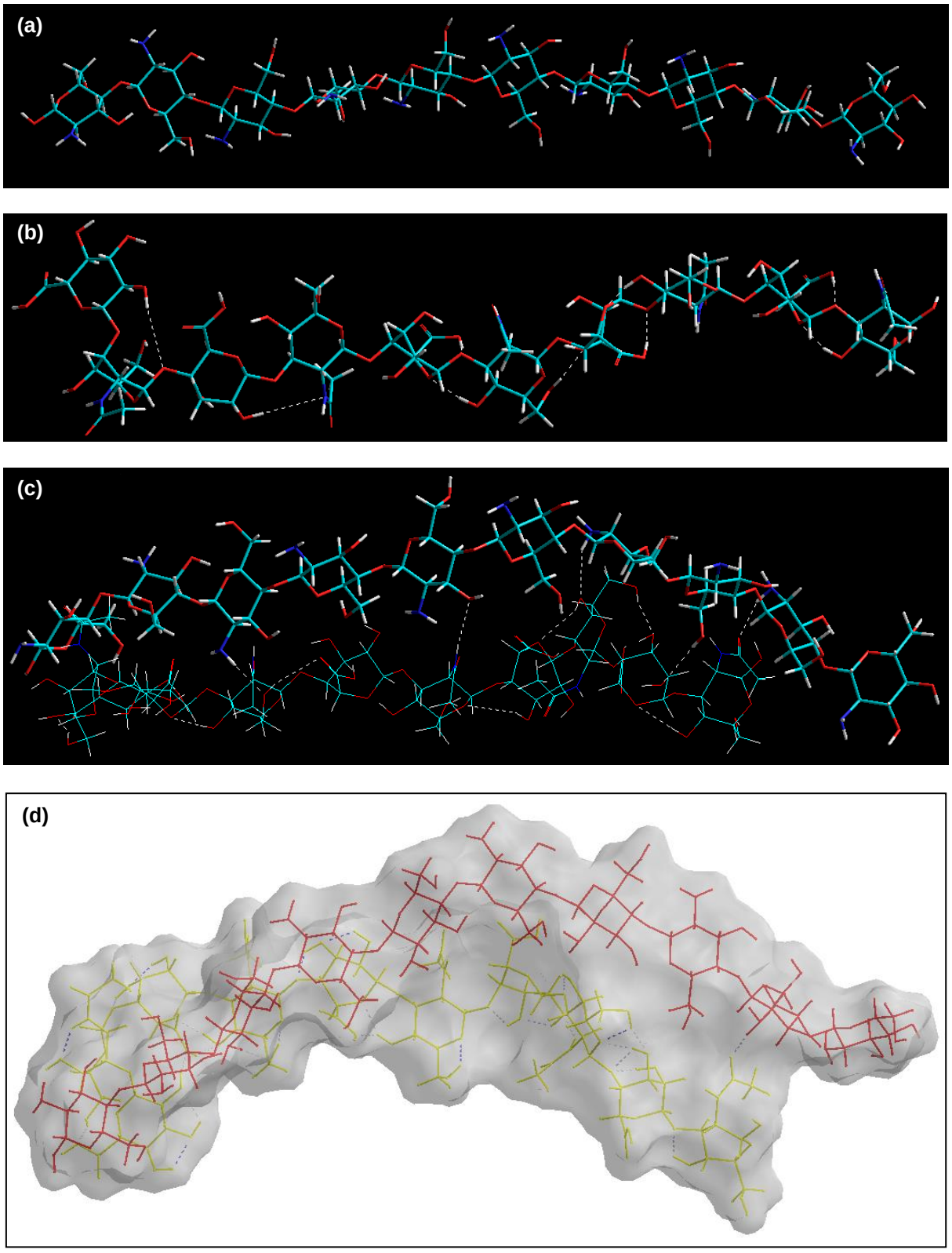

Figure 5.26: Visualization of geometrically minimized and energetically stable model of (a) Chitosan; (b) hyaluronate; (c) chitosan (tube rendering) - hyaluronate (stick rendering) complex; and (d) respective connolly molecular chitosan (red) and hyaluronate (yellow) electrostatic potential surfaces in translucent display mode - after molecular simulations in vacuum. Color codes: C (cyan), O (red), H (white), and N (blue)

5.4. Concluding Remarks

The intricately crosslinked polymeric system comprising the I^3 responds at an innate level predicted by its molecular make-up to inflammatory conditions as indicated by the results of the in-depth system characterization and deductions of the intricate molecular modeling undertaken. Oscillatory studies highlighted that the SRHS employed to form the inner and outer BPM of the I^3 exhibited stimulus-responsive rheological behavior on exposure to and removal of the inflammatory environment. The average loss tangent was highest when exposed to inflammatory conditions. FTIR highlighted that the final crosslinked BPMs showed the presence of bands inherent to all its components, with a reduction in intensity of selected bands and the appearance of new bands, attributable to the intra- and intermolecular crosslinking instigated in the presence of the chemical crosslinkers and initiators, namely DCC and NHS in the outer core and gluteraldehyde in the inner core. Overall, there was a significant shift in the T_g in the I^3, represented as the outer and inner BPM, compared to the native components, indicative of the high degree of crosslinking within the I^3. MRI highlighted that fluid ingress with device hydration and gelling can be considered as a significant predictor of the drug release profiles of the I^3 with the minimal change in the device area (which had a high degree of gelling) showing a notable negative correlation with both indomethacin and ciprofloxacin release under normal conditions (R^2= -0.8856, and R^2= -0.8783, respectively). However, under inflammatory conditions, there was a notable decrease in the area of the I^3, which exhibited a comparatively lower degree of hydration and gelling. This correlated positively and significantly with the observed drug release of both indomethacin and ciprofloxacin (R^2= 0.9695 and 0.9888, respectively). The porosity ascertained for both the inner and outer BPMs was a predictor of the overall internal architecture and potential drug release characteristics of the BPMs comprising the I^3, as were critical morphological changes, visualized via SEM and interpreted via image analysis displayed during device erosion. Tensile analysis provided an indication of the overall mechanical performance of the implant, indicating the potential of the I^3 to withstand physical stressors on implantation, and emphasized the physicomechanical advantages on incorporation of a NS within a matrix.

Finally, in order to tie together the overall molecular make-up of the device, as a progression from the previous two chapters, computational modeling undertaken succinctly confirmed the formation of a ‘secure-fit’ dual polymeric matrix system by highlighting the anticipated interconnectivity between the inner and outer BPM of the I^3.

Physicochemical and physicomechanical characterization was therefore an essential step for delineating *in vitro* attributes (with especial reference to its inflammation-responsive

transitions) for predicting the *in vivo* performance of the device, prior to determination of the clinical potential of the I^3 in an animal model.

CHAPTER 6

EVALUATION OF THE *IN VIVO* POTENTIAL OF THE I^3 IN THE HEALTHY AND INFLAMED RABBIT EYE

6.1. Introduction

**Ethics clearance for this in vivo investigation was obtained from the Animal Ethics Committee of the University of the Witwatersrand for this study, Ethics Clearance No 2009/02/05, see Appendix 8.1).*

6.1.1. The pertinence of *in vivo* analysis of novel drug delivery systems

In vitro release testing can supply valuable and valid information regarding the release of bioactives from a drug delivery system; however, it cannot totally simulate *in vivo* conditions. *In vivo* release studies are currently still imperative to define pharmacokinetic parameters and to foster an *in vitro/ in vivo* correlation. The rabbit model is a suitable and commonly used animal in ocular pharmacology, and was employed in this research to assess the ocular bioavailability of the model antibiotic and anti-inflammatory agents from the I^3 in the healthy and inflamed rabbit eye at predetermined intervals. *In vivo* studies are also required for safety evaluation of the intraocular implant. The acquisition of *in vivo* data from device implantation in the rabbit eye is essential to corroborate the feasibility and clinical viability of the I^3 in human patients.

The clinical potential of the I^3 in a suitable animal model was assessed for its ability to respond to an induced inflammatory state, and subsequently target ocular inflammation - demonstration of the like could present a significant advance in the treatment of ocular inflammatory diseases and associated intraocular infections. Specific objectives inherent in this were:

- To determine the polymer biodegradability and biocompatibility as inherent properties of both the BPMs and NS, with minimal tendency to induce inflammation upon implantation.
- To assess the gross toxicity of the device employing histopathology via assessing whether the I^3 induced any ocular toxicity over 28 days. Histomorphological assessment of cellular infiltrates was also significant in demonstrating the potential of the device to reduce the induced intraocular inflammation on release of the drug/s from the respective BPMs.

- To determine the pharmacokinetic parameters of *in vivo* release in the healthy and inflamed rabbit eye for assessment of the inflammation-responsive capabilities of the implant, and to develop an *in vitro/ in vivo* correlation, where possible.

6.1.2. Pharmacokinetic considerations and model selection for drug delivery from the I^3 to the intraocular structures via the periocular route

Uveitis is essentially a broad term comprising a large group of diverse diseases affecting the retina, uvea, and vitreal compartment, with simultaneous manifestations in several territories, and would necessitate drug targeting to multiple sites (Asencio-Duran et al., 2012). Three possible implantation sites were considered during pilot studies i.e. at the pars plana, intrascleral, and sub-Tenon - therefore periocular routes may be involved. Although delivery of drugs to the posterior segment tissues is attainable, a sound description of the bioavailability of the route is not available and few models describe the pharmacokinetics of drugs in the posterior segment. There is limited literature on the pharmacokinetics of periocular injections in comparison with that on the topical or intravitreous modes of administration. Elaboration of the pharmacokinetics is essential for explicating the potential of a novel drug delivery system (Amrite et al., 2008b).

6.1.3. The significance of defining an *in vitro-in vivo* correlation

The establishment of a relationship between *in vitro* release data and *in vivo* performance of the I^3 is pivotal for further development of the device. The Food and Drug Administration (FDA) guidelines define rules and reliability criteria of IVIVC for extended release forms. The following levels of correlations are exemplified (Ostrowski and Baczek, 2010):

1. Level A - directly associated with a linear relationship between rate of absorption *in vivo* and dissolution rate *in vitro* through all available time points. In some cases, a non-linear relationship may also be applicable.
2. Level B - based on statistical moment analysis, where mean residence time *in vivo* is compared to mean dissolution time *in vitro*. Because a number of *in vivo* curves could result in similar residence time values, the obtained relationship is not direct.
3. Single point level C - represents a single point relationship between one pharmacokinetic parameter (e.g. AUC) and one dissolution parameter (e.g. amount of substance released at a certain time point).
4. Multiple point level C - indicates the existence of a relationship between one or more pharmacokinetic parameters and dissolution at several *in vitro* time points, and should be represented by the early, middle and late stage of a dissolution profile.
5. Level D - exemplifies a semiquantitative rank order correlation, which is not useful for regulatory purposes.

Level A therefore represents a correlation of the highest order and is the preferred scenario for enabling reliable predictability of the *in vivo* behavior of a drug delivery system. A level A IVIVC is evaluated by the predicted error (PE) criteria defined in the FDA guidelines. A reliable level A correlation exists when an average absolute PE for AUC and C_{max} is below 10% and the PE for the individual formulation does not exceed 15%. In addition to criteria based on PE, the correlation coefficient (*R*) may be useful tool to evaluate a level A correlation (% *in vivo* absorbed *vs*. % *in vitro* dissolved. Literature indicates that an *R* value greater than 0.9 indicates an existing IVIVC (Ostrowski and Baczek, 2010).

This chapter therefore discusses the in-depth *in vivo* studies conducted on the I^3 through determination of intraocular drug concentrations furnished by the device in normal and inflamed rabbit eyes, device erosion *in vivo*, histological analysis, and pharmacokinetic analysis with establishment of an IVIVC; all as pertinent predictors of the overall clinical capacity of the device.

6.2. Materials and Methods

6.2.1. Materials and preparative work

Gamma sterilization employing a ^{60}Cobalt source at 25 kGy of the batches of the optimum I^3 (implant weights were ~15mg) was undertaken at Isotron (Isotron (Pty) Ltd., Isando, Johannesburg, South Africa). Anesthetics (ketamine), painkillers, topical antibiotics (chloramphenicol ointment) and euthanasia agents (phenobarbitone) for administration to the rabbits were supplied by the Central Animal Services of the University of the Witwatersrand, Johannesburg, South Africa. All other reagents used were of standard analytical grade of the highest purity.

All drugs and their respective dosages as administered to the rabbits are provided in Table 6.1.

Table 6.1: Drugs and recommended dosages as administered to rabbits

Drug	Route (e.g., I.V., I.M.)	Dose	Frequency
Ketamine HCl (dissociative anaesthetic)	I.M.	40mg/kg	On surgical implantation
Xylazine HCl (sedation, anesthesia, muscle relaxation, and analgesia)	I.M.	10mg/kg	On surgical implantation
Tetracaine HCl (topical anesthetic) 0.5% $^{w}/_{w}$	Topical	1-2 drops	On surgical implantation
Chloramphenicol ointment 1% $^{w}/_{w}$ (antibiotic)	Topical	Thin layer to lower lid	On surgical implantation
Sodium pentobarbitone	I.V.	> 50 mg/kg	On euthanasia

6.2.2. *In vivo* design and surgical technique

6.2.2.1. Selection of an animal model and pilot study for identification of an implantation site

The rabbit model is a suitable and commonly used animal in ocular pharmacology; however, differences in the anatomy of the rabbit eye compared to humans must be borne in mind (Worakul and Robinson, 1997). In the ensuing investigations, male and female New Zealand Albino rabbits (~2.5-4.0kg) were employed. Throughout the *in vivo* study, food and water was available *ad libitum* and the rabbits were continuously observed each day for alterations in eating behavior, and untoward changes as further defined. The entire postoperative course was logged in a protocol.

For the treatment of posterior segment inflammatory disorders or intraocular infections, the implant may be placed intravitreally - at the pars plana of the eye (posterior to the lens and anterior to the retina), intrasclerally, or sub-Tenon (these sites of implantation were represented in Chapter 2, Figure 2.1). The preferred implantation site was identified following pilot study A in a group comprising three New Zealand Albino rabbits (Figure 6.1). All surgical procedures described were undertaken by Professor Trevor Carmichael of the Department of Neurosciences, Ophthalmology Division, University of the Witwatersrand, who is skilled in ocular surgical techniques and possesses the following qualifications: MB BCh, FCS, MSc (Med), PhD (Med); and in accordance with the Association for Research in Vision and Ophthalmology (ARVO) Statement for the Use of Animals in Ophthalmic and Vision Research. Animals were housed at room temperature with a 12-h light/dark cycle

(light from 6am to 6pm), and were fed a standard rabbit diet with water available *ad libitum*. In each animal, the prototype optimized drug-free device was implanted either intrasclerally, sub-Tenon, or at the pars plana of one eye (the right eye) following general anesthesia via intramuscular administration of ketamine HCl, 40mg/kg (a dissociative anesthetic) and xylazine HCl, 10mg/kg (a sedative, anesthetic, muscle relaxant, and analgesic) and local anesthesia via instillation of tetracaine HCl 0.5%$^{w}/_{w}$ (topical anaesthetic) into the eye. The onset of sedation, duration of anesthesia and recovery time for the ketamine-xylazine combination has been shown to be ~3, 45 and 160 minutes, respectively (Green et al., 1981). The duration of the surgical procedure did not exceed 30 minutes. For pars plana implantation, a microblade was instituted to create a 5mm sclerotomy at the supra-temporal quadrant 2.0mm from the limbus, and the I^3 placed at the specified site. Vitreous penetration was verified with direct visualization and the implant was inserted into the vitreous cavity and secured via a 9-0 Nylon suture. For sub-Tenon placement, a small peritomy was created supero-temporally and a tunnel made into the sub-Tenon space extending as far posterior as possible. The device was grasped with a blunt forceps and pushed far enough posteriorly into the sub-Tenon pocket so that the anterior edge of the device was at least 10mm back from the limbus. The device was left between the superior and lateral rectus muscles and not secured. The conjunctiva and Tenon's capsule were pulled over to cover the device completely and secured at the limbus with a single 9-0 Nylon suture with the knot buried. The scleral procedure implicated performing a conjunctival peritomy superiorly (the conjunctiva was cut at the limbal attachment and recessed). The superior rectus muscle was located with a muscle hook and the eye rotated downwards exposing the super-nasal area of sclera between the medial and superior rectus muscles. A half thickness incision was made into the sclera creating a hinged trap-door over a pocket into which the device was inserted. The thin sclera in the rabbit makes it technically difficult to create an adequate pocket and the sides of the pocket needed to be closed with a 9-0 Nylon suture placed with several interrupted sutures. The conjunctiva was then pulled back to the limbus to cover the area and held in place with a buried 9-0 Nylon suture.

Chloramphenicol ointment 1%$^{w}/_{w}$ was instilled into each eye after each surgery and for 3 days thereafter to prevent surface ocular infections of the conjunctiva and/ or cornea. Once the procedure was completed the rabbits entered the recovery period and post-surgical care was initiated. Reflexes were checked with increasingly strong responses indicating recovery from anesthesia. Warmth was provided until recovery. Respiration and heart rate were monitored, usually by direct observation and stethoscope, until the rabbit was fully awake. The rabbits were observed each day for alterations in eating patterns signifying distress, with recordings made on the provided bed letter. On day 3, each animal in pilot group A was

euthanized with an overdose of IV sodium pentobarbitone (>50mg/kg, ~2mL) with consequent enucleation of both eyes and fixing in formalin, followed by embedding in paraffin and staining with hematoxylin-eosin for histological assessment. The following was noted: i) ease of implantation at the defined site, and ii) presence of any untoward reactions in the rabbit eye following visual assessment of the implanted and unimplanted eyes at 24, 48 and 72 hours for any untoward changes (e.g. retinal detachment and intravitreal hemorrhage) which would warrant termination of the pilot study, and iii) histological changes in the enucleated eye. The opposing eye in which no device was implanted was also enucleated, immediately snap-frozen at -80^{o}C and retained for *ex vivo* permeation studies, which were conducted concurrently, as reported in Chapter 3, Section 3.3.7.

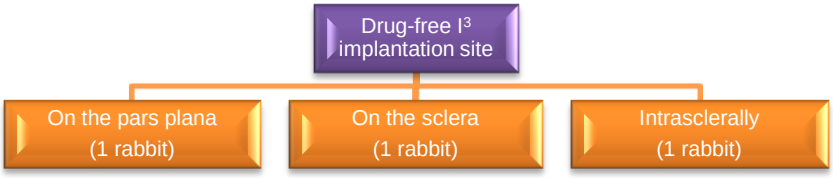

Figure 6.1: Pilot study A undertaken in New Zealand Albino Rabbits for identification of site of I^3 implantation

6.2.2.2. Pilot study for identification of a suitable model for induction of intraocular inflammation

The preliminary inflammation instigated on I^3 implantation is insufficient to quantify its inflammation-responsive degradation, thus inflammation was induced within a few days of implantation. Reports of induction of ocular inflammation in the anterior chamber are common for *in vivo* evaluation of anti-inflammatory activity of topically administered agents (Gupta et al., 2000; Bucolo and Maltese, 2002). However, reports of inflammation induction in the posterior segment are scarce and well-defined animal models of posterior segment inflammation are still lacking. Gatti and Panozzo (1995) reported that paracentesis is a well-recognized inflammatory stimulus; ocular inflammation may be induced by paracentesis of the vitreous i.e. hyalocentesis where a standardized model of posterior penetrating ocular trauma is made and then repaired (Öztürk et al., 2000). Other models include endotoxin-induced uveitis (EIU), which is an animal and human model of acute intraocular inflammation/ uveitis, induced by injection of the LPS component of the Gram-negative cell wall which leads to the production of pro-inflammatory cytokines (Rosenbaum et al., 1980; Jin et al., 2006). The main feature of EIU is the infiltration of PMNs and proteinaceous exudates in the aqueous humor and vitreous (Cousins et al., 1984; Herbort et al., 1989). Following LPS injection, acute inflammation is initiated as early as 0.5 h and peaks 18 h after the inoculation. Histopathologically, cellular infiltrates and proteinaceous exudates are

observed in the anterior segment (anterior chamber, iris and ciliary body). The posterior segment exhibits retinal vasculitis, hemorrhagic exudates, focal destruction of photoreceptor cells and choroidal infiltration (Ruiz-Moreno et al., 1992).

An effective model of posterior segment inflammation induction, which causes minimal trauma in the animal, was identified via comparison of two approaches. In order to establish the validity of the proposed models, and identify the most suitable model for induction of intraocular inflammation, pilot study B was conducted in a group comprising two New Zealand Albino rabbits (Figure 6.2).

In one rabbit, surgical puncture of the vitreous cavity i.e. hyalocentesis, was performed in the right eye (a microblade was used to make a 5mm laceration 2.0mm posterior to the limbus, with aspiration/ excision of ≈200µL vitreous humour from the posterior segment and suturing of the wound), as reported by Gatti and Panozzo (1995) and Öztürk and coworkers (2000) following general anesthesia via intramuscular administration of ketamine HCl, 40 mg/kg (a dissociative anesthetic) and xylazine HCl, 10mg/kg (a sedative, anesthetic, muscle relaxant, and analgesic) and local anesthesia via instillation of tetracaine HCl 0.5%$^{w}/_{w}$ (topical anesthetic) into the eye.

In the second rabbit, intraocular injection of LPS for induction of ocular inflammation as an acute uveitis (EIU) in the right eye of the rabbit was performed (Koura et al, 2006), i.e. one eye was exposed to the inflammatory stimulus. Intravitreal injection (100µL) of *Salmonella typhimurium* LPS (100-200ng/10µL of phosphate-buffered saline) into one eye was undertaken (Koura et al, 2006). The diluted LPS was injected intravitreally at the pars plana 2.0mm posterior to the limbus using a needle, taking care to avoid injury to the lens, following general anesthesia via intramuscular administration of ketamine HCl (40 mg/kg) and xylazine HCl (10mg/kg) and local anesthesia via instillation of tetracaine HCl (0.5%$^{w}/_{w}$) into the eye. The opposing eye of both rabbits, in which no hyalocentesis or intravitreal LPS injection was performed, was maintained as a control for comparative purposes.

Visual assessment was conducted at 24, 48 and 72 hours, and the rabbits were observed for any untoward changes (e.g. retinal detachment and intravitreal hemorrhage) which would warrant termination of the pilot study.

Thereafter, each rabbit was sacrificed 72 hours after hyalocentesis or LPS (endotoxin) injection with sodium pentobarbitone (>50mg/kg, ~2mL). For the histopathological evaluation, both eyes were enucleated, fixed in formalin, and embedded in paraffin and stained with

hematoxylin-eosin. Assessment of the level of inflammation was histopathologically graded: where Grade 0 = absent, Grade 1 = mild, Grade 2 = moderate, and Grade 3 = severe (Dunne and Travers, 1979). To ascertain the propensity of each method to induce an ocular inflammatory response, the infiltration of inflammatory cells into the vitreous cavity was visualized (Hashida et al., 2000). Previous investigators have reported that significantly more cells infiltrated into aqueous humor in a LPS-injected group (~4.9 x 10^6 cells/mL) than in a non-LPS-injected group (~7.5 x 10^5 cells/mL) (Koura et al., 2006). A model was selected based on tolerability in the rabbit and ability to induce an adequate level of inflammation within 72 hours.

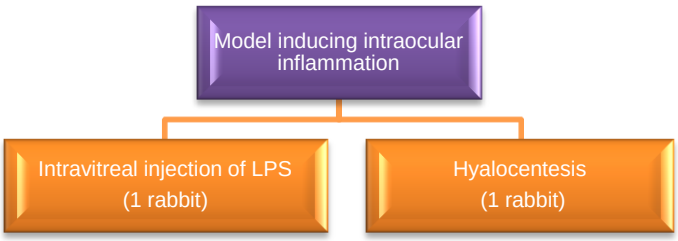

Figure 6.2: Pilot study B undertaken in New Zealand Albino Rabbits for identification of model for induction of intraocular inflammation

6.2.2.3. Intraocular inflammation and tissue sampling considerations

As discussed in Chapter 2, known posterior inflammatory changes due to LPS (as a described model for uveitis) include recruitment of macrophages, serous and hemorrhagic exudation, disruption of the BRB, and development of epiretinal membranes (Hiscott et al., 1988; Ruiz-Moreno et al., 1992; Yang et al., 1997; Zhang et al., 2005). The extensively diverse physiological and pathological functions of prostaglandins within the eye have been described in Chapters 1 and 2 (Adamis et al., 1994; Aiello et al., 1995 Ayalasomayajula and Kompella, 2003; Leung et al., 2003). The ciliary body (choroid), RPE and specific cells in the retina all express COX enzymes and are thus potential sources of endogenous prostaglandin production (Chin et al., 2001; Ju et al., 2002).

Following implantation of a device for drug delivery to the posterior segment tissues, measurement of drug concentrations in the vitreous is the most common approach, as this is considered to be representative of the retinal or choroidal concentrations of the bioactive. It is also important to consider the retinal or choroidal concentrations and pharmacokinetics of drugs, as these are essentially the target organs for posterior segment disorders. In this investigation, it was thus pivotal to include drug concentrations in the ocular structures (RCS) together with the vitreous levels. Eye afflictions such as uveitis possess their origin in various structures of the eye but cause secretion of cells into the vitreous (Asencio-Duran et al.,

2012). The NS, specifically, is designed to penetrate the ocular barriers and essentially target any inflammatory cells it may encounter on its path and have been demonstrated to undergo tissue and ultimately intracellular uptake (whether in the RCS or vitreous humor).

6.2.2.4. In vivo design and surgical technique in the healthy rabbit eye (Set A)

The implant was placed intravitreally, at the pars plana of the eye (posterior to the lens and anterior to the retina), intrasclerally, or sub-Tenon, in accordance with the preferred site as identified in pilot study A. Fifty New Zealand Albino rabbits free of any signs of ocular inflammation or gross abnormality (Set A) were used, randomly assigned to the experimental (25 rabbits) and control (25 rabbits) groups in accordance with the schematic presented in Figure 6.3. A placebo (drug-free) device was implanted into one eye of the control group and the drug-loaded implant into one eye of the experimental group. The minimum animal sample size for testing was ascertained from the specifications of the Animal Ethics Committee of the University of the Witwatersrand for statistical significance (i.e. n=5 for each sample point).

Following induction of general anesthesia as described in the pilot studies, the operative eye was prepared in a sterile manner and a wire lid speculum inserted. Sub-Tenon implantation was preferentially identified for device placement. A small peritomy was created supero-temporally and a tunnel made into the sub-Tenon space extending as far posterior as possible. The device was grasped with a blunt forceps and pushed into the sub-Tenon pocket far enough back so that the anterior edge of the device was at least 10mm back from the limbus. The device was left between superior and lateral rectus muscles and not secured. The conjunctiva and Tenon's capsule were pulled over to cover the device completely and secured at the limbus with a single 9-0 Nylon suture with the knot buried. Chloramphenicol ointment $1\%^{w}/_{w}$ was instilled into each eye after surgery for the prevention of surface ocular infections of the conjunctiva and/ or cornea.

Recovery and post-surgical care was as described for the pilot studies. Visual assessment was conducted on days 0, 3, 7, 14, 21, and 28, and the rabbits observed for any untoward changes (e.g. retinal detachment and intravitreal hemorrhage) which would warrant termination of the study.

For each study, one animal in each group was euthanized with an overdose of IV sodium pentobarbitone (>50mg/kg, ~2mL) at each sampling point (3, 7, 14, 21, 28 days) with consequent enucleation (surgical removal of the eyeball that leaves the eye muscles and remaining orbital contents intact). The central vitreous humor (approximately 2mL) from the

enucleated eye was aspirated employing a 15" needle (hyalocentesis). Therefter, the adherent muscle tissue was removed from the eye and the anterior segment of the eye was removed with a circumferential cut behind the limbus. The remaining orbital tissues were stored with the vitreous samples to enable measurement of drug (not yet internalized for intracellular mechanisms) in the choroid (posterior component of uvea), retina and RPE tissues. The tissues and vitreous were immediately snap-frozen at -80^{o}C in an ultra-low freezer (Sanyo VIP™ Series, Sanyo North America Corporation, Wood Dale, IL, USA). The study was performed in quintuplicate to ensure reproducibility (n=5 for each sampling point, i.e. 10 rabbits for each study). Two of the 5 eyes at each sampling point were not subjected to sectioning and storage with the vitreous humor but fixed in formalin, and embedded in paraffin and stained with hematoxylin-eosin for subsequent histological analysis.

In each animal receiving a drug-free device, the opposing eye in which no device was implanted was also enucleated, and either immediately snap-frozen at -80^{o}C for subsequent tissue sampling or fixed in formalin, and embedded in paraffin and stained with hematoxylin-eosin for subsequent histological analysis. This was for comparative purposes.

6.2.2.5. In vivo design and surgical technique in the inflamed rabbit eye (Set B)

Ten New Zealand Albino rabbits (Set B) were used, assigned to experimental (5 rabbits) and control (5 rabbits) groups as depicted in the schematic presented in Figure 6.5 (n=5 at the sampling point on day 7). Device implantation in the control and experimental groups was on day 0. Intraocular inflammation was induced as per the method identified in pilot study B on day 3 following surgical anaesthesia (Figure 6.5). Post-surgical care was as described for Set A, following device implantation and inflammation induction. The degree of inflammation induced following implantation was visually assessed and graded, as described, on days 3 and 7. One animal in each group was euthanized on day 7 with sodium pentobarbitone, the implant removed, and the central vitreous humor (≈2mL) from the enucleated eye was aspirated with a needle. Therefter, the adherent muscle tissue was removed from the eye and the anterior segment of the eye was removed with a circumferential cut behind the limbus. The remaining orbital tissues were stored with the vitreous samples to enable measurement of drug in the choroid, retina and RPE tissues. The tissues and vitreous were immediately snap-frozen at -80^{o}C an ultra-low freezer (Sanyo VIP™ Series, Sanyo North America Corporation, Wood Dale, IL, USA). The study was performed five times (n=5). Two of the 5 eyes at each sampling point were not subjected to sectioning and storage with the vitreous humor but fixed in formalin, and embedded in paraffin and stained with hematoxylin-eosin for subsequent histological analysis. The results of the investigations from both Sets would allow ascertainment of the purported differences

in device erosion and drug release behavior in the healthy versus the inflamed rabbit eye for ultimate description of the clinical potential of the I^3.

**Note that ethics approval was contingent on the fact that inflammation not be continued after the 7 day mark; hence only one drug concentration measurement could be obtained in the inflamed rabbit eye model.*

6.2.3. Histomorphological analysis for assessment of ocular inflammation, implant biocompatibility and biodegradability

The enucleated eyeballs (fixed in 10%$^{v}/_{v}$ formalin) were sent to IDEXX laboratories (Pretoria, South Africa) and were sectioned along the sagittal axis close to the optic nerve at three different levels. The sections were processed overnight in an automated tissue processor according to their standard operating procedure (PTA-his-SOP-27). Following the routine histological processing, wax blocks were produced in paraffin wax and sections of approximately 6µm cut according to IDEXX SOPs (PTA-his-SOP-30). The slides were stained with hematoxylin and eosin according to the IDEXX SOPs (PTA-his-SOP-49).

Cellular infiltration (degree of infiltration by lymphocytes, plasma cells, and mononuclear and polymorphonuclear leukocytes) was graded from 0 to 3+ in accordance with IDEXX laboratory protocols, as instituted in related investigations (Kobayashi et al., 2007).

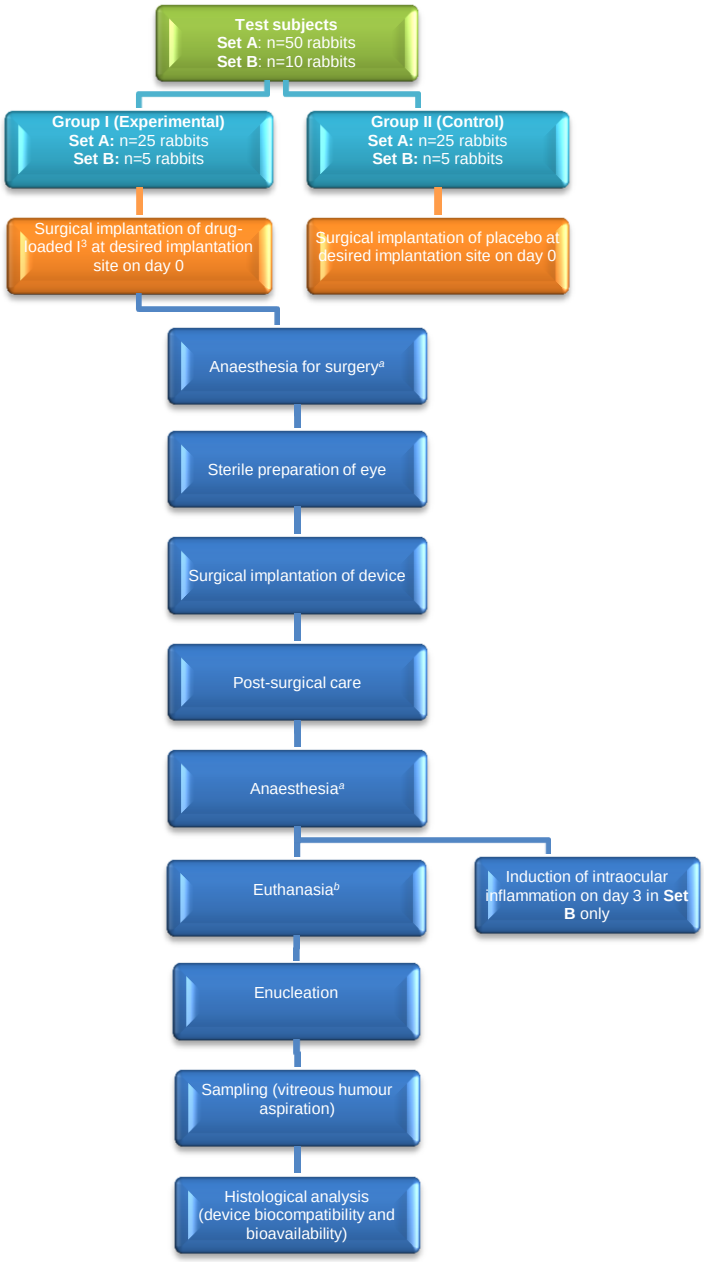

Figure 6.3: *In vivo* testing of the I^3 in animal species (Note: Rabbits underwent surgical implantation with device at day 0. Euthanasia and sampling occured on days 3, 7, 14, 21, 28 in Set A and on day 7, Set B)
[a] induced following I.M. administration of ketamine HCl, 40mg/kg and xylazine HCl, 10mg/kg; and instillation of tetracaine HCl 0.5% into the eye
[b] induced via an overdose of IV sodium pentobarbitone (> 50mg/kg, ~2mL)

6.2.4. Quantification of *in vivo* anti-inflammatory and antibiotic concentrations released from the I^3 into the posterior segment of the rabbit eye model under normal and inflammatory conditions

A method was required for simultaneous detection of ciprofloxacin and indomethacin in rabbit posterior ocular fluid. An ultraperformance liquid chromatographic (UPLC) method was developed employing a Waters® ACQUITY™LC system (Waters®, Milford, MA, USA) coupled

with a photodiode array detector (PDA), and Empower® Pro Software (Waters®, Milford, MA, USA). The UPLC was fitted with an Aquity UPLC® Bridged Ethyl Hybrid (BEH) Shield RP_{18} column, with a pore size of 1.7µm. A gradient method with a run time of 4 minutes was developed using acetonitrile and 0.1%$^{v}/_{v}$ formic acid in double deionized water as the mobile phase (Table 6.2). UPLC analysis enabled accurate simultaneous detection of micro-levels of both drugs.

A solvent flow rate of 0.25mL/min was maintained with an average initial pressure of 6500psi. The extracted and pre-filtered samples (0.2-1.0µL) were injected onto the column. The column and sample manager temperature was maintained at 21±0.5ºC. Prior to use, the column was equilibrated by passing 45mL of mobile phase solvent through the system. The eluent was monitored at analytical wavelengths set at 254, 278 and 318nm and the entire assay procedure was performed at room temperature (21±0.5ºC).

Table 6.2: Gradient method for the separation of indomethacin and ciprofloxacin indicating mobile phase concentrations at flow rates at each time point over the 3 minute run time

Time (min)	***Flow rate (mL/min)***	***0.1%$^{v}/_{v}$ Formic acid solution***	***Acetonitrile***
Initial	0.5	85	15
1.00	0.5	20	80
3.00	0.5	85	15

Nicotinic acid was identified via preliminary screening assays as an appropriate internal standard for both indomethacin and ciprofloxacin, being separated employing the mobile phase system instituted, and possessing an isolated retention time for sound analysis of peak areas. A standard linear curve was generated, as subsequently described to assess the respective drug concentrations released from the device at various time points.

6.2.4.1. Preparation of calibration standards and generation of corresponding in vitro drug release samples

In order to prepare the blank rabbit vitreous humor-posterior segment tissue dissolutes sample, a sample eye in which a no I^3 was implanted was employed: the stored and frozen sample (vitreous humor and posterior segment tissues, inclusive of choroid, retina, and RPE) were thawed at room temperature (21±0.5^{o}C) and allowed to environmentally equilibrate, followed by centrifugation at 15000×*g* for 10 min. Centrifugation was repeated twice in order to release any drug present in the tissues (which would be absent in the unimplanted eye). The supernatant was isolated and henceforth referred to as the total posterior ocular fluid (TPOF). Stock solutions of indomethacin and ciprofloxacin were prepared (0.2mg/mL) and diluted further with deionized water to prepare spiking solutions with indomethacin and

ciprofloxacin concentrations ranging between 0.02 and 0.1mg/mL. Calibration standards were prepared for generating a standard curve of indomethacin and ciprofloxacin in TPOF and for method validation; 50µL aliquots of both indomethacin and ciprofloxacin spiking solutions and the internal standard solution of nicotinic acid (100µL; initial concentration of 0.2mg/mL) were added to inert polypropylene tubes, each tube contained a 200µL aliquot of blank rabbit TPOF previously thawed and centrifuged at 15000×*g* for 10min. A liquid-liquid phase extraction methodology was used for the extraction of all drugs added from the blank rabbit TPOF to prepare a calibration profile. To each calibration standard, 300µL of acetonitrile was added. The tubes were then capped, vortexed (Vortex-Genie 2; Scientific Industries Inc., Bohemia, New York) for 15 s and centrifuged (Optima R LE- 80K, Beckman Coulter Inc., Fullerton, California) at 15000×*g* for 10 min. Aliquots (300µL) of the supernatants were filtered through a 0.22µm Millipore® filter and transferred to UPLC injection vials. Thereafter, 0.2µL of the filtered solution was injected onto the UPLC column for simultaneous indomethacin and ciprofloxacin content analysis. The ratio of the peak areas (between the internal standard nicotinic acid, and indomethacin and ciprofloxacin) versus the concentration data for the calibration standards was fit by linear regression to generate the calibration curves. This procedure generated a set of five calibration standards with concentrations ranging from 0.109645 to 0.520813µg/mL of indomethacin/ ciprofloxacin in rabbit TPOF. A standard linear curve was constructed from the five calibration standards and additional calibration standards were prepared and analyzed for validation runs for precision and accuracy analysis of the assay method (n=3). Determination of accuracy was via the mean recovery, i.e., the ratio of the mean found concentration to nominal concentration. Recovery of both drugs during the extraction procedures in the TPOF samples was thus assessed by replicate analysis (n=3) of the lower and upper concentration limits of the calibration standards and compared to those obtained by injection of aqueous solutions of indomethacin and ciprofloxacin prepared at the same concentrations corresponding to the standards. Both extracted calibration standards and the aqueous samples were injected onto the UPLC column employing the same chromatographic conditions as in the assay method developed.

In order to generate corresponding *in vitro* drug release samples for development of the IVIVC, drug release studies were conducted on the optimal I^3 formulation (containing ~60µg indomethacin and ~70µg ciprofloxacin) in 2mL normal SVH pH 7.4 (to replicate the rabbit vitreous humor volume) in an oscillating laboratory incubator, with balancing withdrawal of samples at 3, 7, 14, 21 and 28 days and filtration (0.22µm PVDF, Millipore Corporation, USA). Filtered samples were subsequently analysed via UPLC as described for the calibration standards for simultaneous determination of indomethacin and ciprofloxacin.

6.2.4.2. Extraction of indomethacin and ciprofloxacin from the aspirated vitreous fluid and posterior segment tissue samples

Rather than homogenize the posterior segment tissues together with the vitreous (as has been previously undertaken in certain investigations such as those of Cheruvu et al., 2003) the posterior segment tissues (inclusive of choroid, retina, and RPE) together with the associated 2mL vitreous were prepared as follows to extract the drugs: the stored and frozen study samples were thawed at room temperature (21±0.5^{o}C) and allowed to environmentally equilibrate, followed by centrifugation at 15000×*g* for 10 min. Centrifugation was repeated twice in order to release any drug present in the tissues. The supernatant was isolated, representing the TPOF and total drug. The sample biological matrix was replicated in the matrix employed for the calibration standards. Aliquots (200µL) of the TPOF samples were transferred using a graded microsyringe (0.5µL) [Hamilton (Pty) Ltd., Bonaduz, GR, Switzerland] into polypropylene tubes. The internal standard in deionized water (nicotinic acid; 0.2mg/mL; 100µL) was added to each tube, and the tubes were vortexed for 15 s. The same procedure used for the extraction of the calibration standards (with the addition of 300µL acetonitrile), and UPLC injection of calibration standards, were applied to the diluted TPOF samples for simultaneous measurement of indomethacin and ciprofloxacin content. Measurements were conducted on each three samples in triplicate (n=3).

6.2.5. Determination of the erosional behavior of the I^3 in the normal and inflamed rabbit eye

In order to correlate the *in vivo* drug release characteristics of the device under normal and inflammatory conditions with that of the overall bulk erosion transitions of the I^3, the dynamic weight change of the device before implantation and following removal from the euthanized rabbit at each time point was assessed (0, 3, 7, 14, 21 and 28 days in the normal rabbit eye; and 0 and 7 days in the inflamed rabbit eye). Following removal of the I^3 from the eye, it was allowed to dry under normal conditions to constant weight. The following empirical relationship was used to demonstrate the overall gravimetric transition of the I^3 from 100% to 0% initial weight:

$$I^3\ erosion\ (\%) = \left(\frac{initial\ weight - final\ weight}{initial\ weight}\right) \times 100 \qquad \text{[Equation 6.1]}$$

The initial and final weights represent the pre-implantation and dried post-implantation weights of the I^3, respectively. Measurements were undertaken in quintuplicate (n=5).

6.2.6. Visualization of *in vivo* surface morphological transitions of the I^3 in the normal and inflamed rabbit eye

In congruence with *in vitro* observations, the changes in the surface architecture of the I^3 in the normal and inflamed rapid eye were evaluated on a desktop SEM system (Phenom™ scanning electron microscope, FEI Company, OR, USA) to view the overall and in-depth surface architecture at various magnifications. Following removal from the rabbit eye, I^3 samples were dried to constant weight under ambient conditions (25^{o}C). Samples were made electrically conductive prior to analysis through the process of gold-sputter coating (SPI Module™ Sputter Coater, SPI Supplies, PA, USA).

6.2.7. Pharmacokinetic modeling of drug release data employing compartmental and noncompartmental algorithms and establishment of an *in vitro-in vivo* correlation

Pharmacokinetic data analysis was achieved using PKSolver, a menu-driven add-in program for Microsoft Excel written in Visual Basic for Applications (VBA). The program was instituted to undertake noncompartmental and compartmental analysis (Zhang et al., 2010).

Noncompartmental analysis is extensively employed in PK analysis. Calculation of the area under the zero and first moment curves from 0 to last time *t* ($AUC_{0\text{-}t}$, $AUMC_{0\text{-}t}$) is generally via the trapezoidal method (linear or log). The terminal elimination slope, λ_z, can be calculated based on user-specified terminal data points or automatically estimated using the regression with the largest adjusted R^2.

$$Adjusted\ R^2 = 1 - \frac{(1-R^2)(n-1)}{n-2} \qquad \text{[Equation 6.2]}$$

Where *n* is the number of data points in the regression and R^2 is the square of the correlation coefficient. In the case of the specified I^3 (extravascular input data) the time delay of absorption *T*lag was specified or set *T*lag = 0. Area under the zero and first moment curves from the last sampling time to infinity ($AUC_{t\text{-}\infty}$, $AUMC_{t\text{-}\infty}$) were calculated based on the last observed or predicted concentration employing the following equations:

$$AUC_{t-\infty} = \frac{C_{last}}{\lambda_Z} \qquad \text{[Equation 6.3]}$$

$$AUMC_{t-\infty} = \frac{C_{last} \times t_{last}}{\lambda_Z} + \frac{C_{last}}{\lambda_Z^2} \qquad \text{[Equation 6.4]}$$

Additional parameters including $t_{1/2}$, mean residence time (*MRT*), clearance (*Cl*), and volume of distribution based on the terminal slope (V_z) were subsequently calculated.

Quantitative evaluation of the drug transport process occurring in the eye necessitates selection of a suitable PK model for fitting concentration-time data. Appropriate model selection required the use of diagnostics such as the correlation coefficient, sum of squares of residuals (SS), standard error of weighted residuals (SE), Akaike's Information Criterion (AIC) and Schwarz's Bayesian Criterion (SBC). AIC and SBC hold the most significance (Zhang et al., 2010), and were calculated as described in Chapter 4, Equations 4.10 and 4.11.

Compartmental analysis was instituted to quantitatively evaluate and predict the *in vivo* fate of a both drugs in the I^3 by modeling the concentration-time data with a suitable PK compartment model. Pharmacokinetic and pharmacodynamic considerations of the drugs included in the I^3 led to tentative consideration of four PK models, with the I^3 considered as a single extravascular dose with sub-Tenon placement:

1. Noncompartmental model
2. One compartment model
3. One compartment model with *Tlag*
4. Two compartment model

Subsequent to definition of the PK parameters, WinNonLin® software (V5.3 with IVIVC Toolkit Build 20091211139, Pharsight Software, Statistical Consultants Inc., Apex, NC, USA) was employed for establishing a Level A IVIVC. Input data comprised *in vitro* indomethacin and ciprofloxacin release data, as well as relevant PK data. As discussed, an IVIVC is the correlation between the *in vitro* drug dissolution profile and *in vivo* drug absorption profile. Evaluation of an IVIVC model implicates development and validation. Therefore, firstly, development of level A IVIVC model follows a two-stage process:

1. *Deconvolution*: the observed fraction of the drug absorbed is estimated based on the Wagner-Nelson method. Following estimation of pharmacokinetic parameters, the IVIVC model is developed using the observed fraction of the drug absorbed and that of the drug dissolved. Based on the IVIVC model, the predicted fraction of the drug absorbed is calculated from the observed fraction of the drug dissolved.
2. *Convolution*: the predicted fraction of the drug absorbed is then convolved to the predicted plasma concentrations (or other relevant body fluid concentration in the case of this investigation) instiuting the convolution method. Thereafter, determination of the predictability of a level A correlation focuses on estimating the percent prediction error

(%PE) between the observed and predicted plasma concentration profiles, such as the difference in pharmacokinetic parameters (C_{max}, and the area under the curve from time zero to infinity, $AUC_{0-\infty}$).

6.3. Results and Discussion

6.3.1. Surgical procedures and post-surgical assessment of the rabbit model following implantation of the I^3

The I^3 was well tolerated and its efficacy successfully demonstrated in the rabbit eye model. No untoward reactions (e.g. retinal detachment, vitreous hemorrhage) were observed in any of the 65 rabbits, some of which were evaluated up to the full 28 days of analysis. Clinically no changes were observed in the vitreous humor, retina or choroid such as vitritis, vascular changes, exudative changes, necrosis or traction. This was attributed to the ease and relatively minimal trauma of the implantation procedure and lack of toxicity associated with the device. Two rabbits demonstrated changes in eating habits but this was remedied by an alteration in diet. One rabbit suffered mortality before completion of the study due to causes unrelated to any component of the surgeries. Figure 6.4 portrays the general procedure adopted in the housing, handling, anesthetization, examination, and post-surgical care of the rabbit. The gross clinical presentation of the rabbits following implantation of the I^3 at the proposed sites following pilot study A is depicted in Figure 6.5. It was initially evident from the overall visual appearance of the rabbits' eyes that sub-Tenon implantation was best tolerated (affirmed subsequently via histopathology in Section 6.3.2).

Figure 6.4: Photographic evidence of (a) Housing of the rabbits (b) preparation for surgery with anesthetization (c) post-surgical recovery of the rabbit (d) slit-lamp examination of the rabbit eye following surgical implantation

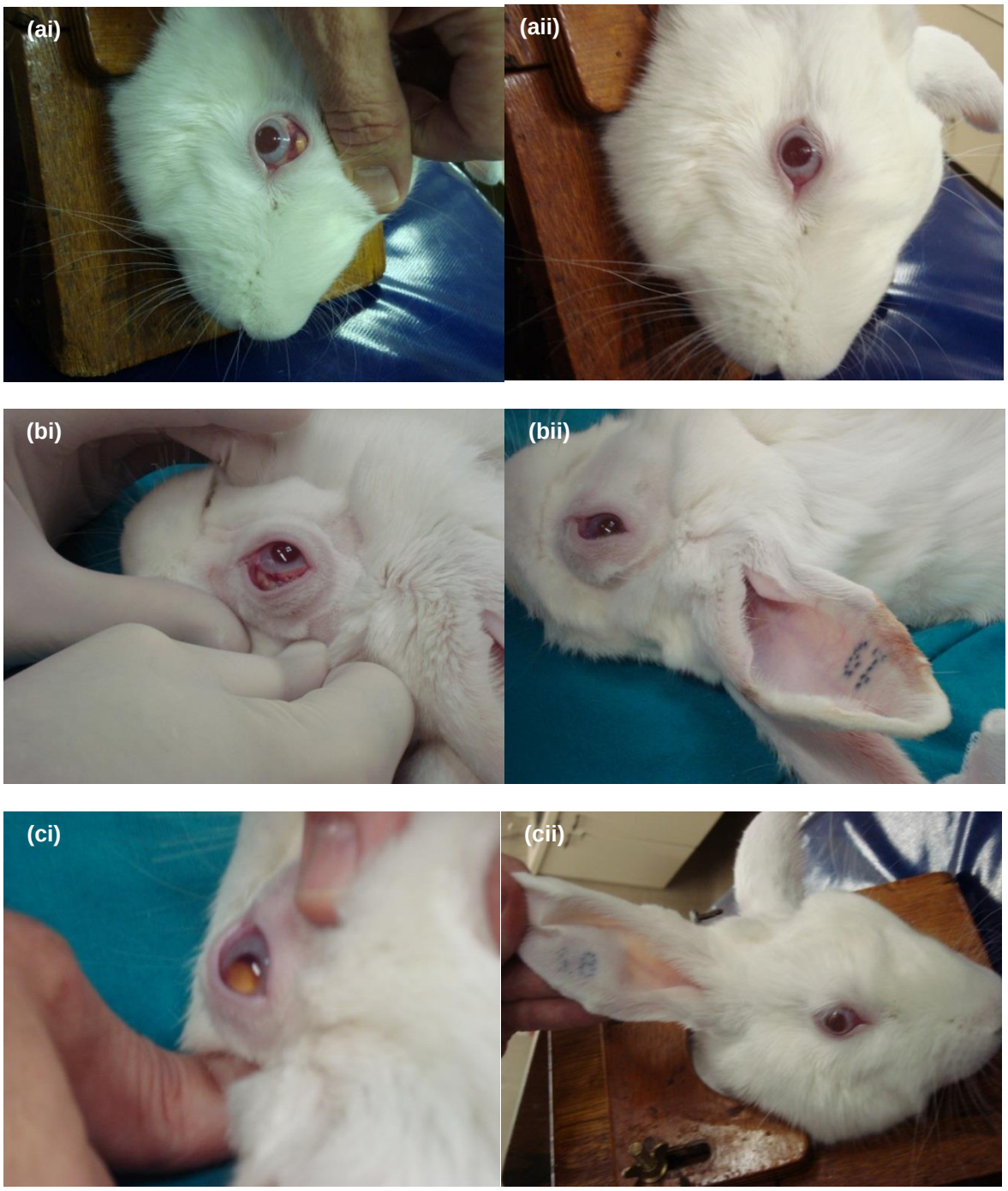

Figure 6.5: View of the rabbit eye (i) eyelids drawn open and (ii) normal view following (a) sub-Tenon (b) intrascleral and (c) pars plana implantation

As evidenced from Figure 6.6, the implantation procedure ultimately selected for the main investigation (i.e. sub-Tenon implantation) was drastically simplified, as no incision into the posterior segment was required (Retisert^{TM} for uveitis management is implanted at the pars plana, therefore requiring incision into the posterior segment), which often culminates in loss of vitreous and unfavorable pressure changes, and is an invasive procedure overall. The I^3 was readily recovered following euthanasia of the rabbit prior to enucleation (Figure 6.7).

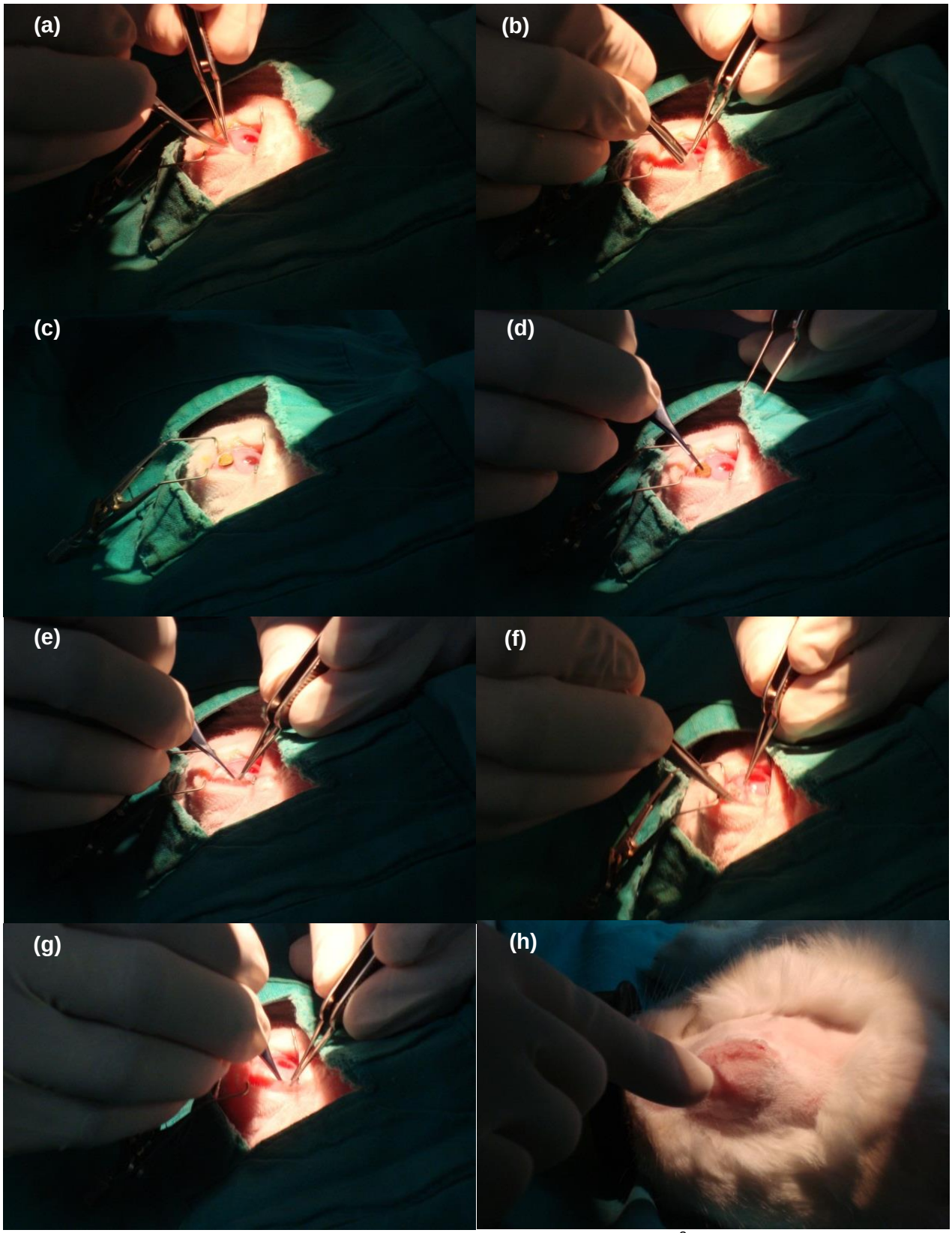

Figure 6.6: Successive images (a-h) depicting implantation of the I^3 into sub-Tenon's space of the rabbit eye

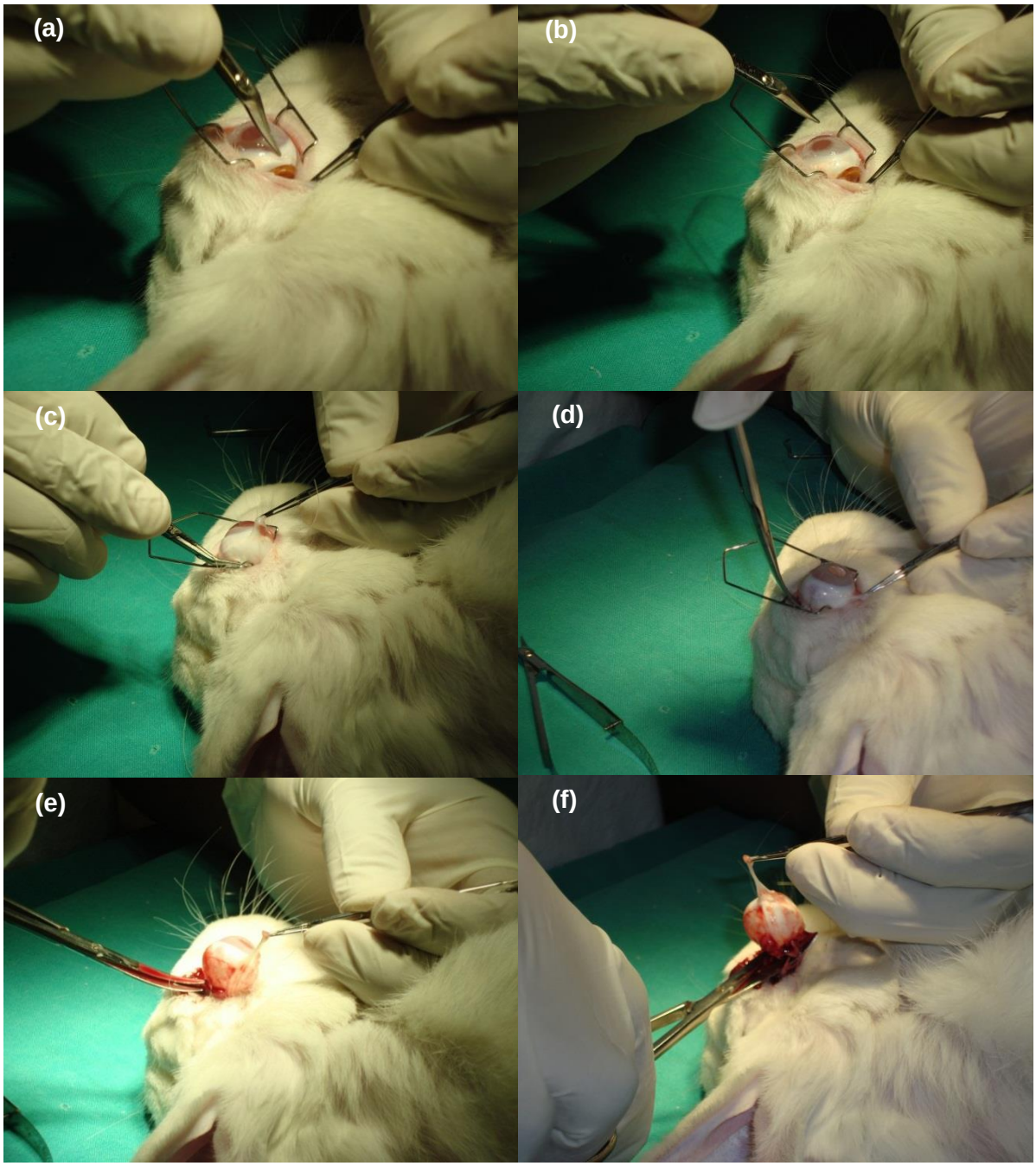

Figure 6.7: Successive photographic images (a-f) depicting device removal and enucleation

6.3.2. Histomorphological findings for the pilot studies for identification of the preferred implantation site for the I^3 and a suitable model for induction of intraocular inflammation

Histomorphological evaluation of the ocular milieu and the I^3 biocompatibility and biodegradability was undertaken on all representative samples. Table 6.3 exemplifies the levels of anterior and posterior inflammation induced following the different methodologies for induction of inflammation, and following implantation at the proposed ocular sites.

Table 6.3: Levels of anterior and posterior inflammation observed following evaluation of the various implantation sites and the different methodologies for induction of inflammation

IDEXX Ref	*Animal Id*	*Methodology*	*Anterior Inflammation*	*Posterior Inflammation*
1199A/11	48C	Control	0	0
1199B/11	35T	LPS	1+	3+
1199G/11	48T	Hyalocentesis	0	0
1199C/11	35C	Control	0	0
1199D/11	18I	IP Sub-Tenon/ scleral (external)	0	0
1199E/11	19I	IP Pars plana	1+	1+
1199F/11	21I	IP Intrascleral	0	1+

Legend:

0	-	no detectable inflammation
1+	-	mild inflammation
2+	-	moderate inflammation
3+	-	severe inflammation
IP	-	implant
LPS	-	lipopolysaccharide

6.3.2.1. Histological identification of a suitable model for induction of posterior segment inflammation

Sagittal sections from the control eye of the rabbit eye in which no device was implanted are provided in Figure 6.8 as a point of comparison and showed normal morphology without any inflammation visible in the anterior and posterior chambers. Part of the lens was included in one section and appeared morphologically normal.

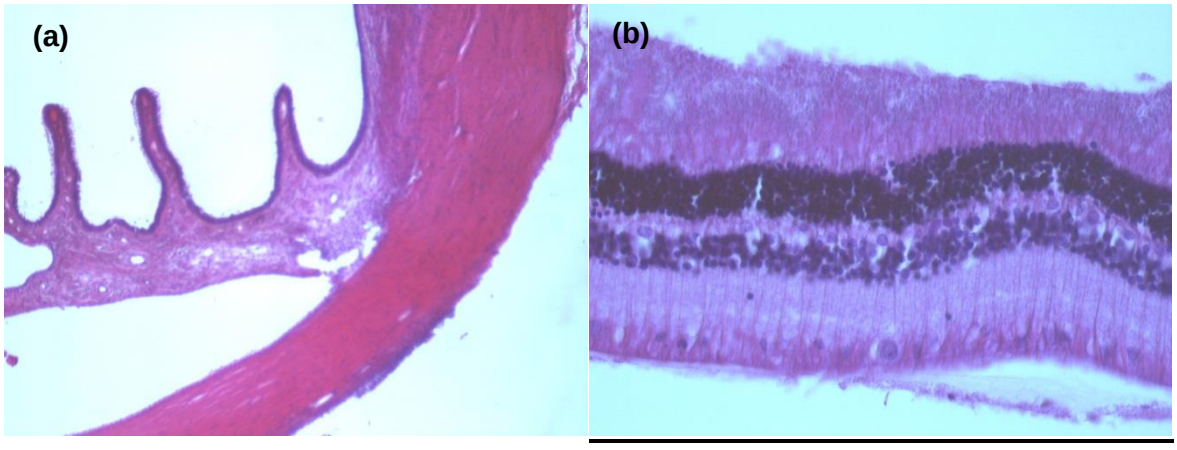

Figure 6.8: Images of (a) the normal eye and (b) the retina of the normal device-free eye in the control rabbit (10x magnification)

In the eye in which LPS was injected, acute purulent panopthalmitis could be confirmed with severe exudation into the posterior chamber and vitreous humor as well as mild inflammation visible in the anterior chamber of the eye. Polymorphonuclear leukocytes (heterophils) appeared to predominate in the exudative inflammatory process, but some mononuclear leukocytes as well as macrophages were scattered in the protein-rich inflammatory exudate.

Additionally, cell debris and desquamated epithelium cells were observed in the vitreous material. The exudate extended up to the retina and was also present in the ciliary processes, but did not penetrate into the sub-epithelial stroma. A focal scleritis was present at the sclera-corneal junction, which was possibly associated with needle penetration on LPS injection. Macrophages and lymphoplasma predominated in this focal scleritis (Figure 6.9).

Where hyalocentesis was performed, sections from the eye could not confirm inflammatory infiltrates into the anterior and posterior chambers, as well as the vitreous body. A focal scleritis was evident where mononuclear cells predominated. No inflammatory infiltrates were detected in the eyeball.

From the histological evaluation it appears that the intraocular injection of the LPS component of the cell wall from the Gram negative *Salmonella typhimurium* is responsible for panopthalmitis with severe exudative inflammation in the posterior chamber and vitreous and mild exudation into the anterior chamber of the eye. This approach was thus identified as the most suitable model for induction of posterior segment inflammation.

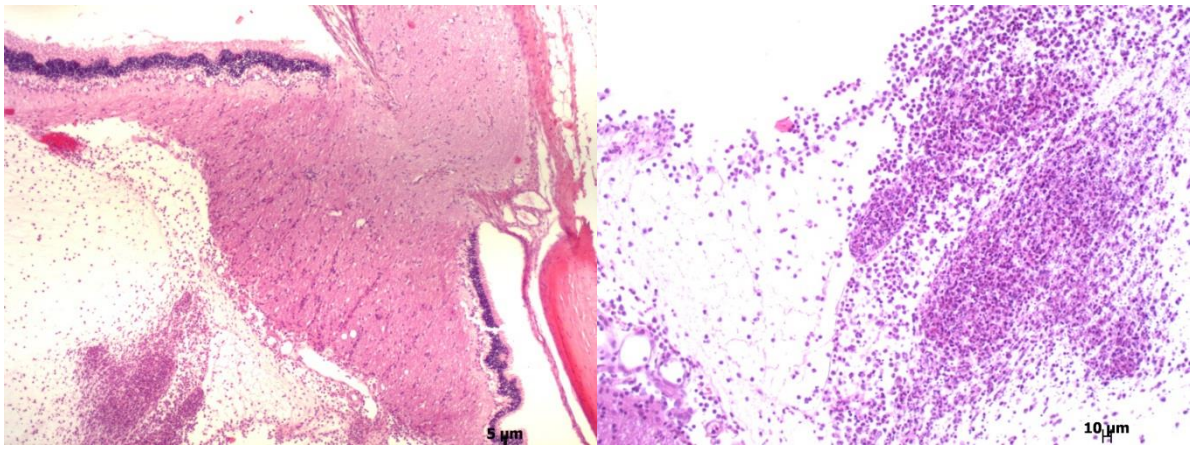

Figure 6.9: Histological slides following LPS injection (10x magnification)

6.3.2.2. Histological identification of a suitable site for implantation of the I^3

The histological evaluation of the eye in which the implant was placed sub-Tenon (on the sclera) confirms a focal episcleral implant detected as a basophilic vacuolated material at the conjunctival-scleral reflection. There was minimal to mild inflammation observed in the vicinity of the implant on the external surface of the sclera where heterophils and a few macrophages appeared to predominate. No exudative inflammation was present in the anterior or posterior segments of the eye (Figure 6.10). A mild lymphocytic conjunctivitis was detected.

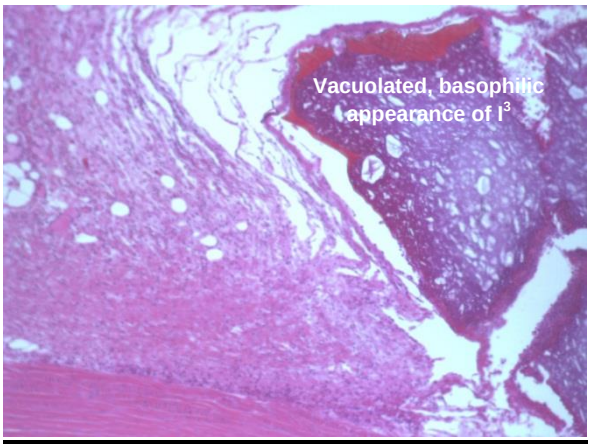

Figure 6.10: Histological slide depicting the I^3 and associated tissue following sub-Tenon placement (10x magnification)

When the device was implanted intravitreally (pars plana), in the sagittal section of the eye it was possible to demonstrate the I^3 in the pars plana, posterior to the lens and within the posterior vitreous intraocular fluid (Figure 6.11). Again, the implant revealed a vacuolated appearance with basophilic staining. Around the implant the vitreous humor revealed dissociation as well as a mild degree of intraocular inflammation. Heterophils predominated among the inflammatory infiltrates. In the remainder of the intraocular fluid minimal cell infiltrates were present. A mild inflammation was visible in the posterior and vitreous chamber, but some heterophils were also observed within the anterior chamber of the eye. The inflammation in the anterior chamber was classified as minimal to mild. Few inflammatory cells were observed at the iridocorneal angle. A focal mild episcleritis was present.

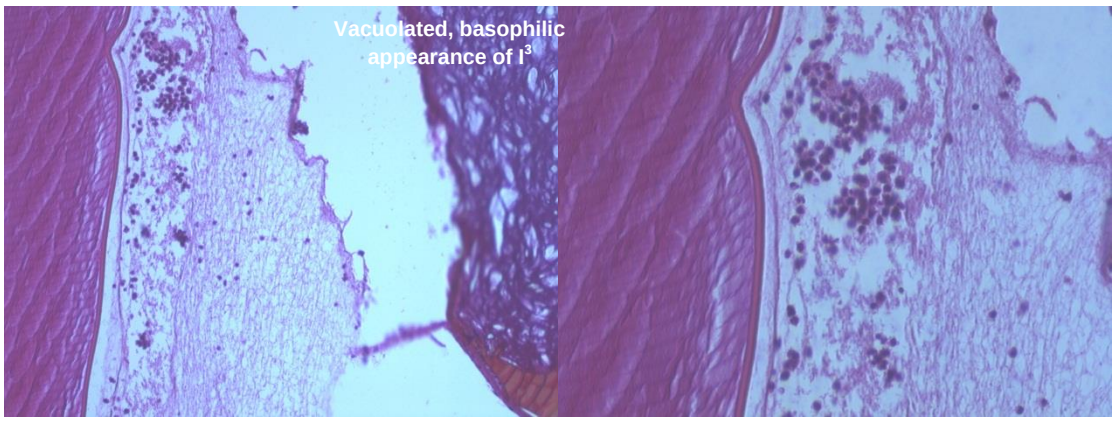

Figure 6.11: Histological slides depicting (a) the I^3 and lens and associated inflammation at 10x magnification and (b) the lens and associated inflammation at 20x magnification

With regard to the final implantation procedure, the I^3 could be identified intrasclerally on the lateral part of the sclera and there was a mild inflammation observed on the external surface of the sclera in the loose connective tissue with neutrophils predominating (Figure 6.12). The

capillaries appeared dilated and congested. In the posterior chamber, directly underneath the implant, heterophils were found in the sclera. The capillaries were prominently dilated. Minimal extension into the vitreous humor of the posterior segment was visible. All of the other intraocular structures appeared normal.

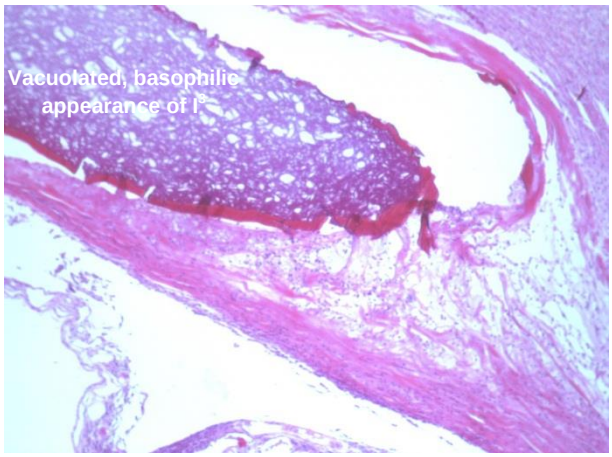

Figure 6.12: Histological slide depicting the I^3 implanted intrasclerally (10x magnification)

To summarize, a mild to minimal inflammatory response was detected in both the posterior and anterior eye chambers where the I^3 was introduced in the pars plana within the posterior chamber. A focal mild inflammatory process was present in the deeper segment of the sclera where the I^3 was placed intrasclerally. Minimal inflammation was observed upon sub-Tenon implantation. This was identified as the most favorable site for successive implantations, as it is minimally invasive and the surgery could be conducted on an outpatient basis. Since the NS incorporated within the I^3 effectively penetrates the scleral membrane (demonstrated in Chapter 2), the choice of a periocular implantation site was envisaged as not being a limiting factor.

6.3.3. Histomorphological findings following implantation of the I^3 in the normal and inflamed rabbit eye

6.3.3.1. Effects of the drug-loaded I^3 in the normal rabbit eye

Microscopic examination at day 3 confirmed normal intraocular morphology with only mild acute inflammation on the external surface of the sclera where incisions into sub-Tenon's space were conducted. Three days following implantation of the drug-loaded I^3, no intraocular pathological changes could be confirmed. The optic nerve appeared morphologically normal. Within the muscle attached to the external surface of the sclera, mild rhabdomyolysis and inflammation were found, while some hemorrhages and fibrin exudation

was also visible in the stromal tissue. No pathology was observed in the anterior chamber of the eye or within the vitreous chamber posterior to the lens (Figure 6.13).

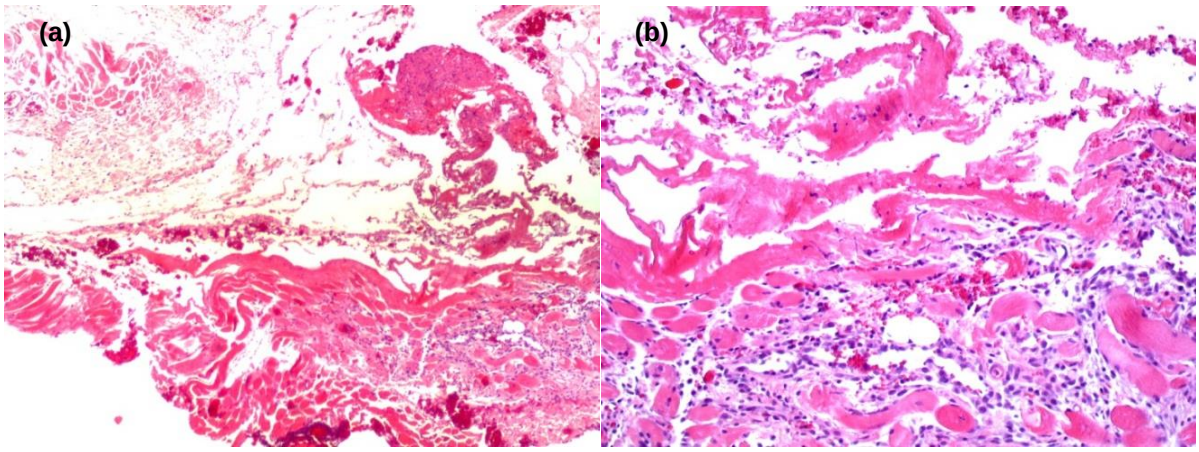

Figure 6.13: Histological slides at day 3 for the drug-loaded I^3 in the normal eye at (a) 4x and (b) 20x magnification

At day 7, morphological evaluation of sections from the eyeball showed no intraocular pathological changes with no specific lesions present in the soft tissues around the eyeball in these sections. The optic nerve appeared morphologically normal. In one eye specimen, a few hemorrhages could be detected in the muscle of the external surface of the eye.

The histological evaluation could not demonstrate any pathological changes within the internal structures of the eyeball at day 14. The anterior chamber of the eye, posterior chamber, as well as the vitreous chamber, were all normal. No morphological pathology of the optic nerve was noted. The soft tissues around the eye appeared morphologically normal. A few hemorrhages could be detected in the muscles around the eyeball in one specimen.

At day 21, histological evaluation of the sections from the eye demonstrated no inflammation or any morphological pathology in the internal structures of the eye. Generally no pathology was found in the sclera and extrascleral soft tissue. A focal mild subacute inflammation process was present on the external surface of the sclera of one specimen with macrophages predominating, most likely at the incision site of the drug-loaded implant (Figure 6.14).

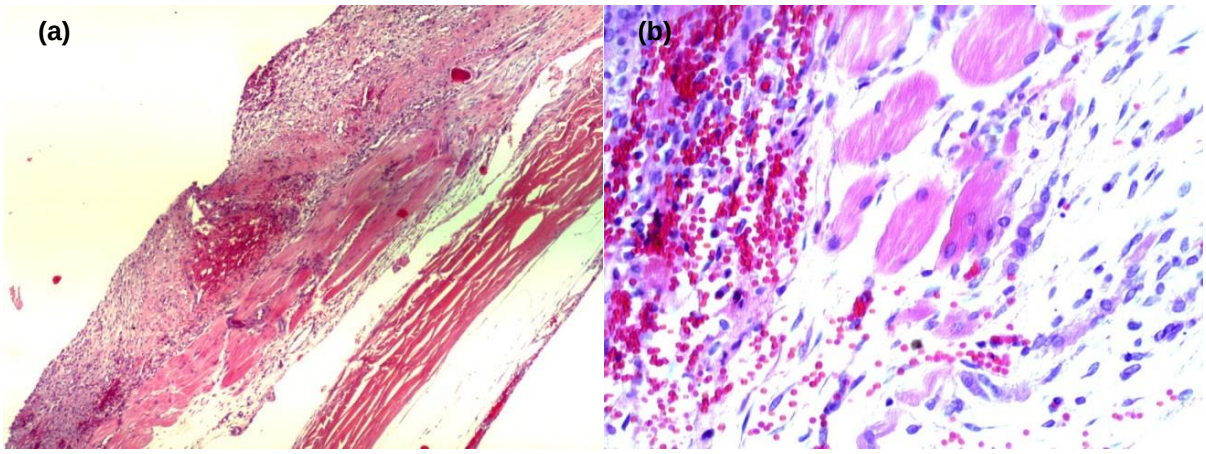

Figure 6.14: Histological slides at day 21 for the drug-loaded I^3 in the normal eye at (a) 4x and (b) 20x magnification

In the eyeball sections at 28 days of the experiment, no pathology could be recorded in intraocular structures of the eye. The extrascleral soft tissue, as well as the optic nerve appeared morphologically normal.

6.3.3.2. Effects of the drug-free I^3 in the normal rabbit eye

At day 3, no pathology could be confirmed in the intraocular structures from the anterior, posterior, as well as the vitreous chamber of the eye. In addition, the extraocular soft tissue was morphologically normal. In one specimen, the sections from the eyeball revealed no intraocular lesions, but a mild inflammatory process could be detected in the muscle attached to the sclera. Macrophages appeared to predominate (Figure 6.15).

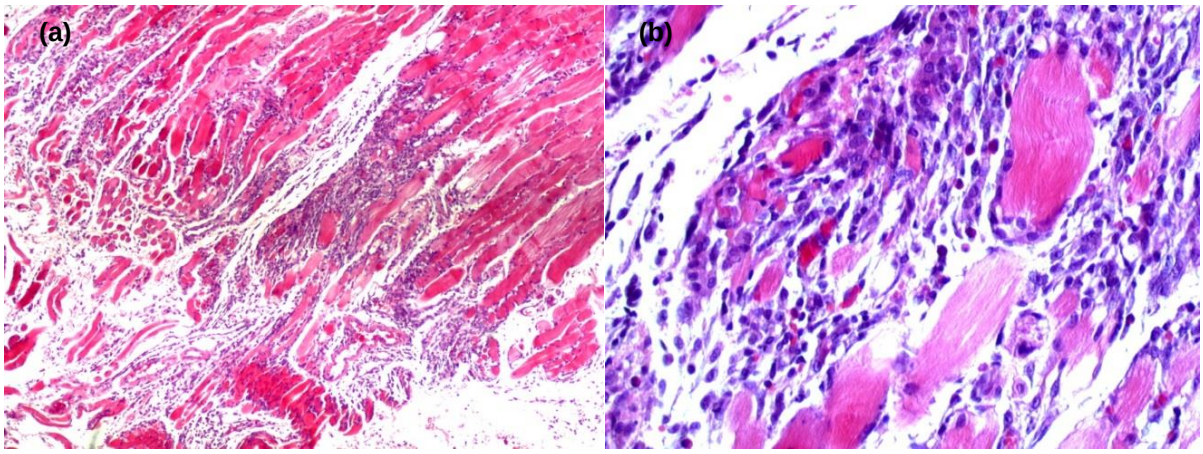

Figure 6.15: Histological slides at day 3 for the drug-free I^3 in the normal eye at (a) 4x and (b) 20x magnification

Normal anatomical features are observed in the intraocular structures as well as the sclera and extraocular soft tissues at day 7. No lesions were present in the intraocular spaces as well as the optic nerve and extraocular soft tissues.

In general, at day 14, the intraocular tissues appeared morphologically normal and no specific pathology could be confirmed in the sections from the eye as well as the optic nerve and periocular soft tissue. In one specimen, sections from the eye did not reveal pathology in the intraocular structures and a mild focal granulomatous inflammatory reaction was present on the external surface of the sclera, possibly at the implantation site into the sub-Tenon's space, and macrophages predominated.

At day 21, the morphological evaluation could not demonstrate any intraocular and extraocular pathology in these sections and the optic nerve appeared morphologically normal. Focal hemorrhages were detected within the muscles around the eye. In one specimen, sections from the eye did not reveal pathology in the intraocular structures at day 21, but a mild focal periocular granulomatous inflammation could be detected. Epitheloid macrophages predominated with few multinucleated giant cells also visible in the soft tissue around the eyeball.

Sections from the eyeball at day 28 did not reveal intraocular pathological changes (of the intraocular chambers and structures). The sclera and cornea were intact and normal. Furthermore, extraocular soft tissues were non-inflamed and morphologically normal.

6.3.3.3. Effects of the drug-loaded I^3 in the inflamed rabbit eye

In the sections from the eye at day 7, exudative inflammation was demonstrated in the posterior chamber and in the vitreous chamber of the eye. The intraocular inflammatory process appeared acute and mild. Polymorphonuclear leukocytes (heterophils) predominated with some protein-rich fibrinous exudate also present. The anterior chamber of the eye was clear of any inflammatory infiltrates. The exudative panopthalmitis was visualized as mild and acute in the posterior vitreous chamber of the eye. In the surrounding soft tissue mild subacute inflammation was detected where neutrophils and some mononuclear leukocytes were observed in the peri-orbital fat and loose connective tissue. This was focal and most likely associated with the implantation site. The subacute inflammation on the extraocular stroma was graded as mild (Figure 6.16).

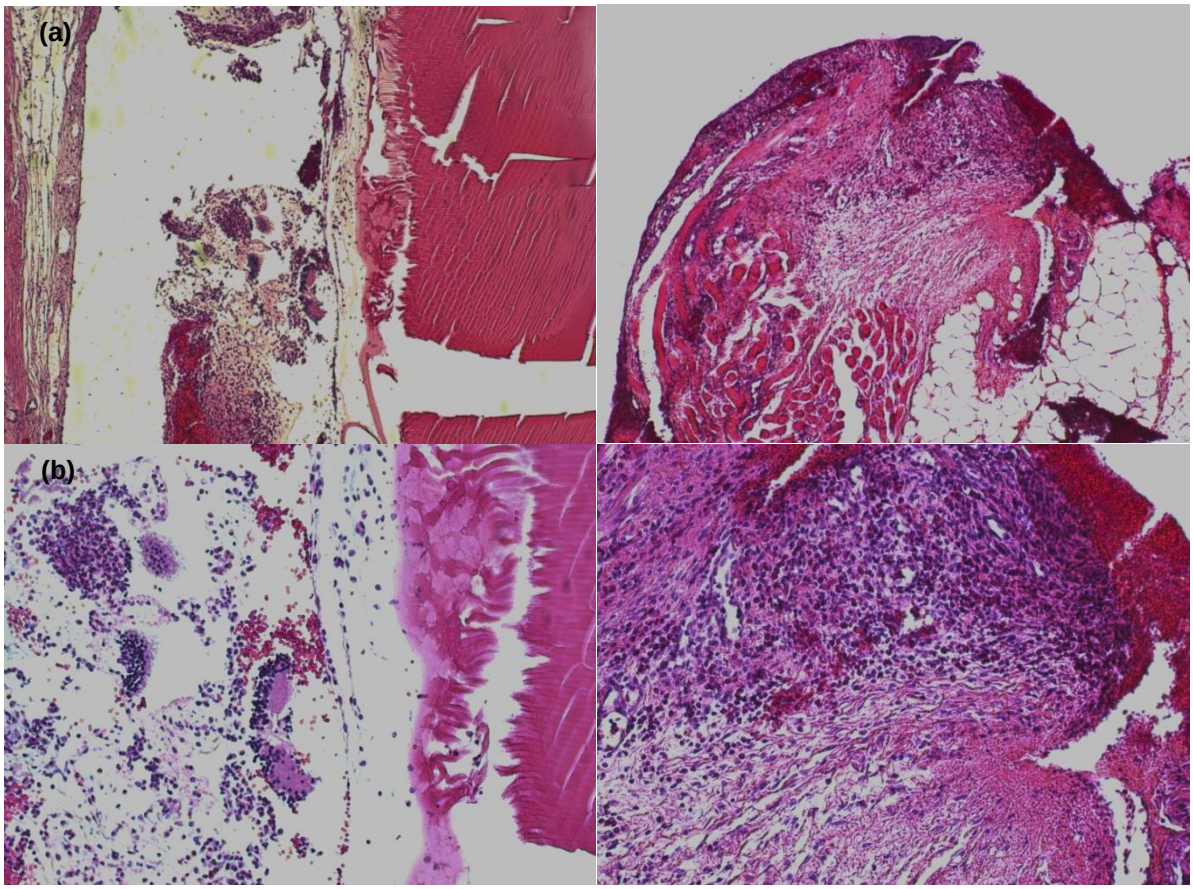

Figure 6.16: Histological slides at day 7 for the drug-loaded I^3 in the inflamed rabbit eye at (a) 4x and (b) 10x magnification

6.3.3.4. Effects of the drug-free I^3 in the inflamed rabbit eye

At day 7, acute fibrinous exudative panopthalmitis was detected where heterophils and fibrin exudation were found in the anterior, and posterior, and vitreous chambers of the eye. A section from the optic nerve highlighted lymphocytic perivascular cuffing within the optic nerve where prominent lymphoplasmacytic infiltrates were found around some of the capillaries in the nerve. The extraocular soft tissues demonstrated mild focal granulomatous inflammation with macrophages predominating. This is most likely the area where the implant was deposited (Figure 6.17).

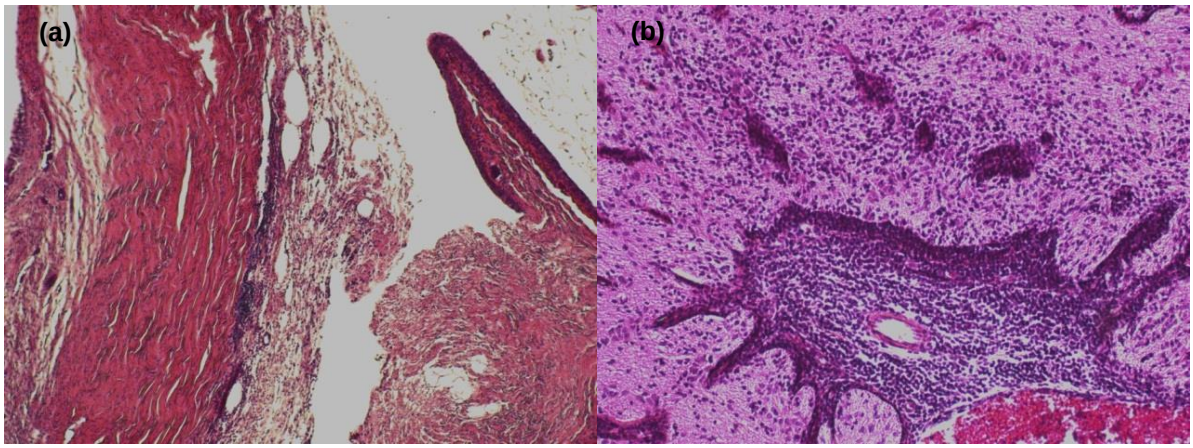

Figure 6.17: Histological slides at day 7 for the drug-free I^3 in the inflamed eye at (a) 4x and (b) 10x magnification (this highlights the optic nerve with lymphoplasmocytic infiltrates)

Ultimately, it can be concluded that the morphological findings in several sections where drug-loaded and placebo implants were left for 3, 7, 14, 21 and 28 days in the sub-Tenon's space in the normal rabbit eye showed no morphological differences between the two groups. The mild inflammation on the external surface of the sclera observed in some of the rabbit eyes appeared subacute and was associated with the I^3 in the sub-Tenon's space. In a few cases, focal hemorrhages were detected within the soft tissue and muscles around the eye, but this is regarded as an incidental observation, possibly associated with the final enucleation of the eye for histological evaluation.

In the inflamed rabbit eye specimens, inflammation suggesting a mild, acute, intraocular panopthalmitis could be confirmed in all of the sections with polymorphonuclear leukocytes (heterophils) predominating. This is a by-product of the inflammation that was induced via LPS injection. In the drug-free specimens a lymphocytic optic neuritis was confirmed. Because no drug was present in this instance, there was no opportunity for a reduction in the inflammation induced as opposed to where there was implantation of a drug-loaded device. However, with a drug-loaded implant in the inflamed rabbit eye, morphological evaluation revealed only mild intraocular heterophil infiltrates in the vitreous chamber with no inflammation in the anterior portion of the eye. This highlights a reduction in level of induced inflammation attributed to adequate release of drug from the I^3 in the presence of inflammation, and ultimately proves the efficacy of the I^3 in commencing to counteract the pathological tissue changes that occur when ocular inflammation is instigated.

6.3.5. Quantification of *in vivo* anti-inflammatory and antibiotic concentrations released from the I^3 into the total posterior ocular fluids of the rabbit eye model under normal and inflammatory conditions

Chromatographic analysis revealed three separated and defined peaks at 318nm at the respective retention times of 0.515 (nicotinic acid), 0.820 (ciprofloxacin), and 1.620 (indomethacin) minutes, in order of increasing lipophilicity (as the solvent program shifts towards a greater ACN ratio) as highlighted in Figure 6.18. Absolute recovery of indomethacin and ciprofloxacin from the TPOF samples by the liquid-liquid phase extraction process employed was performed by comparison of peak areas from extracted low and high calibration standards to those from aqueous standards. The recovery of both indomethacin and ciprofloxacin obtained during the extraction procedure spiked into blank TPOF samples from the non-test rabbit eyes ranged from 92.8-97.4% for indomethacin and 95.4-101.6% for ciprofloxacin, indicating acceptable methodological conditions for evaluation of drug concentrations in the TPOF of the rabbit eye model. Calibration curves generated for both indomethacin and ciprofloxacin were satisfactory (Figure 6.19).

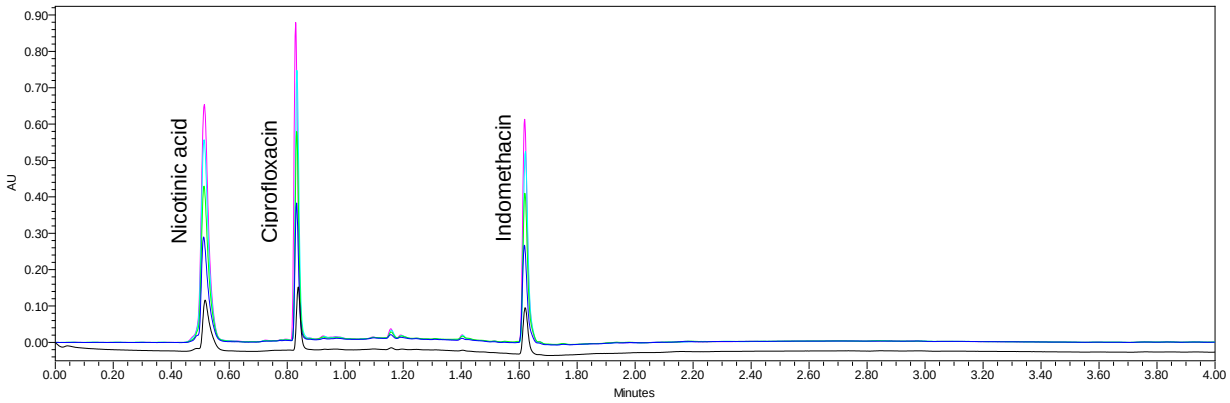

Figure 6.18: Overlaid calibration standard curves depicting the internal standard, ciprofloxacin and indomethacin at 318nm

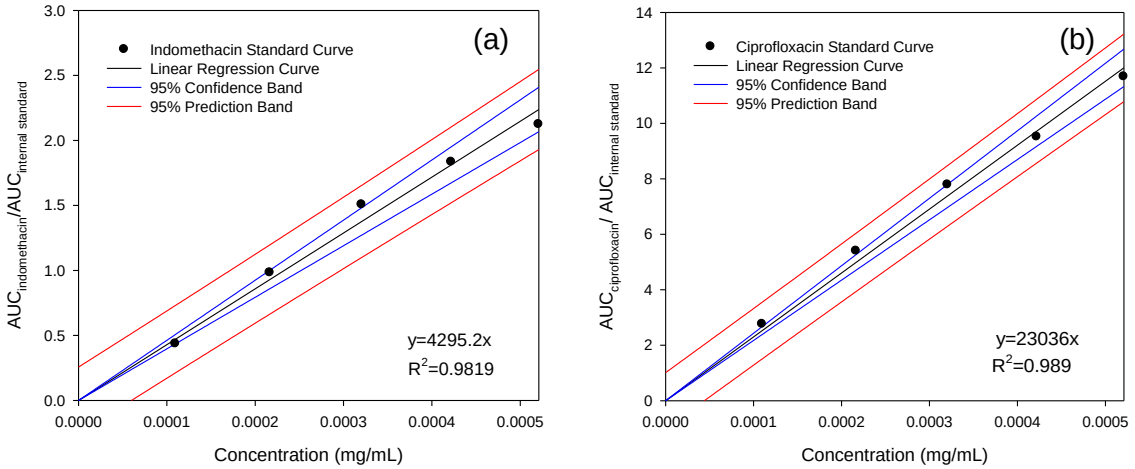

Figure 6.19: Calibration curves generated for (a) indomethacin and (b) ciprofloxacin spiked with the internal standard, nicotinic acid, in blank rabbit TPOF

In vivo results demonstrated good penetration of drug from sub-Tenon's space, through the sclera, into the TPOF. There was enhanced release of both drugs in the inflamed rabbit eye even after 7 days (the maximum period in which the induced inflammation was permitted to ensue), with indomethacin levels of 0.749±0.126µg/mL and 1.168±0.186µg/mL, and ciprofloxacin levels of 1.181±0.150µg/mL and 6.653±0.605µg/mL being attained in the normal and inflamed eye, respectively. At 28 days in the normal eye, concentrations of indomethacin detected were only 0.564±0.111µg/mL and those of ciprofloxacin were 1.226±0.209µg/mL. This is visualized in the UPLC-derived graphs (Figure 6.20) and *in vivo* release profiles (Figures 6.21 and 6.22). Furthermore, the enhanced erosion of the I^3 in the inflamed eye is also exemplified (Figure 6.24), with the I^3 eroding 1.504±0.505% in the normal eye and 22.609±2.421% in the inflamed eye after 7 days; and only reaching 13.830±1.010% erosion after 28 days in the normal rabbit eye. Very few studies report on the inflammation-responsive behavior of implants; however the investigation of Yui et al. (1993) on the inflammation-responsive degradation of crosslinked HA revealed erosion of 5-55% at 175 hours (~7days) at Fenton's reagent concentrations of 0.01-0.05M. There was no comparator under normal conditions, and no drug was included for comparison with our data on inflammation-responsive drug release patterns. The degree of erosion of the I^3 at the same Fenton's reagent concentration was half that described as 'rapid [responsive] degradation' by Yui et al. (1993), highlighting a more controlled erosion due to the intimately crosslinked system. However, the erosion of the I^3 under inflammatory conditions was notably greater than that observed in a normal ocular milieu.

(a)

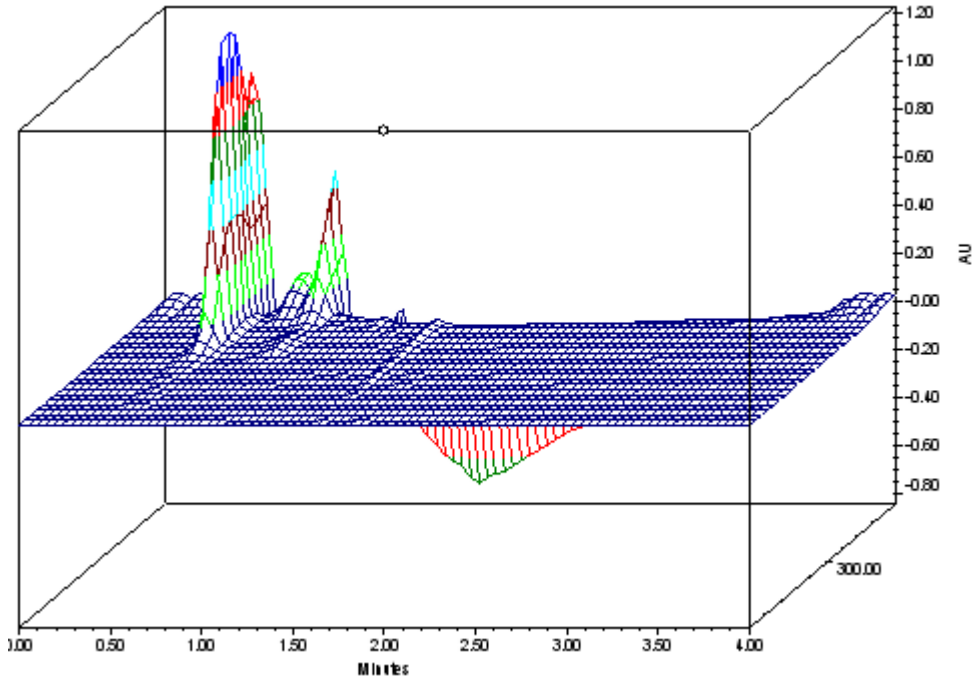

(b)

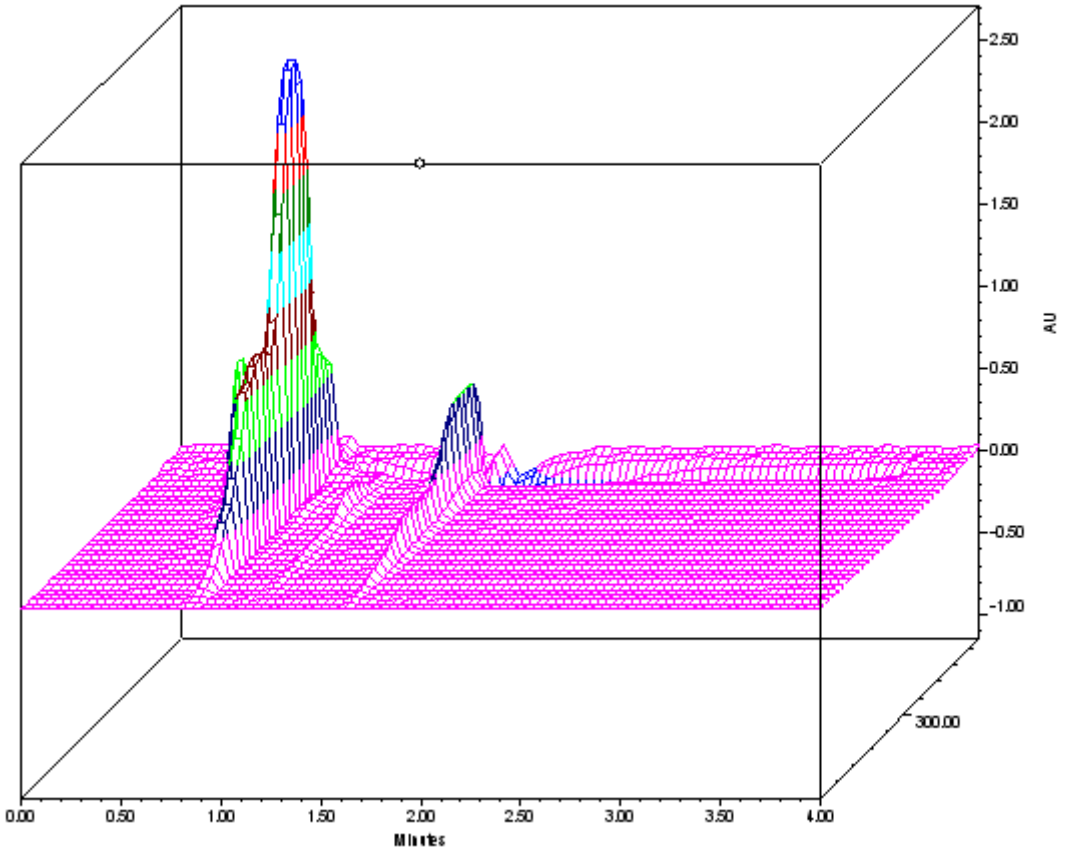

Figure 6.20: UPLC-derived 3D graphs representing concentrations of indomethacin and ciprofloxacin in the vitreous humour and tissues at 7 days for (a) the normal rabbit eye and (b) the inflamed rabbit eye. Note the enlarged areas representing drugs in the inflamed rabbit eye demonstrating enhanced release of both ciprofloxacin and indomethacin into the vitreous cavity in the inflamed rabbit eye

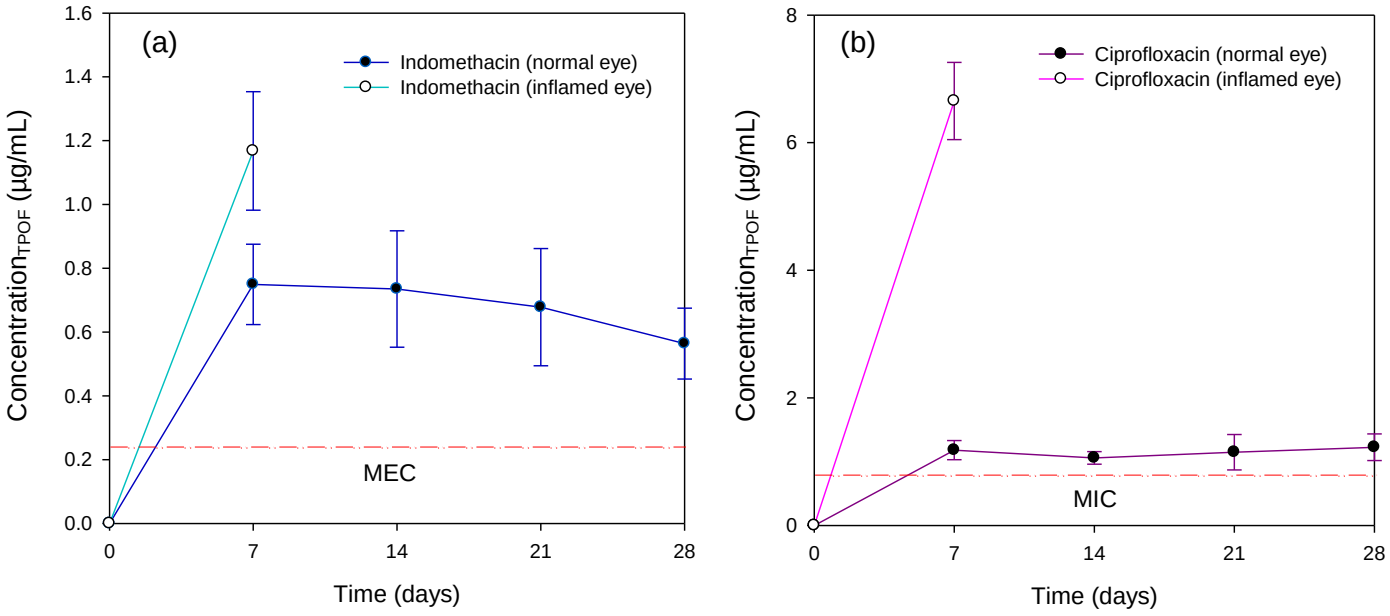

Figure 6.21: *In vivo* drug concentrations attained of (a) indomethacin and (b) ciprofloxacin in the normal and inflamed rabbit eye indicating the MEC of indomethacin (0.225µg/mL) and MIC of ciprofloxacin (0.8µg/mL) (n=3)

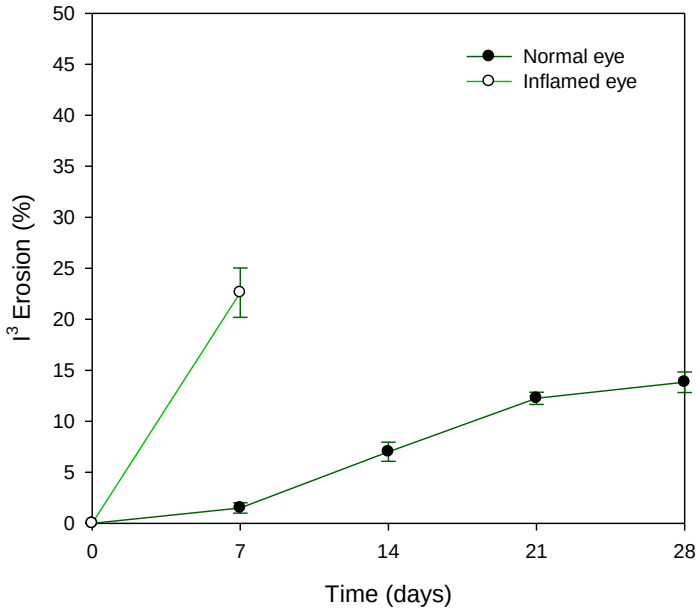

Figure 6.22: Device erosion in the normal and inflamed rabbit eyes (n=3)

Multipoint analysis of intravitreal drug concentrations and erosion was only achievable for the normal eye studies, demonstrating no appreciable correlation between indomethacin concentrations and device erosion (R^2=0.45), with a degree of correlation between

ciprofloxacin concentrations and I^3 erosion (R^2=0.64). This emphasized that available concentrations of ciprofloxacin were more dependent on intrinsic erosion of the I^3 than those of indomethacin, confirming *in vitro* predictions that drug release under normal conditions was not based on an erosion mechanism.

6.3.6. Visualization of *in vivo* surface morphological transitions of the I^3 in the normal and inflamed rabbit eye

The implant exposed to normal physiological conditions in the rabbits' eye for both 7 days (Figure 6.23a) and 28 days (Figure 6.23b) indicated that surface changes, although present, were minimal in comparison to the implant that was exposed to the environment of the inflamed rabbit eye for just 7 days (Figure 6.23c). It can be seen that the surface of the I^3 when exposed to inflammatory conditions erodes to a greater extent than the implant exposed to normal physiological conditions, which is congruent with *in vitro* morphological observations (Chapter 5, Section 5.3.7) and the *in vivo* erosion data.

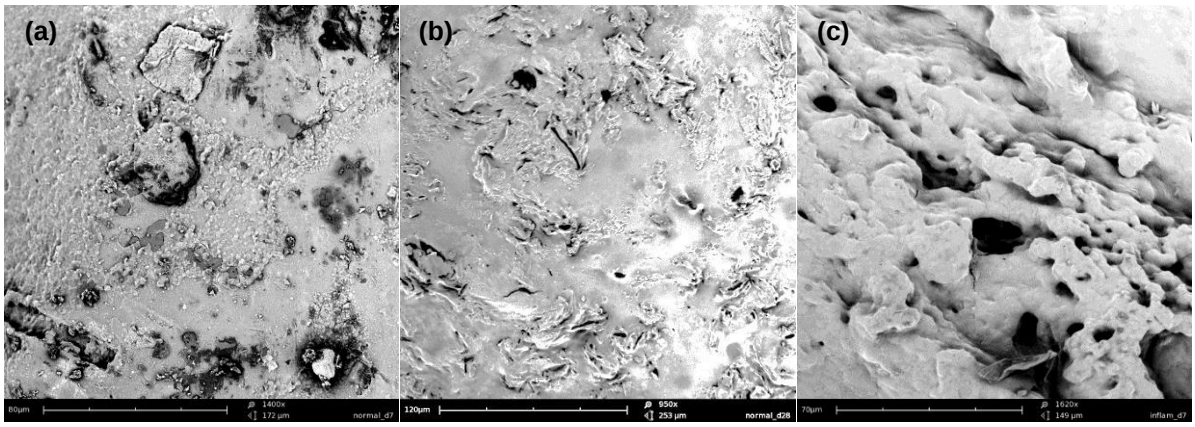

Figure 6.23: SEM images of implant exposed to (a) normal physiological conditions for 7 days at 1400x, (b) normal physiological conditions for 28 days at 950x and (c) inflammatory conditions for 7 days at 1620x magnification

6.3.7. Pharmacokinetic analysis

6.3.7.1. Indomethacin noncompartmental and compartmental analysis

The results of the noncompartmental and compartmental analysis for indomethacin are presented in Tables 6.4 and 6.5 and Figure 6.24. PK analysis revealed that indomethacin release was best described by a one compartment model without lag, as the most favorable AIC and SC values were generated for that case (Table 6.5) (the R^2 did not allow adequate differentiation between models). The values obtained for the first order absorption rate constant for indomethacin in the eye (K_a) was 0.8377/day (literature: 2.06±0.53/h, Gurnasinghani et al., 1989); elimination half-life (K_{el}) of 0.01281 days (literature: 2.6-11.2 h

Gurnasinghani et al., 1989), a C_{max} of 0.7845µg/mL and a T_{max} of 5.0675 days. PK parameters generated thus all point to the prolonged release of indomethacin, which was enhanced in the presence of the NS. The simplest PK model for the eye is the single compartment model (Worakul and Robinson, 1997). The equation describing this process in terms of drug concentration is:

$$C = \left(\frac{FD}{V_d}\right)\left(\frac{k}{k-K}\right)\left(e^{-Kt} - e^{-kt}\right) \qquad \text{[Equation 6.5]}$$

Where *F* is the fraction of dose absorbed, *D* is the dose, *k* and *K* are absorption and elimination rate constants, respectively, and *V*, is the apparent volume of distribution (Worakul and Robinson, 1997).

The fact that the release of indomethacin from the I^3 is superlatively described via a one-compartment model, without lag, emphasizes that the drug achieves instantaneous distribution within the vitreous and ocular tissues, and the drug concentration-time profile exhibits a monophasic response. There are no impediments to drug availability to the tissues due to the apt placement of the I^3 within the posterior sub-Tenon space, and ready penetration of the indomethacin-loaded NS through the sclera to the tissues of interest and vitreous.

Data was not readily available on the posterior segment pharmacokinetics of indomethacin; however Barañano and co-workers (2009) assessed the intraocular efficacy of two NSAIDs for reducing inflammation in the same animal model of EIU employed in this investigation, in addition to investigating the intraocular pharmacokinetics of both NSAIDs and their penetration into the retina. Drug concentrations in the vitreous and retina/ choroid were measured up to 48 hours after injection of either 3mg of ketorolac or 0.3mg of diclofenac (two eyes per NSAID time point). Measurement of ketorolac in the vitreous over time revealed a peak concentration of 234mg/mL 15 min after injection. By 48 h, ketorolac was barely detectable in the vitreous at 0.06mg/mL. Fifteen minutes after injection, ketorolac could be readily detected in the retina/ choroid and achieved peak levels by 2 h at a concentration of 280mg/g of tissue. After 48 h, ketorolac was no longer detectable in the retina/ choroid. The maximum concentration of diclofenac achieved in the vitreous was 72.98mg/mL 1 h after injection but was no longer detectable at 24 h. Diclofenac could be detected at a concentration of 4.1mg/g of tissue in the retina/choroid 15 min after injection but was undetectable after 24 h. Both NSAIDs were readily described by a one-compartment model and possessed half-lives of 4.27 h and 2.05 h for ketorolac and diclofenac, respectively. In

terms of MRT in the vitreous, that of ketorolac was more protracted (6.16 h vs. 2.95 h). Although both ketorolac and diclofenac demonstrated excellent penetration into the retina, clearance was already at 48 h. Barañano et al. (2009) therefore suggested the application of novel drug technologies for controlled delivery of intraocular NSAIDs as being currently feasible and essentially necessary to maximize their efficacy. The I^3 attains lower levels of the incorporated NSAID (but above the minimum effective level) with a T_{max} only being attained after 5 days, thus providing prolonged levels of NSAID. Owing to the responsive nature of the system, it can be extrapolated from the limited data that in the inflamed eye, the C_{max} and ultimately the *AUC* and *AUMC* would be increased thus prompting enhanced drug effects under inflammatory conditions.

Table 6.4: Results of noncompartmental analysis for indomethacin release

Parameter	Unit	Value
λ_z	1/d	0.0189
$t_{1/2}$	D	36.6181
T_{max}	D	3.0000
C_{max}	µg/mL	0.7513
T_{lag}	D	0.0000
C_{last_obs}/C_{max}		0.7505
AUC $_{0\text{-}t}$	µg/mL*d	18.6169
AUC $_{0\text{-}inf\ obs}$	µg/mL*d	48.4043
AUC $_{0\text{-}t/0\text{-}inf\ obs}$		0.3846
AUMC $_{0\text{-}inf\ obs}$	µg/mL*d^2	2671.3887
MRT $_{0\text{-}inf\ obs}$	D	55.1890
Cl/F $_{obs}$	(mg)/(µg/mL)/d	0.0083

Table 6.5: Results of compartmental analysis for indomethacin release

Parameter	Unit	Value	Diagnostics	Value
One compartment model without T_{lag}				
A	µg/mL	0.8502	r obs-pre	0.9966
K_a	1/d	0.8377	SS	0.002948
k_{10}	1/d	0.01281	WSS	0.002948
$t_{1/2ka}$	D	0.8274	R^2	0.9988
$t_{1/2k10}$	D	54.090	WR^2	0.9988
V/F	(mg)/(µg/mL)	0.4778	SE	0.03135
CL/F	(mg)/(µg/mL)/d	0.00612	AIC	-28.961
T_{max}	D	5.0675	SBC	-29.585
C_{max}	µg/mL	0.7845		
AUC_{0-t}	µg/mL*d	18.988		
AUC_{0-inf}	µg/mL*d	65.329		
AUMC	µg/mL*d^2	5175.96		
MRT	D	79.229		
One compartment model with T_{lag}				
A	µg/mL	0.8502	r obs-pre	0.9966
K_a	1/d	0.8377	SS	0.002948
k_{10}	1/d	0.01281	WSS	0.002948
T_{lag}	D	1E-06	R^2	0.9988
$t_{1/2ka}$	D	0.8274	WR^2	0.9988
$t_{1/2k10}$	D	54.090	SE	0.03839
V/F	(mg)/(µg/mL)	0.4778	AIC	-26.961
CL/F	(mg)/(µg/mL)/d	0.00612	SBC	-27.794
T_{max}	D	5.0675		
C_{max}	µg/mL	0.7845		
AUC_{0-t}	µg/mL*d	18.988		
AUC_{0-inf}	µg/mL*d	65.329		
AUMC	µg/mL*d^2	5175.96		
MRT	D	79.229		
Two compartment model				
A	µg/mL	0.8502	r obs-pre	0.9966
Alpha	1/d	0.01281	SS	0.002948
B	µg/mL	5.0014E-06	WSS	0.002948
Beta	1/d	0.01065	R^2	0.9988
K_a	1/d	0.8375	WR^2	0.9988
k_{10}	1/d	0.01282	SE	0.05429
k_{12}	1/d	2.5798E-09	AIC	-24.961
k_{21}	1/d	0.01066	SBC	-26.002
$t_{1/2Alpha}$	D	54.082		
$t_{1/2Beta}$	D	65.038		
$t_{1/2ka}$	D	0.8276		
V/F	(mg)/(µg/mL)	0.4778		
CL/F	(mg)/(µg/mL)/d	0.006124		
V_2/F	(mg)/(µg/mL)	1.1565E-07		
CL_2/F	(mg)/(µg/mL)/d	1.2326E-09		
T_{max}	D	5.0683		
C_{max}	µg/mL	0.7845		
AUC_{0-t}	µg/mL*d	18.987		
AUC_{0-inf}	µg/mL*d	65.322		
AUMC	µg/mL*d^2	5174.64		
MRT	D	79.218		

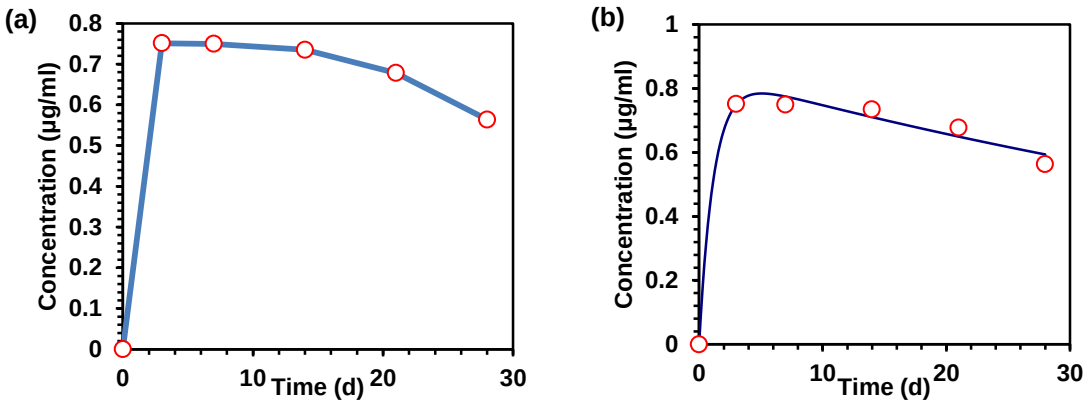

Figure 6.24: Graphical results for (a) noncompartmental and (b) compartmental PK analysis of indomethacin release. The blue line represents the predicted values whereas the red dots represent the observed values

6.3.7.2. Ciprofloxacin noncompartmental and compartmental analysis

The results of the noncompartmental and compartmental analysis for ciprofloxacin are presented in Tables 6.6 and 6.7 and Figure 6.25. Ciprofloxacin release was also best elaborated via a one compartment kinetic model without lag, with the AIC and SC being most favorable (Table 6.7). A C_{max} of 1.2162µg/mL and a T_{max} of 1.0883 days were evidenced for ciprofloxacin release from the I^3, and a K_a of 7.5361/day and K_{el} of 0.002071/day were obtained.

In terms of the intraocular pharmacokinetics of ciprofloxacin, some investigations have been reported. Rootman and co-workers (1992) assessed the pharmacokinetics of intraocular injection of ciprofloxacin (for use in aminoglycoside-resistant bacterial endophthalmitis) via aqueous and vitreous humor sampling over 24 hours after midvitreal injection of 100µg of the drug in one eye each of 25 New Zealand Albino rabbits and analysis of samples via means of a disc diffusion bioassay. Peak aqueous and vitreous levels of ciprofloxacin were obtained at 1 hour (0.59 and 27.26µg/mL, respectively); the vitreous level fell to below 1.0µg/mL 12 hours after injection (Rootman et al., 1992). It is evident that the I^3 can maintain therapeutic intraocular ciprofloxacin levels for significantly prolonged periods compared to intravitreal administration.

Table 6.6: Results of noncompartmental analysis for ciprofloxacin release

Parameter	Unit	Value
λ_z	1/d	0.0018
$t_{1/2}$	D	374.7449
T_{max}	D	3.0000
C_{max}	µg/mL	1.3035
T_{lag}	D	0.0000
$C_{last\ obs}/C_{max}$		0.9401
AUC_{0-t}	µg/mL*d	30.7901
$AUC_{0-inf\ obs}$	µg/mL*d	693.3616
$AUC_{0-t/0-inf\ obs}$		0.0444
$AUMC_{0-inf\ obs}$	µg/mL*d^2	377218.1313
$MRT_{0-inf\ obs}$	D	544.0424
Cl/F_{obs}	(mg)/(µg/mL)/d	0.0001

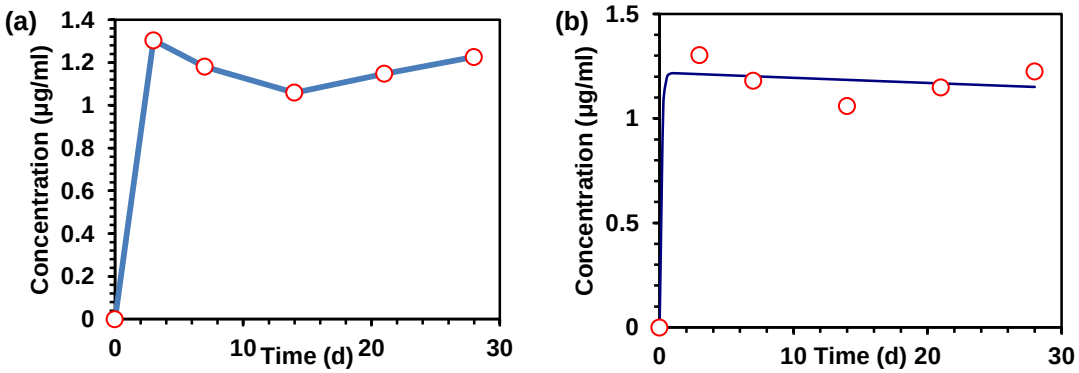

Figure 6.25: Graphical results for (a) noncompartmental and (b) compartmental PK analysis of ciprofloxacin release. The blue line represents the predicted values whereas the red dots represent the observed values

Table 6.7: Results of compartmental analysis for ciprofloxacin release

Parameter	Unit	Value	Diagnostics	Value
One compartment model without T_{lag}				
A	µg/mL	1.2193	r obs-pre	0.9871
K_a	1/d	7.5361	SS	0.03065
k_{10}	1/d	0.002071	WSS	0.03065
$t_{1/2ka}$	D	0.09197	R^2	0.9956
$t_{1/2k10}$	D	334.713	WR^2	0.9956
V/F	(mg)/(µg/mL)	0.05743	SE	0.1011
CL/F	(mg)/(µg/mL)/d	0.0001189	AIC	-14.910
T_{max}	D	1.0883	SBC	-15.535
C_{max}	µg/mL	1.2162		
AUC_{0-t}	µg/mL*d	33.008		
AUC_{0-inf}	µg/mL*d	588.630		
AUMC	µg/mL*d^2	284320.96		
MRT	D	483.022		
$t_{1/2ka}$	D	0.09198		
One compartment model with T_{lag}				
A	µg/mL	1.2191	r obs-pre	0.9871
K_a	1/d	4.0818	SS	0.03065
k_{10}	1/d	0.002066	WSS	0.03065
T_{lag}	D	1E-06	R^2	0.9956
$t_{1/2ka}$	D	0.1698	WR^2	0.9956
$t_{1/2k10}$	D	335.549	SE	0.1238
V/F	(mg)/(µg/mL)	0.05744	AIC	-12.910
CL/F	(mg)/(µg/mL)/d	0.0001187	SBC	-13.743
T_{max}	D	1.8601		
C_{max}	µg/mL	1.2139		
AUC_{0-t}	µg/mL*d	32.870		
AUC_{0-inf}	µg/mL*d	589.90		
AUMC	µg/mL*d^2	285713.82		
MRT	D	484.339		
Two compartment model				
A	µg/mL	0.1219	r obs-pre	0.9871
Alpha	1/d	0.003489	SS	0.03064
B	µg/mL	1.0979	WSS	0.03064
Beta	1/d	0.001951	R^2	0.9956
K_a	1/d	3.8130	WR^2	0.9956
k_{10}	1/d	0.002041	SE	0.1750
k_{12}	1/d	6.3763E-05	AIC	-10.910
k_{21}	1/d	0.003335	SBC	-11.952
$t_{1/2Alpha}$	D	198.6340		
$t_{1/2Beta}$	D	355.1125		
$t_{1/2ka}$	D	0.1817		
V/F	(mg)/(µg/mL)	0.05741		
CL/F	(mg)/(µg/mL)/d	0.0001172		
V_2/F	(mg)/(µg/mL)	0.001097		
CL_2/F	(mg)/(µg/mL)/d	3.6609E-06		
T_{max}	D	1.9684		
C_{max}	µg/mL	1.2141		
AUC_{0-t}	µg/mL*d	32.8501		
AUC_{0-inf}	µg/mL*d	597.1104		
AUMC	µg/mL*d^2	298184.068		
MRT	D	499.3784		

6.3.8. Establishment of an *in vitro-in vivo* correlation for bioactive release from the I^3

6.3.8.1. Establishment of an in vitro-in vivo correlation for indomethacin

There is a notable scarcity of published IVIVC data for implantable drug delivery systems (Iyer et al., 2006; Amann et al., 2010). Currently, no single method exists for treating data that can be applied to the majority of implantable dosage forms, and a case-by-case analysis is most often reported. Besides plasma drug levels, approaches involving tissue concentrations or surrogate markers has been highlighted for IVIVC development for implants (Iyer at el., 2006). In this case, drug concentrations in the ocular fluid were considered as this is of relevance here.

For indomethacin, an extravascular single dose, first order absorption, one compartment model without lag was selected for development of the IVIVC model, being the best fit as predicted by initial PK analysis. In addition to the mechanistic modeling of *in vitro* dissolution data as described in Chapter 4, Section 4.3.6, dissolution data was also fitted against empirical models for the purposes of IVIVC development. In terms of the R^2, AIC and SBC, indomethacin dissolution data was best described in terms of the Makoid-Banaker model (a multiple linear regression method).

A Level A correlation was developed, which uses all the information of the dissolution and absorption curves, in contrast to levels B or C, and is based directly upon each of the assayed time points (Amann et al., 2010). Level A analysis is therefore able to account for both qualitative patterns of release in addition to time-based positioning. Therefore, the amount of drug absorbed following implantation of the I^3, which is pertinent in terms of its further clinical development, was calculated by the Wagner Nelson method using the linear trapezoidal rule. For testing a level A IVIVC, the percentage of drug absorbed up to time *t* was plotted versus the amount of drug released *in vitro*.

The PK conditions derived from this investigation conforms to the requirements of deconvolution through convolution as the drug release from the I^3 device into the TPOF was aptly described via simple one-compartmental pK models due to the enclosed environment of the posterior segment of the eye facilitated by the highly restrictive blood-ocular barriers. Deconvolution of observed TPOF indomethacin concentration-time data against the in vitro release profile provided the cumulative in vivo release-time profile (Figure 6.26a).

When considering IVIVCs for implant formulations, a pertinent consideration is the burst effect, in which a high concentration of drug is released during a short period of time. Such a

burst generally occurs within 24 h of either *in vitro* or *in vivo* placement, but may also occur later, for instance, after a certain threshold of solvent is absorbed by the implant (Amann et al., 2010). Although there was an initial peak in indomethacin levels, drug release was minimized from the I^3 (<8%) due to extensive crosslinking of the device, as well as incorporation of the anti-inflammatory into a NS. Level A analysis yielded an R^2 value of 0.8821 (Figure 6.26b) (p=0.01424). Thus *in vitro* data was predictive of *in vivo* data with 88.21% accuracy. The prediction errors (PE) for C_{max} and $AUC_{0-\infty}$ were 13.33 and 12.05%, respectively, which is slightly more than the specified 10% PE specified for a good Level A correlation. The plots were not directly superimposable; however, based on the qualitative patterns of this fit, a level A correlation was approached. The rationalization of the imperfect superimposability between *in vitro* and *in vivo* data may lie in the complexity of the indomethacin delivery mechanism as, *in vivo*, the indomethacin, incorporated within the NS, encounters diverse cellular barriers and has an inherent propensity for cellular uptake, even in the normal rabbit eye. Furthermore, in the normal rabbit eye, the I^3 would become encapsulated with time (which cannot be replicated *in vitro*), and with a lack of an instigating inflammatory stimulus, erosion of the device would slow with decreasing indomethacin absorption - the preferred scenario under normal conditions. This may emanate in a discrepancy with regard to *in vitro* versus *in vivo* behavior. This extenuating fact has been noted by other investigators in the development of IVIVCs, that, in general, *in vitro* results tend to run ahead of *in vivo* data.

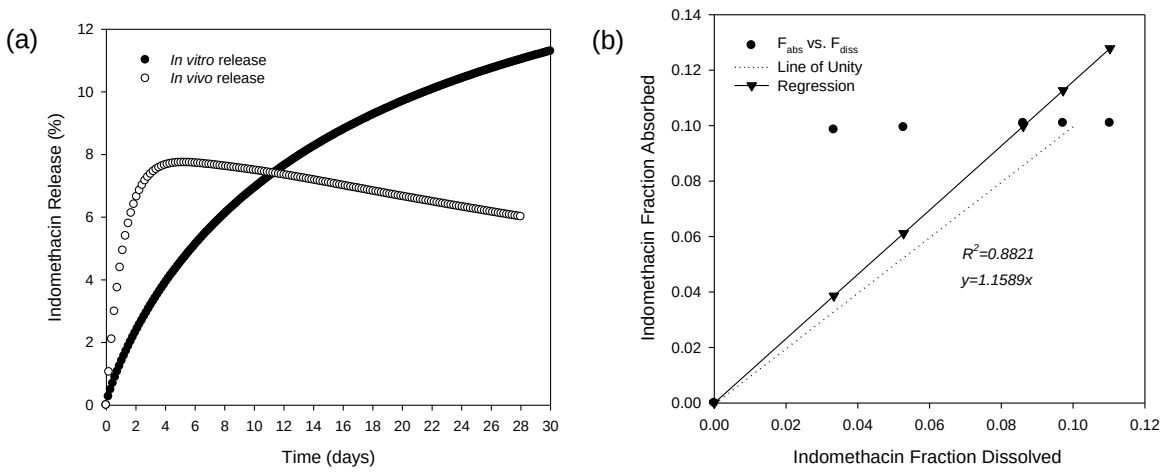

Figure 6.26: (a) Drug release profiles of the *in vitro* indomethacin release and the observed mean *in vivo* release profile extracted using deconvolution analysis for single-dose indomethacin released from the I^3 (b) Regression plot showing the relationship between the fraction of indomethacin absorbed *in vivo* and the fraction released *in vitro*

6.3.8.2. Establishment of an in vitro-in vivo correlation for ciprofloxacin

An extravascular single-dose, first-order absorption one compartment model without lag was selected for ciprofloxacin for development of the IVIVC model, being the best fit as predicted by initial PK analysis. Ciprofloxacin dissolution data was best described in terms of the Makoid-Banaker model in terms of the R^2, AIC and SBC.

Level A analysis yielded an R^2 value of 0.9760 (p=1.803e-07), signifying a very good level of superimposability (Figure 6.27b). *In vitro* data derived for ciprofloxacin could thus predict *in vivo* results with 97.6% accuracy. The PE's for C_{max} and $AUC_{0-\infty}$ were 5.77 and 5.71%, respectively, which is less than the specified 10% PE necessitated for a good Level A correlation. Thus quantitative analysis and visualization of the qualitative patterns of this fit pertinently confirm the attainment of a level A correlation. There are few extenuating factors influencing the *in vivo* absorption of ciprofloxacin following its release from the I^3. The fact that it is not incorporated within a NS avails the drug more immediately for absorption (therefore an earlier T_{max} and higher C_{max} than reported for indomethacin), which is important for amelioration of an initial infection, and *in vitro* data thus matches *in vivo* results more closely than evidenced for indomethacin.

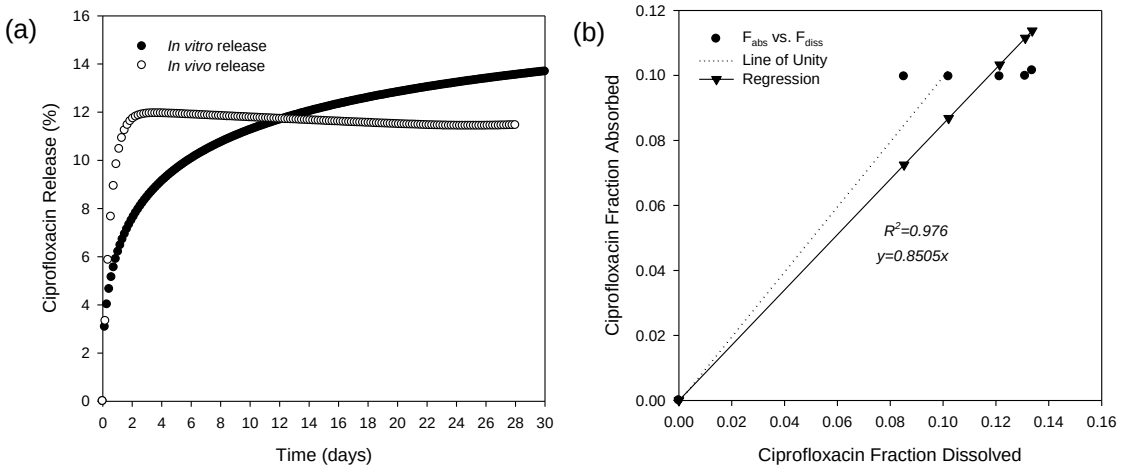

Figure 6.27: (a) Drug release profiles of the *in vitro* ciprofloxacin release and the observed mean *in vivo* release profile extracted using deconvolution analysis for single-dose ciprofloxacin released from the I^3 (b) Regression plot showing the relationship between the fraction of ciprofloxacin absorbed *in vivo* and the fraction released *in vitro*

6.4. Concluding Remarks

The device was well-tolerated following implantation in the rabbit eye. Investigations of drug concentrations attained and device erosion were a good preliminary indication that the I^3 expressed bioresponsive capabilities *in vivo.* There was enhanced release of both drugs in the inflamed rabbit eye even at the 7 day mark (the maximum period in which the induced inflammation was permitted to ensue), with indomethacin levels of 0.749±0.126µg/mL and 1.168±0.186µg/mL, and ciprofloxacin levels of 1.181±0.150µg/mL and 6.653±0.605µg/mL being attained in the normal and inflamed eye, respectively. At 28 days in the normal eye, concentrations of indomethacin detected were only 0.564±0.111µg/mL and those of ciprofloxacin were 1.226±0.209µg/mL. Furthermore, the enhanced erosion of the I^3 in the inflamed eye was also exemplified, with the I^3 eroding 1.504±0.505% in the normal eye and 22.609±2.421% in the inflamed eye after 7 days; and only reaching 13.830±1.010% erosion after 28 days in the normal rabbit eye. Elaboration of the IVIVC undertaken for both indomethacin and ciprofloxacin approached or attained a Level A correlation and provided further evidence for the feasibility of the I^3 and advances this concept toward application in a clinical setting. Establishment of such a correlation for the inflamed rabbit eye would be the main consideration in prospective investigations. Comparison of the I^3 with other ocular implants in terms of bioresponsive behavior and intraocular levels of indomethacin and ciprofloxacin was challenging as related bioresponsive ocular systems (incorporating these drugs) do not specifically exist.

CHAPTER 7

CONCLUSION AND RECOMMENDATIONS

'The science of today is the technology of tomorrow.'

Edward Teller

Hungarian-born American nuclear physicist

7.1. Conclusion

Conceptualization of novel polymeric systems with intelligent (e.g. stimulus-responsive) mechanisms and advances in nanotechnology are at the forefront of achieving directed and controlled delivery for treating vision-threatening diseases. It was thus the pertinent goal of this investigation to assimilate these observations in the design of an intelligent ocular drug delivery system. This investigation culminated in the development of an intelligent inflammation-responsive intraocular device as a novel approach for delivering therapeutic agents such as anti-inflammatories and antibiotics for the proposed enhanced treatment of posterior segment inflammatory disorders. To date, there has been limited application of the concept of specifically designing a nano-enabled inflammation-responsive drug delivery system for application in the eye with the proposed embodiment emanating in the achievement of drug delivery which is responsive to and targeted to inflammation.

The drug release pattern obtained from the I^3 is thus differential in normal versus pathological (inflammatory) conditions, with reversibility demonstrated *in vitro*, which has not been considered or demonstrated for intraocular implants on the market for the treatment of posterior segment inflammation, such as the market leader, Retisert™, introduced in Chapter 1. The Retisert™ provides continuous delivery of the corticosteroid (Ahn and Moshfeghi, 2008). Because there is continuous release of anti-inflammatory drug, irrespective of the presence or absence of inflammation, there is an increased propensity for the occurrence of side effects, such as, cataract development, intraocular pressure elevation, procedural complications and eye pain. This would be minimized from the I^3 which provides enhanced drug release when exposed to an inflammatory stimulus compared to when the implant is subjected to normal intraocular conditions. Furthermore, minimal surgical complications were observed attributed to the ease of implantation of the I^3 at the sub-Tenon site (with in-built nanotechnology enabling good drug levels in the posterior segment), and biodegradability of the device, obliterating the need for removal of the device which is necessitated in non-biodegradable implants such as Retisert™.

The research culminating in this thesis has brought the I^3 from the stage of conception to the completion of preclinical studies. Systems already on the market and those in various stages of research and development have been referred to in Chapter 1 and 2, and its advantages over the market leader for uveitis treatment (Retisert®) presented. However, at the final culmination of this thesis, in order to see the I^3 ultimately obtain regulatory approval we must take a final look at the latest stage of development (referring to updated 2012/ 2013 reports) of related ocular drug delivery systems for posterior segment disorders and whether the overall essence of our system in any way encroaches on what has already been achieved, as summarized in Table 7.1.

Table 7.1: Comparison of the I^3 with related ocular systems at the Preclinical or Clinical Stage of development (adapted from Kuno and Fujii, 2012)

Drug Delivery System (DDS)	Description	Clinical Trial Status	Shortfall of DDS compared to the I^3
Nonbiodegradable polymeric drug delivery systems			
I-vation (Surmodics Inc.)	Sustained delivery of triamcinolone acetonide (TA) to the vitreous using I-vation is in development for diabetic macular edema (DME). The I-vation intravitreal implant is a titanium helical coil coated with TA (925 μg) and the nonbiodegradable polymers poly(methyl methacrylate) and ethylene-vinyl acetate. It is predicted that this implant will have an *in vivo* sustained delivery of at least 2 years.	The proportion of patients demonstrating improved visual was 64% in the slow-release group and 72% in the fast-release group. No further clinical trial has commenced (Clinicaltrials.gov(b))	It is not biodegradable or inflammation responsive. It has demonstrated sustained release for extended periods and demonstrated clinical efficacy in DME.
Renexus, formerly NT-501 (Neurotech)	Encapsulated cell technology providing extracellular delivery of ciliary neurotrophic factor (CNTF) with long-term and stable intraocular release at constant doses through the Renexus device implanted in the vitreous. It contains human cell line of RPE, NTC-200, genetically modified to secrete recombinant human CNTF. Renexus consists of a sealed semipermeable hollow fiber membrane capsule surrounding a scaffold of 6 strands of polyethylene terephthalate yarn, which can be loaded with cells. The device is surgically implanted in the vitreous through a small scleral incision and is anchored by a single suture through a titanium loop at one end of the device and allows the outward diffusion of CNTF and other cellular metabolites and the inward diffusion of nutrients necessary to support the cell survival in the vitreous cavity while protecting the contents from host cellular immunologic attack.	Phase I and Phase II clinical studies for various indications (retinitis pigmentosa and age-related macular degeneration) have demonstrated stabilized visual acuity accompanied by dose dependent structural changes.	Device is not biodegradable. Different mechanism of action to the I^3 based on semi-permeability of the cell-entrapping device.
NT-503 (Neurotech)	NT-503 encapsulates VEGF receptor Fc-fusion protein (VEGFR-Fc)-releasing cells. This VEGFR-Fc is reportedly 20-fold more efficient in neutralizing VEGF in comparison to ranibizumab. NT-503 is confirmed to release VEGFR-Fc constantly up to 1 year in the rabbit vitreous (Kauper et al., 2012).	A Phase I clinical trial of NT-503 for neovascular AMD is currently underway (Ling, 2011).	Constant release of the anti-VEGF protein.

ODTx (On Demand Therapeutics)	It is an injectable, biocompatible, nonresorbable device containing reservoirs designed for drug release in optimized doses for laser activation (OnDemandTx.com). The reservoirs are capable of storing small- or large-molecule drugs that can be released via a standard, noninvasive laser activation procedure. The multiple reservoir system allows ophthalmologists to control drug delivery by activating specific reservoirs, while unactivated reservoirs remain intact.	Clinical trials of ODTx have not commenced.	This is the closest match in terms of a *defined modus oprandi* to the I^3 as it embodies a 'stimulus-responsive' concept, but the actual activation of drug release is external rather than an internal disease-related stimulus.
Biodegradable polymeric drug delivery systems			
Brimonidine intravitreal implant (Allergan)	Allergan have developed a a biodegradable, rod-shaped poly(lactide-co-glycolide) intravitreal implant containing brimonidine tartrate (an alpha-2 adrenergic agonist that can release various neurotrophins)	A Phase II/III clinical trial has been conducted in patients with retinitis pigmentosa, and a phase 2 clinical study in atrophic AMD is currently underway (ClinicalTrials.gov(c))	No mention of stimulus-responsive capabilities. Intravitreal rather than sub-Tenon placement.
Thethadur (pSivida)	Thethadur embodies a honeycomb-like nanostructured porous silicon (biosilicon), which is both biocompatible and biodegradable. Thethadur can purportedly deliver various drugs including small chemical entities, peptides and proteins and can provide sustained drug release(pSivida.com).	Further details regarding Thethadur have not, as yet, been disclosed by the company.	Is also a nanostructured system as embodied in the I^3. Sustained rather than stimulus-responsive release.
DE-102 (Santen Pharmaceutical Co. Ltd)	Injectable biodegradable microspheres loaded with betamethasone for sub-Tenon injection. They provide sustained release has been for the treatment of DME (ClinicalTrials.gov(d)) and for branch retinal vein occlusion (ClinicalTrials.gov(e)).	Have been subjected to a randomized, multicenter, controlled, Phase II/III clinical trial in Japan	Injectable rather than implantable system providing only sustained release.
Ranibizumab-loaded microspheres (SurModics Inc. and Genentech)	SurModics Inc. and Genentech are in the process of developing biodegradable microparticles that incorporate ranibizumab and are anticipated to deliver the agent over a period of approximately 4 to 6 months.	They were reportedly in preclinical stages, but the details of this cannot be readily accessed online.	Microparticles rather than a nanosystem which may not facilitate penetration of ocular barriers.
Oil/ lipid-based drug delivery systems			
IBI-20089 (Icon Bioscience Inc.)	Verisome drug delivery platform technology has been employed by Icon Bioscience Inc. in developing IBI-20089	An open-label, phase 1 study for cystoid macular edema associated with branch	Intravitreal injection rather than implant. Purely lipid

	containing TA. The Verisome is a translucent liquid. When IBI-20089 mixes with saline, the solution becomes a milky, slightly opaque color and forms a gel. The Patent of Icon states that IBI-20089 might be a solution of TA in benzyl benzoate. IBI-20089 is designed to last up to 1 year with a single intravitreal injection (Wong and Wood, 2006).	retinal vein occlusion or central retinal vein occlusion has been completed, and the results have been published and reported a decrease in mean central subfield OCT thickness. The reported side effects include IOP elevation with neovascular glaucoma (Lim et al., 2011). IBI-20089 adjunctively with 0.5 mg of ranibizumab is now being tested in a phase 2 clinical study for neovascular AMD.22 The results highlight that IBI-20089 may decrease the frequency of as-needed ranibizumab treatment (ClinicalTrials.com(f))	based formulation as opposed to the composite system embodied by the I^3.
Cortiject (NOVA63035, Novagali Pharma SA, acquired by Santen Pharmaceutical Co. Ltd.)	Cortiject is a preservative-free emulsion composed of oily carrier and phospholipid as surfactant, encapsulating a target tissue-activated dexamethasone prodrug which can provide sustained release over 6 to 9 months following a single intravitreal injection (Novagali.com).	An open-label, phase 1 study for DME is currently under way (ClinicalTrials.com(g)). According to an interim report mean foveal thickness decreased after an intravitreal injection (Kupperman, 2009), however, further results of this trial have not been reported since 2009.	Intravitreal injection rather than implant. Purely lipid based formulation as opposed to the composite system embodied by the I^3.

It is tantamount in closing this investigation to investigate whether the research questions put forward in Chapter 1 (Figure 1.2), have, in fact, been adequately addressed, as divulged in Figure 7.1.

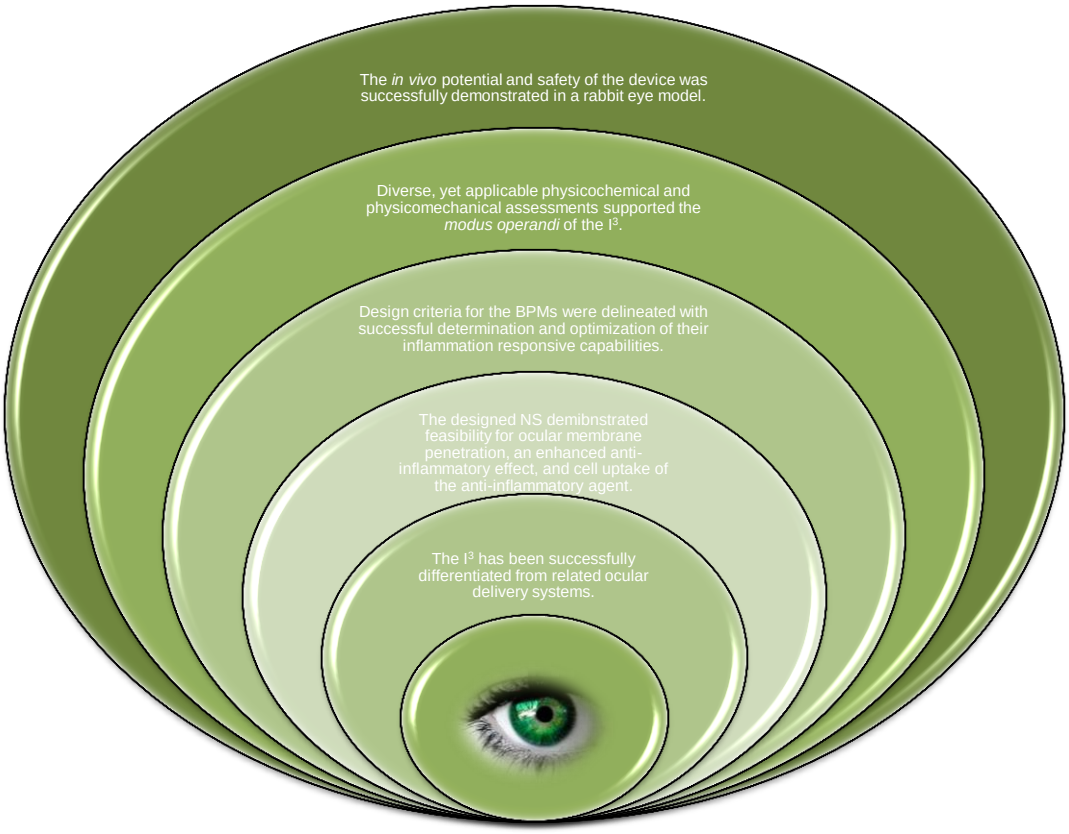

Figure 7.1: Outflow of solutions to critical pharmaceutical design questions presented at the inception of this thesis

It is evident that most posterior segment disorders are induced by complex pathophysiological conditions. The most efficacious combinations of drugs, delivery route, and drug release patterns based on the pathophysiology and progressive courses of the targeted diseases was thus taken into consideration to embrace a novel concept in ocular drug delivery of inflammation responsiveness. A novelly configured I^3, displaying desirable inflammation-responsive traits, was thus conceptualized and optimized.

7.2. Recommendations

In vivo studies undertaken successfully demonstrated enhanced drug levels in the inflamed rabbit eye; however, studies in the inflamed eye were limited to a time point of 7 days. In future, it is anticipated that, due to the success of this investigation, a more prolonged inflammatory state could be induced, for a period of at least 28 days. Furthermore, *in vivo*

studies demonstrating the reversibility of the responsive nature of the device, to correlate with *in vitro* findings, would add even more gravity to the clinical findings attained thus far.

It is an ultimate goal to introduce the I^3, being a new product to the market. This certainly implicates numerous stages of research and development. The I^3 has been refined to a state of formulation optimization and preclinical investigation. It is pertinent to further consider manufacturing processes and product presentation. Included in these additional deliberations for licensing of the I^3 to a pharmaceutical company are scale-up considerations. The scale-up phase includes the integration of procedures, as well as the transfer of technology, for realizing the large-scale manufacture of a given product (Galindo-Rodr´ıguez et al., 2005). It essentially implicates increasing the batch size and is concerned with increasing the linear dimensions from the laboratory to the plant size (Levin, 2001). In this instance, scale-up procedures are necessitated for firstly NS manufacture and ultimately simultaneous manufacture of both BPMs to form the I^3.

The scale-up approach for NS elaboration could implicate a continuous method based on a flow-through ultrasonicator as suggested by Freitas et al. (2006). The continuous phase would be fed by a double-piston pump, and the disperse phase by a syringe pump, and would be pre-mixed in a glass cell by means of a cross-shaped magnetic stirrer. The pre-mixed coarse emulsion would be transported to the ultrasonic flow-through cell for further homogenization. Thereafter, the nascent NS emulsion would be collected and gently stirred in a large collecting beaker to enable evaporation of the organic solvents.

With regard to scale-up manufacture of the BPMs for the I^3, techniques commonly implemented for molding of intraocular implants could be considered, including injection-molding, extrusion and compression-molding. However, the limited stability of commercially available biodegradable polymers at high temperatures and especially under shearing forces, is a main concern when using melt-processing (Rothen-Weinhold. 1999). Dual-injection (or bi-injection) molding of both the anionic and cationic polymeric blends at low temperatures could hold suitability (conceptualized for the I^3 in Figure 7.2). The anionic solution (forming the outer BPM) would be pumped initially to reach an $AlCl_3$-saturated mold. Following migration of the moving plate, the cationic solution (forming the inner BPM) would be channelled to the inner part of the mold for simultaneous formation of the inner and outer BPM.

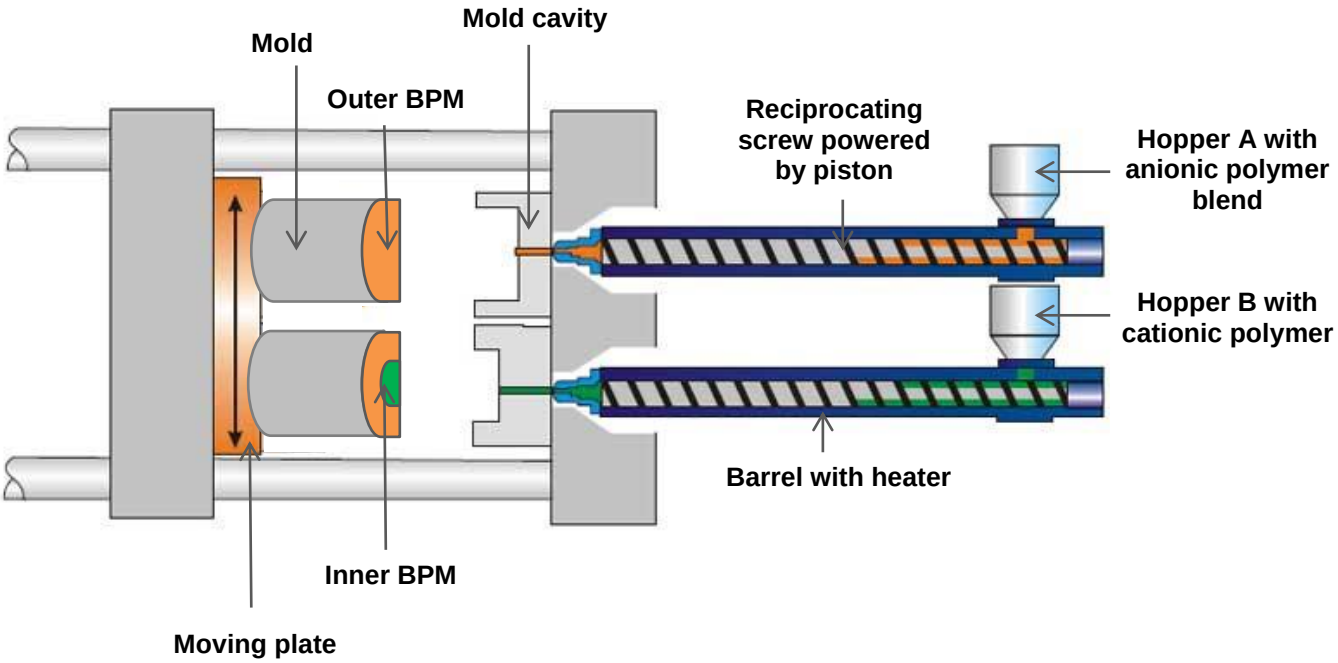

Figure 7.2: Proposed configuration of machinery dual-injection molding (Adapted from: Dakumar machinery, www.dakumar.com/bi-injection-moulding-machine.htm)

Bioresponsive/ intelligent polymeric implants have gained wider attention because of the feasibility in therapeutic applications, product scale-up and cost considerations. The proposed I^3 may also prove to be a suitable platform for the delivery of anti-glaucoma agents for lowering intraocular pressure. Furthermore, because glaucoma patients often have coexisting posterior segment diseases (Scott et al. 2000); the device may incorporate multiple drugs for combinatory disease management. The superior properties conferred through implementation of intelligent polymeric crosslinking and nanotechnological principles would allow the design of a suitable multicomponent delivery system that could be used as platform for the bioresponsive, site-specific delivery of a potentially diverse array of bioactives to various tissue sites. In so doing trends in drug delivery would be enforced. Localized elution of corticosteroids has been used in suppressing inflammation and fibrosis associated with implantation and continuous *in vivo* residence of bio-medical devices (Patil et al., 2007). An optimally developed implant for anti-inflammatory delivery could find application in the site-specific therapeutic management of inflammatory states throughout the body. Attainment of research objectives will, and has, permitted presentation of results at conferences, and publication in peer-reviewed journals. As a novel device with potential for commercialization, the I^3 can be patented. Innovative research into novel drug delivery systems forms a pivotal thrust of South Africa's research goals, through enhancement of the technological platform.

8. REFERENCES

Adamis AP, Miller JW, Bernal MT, et al. Increased vascular endothelial growth factor levels in the vitreous of eyes with proliferative diabetic retinopathy. *Am J Ophthalmol* 1994, 118: 445-450.

Aggarwal P, Hall JB, McLeland CB, Dobrovolskaia MA, McNeil SE. Nanoparticle interaction with plasma proteins as it relates to particle biodistribution, biocompatibility and therapeutic efficacy. *Adv Drug Deliv Rev* 2009, 61: 428-437.

Ahmed I. The noncorneal route in ocular drug delivery. In: Mitra AK (ed). Ophthalmic drug delivery systems. New York: Marcel Dekker, 2003. pp. 335-363.

Ahn BJ, Moshfeghi AA. Implantable Posterior Segment Drug Delivery Devices. Ophthalmology Web 2008. http://www.ophthalmologyweb.com/Spotlight.aspx?spid=23&aid=253&headerid=23.

Ahuja M, Dhake AS, Sharma SK, Majumdar DK. Topical Ocular Delivery of NSAIDs. *AAPS J* 2008, 10(2): 229-241.

Aiello LP, Pierce EA, Foley ED, et al. Suppression of retinal neovascularization in vivo by inhibition of vascular endothelial growth factor (VEGF) using soluble VEGF-receptor chimeric proteins. *Proc Natl Acad Sci USA* 1995, 92: 10457-10461.

Albensi BC, Mattson MP. Evidence for the involvement of TNF and NF-κB in hippocampal synaptic plasticity. *Synapse* 2000, 35(2): 151-159.

Ali Y, Lehmussaari K. Industrial perspective in ocular drug delivery. *Adv Drug Deliv Rev* 2006, 58: 1258-1268.

Allen HF, Mangiaracine AB. Bacterial endophthalmitis after cataract extraction: a study of 22 infections in 20.000 operations. *Arch Ophthalmol* 1964, 72: 454-462.

Allergan Inc. EP1750688 - Steroid intraocular implants having an extended sustained release for a period of greater than 2 months, 2007 (patent filed). Retrieved from URL: https://register.epo.org/espacenet/application?number=EP05744945. [Accessed 5 March 2008].

Alonso MJ, Sanchez A. The potential of chitosan in ocular drug delivery. *J Pharm Pharmacol* 2003, 55: 1451-1463.

Alvarez-Lorenzo C, Concheiro A. Molecularly imprinted polymers for drug delivery. *J Chrom B* 2004, 804(1): 231-245.

Amann LC, Gandal MJ, Lin R, Liang Y, Siegel SJ. In vitro–in vivo correlations of scalable PLGA-risperidone implants for the treatment of schizophrenia. *Pharm Res* 2010, 27: 1730-1737.

Amrite AC, Edelhauser HF, Singh SR, Kompella UB. Effect of circulation on the disposition and ocular tissue distribution of 20 nm nanoparticles after periocular administration. *Mol Vis* 2008a,14: 150-160.

Amrite AC, Edelhauser HF, Kompella UB. Modeling of Corneal and Retinal Pharmacokinetics after Periocular Drug Administration. *Invest Ophthalmol Vis Sci* 2008b, 49(1): 320-332.

Amrite AC, Kompella UB. Size-dependent disposition of nanoparticles and microparticles following subconjunctival administration. *J Pharm Pharmacol* 2005, 57(12): 1555-1563.

Ananthula HK, Vaishya RD, Barot M, Mitra AK. Duane's Ophthalmology. In: Tasman W, Jaeger EA (eds). *Bioavailability.* Philadelphia: Lippincott Williams & Wilkins, 2009.

Andrieu-Soler C, Aubert-Pouessel A, Doat M, Picaud S, Halhal M, Simonutti M, Venier-Julienne MC, Benoit JP, Behar-Cohen F. Intravitreous injection of PLGA microspheres encapsulating GDNF promotes the survival of photoreceptors in the *rd1/rd1* mouse. *Mol Vis* 2005, 11: 1002-1011.

Araújo J, Vega E, Lopes C, Egea MA, Garcia ML, Souto EB. Effect of polymer viscosity on physicochemical properties and ocular tolerance of FB-loaded PLGA nanospheres. *Coll Surfaces B: Biointerfaces* 2009, 72: 48-56.

Asencio-Duran M, Vallejo-Garcia JL, Pastora-Salvador N, Fonseca-Sandomingo A, Romano MR. Vitreous diagnosis in neoplastic diseases. Med Inflamm 2012, 2012(Article ID 930704): 10 pages.

Axelrod J-L, Newton JC, Klein RM, Bergen RL, Sheikh MZ. Penetration of imipenem into human aqueous and vitreous humor. *Am J Ophthalmol* 1987, 104: 649-653.

Ayalasomayajula SP, Kompella UB. Celecoxib, a selective cyclooxygenase-2 inhibitor, inhibits retinal vascular endothelial growth factor expression and vascular leakage in a streptozotocin-induced diabetic rat model. *Eur J Pharmacol* 2003, 458: 283-289.

Badawi AA, El-Laithy HM, El Qidra RK, El Mofty H, El Dally M. Chitosan based nanocarriers for indomethacin ocular delivery. *Arch Pharm Res* 2008, 31: 1040-1049.

Balazs AC, Buxton GA. Supramolecular networks synthesized in nanoparticle-polymer mixtures. In: Schwarz JA, Contescu CI, Putyera K. Dekker Encyclopedia of Nanoscience and Nanotechnology. CRC Press: Florida, USA; London, UK, 2004, pp. 3785-3794.

Barañano DE, Kim SJ, Edelhauser HF, Durairaj C, Kompella UB, Handa JT. Efficacy and pharmacokinetics of intravitreal non-steroidal anti-inflammatory drugs for intraocular inflammation. *Br J Ophthalmol* 2009, 93: 1387-1390.

Barar J, Javadzadeh AR, Omidi Y. Ocular novel drug delivery: impacts of membranes and barriers. *Expert Opin Drug Deliv* 2008, 5(5): 567-581.

Barbu E, Verestiuc L, Nevell TG, Tsibouklis J. Polymeric materials for ophthalmic drug delivery: trends and perspectives. *J Mater Chem* 2006, 16: 3439-3443.

Barbu E, Sarvaiya I, Green KL, Nevell TG, Tsibouklis J. Vinylpyrrolidone-co-(meth) acrylic acid inserts for ocular drug delivery: synthesis and evaluation. *J Biomed Mater Res* 2005, 74A: 598.

Barbucci R, Rappuoli R, Borzacchiello A, Ambrosio L. Synthesis, chemical and rheological characterization of new hyaluronic acid-based hydrogels. *J Biomat Sci, Polym Ed* 2000, 11(4): 383-399.

Barcia E, Herrero-Vanrell R, Dı´ez A, Alvarez-Santiago C, Lo´ pez I, Calonge M. Downregulation of endotoxin-induced uveitis by intravitreal injection of polylactic-glycolic acid (PLGA) microspheres loaded with dexamethasone. *Exp Eye Res* 2009, 89: 238-245.

Bareford LM, Swaan PW. Endocytic mechanisms for targeted drug delivery. *Adv Drug Deliv Rev* 2007, 59: 748-758.

Bar-Ilan A, Aviv H, Friedman D, Vered M,. Belkin M, Amselem S, Baru H, Beilin M, Wellner E, Wolf Y, Schwarz J, Newmann R. Improved performance of ocular drugs formulated in submicron emulsions. *Invest Ophthalmol Vis Sci* 1993, 34: 1488 (Suppl.).

Barnes PJ, Adcock IM, Ito K. Histone acetylation and deacetylation: importance in inflammatory lung diseases. *Eur Respir J* 2005; 25: 552-563.

Beeley NRF, Rossi JV, Mello PAA, Mahmoud MI, Fujii GY, De Juan E, Varner SE. Fabrication, implantation, elution, and retrieval of a steroid-loaded polycaprolactone subretinal implant. *J Biomed Mater Res* 2005, 73A: 437-444.

Bejjani RA, BenEzra D, Cohen H, Rieger J, Andrieu C, Jeaanny J-C, Golomb G, Behar-Cohen FF. Nanoparticles for gene delivery to retinal pigment epithelial cells. *Mol Vis* 2005, 11: 124-132.

Benotmane AM, Hoylaerts MF, Collen D, Belayew A. Nonisotopic quantitative analysis of protein-DNA interactions at equilibrium. *Anal Biochem* 1997, 250: 181-185.

Beppu MM, Vieira RS, Aimoli CG, Santana CC.Crosslinking of chitosan membranes using glutaraldehyde: Effect on ion permeability and water absorption. *J Membr Sci* 2007, 301(1-2): 126-130.

Bernkop-Schnurch A. Thiomers: A new generation of mucoadhesive polymers. *Adv Drug Deliv Rev* 2005, 57: 1569-1582.

Bhattarai NN, Gunn J, Zhang M. Chitosan-based hydrogels for controlled, localized drug delivery. *Adv Drug Deliv Rev* 2009, 62: 83-99.

Bilensoy E, Sarisozen C, Esendağlı G, Lale Doğan A, Aktaş Y, Şen M, Aydın Mungan N. Intravesical cationic nanoparticles of chitosan and polycaprolactone for the delivery of Mitomycin C to bladder tumors. *Int J Pharm (Pharmaceutical Nanotechnology)* 2009, 371(1-2): 170-176.

Biron M. Extrinsic smart polymers. Technical Paper. 2 February 2005. Retrieved from URL: www.specialchem4polymers.com/2456/eng/article...[Accessed 5 March 2008].

Bishop PN. Structural macromolecules and supramolecular organisation of the vitreous gel. *Progr Ret Eye Res* 2000,19(3): 323-344.

Bloquel C, Bourges JL, Touchard E, Berdugo M, BenEzra D, Behar-Cohen F. Non-viral ocular gene therapy: potential ocular therapeutic avenues. *Adv Drug Deliv Rev* 2006, 58: 1224-1242.

Bodnar M, Hartmann JF, Borbely J. Preparation and characterization of chitosan-based nanoparticles. *Biomacromol* 2005, 6: 2521-2527.

Bodor N, Buchwald P. Ophthalmic Drug Design Based on the Metabolic Activity of the Eye: Soft Drugs and Chemical Delivery Systems. *AAPS Journal* 2005, 7(4): E820-E833.

Bodor N. Designing safer ophthalmic drugs. In: van der Goot H, Domany G, Pallos L, Timmerman H (eds.). Trends in Medicinal Chemistry '88. Elsevier Science Publishers: Amsterdam, 1988, p. 145.

Bodor N. Novel approaches to the design of safer drugs: soft drugs and site-specific chemical delivery systems. In: Testa B (ed.). Advances in Drug Research. Vol. 13, Academic Press: London, 1984, p. 255.

Bodor N, Brewster BE. Problems of delivery of drugs to the brain. *Pharm Ther* 1983, 19: 332-389.

Borzacchiello A, Mayol L, Schiavinato A, Ambrosio, L. Effect of hyaluronic acid amide derivative on equine synovial fluid viscoelasticity. *J Biomed Mat Res Part A* 2010, 92(3): 1162-1170.

Bourges J-L, Gautier SE, Delie F, Bejjani RA, Jeanny JC, Gurny R, BenEzra D, Behar-Cohen F. Ocular drug delivery targeting the retina and retinal pigment epithelium using polylactide nanoparticles. *Invest Ophthalmol Vis Sci* 2003, 44: 3562-3569.

Bourne DWA. Pharmacokinetics. In: Banker GS, Rhodes CT (eds.). Modern Pharmaceutics, 4th ed., Marcel Dekker Inc.: New York, 2002, pp.67-92.

Brasier AR. The NF-κB regulatory network. *Cardiovasc Toxicol* 2006, 6(2): 111-130.

Brunauer S, Emmett PH, Teller E. Adsorption of gases in multimolecular layers. *J Am Chem Soc* 1938, 60: 309-319.

Brunel F, Véron L, Ladavière C, David L, Domard A, Delair T. Synthesis and structural characterization of chitosan nanogels. *Langmuir* 2009, *25*(16): 8935–8943.

Bucolo C, Maltese A, Drago F. When nanotechnology meets the ocular surface. *Expert Rev Ophthalmol* 2008, 3: 325-332.

Bucolo C, Maltese A, Puglisi G, Pignatello R. Enhanced ocular anti-inflammatory activity of ibuprofen carried by an Eudragit RS100 nanoparticle suspension*. Ophthal Res* 2002, 34*;* 319-323*.*

Buculo C, Maltese A. Pharmacological profile of oxaprozin eye drops. *J Ocul Pharmacol Ther* 2002, 18(1): 75-81.

Cadete A, Fifueiredo L, Lopes R, Calado CCR, Almeida AJ, Gonçalves LMD. Development and characterization of a new plasmid delivery system based on chitosan–sodium deoxycholate nanoparticles*. Eur J Pharm Sci* 2012, 45(4): 451-458.

Cai Q, Bei J, Wang S. Synthesis and degradation of a tri-component copolymer derived from glycolide, L-lactide and *ε*-caprolactone. *J Biomat Sci (Polymer Edition)* 2000, 11: 273.

Callegan MC, Gilmore MS, Gregory M, Ramadan RT, Wiskur BJ, Moyer AL, Hunt JJ, Novosad BD. Bacterial endophthalmitis: Therapeutic challenges and host-pathogen interactions. *Prog Ret Eye Res* 2007, 28(2): 189-203.

Calvo P, Remuñán-López C, Vila-Jato JL, Alonso MJ. Novel hydrophilic chitosan-polyethylene oxide nanoparticles as protein carriers. *J Appl Polym Sci* 1997a, 63: 125-132.

Calvo P, Vila-Jato JL, Alonso MJ. Evaluation of cationic polymer-coated nanocapsules as ocular drug carriers. *Int J Pharm* 1997b, 153: 41-50.

Calvo P, Alonso MJ, Vila-Jato JL, Robinson JR. Improved ocular bioavailability of indomethacin by novel ocular drug carriers. *J Pharm Pharmacol* 1996a, 48: 1147-1152.

Calvo P, Sanchez A, Martinez J, Lopez MI, Calonge M, Pastor JC, Alonso MJ. Polyester nanocapsules as new topical ocular delivery systems for cyclosporin A. *Pharm Res* 1996b, 13: 311-315.

Calvo P, Vila-Jato JL, Alonso MJ. Comparative in vitro evaluation of several colloidal systems, nanoparticles, nanocapsules, and nanoemulsions, as ocular drug carriers. *J Pharm Sci* 1996c, 85: 530-536.

Camelo S, Lajavardi L, Bochot A, Goldenberg B, Naud MC, Fattal E, Behary-Cohen F, de kozak Y. Drainage of fluorescent liposomes from the vitreous to cervical lymph nodes via conjunctival lymphatics. *Ophthal Res* 2008, 40: 145-150.

Cao Y, Zhang C, Ping Q. Preparation and characterization of a novel poly (*N*-isopropyl acrylamide)-chitosan. *Polym Mater Sci Eng* 2005, 21(6): 236.

Capadona JR, Shanmuganathan K, Tyler DJ, Rowan SJ, Weder C. Stimuli-responsive polymer nanocomposites inspired by the sea cucumber dermis. *Science* 2008, 319 (5868): 1370-1374.

Carafa M, Santucci E, Alhaique F, Coviello T, Murtas E, Riccieri FM, Lucania G, Torrisi MR. Preparation and properties of new unilamellar non-ionic surfactant vesicles. *Int J Pharm* 1998, 160: 51-59.

Caron JM, Berlin RD. Dynamic interactions between microtubules and artificial membranes. *Biochem* 1987, 26: 3681-3688.

Chadwick S, Kriegel C, Amiji M. Nanotechnology solutions for mucosal immunization. *Adv Drug Deliv Rev* 2010, 62: 394-407.

Champagne ES. Ocular Pharmacology. *Clin Tech Small Anim Prac* 2001, 16(1): 13-16.

Chan C-K, Chu I-M. Effect of hydrogen bonding on the glass transition behavior of poly(acrylic acid)/silica hybrid materials prepared by sol-gel process. *Polymer* 2001, 42(14): 6089-6093.

Chen W, Varadarajan S. Integration of Design of Experiments and Artificial Neural Networks for achieving affordable concurrent design. *American Institute of Aeronautics and Astronautics* 1997: 1-9.

Cheng SZD (ed.). Handbook of Thermal Analysis and Calorimetry. Applications to Polymers and Plastics. Vol. 3, Elsevier: Amsterdam, The Netherlands, 2002.

Cheruvu NP, Amrite AC, Kompella UB. Effect of diabetes on transscleral delivery of celecoxib. *Pharm Res* 2009, 26(2): 404-414.

Cheruvu NP, Amrite AC, Kompella UB. Effect of eye pigmentation on transscleral drug delivery. *Invest Ophthalmol Vis Sci* 2008, 49(1): 333-341.

Cheruvu NP, Ayalasomayajula SP, Kompella UB. retinal delivery of sodium fluorescein, budesonide & celecoxib following subconjunctival injection. *Drug Dev Deliv* 2003, 3(6), posted on: 3/28/2008.

Chin MS, Nagineni CN, Hooper LC, Detrick B, Hooks JJ. Cyclooxygenase-2 gene expression and regulation in human retinal pigment epithelial cells. Invest Ophthalmol Vis Sci 2001, 42: 2338-2346.

Chong DY, Johnson MW, Huynh TH, Hall EF, Comer GM, Fish DN. Vitreous penetration of orally administered famciclovir. *Am J Ophthalmol* 2009, 148(1): 38-42.

Choonara YE, Pillay V, Ndesendo VMK, du Toit LC, Kumar P, Khan RA, Murphy CS, Jarvis D-L. Design of polymeric nanoparticles by synthetic wet chemical processing strategies for the sustained delivery of anti-tuberculosis drugs. *Coll Interf B: Biointerface* 2011, 87: 243-254.

Choonara YE, Pillay V, Carmichael T, Danckwerts MP. Studies on a Novel Doughnut-Shaped Minitablet for Intraocular Drug Delivery. *AAPS PharmSciTech* 2007, 8(4), Article 118. DOI: 10.1208/pt0804118.

Choonara YE, Pillay V, Carmichael T, MP Danckwerts. An in vitro study of the design and development of a novel doughnut-shaped minitablet for intraocular implantation. *Int J Pharm* 2006, 310(1-2): 15-24

Choonara YE. *In vivo* evaluation of a novel donut-shaped minitablet for intraocular implantation. University of the Witwatersrand, JHB, Electronic Theses and Dissertations, 2009. *wiredspace.wits.ac.za/.../YE%20Choonara%20PhD%20Thesis%20301009.pdf?...*

Clement DB, Tailor V. A study of aqueous and serum levels of ceftazidime following subconjunctival administration. *Br J Ophthalmol* 1987, 71: 433-435.

ClinicalTrials.gov(a). Infectious Causes of Uveitis. Retrieved from URL: http://clinicaltrials.gov/show/NCT00676624. ClinicalTrials.gov updated this record on 12 May 2008. [Accessed 25 May 2010].

ClinicalTrials.gov(b). A study of MK0140 in diabetic patients with macular edema. Retrieved from URL: http://clinicaltrials.gov/ct2/show/NCT00692614?term=I-vation&rank=1. ClinicalTrials.gov updated this record on 29 January 2013. [Accessed 14 February 2013].

ClinicalTrials.gov(c). Safety and efficacy of brimonidine intravitreal implant in patients with geographic atrophy due to age-related macular degeneration (AMD). Retrieved from URL: http://clinicaltrials.gov/ct2/show/NCT00658619. ClinicalTrials.gov processed this record on 13 March 2013. [Accessed 14 February 2013].

ClinicalTrials.gov(d). Efficacy and safety of betamethasone micropsheres in patients with diabetic macular edema (Tsubasa). Retrieved from URL: http://clinicaltrials.gov/ct2/show/NCT01411254?term=DE-102&rank=1. ClinicalTrials.gov processed this record on 13 March 2013. [Accessed 14 February 2013].

ClinicalTrials.gov(e). Efficacy and safety of betamethasone microspheres in patients with macular edema following branch retinal vein occlusion (HIKARI). Retrieved from URL: http://clinicaltrials.gov/ct2/show/NCT01512901?term=DE-102&rank=2. ClinicalTrials.gov processed this record on 29 July 2012. [Accessed 14 February 2013].

ClinicalTrials.gov(f). IBI 20089+Lucentis combo intravitreal injections for treatment of neovascular age-related macular degeneration (AMD) (Icon Combo). Retrieved from URL: http://clinicaltrials.gov/ct2/show/NCT01175395?term=IBI20089&rank=1. ClinicalTrials.gov processed this record on 28 June 2012. [Accessed 14 February 2013].

ClinicalTrials.gov(g). Safety and tolerability of NOVA63035 “Corticosteroid” in patients with diabetic macular edema secondary to diabetic retinopathy. Available at: http://clinicaltrials.gov/ct2/show/NCT00665106?term=NOVA63035&rank=1. ClinicalTrials.gov processed this record on 15 July 2010. [Accessed 14 February 2013].

Collins MN, Birkinshaw C. Physical properties of crosslinked hyaluronic acid hydrogels. *J Mater Sci: Mater Med* 2008, 19: 3335-3343.

Collins MN, Birkinshaw C. Comparison of the effectiveness of four different crosslinking agents with hyaluronic acid hydrogel films for tissue-culture applications. *J Appl Polym Sci* 2007, 104: 3183-3191.

Cong W, Liu Q, Liang Q, Wang Y, Luo G. Investigation on the interactions between pirarubicin and phospholipids. *Biophys Chem* 2009, 143(3): 154-160.

Conley SM, Naash MI. Nanoparticles for retinal gene therapy. *Prog Retin Eye Res* 2010, 29(5): 376-397.

Coppens M, Versichelen L, Mortier E. Treatment of postoperative pain after ophthalmic surgery. *Bull Soc Belge Ophtalmol* 2002, 285: 27-32.

Corcoran S. Drug delivery to the eye. Highlights in Chem Sci 2006, 9. Retrieved from URL: http://www.rsc.org/Publishing/ChemScience/Volume/2006/09/nanoparticles_in_the_eye.asp. [Accessed 12 March 2008].

Cousins SW, Guss RB, Howes EL Jr, Rosenbaum JT. Endotoxin induced uveitis in the rat: observations on altered vascular permeability, clinical findings, and histology. *Exp Eye Res* 1984, 39: 665-676.

Couvreur P, Stella B, Reddy LH, Hillaireau H, Dubernet C, Desmaele D, Lepetre-Mouelhi S, Rocco F, Dereuddre-Bosquet N, Clayette P. Squalenoyl nanomedicines as potential therapeutics. *Nano Lett* 2006, 6: 2544-2548.

Couvreur P, Tulkenst P, Roland M, Trouet A, Speiser P. Nanocapsules: a new type of lysomotropic carrier. *FEBS Lett 1977*, 84: 323-326.

Coviello T, Palleschi A, Grassi M, Matricardi P, Bocchinfuso G, Alhaique F. Scleroglucan: a versatile polysaccharide for modified drug delivery. *Molecules* 2005, 10: 6-33.

Cunha-Vaz JG. The blood–retinal barriers system. Basic concepts and clinical evaluation. *Exp Eye Res* 2004, 78: 715-721.

Dakumar machinery. Bi-injection moulding machine. Retrieved from URL: http://www.dakumar.com/bi-injection-moulding-machine.htm. [Accessed 15 February 2013].

Davda J, Labhasetwar V. Characterization of nanoparticle uptake by endothelial cells. *Int J Pharm* 2002, 233(1-2): 51-59.

Day AJ, de la Motte CA. Hyaluronan crosslinking: a protective mechanism in inflammation? *Tr Immunol* 2005, 26(12): 638-643.

De Campos AM, Diebold Y, Carvalho EL, Sanchez A, Alonso MJ. Chitosan nanoparticles as new ocular drug delivery systems: in vitro stability, in vivo fate, and cellular toxicity. *Pharm Res* 2004, 21: 803-810.

De Campos AM, Sanchez A, Gref R, Calvo P, Alonso MJ. The effect of a PEG versus a chitosan coating on the interaction of drug colloidal carriers with the ocular mucosa. *Eur J Pharm Sci* 2003, 20: 73-81.

De Campos AM, Sanchez A, Alonso MJ, Chitosan nanoparticles: a new vehicle for the improvement of the delivery of drugs to the ocular surface. Application to cyclosporin A. *Int J Pharm* 2001, 224: 159-168.

de Gennes PG. The Physics of Liquid Crystals, Oxford University Press: Oxford, 1974.

de la Fuente M, Raviña M, Paolicelli P, Sanchez A, Seijo B, Alonso MJ. Chitosan-based nanostructures: A delivery platform for ocular therapeutics. *Adv Drug Del Rev* 2010, 62: 100-117.

de la Fuente M, Csaba N, Garcia-Fuentes M, Alonso MJ. Nanoparticles as protein and gene carriers to mucosal surfaces. *Nanomed* 2008, 3: 845-857.

Del Amo EM, Urtti A. Current and future ophthalmic drug delivery systems: A shift to the posterior segment. *Drug Discovery Today* 2008, 13(3-4): 135-143.

Desai MP, Labhasetwar V, Walter E, Levy RJ, Amidon GL. The mechanism of uptake of biodegradable microparticles in Caco-2 cells is size dependent. *Pharm Res* 1997, 14: 1568-1573.

Diebold Y, Calonge M. Applications of nanoparticles in ophthalmology. *Progr Ret Eye Res* 2010, 29: 596-609.

Diebold Y, Jarrín M, Sáez V, Carvalho ELS, Orea M, Calonge M, Seijo B, Alonso MJ. Ocular drug delivery by liposome–chitosan nanoparticle complexes (LCS-NP). *Biomaterials* 2007, 28(8): 1553-1564.

Dillen K, Bridts C, Van der Veken P, Cos P, Vandervoort J, Augustyns K, Stevens W, Ludwig A. Adhesion of PLGA or Eudragit®/PLGA nanoparticles to Staphylococcus and Pseudomona. *Int J Pharm* 2008; 349(1-2): 234-240.

Ding S. Recent developments in ophthalmic drug delivery. *PSTT* 1998, 1(8): 328-335.

Doan T, Melvold R, Viselli S, Waltenbaugh C. The Well Patient: How Innate and Adaptive Immune Responses Maintain Health (Chapter 13). In: RA Harvey, PC Champ. Lippincott's Illustrated Reviews: Immunology. Lippincott Williams and Wilkins, Wolters Kluwer: Philadelphia, USA, 2007, pp. 165-194.

Dobrovolskaia MA, Aggarwal P, Hall JB, McNeil SE. Preclinical studies to understand nanoparticles interaction with the immune system and its potential effects on nanoparticles biodistribution. *Mol Pharmacol* 2008, 5: 487-495.

Dobrovolskaia MA, McNeil SE. Immunological properties of engineered nanomaterials. *Nat Nanotechnol* 2007, 2: 469-478.

Dong YM, Ruan YH, Wang HW, Zhao YG, Bi DX. Properties of chitosan. *J Appl Polym Sci* 2004, 93: 1553.

Dot C, Behar-Cohen F, BenEzra D, Doat M, Jonet L, May F, Jeanny JC. Influence of triamcinolone intravitreal injection on retinochoroidal healing processes. *Exp Eye Res* 2007, 84(6): 1081-1089.

DrugBank: a knowledgebase for drugs, drug actions and drug targets. Wishart DS, Knox C, Guo AC, Cheng D, Shrivastava S, Tzur D, Gautam B, Hassanali M. *Nucleic Acids Res* 2008, 36(Database issue): D901-906. Retrieved from URL: www.drugbank.ca. [Accessed 30 June 2011].

du Toit LC, Pillay V, Choonara YE, Govender T, Carmichael T. Ocular drug delivery - a look towards nanobioadhesives. *Expert Opin Drug Deliv* 2011a, 8(1): 71-94.

du Toit LC, Govender T, Pillay V, Choonara YE, Kodama T. Investigating the effect of polymeric approaches on circulation time and physical properties of nanobubbles. *Pharm Res* 2011, 28: 494-504.

Dunne JA, Travers JP. Double-blind clinical trial of topical steroids in anterior uveitis. *Br J Ophthalmol* 1979, 63: 762-767.

Ebrahim S, Peyman GA, Lee PJ. Applications of liposomes in ophthalmology. *Surv Ophthalmol* 2005, 50: 167-182.

El-Sayed MEH, Hoffman AS, Stayton PS. Smart polymeric carriers for enhanced intracellular delivery of therapeutic macromolecules. *Expert Opin Biol Ther* 2005, 5: 23.

Espana E, Chipont E, Sanchez S, Romero FJ, Navea A, Diaz M.) Collagen shields enhanced penetration of topical cyclosporine. *Invest Ophthalmol Vis Sci* 1993, 34(Suppl.): 1488.

European Science Foundation. Nanomedicine. An ESF – European Medical Research Councils (EMRC) Forward Look report. 2005.

Farjo R, Skaggs J, Quiambao AB, Cooper MJ, Naash MI. Efficient nonviral ocular gene transfer with compacted DNA nanoparticles. PLoS ONE 2006, 1-38.

FDA. Draft Guidance for Industry: Waiver of In Vivo Bioavailability and Bioequivalence Studies for Immediate Release Solid Oral Dosage Forms containing certain Active Moieties/ Active Ingredients based on Biopharmaceutical Classification System, 1999.

Felt O, Furrer P, Mayer JM, Plazonnet B, Buri P, Gurny R. Topical use of chitosan in ophthalmology: tolerance assessment and evaluation of precorneal retention. *Int J Pharm* 1999, 180: 185-193.

Fenske DB, Palmer LR, Chen T, Wong KF, Cullis PR. Cationic poly(ethyleneglycol) lipids incorporated into pre-formed vesicles enhance binding and uptake to BHK cells. *Biochim Biophys Acta* 2001, 1512(2): 259-272.

Fialho SL, Cunha AD. Manufacturing techniques of biodegradable implants intended to intraocular application. *Drug Deliv* 2005, 12: 109-116.

Fleisher LN, Ferrell JB, Smith MG, McGahan MC. Lipid mediators of tumor necrosis factor-alpha-induced uveitis. *Invest Ophthalmol Vis Sci* 1991, 32(8), 2393-9.

Fox TG, Flory, PJ. Second-order transition temperatures and related properties of polystyrene. *J Appl Phys* 1950, 21: 581-591.

Foxall C, Watson SR, Dowbenko D, Fennie C, Lasky LA, Kiso M, Hasegawa A, Asa D, Brandley BK. The three members of the selectin receptor family recognize a common carbohydrate epitope, the sialyl Lewis (x) oligosaccharide. J Cell Biol 1992, 117: 895-902.

Freitas S, Hielscher G, Merkle HP, Gander B. Continuous contact- and contamination-free ultrasonic emulsification - a useful tool for pharmaceutical development and production. Ultrason Sonochem 2006, 13(1): 76-85.

Frenkel V. Ultrasound mediated delivery of drugs and genes to solid tumors. Adv Drug Deliv Rev 2008, 30: 1193-1208.

Galindo-Rodr´ıguez SA, Puel F, Brianc S, All´emannb E, Doelker E, Fess Hi. Comparative scale-up of three methods for producing ibuprofen-loaded nanoparticles. Eur J Pharm Sci 2005, 25: 357-367.

Gao P, Nixon PR, Skoug JW. Diffusion in HPMC gels. II. Prediction of drug release rates from hydrophilic matrix extended-release dosage forms. *Pharm Res* 1995, 12: 965-971.

Gaserod O, Smidsrod O, Skjask-Brñk G. Microcapsules of alginate-chitosan: A quantitative study of the interaction between alginate and chitosan. *Biomaterials* 1998, 19: 1815-1825.

Gatti G, Panozzo G. Effect of inflammation on intraocular penetration of intravenous ofloxacin in albino rabbits. *Antimicrob Agents Chemother* 1995, 39(2): 549-552.

Gaudana R, Krishna Ananthula H, Parenky A, Mitra AK. Ocular drug delivery. *AAPS J* 2010, 12(3): 348-360.

Gaudana R, Jwala J, Boddu SHS, Mitra AK. Recent perspectives in ocular drug delivery. *Pharm Res* 2009, 26(5): 1197-1216.

Geroski DH, Edelhauser HF. Transscleral drug delivery for posterior segment disease. *Adv Drug Deliv Rev* 2001, 52(1): 37-48.

Ghate D, Edelhauser HF. Ocular drug delivery. *Expert Opin Drug Deliv* 2006, 3(2): 275-287.

Gillies MC, Kuzniarz M, Craig J, Ball M, Luo W, Simpson JM. Intravitreal triamcinolone-induced elevated intraocular pressure is associated with the development of posterior subcapsular cataract. *Ophthalmology* 2005, 112: 139-43.

Gillies MC, Simpson JM, Billson FA, Luo W, Penfold P, Chua W, Mitchell P, Zhu M, Hunyor ABL. Safety of an intravitreal injection of triamcinolone. *Arch Ophthalmol* 2004, 122: 336-340.

Gilmore TD. Introduction to NF-κB: players, pathways, perspectives. *Oncogene* 2006, 25(51): 6680-6684.

Gipson IK, Argueso P. Role of mucins in the function of the corneal and conjunctival epithelia. *Int Rev Cytol* 2003, 231: 1-49.

Goldblum D, Rohrer K, Frueh BE, Theurillat R, Thormann W, Zimmerli S. Ocular distribution of intravenously administered lipid formulations of amphotericin B in a rabbit model. *Antimicrob Agents Chemother* 2002, 46(12): 3719-3723.

Gonçalves C, Pereira P, Gama M. Self-assembled hydrogel nanoparticles for drug delivery applications. *Materials* 2010, 3, 1420-1460.

Gong K, Darr JA, Rehman IU. Supercritical fluid assisted impregnation of indomethacin into chitosan thermosets for controlled release applications. *Int J Pharm* 2006, 315(1-2); 93-98.

Gopferich A. Mechanisms of polymer degradation and elimination. In: Wiseman DM, Kost J, Domb AJ (eds.). Handbook of Biodegradable Polymers. CRC Press: Florida, USA; London, UK, 1998.

Govender S, Pillay V, Chetty DJ, Essack SY, Dangor CM, Govender T: Optimisation and characterisation of bioadhesive controlled release tetracycline microspheres. *Int J Pharm* 2005, 306(1-2): 24-40.

Goyal A, Kumar A, Patra PK, Mahendra S, Tabatabaei S, Alvarez PJJ, John G, Ajayan PM. In situ synthesis of metal nanoparticle embedded free standing multifunctional PDMS Films. *Macromol Rapid Commun* 2009, 30: 1116-1122

Green CJ, Knight J, Precious S, Simpkin, S. Ketamine alone and combined with diazepam or xylazine in laboratory animals: a 10 year experience. *Lab Anim* 1981, 15: 163-170.

Gref R, Minamitake Y, Peracchia MT, Trubetskoy V, Torchilin V, Langer R. Biodegradable long-circulating polymeric nanospheres. *Science* 1994, 263: 1600-1603.

Guo W, Guo Y, Gao H, Zheng Q, Zhong W. Energy Dissipation in Gigahertz Oscillators from Multiwalled Carbon Nanotubes. *Phys Rev Lett 2003,* 91(12): 125501-1.

Gupta AK, Madan S, Majumdara DK, Maitra A. Ketorolac entrapped in polymeric micelles: preparation, characterisation and ocular anti-inflammatory studies*. Int J Pharm* 2000, 209(1-2): 1-14.

Gurnasinghani ML, Bhatt HR, Lalla JK. Indomethacin delivery from matrix controlled release indomethacin tablets. *J Contr Rel* 1989, 8: 211-222.

Ha CS, Gardella JA. Surface chemistry of biodegradable polymers for drug delivery systems. *Chem Rev* 2005, 105: 4205.

Hadjiioannou TP, Christian GD, Koupparis MA, Macheras PE. Quantitative Calculations in Pharmaceutical Practice and Research, VCH Publishers Inc.: New York, 1993, pp.345-348.

Haesslein A, Hacker MC, Ueda H, Ammonb DM, Borazjani RN, Kunzler JF, Salamone JC, Mikos AG. Matrix modifications modulate ophthalmic drug delivery from photo-cross-linked poly(propylene fumarate)-based networks. *J Biomat Sci* 2009, 20: 49-69.

Haesslein A, Ueda H, Hacker MC, Jo S, Ammon DM, Borazjani RN, Kunzler JJ, Salamone JC, Mikos AG. Long-term release of fluocinolone acetonide using biodegradable fumarate-based polymers. *J Contr Rel* 2006, 114(2): 251-260.

Hainsworth DP, Conklin JD, Bierly JR, Ax D, Ashton P. Intravitreal delivery of ciprofloxacin. *J Ocul Pharmacol Ther* 1996, 12: 183-191.

Hamidi M, Azadi A, Rafiei P. Hydrogel nanoparticles in drug delivery. *Adv Drug Deliv Rev* 2008, 60: 1638-1649.

Harush-Frenkel O, Altschuler Y, Benita S. Nanoparticle-cell interactions: drug delivery implications. *Crit Rev Ther Drug Carrier Syst* 2008, 25: 485-544.

Hashida N, Ohguro N, Yamazaki N, Arakawa Y, Oiki E, Mashimo H, Kurokawa N, Tano Y. High-efficacy site-directed drug delivery system using sialyl-Lewis X conjugated liposome. *Exp Eye Res* 2008, 86: 138-149.

Hashida M, Fukushima A, Zhang J, Kodama H, Ueno H. Involvement of superoxide generated by polymorphonuclear leukocytes in endotoxin-induced uveitis. *Graefe's Arch Clin Exp Ophthalmol* 2000, 238: 359-365.

Hawkins CL, Davies MJ. Direct detection and identification of radicals generated during the hydroxyl radical-induced degradation of hyaluronic acid and related materials. *Free Radical Biol Med* 1996, 21: 275–290

Heller J. Ocular delivery using poly(ortho esters). *Adv Drug Deliv Rev* 2005, 57: 2053-2062.

Henderer JD, Rapuano CJ. Chapter 64. Ocular Pharmacology. In: Chabner BA, Brunton LL, Knollman BC (eds). Goodman & Gilman's The Pharmacological Basis of Therapeutics. 12th ed. New York: McGraw-Hill, 2011. Retrieved from URL: http://www.accesspharmacy.com/content.aspx?aID=16681771. [Accessed 12 March 2008].

Herbort CP, Okumura A, Mochizuki M. Immunopharmacological analysis of endotoxin-induced uveitis in the rat. *Exp Eye Res* 1989, 48:693-705.

Herh P, Tkachuk J, Wu S, Bernzen M, Rudolph B. The rheology of pharmaceutical and cosmetic semisolids. *ATS RheoSystems* 1998, 12-14.

Hermanson T (ed.). Bioconjugate Techniques. 2nd Ed, Elsevier: London, UK, 2008, p. 220.

Herrero-Vanrell R, Refojo MF. Biodegradable microspheres for vitreoretinal drug delivery. *Adv Drug Del Rev* 2001, 52(1): 5-16.

Higuchi T. Mechanism of sustained action medication. Theoretical analysis of rate of release of solid drugs dispersed in solid matrices. *J Pharm Sci* 1963, 52: 1145-1149.

Hillaireau H, Couvreur C. Nanocarriers' entry into the cell: relevance to drug delivery. *Cell Mol Life Sci* 2009, 66: 2873-2896.

Hilt JZ, Peppas NA. Microfabricated drug delivery devices. *Int J Pharm* 2005, 306: 15-23.

Hippalgoankar K, Hippalgaonkar K, Majumdar S. Transcorneal and transcleral transport of indomethacin using different formulation approaches. *The AAPS Journal* 2009, 11(S2). http://www.aapsj.org/abstracts/AM_2009/AAPS2009-003357.PDF.

Hirano S, Seino H, Akiyama I, Nonaka I. Chitosan: a biocompatible material for oral and intravenous administration. In: Gebelein CG, Dunn RL (eds.). Progress in Biomedical Polymers, New York: Plenum Press, 1990, pp. 283-289.

Hiscott PS, Unger WG, Grierson I, McLeod D. The role of inflammation in the development of epiretinal membranes. *Curr Eye Res* 1988, 7: 877-892.

Hixson AW, Crowell JH. Dependence of reaction velocity upon surface and agitation (I) theoretical consideration. *Ind Eng Chem* 1931, 23: 923-931.

Hoare TR, Kohane DS. Hydrogels in drug delivery: Progress and challenges. *Polymer* 2008, 49: 1993-2007.

Hogan MJ. Inflammation and its effect on the vitreous. *Trans Ophthalmol Soc UK* 1975, 95(3): 378-81.

Holekamp NM, Thomas MA, Pearson A. The safety profile of long-term, high-dose intraocular corticosteroid delivery. *Am J Ophthalmol* 2005, 139(3): 421-428.

Hosseini K, Matsushima D, Johnson J, Widera G, Nyam K, Kim L, Xu Y, Yao Y, Cormier M. Pharmacokinetic study of dexamethasone disodium phosphate using intravitreal, subconjunctival, and intravenous delivery routes in rabbits. *J Ocul Pharmacol Ther* 2008, 24(3): 301-308.

Huang SF, Chen JL, Yeh MK, Chiang CH. Physicochemical properties and in vivo assessment of timolol-loaded poly(D,L-lactide-co-glycolide) films for long-term intraocular pressure lowering effects. *J Ocul Pharmacol Ther* 2005, 21: 445.

Irache JM, Merodio M, Arnedo A, Campanero MA, Mirshahi M, Espuelas S. Albumin nanoparticles for the intravitreal delivery of anticytomegaloviral drugs. *Mini Rev Med Chem* 2005, 5: 293-305.

Islam MT, Rodríguez-Hornedo N, Ciotti S, Ackermann C. Fourier transform infrared spectroscopy for the analysis of neutralizer-carbomer and surfactant-carbomer interactions in aqueous, hydroalcoholic, and anhydrous gel formulations. *AAPS J* 2004, 6(4): article 35.

Isowaki A, Ohtori A, Matsuo Y, Tojo K. Drug delivery to the eye with a transdermal therapeutic system. *Bio Pharm Bull* 2003*,* 26: 69-72.

Iyer SS, Barr WH, Karnes HT. Profiling in vitro drug release from subcutaneous implants: a review of current status and potential implications on drug product development. *Biopharm Drug Dispos* 2006, 27(4): 157-170.

Jarvis MA, Wang CE, Meyers HL, Smith PP, Corless CL, Henderson GJ, Vieira J, Britt WJ, Nelson JA. Human Cytomegalovirus infection of Caco-2 cells occurs at the basolateral membrane and is differentiation state dependent. *J Virol* 1999, 73: 4552-4560**.**

Jiang Z, Imrie CT, Hutchinson JM. An introduction to temperature modulated differential scanning calorimetry (TMDSC): a relatively non-mathematical approach. *Thermochimica Acta* 2002, 387: 75-93.

Jin X, Ohgami K, Shiratori Y, Koyama Y, Yoshida K, Illeva I, Tanaka T, Onoe K, Ohno S. Effects of blue honeysuckle (Lonicera caerula L.) extract on lipopolysaccharide-induced inflammation in vitro and in vivo. *Exp Eye Res* 2006, 82(5): 860-867.

Jonas JB, Degenring RF, Kreissig I, Akkoyun I, Kamppeter BA. Intraocular pressure elevation after intravitreal triamcinolone acetonide injection. *Ophthalmology* 2005, 112(4): 593-598.

Jonas JB, Kreissig I, Degenring RF. Intravitreal triamcinolone acetonide for pseudophakic cystoid macular edema. *Am J Ophthalmol* 2003, 136: 384-386.

Jonas JB, Sofker A. Intraocular injection of crystalline cortisone as adjunctive treatment of diabetic macular edema. *Am J Ophthalmol* 2001, 132: 425-427.

Jonas JB, Hayler J, Sofker A, Panda-Jonas S.. Intravitreal injection of crystalline cortisone as adjunctive treatment of proliferative diabetic retinopathy. *Am J Ophthalmol* 2001, 131: 468-471.

Jonas JB, Hayler JK, Panda-Jonas S. Intravitreal injection of crystalline cortisone as adjunctive treatment of proliferative vitreoretinopathy. *Br J Ophthalmol* 2000, 84: 1064-1067.

Ju WK, Neufeld AH. Cellular localization of cyclooxygenase-1 and cyclooxygenase-2 in the normal mouse, rat, and human retina. *J Comp Neurol* 2002, 452 : 392-399.

Kampougeris G, Antoniadou A, Kavouklis E, Chryssouli Z, Giamarellou H. Penetration of moxifloxacin into the human aqueous humour after oral administration. *Br J Ophthalmol* 2005, 89(5): 628-631.

Kaneko K. Determination of pore size and pore size distribution: 1. Adsorbents and catalysts. *J Membr Sci* 1994, 96: 59-89.

Kanis LA, Viel FC, Crespo JS, Bertolino JR, Pires ATN, Soldi V. Study of poly(oxyethylene oxide)/carbopol blends through thermal analysis and infrared spectroscopy. *Polymer* 2000, 41: 3303-3309.

Kassem MA, Abdel Rahman AA, Ghorab MM, Ahmed MB, Khalil RM. Nanosuspension as an ophthalmic delivery system for certain glucocorticoid drugs. *Int J Pharm* 2007, 340 (1-2): 126-133.

Kauper K, Ling V, Elliot S, McGovern C, Sherman S, Dean B, Orecchio L, Rivera M, Heatherton P, Too W. Long-term, sustained intraocular delivery of escalating doses of VEGF antagonist using encapsulated cell technology implant for the treatment of choroidal neovascular diseases. Presented at the Association for Research in Vision and Ophthalmology Annual Meeting, May 2012, Fort Lauderdaule, FL.

Kaur IP, Aggarwal D, Singh H, Kakkar S. Improved ocular absorption kinetics of timolol maleate loaded into a bioadhesive niosomal delivery system. *Graefes Arch Clin Exp Ophthalmol* 2010, 248(10): 1467-1472.

Kaur IP, Kanwar M. Ocular preparations: the formulation approach*. Drug Dev Ind Pharm* 2002, 28*:* 473-493*.*

Kayser O, Lemke A, Hernandez-Trejo N. The impact of nanobiotechnology on the development of new drug delivery systems. *Curr Pharm Biotechnol* 2005, 6:3-5.

Keister JC, Cooper ER, Missel PJ, Lang JC, Hager DF. Limits on optimizing ocular drug delivery. *J Pharm Sci* 1991, 80: 50-53.

Keller N, Tsao SW, Chandrasekaran K, Hatfield JM. Ocular kinetics of extended duration fluorometholone (0.1%) formulations vs ointment and aqueous suspension. *Invest Ophthalmol Vis Sci* 1993, 34: 1490 (Suppl.).

Kildeeva NR, Perminov PA, Vladimirov LV, Novikov VV, Mikhailov SN. About mechanism of Chitosan cross-linking with glutaraldehyde. *Russ J Bioorg Chem* 2009, 35: 360-369.

Kim JH, Kim KW, Kim MH, Yu YS. Intravenously administered gold nanoparticles pass through the blood-retinal barrier depending on the particle size, and induce no retinal toxicity. *Nanotech* 2009a, 20(50): 505101.

Kim H, Robinson SB, Csaky KG. Investigating the movement of intravitreal human serum albumin nanoparticles in the vitreous and retina. *Pharm Res* 2009b, 26(2): 329-337.

Kim SH, Csaky KG, Wang NS, Lutz RJ. Drug elimination kinetics following subconjunctival injection using dynamic contrast-enhanced magnetic resonance imaging. *Pharm Res* 2008, 25(3): 512-520.

Kim SH, Lutz RJ, Wang NS, Robinson MR. Transport barriers in transscleral drug delivery for retinal diseases. *Ophthalmic Res* 2007, 39(5):244-254.

Klausner RD, Kumar N, Weinstein J N, Blumenthal R, Flavin M. Interaction of tubulin with membrane vesicles. *Biol Chem 1981,* 25, 5879-5885.

Knapczyk J, Krowczynski L, Krzck J, Brzeski M, Nirnberg E, Schenk D, Struszcyk H. Requirements of chitosan for pharmaceutical and biomedical applications. In: Skak- Braek G, Anthonsen T, Sandford P (eds.). Chitin and Chitosan: Sources, Chemistry, Biochemistry, Physical Properties and Applications. Elsevier: London, 1989, pp. 657-663.

Kobayashi A, Naito S, Enomoto H, Shiomoi T, Kimura T, Obata K, Inoue K, Okada Y. Serum Levels of Matrix Metalloproteinase 3 (Stromelysin 1) for Monitoring Synovitis in Rheumatoid Arthritis. *Arch Path Lab Med* 2007, 131(4): 563-570.

Kokke KH, Morris JA, Lawrenson JG. Oral omega-6 essential fatty acid treatment in contact lens associated dry eye. *Cont Lens Anterior Eye* 2008, 31(3): 141-146.

Kolhe P, Kannan RM. Improvement in ductility of chitosan through blending and copolymerization with PEG: FTIR investigation of molecular interactions. *Biomacromolecules* 2002, 4: 173-180.

Korsmeyer RW, Lustig SR, Peppas NA. Solute and penetrant diffusion in swellable polymers. I. Mathematical modeling. *J Polym Sci Polym Phys Ed* 1986a, 24: 395-408.

Korsmeyer RW, von Meerwall E, Peppas NA. Solute and penetrant diffusion in swellable polymers. II. Verification of theoretical models. *J Polym Sci Polym Phys Ed* 1986b, 24: 409-434.

Korsmeyer RW, Gurny R, Doelker E, Buri P, Peppas NA. Mechanisms of solute release from porous hydrophilic polymers. *Int J Pharm* 1983, 15: 25-35.

Koura Y, Fukushima A, Nishino K, Ishida W, Nakakuki T, Sento M, Yamazoe K, Yamaguchi T, Misyoshi T, Ueno H. Inflammatory reaction following cataract surgery and implantation of acrylic intraocular lens in rabbits with endotoxin-induced uveitis. *Eye (Lond)* 2006, 20(5): 606-610.

Kumar P, Pillay V, Choonara YE, Modi G, Naidoo D, du Toit LC. In silico theoretical molecular modeling for Alzheimer's disease: The nicotine-curcumin paradigm in neuroprotection and neurotherapy. *Int J Mol Sci* 2011, 12(1): 694-724.

Kumar N, Ravikumar MN, Pomb AJ. Biodegradable block copolymers*. Adv Drug Deliv Rev* 2001, 53*:* 23-44*.*

Kuno N, Fujii S. Ocular Drug Delivery Systems for the Posterior Segment: A Review. Retina Today 2012, May/ June: 54-59.

Kuppermann B. Cortiject dexamethasone lipid emulsion for the treatment of diabetic macular edema: A pilot study. The 8th International Symposium on Ocular Pharmacology and Therapeutics 2009: 33-31.

Kuznetsova TF. Adsorption Properties and Porous Structure of h-Al2O3: Effect of Hydroxybenzenes. *Coll J* 2003, 65(4): 454-458. Translated from *Kolloidnyi Zhurnal* 2003, 65(4): 495-499.

Lajavardi L, Bochot A, Carmeto S, Goldenberg B, Nand M-C, Behar-Cohen F, Fattal E, de tozak Y. Downregulation of endotoxin-induced uveitis by intravitreal injection of vasoactive intestinal peptide encapsulated in liposomes*. Invest Ophthalmol Vis Sci* 2007, 48*:* 3230-3238*.*

Lampe JW, Chen C, Li S, Prunty J, Grate MT, Meehan DE, Barale KV, Dightman DA, Feng Z, Potter JD. Modulation of human glutathione s-transferases by botanically defined vegetable diets. *Cancer Epidemiol Biomarkers Prev* 2000, 9: 787.

Lang JC. Ocular drug delivery conventional ocular formulations. *Adv Drug Deliv Rev* 1995, 16: 39-43.

Lanone S, Rogerieux F, Geys J, Dupont A, Maillot-Marechal E, Boczkowski J, Lacroix G, Hoet P. Comparative toxicity of 24 manufactured nanoparticles in human alveolar epithelial and macrophage cell lines. *Particle Fibre Toxicol* 2009, 6: 14.

Lasic DD, Belic A, Valentincic T. A new method for the instant preparation of large unilamellar vesicles. *J Am Chem Soc* 1988, 110: 970-971.

Lasic DD. The mechanism of liposome formation. A review. *Biochem J* 1988, 256: 1-11.

Layek B, Mukherjee B. Tamoxifen Citrate Encapsulated Sustained Release Liposomes: Preparation and Evaluation of Physicochemical Properties. *Sci Pharm* 2010, 78(3): 507-515.

Lehr CM, Bouwstra JA, Schacht EH, Junginger HE. In vitro evaluation of mucoadhesive properties of chitosan and some other natural polymers. *Int J Pharm* 1992, 78: 43-48.

Lemarchand C, Gref R, Couvreur P. Polysaccharide-decorated nanoparticles. *Eur J Pharm Biopharm* 2004, 58(2): 327-341.

Leung WK, To KF, Go MY, Chan KK, Chan FK, Ng EK, Chung SC, Sung JJ. Cyclooxygenase-2 upregulates vascular endothelial growth factor expression and angiogenesis in human gastric carcinoma. *Int J Oncol* 2003, 23: 1317-22.

Lewis RNAH, McElhaney RN. Vibrational spectroscopy of lipids. In: Chalmers JM, Griffith PR (eds.). Handbook of Vibrational Spectroscopy, Vol. 5, John Wiley and Sons: Chichester, England, 2002, pp. 3447-3464.

Levin M (ed.). Pharmaceutical Process Scale-Up. Marcel Dekker, New York, NY, 2001, p. vii.

Li W, Huang Z, MacKay JA, Grube S, Szoka Jr FC. Low-pH-sensitive poly(ethylene glycol) (PEG)-stabilized plasmid nanolipoparticles: effects of PEG chain length, lipid composition and assembly conditions on gene delivery. *J Gene Med* 2005, 7: 67–79.

Liao Y-H, Jones SA, Forbes B, Martin GP, Brown MB. Hyaluronan: pharmaceutical characterization and drug delivery. *Drug Deliv* 2005, 12: 327-342.

Ligório Fialho S, Behar-Cohen F, Silva-Cunha A. Dexamethasone-loaded poly(ε-caprolactone) intravitreal implants: A pilot study. *Eur J Pharm Biopharm* 2008, 68(3): 637-646.

Lim JI, Fung AE, Wieland M, Hung D, Wong V. Sustained-release intravitreal liquid drug delivery using triamcinolone acetonide for cystoid macular edema in retinal vein occlusion. Ophthalmol 2011, 118: 1416-1422.

Ling V. Encapsulated cell technology: a new therapy for biologics delivery. Presented at the Annual Meeting of the Antibody Society, December 2011, San Diego.

Liu L, Sheardown H. Polydimethylsiloxane poly (N-isopropyl acrylamide) network polymers as ophthalmic biomaterials. *Biomat* 2005, 26: 233.

López T, Ortiz E, Quitana P, González RD. A nanostructured titania bioceramic implantable device capable of drug delivery to the temporal lobe of the brain. *Coll Sur A: Physicochem Eng Aspects* 2007, 300(1-2): 3-10.

Losa C, Marchal-Heussler L, Orallo F, Vila Jato JL, Alonso MJ. Design of new formulations for topical ocular administration: polymeric nanocapsules containing metipranolol. *Pharm Res* 1993, 10: 80-87.

Losa C, Alonso MJ, Vila JL, Orallo F, Martinez J, Saavedra JA, Pastor JC. Reduction of cardiovascular side effects associated with ocular administration of metipranolol by inclusion in polymeric nanocapsules. *J Ocul Pharmacol* 1992, 8: 191-198.

Losa C, Calvo P, Castro E, Vila-Jato JL, Alonso MJ. Improvement of ocular penetration of amikacin sulphate by association to poly(butylcyanoacrylate) nanoparticles. *J Pharm Pharmacol* 1991, 43: 548-552.

Love WG, Amos N, Kellaway IW, Williams BD. Specific accumulation of cholesterol-rich liposomes in the inflammatory tissue of rats with adjuvant arthritis. *Ann Rheum Dis* 1990, 49: 611-614.

Lozano MM, Longo ML. Microbubbles coated with disaturated lipids and DSPE-PEG2000: phase behaviour, collapse transitions, and permeability. *Langmuir* 2009, 25: 3705-3712.

Ludwig A. The use of mucoadhesive polymers in ocular drug delivery. Adv Drug Deliv Rev 2005, 57: 1595-1639.

Luo Y, Kirker K, Prestwich G. Cross-linked hyaluronic acid hydrogel films: New biomaterials for drug delivery. *J Contr Rel* 2000, 69(1): 169-184.

Lyons NM, O'Brien NM. Modulatory effects of an algal extract containing astaxanthin on UVA-irradiated cells in culture. *J Derm Sci* 2002, 30: 73-84.

Ma G, Liu Y, Fang D, Chen J, Peng C, Fei X, Nie J. Hyaluronic acid/chitosan polyelectrolyte complexes nanofibers prepared by electrospinning. *Mat Lett* 2012, 74: 78-80.

Ma Z, Lim L-Y. Uptake of chitosan and associated insulin in Caco-2 cell monolayers: a comparison between chitosan molecules and chitosan nanoparticles. *Pharm Res* 2003, 20(11): 1812-1819.

Magnani A, Rappuoli R, Lamponi S, Barbucci R. Novel polysaccharide hydrogels: Characterization and properties. *Polym Adv Tech* 2000, 11(8–12): 488-495.

Mainardes RM, Urban MC, Cinto PO, Khalil NM, Chaud MV, Evangelista RC, Gremiao MP, Colloidal carriers for ophthalmic drug delivery. *Curr Drug Targets* 2005, 6: 363-371.

Mannermaa E, Vellonen K-S, Urtti A. Drug transport in corneal epithelium and blood–retina barrier: Emerging role of transporters in ocular pharmacokinetics. *Adv Drug Deliv Rev* 2006, 58(11): 1136-1163.

Mao Z, Wang B, Ma L, Gao C, Shen J. The influence of polycaprolactone coating on the internalization and cytotoxicity of gold nanoparticles. *Nanomedicine* 2007, 3(3): 215-223.

Marriot C. Rheology. In: Marriot ME (ed.). Marriot's Pharmaceutics: the Design and Manufacture of Medicines. Churchill Livingstone Elsevier: Philadelphia, USA, 2008, pp. 42-58.

McEver RP. Leukocyte-endothelial cell interactions. *Curr Opin Cell Biol* 1992, 4: 840-849.

Meadows DL, Paugh JR, Joshi A, Mordaunt J. A novel method to evaluate residence time in humans using a nonpenetrating fluorescent tracer. *Invest Ophthalmol Vis Sci* 2002, 43: 1032-1039.

Meffert MK, Chang JM, Wiltgen BJ, Fanselow MS, Baltimore D. NF-kappa B functions in synaptic signaling and behavior. *Nat Neurosci* 2003, 6(10): 1072-1078.

Merodio M, Espuelas MS, Mirshahi M, Arnedo A, Irache JM. Efficacy of ganciclovir-loaded nanoparticles in human cytomegalovirus (HCMV)-infected cells. *J Drug Target* 2002a, 10: 231-238.

Merodio M, Irache JM, Valamanesh F, Mirshahi M. Ocular disposition and tolerance of ganciclovir-loaded albumin nanoparticles after intravitreal injection in rats. *Biomaterials* 2002b, 23: 1587-1594.

Merodio M, Arnedo A, Renedo MJ, Irache JM. Ganciclovir-loaded nanoparticles: characterization and in vitro release properties. *Eur J Pharm Sci* 2001, 12: 251-259.

Mettler Toledo. Temperature Modulated DSC. 2010. Retrieved from URL: http://www.mt.com. [Accessed 20 April 2012].

Mitra AK, Anand BS, Duvvuri S. Drug delivery to the eye. In: Fischbarg J (ed.). The Biology of the Eye. Academic Press: New York, 2006, pp. 307-351.

Miura K, Kimura N, Suzuki H, Miyashita Y, Nishio Y. Thermal and viscoelastic properties of alginate/poly(vinyl alcohol) blends cross-linked with calcium tetraborate. *Carb Polym* 1999, 39: 139-144.

Mlčochová P, Bystrický S, Steiner B, Machová E, Kóš M, Velebný V, Krčmář M. Synthesis and characterization of new biodegradable hyaluronan alkyl derivatives. *Biopolymers* 2006, 82(1): 74-79.

Monson PA. Contact angles, pore condensation and hysteresis: Insights from a simple molecular model. *Langmuir* 2008, 24: 12295-12302.

Moshfeghi DM, Kaiser PK, Scott IU, Sears JE, Benz M, Sinesterra JP, Kaiser RS, Bakri SJ, Maturi RK, Belmont J, Beer PM, Murray TG, Quiroz-Mercado H, Mieler WF. Acute

endophthalmitis following intravitreal triamcinolone acetonide injection. *Am J Ophthalmol* 2003, 136: 791-796.

Mosquera MJ, Bejarano M, de la Rosa-Fox N, Esquivias L. Producing crack-free colloid-polymer hybrid gels by tailoring porosity. *Langmuir* 2003, 19: 951-957.

Motwani SK, Chopra S, Talegaonkar S, Kohli K, Ahmad FJ, Khar RK. Chitosan–sodium alginate nanoparticles as submicroscopic reservoirs for ocular delivery: Formulation, optimisation and in vitro characterisation. *Eur J Pharm Biopharm* 2008, 68(3): 513-525.

Myles ME, Neumann DM, Hill JM. Recent progress in ocular drug delivery for posterior segment disease: Emphasis on transscleral iontophoresis. *Adv Drug Del Rev (Drug Delivery Strategies to Treat Age-Related Macular Degeneration)* 2005, 57(14): 2063-2079.

Nagarsenker MS, Londhe VY, Nadkarni GD. Preparation and evaluation of liposomal formulations of tropicamide for ocular delivery. *Int J Pharm* 1999, 190(1): 63-71.

Nagarwal RC, Kant S, Singh PN, Maiti P, Pandit JK. Polymeric nanoparticulate system: A potential approach for ocular drug delivery. *J Contr Rel* 2009, 136: 2-13.

Nanjawade BK, Manvi FV, Manjappa AS. In situ-forming hydrogels for sustained ophthalmic drug delivery. *J Contr Rel* 2007, 122(2): 119-134.

Nanosight. Zeta Potential Analysis using Z-NTA. Retrieved from URL: http://www.nanosight.com/applications/nanoparticles/zeta-potential [Accessed 21 February 2013].

Nemoto E, Ueda H, Akimoto M, Natsume H, Morimoto Y. Ability of poly-l-arginine to enhance drug absorption into aqueous humor and vitreous body after instillation in rabbits. *Biol Pharm Bull* 2007, 30: 1768-1772.

Ng S-F, Rouse JJ, Sanderson FD, Meidan V, Eccleston GM. Validation of a static franz diffusion cell system for *in vitro* permeation studies. *AAPS PharmSciTech* 2010, 11(3): 1432-1441.

Nielson LE (ed.). Mechanical Properties of Polymers and Composites. Vol. 1, Marcel Dekker: New York, NY, USA, 1974.

Normand N, Valamanesh F, Savoldelli M, Mascarelli F, BenEzra D, Courtois Y, Behar-Cohen FF. VP22 light controlled delivery of oligonucleotides to ocular cells in vitro and in vivo. *Mol Vis* 2005, 11: 184-191.

Novagali.com. Novagli Pharma. Eyeject. Retrieved from URL: http://www.novagali.com/en/our-research/eyeject/. [Accessed 14 February 2013].

O'Doherty M. Liposome Literature Review. Nanobiotechnology and Bioanalysis Group, 2004. Retrieved from URL: www.etseq.urv.cat/dinamic/catala/places/liposome_lit_review. [Accessed 30 October 2008].

Ogawa T. Effects of molecular weight on mechanical properties of polypropylene. *J Appl Polym Sci* 1992, 44(10): 1869-1871.

Oh SH, Kang SG, Lee JH. Degradation behavior of hydrophilized PLGA scaffolds prepared by melt-molding particulate-leaching method: comparison with control hydrophobic one. *J Mater Sci: Mater Med* 2006, 17: 131-137.

Okada AA, Johnson RP, Liles CW, D'Amico DJ, Baker AS. Endogenous bacterial endophthalmitis: report of a ten-year retrospective study. *Ophthalmol* 1994,101: 832-838.

Olojo RO, Xia RH, Abramson JJ. Spectrophotometric and fluorometric assay of superoxide ion using 4-chloro-7-nitrobenzo-2-oxa-1,3-diazole. *Anal Biochem* 2005, 339: 338-344.

OnDemandTx.com. The ODTx solution. Retrieved from URL: http://www.ondemandtx.com/the-odtx-solution.aspx. [Accessed 14 February 2013].

Ostrowski M, Baczek T. The Progress on the *In Vivo-In Vitro* Correlation (IVIVC) for ImmediatevRelease Dosage Form as an Alternative to Bioavailability Studies *Curr Pharm Anal* 2010*, 6,* 289-298.

Otsubo Y. Dilatant flow of flocculated suspensions. *Langmuir* 1992, 8: 2336-2340

Öztürk F, Kurt E, Inan ÜÜ, Kortunay S, Ilker SS, Bascı NE, Bozkurt A. The effects of prolonged acute use and inflammation on the ocular penetration of topical ciprofloxacin. *Int J Pharm* 2000, 204(1-2): 97-100.

Paasonen L, Laaksonen T, Johans C, Yliperttula M, Kontturi K, Urtti A. Gold nanoparticles enable selective light-induced contents release from liposomes. *J Contr Rel* 2007, 11: 86-93.

Paddock SW, Fellers TJ, Davidson MW. Confocal microscopy. 2012. http://www.microscopyu.com/articles/confocal/confocalintrobasics.html.

Panyam J. Inflammation-responsive drug delivery system. Pharmaceutical Sciences, WSU__.htm. http://research.wayne.edu/idre/db/?view=person&id=42. Last retrieved 2 February 2008. Relocated in part to: http://research.wayne.edu/idre/tools/faculty-interests.php?id=70.

Park CH, Jaffe GJ, Fekrat S. Intravitreal triamcinolone acetonide in eyes with cystoid macular edema associated with central retinal vein occlusion. *Am J Ophthalmol* 2003, 136: 419-425.

Partini M, Argenio O, Coccorullo I, Pantani P. Degradation kinetics and rheology of biodegradable polymers. *J Therm Anal Calor* 2009, 98: 645-653.

Pearlman DA, Case DA, Caldwell JW, Ross WS, Cheatham TE, De-Bolt S III, Ferguson D, Seibel G and Kollman P. AMBER, a package of computer programs for applying molecular mechanics, normal mode analysis, molecular dynamics and free energy calculations to simulate the structural and energetic properties of molecules. *Comp Phys Commun* 1995, 91 1-41.

Peeters L, Lentacker I, Vandenbroucke RE, et al. Can ultrasound solve the transport barrier of the neural retina? *Pharm Res* 2008, 25(11): 2657-2665.

Peeters L, Sanders NN, Braeckmans K, Boussery K, Van de Voorde J, De Smedt SC, Demeester J. Vitreous: a barrier to nonviral ocular gene therapy. *Invest Ophthalmol Vis Sci.* 2005, 46(10): 3553-3561.

Perkins ND. Integrating cell-signalling pathways with NF-κB and IKK function. *Nat Rev Mol Cell Biol* 2007, 8 (1): 49-62.

Pertuit D, Moulari B, Betz T, Nadaradjane A, Neumann D, Ismaïli L, Refouvelet B, Pellequer Y, Lamprecht A. 5-amino salicylic acid bound nanoparticles for the therapy of inflammatory bowel disease. *J Contr Rel* 2007, 123(3): 211-218.

Peyman GA, Ganiban GJ. Delivery systems for intraocular routes. *Adv Drug Deliv Rev* 1995, 16: 107-123.

Pignatello R, Bucolo C, Ferrara P, Maltese A, Puleo A, Puglisi G. Eudragit RS100® nanosuspensions for the ophthalmic controlled delivery of ibuprofen. *Eur J Pharm Sci* 2002a, 16: 53-61

Pignatello R, Bucolo C, Spedalieri G, Maltese A, Puglisi G. Flurbiprofen-loaded acrylate polymer nanosuspensions for ophthalmic application. *Biomaterials* 2002b, 23(15): 3247-3255.

Pillay V, Fassihi R. Evaluation and comparison of dissolution data derived from different modified release dosage forms: an alternative method. *J Contr Rel* 1998, 55: 45-55.

Pişkin E. Molecularly designed water soluble, intelligent, nanosize polymeric carriers. *Int J Pharm* 2004, 277: 105-118.

Pitkanen L, Ruponen M, Nieminen J, Urtti A. Vitreous is a barrier in nonviral gene transfer by cationic lipids and polymers. *Pharm Res* 2003, 20(4): 576-583.

Polley MJ, Phillips ML, Wayner E, Nudelman E, Singhal AK, Hakomori S, Paulson JC. CD62 and endothelial cell-leukocyte adhesion molecule 1 (ELAM-1) recognize the same carbohydrate ligand, sialyl-Lewis X. *Proc Natl Acad Sci USA* 1991, 88: 6224-6228.

Polyak B, Geresh S, Marks RS. Synthesis and characterization of a biotin-alginate conjugate and its application in a biosensor construction. *Biomacromol* 2004, 5: 389-396.

Prabaharan M, Mano JF. Chitosan-based particles as controlled drug delivery systems. *Drug Deliv* 2005, 12: 41-57.

Prestwich GD. Biomaterials from Chemically-Modified Hyaluronan. 2001. Retrieved from URL: http://glycoforum.gr.jp/science/hyaluronan/HA18/HA18E.html. [Accessed 22 February 2008].

pSivida.com. Products/Thethadur. Available at: http://psivida.com/products-biosilicon.html.

Qaddoumi MG, Ueda H, Yang J, Davda J, Labhasetwar V, Lee VHL. Uptake of biodegradable nanoparticles in pigmented rabbit conjunctival epithelial cells. *Invest Ophthalmol Vis Sci* 2000, 41: S765.

Qiu LY, Bae YH. Polymer architecture and drug delivery. *Pharm Res* 2006, 23: 1-30.

Rabinovich-Guilatt L, Couvreur P, Lambert G, Dubernet C. Cationic vectors in ocular drug delivery. *J Drug Target* 2004, 12(9-10): 623-33.

Rabiah PK, Fiscella RG, Tessler HH. Intraocular penetration of periocular ketorolac and efficacy in experimental uveitis. *Invest Ophthalmol Vis Sci* 1996, 37(4): 613-618.

Rajpal, Srinivas A, Azad RV, Sharma YR, Kumar A, Satpathy G, Velpandian T. Evaluation of vitreous levels of gatifloxacin after systemic administration in inflamed and non-inflamed eyes. *Acta Ophthalmol* 2009, 87(6): 648-652.

Raju HB, Goldberg JL, Nanotechnology for ocular therapeutics and tissue repair. *Expert Rev Ophthalmol 2008*, 3: 431-436.

Ramachandran KI, Deepa G, Namboori K (eds.). Computational Chemistry and Molecular Modeling Principles and Applications, Springer-Verlag: Berlin, Heidelberg, Germany, 2008, p. vii.

Rao NA. Role of oxygen radicals in retinal damage associated with experimental uveitis. *Tr Am Opth Soc* 1990, 87:797-850.

Ratajska M, Boryniec S. Physical and chemical aspects of biodegradation of natural polymers. *React Funct Polym* 1998, 38: 35-49.

Ravi Kumar MNV. A review of chitin and chitosan applications. *React Func Polym* 2000, 46: 1-27.

Regnier A, Schneider M, Concordet D, Toutain PL. Intraocular pharmacokinetics of intravenously administered marbofloxacin in rabbits with experimentally induced acute endophthalmitis. *Am J Vet Res* 2008, 69(3): 410-515.

Reichle ML. Complications of intravitreal steroid injections. *Optometry* 2005, 76(8): 450-460.

Ringe K, Walz CM, Sabel BA. Nanoparticle Drug Delivery to the Brain. In: Nalwa HS (ed.). Encyclopedia of Nanoscience and Nanotechnology. Vol. 7, American Scientific Publishers: USA, 2004, pp. 91-104.

Robinson JC. Ocular anatomy and physiology relevant to ocular drug delivery. In: Mitra AK (ed.). *Ophthalmic Drug Delivery Systems*. Marcel Dekker: New York, 1993, pp. 29-58.

Rodrigues GB, Passos GF, Di Giunta G, Figueiredo C, Rodrigues EB, Grumman Jr. A, Medeiros R, Calixto JB. Preventive and therapeutic anti-inflammatory effects of systemic and topical thalidomide on endotoxin-induced uveitis in rats. *Exp Eye Res* 2007, 84(3): 553-560.

Roger S, Bee A, Balnois E, Bourmaud A, Le Deit H, Grohens Y, Cabuil V. Physical and mechanical properties of alginate films containing calcium cations and ferrofluids. Fifth International Conference Polymer-Solvent Complexes & Intercalates, Lorient, France, July 11-14, 2004.

Romero L, Andrews K, Ng L, O'Rourke K, Maslen A, Kirby G. Human GSTA1-1 reduces c-Jun N-terminal kinase signalling and apoptosis in Caco-2 cells. *Biochem J* 2006, 400: 135-141.

Rootman DS, Savage P, Hasany SM, Chisholm L, Basu PK. Toxicity and pharmacokinetics of intravitreally injected ciprofloxacin in rabbit eyes. *Can J Ophthalmol* 1992, 27(6): 277-282.

Rosenbaum JT, McDevitt HO, Guss RB, Egbert PR. Endotoxin induced uveitis in rats as a model for human disease. *Nature* 1980, 286: 611-612.

Roth DB, Chieh J, Spirn, Green SN, Yarian DL, Chaudhry NA. Noninfectious endophthalmitis associated with intravitreal triamcinolone injection. *Arch Ophthalmol* 2003, 121: 1279-1282.

Rothen-Weinhold A, Besseghir K, Vuaridel E, Sublet E, Oudry N, Kubel F, Gurny R. Injection-molding versus extrusion as manufacturing technique for the preparation of biodegradable implants. Eur J Pharm Biopharm 1999, 48(2): 113-121.

Ruiz-Moreno JM, Thillaye B, de Kozak Y. Retino-choroidal changes in endotoxin-induced uveitis in the rat. *Ophthal Res* 1992, 24: 162-168.

Rusu D, Cimpoiu C, Hodisan T. The control over the new obtaining procedeum of indomethacin. *J Pharm Biomed Anal* 1998, 17: 409-413.

Ryu M, Nakazawa T, Akagi T, Tanaka T, Watanabe R, Yasuda M, Himori N, Maruyama K, Yamashita T, Abe T, Akashi M, Nishida K. Suppression of phagocytic cells in retinal disorders using amphiphilic poly(γ-glutamic acid) nanoparticles containing dexamethasone. *J Contr Rel* 2011, 151(1): 65-73.

Sahoo S, Sasmal A, Sahoo D, Nayak P. Synthesis and characterization of chitosan-polycaprolactone blended with organoclay for control release of doxycycline. *J Appl Polym Sci* 2010, 118: 3167-3175.

Sahoo SK, Dilnawaz F, Krishnakumar S. Nanotechnology in ocular drug delivery. *Drug Discov Today* 2008, 13(3-4): 144-151.

Sahoo SK, Labhasetwar V. Nanotech approaches to drug delivery and imaging. *Drug Discov Today* 2003, 8: 1112-1120.

Sakai T, Kohno H, Ishihara T, Higaki M, Saito S, Matsushima M, Mizushima Y, Kitahara K. Treatment of experimental autoimmune uveoretinitis with poly(lactic acid) nanoparticles encapsulating betamethasone phosphate. *Exp Eye Res* 2006, 82(4): 657-663.

Sakamoto H, Sakamoto M, Hata Y, Kubota T, Ishibashi T. Aqueous and vitreous penetration of levofloxacin after topical and/or oral administration. *Eur J Ophthalmol* 2007, 17(3): 372-376.

Sakurai, K.; Maegawa, T.; Takahashi, T. Glass transition temperature of chitosan and miscibility of chitosan/poly(*N*-vinyl pyrrolidone) blends. *Polymer* 2000, 41: 7051-7056.

Saliba JB, Gomes Faraco AA, Yoshida MI, de Vasconcelos WL, da Silva-Cunha A, Mansur HS. Development and characterization of an intraocular biodegradable polymer system containing cyclosporine A for the treatment of posterior uveitis. *Mat Res* 2008, 11(2): 207-211.

Saltzman WM (ed.) Drug Delivery: Engineering Principles for Drug Therapy. Oxford University Press: Oxford, New York, 2001.

Samtani S, Amaral J, Campos MM, Fariss RN, Becerra SP. Doxycycline-mediated inhibition of choroidal neovascularization. *Invest Ophthalmol Vis Sci* 2009, 50(11): 5098-5106.

Sanchez A, Alonso MJ, Nanoparticular carriers for ocular drug delivery. In: Torchilin VP (ed.). Nanoparticulates as Drug Carriers. Imperial College Press: London, 2006, pp. 649-673.

Santulli RJ, Kinney WA, Ghosh S, et al. Studies with an orally bioavailable alpha V integrin antagonist in animal models of ocular vasculopathy: retinal neovascularization in mice and retinal vascular permeability in diabetic rats. *J Pharmacol Exp Ther* 2008, 324(3): 894-901.

Sarasam A, Madihally SV. Characterization of chitosan–polycaprolactone blends for tissue engineering applications. *Biomaterials* 2005, 26(27): 5500-5508.

Sarmila S, Abhishek S, Rajashree N, Phani AR, Nayak PL. Synthesis of chitosan-polycaprolactone blend for control delivery of ofloxacin drug. *Carbohyd Polym* 2009, 79: 106-113.

Sastry SV, Reddy IK, Khan MA: Atenolol gastrointestinal therapeutic system: optimization of formulation variables using response surface methodology. *J Contr Rel* 1997, 45(2): 121-130.

Schante CE, Zuber G, Herlin C, Vandamme TF. Chemical modifications of hyaluronic acid for the synthesis of derivatives for a broad range of biomedical applications. *Carbohyd Polym* 2011, 85(3): 469-489.

Schipper NGM, Olsson S, Hoogstraate JA, DeBoer AG, Varum KM, Artursson P. Chitosans as absorption enhancers for poorly absorbable drugs 2: mechanism of absorption enhancement. *Pharm Res* 1997, 14: 923-929.

Schmaljohann D. Thermo- and pH-responsive polymers in drug delivery. *Adv Drug Deliv Rev* 2006, 58: 1655-1670.

Scott IU, Alexandrakis G, FlynnJr HW, Smiddy WE, Murray TG, Schiffman J, Gedde SJ, Budenz DL, Fantes F, ParrishII RK. Combined pars plana vitrectomy and glaucoma drainage implant placement for refractory glaucoma. *Am J Ophth* 2000, 129(3): 334-341.

Scott JE, Tigwell MJ. Periodate-induced viscosity decreases in aqueous solutions of acetal- and ether-linked polymers. *Carbohyd Res* 1973, 28: 53.

Shaikh RP, Kumar P, Choonara YE, du Toit LC, Pillay. Crosslinked electrospun PVA nanofibrous membranes: elucidation of their physicochemical, physicomechanical and molecular disposition. *Biofabr* 2012, 4(025002):doi:10.1088/1758-5082/4/2/025002.

Sharir M, Triester G, Kneer J, Rubinstein E. The intravitreal penetration of ceftriaxone in man following systemic administration. *Invest Ophthalmol Vis Sci* 1989, 30: 2179-2183.

Sharma A, Sharma US. Liposomes in drug delivery: progress and limitations. *Int J Pharm* 1997, 154: 123-140.

Shen Z, Peedikayil J, Olson GK, Siebert PD, Fang Y. Multiple transcription factor profiling by enzyme-linked immunoassay. *BioTechniques* 2002, 32(5): 1168-1177.

Shin HS, Zhao Z, Satsu H, Totsuka M, Shimizu M. Synergistic effect of tumor necrosis factor-alpha and hydrogen peroxide on the induction of IL-8 production in human intestinal Caco-2 cells. *Inflammation* 2011, 34(5): 440-447.

Shirasaki Y, Miyashita H, Yamaguchi M. Exploration of orally available calpain inhibitors. Part 3: Dipeptidyl alpha-ketoamide derivatives containing pyridine moiety. *Bioorg Med Chem* 2006, 14(16): 5691-5698.

Shoaib MH, Tazeen J, Merchant H, Yousuf RI. Evaluation of drug release kinetics from ibuprofen matrix tablets using HPMC. *Pak J Pharm Sci* 2006, 19(2): 119-124.

Siepmann J, Kranz H, Peppas NA and Bodmeier R. Calculation of the required size and shape of hydroxypropyl methylcellulose matrices to achieve desired drug release profiles. *Int J Pharm* 2000, 201: 151-164.

Siepmann J, Podual K, Sriwongjanya M, Peppas NA, Bodmeier R. A new model describing the swelling and drug release kinetics from hydroxypropyl methylcellulose tablets. *J Pharm Sci* 1999a, 88: 65-72.

Siepmann J, Kranz H, Bodmeier R and Peppas NA. HPMC-matrices for controlled drug delivery: a new model combining diffusion, swelling and dissolution mechanisms and predicting the release kinetics. *Pharm Res* 1999b, 16: 1748-1756.

Sihorkar V, Vyas SP. Biofilm consortia on biomedical and biological surfaces: delivery and targeting strategies. *Pharm Res 2001,* 18: 1247-1254.

Simone E, Ding BS, Muzykantov V. Targeted delivery of therapeutics to endothelium*. Cell Tissue Res* 2009, 335*:* 283-300*.*

Sing KSW, Everett DH, Haul RAW, Moscou L, Pierotti RA, Rouquerol J, Siemieniewska T. Reporting physisorption data for gas/solid systems with special reference to the determination of surface area and porosity. *Pure Appl Chem* 1985, 57: 603-619.

Singh R, Lillard Jr. JW. Nanoparticle-based targeted drug delivery *Exp Mol Path (Special Issue: Structural Biology)* 2009, 86(3): 215-223.

Singh SR, Grossniklaus HE, Kang SJ, Edelhauser HF, Ambati BK, Kompella UB. Intravenous transferrin, RGD peptide and dual-targeted nanoparticles enhance anti-VEGF intraceptor gene delivery to laser-induced CNV. *Gene Ther* 2009, 16(5): 645-659.

Singh B, Kumar R, Ahuja N. Optimizing drug delivery systems using systematic "design of experiments." Part I: fundamental aspects. *Crit Rev Ther Drug Carrier Syst* 2005, 22(1): 27-105.

Soppimath KS, Aminabhavi TM, Kulkarni AR, Rudzinski WE. Biodegradable polymeric nanoparticles as drug delivery devices. *J Contr Rel* 2001, 70: 1-20.

Srinath P, Vyas SP, Diwan PV. Preparation and pharmacodynamic evaluation of liposomes of indomethacin. *Drug Dev Ind Pharm* 2000, 26(3): 313-321.

Steeber DA, Venturi GM, Tedder TF. A new twist to the leukocyte adhesion cascade: intimate cooperation is key. *Trends Immunol* 2005, 26: 9-12.

Stein J, Ries J, Barrett KE. Disruption of intestinal barrier function associated with experimental colitis: possible role of mast cells. *Am J Physiol* 1998, 274: G203-G209.

Steuer H, Jaworski A, Elger B, Kaussmann M, Keldenich J, Schneider H, Stoll D, Schlosshauer B. Functional characterization and comparison of the outer blood–retina barrier and the blood–brain barrier. *Invest Ophthalmol Visual Sci* 2005, 46: 1047-1053.

Stofan DA, Calllahan LA, DiMarco AF, Nethery DE, Supinski GS. Modulation of Release of Reactive Oxygen Species by the Contracting Diaphragm. *Am J Respir Crit Care Med* 2000, 161(3): 891-898.

Strübing S, Metz H, Mäder K. Characterization of poly(vinyl acetate) based floating matrix tablets. *J Contr Rel* 2008, 126(2): 149-155.

Sultana Y, Aqil M, Ali A. Ocular inserts for controlled delivery of pefloxacin mesylate: Preparation and evaluation. *Acta Pharm* 2005, 55: 305.

Sun J, Wang S, Zhao D, Han Hun F, Weng L, Liu H. Cytotoxicity, permeability, and inflammation of metal oxide nanoparticles. *Cell Biol Toxicol* 2011, 27: 333-342.

Sunkara GKU. Membrane transport processes in the eye. In: Mitra AK (ed). Ophthalmic drug delivery systems. New York: Marcel Dekker, Inc, 2003. pp. 13-58.

Suri SS, Fenniri H, Singh B. Nanotechnology-based drug delivery systems. *J Occup Med Toxicol* 2007, 2: 16.

Surmodics.com. I-vation™ Sustained Drug Delivery System. Retrieved from URL: www.surmodics.com/pageDetail.aspx?pageId=70... [Accessed 27 February 2008].

Susan B, Maryadele JON, Ann S, Patricia EH. The Merck Index: An encyclopedia of chemicals, drugs and biological. 11th ed., Merck and Co., 1991, p. 1071.

Suzuki T, Uno T, Chen G, Ohashi Y. Ocular distribution of intravenously administered micafungin in rabbits. *J Infect Chemother* 2008, 14(3): 204-207.

Svenson S, Tomalia D. Dendrimers in biomedical applications – reflections on the field. *Adv Drug Del Rev* 2005, 57, 2106-2129.

Szoka FC, Papahadjopoulos D. Procedure for preparation of liposomes with large internal aqueous space and high capture by reverse-phase evaporation. *Proc Natl Acad Sci USA* 1978, 75(9): 4194-4198.

Tabata Y, Inoue Y, Ikada Y. Size effect on systemic and mucosal immune responses induced by oral administration of biodegradable microspheres*. Vaccine* 1996, 14*:* 1677-1685*.*

Taheri SM, Fischer S, Förster S. Routes to nanoparticle-polymer superlattices. *Polymers* 2011, 3: 662-673.

Tajiri T, Morita S, Sakamoto R, Suzuki M, Yamanashi S, Ozaki Y, Kitamura S. Release mechanisms of acetaminophen from polyethylene oxide/polyethylene glycol matrix tablets utilizing magnetic resonance imaging*. Int J Pharm* 2010, 395(1-2): 147-153.

Takahashi K, Saishin Y, King AG, Levin R, Campochiaro PA. Suppression and regression of choroidal neovascularization by the multitargeted kinase inhibitor pazopanib. *Arch Ophthalmol* 2009, 127(4): 494-499.

Takeuchi H, Yamamoto H, Niwa T, Hino T, Kawashima Y. Enteral absorption of insulin in rats from mucoadhesive chitosan-coated liposomes. *Pharm Res* 1996; 13: 896–901.

Takka S. Propranolol hydrochloride–anionic polymer binding interaction. *Il Farmaco* 2003, 58(10): 1051-1056.

Tamm LK, Tatulian SA. Infrared spectroscopy of proteins and peptides in lipid bilayers. *Q Rev Biophys* 1997, 30(4): 365-429.

Tammi MI, Day AJ, Turley EA. Hyaluronan and homeostasis: a balancing act. *J Biol Chem* 2002, 277(7): 4581-4584.

Thilek Kumar M, Pandit JK, Balasubramaniam J. Novel therapeutic approaches for uveitis and retinitis. *J Pharm Pharmaceut Sci* 2001, 4(3), 248-254.

Thomas AA, Kim IT, Kiser PF. Symmetrical biodegradable crosslinkers for use in polymeric devices. *Tetrahedron Lett* 2005, 46: 8921-5.

Thommes M. Physical adsorption characterization of nanoporous materials. *Chemie Ingenieur Technik* 2010, 82(7): 1059-1073.

Tian Y, Li Y, Xu X, Jin Z, Jiao A, Wang J, Yu B. A novel size-exclusion high performance liquid chromatography (SE-HPLC) method for measuring degree of amylose retrogradation in rice starch. *Food Chem* 2010, 118: 445-448.

Tinke AP. Monitoring pharmaceutical products with tabletop SEM: Customer Testimonial. Phenom-World BV: The Netherlands, 2009.

Tiwary AK, Rana V. Cross-linked chitosan films: effect of cross-linking density on swelling parameters. *Pak J Pharm Sci* 2010, 23(4): 443-448.

Tomihata K, Ikada Y. Crosslinking of hyaluronic acid with glutaraldehyde. *J Polym Sci Part A: Polym Chem* 2000, 35(16): 3553-3559.

Twaites B, Alarcon CD, Alexander C. Synthetic polymers as drugs and therapeutics. *J Mater Chem* 2005, 15: 441.

Ulanski P, von Sonntag C. OH-Radical-induced chain scission of chitosan in the absence and presence of dioxygen *J Chem Soc, Perkin Trans* 2000, *2*: 2022-2028.

Ulbrich W, Lamprecht A.Targeted drug-delivery approaches by nanoparticulate carriers in the therapy of inflammatory diseases. *J R Soc Interface* 2010, 7(Suppl 1): S55-S66.

Umemoto M, Takahashi K, Higashi K. Evaluation of ophthalmic suspension containing pilocarpine microcapsules: pharmacodynamic and pharmacokinetic studies. *Invest Ophthalmol Vis Sci* 1993, 34: 1488 (Suppl.).

Urtti A. Challenges and obstacles of ocular pharmacokinetics and drug delivery. *Adv Drug Deliv Rev* 2006, 58(11): 1131-1135.

Vandamme TF, Brobeck L. Poly(amidoamine) dendrimers as ophthalmic vehicles for ocular delivery of pilocarpine nitrate and tropicamide. *J Contr Rel* 2005, 102: 23.

Vandervoort J, Ludwig A. Preparation and evaluation of drug-loaded gelatine nanoparticles for topical ophthalmic use. *Eur J Pharm Biopharm* 2004, 57: 251-261

Vasir JK, Reddy MK, Labhasetwar V. Nanosystems in drug targeting: opportunities and challenges. *Curr Nanosci* 2005, 1: 47-64.

Vega E, Egea MA, Valls O, Espina M, Garcia ML. Flurbiprofen loaded biodegradable nanoparticles for ophtalmic administration. *J Pharmacol Sci* 2006, 95: 2393-2405.

Visor GC. Drug design strategies for ocular therapeutics. *Adv Drug Del Rev* 1994, 14: 269-279

Voigt M, Kralinger M, Kieselbach G, Chapon P, Ananoste S, Hayden B, Parel JM. Ocular aspirin distribution: a comparison of intravenous, topical, and coulomb-controlled iontophoresis administration. *Investig Ophthalmol Vis Sci* 2002, 43: 3299-3306.

Von Sallmann L, Meyer K, Di Grandi J. Experimental study on penicillin treatment of ectogenous infection of vitreous. *Arch Ophthalmol* 1944, 32: 179-189.

Von Sallmann L. Controversial points in penicillin therapy for ocular diseases. *Arch Ophthalmol* 1948, 39: 752-804.

Warhurst DC, Craig JC, Adagu IS, Meyer DJ, Lee SY. The relationship of physico-chemical properties and structure to the differential antiplasmodial activity of the cinchona alkaloids *Malaria J* 2003, 2: 26.

Waterbury LD, Flach AJ. Comparison of ketorolac tromethamine, diclofenac sodium, and loteprednol etabonate in an animal model of ocular inflammation. *J Ocul Pharmacol Ther* 2006, 22(3): 155-159.

Waterbury LD, Flach AJ. Efficacy of low concentrations of ketorolac tromethamine in animal models of ocular inflammation. *J Ocul Pharmacol Ther* 2004, 20(4): 345-352.

Weiner AL, Marsh DA. Chapter 22: Systems for Drug Delivery to the Posterior Segment of the Eye. In: Penn JS (ed.). Retinal and Choroidal Angiogenesis. Springer Science + Business Media, 2008, pp. 419-444.

Wong V, Wood, L. Conveniently Implantable Sustained Release Drug Compositions. US Patent WO2006/039336, 6 April 2006.

Woodward SC, Brewer PS, Moatamed F, Schindler A, Pitt CG. The intracellular degradation of poly(epsilon-caprolactone). *J Biomed Mater Res* 1985, 19: 437-444.

Worakul N, Robinson JR. Ocular pharmacokinetics/pharmacodynamics. *Eur J Pharm Biopharm* 1997, 44(1627): 71-83.

Xie YH, Soh AK. Investigation of non-covalent association of single-walled carbon nanotube with amylose by molecular dynamics simulation. *Mat Lett* 2005, 59(8-9): 971-975.

Yadav AK, Mishra P, Mishra AK, Mishra P, Jain S, Agrawal GP. Development and characterization of hyaluronic acid-anchored PLGA nanoparticulate carriers of doxorubicin. *Nanomed: Nanotech Biol Med* 2007, 3(4): 246-257.

Yagci R, Oflu Y, Dincel A, Kaya E, Yagci S, Bayar B, Duman S, Bozkurt A. Penetration of second-,third-, and fourth-generation topical fluoroquinolone into aqueous and vitreous humour in a rabbit endophthalmitis model. *Eye* 2007, 21: 990-994.

Yang L, Chu JS, Fix JA. Colon-specific drug delivery: new approaches and in vitro/in vivo evaluation. *Int J Pharm* 2002, 235: 1-15.

Yang P, de Vos AF, Kijlstra A. Macrophages and MHC class II positive cells in the choroid during endotoxin induced uveitis. *Br J Ophthalmol* 1997, 81: 396-401.

Yasukawa T, Ogura Y, Sakurai E, Tabata Y, Kimura H. Intraocular sustained drug delivery using implantable polymeric devices. *Adv Drug Del Rev* 2005*,* 57(14): 2033-2046.

Yoo MK, Cho KY, Song HH, Choi YJ. Release of Ciprofloxacin from Chondroitin 6-Sulfate-Graft-Poloxamer Hydrogel In Vitro for Ophthalmic Drug Delivery. *Drug Dev Ind Pharm* 2005, 31: 455-463.

Young S, Larkin G, Branley M, Lightman S. Safety and efficacy of intravitreal triamcinolone for cystoid macular oedema in uveitis. *Clin Exp Ophthalmol* 2001, 29: 2-6.

Yu BY, Chung JW, Kwak S-Y. Reduced migration from flexible poly(vinyl chloride) of a plasticizer containing β-cyclodextrin derivative. *Environ Sci Technol* 2008, 42: 7522-7527.

Yui N, Nihira J, Okano T, Sakurai Y. Inflammation responsive degradation of crosslinked hyaluronic acid gels. *J Contr Rel* 1992, 22: 105-116.

Yui N, Nihira J, Okano T, Sakurai Y. Regulated release of drug microspheres from inflammation responsive degradable matrices of crosslinked hyaluronic acid. *J Contr Rel* 1993, 25(1-2): 133-143.

Zeimer R, Goldberg MF. Novel ophthalmic therapeutic modalities based on noninvasive light-targeted drug delivery to the posterior pole of the eye (Drug Delivery to the Posterior Segments of the Eye). *Adv Drug Deliv Rev* 2001, 52(1): 49-61.

Zhang M, Xin H, Atherton SS. Murine cytomegalovirus (MCMV) spreads to and replicates in the retina after endotoxin-induced disruption of the blood-retinal barrier of immunosuppressed BALB/c mice. *J Neurovirol* 2005, 11: 365-75.

Zhang Y, Huo M, Zhou J, Xie S. PKSolver: An add-in program for pharmacokinetic and pharmacodynamic data analysis in Microsoft Excel. *Comp Meth Progr Biomed* 2010, 99(3): 306-314.

Zhao XB, Fraser JE, Alexander C, Lockett C, White BJ. Synthesis and characterisation of novel double crosslinked hyaluronan hydrogel. *J Mat Sci: Materials in Medicine* 2002, 13: 11-16.

Zhu KJ, Xiangzhon L, Shilin Y. Preparation, characterization and properties of polylactide (PLA)–poly-(ethylene glycol) (PEG) copolymers: A potential drug carrier. *J Appl Polym Sci* 1990, 39: 1.

Zimmer A, Kreuter J. Microspheres and nanoparticles used in ocular delivery systems. *Adv Drug Deliv Rev* 1995, 16: 61-73.

9. APPENDICES

9.1. Animal Ethics Clearance Certificate

AESC 3

UNIVERSITY OF THE WITWATERSRAND, JOHANNESBURG

STRICTLY CONFIDENTIAL

ANIMAL ETHICS SCREENING COMMITTEE (AESC)

CLEARANCE CERTIFICATE NO. 2009/2/5

APPLICANT: Ms L du Toit

SCHOOL: Pharmacy and Pharmacology
DEPARTMENT:
LOCATION:

PROJECT TITLE: **In vivo assessment of the efficacy of an intelligent intraocular implant for site specific prolonged drug delivery in the rabbit eye**

Number and Species

65 New Zealand albino rabbits.

Approval was given for the use of animals for the project described above at an AESC meeting held on 27.01.2009. This approval remains valid until 27.01.2011

The use of these animals is subject to AESC guidelines for the use and care of animals, is limited to the procedures described in the application form and to the following additional conditions:

The main body of the study can only be initiated once an effective model of posterior segment inflammation has been established in 2 rabbits.

Signed: _____ (Chairperson, AESC) Date: 31/05/2010

I am satisfied that the persons listed in this application are competent to perform the procedures therein, in terms of Section 23 (1) (c) of the Veterinary and Para-Veterinary Professions Act (19 of 1982)

Signed: _____ (Registered Veterinarian) Date: 31/05/2010

cc: Supervisor:
Director: CAS

Works 2000/lain0015/AESCCert.wps

9.2. Doctoral Publications (2008-2013)

9.2.1. Review Paper 1

Review

Expert Opinion

informa
healthcare

Ocular drug delivery – a look towards nanobioadhesives

Lisa C du Toit, Viness Pillay†, Yahya E Choonara, Thirumala Govender & Trevor Carmichael
†*University of the Witwatersrand, Department of Pharmacy and Pharmacology, Johannesburg, South Africa*

Importance of the field: A major challenge emanating in the design of topical ophthalmic preparations is their short precorneal residence time. Retention of a drug delivery system in the front of the eye is thus desirable. One solution identified to address this concern is a retentive system that can preferably be delivered in a liquid drop form and ultimately remain attached to the corneal tissue owing to incorporation of a bioadhesive component. Forward-thinking approaches are required to achieve advancements in this approach for the attainment of an effective drug concentration at the site of action. Accordingly, several investigators have identified the benefits of nanotechnology-based drug delivery systems for ophthalmic drug delivery.
Areas covered in this review: A concerted effort was made to review critically all 'nanobioadhesives', that is, nanosystems designed for ocular drug delivery with the goal of attaining prolonged ocular retention, in a systematic, chronological manner, from their reported point of inception to the present.
What the reader will gain: A perspective on possible future trends in this growing field of ocular drug delivery is formulated.
Take home message: The importance of and need for new developments in the field of ocular nanobioadhesives is emphasized.

Keywords: bioadhesive, colloidal carriers, liposome, mucoadhesive, nanocapsule, nanoparticle, nanosphere, ophthalmic drug delivery

Expert Opin. Drug Deliv. (2011) 8(1):71-94

1. Introduction

The eye – a precious, unique and anatomically isolated specialized sensory organ – shows unique pharmacodynamic and pharmacokinetic properties. This is a consequence of its seclusion from systemic access by the blood–retinal, blood–aqueous and blood–vitreous barriers. Significantly, the eye can be viewed as an apt 'laboratory' for the investigation of drug delivery in inflammatory and infectious afflictions. According to Robinson [1] 'no other organ is so readily accessible or as visible for observation'; undoubtedly a distinct test for the pharmaceutical scientist in drug delivery system design.

The eye is divided into anterior and posterior segments, which function both independently and in tandem on application of an ocular preparation [2]. Targeting the drug to the appropriate site of action in the eye is usually one of the greatest challenges in drug delivery because of its anatomical and physiological defense mechanisms. Furthermore, most of the biodisposition studies in ocular drug delivery have been carried out using animal models, and the physiological and anatomical variation of the eye among species highlights that outcomes may not be directly applicable to human use. Ocular drug delivery systems thus necessitate specified criteria according to the physiological structure of the eye [3,4].

Ocular therapeutic preparations are centuries old and comprise topical ophthalmic solutions, suspensions and semisolids, which hold the disadvantage of

10.1517/17425247.2011.542142 © 2011 Informa UK, Ltd. ISSN 1742-5247

9.2.2. Review Paper 2

Advanced Drug Delivery Reviews 62 (2010) 532–546

Contents lists available at ScienceDirect

Advanced Drug Delivery Reviews

journal homepage: www.elsevier.com/locate/addr

Nano-microbicides: Challenges in drug delivery, patient ethics and intellectual property in the war against HIV/AIDS☆

Lisa C. du Toit, Viness Pillay *, Yahya E. Choonara

University of the Witwatersrand, Department of Pharmacy and Pharmacology, 7 York Road, Parktown, 2193, Johannesburg, South Africa

ARTICLE INFO

Article history:
Received 28 May 2009
Accepted 14 September 2009
Available online 14 November 2009

Keywords:
Human immunodeficiency virus
Microbicide
Drug delivery systems
Dendrimer
Nanoparticle
Nano-enabled
Intellectual property
Patents

ABSTRACT

As we continue to be embroiled in the global battle against the human immunodeficiency virus (HIV), there has been an ongoing evolution in the understanding of the molecular mode of sexual transmission of HIV. This has gone hand-in-hand with a paradigm shift and research focus on the development of microbicides – compounds designed for vaginal (and possibly rectal) administration that are envisaged to put safe, affordable and accessible protection into the hands of women. However, an effective microbicide is not yet available; innovative approaches for the design of topical vaginal microbicides are urgently needed. The potential of the advancing field of nanomedicine has been earmarked in the increasing efforts to address the major health problems of the developing world. In this review, advances in the design of innovative microbicide nanocarriers and nano-enabled microbicides, henceforth referred to as 'nano-microbicides', are presented; elaborating on nanotechnology's role in the antiviral arena. The role of nanotechnology in the antiviral arena and the unique issues facing the generation of intellectual property relating to nano-microbicides in the ongoing global 'tug-of-war' of 'patients versus patents' are also explicated.

Contents

☆ This review is part of the *Advanced Drug Delivery Reviews* theme issue on "Nanotechnology Solutions for Infectious Diseases in Developing Nations".

* Corresponding author. Tel.: +27 11 717 2274; fax: +27 86 553 4733.
E-mail address: viness.pillay@wits.ac.za (V. Pillay).

0169-409X/$ – see front matter © 2009 Elsevier B.V. All rights reserved.
doi:10.1016/j.addr.2009.11.022

9.2.3. Research Paper 1

Pharm Res (2011) 28:494–504
DOI 10.1007/s11095-010-0247-y

RESEARCH PAPER

Investigating the Effect of Polymeric Approaches on Circulation Time and Physical Properties of Nanobubbles

Lisa C. du Toit • Thirumala Govender • Viness Pillay • Yahya E. Choonara • Tetsuya Kodama

Received: 19 March 2010 / Accepted: 13 August 2010 / Published online: 23 December 2010

ABSTRACT

Purpose A challenge in the field of nanobubbles, including lipobubbles and polymeric nanobubbles, is identification of formulation approaches to enhance circulation time or "bubble life" in the specific organ to allow for organ visualization. The aim of this study was to investigate the potential of two specific preparation approaches, polymeric surface modification to lipobubbles and a one-step approach for the preparation of ionotropically originated polymeric hydrogel nanobubbles for the production of biocompatible, biodegradable, and sufficiently echogenic ('flexible') bubbles, preferably within the nanometer range, that possess an enhanced *in vivo* lifetime compared to an unmodified lipobubble to allow visualization of the lymph node vasculature.

Methods In the first approach, formed liposomes (basic and polymerically enhanced) were sequentially layered with appropriate cationic and anionic polyelectrolytes followed by transformation into polymer-coated nanobubbles. In addition, a one-step approach was employed for the fabrication of ionotropically originated polymeric hydrogel bubbles.

Results Bubble lifetime was marginally enhanced by self-deposition of polyelectrolytes onto the normal lipobubble, however, not significantly ($P=0.0634$). In general, formulations possessing a higher ratio of anionic:cationic coats and highly anionic overall surface charge (−20.62 mV to −17.54 mV) possessed an enhanced lifetime. The improvement in bubble lifetime was significant when a purely polymeric polyionic hydrogel bubble shell was instituted compared to a normal unmodified lipobubble ($P=0.004$). There was enhanced persistence of these systems compared to lipobubbles, attributed to the highly flexible, interconnected hydrogel shell which minimized gas leakage. The prolonged contrast signal may also be attributed to a degree of polymeric deposition/endothelial attachment.

Conclusions This study identified the relevance of polymeric modifications to nanobubbles for an improved circulating lifetime, which would be essential for application of these systems in passive drug or gene targeting via the enhanced permeability and retention effect.

KEY WORDS hydrogel · layer-by-layer self-deposition · liposome · nanobubble · polymer

L. C. du Toit · V. Pillay · Y. E. Choonara
Department of Pharmacy and Pharmacology
University of the Witwatersrand
7 York Road, Parktown
2193 Johannesburg, South Africa

T. Govender
School of Pharmacy and Pharmacology, University of KwaZulu Natal
Durban, South Africa

T. Kodama (✉)
Graduate School of Biomedical Engineering, Tohoku University
2-1 Seiryo-machi, Aoba
Sendai 980-7583, Japan
e-mail: kodama@bme.tohoku.ac.jp

INTRODUCTION

Nanobubbles are recent nanostructures and are termed as such since their internal core surrounded by a shell/membrane is gas-filled. The shell membrane of nanobubbles consists of albumin, lipid or biocompatible polymer for the purpose of stability enhancement against gas loss, dissolution, bubble coalescence and the attainment of an improved particle size distribution (1). The internal gas core comprises either air or perfluorocarbons. The presence of a gas core, specifically, confers the capability of *in vivo*

Design of an Anti-Inflammatory Composite Nanosystem and Evaluation of Its Potential for Ocular Drug Delivery

LISA C. DU TOIT,[1] THIRUMALA GOVENDER,[2] TREVOR CARMICHAEL,[3] PRADEEP KUMAR,[1] YAHYA E. CHOONARA,[1] VINESS PILLAY[1]

[1]Department of Pharmacy and Pharmacology, University of the Witwatersrand, Parktown, Johannesburg 2193, South Africa

[2]Department of Pharmaceutical Sciences, University of KwaZulu Natal, Berea, Durban 4041, South Africa

[3]Ophthalmology Division, Department of Neurosciences, University of the Witwatersrand, Parktown, Johannesburg 2193, South Africa

Received 26 March 2013; revised 17 May 2013; accepted 10 June 2013

Published online 4 July 2013 in Wiley Online Library (wileyonlinelibrary.com). DOI 10.1002/jps.23650

ABSTRACT: This study compared two specific embodiments of an ocular nanosystem (NS): one portraying a purely polymeric system, referred to as the chitosan–poly(ε-caprolactone) nanosystem, and the other based on a composite lipoidal–polymeric NS architecture utilizing phospholipids—the lipoidal–chitosan–poly(ε-caprolactone) nanosystem. Investigations undertaken were implicit to warrant inclusion in an implantable system for the intelligent treatment of inflammatory disorders (specifically ocular afflictions). Results obtained highlighted the enhanced efficacy of both NS to an indomethacin suspension in terms of tissue permeation, cell uptake, and anti-inflammatory activity. Furthermore, the size (134.3 vs. 140.7 nm); surface charge (+49.4 vs. +55.7 mV); drug incorporation efficiency (75.00% vs. 67.20%); flux across the retinal pigment epithelium–choroid–sclera (0.002951 vs. 0.001255 mg cm $^{-2}$ h^{-1}); anti-inflammatory efficacy, demonstrated by a decrease in 4-chloro-7-nitrobenzo-2-oxa-1,3-diazole complex formation (0.0031 vs. 0.0023 mmol L^{-1}) and decrease in NFκB formation (decrease in relative optical density of 0.2027 vs. 0.2420); and enhanced inflammatory cell uptake, visualized via high-speed fluorescence and confocal microscopy, all highlighted the enhanced potential of the lipoidal system compared with the purely polymeric NS for potentially targeting inflammatory disorders of the posterior segment of the eye. Mechanics energy relationships revealed the favorable hydrophilic–lipophilic balance of the composite NS compared with the purely polymeric NS. © 2013 Wiley Periodicals, Inc. and the American Pharmacists Association J Pharm Sci 102:2780–2805, 2013

Keywords: ophthalmic drug delivery; nanotechnology; nanoparticles; lipids; liposomes; permeation; cell uptake; ELISA; confocal microscopy; computational modeling

INTRODUCTION

In terms of research spurring the pharmaceutical scientist, ophthalmic drug delivery is an increasingly demanding sector.[1] In their investigations, authors have pointed to inflammatory posterior segment ocular (vitreoretinal) disorders, such as uveitis, as the foremost contributors to visual impairment, and ultimately blindness.[2,3] Ensuring delivery of the indicated bioactive to the posterior segment of the eye is fundamental for the effectual treatment of internal eye structure disorders.[3] Nonetheless, anterior segment drug delivery systems, most notably, eye drops, still lead trends in the ocular market. The goal in ocular therapeutics is to maintain an effective drug concentration at the site of action for an appropriate period of time, to achieve the expected pharmacological response.[4] Drug delivery systems undoubtedly form a crucial component of the "therapeutic armamentarium" in ophthalmology. Accordingly, investigators have stated that, "ophthalmic drug delivery, probably more than any other route of administration, may benefit from the characteristics of nanotechnology-based drug delivery systems."[5,6] Knowledge derived

Additional Supporting Information may be found in the online version of this article. Supporting Information

Correspondence to: Viness Pillay (Telephone: +27-7172274; Fax: +27-86-553-4733; E-mail: viness.pillay@wits.ac.za)

Journal of Pharmaceutical Sciences, Vol. 102, 2780–2805 (2013)

9.2.5. Research Paper 3

Available online:

Pharm Res
DOI 10.1007/s11095-013-1184-3

RESEARCH PAPER

In Vitro, In Vivo, and *In Silico* Evaluation of the Bioresponsive Behavior of an Intelligent Intraocular Implant

Lisa C. du Toit · Trevor Carmichael · Thirumala Govender · Pradeep Kumar · Yahya E. Choonara · Viness Pillay

Received: 2 May 2013 / Accepted: 9 August 2013

ABSTRACT

Purpose An autofeedback complex polymeric platform was used in the design of an intelligent intraocular implant the I^3 using stimuli responsive polymers, producing a smart release system capable of delivering therapeutic levels of an anti inflammatory agent (indomethacin) and antibiotic (ciprofloxacin) for posterior segment disorders of the eye in response to inflammation.

Methods Physicochemical and physicomechanical analysis of the I^3 was undertaken to explicate the highly crosslinked make up and 'on off' inflammation responsive performance of the I^3. In addition, energetic profiles for important complexation reactions were generated using Molecular Mechanics Energy Relationships by exploring the spatial disposition of energy minimized molecular structures. Furthermore, preliminary *in vivo* determination of the inflammation responsiveness of the I^3 was ascertained following implantation in the normal and inflamed rabbit eye.

Results *In silico* modeling simulating a pathological inflammatory intraocular state highlighted the interaction potential of hydroxyl radicals with the selected polysaccharides comprising the I^3. The intricately crosslinked polymeric system forming the I^3 thus responded at an innate level predicted by its molecular make up to inflammatory conditions as indicated by the results of the drug release studies, rheological analysis, magnetic resonance imaging and scanning electron microscopic imaging. *In vivo* drug release analysis demonstrated indomethacin levels of 0.749 ± 0.126 μg/mL and 1.168 ± 0.186 μg/mL, and ciprofloxacin levels of 1.181 ± 0.150 μg/mL and 6.653 ± 0.605 μg/mL in the normal and inflamed eye, respectively.

Conclusions Extensive *in vitro*, molecular, and *in vivo* characterization therefore highlighted successful inflammation responsiveness of the I^3. The I^3 is a proposed step forward from other described ocular systems owing to its combined bioresponsive, nano enabled architecture.

KEY WORDS *in vivo* test · inflammation · intraocular implant · molecular modeling · physicochemical properties · physicomechanical properties · stimulus responsive

ABBREVIATIONS

ALG	Alginate
BPMs	Bioresponsive polymeric matrices
CMV	Cytomegalovirus
DCC	*N,N'* dicyclohexylcarbodiimide
DSPC	Distearoylphosphatidylcholine
DSPE	Distearoylphosphatidylethanolamine
HA	Hyaluronic acid
I^3	Intelligent Intraocular Implant
Lipo CHT PCL NS	Lipoidal chitosan poly(ε caprolactone) nanosystem
LPS	Lipopolysaccharide
MMER	Molecular Mechanics Energy Relationships
NS	Nanosystem/s
OH	Hydroxyl radicals
PAA	Poly(acrylic acid)
PCL	Poly(ε caprolactone)
SRHS	Stimulus responsive hydrogel system
SVH	Simulated vitreous humor

Electronic supplementary material The online version of this article (doi:10.1007/s11095-013-1184-3) contains supplementary material, which is available to authorized users.

L. C. du Toit · P. Kumar · Y. E. Choonara · V. Pillay (✉)
Department of Pharmacy and Pharmacology, Faculty of Health Sciences
University of the Witwatersrand, 7 York Road
Parktown, 2193 Johannesburg, South Africa
e-mail: viness.pillay@wits.ac.za

T. Carmichael
Ophthalmology Division, Department of Neurosciences
Faculty of Health Sciences, University of the Witwatersrand
7 York Road, Parktown, 2193 Johannesburg, South Africa

T. Govender
Department of Pharmaceutical Sciences, School of Health Sciences
University of KwaZulu Natal University Road
Westville, 4000 Durban, South Africa

Published online: 04 September 2013